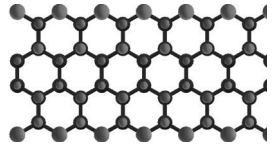


edited by Toshiaki Enoki | Tsuneya Ando

PHYSICS AND CHEMISTRY OF
GRAPHENE
Graphene to Nanographene



PHYSICS AND CHEMISTRY OF
GRAPHENE



This page intentionally left blank

edited by Toshiaki Enoki | Tsuneya Ando

PHYSICS AND CHEMISTRY OF
GRAPHENE
Graphene to Nanographene

CRC Press
Taylor & Francis Group
6000 Broken Sound Parkway NW, Suite 300
Boca Raton, FL 33487-2742

© 2014 by Taylor & Francis Group, LLC
CRC Press is an imprint of Taylor & Francis Group, an Informa business

No claim to original U.S. Government works
Version Date: 20130321

International Standard Book Number-13: 978-981-4241-49-6 (eBook - PDF)

This book contains information obtained from authentic and highly regarded sources. Reasonable efforts have been made to publish reliable data and information, but the author and publisher cannot assume responsibility for the validity of all materials or the consequences of their use. The authors and publishers have attempted to trace the copyright holders of all material reproduced in this publication and apologize to copyright holders if permission to publish in this form has not been obtained. If any copyright material has not been acknowledged please write and let us know so we may rectify in any future reprint.

Except as permitted under U.S. Copyright Law, no part of this book may be reprinted, reproduced, transmitted, or utilized in any form by any electronic, mechanical, or other means, now known or hereafter invented, including photocopying, microfilming, and recording, or in any information storage or retrieval system, without written permission from the publishers.

For permission to photocopy or use material electronically from this work, please access www.copyright.com (<http://www.copyright.com/>) or contact the Copyright Clearance Center, Inc. (CCC), 222 Rosewood Drive, Danvers, MA 01923, 978-750-8400. CCC is a not-for-profit organization that provides licenses and registration for a variety of users. For organizations that have been granted a photocopy license by the CCC, a separate system of payment has been arranged.

Trademark Notice: Product or corporate names may be trademarks or registered trademarks, and are used only for identification and explanation without intent to infringe.

Visit the Taylor & Francis Web site at
<http://www.taylorandfrancis.com>

and the CRC Press Web site at
<http://www.crcpress.com>

Contents

<i>Preface</i>	xi
1 Introduction	1
2 Theory of Electronic States and Transport in Graphene	9
<i>Tsuneya Ando</i>	
2.1 Introduction	9
2.2 Electronic States of Monolayer Graphene	10
2.2.1 Massless Dirac Electron	10
2.2.2 Berry's Phase and Topological Anomaly	15
2.2.3 Landau Levels in Magnetic Fields	17
2.2.4 Effects of Bandgap Opening	19
2.3 Magnetic Properties	20
2.3.1 Singular Diamagnetism	20
2.3.2 Effects of Bandgap Opening	23
2.3.3 Magnetic Screening and Mirroring	25
2.4 Optical Properties	28
2.5 Transport Properties	30
2.5.1 Boltzmann Conductivity	30
2.5.2 Charged Impurities	34
2.5.3 Self-Consistent Born Approximation and Zero-Mode Anomalies	36
2.5.4 Resonant Scattering by Lattice Defects	43
2.5.5 Crossover between Localization and Antilocalization	45
2.6 Phonons and Electron-Phonon Interaction	49
2.6.1 Acoustic Phonon	49
2.6.2 Optical Phonon	50
2.6.3 Zone-Boundary Phonon	53

2.7	Bilayer Graphene	55
2.7.1	Electronic States	55
2.7.2	Magnetic Properties	60
2.7.3	Optical Properties	61
2.7.4	Transport Properties	66
2.7.5	Phonons and Electron–Phonon Interaction	71
2.8	Multilayer Graphene	74
3	Experimental Approaches to Graphene Electron Transport for Device Applications	89
	<i>Akinobu Kanda</i>	
3.1	Introduction	89
3.2	Formation of Graphene	91
3.2.1	Scotch Tape Method	94
3.2.2	Determination of the Number of Layers	97
3.2.3	Other Techniques for Formation of Graphene	106
3.2.3.1	Thermal decomposition of SiC	107
3.2.3.2	Chemical vapor deposition on metallic substrates	109
3.3	Experiments on Transport Properties of Graphene for Device Applications	111
3.3.1	Sample Geometries	111
3.3.2	Gate Voltage Dependence of Conductance	118
3.3.3	Quantum Hall Effect	131
3.3.4	Klein Tunneling	134
3.3.5	Improving Mobility of Graphene	135
3.3.5.1	Effect of phonon scattering	135
3.3.5.2	Experimental techniques to improve mobility	143
3.3.6	Bandgap Engineering	147
3.3.6.1	Graphene nanoribbons	148
3.3.6.2	Bilayer graphene under perpendicular electric fields	157
3.3.6.3	Other methods for bandgap formation	162
3.3.7	Graphene Quantum Effect Devices: Mesoscopic Electron Transport in Graphene	163
3.3.8	Application to Chemical Sensors	165

3.3.9	Graphene Spintronics	167
3.3.9.1	Spintronics	167
3.3.9.2	Experimental techniques for determining spin relaxation length of graphene	171
3.3.9.3	Experimental values vs. theoretical expectations of the spin relaxation length	176
3.3.10	Cooper-Pair Transport	178
3.3.10.1	Superconducting proximity effect	178
3.3.10.2	Josephson effect in single-layer graphene: theoretical aspects	179
3.3.10.3	Josephson effect in single-layer graphene: experiments	184
3.4	Summary	191
4	Electronic Properties of Nanographene	207
	<i>Katsunori Wakabayashi</i>	
4.1	Introduction	207
4.2	Electronic States of Graphene	210
4.3	Graphene Nanoribbons and Edge States	214
4.4	Energy Spectrum and Wave Functions: Tight-Binding Model	222
4.4.1	Armchair Nanoribbons	222
4.4.2	Zigzag Nanoribbons	225
4.5	Energy Bandgap	232
4.5.1	Armchair Nanoribbons	232
4.5.2	Zigzag Nanoribbons	233
4.6	Energy Spectrum and Wave Function: Massless Dirac Equation	234
4.6.1	Semi-Infinite Graphene Sheet with a Zigzag Edge	235
4.6.2	Zigzag Nanoribbons	238
4.6.3	Armchair Nanoribbons	240
4.7	Bearded Edges and Cove Edges	243
4.8	Electronic States in a Magnetic Field	247
4.8.1	Tight-Binding Model with Peierls Phase	248
4.9	Orbital Diamagnetism and Pauli Paramagnetism	252

4.9.1	Orbital Magnetization and Susceptibility	252
4.9.2	Pauli Paramagnetism	257
4.10	Magnetic Instability	259
4.10.1	Electric Field-Induced Half-Metallicity	269
4.11	Electronic Transport Properties	272
4.11.1	One-Way Excess Channel System	273
4.11.2	Perfectly Conducting Channel: Absence of Anderson Localization	277
4.12	Summary	280
5	Spin Structure of Polycyclic Aromatic Hydrocarbons	289
	<i>Akihito Konishi and Takashi Kubo</i>	
5.1	Introduction	289
5.2	A Brief Introduction of PAHs	290
5.2.1	Categories of Polycyclic Aromatic Hydrocarbons	290
5.2.2	Brief History of Aromatic Sextet	292
5.2.3	Clar Sextet in Relation to the Property of PAHs	294
5.3	Recent Advanced Studies on PAHs: Synthesis, Property, and Application	298
5.4	Electronic Structure of PAHs	302
5.4.1	Effects of Edge Shapes on the Electronic Structure of PAHs	302
5.4.2	Prediction of the Spin Multiplicity in the Ground State: Ovchinnikov Rule	305
5.4.3	Non Kekulé-Type PAHs	308
5.4.4	Kekulé-Type PAHs	312
5.4.4.1	Theoretical treatment of singlet biradical character	312
5.4.4.2	Linear system: quantum chemical prediction of spin structure in the ground state	313
5.4.4.3	Linear system: isolation and characterization of large acenes	314
5.4.4.4	Two-dimensional system: quantum chemical prediction of spin structure in the ground state	317

5.4.5	Detailed Discussion on Spin-Polarized State at Zigzag Edges of Kekulé-Type PAHs	320
5.4.5.1	Synthesis of bisanthene and teranthene	323
5.4.5.2	Geometrical consideration of singlet biradical character	326
5.4.5.3	Singlet–triplet energy gap	328
5.4.5.4	HOMO–LUMO energy gap	329
5.4.5.5	Transition probability from S_0 to S_1 state	331
5.5	Highly Stable Antiferromagnetic PAHs	332
5.5.1	Molecular Design for Thermodynamically Stabilized Antiferromagnetic Molecules	332
5.5.2	Theoretical Assessment of Singlet Biradical Character	333
5.5.3	Antiferromagnetic Couplings of Two Unpaired Electrons	335
5.5.4	Coexistence of Intra- and Intermolecular Antiferromagnetic Couplings	336
5.5.5	Non-Linear Optical Property	338
5.5.6	Experimental Estimation of the Amount of Singlet Biradical Character	340
5.6	Concluding Remarks	340
6	Experimental Approach to Electronic and Magnetic Properties of Nanographene	353
	<i>Toshiaki Enoki</i>	
6.1	Introduction	353
6.2	Fabrication of Graphene Nanostructures	355
6.2.1	Chemical Vapor Deposition	356
6.2.2	Graphene Oxides	358
6.2.3	Unzipping of Carbon Nanotubes	360
6.2.4	Heat-Induced Structural Changes	360
6.2.5	Electron Beam Lithography and STM/AFM Lithography	365
6.2.6	Chemical Reactions with Crystallographic Selectivity	368

6.2.7	Bottom-Up Fabrication from Aromatic Molecules	371
6.3	Electronic Structure of Nanographene and Graphene Edges	373
6.3.1	Theoretical Background of the Edge State	373
6.3.2	Experimental Evidence of Edge States	381
6.3.2.1	STM/STS observations	381
6.3.2.2	Angle-resolved photoemission spectroscopy	388
6.3.2.3	X-ray absorption spectroscopy	391
6.3.2.4	Transmission electron microscopy	395
6.3.3	Electron Confinement and Gap Opening in Nanographene	398
6.3.4	Electron Wave Interference: Theory and Experiments	404
6.3.4.1	Raman spectra: G and D bands	405
6.3.4.2	STM image of superlattice	410
6.4	Magnetic Structures of Nanographene	412
6.4.1	Theoretical Background	412
6.4.2	Experiments on Magnetic Properties of Edge-State Spins	418
6.4.2.1	Edge-state spins in defects	418
6.4.2.2	Edge-state spins in nanographene and nanographite	422
6.4.2.3	Interaction between edge-state spins and conduction π -electron carriers (Kondo effect)	427
6.5	Chemical Activity of Nanographene and Graphene Edges	429
6.5.1	Stability and Chemical Activity of Graphene Edges	429
6.5.2	Interaction of Guest Molecules with Nanographene	433
6.6	Summary	436
	<i>Index</i>	451

Preface

From the early stage in the research history of graphite, starting from the 1920s, it has been recognized that graphene, or single-layer graphite, is a two-dimensional infinite sheet of carbon in a hexagonal network and is the basic unit of graphite. However, until 2004, no one had ever observed a graphene sheet with the naked eye by extracting it from graphite. The successful isolation of a graphene sheet in 2004 has attracted great attention in the fields of physics, chemistry, materials science, and device applications. Indeed, graphene has now become not only a central topic in fundamental science but also a challenging target in cutting-edge nanotechnology. For this historic contribution to graphene science, the Nobel Prize in Physics 2010 was awarded to Andre Geim and Konstantin Novoselov.

Graphite and diamond are the most prevalent carbon allotropes. The former is an electrically conductive layered material consisting of a stack of graphene sheets, while the latter is three-dimensional tetrahedral network with insulating properties. The highly conducting properties of graphite originate from π -electrons delocalized throughout the entire hexagonal network of graphene built with the sp^2 hybrid orbital of the σ -state, in contrast to the insulating properties of diamond built with the sp^3 hybrid orbital. Accordingly, graphene is the most basic entity by which the electronic structure of graphite is understood.

What is most interesting about graphene is the unconventional physics behind its electronic properties as observed experimentally. Indeed, the electron motion in graphene is governed by the Dirac equation with vanishing rest mass. This has been shown to give rise to various unprecedented electronic phenomena, such as the half-integer quantum Hall effect, Klein tunneling due to the absence

of backscattering, and Berry's phase leading to singularities in the diamagnetic susceptibility and the conductivity. It should be noted that this equation of motion for π -electrons was first derived by Wallace more than 60 years ago.

When we cut a graphene sheet into fragments and terminate the resultant edges with hydrogen, a variety of fragments are obtained. These range from benzene itself to small polycyclic aromatic hydrocarbon molecules consisting of fused benzene rings, to nano-sized fragments (nanographene), and to semi-infinite graphene. Accordingly, it is natural to suppose that we can apply the rules of chemistry to all of these fragments. In molecules, the geometrical structures crucially depend on how constituent atoms are bonded. This tells us that the properties of molecules are owing to geometry, in which chemical bonds play the role of fundamental units. Indeed, in polycyclic aromatic hydrocarbon molecules, the stability and chemical activity depend on how benzene rings are fused, and these are subject to Clar's aromatic sextet rule. From this geometrical viewpoint, we have two important types of geometry in the edge shapes of nanographene and graphene, namely, zigzag edges and armchair edges. The less aromatic zigzag edges have nonbonding π -electron states (edge states), which play an important role in the electronic and chemical activities of graphene.

Going back to the 1970s, graphite intercalation compounds were a central topic in physics, chemistry, and materials science. In these graphite-based materials, guest molecules (intercalates) are accommodated by the graphitic galleries, with exotic metallic properties being produced. In the 1980s, soccer-ball-shaped C_{60} was discovered as the first member of fullerenes. Carbon nanotubes were discovered at the beginning of the 1990s. Graphene is the fundamental unit from which graphite, graphite intercalation compounds, fullerenes, and carbon nanotubes are created. Accordingly, graphene is particularly important as a basis for understanding and manipulating carbon-based π -electron materials.

With the impetus mentioned above, this book is devoted to understanding graphene comprehensively through a wide range of issues from chemistry to physics. It has been written as a textbook for graduate students of condensed matter physics, physical chemistry, and materials science who want to study

graphene and related carbon-based low-dimensional materials. We are convinced about the importance of this book as a resource of comprehensive knowledge pertinent to graphene and to expanding related areas.

The book consists of the introductory Chapter 1 and five subsequent chapters, which are authored as follows:

Chapter 2

Tsuneya Ando

Department of Physics, Tokyo Institute of Technology
Ookayama, Meguro-ku Tokyo, 152-8551, Japan
ando@stat.phys.titech.ac.jp

Chapter 3

Akinobu Kanda

Institute of Physics, University of Tsukuba
Tsukuba 305-8571, Japan
kanda@lt.px.tsukuba.ac.jp

Chapter 4

Katsunori Wakabayashi

WPI Center for Materials Nanoarchitectonics (MANA)
National Institute for Materials Science (NIMS)
Namiki, Tsukuba 305-0044, Japan
Wakabayashi.Katsunori@nims.go.jp

Chapter 5

Takashi Kubo

Department of Chemistry, Osaka University
Machikaneyama, Toyonaka 560-0043, Japan
kubo@chem.sci.osaka-u.ac.jp

Akihito Konishi

Department of Chemistry, Osaka University
Machikaneyama, Toyonaka 560-0043, Japan

Chapter 6

Toshiaki Enoki

Department of Chemistry, Tokyo Institute of Technology
Ookayama, Meguro-ku, Tokyo 152-8551, Japan
tenoki@chem.titech.ac.jp

The authors would like to recognize Mitsutaka Fujita and his contribution to graphene science in the early stage of the research history of graphene. In fact, Mitsutaka Fujita investigated theoretically the electronic structure of nanographene and in the mid-1990s found the nonbonding edge state, which is the origin of electronic and chemical activities in graphene edges. The question of nanographene and graphene edges, which he initiated, is now one of the important issues about graphene. He passed away prematurely in 1998 at the age of 38. Publishing this book commemorates his great achievements on graphene.

Some of the work in Chapter 2 was supported by a Grant-in-Aid for Scientific Research on the Priority Area “Carbon Nanotube Nanoelectronics,” by a Grant-in-Aid for Scientific Research, and by the Global Center of Excellence Program “Nanoscience and Quantum Physics” at Tokyo Tech., all from the Ministry of Education, Culture, Sport, Science and Technology of Japan. T. Ando, author of Chapter 2, acknowledges collaboration and discussion with Mikito Koshino and Hidekatsu Suzuura. A. Kanda, author of Chapter 3, would like to thank his collaborators: Hidenori Goto, Hikari Tomori, Yosuke Nukui, Yukinori Toyota, Takashi Sato, Takuya Moriki, Youiti Ohtuka, Hisao Miyazaki, and Kazuhito Tsukagoshi, who made valuable contributions to his graphene research. The work presented in Chapter 4 was partly supported by the PRESTO project “Materials and Processes for Innovative Next-generation Devices” from the Japan Science Technology Agency and by a Grant-in-Aid for Scientific Research (No. 23310083) from the Japan Society for the Promotion of Science. The work presented in Chapter 5 was partly supported by a Grant-in-Aid for Scientific Research on an Innovative Area (No. 2105) from the Ministry of Education, Culture, Sports, Science and Technology of Japan. A. Konishi and T. Kubo, authors of Chapter 5, wish to thank Masayoshi Nakano, Benoît Champagne, Akihiro Shimizu, and Yasukazu Hirao for useful discussions. Some of the works presented in Chapter 6 were supported by a Grant-in-Aid for Scientific Research (No. 20001006) from the Ministry of Education, Culture, Sports, Science and Technology of Japan.

The authors would like to thank all those who have given fruitful suggestions and encouragement, in particular, Hiroshi Ajiki, Luiz Gustavo Cançado, Mildred S. Dresselhaus, Sudipta Dutta, Shintaro

Fujii, Mitsutaka Fujita, Kikuo Harigaya, Haruo Hosoya, Masatsura Igami, Hiroo Inokuchi, Manabu Kiguchi, Koichi Kusakabe, Klaus Müllen, Kyoko Nakada, Takeshi Nakanishi, Kenji Nakao, Konstantin Novoselov, Chuhei Oshima, Susumu Okada, Makoto Okazaki, Marcos Pimenta, C. N. R. Rao, Riichiro Saito, Kenichi Sasaki, Manfred Sigrist, Yoshiteru Takagi, Kazuyuki Takai, Yositate Takane, Mauricio Terrones, and Kazuhito Tsukagoshi.

We are also grateful to Tomoko Kuroiwa for her assistance in preparing this manuscript. We would like to express our gratitude to the publishers for their help in many ways.

The publication of this book was supported by a Grant-in-Aid for Scientific Research (No. 20001006) from the Ministry of Education, Culture, Sports, Science and Technology of Japan.

Toshiaki Enoki
Tsuneya Ando
Winter 2012

This page intentionally left blank

Chapter 1

Introduction

Graphite, which is one of the most prevalent carbon allotropes, is a layered material in which infinite sheets of hexagonal carbon networks are stacked in the AB fashion (Bernal stacking) with the aid of weak intersheet interaction [1], as shown in Fig. 1.1. Each two-dimensional (2D) sheet is called graphene. The unit cell of graphene, with a lattice constant of $a = 0.246$ nm, is formed of two independent carbon sites, where the strong σ -bonds and weak π -bonds of the carbon atoms give a bond length of 0.142 nm. The σ -bonds consist of threefold symmetric sp^3 hybrid orbitals of $2s$, $2p_x$, and $2p_y$ orbitals, while the π -bonds consist of $2p_z$ orbitals. Graphite has two independent graphene sheets, where some carbon atoms in a graphene sheet are on top of carbon atoms in the sheet underneath and others are over the centers of hexagons in the sheet underneath.

The quasi-2D structural feature of graphite makes its electronic band structure quasi-2D [2]. Figure 1.2(a) shows the energy band structure of graphite for the lattice structure shown in Fig. 1.1(b), which is obtained on the basis of the density functional theory with the local density approximation. The quasi-2D character can be seen in the less dispersive energy band feature for both the σ - and π -bands in the intersheet directions $K \leftrightarrow H$ and $\Gamma \leftrightarrow A$ in the Brillouin zone, even though the bands have strong wave number

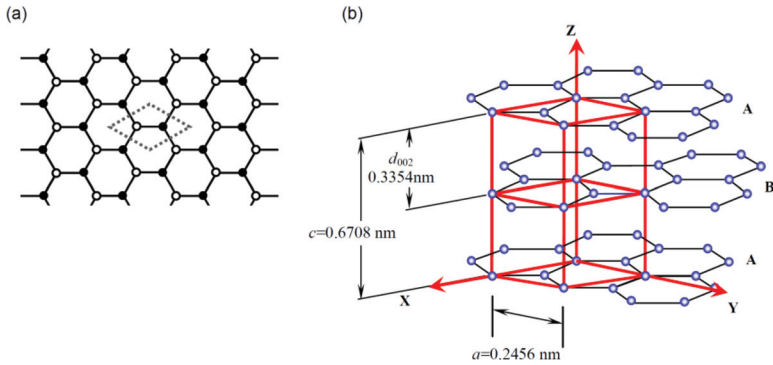


Figure 1.1 The structures of (a) graphene and (b) graphite. The unit cell (dotted lines) of graphene with a lattice constant of $a = 0.2456$ nm has two independent carbon atoms (filled and open circles). Graphene sheets in graphite are stacked in AB fashion. The unit cell of graphite (bold red lines) has four independent carbon atoms. The intra-sheet and c -axis lattice constants are 0.2456 nm and 0.6708 nm, respectively.

dependence in the intrasheet directions. The valence π -band and the conduction π^* -band are each split into two subbands due to the presence of two independent graphene sheets interacting with each other in a unit cell. What is important is that these bands touch each other at the K point, giving a semimetallic electronic structure. Indeed, the weakly dispersive π -band crosses the Fermi level along the direction $K \leftrightarrow H$, resulting in the coexistence of the same small number of electrons and holes. A single graphene sheet extracted from graphite is free from the intersheet interaction and thus a pure 2D electronic structure is formed as shown in Fig. 1.2(b). The feature of the electronic structure of graphite is roughly preserved in graphene.

What distinguishes graphene from graphite is the zero-gap semiconducting feature that appears at the K point, where the valence π -band and conduction π^* -band having a linear wave number dependence touch each other. Interestingly, the linear dispersion of the π - and π^* -bands in the vicinity of the Fermi level indicates the feature of massless electrons at the Fermi level. This unconventional electronic structure of graphene, first predicted theoretically by Wallace in 1947 [3], is effectively equivalent to

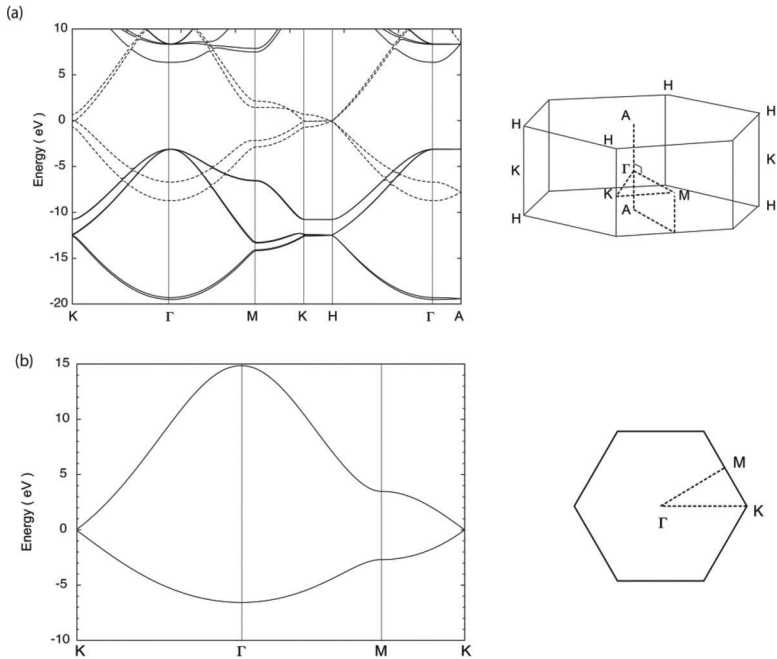


Figure 1.2 (a) The band structure of graphite with its Brillouin zone. The band structure of graphite is calculated by a mixed-basis pseudopotential method. The solid and dotted lines denote the σ - and π -bands, respectively. (b) π -bands of graphene are derived from the tight binding method.

what we observe for the massless fermion in the relativistic Dirac equation (Weyl equation for neutrinos) [4]. Moreover, in graphene we can expect phenomena the same as those observed for neutrinos. After the successful isolation of graphene in 2004 [5], theoretical and experimental efforts have unveiled a variety of phenomena related to the intriguing features of the massless Dirac fermion in graphene [6], including the half-integer quantum Hall effect [7, 8]. The massless electrons in graphene, whose Fermi velocity is about $1/300$ the speed of light, has attracted great attention in cutting-edge nanotechnology applications [9, 10].

When we discuss graphene, we involve another aspect from chemistry. The fundamental unit of graphene is the hexagonal benzene ring that we discuss in chemistry. Indeed, graphene is formed

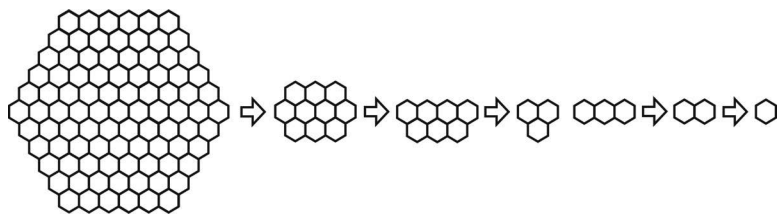


Figure 1.3 Fragmentation of graphene into small polycyclic aromatic hydrocarbon molecules.

by fusing an infinite number of benzene rings two-dimensionally. Accordingly, we expect that the knowledge we use in chemistry is applicable in understanding the properties of graphene. With this viewpoint, we can create a variety of graphene fragments whose sizes extend from small polycyclic aromatic hydrocarbon molecules to macro-size graphene, as shown in Fig. 1.3. Among these, the nano-size graphene (nanographene) is particularly important as this forms a bridge between small polycyclic aromatic hydrocarbon molecules and infinite graphene, which are related to issues of chemistry and physics, respectively. The electronic structures of small polycyclic aromatic hydrocarbon molecules depend on the shapes of the molecules: in other words, on how benzene rings are fused. For example, there are two ways to fuse three benzene rings: fusing them in 1D gives anthracene, while fusing them into a triangle gives phenalene. The former is well stabilized and chemically inactive as a Kekulé molecule having a closed-shell electronic structure, whereas the latter is unstable and very chemically active as a non-Kekulé molecule having an open-shell electronic structure with a spin state of $S = 1/2$. This geometrical dependence is also preserved in the edges of nanographene and graphene, as we can understand on the basis of Clar's aromatic sextet rule [11]. Actually, there are two types of edges: zigzag edges and armchair edges, which give essentially different electronic features owing to Kekulé and non-Kekulé structures, respectively. Importantly, nonbonding π -electron states having a large local density of states with localized spins are created in zigzag edges, and these are the origin of the electronic, magnetic, and chemical activities of nanographene and

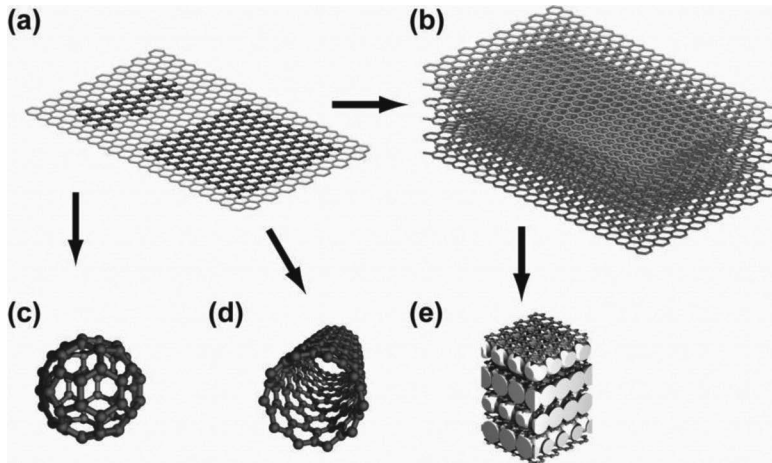


Figure 1.4 Carbon-based π -electron materials: (a) graphene, (b) graphite, (c) fullerene (C_{60}), (d) a carbon nanotube, and (e) a graphite intercalation compound (KC_8). The parts drawn with bold lines in (a) are the precursors of the C_{60} and the carbon nanotube. The large white spheres in (e) are potassium atoms.

graphene edges [12]. This is important for applications such as spintronic devices, batteries, catalysts, and fuel cells.

There exist important carbon-based π -electron materials, which have been at the focal point in physics and chemistry these past three decades, that is, graphite intercalation compounds, fullerenes, and carbon nanotubes, as illustrated in Fig. 1.4. Graphite intercalation compounds (GICs) are obtained when a variety of guest molecules (intercalates) having abilities to donate and accept electrons are accepted into the graphitic galleries through charge transfer interaction with graphene having amphoteric electronic properties. GICs are 2D metallic systems showing exotic electronic features such as high electrical conductivity, superconductivity, and 2D magnetism [13, 14]. Folding a graphene sheet into a spherical shape yields a fullerene [15], while rolling one into a cylindrical shape yields a carbon nanotube [16]. These are carbon nanomaterials having electronic properties that are interesting not only in fundamental science but also for device applications. Here, graphene is the most basic material, from which are created all the π -electron-based

carbon systems such as graphite, fullerenes, carbon nanotubes, and graphite intercalation compounds. Therefore, knowledge about graphene is particularly important in understanding these carbon-based materials.

In the following chapters, we discuss the properties of graphene from the viewpoints of physics and chemistry as follows: Chapter 2, “Theory of Electronic States and Transport in Graphene”; Chapter 3, “Experimental Approach to Graphene and Device Applications”; Chapter 4, “Theory of Electronic Properties of Nanographene”; Chapter 5, “Spin Structure of Polycyclic Aromatic Hydrocarbons (PAHs)”; and Chapter 6, “Experimental Approach to Electronic and Magnetic Properties of Nanographene.”

References

1. Kelly, B. T. (1981). *Physics of graphite* (Applied Science Publishers, London).
2. Horzwarth, N. A. W., Louie, S. G. and Rabii, S. (1982). X-ray form factors and the electronic structure of graphite, *Phys. Rev. B*, **26**, pp. 5382–5390.
3. Wallace, P. R. (1947). The band theory of graphite, *Phys. Rev.*, **71**, pp. 476 and pp. 622–634.
4. Shon, N. H. and Ando, T. (1998). Quantum transport in two-dimensional graphite system, *J. Phys. Soc. Jpn.*, **67**, pp. 2421–2429.
5. Novoselov, K. S., Geim, A. K., Morozov, S. V., Jiang, D., Zhang, Y., Dubonos, S. V., Grigorieva, I. V. and Firsov, A. A. (2004). Electric field effect in atomically thin carbon films, *Science*, **306**, pp. 666–669.
6. Castro Neto, A. H., Guinea, F., Peres, N. M. R., Novoselov, K. S. and Geim, A. K. (2009). The electronic properties of graphene, *Rev. Mod. Phys.*, **81**, pp. 109–162.
7. Novoselov, K. S., Geim, A. K., Morozov, S. V., Jiang, D., Katsnelson, M. I., Grigorieva, I. V., Dubonos, S. V. and Firsov, A. A. (2005). Two-dimensional gas of massless Dirac fermion in graphene, *Nature*, **438**, pp. 197–200.
8. Zhang, Y., Tan, Y-W., Stormer, H. L. and Kim, P. (2005). Experimental observation of the quantum Hall effect and Berry’s phase in graphene, *Nature*, **438**, pp. 201–204.
9. Berger, C., Song, Z., Li, T., Li, X., Ogbazghi, A. Y., Feng, R., Dai, Z., Marchenkov, A. N., Conrad, E. H., First, P. N. and de Heer, W. A. (2004).

- Ultrathin epitaxial graphite: 2D electron gas properties and a route toward graphene-based nanoelectronics, *J. Chem. Phys. B*, **108**, pp. 19912–19916.
10. Cheianov, V. V., Fal'ko, V. and Altshuler, B. L. (2007). The focusing of electron flow and a Veselago lens in graphene p–n junctions, *Science*, **315**, pp. 1252–1255.
 11. Clar, E. (1972). *The Aromatic Sextet* (Wiley, London).
 12. Fujita, M., Wakabayashi, K., Nakada, K. and Kusakabe, K. (1996). Peculiar localized state at zigzag graphite edge, *J. Phys. Soc. Jpn.*, **65**, pp. 1920–1923.
 13. Dresselhaus, M. S. and Dresselhaus, G. (1981). Intercalation compounds of graphite, *Adv. Phys.*, **30**, pp. 139–326.
 14. Enoki, T., Suzuki, M. and Endo, M. (2003). *Graphite Intercalation Compounds and Applications* (Oxford University Press, New York).
 15. Dresselhaus, M. S., Dresselhaus, G. and Eklund, P. C. (1996). *Science of Fullerenes and Carbon Nanotubes* (Academic Press, San Diego).
 16. Saito, R., Dresselhaus, G., and Dresselhaus, M. S. (1998). *Physical Properties of Carbon Nanotubes* (Imperial College Press, London).

This page intentionally left blank

Chapter 2

Theory of Electronic States and Transport in Graphene

Tsuneya Ando

*Department of Physics, Tokyo Institute of Technology
2-12-1 Ookayama, Meguro-ku, Tokyo 152-8551, Japan
ando@phys.titech.ac.jp*

2.1 Introduction

Graphene is a monolayer graphite sheet recently fabricated [1–3] and has been attracting attention theoretically and experimentally since the observation of the integer quantum Hall effect [4, 5]. Several reviews have already been published [6–9]. Actually, graphene has been a subject of study prior to the experimental realization because of the peculiar electronic structure responsible for intriguing properties of carbon nanotubes [10] and because of theoretical interest in special properties of systems in relativistic limit. The purpose of this chapter is to give a brief review on electronic properties of graphenes mainly from a theoretical point of view. The topics include effective-mass description of electronic states, transport and optical properties, and phonons and their interaction with electrons.

Physics and Chemistry of Graphene: Graphene to Nanographene

Edited by Toshiaki Enoki and Tsuneya Ando

Copyright © 2013 Pan Stanford Publishing Pte. Ltd.

ISBN 978-981-4241-48-9 (Hardcover), 978-981-4241-49-6 (eBook)

www.panstanford.com

Within an effective-mass approximation or a $\mathbf{k}\cdot\mathbf{p}$ scheme, the electron motion in graphene is governed by the Weyl equation for a neutrino or the Dirac equation with vanishing rest mass or in the relativistic limit [6–16]. An important feature is the presence of a topological singularity at $\mathbf{k} = 0$. This singularity is the origin of the absence of backscattering in metallic carbon nanotubes [17, 18]. It also leads to the presence of a Landau level at $\varepsilon = 0$, responsible for the singular diamagnetic susceptibility [19–22]. It is considered the origin of the peculiar behavior in transport, such as the minimum conductivity [23], the half-integer quantum Hall effect [24], the dynamical conductivity [25], and the special time reversal symmetry [26–28] leading to antilocalization behavior [29, 30]. A massless Dirac system can also be realized in organic conductors [31]. Bilayer graphene has a zero-gap structure, but with quadratic dispersion unlike monolayer, leading to nonzero density of states even at zero energy [32–39]. Electronic states in multilayer graphene are well understood in terms of decomposition of the Hamiltonian into those of monolayer or bilayers [40–42].

In Sections 2.2–2.5, various properties of monolayer graphene are described: In Section 2.2, effective-mass description of electronic states is briefly reviewed, in Section 2.3 the singular behavior of the orbital diamagnetic response is discussed, in Section 2.4 the dynamical conductivity describing optical absorption is discussed, in Section 2.5 the singular behavior of the conductivity is discussed together with the Hall coefficient and the nonuniversal behavior of the minimum conductivity at the Dirac point, and in Section 2.6 phonons and effects of electron–phonon interactions are reviewed. In Section 2.7, similar discussions are given for bilayer graphene. In Section 2.8, the effective Hamiltonian in multilayer graphenes are shown to be decomposed into those of bilayer graphenes and that of a monolayer graphene when several important parameters characterizing interlayer interactions are considered.

2.2 Electronic States of Monolayer Graphene

2.2.1 Massless Dirac Electron

The lattice structure of monolayer graphene and the first Brillouin zone are shown in Figs. 2.1(a) and (b), respectively. We have the

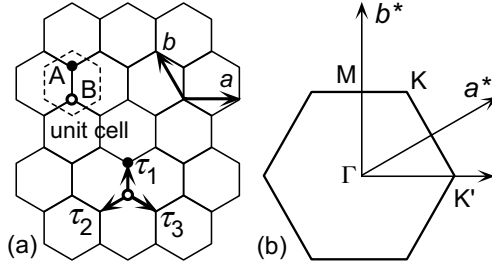


Figure 2.1 (a) The lattice structure of graphene sheet. Two primitive translation vectors are denoted by \mathbf{a} and \mathbf{b} . A unit cell represented by a dashed line contains two carbon atoms denoted by A and B. Three vectors directed from a B site to nearest neighbor A sites are given by $\vec{\tau}_l$ ($l = 1, 2, 3$). (b) The first Brillouin zone. The vertices of the hexagon are called K and K' points and reciprocal lattice vectors are denoted by \mathbf{a}^* and \mathbf{b}^* .

primitive translation vectors $\mathbf{a} = a(1, 0)$ and $\mathbf{b} = a(-1/2, \sqrt{3}/2)$, and the vectors connecting nearest neighbor carbon atoms $\vec{\tau}_1 = a(0, 1/\sqrt{3})$, $\vec{\tau}_2 = a(-1/2, -1/2\sqrt{3})$, and $\vec{\tau}_3 = a(1/2, -1/2\sqrt{3})$, where a is the lattice constant given by $a = 0.246$ nm. A unit cell with area $\Omega_0 = (\sqrt{3}/2)a^2$ contains two carbon atoms, which will be denoted by A and B in the following as shown in Fig. 2.1(a). The primitive reciprocal lattice vectors \mathbf{a}^* and \mathbf{b}^* are given by $\mathbf{a}^* = (2\pi/a)(1, 1/\sqrt{3})$ and $\mathbf{b}^* = (2\pi/a)(0, 2/\sqrt{3})$. The hexagonal first Brillouin zone has area $\Omega_0^* = (2/\sqrt{3})(2\pi/a)^2$.

The K and K' points at the corners of the Brillouin zone are given as $\mathbf{K} = (2\pi/a)(1/3, 1/\sqrt{3})$ and $\mathbf{K}' = (2\pi/a)(2/3, 0)$, respectively. We have the relations $\exp(i\mathbf{K} \cdot \vec{\tau}_1) = \omega$, $\exp(i\mathbf{K} \cdot \vec{\tau}_2) = \omega^{-1}$, $\exp(i\mathbf{K} \cdot \vec{\tau}_3) = 1$, $\exp(i\mathbf{K}' \cdot \vec{\tau}_1) = 1$, $\exp(i\mathbf{K}' \cdot \vec{\tau}_2) = \omega^{-1}$, and $\exp(i\mathbf{K}' \cdot \vec{\tau}_3) = \omega$, with $\omega = \exp(2\pi i/3)$. As will be shown below, the conduction and valence bands consisting of π states touch at the K and K' points, where the Fermi level is located, and therefore electronic properties are determined by the states near the K and K' points.

In a tight-binding model, the wave function is written as

$$\psi(\mathbf{r}) = \sum_{\mathbf{R}_A} \psi_A(\mathbf{R}_A)\phi(\mathbf{r} - \mathbf{R}_A) + \sum_{\mathbf{R}_B} \psi_B(\mathbf{R}_B)\phi(\mathbf{r} - \mathbf{R}_B), \quad (2.1)$$

where $\phi(\mathbf{r})$ is the wave function of the p_z orbital of a carbon atom located at the origin, $\mathbf{R}_A = n_a\mathbf{a} + n_b\mathbf{b} + \vec{\tau}_1$, and $\mathbf{R}_B = n_a\mathbf{a} + n_b\mathbf{b}$ with integer n_a and n_b . Let $-\gamma_0$ be the transfer integral between nearest-neighbor carbon atoms and choose the energy origin at that of the

carbon p_z level. Then, we have

$$\begin{aligned}\varepsilon\psi_A(\mathbf{R}_A) &= -\gamma_0 \sum_{l=1}^3 \psi_B(\mathbf{R}_A - \vec{\tau}_l), \\ \varepsilon\psi_B(\mathbf{R}_B) &= -\gamma_0 \sum_{l=1}^3 \psi_A(\mathbf{R}_B + \vec{\tau}_l),\end{aligned}\quad (2.2)$$

where the overlap integral between nearest A and B sites is completely neglected for simplicity.

Assuming $\psi_A(\mathbf{R}_A) \propto f_A(\mathbf{k}) \exp(i\mathbf{k} \cdot \mathbf{R}_A)$ and $\psi_B(\mathbf{R}_B) \propto f_B(\mathbf{k}) \exp(i\mathbf{k} \cdot \mathbf{R}_B)$, we have

$$\begin{pmatrix} 0 & h_{AB}(\mathbf{k}) \\ h_{AB}(\mathbf{k})^* & 0 \end{pmatrix} \begin{pmatrix} f_A(\mathbf{k}) \\ f_B(\mathbf{k}) \end{pmatrix} = \varepsilon \begin{pmatrix} f_A(\mathbf{k}) \\ f_B(\mathbf{k}) \end{pmatrix}, \quad (2.3)$$

$$h_{AB}(\mathbf{k}) = -\gamma_0 \sum_l \exp(-i\mathbf{k} \cdot \vec{\tau}_l). \quad (2.4)$$

The energy bands are given by

$$\varepsilon_{\pm}(\mathbf{k}) = \pm\gamma_0 \sqrt{1 + 4 \cos \frac{ak_x}{2} \cos \frac{\sqrt{3}ak_y}{2} + 4 \cos^2 \frac{ak_x}{2}}. \quad (2.5)$$

They are shown in Fig. 2.2.

In order to see the behavior in the vicinity of a K point, we replace \mathbf{k} with $\mathbf{K} + \mathbf{k}$. Then, to the lowest order in $|\mathbf{k}|a$, we have

$$-\gamma_0 \sum_{l=1}^3 \exp[-i(\mathbf{K} + \mathbf{k}) \cdot \vec{\tau}_l] = -i\omega^{-1}\gamma(k_x - ik_y). \quad (2.6)$$

with

$$\gamma = \frac{\sqrt{3}a\gamma_0}{2}, \quad (2.7)$$

A similar expansion is possible for the K' point. Therefore, we have $\varepsilon_{\pm}(\mathbf{K}) = \varepsilon_{\pm}(\mathbf{K}') = 0$, showing that there is no gap at the K and K' points. For $f_A(\mathbf{K} + \mathbf{k}) = \tilde{f}_A(\mathbf{k})$ and $f_B(\mathbf{K} + \mathbf{k}) = i\omega\tilde{f}_B(\mathbf{k})$, we have

$$\gamma \begin{pmatrix} 0 & k_x - ik_y \\ k_x + ik_y & 0 \end{pmatrix} \begin{pmatrix} \tilde{f}_A(\mathbf{k}) \\ \tilde{f}_B(\mathbf{k}) \end{pmatrix} = \varepsilon \begin{pmatrix} \tilde{f}_A(\mathbf{k}) \\ \tilde{f}_B(\mathbf{k}) \end{pmatrix}. \quad (2.8)$$

In terms of the Pauli spin matrices

$$\sigma_x = \begin{pmatrix} 0 & 1 \\ 1 & 0 \end{pmatrix}, \quad \sigma_y = \begin{pmatrix} 0 & -i \\ i & 0 \end{pmatrix}, \quad \sigma_z = \begin{pmatrix} 1 & 0 \\ 0 & -1 \end{pmatrix}, \quad (2.9)$$

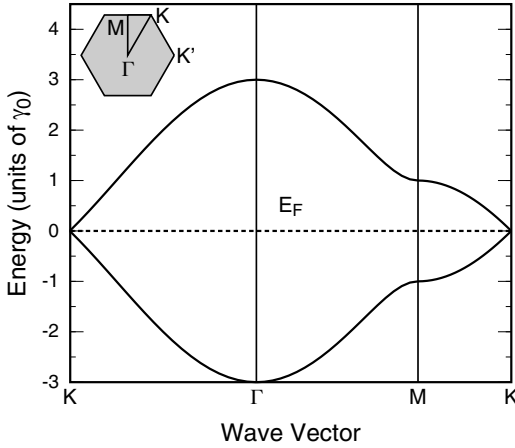


Figure 2.2 The π band structure of graphene obtained in a nearest-neighbor tight-binding model along $K \rightarrow \Gamma \rightarrow M \rightarrow K$ shown in the inset. The Fermi level lies at the center $\varepsilon = 0$.

the above is rewritten as

$$\gamma(\vec{\sigma} \cdot \mathbf{k})\tilde{\mathbf{f}}(\mathbf{k}) = \varepsilon\tilde{\mathbf{f}}(\mathbf{k}), \quad \tilde{\mathbf{f}}(\mathbf{k}) = \begin{pmatrix} \tilde{f}_A(\mathbf{k}) \\ \tilde{f}_B(\mathbf{k}) \end{pmatrix} \quad (2.10)$$

with $\vec{\sigma} = (\sigma_x, \sigma_y)$. For the K' point, we have the same equation except that $\vec{\sigma}$ is replaced with $\vec{\sigma}^*$.

In the vicinity of the K and K' points, the energy becomes

$$\varepsilon_s(\mathbf{k}) = s\gamma|\mathbf{k}|, \quad (s = \pm 1), \quad (2.11)$$

giving the density of states

$$D(\varepsilon) = \frac{g_s g_v}{L^2} \sum_{s, \mathbf{k}} \delta(\varepsilon - s\gamma|\mathbf{k}|) = \frac{g_s g_v |\varepsilon|}{2\pi\gamma^2}, \quad (2.12)$$

with system area L^2 , spin degeneracy $g_s = 2$, and valley degeneracy $g_v = 2$. The corresponding electron or hole concentration at zero temperature is given by

$$n_s = \text{sgn}(\varepsilon) \frac{g_s g_v \varepsilon^2}{4\pi\gamma^2}, \quad (2.13)$$

with

$$\text{sgn}(t) = \begin{cases} +1 & (t > 0); \\ 0 & (t = 0); \\ -1 & (t < 0). \end{cases} \quad (2.14)$$

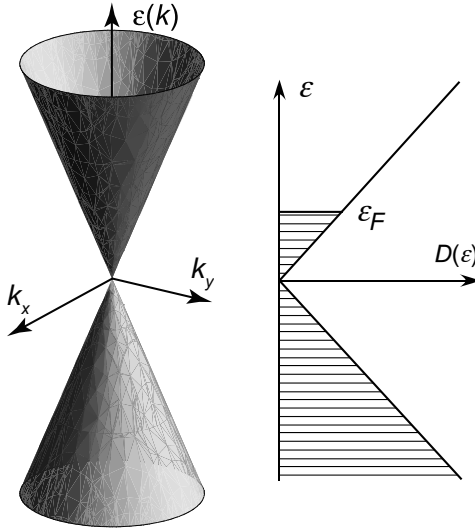


Figure 2.3 The energy bands in the vicinity of the K and K' points and the density of states in monolayer graphene.

This energy dispersion and the density of states are shown in Fig. 2.3. Because the density of states vanishes at $\varepsilon = 0$, to be called the Dirac point, graphene is often called a zero-gap semiconductor. This is quite inappropriate as will be shown later because of its metallic behavior.

In an effective-mass approximation or a $\mathbf{k}\cdot\mathbf{p}$ scheme near the K and K' points, the effective Schrödinger equation is obtained from Eq. (2.10) by replacing \mathbf{k} with operator $\hat{\mathbf{k}} = -i\vec{\nabla}$. Then, we have

$$\begin{aligned} \gamma \begin{pmatrix} 0 & \hat{k}_x - i\hat{k}_y \\ \hat{k}_x + i\hat{k}_y & 0 \end{pmatrix} \mathbf{F}^K(\mathbf{r}) &= \varepsilon \mathbf{F}^K(\mathbf{r}), \\ \gamma \begin{pmatrix} 0 & \hat{k}_x + i\hat{k}_y \\ \hat{k}_x - i\hat{k}_y & 0 \end{pmatrix} \mathbf{F}^{K'}(\mathbf{r}) &= \varepsilon \mathbf{F}^{K'}(\mathbf{r}), \end{aligned} \quad (2.15)$$

where $\mathbf{F}^K(\mathbf{r})$ and $\mathbf{F}^{K'}(\mathbf{r})$ are two-component wave functions

$$\mathbf{F}^K(\mathbf{r}) = \begin{pmatrix} F_A^K(\mathbf{r}) \\ F_B^K(\mathbf{r}) \end{pmatrix}, \quad \mathbf{F}^{K'}(\mathbf{r}) = \begin{pmatrix} F_A^{K'}(\mathbf{r}) \\ F_B^{K'}(\mathbf{r}) \end{pmatrix}. \quad (2.16)$$

These are rewritten as

$$\begin{aligned} \gamma(\vec{\sigma} \cdot \hat{\mathbf{k}})\mathbf{F}^K(\mathbf{r}) &= \varepsilon \mathbf{F}^K(\mathbf{r}), \\ \gamma(\vec{\sigma}^* \cdot \hat{\mathbf{k}})\mathbf{F}^{K'}(\mathbf{r}) &= \varepsilon \mathbf{F}^{K'}(\mathbf{r}). \end{aligned} \quad (2.17)$$

This is equivalent to the Weyl equation for a neutrino or relativistic Dirac electron with vanishing rest mass, moving with the velocity of light, except that the velocity

$$v = \frac{\gamma}{\hbar} \quad (2.18)$$

is about 1/300 of the light velocity. This neutrino description of the electron motion is most suitable for revealing various interesting features of electronic properties of graphene.

In magnetic field B perpendicular to graphene layer, we should make replacement $\hat{\mathbf{k}} = -i\vec{\nabla} + (e/c\hbar)\mathbf{A}$ with vector potential \mathbf{A} , giving $B = \vec{\nabla} \times \mathbf{A} = (\partial A_y/\partial x) - (\partial A_x/\partial y)$. In the presence of external potential $V(\mathbf{r})$, which is slowly varying in a scale of the lattice constant and therefore is the same between A and B sites within a unit cell, $V(\mathbf{r})$ should be added to the diagonal element of Eqs. (2.15) and (2.17). The Schrödinger equation in the presence of potential with range shorter than the lattice constant causing mixing between the K and K' points can also be derived. Readers interested in more details on the effective-mass approximation should refer to Ref. [10], for example.

2.2.2 Berry's Phase and Topological Anomaly

The eigen wave functions and energies of the Hamiltonian for the K point are written in the absence of a magnetic field as

$$\mathbf{F}_{s\mathbf{k}}(\mathbf{r}) = \frac{1}{L} \exp(i\mathbf{k} \cdot \mathbf{r}) \mathbf{F}_{s\mathbf{k}}. \quad (2.19)$$

In general, we can write eigenvector $\mathbf{F}_{s\mathbf{k}}$ as

$$\mathbf{F}_{s\mathbf{k}} = \exp[i\phi_s(\mathbf{k})] R^{-1}[\theta(\mathbf{k})] |s\rangle, \quad (2.20)$$

where $\phi_s(\mathbf{k})$ is an arbitrary phase factor, $\theta(\mathbf{k})$ is the angle between wave vector \mathbf{k} and the k_y axis, i.e., $k_x + ik_y = +i|\mathbf{k}|e^{i\theta(\mathbf{k})}$ and $k_x - ik_y = -i|\mathbf{k}|e^{-i\theta(\mathbf{k})}$, $R(\theta)$ is a spin-rotation operator, given by

$$R(\theta) = \exp\left(i\frac{\theta}{2}\sigma_z\right) = \begin{pmatrix} \exp(+i\theta/2) & 0 \\ 0 & \exp(-i\theta/2) \end{pmatrix}, \quad (2.21)$$

with σ_z being a Pauli matrix, and $|s\rangle$ is the eigenvector for the state with \mathbf{k} in the positive k_y direction, given by

$$|s\rangle = \frac{1}{\sqrt{2}} \begin{pmatrix} -is \\ 1 \end{pmatrix}. \quad (2.22)$$

Obviously, we have

$$\begin{aligned} R(\theta_1)R(\theta_2) &= R(\theta_1 + \theta_2), \\ R(-\theta) &= R^{-1}(\theta). \end{aligned} \quad (2.23)$$

Further, because $R(\theta)$ describes the rotation of a spin, it has the property

$$R(\theta \pm 2\pi) = -R(\theta), \quad (2.24)$$

which gives $R(-\pi) = -R(+\pi)$. The appearance of the spin rotation operator and the corresponding sign change under the 2π rotation around $\mathbf{k} = 0$ correspond to a topological singularity at $\mathbf{k} = 0$. Because phase $\phi_s(\mathbf{k})$ is arbitrary, we can choose the eigen wave function as

$$\mathbf{F}_{s\mathbf{k}} = \frac{1}{\sqrt{2}} \begin{pmatrix} -is \exp[-i\theta(\mathbf{k})] \\ 1 \end{pmatrix}. \quad (2.25)$$

This is the ‘‘spin’’ part of an eigenfunction, obtained by choosing $\phi_s(\mathbf{k}) = -\theta(\mathbf{k})/2$ in such a way that the wave function becomes continuous as a function of $\theta(\mathbf{k})$. It seems that this $\mathbf{F}_{s\mathbf{k}}$ does not change the sign after 2π rotation $\theta(\mathbf{k}) \rightarrow \theta(\mathbf{k}) + 2\pi$. However, the wave function changes the sign when we consider Berry’s phase [43, 44].

Let us consider the case that the Hamiltonian contains parameter η and change η from $\eta(0)$ to $\eta(T)$ as a function of time t from $t = 0$ to $t = T$ and assume that $\mathcal{H}[\eta(T)] = \mathcal{H}[\eta(0)]$. Note that $\eta(T)$ is not necessarily the same as $\eta(0)$. When there is no degeneracy, the state at $t = T$ is completely same as that at $t = 0$ when the process is sufficiently slow and adiabatic. Let us write

$$\psi(T) = \psi(0) \exp\left(-i\varphi - \frac{i}{\hbar} \int_0^T dt' E_0[\eta(t')]\right), \quad (2.26)$$

where $E_0[\eta(t)]$ is eigen energy in the steady state, i.e.,

$$\mathcal{H}[\eta(t)]\psi_0[\eta(t)] = E_0[\eta(t)]\psi_0[\eta(t)], \quad (2.27)$$

and therefore represents phase change corresponding to electron energy. Extra phase φ is called the Berry phase.

In order to obtain an explicit expression of φ , we write

$$\psi(t) = \psi[\eta(t)] \exp\left(-i\varphi(t) - \frac{i}{\hbar} \int_0^t dt' E_0[\eta(t')]\right), \quad (2.28)$$

and substitute $\psi(t)$ into the time-dependent Schrödinger equation. Then, we have

$$\frac{d\varphi(t)}{dt} = -i \left\langle \psi[\eta(t)] \left| \frac{d\psi[\eta(t)]}{dt} \right. \right\rangle, \quad (2.29)$$

and on integration we have

$$\varphi = -i \int_0^T dt \left\langle \psi[\eta(t)] \left| \frac{d\psi[\eta(t)]}{dt} \right. \right\rangle. \quad (2.30)$$

When the wave vector \mathbf{k} is rotated in the anticlockwise direction adiabatically as a function of time t around the origin for a time interval $0 < t < T$, the wavefunction (2.25) is changed into $\psi_s(\mathbf{k}) \exp(-i\varphi)$, where φ is Berry's phase given by

$$\varphi = -i \int_0^T dt \mathbf{F}_{s\mathbf{k}(t)}^\dagger \frac{d}{dt} \mathbf{F}_{s\mathbf{k}(t)} = -\pi. \quad (2.31)$$

This shows that the rotation in the \mathbf{k} space by 2π leads to the change in the phase by $-\pi$, i.e., a sign change. Note that $R^{-1}[\theta(\mathbf{k})|s]$ is obtained from Eq. (2.25) by continuously varying the direction of \mathbf{k} including Berry's phase. Note also that the signature change occurs only when the closed contour encircles the origin $\mathbf{k} = 0$ but not when the contour does not contain $\mathbf{k} = 0$, showing the presence of a singularity at $\mathbf{k} = 0$. This topological singularity at $\mathbf{k} = 0$ causes various zero-mode anomalies as will be discussed in the following as well as the absence of backscattering leading to the perfect conductance in metallic carbon nanotubes [17, 18].

2.2.3 Landau Levels in Magnetic Fields

A singularity at $\varepsilon = 0$ manifests itself in magnetic field B even in classical mechanics. The equation of motion gives the cyclotron frequency $\omega_c(\varepsilon) = eBv^2/c\varepsilon$. The cyclotron frequency diverges and changes its signature at $\varepsilon = 0$ [24, 45]. In quantum mechanics \hat{k}_x and \hat{k}_y satisfy the commutation relation $[\hat{k}_x, \hat{k}_y] = -i/l^2$, where l is the magnetic length given by $l = \sqrt{c\hbar/(eB)}$. Semiclassically, the Landau levels can be obtained by the condition

$$\oint k_x dk_y = \pm \frac{2\pi}{l^2} \left(|n| + \frac{1}{2} \right), \quad (2.32)$$

as $\varepsilon_n = \text{sgn}(n)\sqrt{|n| + \frac{1}{2}} \hbar\omega_B$ with integer n , where

$$\hbar\omega_B = \frac{\sqrt{2}\gamma}{l}. \quad (2.33)$$

Because of the uncertainty principle, $k^2 = 0$ is not allowed and there is no Landau level at $\varepsilon = 0$. However, a full quantum mechanical treatment gives

$$\varepsilon_n = \text{sgn}(n)\sqrt{|n|} \hbar\omega_B, \quad (2.34)$$

leading to the formation of Landau levels at $\varepsilon = 0$, first noted by McClure in 1956 [11]. This can be understood by the cancellation of factor $1/2$ in Eq. (2.32) by Berry's phase corresponding to the rotation in the \mathbf{k} space.

Define $a = (l/\sqrt{2})(\hat{k}_x - i\hat{k}_y)$ and $a^\dagger = (l/\sqrt{2})(\hat{k}_x + i\hat{k}_y)$. Then, we have $[a, a^\dagger] = 1$. In terms of these operators the Hamiltonian for the K point is rewritten as

$$\mathcal{H}_0 = \frac{\sqrt{2}\gamma}{l} \begin{pmatrix} 0 & a \\ a^\dagger & 0 \end{pmatrix}. \quad (2.35)$$

We shall define a function $h_n(x, y)$ such that

$$h_n(x, y) = \frac{(a^\dagger)^n}{\sqrt{n!}} h_0(x, y), \quad (2.36)$$

with

$$a h_0(x, y) = 0. \quad (2.37)$$

Then, we have

$$a^\dagger h_n = \sqrt{n+1} h_{n+1}, \quad a h_{n+1} = \sqrt{n+1} h_n, \quad a^\dagger a h_n = n h_n. \quad (2.38)$$

Therefore, there is a Landau level with vanishing energy $\varepsilon_0 = 0$ with wave function

$$\mathbf{F}_0^K = \begin{pmatrix} 0 \\ h_0 \end{pmatrix}. \quad (2.39)$$

Other Landau levels have wave function

$$\mathbf{F}_n^K = \frac{1}{\sqrt{2}} \begin{pmatrix} \text{sgn}(n)h_{|n|-1} \\ h_{|n|} \end{pmatrix}, \quad (2.40)$$

where $n = \pm 1, \pm 2, \dots$

For the K' point, we should exchange a and a^\dagger in Hamiltonian (2.35). Then, we have

$$\mathbf{F}_0^{K'} = \begin{pmatrix} h_0 \\ 0 \end{pmatrix}, \quad (2.41)$$

$$\mathbf{F}_n^{K'} = \frac{1}{\sqrt{2}} \begin{pmatrix} h_{|n|} \\ \text{sgn}(n)h_{|n|-1} \end{pmatrix}, \quad (n = \pm 1, \pm 2, \dots). \quad (2.42)$$

The presence of the Landau level at $\varepsilon = 0$ independent of the magnetic-field strength is a remarkable feature of the Weyl equation, leading to a divergent magnetic susceptibility as discussed below.

2.2.4 Effects of Bandgap Opening

In the presence of potential difference 2Δ between the A and B sites, the Hamiltonian becomes

$$\mathcal{H}_0 = \begin{pmatrix} \Delta & \gamma(\hat{k}_x - i\hat{k}_y) \\ \gamma(\hat{k}_x + i\hat{k}_y) & -\Delta \end{pmatrix}. \quad (2.43)$$

Such potential asymmetry can arise when graphene is placed on a certain substrate material. In fact, bandgap opening is observed in graphene epitaxially grown on a SiC substrate [46, 47]. From a theoretical point of view, the singular behavior in ideal graphene with vanishing gap is better understood by taking the limit $\Delta \rightarrow 0$, as will be shown below. We can safely assume $\Delta \geq 0$ without loss of generality.

The energy band becomes

$$\varepsilon_s(p) = s\sqrt{\gamma^2 k^2 + \Delta^2}, \quad (s = \pm 1), \quad (2.44)$$

and the density of states becomes [48]

$$D(\varepsilon) = \frac{g_s g_v |\varepsilon|}{2\pi \gamma^2} \theta(|\varepsilon| - |\Delta|), \quad (2.45)$$

where $\theta(t)$ is a step function, defined by

$$\theta(t) = \begin{cases} 1 & (t > 0); \\ 0 & (t < 0). \end{cases} \quad (2.46)$$

Figure 2.4 shows the energy bands and the density of states for nonzero Δ .

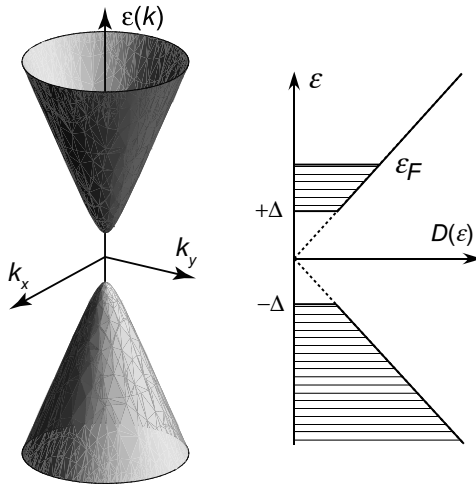


Figure 2.4 The energy bands in the vicinity of the K and K' points and the density of states in graphene with nonzero gap.

In magnetic field B perpendicular to the system, the Landau levels at the K point become

$$\varepsilon_n^K = \begin{cases} \text{sgn}(n)\sqrt{(\hbar\omega_B)^2|n| + \Delta^2} & (n = \pm 1, \pm 2, \dots); \\ -\Delta & (n = 0), \end{cases} \quad (2.47)$$

and at the K' point

$$\varepsilon_n^{K'} = \begin{cases} \text{sgn}(n)\sqrt{(\hbar\omega_B)^2|n| + \Delta^2} & (n = \pm 1, \pm 2, \dots); \\ +\Delta & (n = 0). \end{cases} \quad (2.48)$$

The Landau level $n = 0$ lies just at the top of the valence band for the K point and at the bottom of the conduction band for the K' point. The Landau levels of $n \neq 0$ are doubly degenerate between the K and K' valleys. Figure 2.5 shows some examples of Landau levels for $\Delta = 0$ and $\Delta > 0$.

2.3 Magnetic Properties

2.3.1 Singular Diamagnetism

The unique Landau-level structure gives rise to a singular diamagnetism [11], that is the origin of large diamagnetic susceptibility of

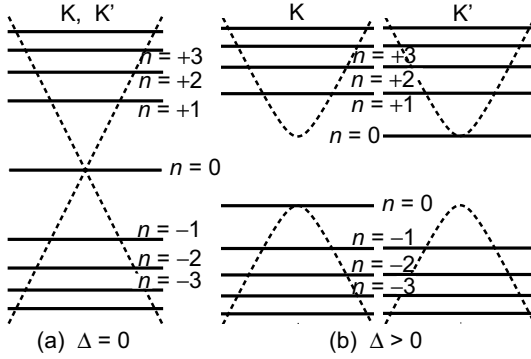


Figure 2.5 Landau levels in graphene with potential asymmetry Δ . (a) $\Delta = 0$. (b) $\Delta > 0$.

bulk graphite [49, 50]. The thermodynamic function Ω is given by

$$\Omega = -k_B T \frac{g_s g_v}{2\pi l^2} \sum_n \varphi(\varepsilon_n), \quad (2.49)$$

$$\varphi(\varepsilon) = \ln \{1 + \exp[\beta(\zeta - \varepsilon)]\},$$

where T is the temperature, k_B the Boltzmann constant, $\beta = 1/k_B T$, and ζ the chemical potential. Let n_s be the electron concentration. Then, the free energy is written as

$$F = n_s \zeta + \Omega. \quad (2.50)$$

With the use of the relation $n_s = -(\partial\Omega/\partial\zeta)_B$, the magnetization is given by

$$M = -\left(\frac{\partial F}{\partial B}\right)_{n_s} = -\left(\frac{\partial\Omega}{\partial B}\right)_{\zeta}. \quad (2.51)$$

Therefore, susceptibility χ , defined by $M = \chi B$ for small B , can be obtained by calculating Ω up to the order of B^2 .

The thermodynamic function is rewritten as

$$\begin{aligned} \Omega = & -k_B T \frac{g_s g_v}{2\pi l^2} \sum_{n=0}^{\infty} g(\hbar\omega_B \sqrt{n}) \left(1 - \frac{1}{2} \delta_{n0}\right) \ln \\ & \times [1 + 2e^{\beta\zeta} \cosh(\beta\hbar\omega_B \sqrt{n}) + e^{2\beta\zeta}], \end{aligned} \quad (2.52)$$

where $1/2\pi l^2$ is the degeneracy of a Landau level due to guiding centers and $g(\varepsilon)$ is a cutoff function that decays smoothly but sufficiently rapidly in such a way that the summation converges. In

order to expand Ω in terms of $\hbar\omega_B$, let us consider a smooth function $F(x)$ and its integral

$$\int_0^\infty F(x)dx = \int_0^{\hbar/2} F(x)dx + \sum_{j=1}^\infty \int_{-\hbar/2}^{\hbar/2} F(x+hj)dx, \quad (2.53)$$

where h is a small positive number. By expanding this with respect to h , we have

$$h \left[\frac{1}{2} F(0) + \sum_{j=1}^\infty F(x+hj) \right] = \int_0^\infty F(x)dx - \frac{1}{12} h^2 \left[F'(0) + \frac{1}{2} F'(\infty) \right], \quad (2.54)$$

up to the second order in h .

The desired expansion in $\hbar\omega_B$ is performed by letting $h = (\hbar\omega_B)^2$, $x = nh$, and

$$F(x) = g(\sqrt{x}) \ln [1 + 2 \exp(\beta\zeta) \cosh(\beta\sqrt{x}) + \exp(2\beta\zeta)]. \quad (2.55)$$

Then, we immediately have

$$\Omega = \Omega_0 + \Delta\Omega, \quad (2.56)$$

where Ω_0 is the thermodynamic potential in the absence of a magnetic field and

$$\begin{aligned} \Delta\Omega &= \frac{1}{12} \frac{g_v g_s (\hbar\omega_B)^2}{2\pi l^2} \frac{\beta \exp(\beta\zeta)}{[1 + \exp(\beta\zeta)]^2} \\ &= \frac{g_v g_s \gamma^2}{12\pi l^4} \int_{-\infty}^\infty \left(-\frac{\partial f(\varepsilon)}{\partial \varepsilon} \right) \delta(\varepsilon) d\varepsilon, \end{aligned} \quad (2.57)$$

where $f(\varepsilon)$ is the Fermi distribution function. The susceptibility becomes

$$\chi = \int_{-\infty}^\infty \left(-\frac{\partial f(\varepsilon)}{\partial \varepsilon} \right) \chi(\varepsilon) d\varepsilon, \quad (2.58)$$

with

$$\chi(\varepsilon) = -\frac{g_v g_s \gamma^2}{6\pi} \left(\frac{e}{c\hbar} \right)^2 \delta(\varepsilon). \quad (2.59)$$

This singular susceptibility is characteristic to graphene and obtained first by McClure [11] and later by many others [51–53].

Consider the average contribution of states around ε_n ($|n| \gg 1$) to the thermodynamic potential in the weak-field limit. We have

$$\begin{aligned} &\int_{-1/2}^{1/2} \text{sgn}(n) \hbar\omega_B \sqrt{|n|+t} \varphi [\text{sgn}(n) \hbar\omega_B \sqrt{|n|+t}] dt \\ &= \varphi(\varepsilon_n) + \frac{\beta}{96} (\hbar\omega_B)^4 [\varepsilon_n^{-3} f(\varepsilon_n) - \varepsilon_n^{-2} f'(\varepsilon_n)] + \dots \end{aligned} \quad (2.60)$$

Therefore, the change in the thermodynamic potential in a magnetic field becomes

$$\Delta\Omega = \frac{g_v g_s}{2\pi l^2} \frac{(\hbar\omega_B)^2}{48} \int_{-\infty}^{\infty} \text{sgn}(\varepsilon) [\varepsilon^{-2} f(\varepsilon) - \varepsilon^{-1} f'(\varepsilon)] d\varepsilon. \quad (2.61)$$

When the Fermi level lies well away from $\varepsilon = 0$, the integral vanishes identically and therefore the susceptibility vanishes.

At $\varepsilon = 0$, the integrand becomes singular and gives the “paramagnetic” contribution

$$\Delta\Omega = -\frac{g_v g_s}{2\pi l^2} \frac{1}{24} (\hbar\omega_B)^2 \int_{-\infty}^{\infty} \left(-\frac{\partial f(\varepsilon)}{\partial \varepsilon} \right) \delta(\varepsilon) d\varepsilon. \quad (2.62)$$

In fact, we have

$$\begin{aligned} & \int_0^{\infty} \left(\frac{f(\varepsilon)}{\varepsilon^2} - \frac{f'(\varepsilon)}{\varepsilon} \right) d\varepsilon - \int_{-\infty}^0 \left(\frac{f(\varepsilon)}{\varepsilon^2} - \frac{f'(\varepsilon)}{\varepsilon} \right) d\varepsilon \\ &= \lim_{\varepsilon \rightarrow +0} \left(\frac{f(\varepsilon)}{\varepsilon} + \frac{f(-\varepsilon)}{-\varepsilon} \right) = 2f'(0). \end{aligned} \quad (2.63)$$

For $n = 0$, the average contribution to the thermodynamic potential in the weak-field limit becomes

$$\begin{aligned} & \int_{-1/2}^{1/2} \varphi[\text{sgn}(t)\hbar\omega_B\sqrt{|t|}] dt = \frac{1}{8} (\hbar\omega_B)^2 \varphi''(0) + \dots \\ &= -\frac{\beta}{8} (\hbar\omega_B)^2 f'(0) + \dots, \end{aligned} \quad (2.64)$$

giving

$$\Delta\Omega = \frac{g_v g_s}{2\pi l^2} \frac{1}{8} (\hbar\omega_B)^2 \int_{-\infty}^{\infty} \left(-\frac{\partial f(\varepsilon)}{\partial \varepsilon} \right) \delta(\varepsilon) d\varepsilon. \quad (2.65)$$

By adding the contribution from $n \neq 0$ given by Eq. (2.62), we have the result given by Eq. (2.57). This shows clearly that the presence of the Landau level at $\varepsilon = 0$ is the origin of the singular behavior of the susceptibility.

2.3.2 Effects of Bandgap Opening

It is instructive to consider diamagnetic response in the presence of nonzero gap Δ . In this case, we should replace $\hbar\omega_B\sqrt{n}$ with

$\sqrt{(\hbar\omega_B)^2|n| + \Delta^2}$ in Eq. (2.52). Then, we immediately obtain [22]

$$\chi(\varepsilon) = -\frac{g_v g_s \gamma^2}{6\pi} \left(\frac{e}{c\hbar}\right)^2 \frac{\theta(\Delta - |\varepsilon|)}{2\Delta}. \quad (2.66)$$

This agrees with Eq. (2.59) for $\Delta \rightarrow 0$.

Because the Hamiltonian is equivalent to that of a Dirac electron with a nonzero mass, the magnetic susceptibility around the band edge should correspond to that of a conventional electron in vacuum. This is clearly illustrated by the effective Hamiltonian expanded in the vicinity of $\mathbf{k} = 0$. For the conduction band, $s = +1$, the effective Hamiltonian for the A site near the band bottom ($\varepsilon = \Delta$) is written apart from the constant energy as

$$\mathcal{H}^K \approx \frac{\gamma^2}{2\Delta} \hat{k}_- \hat{k}_+ = \frac{\hbar^2 \hat{\mathbf{k}}^2}{2m^*} - \frac{1}{2} g^* \mu_B B, \quad (2.67)$$

$$\mathcal{H}^{K'} \approx \frac{\gamma^2}{2\Delta} \hat{k}_- \hat{k}_+ = \frac{\hat{\mathbf{k}}^2}{2m^*} + \frac{1}{2} g^* \mu_B B, \quad (2.68)$$

where μ_B is the Bohr magneton, given by $e\hbar/(2mc)$ with m being the free electron mass, and we used the relation $[\hat{k}_x, \hat{k}_y] = i/l^2$ and defined

$$m^* = \frac{\hbar^2 \Delta}{\gamma^2}, \quad g^* = 2 \frac{m}{m^*}. \quad (2.69)$$

The last term in each Hamiltonian can be regarded as the pseudo-spin Zeeman term, where the different valleys K and K' serve as pseudo-spin up ($\xi = +1$) and down ($\xi = -1$), respectively. This shows that electrons at the K and K' points have intrinsic magnetic moment perpendicular to the graphene sheet in agreement with the self-rotation of wave packet [54, 55]. The combined Hamiltonian is written as

$$\mathcal{H} \approx \frac{\hat{\mathbf{k}}^2}{2m^*} - \frac{\xi}{2} g^* \mu_B B. \quad (2.70)$$

Obviously, the pseudo-spin Zeeman term gives the Pauli paramagnetism and the first term containing $\hat{\mathbf{k}}^2$ gives the Landau diamagnetism in the usual form as

$$\chi_P(\varepsilon) = \left(\frac{g^*}{2}\right)^2 \mu_B^2 D(\varepsilon), \quad (2.71)$$

$$\chi_L(\varepsilon) = -\frac{1}{3} \left(\frac{m}{m^*}\right)^2 \mu_B^2 D(\varepsilon), \quad (2.72)$$

with density of states

$$D(\varepsilon) = \frac{g_v g_s m^*}{2\pi \hbar^2} \theta(\varepsilon). \quad (2.73)$$

The total susceptibility $\chi_P + \chi_L$ actually agrees with the amount of the jump at the conduction band bottom in $\chi(\varepsilon)$ of Eq. (2.66). Because $g = 2m/m^*$ in the present case, we have $\chi_L = -\chi_P/3 \propto 1/m^*$ as in the free electron, giving the paramagnetic susceptibility in total. Therefore the susceptibility exhibits a discrete jump toward the paramagnetic direction when the Fermi energy moves off the Dirac point. The jump height goes to infinity as the gap closes, because the susceptibility is inversely proportional to the effective mass.

In the original Hamiltonian, the Landau-level energies can be rewritten as

$$\varepsilon_{\xi, s, n'} = s \sqrt{(\hbar\omega_B)^2 \left(n' + \frac{1}{2} + \frac{\xi s}{2} \right) + \Delta^2} \quad (n' = 0, 1, 2, \dots). \quad (2.74)$$

For the conduction band, the levels of the same n' with opposite pseudo-spins $\xi = \pm 1$ share the same Landau level function $\phi_{n'}$ on the A site, on which the states near the conduction-band bottom ($\varepsilon = \Delta$) have most of the amplitude. For the valence band, similarly, n' describes the index of the Landau-level function at the B site. The above is nothing but the Landau level of a (two-dimensional) electron in vacuum.

2.3.3 Magnetic Screening and Mirroring

Graphene exhibits singular diamagnetism also in non-uniform magnetic fields [21]. We apply a magnetic field perpendicular to the layer $B(\mathbf{r}) = B(\mathbf{q}) \exp(i\mathbf{q} \cdot \mathbf{r}) + \text{c.c.}$, where 'c.c.' stands for complex conjugate. Within the linear response, the Fourier-transforms of induced current density $\mathbf{j}(\mathbf{r}) = \mathbf{j}(\mathbf{q}) \exp(i\mathbf{q} \cdot \mathbf{r}) + \text{c.c.}$ and $\mathbf{A}(\mathbf{r}) = \mathbf{A}(\mathbf{q}) \exp(i\mathbf{q} \cdot \mathbf{r}) + \text{c.c.}$ are related by

$$j_\mu(\mathbf{q}) = \sum_{\nu=x,y} K_{\mu\nu}(\mathbf{q}) A_\nu(\mathbf{q}), \quad (\mu = x, y), \quad (2.75)$$

with response function $K_{\mu\nu}(\mathbf{q})$. The gauge invariance for $\mathbf{A}(\mathbf{r})$ requires $\sum_\nu K_{\mu\nu}(\mathbf{q}) q_\nu = 0$. The continuous equation in the static

system, $\vec{\nabla} \cdot \mathbf{j}(\mathbf{r}) = 0$, imposes another constraint $\sum_{\mu} q_{\mu} K_{\mu\nu}(\mathbf{q}) = 0$. To meet both requirements, tensor $K_{\mu\nu}(\mathbf{q})$ needs to be in the form,

$$K_{\mu\nu}(\mathbf{q}) = K(\mathbf{q}) \left(\delta_{\mu\nu} - \frac{q_{\mu} q_{\nu}}{q^2} \right). \quad (2.76)$$

On the other hand, because $\vec{\nabla} \cdot \mathbf{j}(\mathbf{r}) = 0$, we can express $\mathbf{j}(\mathbf{r})$ as

$$j_x = c \frac{\partial m}{\partial y}, \quad j_y = -c \frac{\partial m}{\partial x}, \quad (2.77)$$

with $m(\mathbf{r})$ being the local magnetic moment perpendicular to the layer. In the linear response, its Fourier transform is written as

$$m(\mathbf{q}) = \chi(\mathbf{q}) B(\mathbf{q}), \quad (2.78)$$

with magnetic susceptibility $\chi(\mathbf{q})$. Equations (2.75) and (2.78) are complementary, and both response functions $\chi(\mathbf{q})$ and $K(\mathbf{q})$ are related by

$$\chi(\mathbf{q}) = \frac{1}{cq^2} K(\mathbf{q}). \quad (2.79)$$

The Hamiltonian becomes $\mathcal{H} = \mathcal{H}_0 + \delta\mathcal{H}$ with $\delta\mathcal{H} = (e\gamma/c\hbar)\vec{\sigma} \cdot \mathbf{A}(\mathbf{r})$. The local current density at \mathbf{r}_0 is calculated as the expectation value of current-density operator $\hat{\mathbf{j}}(\mathbf{r}_0) = (e\gamma/\hbar)\vec{\sigma} \delta(\mathbf{r} - \mathbf{r}_0)$ over the occupied states. In the first order perturbation in $\delta\mathcal{H}$, we have

$$\begin{aligned} K_{\mu\nu}(\mathbf{q}) = & -\frac{g_s g_v e^2 \gamma^2}{c\hbar^2} \frac{1}{L^2} \sum_{ss'\mathbf{k}} \frac{f(\varepsilon_{s\mathbf{k}}) - f(\varepsilon_{s'\mathbf{k}+\mathbf{q}})}{\varepsilon_{s\mathbf{k}} - \varepsilon_{s'\mathbf{k}+\mathbf{q}}} \\ & \times (\mathbf{F}_{s\mathbf{k}}^\dagger \sigma_\nu \mathbf{F}_{s'\mathbf{k}+\mathbf{q}}) (\mathbf{F}_{s'\mathbf{k}+\mathbf{q}}^\dagger \sigma_\mu \mathbf{F}_{s\mathbf{k}}). \end{aligned} \quad (2.80)$$

At the zero temperature, we can explicitly calculate this to obtain

$$\begin{aligned} \chi(q) = & -\frac{g_s g_v e^2 \gamma}{16\hbar c^2 \hbar} \frac{1}{q} \theta(q - 2k_F) \\ & \times \left[1 + \frac{2}{\pi} \frac{2k_F}{q} \sqrt{1 - \left(\frac{2k_F}{q}\right)^2} - \frac{2}{\pi} \sin^{-1} \frac{2k_F}{q} \right], \end{aligned} \quad (2.81)$$

where $k_F = |\varepsilon_F|/\gamma$ is the Fermi wave number. Significantly, $\chi(q)$ vanishes in range $q < 2k_F$, i.e., no magnetic moment is induced when the external field is smooth enough compared to the Fermi wavelength. At $\varepsilon_F = 0$, particularly, we have

$$\chi(q) = -\frac{g_s g_v e^2 \gamma}{16\hbar c^2 \hbar} \frac{1}{q}. \quad (2.82)$$

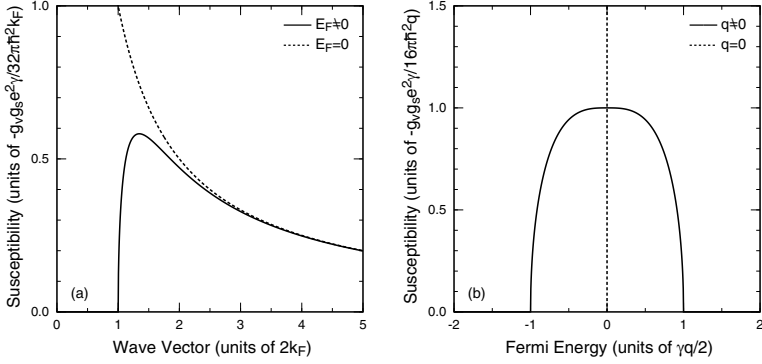


Figure 2.6 Diamagnetic susceptibility (a) versus wave vector q and versus the Fermi energy in ideal graphene.

The susceptibility of the carbon nanotube for a uniform field perpendicular to the axis has the equivalent expression of Eq. (2.82) where q is replaced by $2\pi/L$ with tube circumference L [56, 57]. Figure 2.6(a) shows a plot of $\chi(q)$ of Eq. (2.81) and Fig. 2.6(b) shows the dependence on the Fermi energy for a fixed q . The susceptibility suddenly starts from zero at $q = 2k_F$ and rapidly approaches the universal curve given by Eq. (2.82). As a function of ε_F at fixed q , it is nonzero only in a finite region satisfying $|\varepsilon_F| < \hbar v q/2$, and its integral over ε_F becomes constant $-g_s g_v e^2 \gamma^2 / (6\pi c^2 \hbar^2)$. Thus, in the limit of $q \rightarrow 0$ it goes to

$$\chi(0) = -\frac{g_s g_v e^2 \gamma^2}{6\pi c^2 \hbar^2} \delta(\varepsilon_F). \quad (2.83)$$

This agrees with the susceptibility against uniform magnetic field [11, 19].

Let us consider an undoped graphene ($\varepsilon_F = 0$) under a sinusoidal field $B(\mathbf{r}) = B_0 \cos qx$. With the susceptibility Eq. (2.81), the response current is calculated as

$$\mathbf{j}(\mathbf{r}) = -\frac{g_s g_v e^2 v B_0}{16\hbar c} \mathbf{e}_y \sin qx. \quad (2.84)$$

The current induces a counter magnetic field that reduces the original field. The z component of the induced field on graphene becomes

$$B_{\text{ind}}(\mathbf{r}) = -\alpha_g B(\mathbf{r}), \quad \alpha_g = \frac{2\pi g_s g_v e^2 v}{16\hbar c^2}. \quad (2.85)$$

Because the ratio is independent of q , Eq. (2.85) is actually valid for any external field $B(\mathbf{r})$, i.e., the magnetic field on the graphene is always reduced by the same factor $1 - \alpha_g$. This property holds whenever $\chi(q)$ is proportional to $1/q$. With the typical value $v \approx 1 \times 10^6$ m/s, α_g is estimated as $\approx 4 \times 10^{-5}$, showing that the counter field is much smaller than the original.

The argument of the magnetic field screening can be extended in the three dimensional field distribution. Let us suppose a situation when a certain magnetic object (permanent magnet or electric current) is located above the undoped graphene ($z > 0$), which produces an external magnetic field $\mathbf{B}(\vec{\rho})$ in three-dimensional space $\vec{\rho} = (x, y, z)$. Then, the following can easily be concluded: (i) On the other side of the graphene ($z < 0$), the induced field becomes $-\alpha_g \mathbf{B}(\vec{\rho})$, i.e., the external field is screened by the factor $1 - \alpha_g$. (ii) On the same side ($z > 0$), the induced field is given by $\alpha_g R_z[\mathbf{B}(x, y, -z)]$, where R_z is the vector inversion with respect to $z = 0$. Namely, this is equivalent to a field of the mirror image of the original object reflected with respect to $z = 0$, and reduced by α_g .

2.4 Optical Properties

With the use of the Kubo formula, the dynamical conductivity is given by

$$\sigma(\omega) = \frac{g_v g_s}{L^2} \left(\frac{e\gamma}{\hbar} \right)^2 \frac{\hbar}{i} \sum_{\alpha, \beta} \frac{|\langle \alpha | \sigma_x | \beta \rangle|^2 (f_\alpha - f_\beta)}{(\varepsilon_\alpha - \varepsilon_\beta)(\varepsilon_\alpha - \varepsilon_\beta + \hbar\omega + i\delta)}, \quad (2.86)$$

where α and β are a set of quantum numbers specifying states, and δ is a positive infinitesimal. In ideal graphene, this can be separated into two parts:

$$\sigma(\omega) = \frac{g_v g_s}{L^2} \left(\frac{e\gamma}{\hbar} \right)^2 \frac{\hbar}{i} \left[\sum_{\mathbf{s}\mathbf{k}} \frac{\partial f(\varepsilon_{\mathbf{s}\mathbf{k}})}{\partial \varepsilon_{\mathbf{s}\mathbf{k}}} \frac{|\langle \mathbf{s}\mathbf{k} | \sigma_x | \mathbf{s}\mathbf{k} \rangle|^2}{\hbar\omega + i\delta} - \sum_{\mathbf{s} \neq \mathbf{s}', \mathbf{k}} \frac{|\langle \mathbf{s}\mathbf{k} | \sigma_x | \mathbf{s}'\mathbf{k} \rangle|^2 [f(\varepsilon_{\mathbf{s}\mathbf{k}}) - f(\varepsilon_{\mathbf{s}'\mathbf{k}})] (\hbar\omega + i\delta)}{(\varepsilon_{\mathbf{s}\mathbf{k}} - \varepsilon_{\mathbf{s}'\mathbf{k}})[(\varepsilon_{\mathbf{s}\mathbf{k}} - \varepsilon_{\mathbf{s}'\mathbf{k}})^2 - (\hbar\omega + i\delta)^2]} \right], \quad (2.87)$$

where the first term in the bracket represents the Drude (intra-band) part and the second the interband part.

In order to include effects of level broadening due to scatterers, we shall replace δ by \hbar/τ , where τ is a relaxation time. Because of the energy dependence of the relaxation time, we shall assume $\tau = \tau(\varepsilon)$ with $\varepsilon = \varepsilon_F$ in the first term in the bracket of Eq. (2.86) and $\varepsilon = \hbar\omega/2$ in the second term, corresponding to the energy of the states giving a major contribution to the transition. Then, the dynamical conductivity at zero temperature is calculated as

$$\sigma(\omega) = \frac{g_s g_v e^2}{4} \frac{1}{4\hbar} \left[\frac{4}{\pi} \frac{i\varepsilon_F}{\hbar\omega + i[\hbar/\tau(\varepsilon_F)]} + 1 + \frac{i}{\pi} \ln \frac{\hbar\omega + i[\hbar/\tau(\hbar\omega/2)] - 2\varepsilon_F}{\hbar\omega + i[\hbar/\tau(\hbar\omega/2)] + 2\varepsilon_F} \right]. \quad (2.88)$$

As will be shown in the next section, for scatterers with potential range longer than the lattice constant and shorter than the electron wavelength, we have

$$\frac{\hbar}{\tau(\varepsilon)} = \pi |\varepsilon| W, \quad (2.89)$$

where W is the dimensionless parameter characterizing the strength and concentration of scatterers. Then, the frequency dependence of the dynamical conductivity is scaled by $\hbar\omega/\varepsilon_F$. Figure 2.7 shows $\sigma(\omega)$ as a function of $\hbar\omega/\varepsilon_F$ for several values of W [25].

The scaling of the dynamical conductivity $\sigma(\hbar\omega/\varepsilon_F)$ shows that $\sigma(\omega)$ exhibits a singular behavior at the point $(\omega, \varepsilon_F) = (0, 0)$. In fact, when we set $\omega = 0$ first, the static conductivity is given by

$$\sigma(0) = \sigma_0 \equiv \frac{g_s g_v e^2}{4} \frac{1}{\pi^2 \hbar W}, \quad (2.90)$$

independent of the Fermi energy ε_F in agreement with the Boltzmann result [23]. When we set $\varepsilon_F = 0$ first with nonzero ω , on the other hand, the static conductivity at $\omega \rightarrow 0$ becomes

$$\sigma_\infty \equiv \frac{g_s g_v e^2}{4} \frac{1}{\pi \hbar}, \quad (2.91)$$

which is the universal interband conductivity. The correct way is to let $\omega \rightarrow 0$ at each ε_F , leading to a singular jump of the static conductivity at $\varepsilon_F = 0$. The calculation in a self-consistent Born approximation shows that this anomaly manifests itself as a near singular dependence of σ on ε_F even if level broadening effects are

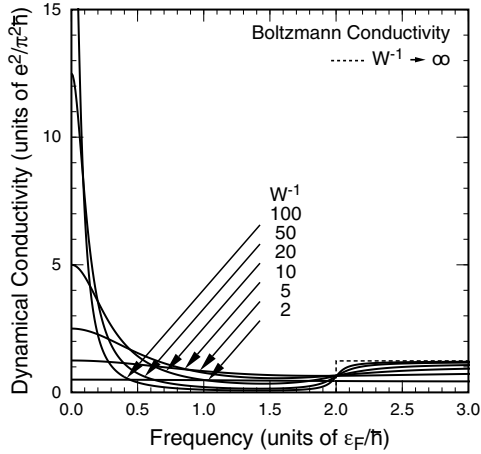


Figure 2.7 The dynamical conductivity calculated using the Boltzmann transport equation. The frequency is scaled by the Fermi energy. After Ref. [25].

included and that the conductivity at $\varepsilon_F = 0$ is given by a universal conductivity quantum $e^2/\pi^2\hbar$ as will be discussed in the following [23].

The transmission of light incident perpendicular to graphene sheet is given by [58]

$$T = \left| 1 + \frac{2\pi}{c} \sigma(\omega) \right|^{-2} \approx 1 - \frac{4\pi}{c} \text{Re}\sigma(\omega) = 1 - \frac{g_s g_v \pi e^2}{4 c \hbar}, \quad (2.92)$$

showing that the absorption is given by $\pi\alpha \approx 0.023$ independent of frequency or wavelength, with fine structure constant $\alpha \equiv e^2/(c\hbar) \approx 1/137$. This small absorption was experimentally observed [59, 60] and is often used to identify the number of layers of graphene flakes created by mechanical exfoliation.

2.5 Transport Properties

2.5.1 Boltzmann Conductivity

In this section, transport theory based on the Boltzmann equation will be reviewed [61]. The transport equation for the distribution

function $f_{s\mathbf{k}}^E$ in the applied electric field \mathbf{E} is given by

$$\frac{d\mathbf{k}}{dt} \cdot \frac{\partial f_{s\mathbf{k}}^E}{\partial \mathbf{k}} = - \sum_{s'} \int \frac{d\mathbf{k}'}{(2\pi)^2} [f_{s\mathbf{k}}^E(1 - f_{s'\mathbf{k}'}^E) - f_{s'\mathbf{k}'}^E(1 - f_{s\mathbf{k}}^E)] W(s'\mathbf{k}', s\mathbf{k}), \quad (2.93)$$

with scattering probability

$$W(s'\mathbf{k}', s\mathbf{k}) = \frac{2\pi}{\hbar} \langle |V_{s'\mathbf{k}', s\mathbf{k}}|^2 \rangle \delta(\varepsilon_{s\mathbf{k}} - \varepsilon_{s'\mathbf{k}'}), \quad (2.94)$$

where $V_{s'\mathbf{k}', s\mathbf{k}}$ is the matrix element of scattering potential and $\langle \dots \rangle$ denotes the average over configurations of scatterers. We shall confine ourselves to the case of elastic scattering and therefore neglect interband processes ($s' \neq s$). To the lowest order in the applied electric field \mathbf{E} , we have

$$f_{s\mathbf{k}}^E = f(\varepsilon_{s\mathbf{k}}) + g_{s\mathbf{k}}, \quad (2.95)$$

where $f(\varepsilon)$ is the Fermi distribution function and $g_{s\mathbf{k}}$ is the deviation proportional to \mathbf{E} . Then, we have

$$\frac{d\mathbf{k}}{dt} \cdot \frac{\partial f_{s\mathbf{k}}^E}{\partial \mathbf{k}} = -e\mathbf{E} \cdot \mathbf{v}_{s\mathbf{k}} \frac{\partial f}{\partial \varepsilon_{s\mathbf{k}}} - \frac{e}{c\hbar} (\mathbf{v}_{s\mathbf{k}} \times \mathbf{B}) \cdot \frac{\partial g_{s\mathbf{k}}}{\partial \mathbf{k}}, \quad (2.96)$$

where \mathbf{B} is the magnetic field perpendicular to the system and $\mathbf{v}_{s\mathbf{k}}$ is the velocity given by

$$\mathbf{v}_{s\mathbf{k}} = \frac{\partial \varepsilon_{s\mathbf{k}}}{\hbar \partial \mathbf{k}} = \frac{\gamma}{\hbar} \frac{s\mathbf{k}}{|\mathbf{k}|}. \quad (2.97)$$

The vector product is defined as $\mathbf{v} \times \mathbf{B} = -\mathbf{B} \times \mathbf{v} = B(v_y, -v_x)$ for vector $\mathbf{v} = (v_x, v_y)$. The transport equation is rewritten as

$$e\mathbf{E} \cdot \mathbf{v}_{s\mathbf{k}} \left(-\frac{\partial f}{\partial \varepsilon_{s\mathbf{k}}} \right) = \frac{e}{c\hbar} (\mathbf{v}_{s\mathbf{k}} \times \mathbf{B}) \cdot \frac{\partial g_{s\mathbf{k}}}{\partial \mathbf{k}} - \int \frac{d\mathbf{k}'}{(2\pi)^2} (g_{s\mathbf{k}} - g_{s'\mathbf{k}'}) \frac{2\pi}{\hbar} \langle |V_{s\mathbf{k}, s'\mathbf{k}'}|^2 \rangle \delta(\varepsilon_{s\mathbf{k}} - \varepsilon_{s'\mathbf{k}'}). \quad (2.98)$$

Let us introduce the transport relaxation time given by

$$\frac{\hbar}{\tau(\varepsilon_{s\mathbf{k}})} = 2\pi \int \frac{d\mathbf{k}'}{(2\pi)^2} \langle |V_{s\mathbf{k}, s'\mathbf{k}'}|^2 \rangle [1 - \cos(\theta_{\mathbf{k}} - \theta_{\mathbf{k}'})] \delta(\varepsilon_{s\mathbf{k}} - \varepsilon_{s'\mathbf{k}'}), \quad (2.99)$$

and the cyclotron frequency

$$\omega_c(\varepsilon_{s\mathbf{k}}) = \frac{eBv^2}{c\varepsilon_{s\mathbf{k}}}. \quad (2.100)$$

Then, the solution becomes

$$g_{s\mathbf{k}} = -e\tau \left(-\frac{\partial f}{\partial \varepsilon_{s\mathbf{k}}} \right) \frac{1}{1 + \omega_c^2 \tau^2} \mathbf{v}_{s\mathbf{k}} \cdot \left(\mathbf{E} + \omega_c \tau \frac{\mathbf{B}}{B} \times \mathbf{E} \right), \quad (2.101)$$

with $\omega_c = \omega_c(\varepsilon_{s\mathbf{k}})$ and $\tau = \tau(\varepsilon_{s\mathbf{k}})$. It should be noted that the cyclotron frequency diverges in proportion to the inverse of the energy at zero energy and changes the sign corresponding to change in the carrier type from electron to hole.

Let us define

$$\bar{D} = \frac{g_s g_v}{2\pi \gamma^2} \int \left(-\frac{\partial f}{\partial \varepsilon} \right) |\varepsilon| d\varepsilon, \quad (2.102)$$

and the average of function $p(\varepsilon)$ by

$$\langle p(\varepsilon) \rangle \equiv \frac{1}{\bar{D}} \int \left(-\frac{\partial f}{\partial \varepsilon} \right) \frac{g_s g_v}{2\pi \gamma^2} |\varepsilon| p(\varepsilon) d\varepsilon. \quad (2.103)$$

Then, we have the diagonal conductivity

$$\sigma_{xx} = \sigma_{yy} = \frac{e^2 \gamma^2}{2\hbar^2} \bar{D} \left\langle \frac{\tau}{1 + \omega_c^2 \tau^2} \right\rangle, \quad (2.104)$$

and the Hall conductivity

$$\sigma_{xy} = -\sigma_{yx} = -\frac{e^2 \gamma^2}{2\hbar^2} \bar{D} \left\langle \frac{\omega_c \tau^2}{1 + \omega_c^2 \tau^2} \right\rangle. \quad (2.105)$$

These are essentially the same as the expressions in conventional semiconductors or metals except that ω_c depends strongly on the energy while the velocity remains independent.

The Hall coefficient is given by

$$R_H = -\frac{\sigma_{yx}}{B(\sigma_{xx}^2 + \sigma_{xy}^2)}, \quad (2.106)$$

and the Hall mobility is given by

$$\mu = c |R_H| \sigma_0, \quad (2.107)$$

in the limit $B \rightarrow 0$, where $\sigma_0 = \sigma_{xx}$ in the absence of a magnetic field. At zero temperature in weak magnetic fields, we have

$$R_H = -\frac{S}{n_s e c}, \quad (2.108)$$

with the electron concentration given by Eq. (2.13). The Hall mobility becomes

$$\mu_0 = \frac{e v^2}{\varepsilon_F} \tau(\varepsilon_F), \quad (2.109)$$

and then the conductivity is given by

$$\sigma_0 = n_s e \mu, \quad (2.110)$$

as in conventional two-dimensional systems.

For scatterers with potential $v(\mathbf{r})$, randomly distributed with concentration n_i per unit area, we have

$$\langle |V_{s'\mathbf{k}',s\mathbf{k}}|^2 \rangle = n_i |v(\mathbf{k}' - \mathbf{k})(\mathbf{F}_{s'\mathbf{k}'}^\dagger \cdot \mathbf{F}_{s\mathbf{k}})|^2, \quad (2.111)$$

with

$$(\mathbf{F}_{s\mathbf{k}}^\dagger \cdot \mathbf{F}_{s'\mathbf{k}'}) = \frac{1}{2} [\exp(i\theta_{\mathbf{k}} - i\theta_{\mathbf{k}'}) + ss'], \quad (2.112)$$

$$v(\mathbf{r}) = \int \frac{d\mathbf{q}}{(2\pi)^2} v(\mathbf{q}) \exp(i\mathbf{q} \cdot \mathbf{r}). \quad (2.113)$$

The transport relaxation time becomes

$$\frac{\hbar}{\tau(\varepsilon)} = 2\pi n_i \frac{|\varepsilon|}{2\pi\gamma^2} \int_0^\pi \frac{d\theta}{\pi} \frac{1}{2} (1 - \cos^2 \theta) |v(q)|^2. \quad (2.114)$$

where $|v(q)|^2$ is the average over different directions of impurities in the case of anisotropic scatterers, i.e., $|v(q)|^2 = \langle |v(\mathbf{q})|^2 \rangle$, and $q = 2(|\varepsilon|/\gamma) \sin(\theta/2)$ in the integrand. On the other hand, the conventional relaxation time representing the electron life time is obtained from above by replacing $1 - \cos^2 \theta$ with $1 + \cos \theta$, i.e.,

$$\frac{\hbar}{\tau_0(\varepsilon)} = 2\pi n_i \frac{|\varepsilon|}{2\pi\gamma^2} \int_0^\pi \frac{d\theta}{\pi} \frac{1}{2} (1 + \cos \theta) |v(q)|^2. \quad (2.115)$$

For scatterers with potential range smaller than the electron wavelength $\lambda = 2\pi/k = 2\pi\gamma/|\varepsilon|$, we can safely neglect the q dependence of $|v(q)|^2$ and set $|v(q)|^2 \approx v_i^2$. Then, we have

$$\frac{\hbar}{\tau(\varepsilon)} = \frac{\hbar}{2\tau_0(\varepsilon)} = \pi |\varepsilon| \frac{n_i v_i^2}{4\pi\gamma^2}. \quad (2.116)$$

This becomes Eq. (2.89), for the dimensionless parameter characterizing the strength of scattering

$$W = \frac{n_i v_i^2}{4\pi\gamma^2}. \quad (2.117)$$

The conductivity at zero temperature is given by Eq. (2.90), independent of the Fermi energy. This shows that graphene should be regarded as a metal rather than a semiconductor.

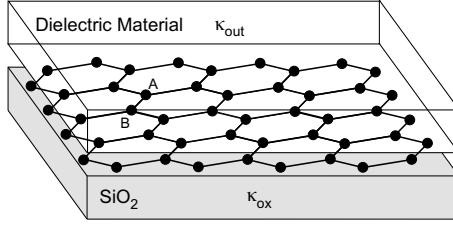


Figure 2.8 Schematic illustration of graphene on SiO_2 substrate covered by dielectric material on top.

2.5.2 Charged Impurities

We consider graphene on SiO_2 covered by dielectric material with dielectric constant κ_{out} on the top side as schematically illustrated in Fig. 2.8. For charged impurities located close to graphene layer, we have

$$v(q) = \frac{2\pi e^2}{\kappa q \varepsilon(q)}, \quad (2.118)$$

where κ is the effective dielectric constant determined by environmental conditions and $\varepsilon(q)$ represents the screening effect due to electrons in graphene. The static screening constant is given by the average of that of the substrate SiO_2 , $\kappa_{\text{ox}} = 3.9$, and that of the covering material κ_{out} due to the image effect [62], i.e., $\kappa = (\kappa_{\text{ox}} + \kappa_{\text{out}})/2$.

Actually, we have to consider contributions of electrons in σ bands and π bands away from the Fermi level. This contribution is known to be $\kappa_0 \approx 2.4$ in bulk graphite [63], but is not known for the present system and may not be written as in Eq. (2.118). In spite of this, we shall use Eq. (2.118) assuming that κ can be larger than that estimated above.

The dielectric function of graphene is written as

$$\varepsilon(q) = 1 + \frac{2\pi e^2}{\kappa q} \Pi(q), \quad (2.119)$$

where the polarization function at zero temperature is calculated as [45]

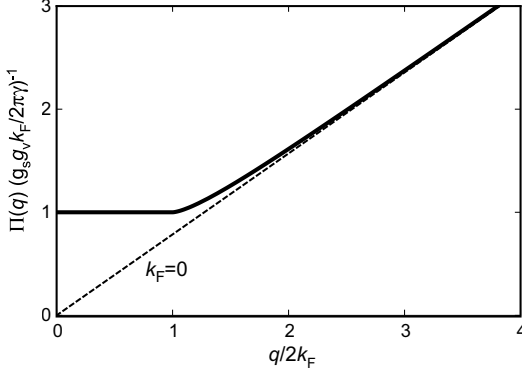


Figure 2.9 Polarization function $\Pi(q)$ in graphene. The dotted line represents pure interband contribution for vanishing electron and hole concentrations.

$$\Pi(q) = \begin{cases} \frac{g_s g_v}{2\pi\gamma} k_F & (q < 2k_F); \\ \frac{g_s g_v}{16\gamma} q + \frac{g_s g_v}{2\pi\gamma} k_F \left[1 - \left(\frac{1}{2} \sqrt{1 - \left(\frac{2k_F}{q} \right)^2} - \frac{q}{4k_F} \sin^{-1} \frac{2k_F}{q} \right) \right] & (q > 2k_F). \end{cases} \quad (2.120)$$

This is shown in Fig. 2.9. In the long-range limit $q = 0$, we have $\Pi(0) = D(\varepsilon_F)$ corresponding to the compressibility sum rule. For the relaxation time at zero temperature or at sufficiently low temperatures, we can safely replace $\Pi(q)$ with $\Pi(0)$ because $q \leq 2k_F$, i.e., we can use the Thomas–Fermi approximation.

The transport relaxation time becomes

$$\tau(\varepsilon) = \frac{n_s}{\pi g_s g_v n_i} \frac{\hbar}{|\varepsilon|} H, \quad (2.121)$$

with

$$H^{-1} = \int_0^\pi \frac{d\theta}{\pi} \frac{1}{2} (1 - \cos^2 \theta) \left(g_s g_v + \frac{\kappa \gamma}{e^2} \frac{q}{k_F} \right)^{-2}, \quad (2.122)$$

where $q = 2k_F \sin(\theta/2)$ and $e^2/\kappa\gamma$ is the effective fine structure constant in graphene, i.e.,

$$\frac{e^2}{\kappa\gamma} = \frac{1}{\kappa} \frac{c}{v} \frac{e^2}{\hbar c} \approx \frac{300}{\kappa} \frac{1}{137}, \quad (2.123)$$

for $v/c \approx 1/300$. The conventional relaxation time representing the electron life time is obtained from above by replacing $1 - \cos^2 \theta$ with $1 + \cos \theta$.

The mobility becomes

$$\mu_0 = \frac{e}{4\pi^2 \hbar n_i} H, \quad (2.124)$$

which is independent of n_s . The conductivity becomes

$$\sigma_0 = \frac{e^2}{4\pi^2 \hbar} \frac{n_s}{n_i} H, \quad (2.125)$$

which is proportional to n_s .

The Boltzmann transport equation, as well as the Einstein relation, gives $\sigma \propto e^2 \tau(\varepsilon_F) v(\varepsilon_F)^2 D(\varepsilon_F)$. In conventional systems characterized by constant effective mass m^* , we have $\varepsilon_F = m^* v(\varepsilon_F)^2 / 2$. With the use of $n_s \propto \varepsilon_F D(\varepsilon_F)$, this leads to the usual expression $\sigma = n_s e \mu$ with mobility $\mu = e \tau(\varepsilon_F) / m^*$, where n_s is the electron concentration.

In graphene, the velocity v is independent of ε_F or $m^* \propto \varepsilon_F$ if we assume $\varepsilon_F = m^* v^2 / 2$ as above. Further, the scattering probability $\hbar / \tau(\varepsilon_F)$ is proportional to the final-state density of states with a coefficient independent of ε_F . Because the density of states is proportional to ε_F , the relaxation time is inversely proportional to ε_F . As a result, the mobility μ becomes proportional to $\varepsilon_F^{-2} \propto n_s^{-1}$, leading to the conductivity independent of the Fermi energy and the electron concentration.

In the case of charged-impurity scattering, the matrix element itself is proportional to the inverse of the Fermi energy, leading to $W \propto \varepsilon_F^{-2} \propto n_s^{-1}$. Consequently, the conductivity increases in proportion to the electron or hole concentration n_s as if there is a mobility independent of n_s [45, 64]. Note, however, that this does not change the situation that graphene should be regarded as a metal rather than a semiconductor.

2.5.3 Self-Consistent Born Approximation and Zero-Mode Anomalies

A more refined treatment has been performed for the density of states and the conductivity in a self-consistent Born approximation

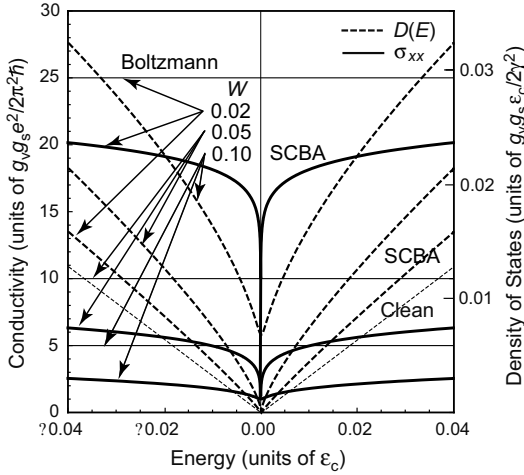


Figure 2.10 Some examples of the density of states (dashed lines) and the conductivity (solid lines), calculated in the self-consistent Born approximation (SCBA) for scatters with potential range smaller than the electron wavelength but larger than the lattice constant [23]. The thin horizontal lines denote the Boltzmann conductivity and the thin dotted line denoted as ‘Clean’ represents the density of states in clean graphene.

[58, 66, 66], in which level-broadening effects are properly taken into account [23]. Figure 2.10 shows some examples of the results. The density of states becomes nonzero at $\varepsilon = 0$ because of level broadening and is also enhanced due to level repulsion effect near $\varepsilon = 0$. Further, the conductivity at $\varepsilon_F = 0$ is given by

$$\sigma_{\min} = \frac{g_s g_v e^2}{2\pi^2 \hbar}, \quad (2.126)$$

which is universal and independent of the scattering strength. The resulting conductivity varies smoothly across $\varepsilon_F = 0$ but exhibits a sharp jump in the limit of weak scattering ($W \ll 1$) from the Boltzmann result σ_0 for $\varepsilon \neq 0$ down to σ_{\min} at $\varepsilon_F = 0$.

The energy scale characterizing this singularity in the vicinity of $\varepsilon_F = 0$ turns out to be

$$\varepsilon_0 = 2W\varepsilon_c e^{-1/2W}, \quad (2.127)$$

where ε_c is the cutoff energy roughly corresponding to a half of the π -band width (~ 9 eV). This becomes extremely small in clean graphene with $W \ll 1$.

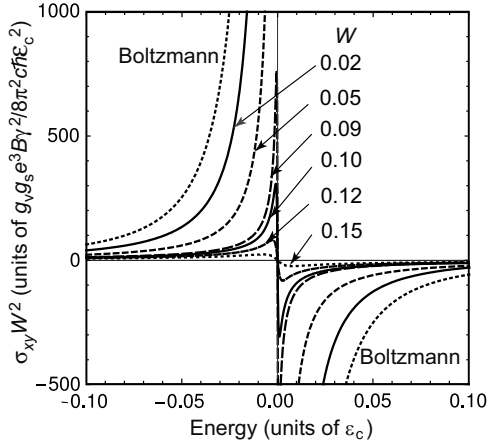


Figure 2.11 Some examples of the Hall conductivity as a function of the Fermi energy calculated in a self-consistent Born approximation for short-range scatterers. After Ref. [65].

As has been discussed in Section 2.5.1, in the Boltzmann theory, the Hall conductivity in weak magnetic field B is given by $\sigma_{xy} = -\omega_c \tau(\epsilon_F) \sigma_0$, where ω_c is the classical cyclotron frequency given by $\omega_c(\epsilon) = eBv^2/c\epsilon$. The cyclotron frequency diverges at the Dirac point, showing the presence of singularity there. In spite of this singularity, the Hall coefficient is simply $R_H = -(n_s ec)^{-1}$ as in conventional systems. Similar calculations in the self-consistent Born approximation were recently performed for the weak-field Hall conductivity [65]. Figure 2.11 shows some examples of calculated σ_{xy} . The Hall conductivity behaves roughly as $-\epsilon_F^{-1}$ outside of the region $|\epsilon_F| > \epsilon_0$, but is considerably reduced from the Boltzmann result. It varies almost linearly in the region $-\epsilon_c < \epsilon_F < +\epsilon_c$ and crosses zero at the Dirac point.

Figure 2.12 shows the inverse Hall coefficient as a function of n_s . In clean systems such as $W < 0.1$, the Hall coefficient is essentially given by $R_H = -(n_s ec)^{-1}$ except in the critical region $|n_s| < n_s^0 = g_s g_v \epsilon_0^2 / 4\pi \gamma^2$. In dirty systems such as $W > 0.1$, R_H^{-1} considerably deviates from $-n_s ec$ and also there seems to be a discrete jump in the values of R_H^{-1} extrapolated to $n_s = 0$ from the electron and hole sides. This jump may be regarded as effective carrier concentration

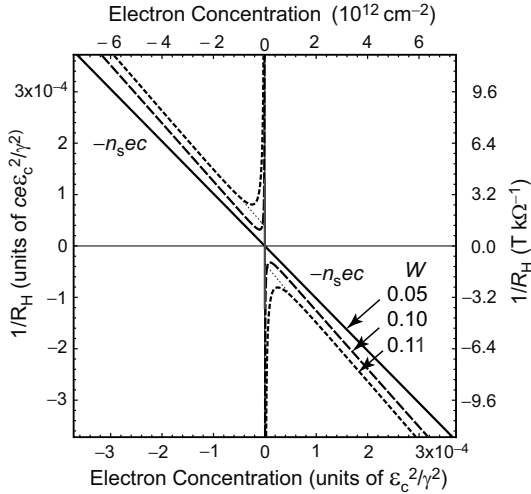


Figure 2.12 Some examples of the inverse of Hall coefficient R_H as a function of the electron concentration. With the decrease of W , R_H^{-1} approaches $-n_s ec$. The thin solid lines are a linear extrapolation of the results for $W = 0.11$ toward $n_s = 0$. After Ref. [65].

associated with the nonvanishing density of states at the Dirac point due to disorder.

Experimentally, the conductivity increases almost linearly with n_s for sufficiently large n_s , showing that the effective scattering strength in actual graphene on SiO_2 substrate varies considerably with n_s . Most plausible scatterers giving rise to such strong n_s dependence are charged impurities [61, 64]. This strong dependence of W on n_s disappears when $|\varepsilon| < \varepsilon_0$, i.e., $|n_s| < n_s^0$, because of the level broadening leading to uncertainty in the effective kinetic energy of electrons. Experimental results [4] can be understood by assuming W , which is ~ 0.11 for $|\varepsilon_F| \lesssim \varepsilon_0$ and decreases in proportion to n_s^{-2} with increasing $|n_s|$. For $W = 0.1$, the broadening is $\Gamma_0 \sim 60$ meV. This Γ_0 is much larger than potential fluctuations ~ 25 meV estimated from observed electron-hole puddles based on ideal density of states [67], suggesting that puddles are actually not important in determining the transport in the vicinity of the Dirac point.

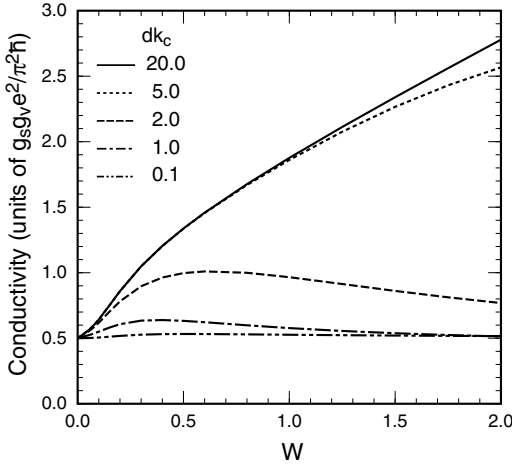


Figure 2.13 Calculated minimum conductivity at the Dirac point versus W for scatterers with Gaussian potential. After Ref. [68].

Calculations can be extended to the case of scatterers with long-range potential [68]. We consider, for example, scatterers with Gaussian potential $U(\mathbf{r}) = \sum_j (v_i / \pi d^2) \exp[-(\mathbf{r} - \mathbf{r}_j)^2 / d^2]$ characterized by potential range d and strength v_i . The energy region affected strongly by the presence of scatterers is limited to $|\varepsilon| \lesssim \gamma / d$ because scattering becomes ineffective for $k > d^{-1}$. Therefore, for long-range scatterers, W is not restricted to small values like $W < 0.1$, but can be much larger.

Figure 2.13 shows the minimum conductivity at the Dirac point. For very short-range case $dk_c < 1$, the conductivity is nearly independent of W , where k_c is the cutoff momentum given by $\gamma k_c \sim \gamma_0$ corresponding to the region where the linear dispersion is approximately valid. For $dk_c > 1$, on the other hand, the conductivity increases with W , depending on dk_c . States at the Dirac point have higher k components because of strong forward scattering caused by long-range scatterers. These higher k states are weakly scattered in backward direction and therefore tend to have large contribution to the conductivity. For short-range scatterers, higher k components do not contribute much to the conductivity and the minimum conductivity remains small.

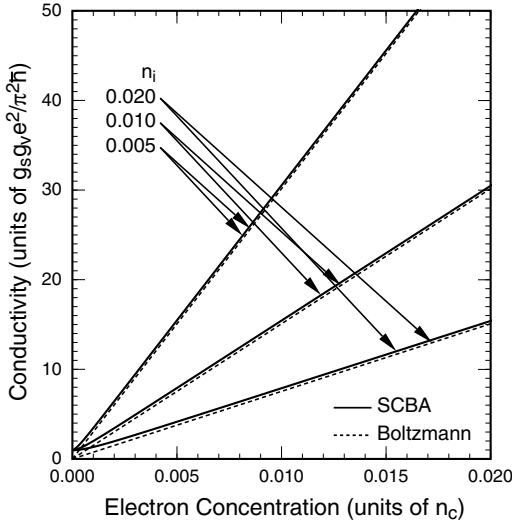


Figure 2.14 Calculated conductivity versus the electron concentration for charged scatterers. After Ref. [68].

Since the first experimental observation of the minimum conductivity [4], which is larger than the theoretical prediction [23, 69, 70], there have been various experimental [71–73] and theoretical works [74–81] to answer the question whether the minimum conductivity is really universal or not. The above clearly shows that the conductivity at the Dirac point is not universal but depends on the degree of the disorder for scatterers with long-range potential when the disorder is sufficiently large.

Calculations can be extended to the case of charged impurities when the screening effect is self-consistently included within a Thomas–Fermi approximation, i.e., the screening is given by the density of states at the Fermi level determined in a self-consistent manner [68]. Figure 2.14 shows the conductivity as a function of the electron density. Here, ε_c is the cutoff energy of the order of $3\gamma_0 \sim 9$ eV, where $-\gamma_0$ is the hopping integral in the simplest tight-binding model [83], and $n_c = \varepsilon_c^2 / (4\pi\gamma^2)$ is the concentration roughly corresponding to an impurity per several unit cells. The conductivity is essentially the same as the Boltzmann conductivity and increases in proportion to n_s except that it approaches a nonzero

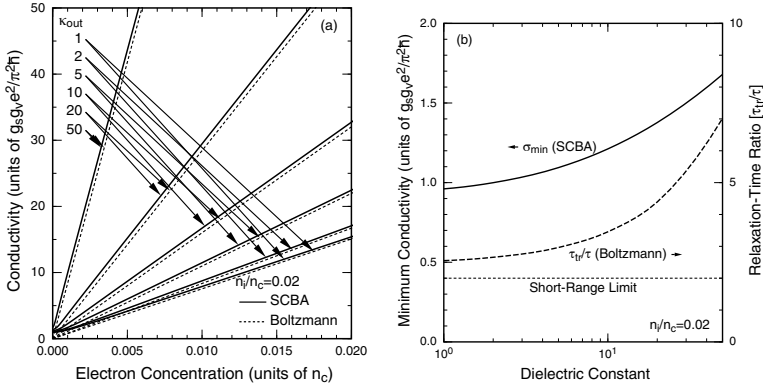


Figure 2.15 (a) Conductivity versus electron concentration for various values of the dielectric constant of dielectric material on top of graphene. (b) Minimum conductivity and the relaxation-time ratio as a function of dielectric constant κ_{out} . After Ref. [82].

value slightly larger than $2 \times \sigma_{min}$ at the Dirac point. This again shows that the minimum conductivity is not universal for realistic scatterers. More elaborate calculations are necessary for various scattering mechanisms and other quantities before reaching full understanding on the behavior of the minimum conductivity.

Calculations can also be extended to the case in the presence of dielectric environmental material [82]. Figure 2.15(a) shows some examples of calculated conductivity for $1 \leq \kappa_{out} \leq 50$. With the increase of κ_{out} , the conductivity does not increase so much, presumably due to the fact that the decrease of potential by dielectric screening is partly canceled by the reduction in the screening by electrons in graphene. Figure 2.15(b) shows the minimum conductivity at the Dirac point as a function of κ_{out} . It increases gradually with κ_{out} . The reason is that the effective potential tends to become of long range due to less screening by electrons in graphene.

Figure 2.15(b) also shows ratio of transport relaxation time τ determining the conductivity and self-energy relaxation time τ_0 corresponding to the inverse of the total scattering probability [82]. For short-range scatterers we have $\tau/\tau_0 = 2$ because of the absence of backscattering [23]. For $\kappa_{out} = 1$ without environmental dielectric

material, we have $2 < \tau/\tau_0 < 3$ not so much different from that for short-range scatterers. This shows that charged impurities should be regarded as short-range scatterers for $\kappa_{\text{out}} = 1$ in contrast to the claim otherwise [84]. For sufficiently large κ_{out} , for which τ/τ_0 is much larger than two, charged impurities tend to have the nature of long-range scatterers. Experiments under different dielectric environments were reported [85–87], but results vary among them and therefore seem to remain inconclusive yet.

2.5.4 Resonant Scattering by Lattice Defects

Direct and clear evidence for the presence of atomic defects in graphene layers, such as vacancies consisting of a single atom, two atoms adjacent to each other, etc., was experimentally demonstrated [88, 89]. Further, graphene is sensitive to adsorbed atoms partly because of their roles as strong scatterers as well as carrier doping [90–92]. The electron scattering by such localized defects with strong and short-range potential is quite interesting. In fact, the scattering of electrons by vacancies was studied in carbon nanotubes both in a tight-binding model and in an effective-mass approximation and was shown to depend critically on the difference in the number of vacancies at A and B sublattices when the strength of the potential is sufficiently large [93–98]. In nanotubes, resonance scattering by defects was experimentally observed [99–101] and various theoretical calculations based on first-principles [102–105] and tight-binding models [106, 107] were reported.

Effects of scattering by several closely located impurities with strong and short-range potential were theoretically studied recently [108]. It was shown that in a defect consisting of a single impurity, a quasi-bound state like a donor or acceptor state emerges near the Dirac point when the potential becomes extremely strong. In the case of AB pair impurities, the quasi-bound state splits into two and the resonance appears near the Dirac point for moderately strong scattering potential. In the case of defects consisting of many atoms, the number of resonances crossing $\varepsilon = 0$ when the potential strength is varied is that of AB pairs. Such resonance scattering can also be a candidate accounting for the experimental observation of the strong energy dependence of the conductivity in graphene.

Within a tight-binding model, a short-range impurity gives rise to change in local site energy u_0 measured from that of a carbon atom. This gives rise to a delta potential with strength $u = u_0\Omega_0$, where Ω_0 is the area of a unit cell. It is possible to calculate effective $\mathbf{k}\cdot\mathbf{p}$ Hamiltonian for such an impurity and formulate the calculation of scattering matrix T_S within the effective-mass scheme based on Green's function technique [108]. In the following, the scattering strength is represented by the effective scattering potential, V_S , giving the transport relaxation time τ , i.e.,

$$\begin{aligned} \frac{1}{\tau} &= \frac{2\pi}{\hbar} \frac{1}{2} \sum_{v,v'} \int \frac{d\mathbf{k}'}{(2\pi)^2} n_i |\langle v_s\mathbf{k} | T_S | v'_s\mathbf{k}' \rangle|_{\text{av}}^2 (1 - \cos\theta_{\mathbf{k},\mathbf{k}'}) \delta(\varepsilon_{s\mathbf{k}} - \varepsilon_{s\mathbf{k}'}) \\ &\equiv \frac{2\pi}{\hbar} n_i V_S^2 \frac{1}{2} \sum_{v,v'} \int \frac{d\mathbf{k}'}{(2\pi)^2} \delta(\varepsilon_{s\mathbf{k}} - \varepsilon_{s\mathbf{k}'}), \end{aligned} \quad (2.128)$$

where v and v' denote the K and K' points, n_i is the defect concentration, and $\theta_{\mathbf{k},\mathbf{k}'}$ is the angle between \mathbf{k} and \mathbf{k}' .

Figure 2.16 shows some examples of effective potential V_S of a defect consisting of a single A site as a function of energy for $u > 0$. Results for $u < 0$ are obtained by mirror reflection with respect to $\varepsilon = 0$. A strong repulsive and attractive short-range impurity causes the appearance of a virtual bound state and its energy is denoted by a downward arrow. Actual peaks in the effective potential are slightly shifted to the zero-energy side because of the large density of states except at the Dirac point. In the limit $u \rightarrow \infty$, the bound states moves to $\varepsilon = 0$ and the effective potential diverges there. In this case, we have $V_S^{-1} \sim (|\varepsilon|/2\pi\gamma^2) \ln|\varepsilon|$, giving $\sigma \propto |n_s|$ apart from weak logarithmic dependence.

Figure 2.17 shows V_S of defect A_1B_1 consisting of a pair of neighboring A and B sites. Because of large splitting of bonding and antibonding combinations of bound states, the energy of antibonding state can lie close to the zero energy even for moderate values of u . Figure 2.17(a) shows that this state crosses the Dirac point at $u/\gamma_0\Omega_0 \approx 2.5$, where the scattering strength at the Dirac point diverges. With the further increase of u , the bound state goes into the conduction band and the scattering potential approaches a small value independent of u in the limit of infinitely large u .

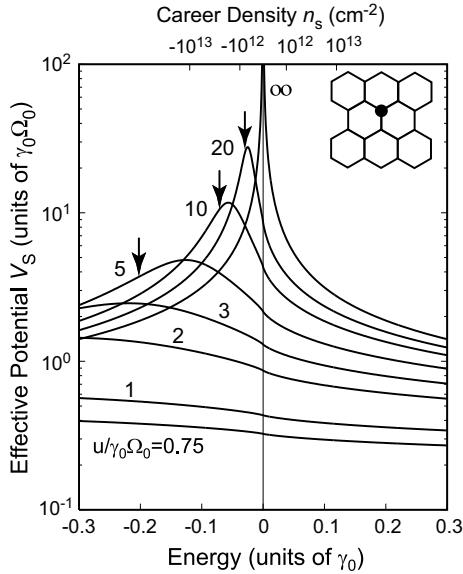


Figure 2.16 Some examples of effective potential V_S of defect A_1 as a function of energy for $u > 0$. The values of $u/\gamma_0\Omega_0$ are denoted in the figure. Results for $u < 0$ are obtained by mirror reflection with respect to $\varepsilon = 0$. The downward arrows indicate energy of a virtual bound state. A clear resonance enhancement becomes apparent for $u/\gamma_0\Omega_0 \gtrsim 10$. After Ref. [108].

Both analytic and numerical calculations for defect $A_n B_m$ ($n \geq m \geq 0$) show the following: (i) The number of bound states that cross the Dirac point for moderate values of u is given by that of AB pairs, i.e., given by m . (ii) In the limit of sufficiently large u , energy of some bound states approaches the Dirac point unless $n = m$. For $n = m$, V_S approaches a small value independent of u and almost independent of energy. These conclusions can be confirmed in Fig. 2.18, which shows V_S of various defects as a function of the potential strength at the Dirac point.

2.5.5 Crossover between Localization and Antilocalization

In the presence of strong disorder, states are known to be localized and the conductivity vanishes at zero temperature. Because of the

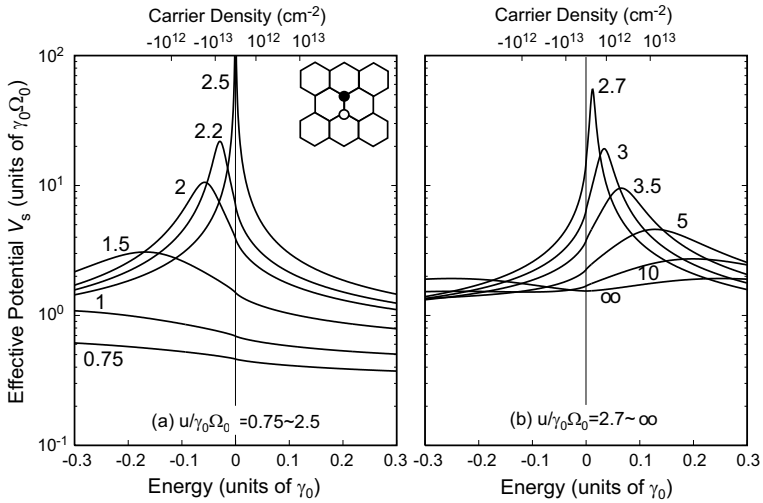


Figure 2.17 Some examples of V_S of defect A_1B_1 consisting of a pair of neighboring A and B sites. Divergent scattering occurs around $u/\gamma_0 \Omega_0 \approx 2.5$ for which the antibonding resonance state crosses the Dirac point. After Ref. [108].

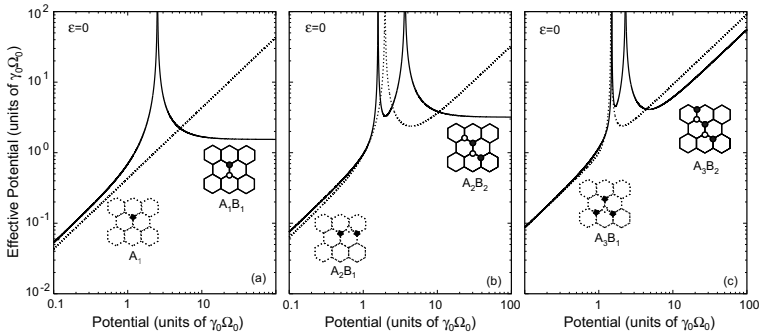


Figure 2.18 Some examples of V_S of various defects as a function of the potential strength at the Dirac point. After Ref. [108].

disorder, various spatial symmetries are all destroyed and only the symmetry related to time reversal may survive. The localization effect is known to vary strongly depending of this remaining

symmetry. The symmetry plays decisive roles in two dimensional systems, which are critical in localization according to scaling theory.

The Weyl equation (2.17) is invariant under a special time reversal operation S ,

$$\mathbf{F}^S = K \mathbf{F}^*, \quad (2.129)$$

where \mathbf{F}^* represents the complex conjugate of the wave function \mathbf{F} and K is an anti-unitary matrix $K = -i\sigma_y$ satisfying $K^2 = -1$. The corresponding operation for an operator P is given by $P^S = K {}^t P K^{-1}$, where ${}^t P$ stands for the transpose of P . This corresponds to the time reversal in systems with spin-orbit interaction and leads to

$$\mathbf{F}^{S^2} \equiv (\mathbf{F}^S)^S = -\mathbf{F}. \quad (2.130)$$

The system belongs to the symplectic universality class when only S constitutes a relevant symmetry [109].

This symmetry prevails even in the presence of impurities unless their potential range is smaller than the lattice constant a . In fact, for such scatterers, the effective potential is the same for the A and B sites and does not cause any mixing between the K and K' points. In this case a quantum correction or a weak-localization correction to the Boltzmann conductivity becomes positive and diverges logarithmically [29]. This so-called antilocalization behavior is the same as that appears in systems with strong spin-orbit interaction.

The operation S is not the real time reversal in graphene. Actually, the Bloch functions at the K and K' points are mutually complex conjugate, and therefore the K point is converted into the K' point and the K' point into the K point under the real time reversal. In the present $\mathbf{k}\cdot\mathbf{p}$ scheme, this operation T is expressed as

$$\mathbf{F}_K^T = e^{-i\psi} \sigma_z \mathbf{F}_{K'}^*, \quad \mathbf{F}_{K'}^T = e^{-i\psi} \sigma_z \mathbf{F}_K^*, \quad (2.131)$$

where ψ is an arbitrary phase factor and \mathbf{F}_K and $\mathbf{F}_{K'}$ are the wave functions at the K and K' points, respectively. This immediately gives

$$\mathbf{F}_K^{T^2} \equiv (\mathbf{F}_K^T)^T = \mathbf{F}_K, \quad \mathbf{F}_{K'}^{T^2} \equiv (\mathbf{F}_{K'}^T)^T = \mathbf{F}_{K'}, \quad (2.132)$$

characteristic of the conventional orthogonal symmetry. When we can neglect mixing between the K and K' points and confine

ourselves to states in each valley, however, the T symmetry is irrelevant and the special S symmetry becomes relevant. In the presence of short-range scatterers causing mixing between K and K' points, the S symmetry is violated, but the T symmetry prevails. As a result, the system now belongs to the orthogonal class [29, 110].

The actual equi-energy line deviates from the circle and has trigonal warping when the energy becomes nonzero. This effect can be included by a higher order $\mathbf{k} \cdot \mathbf{p}$ term. For the K point it is given by

$$\mathcal{H}_1 = \gamma \begin{pmatrix} 0 & h_1(\hat{k}_x, \hat{k}_y) \\ h_1(\hat{k}_x, \hat{k}_y)^\dagger & 0 \end{pmatrix}, \quad h_1(\hat{k}_x, \hat{k}_y) = \beta \frac{a}{4\sqrt{3}} (\hat{k}_x + i\hat{k}_y)^2, \quad (2.133)$$

where β is a constant of the order of unity. This higher order term gives rise to a trigonal warping of the dispersion. This expression with $\beta = 1$ has been derived from a nearest-neighbor tight-binding model [111] but is much more general if we regard β as an adjustable parameter. In the presence of \mathcal{H}_1 , the special time reversal symmetry is destroyed because $\mathcal{H}_1^S = -\mathcal{H}_1$ [112]. As a result, the system now belongs to the unitary class. For the K' point, the effective Hamiltonian is obtained by the replacement of h_1 by $-h_1^\dagger$. It should be noted also that the presence of lattice strain gives rise to an effective vector potential as will be shown in the next section and therefore destroys the S symmetry. A nonzero curvature also gives rise to an effective vector potential and destroys the S symmetry [16, 113].

The time reversal symmetry is known to manifest itself as a quantum correction to the conductivity. If the system has the S symmetry, quantum correction $\Delta\sigma$ given by so-called maximally crossed diagrams exhibits an antilocalization behavior, i.e., the conductivity increases logarithmically with the decrease of the temperature. If the system has only T symmetry, $\Delta\sigma$ exhibits a weak-localization behavior and the conductivity decreases logarithmically with the temperature decrease. The crossover between the weak- and antilocalization behavior caused by short-range scatterers was demonstrated [29] and the crossover between negative and positive magnetoresistance was predicted [30]. A peculiar behavior of the magnetoresistance was experimentally observed [114–118].

2.6 Phonons and Electron–Phonon Interaction

2.6.1 Acoustic Phonon

Acoustic phonons important in the electron scattering are described well by a continuum model [119]. The potential-energy functional for displacement $\mathbf{u} = (u_x, u_y)$ is written as

$$U[\mathbf{u}] = \int dx dy \frac{1}{2} \left(B(u_{xx} + u_{yy})^2 + \mu [(u_{xx} - u_{yy})^2 + 4u_{xy}^2] \right), \quad (2.134)$$

$$u_{xx} = \frac{\partial u_x}{\partial x}, \quad u_{yy} = \frac{\partial u_y}{\partial y}, \quad 2u_{xy} = \frac{\partial u_x}{\partial y} + \frac{\partial u_y}{\partial x}, \quad (2.135)$$

as in a homogeneous and isotropic two-dimensional system. The parameters B and μ denote the bulk modulus and the shear modulus, respectively ($B = \lambda + \mu$ with λ and μ being Lamé's constants). The corresponding kinetic energy is written as

$$K[\mathbf{u}] = \int dx dy \frac{\rho}{2} (\dot{u}_x^2 + \dot{u}_y^2), \quad (2.136)$$

where ρ is the mass density given by the carbon mass per unit area, $\rho = 3.80 \times 10^{-7} \text{ kg/m}^2$.

The corresponding equations of motion are given by

$$\begin{aligned} \rho \ddot{u}_x &= (B + \mu) \frac{\partial^2 u_x}{\partial x^2} + \mu \frac{\partial^2 u_x}{\partial y^2} + B \frac{\partial^2 u_y}{\partial x \partial y}, \\ \rho \ddot{u}_y &= B \frac{\partial^2 u_x}{\partial x \partial y} + (B + \mu) \frac{\partial^2 u_y}{\partial x^2} + \mu \frac{\partial^2 u_y}{\partial y^2}. \end{aligned} \quad (2.137)$$

These give a transverse mode with frequency $\omega_T(q)$ and a longitudinal mode with frequency $\omega_L(q)$, where

$$\begin{aligned} \omega_T(q) &= v_T q, \quad v_T = \sqrt{\frac{\mu}{\rho}}, \\ \omega_L(q) &= v_L q, \quad v_L = \sqrt{\frac{B + \mu}{\rho}}, \end{aligned} \quad (2.138)$$

A long-wavelength acoustic phonon gives rise to an effective potential called the deformation potential

$$V_1 = g_1(u_{xx} + u_{yy}), \quad (2.139)$$

proportional to a local dilation, where g_1 is of the order of the Fermi level measured from the bottom of the σ bands, i.e., $g_1 \sim 30$ eV. This term appears as a diagonal term in the matrix Hamiltonian in the effective-mass approximation and cannot give rise to backscattering in metallic nanotubes. A higher order term appears due to the modification of local bond length,

$$V_2 = g_2 e^{3i\eta} (u_{xx} - u_{yy} + 2iu_{xy}), \quad (2.140)$$

where η is the chiral angle in nanotubes and vanishes in graphene, and $g_2 \sim \gamma_0/2$ or $g_2 \sim 1.5$ eV, which is much smaller than the deformation potential constant g_1 . This term appears as an off-diagonal term. The total Hamiltonian is written as

$$\mathcal{H}'_K = \begin{pmatrix} V_1 & V_2 \\ V_2^* & V_1 \end{pmatrix}, \quad \mathcal{H}'_{K'} = \begin{pmatrix} V_1 & -V_2^* \\ -V_2 & V_1 \end{pmatrix}. \quad (2.141)$$

2.6.2 Optical Phonon

Long-wavelength optical phonons are known to be measured directly by the Raman scattering [120–122]. Usually, they are described perfectly well in a continuum model. Such a model was developed and the Hamiltonian for electron–phonon interactions was derived [123], and effects of electron–phonon interaction on optical phonons were recently studied in graphene [124, 125].

Optical phonons are represented by the relative displacement of two sub-lattice atoms A and B,

$$\mathbf{u}(\mathbf{r}) = \sum_{\mathbf{q}, \mu} \sqrt{\frac{\hbar}{2NM\omega_0}} (b_{\mathbf{q}\mu} + b_{-\mathbf{q}\mu}^\dagger) \mathbf{e}_\mu(\mathbf{q}) e^{i\mathbf{q}\cdot\mathbf{r}}, \quad (2.142)$$

where N is the number of unit cells, M is the mass of a carbon atom, ω_0 is the phonon frequency at the Γ point, $\mathbf{q} = (q_x, q_y)$ is the wave vector, μ denotes the modes ('t' for transverse and 'l' for longitudinal), and $b_{\mathbf{q}\mu}^\dagger$ and $b_{\mathbf{q}\mu}$ are the creation and destruction operators, respectively. Define $q_x = q \cos \varphi_{\mathbf{q}}$ and $q_y = q \sin \varphi_{\mathbf{q}}$ with $q = |\mathbf{q}|$. Then, we have $\mathbf{e}_l(\mathbf{q}) = i(\cos \varphi_{\mathbf{q}}, \sin \varphi_{\mathbf{q}})$ and $\mathbf{e}_t(\mathbf{q}) = i(-\sin \varphi_{\mathbf{q}}, \cos \varphi_{\mathbf{q}})$.

The interaction between optical phonons and an electron in the vicinity of the K and K' points is given by [123]

$$\mathcal{H}_{\text{int}}^K = -\sqrt{2} \frac{\beta_{\Gamma\gamma}}{b^2} \vec{\sigma} \times \mathbf{u}(\mathbf{r}), \quad \mathcal{H}_{\text{int}}^{K'} = +\sqrt{2} \frac{\beta_{\Gamma\gamma}}{b^2} \vec{\sigma} \times \mathbf{u}(\mathbf{r}), \quad (2.143)$$

where the product for vectors $\mathbf{a} = (a_x, a_y)$ and $\mathbf{b} = (b_x, b_y)$ in two dimension is defined by $\mathbf{a} \times \mathbf{b} = a_x b_y - a_y b_x$, b is the bond length ($b = a/\sqrt{3}$), and $\beta_\Gamma = -d \ln \gamma_0 / d \ln b = -(b/\gamma_0)(d\gamma_0/db)$ within a nearest-neighbor tight-binding model. Usually, we expect $\beta_\Gamma \sim 2$. This means that the lattice distortion gives rise to a shift in the origin of the wave vector or an effective vector potential, i.e., u_x in the y direction and u_y in the x direction. The interaction strength is characterized by the dimensionless coupling parameter

$$\lambda_\Gamma = \frac{36\sqrt{3}}{\pi} \frac{\hbar^2}{2M a^2} \frac{1}{\hbar\omega_0} \left(\frac{\beta_\Gamma}{2}\right)^2. \quad (2.144)$$

For $M = 1.993 \times 10^{-23}$ g and $\hbar\omega_0 = 0.196$ eV [126], we have $\lambda_\Gamma \approx 3 \times 10^{-3}(\beta_\Gamma/2)^2$. This shows that the interaction is not strong and therefore the lowest order perturbation gives sufficiently accurate results.

The phonon Green's function is written as

$$D_\mu(\mathbf{q}, \omega) = \frac{2\hbar\omega_0}{(\hbar\omega)^2 - (\hbar\omega_0)^2 - 2\hbar\omega_0\Pi_\mu(\mathbf{q}, \omega)}. \quad (2.145)$$

The phonon frequency is determined by the pole of $D_\mu(\mathbf{q}, \omega)$. In the case of weak interaction, the shift of the phonon frequency, $\Delta\omega_\mu$, and the broadening, Γ_μ , are given by

$$\Delta\omega_\mu = \frac{1}{\hbar} \text{Re} \Pi_\mu(\mathbf{q}, \omega_0), \quad \Gamma_\mu = -\frac{1}{\hbar} \text{Im} \Pi_\mu(\mathbf{q}, \omega_0). \quad (2.146)$$

When we calculate the self-energy of optical phonons starting with the known phonon modes in graphene, its direct evaluation causes a problem of double counting [127]. In fact, if we apply the above formula to the case of vanishing Fermi energy, we get the frequency shift due to virtual excitations of all electrons in the π bands. However, this contribution is already included in the definition of the frequency ω_0 . In order to avoid such a problem, we have to subtract the contribution in the undoped graphene for $\omega = 0$ corresponding to the adiabatic approximation.

Figure 2.19 shows the frequency shift and broadening for various values of $1/\omega_0\tau$ and an example of the spectral function,

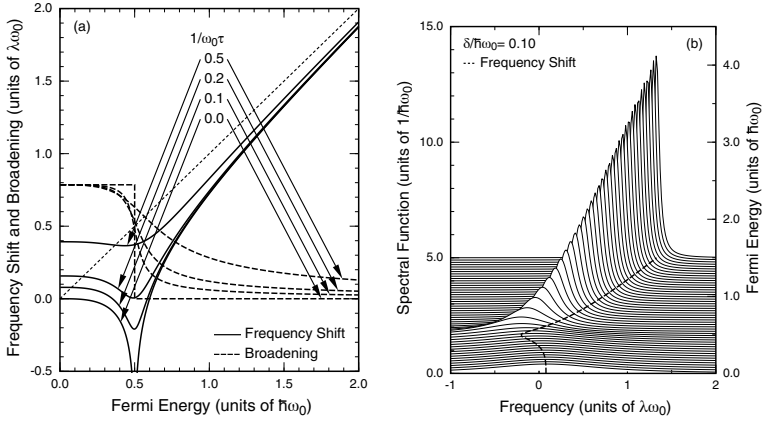


Figure 2.19 (a) The frequency shift and broadening of optical phonons in monolayer graphene as a function of the Fermi energy. τ is a phenomenological relaxation time characterizing the level broadening effect due to disorder. (b) Calculated spectral function of optical phonon for varying Fermi energy. After Ref. [124].

$(-1/\pi)\text{Im}D(q, \omega_0)$ [124]. For nonzero δ or $1/\omega_0\tau$, the logarithmic singularity of the frequency shift and the sharp drop in the broadening disappear, but the corresponding features remain for $1/\omega_0\tau \ll 1$. Similar results were reported independently [128] and experiments giving qualitatively similar results were reported [129–131].

The calculation can easily be extended to the case in the presence of magnetic field B , where discrete Landau levels are formed and oscillations due to resonant interactions appear in the frequency shift and the broadening [125, 132]. Figure 2.20 shows calculated frequency shift and broadening when $\varepsilon_F^0/\hbar\omega_0 = 1/4$ and the corresponding phonon spectral function, where ε_F^0 is the Fermi energy in the absence of a magnetic field. All resonant transitions from $-n$ to $n+1$ and from $-n-1$ to n with $n > 0$ appear at the field where their energy difference becomes equal to $\hbar\omega_0$. At resonances, the phonon spectrum exhibits characteristic behavior. Recently this magneto-phonon resonance was observed in Raman experiments [133].

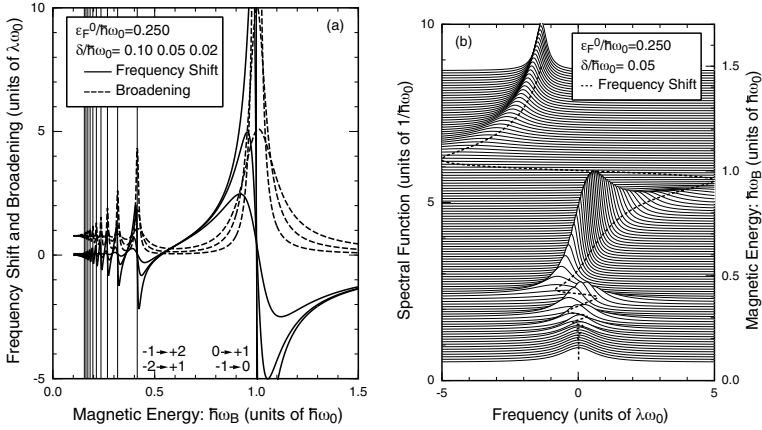


Figure 2.20 (a) The frequency shift and broadening of optical phonons in monolayer graphene as a function of effective magnetic energy $\hbar\omega_B$. Thin vertical lines show resonance magnetic fields. $\varepsilon_F^0/\hbar\omega_0 = 1/4$. The results for $\delta/\hbar\omega_0 = 0.1, 0.05, \text{ and } 0.02$ are shown. (b) The phonon spectral function for $\varepsilon_F^0/\hbar\omega_0 = 1/4$ and $\delta/\hbar\omega_0 = 0.05$. The dotted line shows the peak position as a function of $\hbar\omega_B$. After Ref. [125].

2.6.3 Zone-Boundary Phonon

Phonons near the K and K' points, called zone-boundary phonons, can play important roles in intervalley scattering between the K and K' points. In general, there exist four independent eigen modes for each wave vector. However, after straightforward calculations, we can see that only one mode with the highest frequency contributes to the electron-phonon interaction [134]. This mode is known as a Kekulé type distortion generating only bond-length changes. The interaction Hamiltonian is given by

$$\mathcal{H}_{\text{int}} = 2 \frac{\beta_K \gamma}{b^2} \begin{pmatrix} 0 & \omega^{-1} \Delta(\mathbf{r}) \sigma_y \\ \omega \Delta^\dagger(\mathbf{r}) \sigma_y & 0 \end{pmatrix}, \quad (2.147)$$

where $\omega = e^{2\pi i/3}$ and β_K is another appropriate parameter, which is equal to β_Γ for the tight-binding model. In the second quantized form,

$$\Delta(\mathbf{r}) = \sum_{\mathbf{q}} \sqrt{\frac{\hbar}{2NM\omega_K}} (b_{K\mathbf{q}} + b_{K'-\mathbf{q}}^\dagger) e^{i\mathbf{q}\cdot\mathbf{r}}, \quad (2.148)$$

where ω_K is the frequency of the Kekulé mode. It is worth noting that $\Delta(\mathbf{r})$ cannot be given by a simple summation over the K and K' modes. We should take a proper linear combination of the K and K' modes in order to make the lattice displacement a real variable. We can easily understand the operator form of $\Delta(\mathbf{r})$ and $\Delta(\mathbf{r})^\dagger$ in the interaction Hamiltonian by considering the momentum conservation with the fact that $2\mathbf{K} - \mathbf{K}'$ and $\mathbf{K} - 2\mathbf{K}'$ are reciprocal lattice vectors, where \mathbf{K} and \mathbf{K}' are the wave vectors at the K and K' point. The dimensionless coupling parameter, λ_K , is given by the same expression as Eq. (2.144) except that ω_0 is replaced with ω_K and β_Γ with β_K . For $\hbar\omega_K = 161.2$ meV, we have $\lambda_K = 3.5 \times 10^{-3}(\beta_K/2)^2$.

The lifetime of an electron with energy ε is given by the scattering probability from the initial state to possible final states via emission and absorption of one phonon. For the zone-center phonon, the summation of the contributions of longitudinal and transverse modes gives isotropic scattering probability in each of the K and K' points. For the zone-boundary phonon, any scattering processes are classified into two types: One is the transition between “one K-electron with one K-phonon” and “one K'-electron,” and the other is between “one K-electron” and “one K'-electron with one K'-phonon.” For example, an electron around the K point can be scattered to the K' point accompanied by absorption of one phonon around the K point, and this belongs to the former process. The electron scattering from the K to K' point can also be induced by the emission of one phonon around the K' point, while this is classified into the latter one.

In graphene, the calculated scattering probabilities for both phonons are given by the same formula,

$$\frac{\hbar}{\tau} = \pi\lambda_\alpha|\varepsilon - \hbar\omega_\alpha|. \quad (2.149)$$

where α represents Γ or K and we have neglected the phonon occupation due to large ω_α at room temperature. This simply shows that the electron lifetime is inversely proportional to the coupling parameter λ_α and to the density of states at the energy of the final state. What should be stressed here is that the phonon emission is possible only when the energy of the initial electron is larger than that of the phonon to be emitted. Otherwise, the

final states are fully occupied at zero temperature and the phonon emission never takes place. In this sense, the zone-boundary phonon has another advantage over the zone-center phonon. Therefore, the zone-boundary phonon gives dominant scattering for high-field transport in graphene and in nanotube owing to its smaller frequency and larger coupling constant. It also plays a dominant role in oscillatory magnetophonon resonance appearing in the conductivity in magnetic fields at high temperatures [135].

2.7 Bilayer Graphene

2.7.1 Electronic States

We consider a bilayer graphene that is arranged in the AB (Bernal) stacking as shown in Fig. 2.21. The upper layer is denoted as 1 and the lower layer denoted as 2. In each layer, the unit cell contains two carbon atoms denoted by A_1 and B_1 in layer 1 and A_2 and B_2 in layer 2. For the interlayer coupling, we include only the coupling between vertically neighboring atoms. Then, electronic states are described by the $\mathbf{k}\cdot\mathbf{p}$ Hamiltonian: [32, 33]

$$\mathcal{H} = \begin{pmatrix} A_1 & B_1 & A_2 & B_2 \\ 0 & \gamma\hat{k}_- & 0 & 0 \\ \gamma\hat{k}_+ & 0 & \Delta & 0 \\ 0 & \Delta & 0 & \gamma\hat{k}_- \\ 0 & 0 & \gamma\hat{k}_+ & 0 \end{pmatrix}, \quad (2.150)$$

where Δ ($= \gamma_1 \approx 0.4$ eV) [136] represents the interlayer coupling between sites B_1 and A_2 . We shall completely neglect coupling γ_3 between vertically neighboring atoms $A_1 \leftrightarrow B_2$ (see Fig. 2.21) and γ_4 giving coupling $A_1 \leftrightarrow A_2$ and $B_1 \leftrightarrow B_2$ as shown in Fig. 2.21(a). It is known that they do not play important roles [33, 125].

Let us define

$$\varepsilon(k) = \sqrt{\left(\frac{\Delta}{2}\right)^2 + (\gamma k)^2}, \quad \gamma k = \varepsilon(k) \sin \psi, \quad \frac{\Delta}{2} = \varepsilon(k) \cos \psi, \quad (2.151)$$

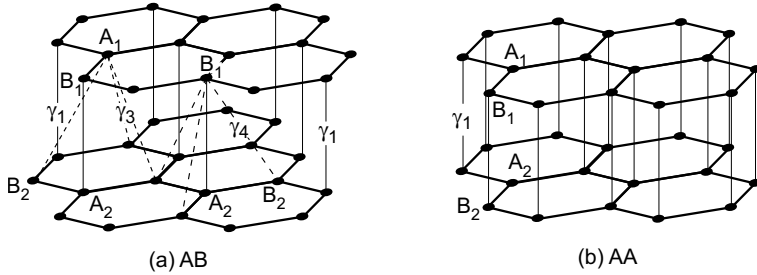


Figure 2.21 The lattice structure of a bilayer graphene. Some representative hopping integrals are shown. (a) Conventional graphene with AB stacking. (b) AA stacking.

where ψ vanishes for $k = 0$ and approaches $\pi/2$ with increasing k . Then, the eigen energies are given by

$$\varepsilon_{\pm 1}(k) = \pm 2\varepsilon(k) \sin^2(\psi/2), \quad \varepsilon_{\pm 2}(k) = \pm 2\varepsilon(k) \cos^2(\psi/2). \quad (2.152)$$

The band $\varepsilon_{+1}(k)$ represents the lowest conduction band that touches the highest valence band $\varepsilon_{-1}(k)$ at $k = 0$. The bands $\varepsilon_{\pm 2}(k)$ are the excited conduction and valence bands and $\varepsilon_{+2}(k) - \varepsilon_{+1}(k) = \Delta$ independent of k . In the vicinity of $\varepsilon = 0$, the Hamiltonian is reduced to the (2,2) form for the basis set $\{A_1, B_2\}$ [32, 33],

$$\mathcal{H} \approx \frac{\hbar^2}{2m^*} \begin{pmatrix} 0 & -\hat{k}_-^2 \\ -\hat{k}_+^2 & 0 \end{pmatrix}, \quad (2.153)$$

with

$$m^* = \frac{\hbar^2 \Delta}{2\gamma^2}. \quad (2.154)$$

We have the energy dispersion $\varepsilon(k) = \pm \hbar^2 k^2 / 2m^*$, giving the density of states $D(\varepsilon) = g_s g_v \Delta / 4\pi \gamma^2$. In the following, the energy bands are also denoted by integer $j = 1, \dots, 4$ in the order of increasing energy as well as by ± 1 and ± 2 .

One important feature is that the band structure can be strongly modified due to opening up of a bandgap by applied electric field [35, 137, 138]. Figure 2.22 shows a schematic illustration of the device structure, where eFd represents the potential difference between layers 1 and 2 (F is the effective electric field and $d = 0.334$ nm is

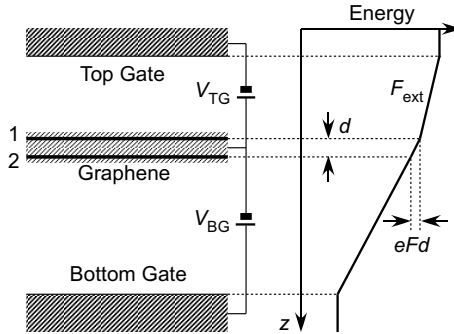


Figure 2.22 A schematic illustration of the bilayer graphene field-effect transistor with a top gate and a bottom gate and the potential energy diagram. The distance between the layers is given by d , the potential difference by eFd , and F_{ext} represents the field due to the top gate.

the interlayer distance). The effective Hamiltonian becomes

$$\mathcal{H} = \begin{pmatrix} eFd/2 & \gamma\hat{k}_- & 0 & 0 \\ \gamma\hat{k}_+ & eFd/2 & \Delta & 0 \\ 0 & \Delta & -eFd/2 & \gamma\hat{k}_- \\ 0 & 0 & \gamma\hat{k}_+ & -eFd/2 \end{pmatrix}. \quad (2.155)$$

In the vicinity of $\varepsilon = 0$, the Hamiltonian is reduced to the (2,2) form,

$$\mathcal{H} \approx \begin{pmatrix} \frac{1}{2}eFd\left(1 - \frac{2}{\Delta} \frac{\hbar^2 \hat{\mathbf{k}}_-^2}{2m^*}\right) & -\frac{\hbar^2 \hat{k}_-^2}{2m^*} \\ -\frac{\hbar^2 \hat{k}_+^2}{2m^*} & -\frac{1}{2}eFd\left(1 - \frac{2}{\Delta} \frac{\hbar^2 \hat{\mathbf{k}}_-^2}{2m^*}\right) \end{pmatrix}, \quad (2.156)$$

The corresponding energy bands are

$$\varepsilon_{\pm}(k) = \pm \sqrt{\frac{1}{4}(eFd)^2 \left(1 - \frac{2}{\Delta} \frac{\hbar^2 k^2}{2m^*}\right)^2 + \left(\frac{\hbar^2 k^2}{2m^*}\right)^2}. \quad (2.157)$$

In the region of small k satisfying $\hbar^2 k^2 / 2m^* \ll \Delta$, we have

$$\varepsilon_{\pm}(k) \approx \pm \frac{1}{2}eFd \left(1 - \frac{2}{\Delta} \frac{\hbar^2 k^2}{2m^*}\right), \quad (2.158)$$

showing that the lowest conduction band has its minima away from $k = 0$ [35]. Figure 2.23 shows the energy bands obtained by the diagonalization of this Hamiltonian. The bandgap appears and the minimum gap is located at a nonzero value of k depending on the field.

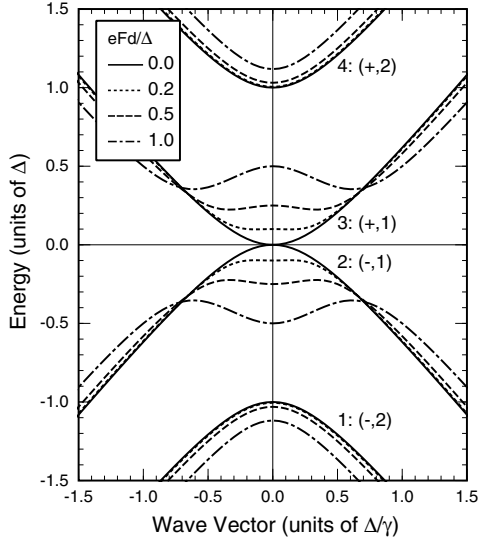


Figure 2.23 The energy dispersion for varying values of the potential difference eFd . The dot-dot-dashed lines show that of a monolayer graphene. After Ref. [138].

The effective field is determined in a self-consistent manner because the electron density distribution between two layers becomes different, giving rise to interlayer potential difference. Some examples of the results of such calculations are shown in Fig. 2.24 [138]. The unit $n_s^0 = g_v g_s \Delta^2 / 2\pi \gamma^2$ is the electron concentration at $\varepsilon_F = \Delta$ for $eFd = 0$. We have $n_s^0 \approx 2.5 \times 10^{13} \text{ cm}^{-2}$ for $\Delta \approx 0.4 \text{ eV}$. We can see eFd can become as large as $\sim \Delta/2$ although being dependent on $eF_{\text{ext}}d$, which represents the field due to an extra gate as shown in Fig. 2.22.

The structure of an AA stacked bilayer graphene is shown in Fig. 2.21(b). When we consider the strongest nearest-neighbor interlayer interaction, the Hamiltonian becomes

$$\hat{\mathcal{H}}_0 = \begin{pmatrix} A_1 & B_1 & A_2 & B_2 \\ +eFd/2 & \gamma \hat{k}_- & \Delta & 0 \\ \gamma \hat{k}_+ & +eFd/2 & 0 & \Delta \\ \Delta & 0 & -eFd/2 & \gamma \hat{k}_- \\ 0 & \Delta & \gamma \hat{k}_+ & -eFd/2 \end{pmatrix}. \quad (2.159)$$

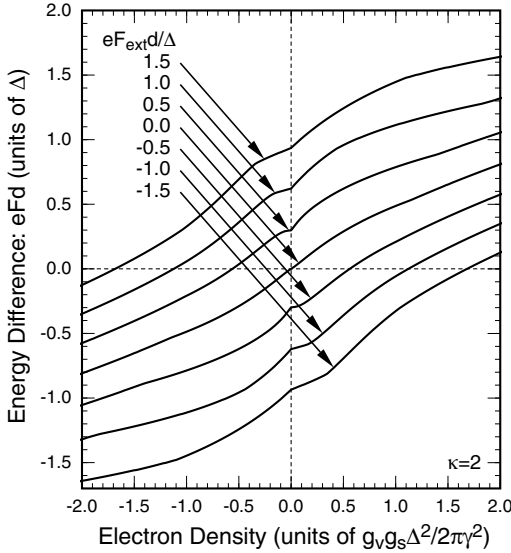


Figure 2.24 Calculated energy difference eFd as a function of the electron concentration for various values of $eF_{\text{ext}}d$. The static dielectric constant of the environment is chosen as $\kappa = 2$. After Ref. [138].

Let us define

$$\Delta = \tilde{\Delta} \sin \psi, \quad \frac{eFd}{2} = \tilde{\Delta} \cos \psi, \quad \tilde{\Delta} = \sqrt{\Delta^2 + \left(\frac{eFd}{2}\right)^2}, \quad (2.160)$$

and

$$V = \begin{pmatrix} \cos(\psi/2) & 0 & -\sin(\psi/2) & 0 \\ 0 & \cos(\psi/2) & 0 & -\sin(\psi/2) \\ \sin(\psi/2) & 0 & +\cos(\psi/2) & 0 \\ 0 & \sin(\psi/2) & 0 & +\cos(\psi/2) \end{pmatrix}. \quad (2.161)$$

Then, we have

$$V^{-1} \hat{\mathcal{H}}_0 V = \begin{pmatrix} \tilde{\Delta} & \gamma \hat{k}_- & 0 & 0 \\ \gamma \hat{k}_+ & \tilde{\Delta} & 0 & 0 \\ 0 & 0 & -\tilde{\Delta} & \gamma \hat{k}_- \\ 0 & 0 & \gamma \hat{k}_+ & -\tilde{\Delta} \end{pmatrix}. \quad (2.162)$$

This immediately shows that the band structure consists of two monolayer-like bands relatively shifted in energy by amount $\pm \tilde{\Delta}$. The presence of potential asymmetry between the top and bottom

layers does not cause significant change except for the increase in the relative shift of two monolayer bands.

2.7.2 Magnetic Properties

Let us consider first the symmetric bilayer graphene with AB stacking. The Landau level in the region $|\varepsilon| \ll \Delta$ in magnetic field B perpendicular to graphene can be calculated from the Hamiltonian (2.153) as [32]

$$\varepsilon_{sn} = s\hbar\omega_c \sqrt{n(n+1)}, \quad (n = 0, 1, \dots, s = \pm 1) \quad (2.163)$$

where $\omega_c = eB/m^*c$. We have doubly degenerate levels at zero energy ($n = 0$ and $s = \pm 1$), while the spacing gradually becomes constant as n goes higher. This degeneracy of the zero-energy Landau level also leads to logarithmic singularity of the magnetic susceptibility. In fact, in a manner similar to but more complicated than in the monolayer graphene, the susceptibility is calculated as

$$\chi = -\left(\frac{e\hbar}{2m^*}\right)^2 \frac{g_s g_v m^*}{2\pi \hbar^2} \int_{-\varepsilon_c}^{\varepsilon_c} \left(\ln \frac{\varepsilon_c}{|\varepsilon|} - 1\right) \left(-\frac{\partial f}{\partial \varepsilon}\right) d\varepsilon, \quad (2.164)$$

where ε_c is a cutoff energy of the order of Δ .

In order to show this logarithmic dependence intuitively, we expand the Landau level energy for large n as

$$\varepsilon_{sn} = s\hbar\omega_c \left[\left(n + \frac{1}{2}\right) - \frac{1}{8} \left(n + \frac{1}{2}\right)^{-1} + \dots \right], \quad (2.165)$$

where the first term gives the constant interval, and the second gives a shift toward zero energy, which is rewritten as $-(\hbar\omega_c)^2/(8\varepsilon_{sn})$. For $\varepsilon_F < 0$, for example, the change in the total energy due to the energy shift is calculated as

$$\Delta E = -\frac{g_s g_v m^*}{2\pi \hbar^2} \int_{-\varepsilon_c}^{\varepsilon_F} \frac{(\hbar\omega_c)^2}{8\varepsilon} d\varepsilon = \frac{B^2}{2} \frac{g_v g_s}{4\pi} \frac{e^2 \gamma^2}{\hbar^2 \Delta} \ln \frac{\varepsilon_c}{|\varepsilon_F|}, \quad (2.166)$$

giving the $\ln |\varepsilon_F|$ dependence of the susceptibility.

An analytic expression for the susceptibility for the full Hamiltonian (2.155) can be derived but will not be presented here because it is too complicated [22]. Figure 2.25 shows the density of states and the susceptibility for $eFd/\Delta = 0, 0.2, \text{ and } 0.5$. In the absence of gap, the susceptibility exhibits logarithmic divergence at zero energy. In the presence of a nonzero gap, this singularity is removed, but

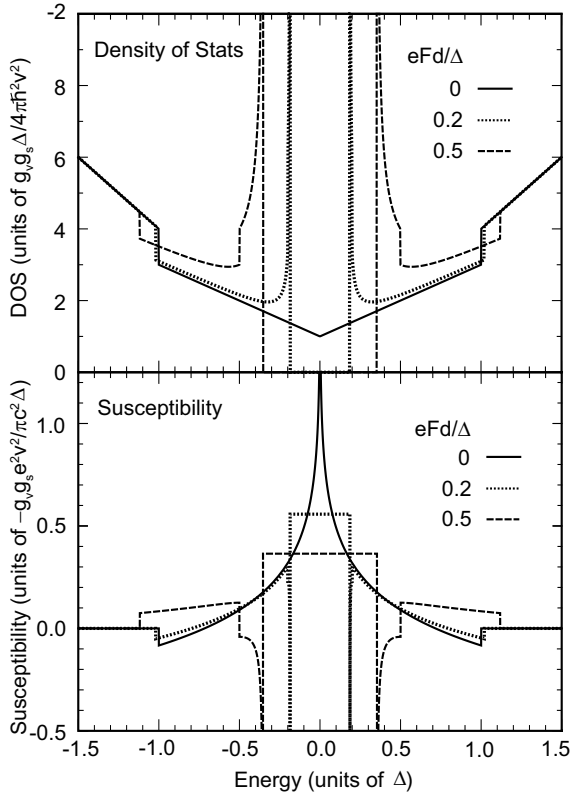


Figure 2.25 The density of states (upper panel) and susceptibility (lower panel) of bilayer graphenes with the asymmetry gap $eFd/\Delta = 0, 0.2,$ and 0.5 . The upward direction represents negative (i.e., diamagnetic) susceptibility. After Ref. [22].

the susceptibility is constant within the gap region together with singular paramagnetic susceptibility at the band edges.

2.7.3 Optical Properties

In bilayer graphene, optical absorption is possible in two different configurations, electric field of light parallel and perpendicular to the layer. It is straightforward to calculate the dynamical conductivity describing optical absorption for electric field parallel

to the layer [139, 140]. It is obtained by replacing σ_x with Σ_x in Eq. (2.86), where

$$\Sigma_x = \begin{pmatrix} 0 & 1 & 0 & 0 \\ 1 & 0 & 0 & 0 \\ 0 & 0 & 0 & 1 \\ 0 & 0 & 1 & 0 \end{pmatrix}. \quad (2.167)$$

The effective conductivity for perpendicular electric field is calculated as follows [140]: We apply external electric field $E_{\text{ext}}(\omega)e^{-i\omega t} + \text{c.c.}$ perpendicular to the layer, where ‘c.c.’ stands for complex conjugate. Let n_1 and n_2 be the electron density in layers 1 and 2, respectively, per unit area. The asymmetry in the density distribution $\Delta n(\omega)$ is defined as $\Delta n(\omega) = n_2(\omega) - n_1(\omega)$. This induces electric field

$$(-e)E_{\text{ind}}(\omega) = -\frac{4\pi e^2}{\kappa} \frac{\Delta n(\omega)}{2}, \quad (2.168)$$

in the region $-d/2 < z < +d/2$, where κ is the static dielectric constant of the environment.

We shall define the polarizability $\alpha(\omega)$ through

$$(-e)\frac{\Delta n(\omega)}{2} = \alpha(\omega)E_{\text{tot}}(\omega), \quad (2.169)$$

where $E_{\text{tot}}(\omega)e^{-i\omega t} + \text{c.c.}$ is the total electric field. Then, we have

$$(-e)E_{\text{tot}}(\omega) = (-e)E_{\text{ext}}(\omega) - \frac{4\pi e^2}{\kappa} \frac{\Delta n(\omega)}{2}, \quad (2.170)$$

giving

$$E_{\text{tot}}(\omega) = \frac{E_{\text{ext}}(\omega)}{\varepsilon(\omega)}, \quad (2.171)$$

$$\varepsilon(\omega) = 1 + \frac{4\pi}{\kappa}\alpha(\omega). \quad (2.172)$$

With the use of the equation of continuity, we have induced current

$$j(\omega) = -i\omega(-e)\frac{\Delta n(\omega)}{2} = \frac{1}{d}\sigma_{zz}(\omega)E_{\text{tot}}(\omega), \quad (2.173)$$

in the region $-d/2 < z < +d/2$, with two-dimensional conductivity

$$\sigma_{zz}(\omega) = -i\omega\alpha(\omega)d. \quad (2.174)$$

Then, we have

$$\varepsilon(\omega) = 1 + \frac{4\pi i}{\omega\kappa d} \sigma_{zz}(\omega), \quad (2.175)$$

$$j(\omega) = \frac{1}{d} \tilde{\sigma}_{zz}(\omega) E_{\text{ext}}(\omega), \quad (2.176)$$

with

$$\tilde{\sigma}_{zz}(\omega) = \frac{\sigma_{zz}(\omega)}{\varepsilon(\omega)}. \quad (2.177)$$

The power absorption per unit area is given by

$$P = \frac{d}{2} \text{Re} [j(\omega) E_{\text{tot}}(\omega)^*] = \frac{1}{2} \text{Re} \tilde{\sigma}_{zz}(\omega) |E_{\text{ext}}(\omega)|^2. \quad (2.178)$$

The dynamical conductivity can easily be calculated in a linear response theory. Define

$$\hat{\tau} = \begin{pmatrix} +1 & 0 & 0 & 0 \\ 0 & +1 & 0 & 0 \\ 0 & 0 & -1 & 0 \\ 0 & 0 & 0 & -1 \end{pmatrix}. \quad (2.179)$$

Then, we have

$$\sigma_{zz}(\omega) = i\omega e^2 d^2 \frac{g_s g_v}{4} \frac{1}{L^2} \sum_{\alpha, \beta} \frac{(f_\alpha - f_\beta) |\hat{\tau}_{\alpha\beta}|^2}{\varepsilon_\alpha - \varepsilon_\beta + \hbar\omega + i\delta}, \quad (2.180)$$

where α and β stand for a set of quantum numbers (j, \mathbf{k}) and $f_\alpha = f(\varepsilon_\alpha)$ is the Fermi distribution function. We have used the fact that both K and K' points give the same contribution. Explicitly, we have

$$\begin{aligned} \sigma_{zz}(\omega) &= i\omega e^2 d^2 \frac{g_s g_v}{4} \frac{1}{2\pi\gamma^2} \sum_{j, j'} \int_0^\infty \gamma^2 k dk g(\gamma k) \\ &\times \frac{[f(\varepsilon_{jk}) - f(\varepsilon_{j'k})] |\hat{\tau}_{jj'}(k)|^2}{\varepsilon_{jk} - \varepsilon_{j'k} + \hbar\omega + i\delta}. \end{aligned} \quad (2.181)$$

In the above, we have introduced cutoff function $g(\varepsilon)$ decaying rapidly for energy comparable to the half of the π -band width. The typical magnitude of the conductivity becomes

$$\sigma_1 = \frac{e^2}{\hbar} \frac{g_s g_v}{4} \frac{d^2}{2\pi\gamma^2} \Delta^2 \sim \frac{e^2}{\pi\hbar} \frac{g_s g_v}{4} \times 0.022, \quad (2.182)$$

where we have used $a = 2.46 \text{ \AA}$, $d = 3.34 \text{ \AA}$, $\Delta \approx 0.4 \text{ eV}$, and $\gamma_0 \approx 3 \text{ eV}$ in the last expression.

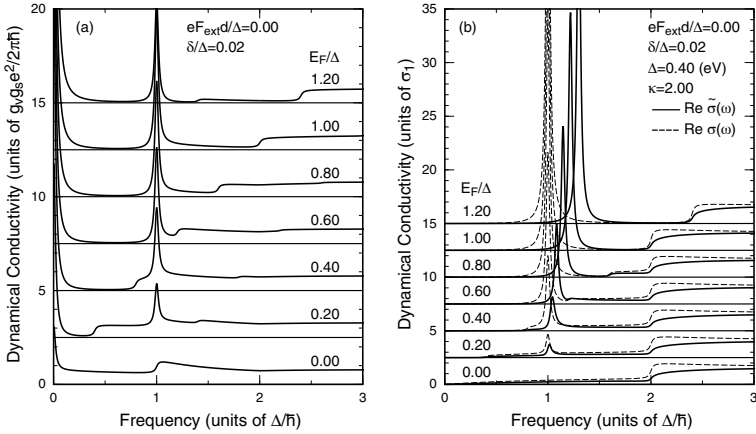


Figure 2.26 Calculated dynamical conductivity for (a) parallel and (b) perpendicular polarization in a symmetric bilayer graphene. The dashed lines in (a) represent $\sigma_{zz}(\omega)$ without depolarization effect and the solid lines $\tilde{\sigma}_{xx}(\omega)$ with depolarization effect. After Ref. [140].

Figure 2.26 shows some examples of calculated dynamical conductivity for (a) parallel and (b) perpendicular polarization in a symmetric case $eFd = 0$, with several values of the Fermi energy. The dashed lines in (b) represent $\sigma_{zz}(\omega)$ without depolarization effect and the solid lines $\tilde{\sigma}_{zz}(\omega)$ with depolarization effect. The dynamical conductivity for $\varepsilon_F = 0$ has essentially no prominent structure except a step-like increase corresponding to transitions from $(-, 1)$ to $(+, 2)$ [139]. In a symmetric bilayer, with increase in ε_F , a delta-function peak appears at $\hbar\omega = \Delta$ with intensity proportional to $|\varepsilon_F|$, corresponding to allowed transitions $(+, 1) \rightarrow (+, 2)$. For perpendicular polarization, this sharp peak is shifted to the higher energy side due to the depolarization effect. When the Fermi level reaches the bottom of band $(+, 2)$, this shift is as large as 30 %.

Figure 2.27 shows the dynamical conductivity for varying electron concentration n_s for $F_{\text{ext}} = 0$, i.e., when the bilayer is symmetric for $n_s = 0$ and the asymmetry potential eFd increases with the change of n_s . The energies where interband transitions start to appear are shown by thin dotted lines. For transitions from $(+, 1)$ to $(+, 2)$, i.e., $3 \rightarrow 4$, the upper edge

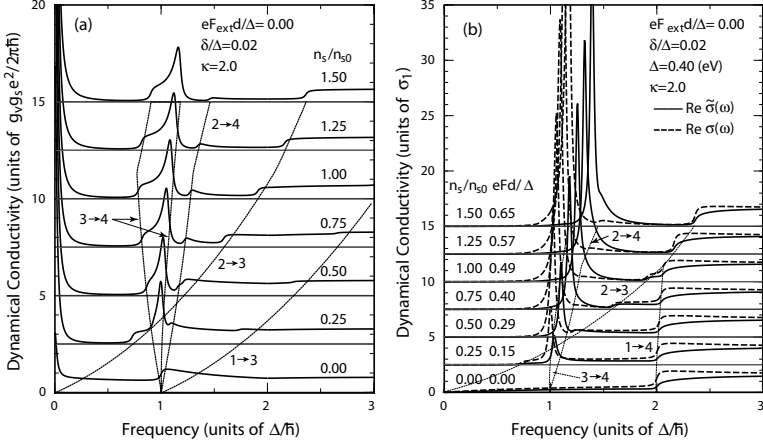


Figure 2.27 Calculated dynamical conductivity for parallel (a) and perpendicular (b) polarization for $eF_{\text{ext}}d = 0$. The potential difference between two layers, eFd/Δ , self-consistently determined is listed in the figure. Thin dotted lines denote edges of interband transitions ($j \rightarrow j'$ means those from band j to band j'). After Ref. [140].

where the transition disappears is also included. For the parallel polarization, the absorption corresponding to transitions $(+, 1) \rightarrow (+, 2)$ becomes broadened with increase of n_s due to the gap opening. For the perpendicular polarization, this broadening is not significant, because the resonance occurs at an energy higher than the interband continuum due to the depolarization effect. A weak structure appears near the line denoted as $2 \rightarrow 4$ with the increase of n_s . This corresponds to the transition from $(-, 1)$ to $(+, 2)$, which becomes allowed by the bandgap opening.

The strength of the absorption for the perpendicular polarization is determined by conductivity $\tilde{\sigma}_{zz}(\omega)$ of the order of σ_1 , while that for the parallel polarization by $\sigma_{xx}(\omega)$ of the order of $(g_v g_s e^2)/(4\pi\hbar)$. Because $\sigma_1 \sim 0.022 \times (g_v g_s e^2)/(4\pi\hbar)$, the absorption intensity for perpendicular polarization is much smaller. This smallness of $\tilde{\sigma}_{zz}(\omega)$ mainly comes from the fact that interlayer coupling γ_1 (~ 0.4 eV) is much smaller than intra-layer coupling γ_0 (~ 3 eV) in spite of the fact that interlayer separation d ($= 3.34$ Å) is not so much different from the intralayer lattice constant a ($= 2.46$ Å). The weak

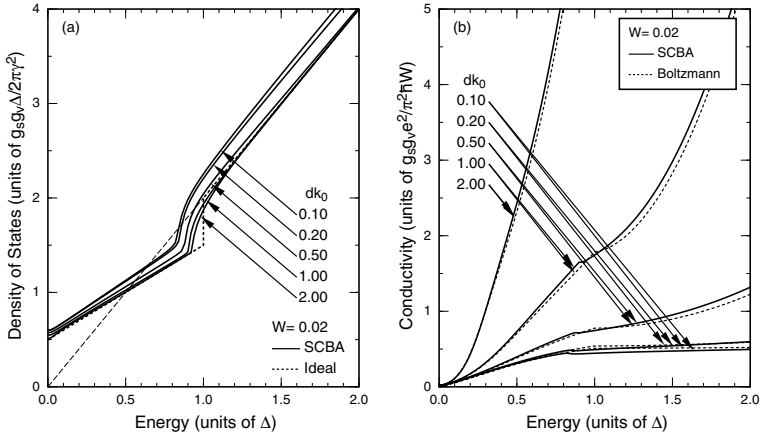


Figure 2.28 (a) Calculated density of states and (b) conductivity as a function of energy for scatterers with Gaussian potential with range d in units of $k_0 = \Delta/\gamma$ and dimensionless scattering strength $W = 0.02$. The dotted line in (a) represents the density of states of ideal bilayer graphene and the thin dashed line represents that of two independent monolayer graphenes. The dotted line in (b) shows the Boltzmann conductivity. After Ref. [141].

absorption intensity requires the use of bilayer graphene with large area.

2.7.4 Transport Properties

It is easy to theoretically formulate transport theory in bilayer graphene within the Boltzmann scheme. In the following, however, we shall exclusively discuss results obtained in the self-consistent Born approximation [141]. Figure 2.28 shows calculated (a) density of states and (b) conductivity as a function of energy for scatterers with a Gaussian potential with range d and for scattering strength $W = 0.1$. In Fig. 2.28(a) the dotted line represents the ideal density of states and the dashed line represents twice of that in monolayer graphene and in 2.28(b) the dotted lines represent the Boltzmann conductivity.

The density of states clearly shows that the energy region affected strongly by the presence of scatterers is limited to $|\varepsilon| \lesssim \gamma/d$

for small d such that $dk_0 \leq 0.2$, where $k_0 = \Delta/\gamma$. When the range becomes larger such that $dk_0 \geq 2$, the region affected by scatterers is separated into two, those close to zero energy and close to the bottom of the excited conduction band Δ . In fact, the excited conduction band has significant band tail due to disorder.

At zero energy, the Boltzmann conductivity vanishes due to the vanishing velocity. In the self-consistent Born approximation, the conductivity becomes close to the universal value obtained previously for short-range scatterers [33, 39]

$$\sigma_2 = \frac{g_s g_v e^2}{\pi^2 \hbar}, \quad (2.183)$$

which is twice as large as that in monolayer graphene [23], the universality of which remains as a hot topic [74–81]. It increases rapidly with energy, becoming larger than the Boltzmann conductivity at sufficiently high energy for long-range scatterers $dk_0 > 0.5$.

The conductivity exhibits a kink-like structure when the energy crosses the bottom of the excited conduction band. This behavior also seen in the Boltzmann conductivity arises due to sudden appearance of interband scattering, which is more dominant than the appearance of extra conductivity due to additional carriers in the excited conduction band. Apart from the difference in the kink position, the overall behavior of the conductivity is very close to that of the Boltzmann result. Interband matrix elements between the state $\mathbf{k} = 0$ at the bottom of the excited conduction band and those of the lowest conduction band vanish, and therefore the conductivity does not exhibit stronger step-like decrease at the band-crossing point.

Figure 2.29 shows the minimum conductivity at zero energy. For very short-range case $dk_0 < 1$, the conductivity is nearly independent of W and close to σ_2 . With the increase in the range, the conductivity increases with W , takes a maximum at a certain value of W and then starts to decrease. The value of W where the minimum conductivity becomes maximum increases with the range. This figure clearly shows that the conductivity at zero energy is not universal but depends on the degree of the disorder for scatterers with long-range potential. This situation is the same as in monolayer graphene [68].

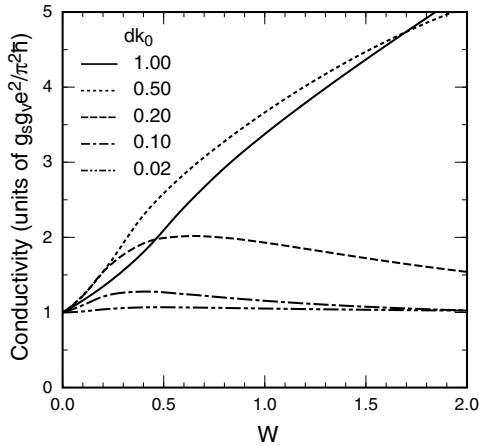


Figure 2.29 Calculated minimum conductivity at zero energy versus W for scatterers with Gaussian potential. After Ref. [141].

Calculations can also be performed for charged impurities within the Thomas–Fermi approximation for screening [141]. Figure 2.30 shows some examples of calculated (a) density of states and (b) conductivity. The density of states in the low-energy region becomes larger with the concentration of scatterers. Further, the excited conduction band has a long tail in the density of states, its amount being roughly proportional to the concentration.

The minimum conductivity at zero energy becomes slightly larger than the universal value given by Eq. (2.183) and increases with the impurity concentration. However, it approximately remains universal because the dependence on n_i is weak as shown in the inset of Fig. 2.30(b). When the energy exceeds the bottom of the excited conduction band, the Boltzmann conductivity exhibits a discrete jump. This jump is also present in the conductivity in the self-consistent Born approximation, although it is considerably smoothed out. This increase when the excited band is occupied comes from the sudden increase in the screening effect.

Figure 2.31 shows some examples for an asymmetric bilayer with nonzero gap. The density of states does not easily vanish and has low energy tail. This is partly due to the self-consistency between the screening constant and the density of states. In fact, smaller density

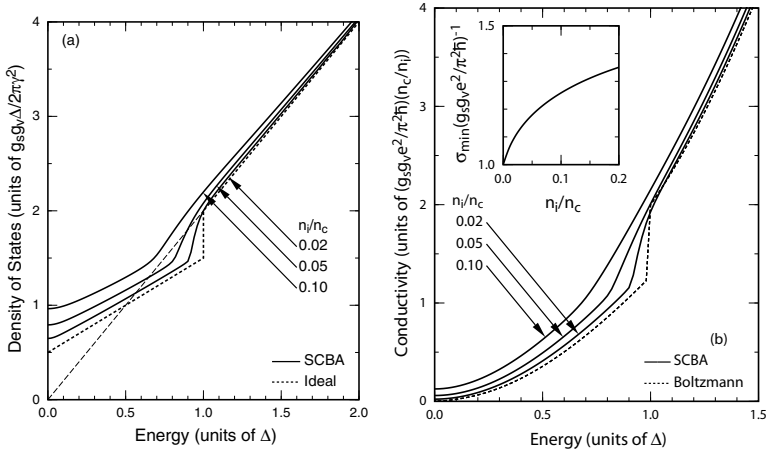


Figure 2.30 Density of states (a) and conductivity (b) versus the Fermi energy for charged scatterers screened in the Thomas–Fermi approximation, calculated in a self-consistent Born approximation. The inset in (b) shows the minimum conductivity versus the impurity concentration. After Ref. [141].

of states causes less screening and causes effectively large scattering strength giving rise to long tail in the density of states. In spite of the considerable density of states, the conductivity within the gap region is much smaller than that outside, in particular for large gap $eFd/\Delta = 1$.

Calculations can also be performed for bilayer graphene with AA stacking. Figure 2.32 shows some examples of calculated (a) density of states and (b) conductivity as a function of energy for symmetric bilayer $eFd = 0$ with AA stacking. Results for asymmetric bilayer can be obtained by replacing Δ with $\tilde{\Delta}$ given in Eq. (2.160). The density of states in the clean limit is independent of energy in the region given by $-\Delta < \varepsilon < +\Delta$ and starts to increase linearly outside this region, as shown by a dotted line in Fig. 2.32(a). In the presence of charged impurities, the density of states is enhanced symmetrically around $\pm\Delta$ corresponding to the Dirac points of the two bands given by Eq. (2.162). As a result, the total density of states is most strongly enhanced near zero energy.

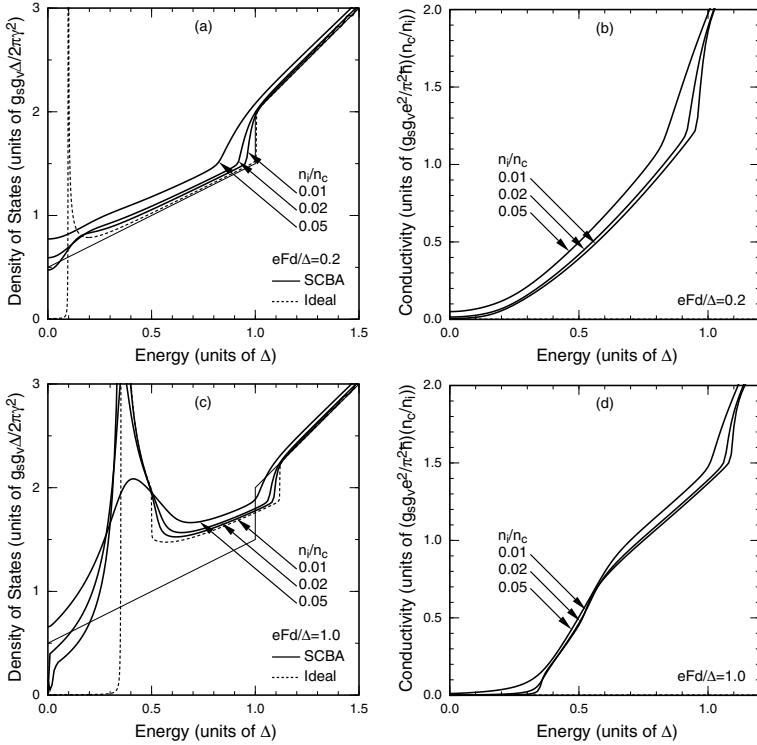


Figure 2.31 Calculated density of states (a) and (c), and conductivity (b) and (d) of asymmetric bilayer graphene. (a) and (b) $eFd/\Delta = 0.2$. (c) and (d) $eFd/\Delta = 1$. After Ref. [82].

For small impurity concentration $n_i/n_c = 0.05$, the conductivity exhibits a singularly sharp drop at $\pm\Delta$. This is a manifestation of the zero-mode anomaly appearing in the conductivity for short-range scatterers with strength independent of energy or electron concentration predicted previously [23], shown in Fig. 2.10. In fact, the screening effect is essentially independent of the energy in the vicinity of $\pm\Delta$ as shown in Fig. 2.32(a), making charged impurities effectively “short-range scatterers” with energy independent strength. Therefore, the zero-mode anomalies characteristic of massless Dirac electrons can be experimentally observed in an AA stacked bilayer graphene even if scattering is dominated by charged

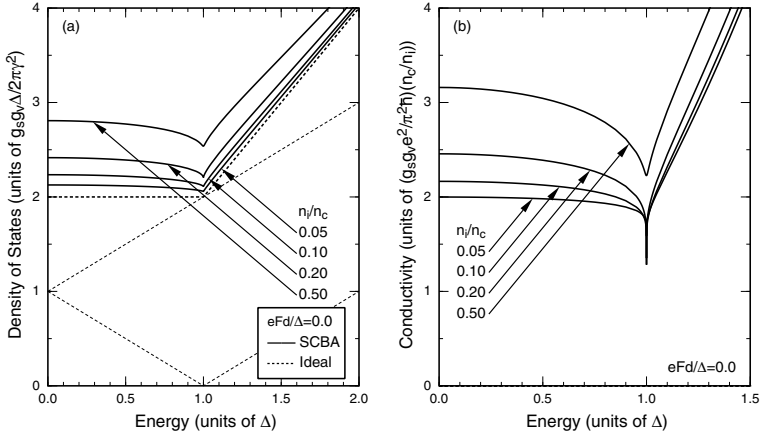


Figure 2.32 Calculated density of states (a) and conductivity (b) of AA-stacked bilayer graphene for charged impurities with screening effect being included within the Thomas–Fermi approximation. After Ref. [82].

impurities. In monolayer graphenes, this singularity is obscured by diverging scattering strength at the Dirac point.

2.7.5 Phonons and Electron–Phonon Interaction

When we neglect small interlayer coupling and interaction with electrons in the vicinity of the Fermi level, acoustic phonons in each layer are regarded as independent and the same as those in monolayer graphene. As a result, the interaction Hamiltonian in each layer is the same as in monolayer. The same is applicable to optical phonons and zone boundary phonons. Within such an approximation scheme, it is straightforward to make theoretical formulation on electron–phonon interactions. In the following, we shall consider interaction effects on optical phonons as an example.

In symmetric bilayer graphene, optical phonons are classified into symmetric and antisymmetric modes in which the displacement of the top and bottom layers are in-phase and out-of-phase, respectively. They are affected by electron–phonon interactions in a different manner [142]. The symmetric mode causes interband transitions between $\varepsilon_{\pm 1}(k)$ and therefore exhibits logarithmic singularity in a manner same as in monolayer graphene when $\varepsilon_F =$

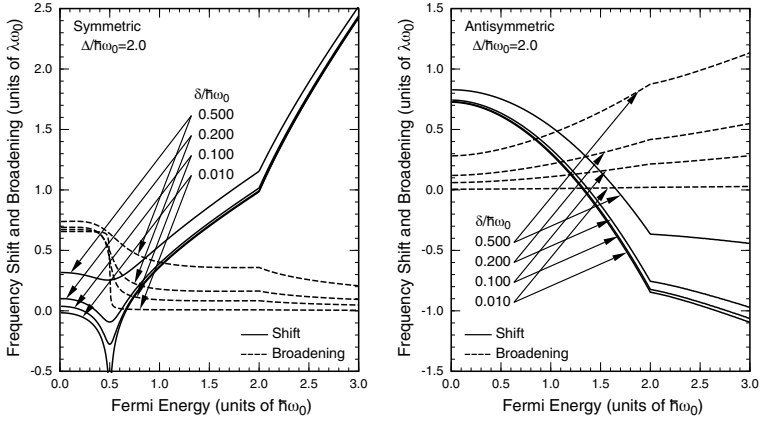


Figure 2.33 Some examples of calculated frequency shift and broadening of the symmetric (a) and antisymmetric mode (b) at the Γ point in a bilayer graphene. $\Delta/\hbar\omega_0 = 2$. The amount of the broadening due to disorder is denoted by δ . After Ref. [142].

$\hbar\omega_0/2$. On the other hand, this transition is not allowed for the antisymmetric mode, but interband transitions between $\varepsilon_{+1}(k)$ and $\varepsilon_{+2}(k)$ contribute to the phonon renormalization when band $\varepsilon_{+1}(k)$ is occupied by electrons.

Figure 2.33 shows calculated frequency shift and broadening for two phonon modes. For the symmetric mode, the shift increases almost linearly in the range $1/2 < \varepsilon_F/\hbar\omega_0 < 2$. Above $\varepsilon_F = \Delta$, corresponding to $\varepsilon_F/\hbar\omega_0 = 2$ for $\Delta/\hbar\omega_0 = 2$, the second conduction band is populated by electrons and the dependence on ε_F becomes steeper. For the antisymmetric mode, the frequency is enhanced from ω_0 of the mono-layer graphene at $\varepsilon_F = 0$ and the broadening is absent, because the contribution of interband transitions between the bands $\varepsilon_{\pm 1}(k)$ is suppressed. With the increase of ε_F interband transitions between $\varepsilon_{+1}(k)$ and $\varepsilon_{+2}(k)$ contribute to the self-energy and the frequency gradually decreases.

When the electron concentration is changed by a gate voltage, potential asymmetry is introduced, and as a result, the symmetric and antisymmetric modes are mixed with each other through electron-phonon interactions [138]. Figure 2.34 shows the frequency shift (top panel), broadening (middle panel), and the spectral intensity

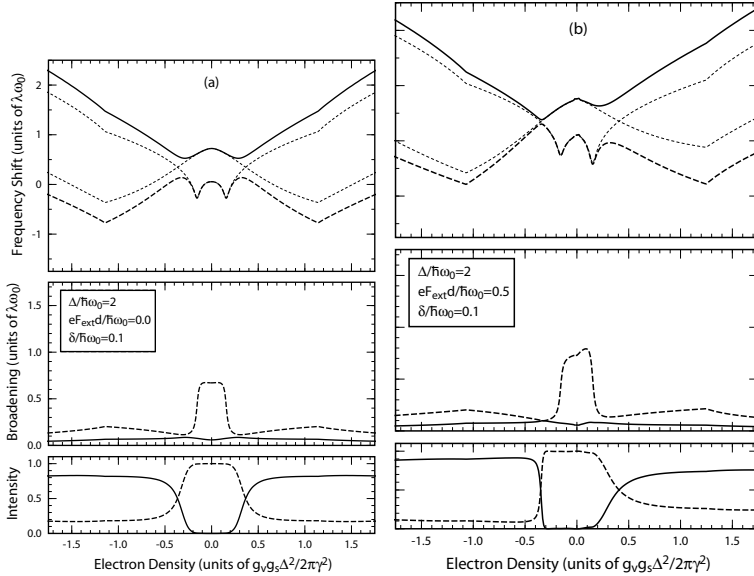


Figure 2.34 Calculated frequency shift, broadening, and strength of the symmetric component. The solid and dashed lines denote the high- and low-frequency modes, respectively. The thin dotted lines in the top panel show the frequencies for symmetric and antisymmetric modes calculated without inclusion of their mixing. $\Delta/\hbar\omega_0 = 2$. $\delta/\hbar\omega_0 = 0.1$. (a) $eF_{\text{ext}}d/\Delta = 0$ and (b) 0.5. After Ref. [138].

(bottom panel) of the symmetric component as a function of the electron concentration for $eF_{\text{ext}}d = 0$. We have assumed $\Delta/\hbar\omega_0 = 2$ corresponding to $\Delta \approx 0.4$ eV and $\hbar\omega_0 \approx 0.2$ eV and $\delta/\hbar\omega_0 = 0.1$. The symmetric component shown in the figure describes the relative intensity of the Raman scattering. At $n_s = 0$ with $eFd = 0$, the optical phonons are exactly classified into symmetric and antisymmetric modes. With the increase of n_s , they become mixed with each other, which becomes particularly important when they cross each other.

In the presence of nonzero external field as $eF_{\text{ext}}d/\hbar\omega_0 = 0.5$ as shown in Fig. 2.34(b), the results are asymmetric between positive and negative n_s . In fact, the intensity of the low-frequency mode is much stronger for $n_s > 0$ than for $n_s < 0$. The appearance of two peaks at sufficiently high electron concentration is in agreement

with that of recent experiments showing double peaks in a highly doped bilayer graphene [143–148]. In order to make detailed comparison with experiments, we may have to consider a small frequency splitting of symmetric and antisymmetric modes that is independent of the change in the electron concentration.

2.8 Multilayer Graphene

We consider a multilayer graphene composed of N graphene layers arranged in the AB (Bernal) stacking. For simplicity we include the nearest-neighbor intra-layer coupling parameter γ_0 and the interlayer coupling $\Delta = \gamma_1$ between A and B atoms located vertically with respect to the layer plane. We can show that the Hamiltonian of a multilayer graphene can be decomposed into those equivalent to monolayer or bilayer, which allows us to systematically study the dependence of various quantities on layer numbers [40–42]. This exact decomposition rule is not destroyed by the presence of next-nearest-neighbor interlayer coupling γ_3 causing trigonal warping of the bands.

Let $|A_j\rangle$ and $|B_j\rangle$ be the Bloch functions at the K point, corresponding to the A and B sublattices, respectively, of layer j . For convenience we divide carbon atoms into two groups as

$$\begin{aligned} \text{Group I: } & B_1, A_2, B_3, \dots \\ \text{Group II: } & A_1, B_2, A_3, \dots \end{aligned} \quad (2.184)$$

The atoms of group I are arranged along vertical columns normal to the layer plane, while those in group II are above or below the center of hexagons in the neighboring layers. If the basis is taken as $|A_1\rangle, |B_1\rangle; |A_2\rangle, |B_2\rangle; \dots; |A_N\rangle, |B_N\rangle$, the Hamiltonian for the multilayer graphene around the K point becomes

$$\mathcal{H} = \begin{pmatrix} H_0 & V & & & \\ V^\dagger & H_0 & V^\dagger & & \\ & V & H_0 & V & \\ & & \ddots & \ddots & \ddots \end{pmatrix}, \quad (2.185)$$

with

$$H_0 = \begin{pmatrix} 0 & \gamma \hat{k}_- \\ \gamma \hat{k}_+ & 0 \end{pmatrix}, \quad V = \begin{pmatrix} 0 & 0 \\ \Delta & 0 \end{pmatrix}. \quad (2.186)$$

The effective Hamiltonian for K' is obtained by exchanging \hat{k}_+ and \hat{k}_- .

The Hamiltonian (2.185) can be decomposed into smaller subsystems for the basis appropriately chosen [40, 41]. First, we define the orthonormal sets

$$\begin{aligned}\phi_l^{(1)} &= \psi_l^{(1)}|B_1\rangle + \psi_l^{(2)}|A_2\rangle + \psi_l^{(3)}|B_3\rangle + \dots, \\ \phi_l^{(II)} &= \psi_l^{(1)}|A_1\rangle + \psi_l^{(2)}|B_2\rangle + \psi_l^{(3)}|A_3\rangle + \dots,\end{aligned}\quad (2.187)$$

where

$$\begin{aligned}\psi_l^{(j)} &= \sqrt{\frac{2}{N+1}} \sin j\kappa_l, \quad \kappa_l = \frac{\pi}{2} - \frac{l\pi}{2(N+1)}, \\ l &= -(N-1), -(N-3), \dots, N-1.\end{aligned}\quad (2.188)$$

Here, l is an odd integer when N is even, while l is even when N is odd, and therefore $l = 0$ is allowed only for odd N .

Next, for $m > 0$, we take the basis

$$\begin{aligned}\left\{ (\phi_m^{(II)} + \phi_{-m}^{(II)})/\sqrt{2}, \quad (\phi_m^{(I)} + \phi_{-m}^{(I)})/\sqrt{2}, \right. \\ \left. (\phi_m^{(I)} - \phi_{-m}^{(I)})/\sqrt{2}, \quad (\phi_m^{(II)} - \phi_{-m}^{(II)})/\sqrt{2} \right\}.\end{aligned}\quad (2.189)$$

For $m = 0$, we take the basis $\{\phi_0^{(II)}, \phi_0^{(I)}\}$. Then, the Hamiltonian has no off-diagonal elements between different m 's. For $m > 0$, the sub-Hamiltonian becomes

$$\mathcal{H}_m = \begin{pmatrix} 0 & \gamma\hat{k}_- & 0 & 0 \\ \gamma\hat{k}_+ & 0 & \lambda_m\Delta & 0 \\ 0 & \lambda_m\Delta & 0 & \gamma\hat{k}_- \\ 0 & 0 & \gamma\hat{k}_+ & 0 \end{pmatrix}, \quad (2.190)$$

with

$$\lambda_m = 2 \cos \kappa_m, \quad (2.191)$$

which is equivalent to the Hamiltonian of bilayer graphene, while the interlayer coupling Δ is multiplied by λ_m . For $m = 0$, we have the Hamiltonian identical to that of the monolayer graphene. These subsystems are labeled as $m = 0, 2, 4, \dots, N-1$ for odd N and $m = 1, 3, 5, \dots, N-1$ for even N .

The eigenstate of a finite-layer graphene can be regarded as a part of a standing wave in bulk graphite, which is a superposition

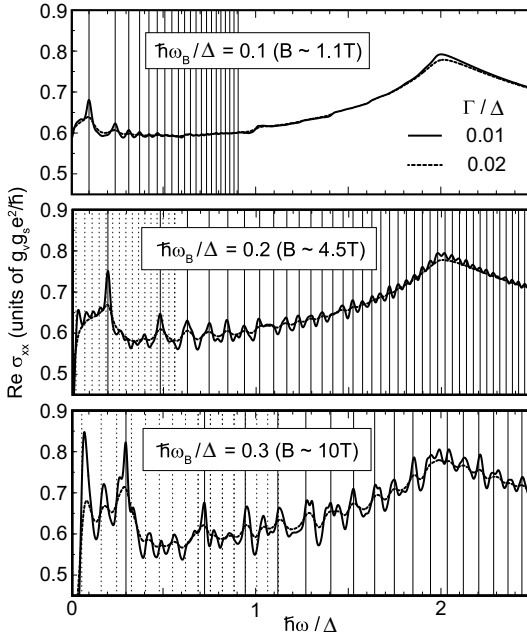


Figure 2.35 Examples of the real part of the dynamical conductivity averaged over the layer numbers from $N = 1$ to 20, for magnetic fields with $\hbar\omega_B/\Delta = 0.1, 0.2$ and 0.3 . Vertical solid and dashed lines represent transition energies for monolayer-type ($\kappa = \pi/2$) and bilayer-type ($\kappa = 0$) subbands, respectively. After Ref. [41].

of opposite traveling waves with $\pm k_z$. The quantity κ ($= \kappa_m$) in our representation corresponds to a wave number via $\kappa = |k_z|d$, where d is the interlayer distance. Thus the monolayer-type subband $\kappa = \pi/2$ is related to an H point in the Brillouin zone of graphite, while no states correspond to $k_z = 0$ since κ never becomes zero.

Thus, the Hamiltonian has been decomposed into those equivalent to the monolayer or bilayer bands. The monolayer-like band exists only in odd-layered graphenes, while the bilayer-like bands always exist. This decomposition can be used for the analysis of diamagnetic response of multilayer graphenes [40]. In fact, in odd-layered graphenes, the monolayer-like band gives a strong diamagnetic peak at $\varepsilon_F = 0$, while the bilayer-like bands

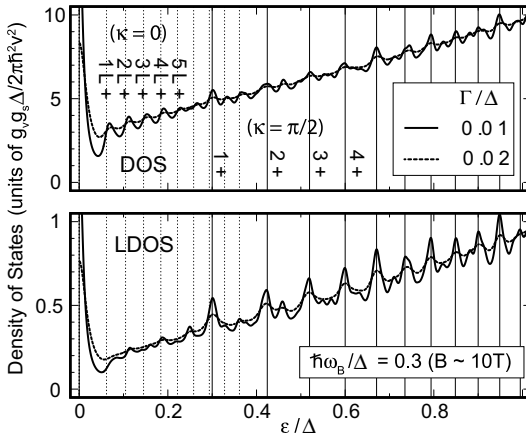


Figure 2.36 (Top) Density of states averaged over the layer numbers $N = 1$ to 20, at $\hbar\omega_B/\Delta = 0.3$. (Bottom) Corresponding plot for the local density of states on the top layer. Vertical solid and dashed lines indicate the ideal Landau level energies for the monolayer-type ($\kappa = \pi/2$) and the bilayer-type ($\kappa = 0$) subbands, respectively. After Ref. [41].

present a broad peak. With the increase of the layer number, the susceptibility is dominated by that of bilayer-like bands. Thus, the large diamagnetic susceptibility of bulk graphite can be understood in terms of the logarithmic singularity of bilayer graphene.

This decomposition rule can also be used for the dynamical conductivity describing optical absorption and the local density of states observed by scanning tunneling spectroscopy [41]. Figure 2.35 shows the dynamical conductivity averaged over the samples $N = 1, 2, \dots, 20$. Surprisingly, we still see the series of peaks in the monolayer graphene $\hbar\omega \propto \sqrt{B}$. This comes from the monolayer-type subbands that appears in every odd layered graphene.

In Fig. 2.36, the top panel shows the total density of states and the bottom panel shows the corresponding plot for the local density of states on the top layer. In the total density of states, we observe the several peaks coming from the monolayer-type subband similarly to the optical absorption spectra. In the local density of states, interestingly, the peaks of the monolayer-type subband are much more pronounced.

References

1. K. S. Novoselov, A. K. Geim, S. V. Morozov, D. Jiang, Y. Zhang, S. V. Dubonos, I. V. Grigorieva, and A. A. Firsov, Electric field effect in atomically thin carbon films, *Science* **306**, 666 (2004).
2. C. Berger, Z. Song, T. Li, X. Li, A. Y. Ogbazghi, R. Feng, Z. Dai, A. N. Marchenkov, E. H. Conrad, P. N. First, and W. A. de Heer, Ultrathin epitaxial graphite: 2D electron gas properties and a route toward graphene-based nanoelectronics., *J. Phys. Chem. B* **108**, 19912 (2004).
3. K. S. Kim, Y. Zhao, H. Jang, S. Y. Lee, J. M. Kim, K. S. Kim, J. -H. Ahn, P. Kim, J.-Y. Choi, and B. H. Hong, Large-scale pattern growth of graphene films for stretchable transparent electrodes, *Nature* **457**, 706 (2009).
4. K. S. Novoselov, A. K. Geim, S. V. Morozov, D. Jiang, M. I. Katsnelson, I. V. Grigorieva, S. V. Dubonos, and A. A. Firsov, Two-dimensional gas of massless Dirac fermions in graphene, *Nature* **438**, 197 (2005).
5. Y. Zhang, Y.-W. Tan, H. L. Stormer, and P. Kim, Experimental observation of the quantum Hall effect and Berry's phase in graphene, *Nature* **438**, 201 (2005).
6. T. Ando, Exotic electronic and transport properties of graphene, *Physica E* **40**, 213 (2007).
7. T. Ando, The electronic properties of graphene and carbon nanotubes, *NPG Asia Mater.* **1**, 17 (2009).
8. A. H. Castro Neto, F. Guinea, N. M. Peres, K. S. Novoselov, and A. K. Geim, The electronic properties of graphene, *Rev. Mod. Phys.* **81**, 109 (2009).
9. D. S. L. Abergel, V. Apalkov, J. Berashevich, K. Ziegler, and T. Chakraborty, Properties of graphene: A theoretical perspective, *Adv. Phys.* **59**, 261 (2010).
10. T. Ando, Theory of electronic states and transport in carbon nanotubes, *J. Phys. Soc. Jpn.* **74**, 777 (2005).
11. J. W. McClure, Diamagnetism of graphite, *Phys. Rev.* **104**, 666 (1956).
12. J. C. Slonczewski and P. R. Weiss, Band structure of graphite, *Phys. Rev.* **109**, 272 (1958).
13. D. P. DiVincenzo and E. J. Mele, Self-consistent effective-mass theory for intralayer screening in graphite intercalation compounds, *Phys. Rev. B* **29**, 1685 (1984).
14. G. W. Semenoﬀ, Condensed-matter simulation of a three-dimensional anomaly, *Phys. Rev. Lett.* **53**, 2449 (1984).
15. H. Ajiki and T. Ando, Electronic states of carbon nanotubes, *J. Phys. Soc. Jpn.* **62**, 1255 (1993).

16. C. L. Kane and E. J. Mele, Size, shape, and low energy electronic structure of carbon nanotubes, *Phys. Rev. Lett.* **78**, 1932 (1997).
17. T. Ando and T. Nakanishi, Impurity scattering in carbon nanotubes — absence of back scattering, *J. Phys. Soc. Jpn.* **67**, 1704 (1998).
18. T. Ando, T. Nakanishi, and R. Saito, Berry's phase and absence of back scattering in carbon nanotubes, *J. Phys. Soc. Jpn.* **67**, 2857 (1998).
19. M. Koshino and T. Ando, Diamagnetism in disordered graphene, *Phys. Rev. B* **75**, 235333 (2007).
20. H. Fukuyama, Anomalous orbital magnetism and Hall effect of massless fermions in two dimension, *J. Phys. Soc. Jpn.* **76**, 043711 (2007).
21. M. Koshino, Y. Arimura, and T. Ando, Magnetic field screening and mirroring in graphene, *Phys. Rev. Lett.* **102**, 177203 (2009).
22. M. Koshino and T. Ando, Anomalous orbital magnetism in Dirac-electron systems: Role of pseudo-spin paramagnetism, *Phys. Rev. B* **81**, 195431 (2010).
23. N. H. Shon and T. Ando, Quantum transport in two-dimensional graphite system, *J. Phys. Soc. Jpn.* **67**, 2421 (1998).
24. Y. Zheng and T. Ando, Hall conductivity of two-dimensional graphite system, *Phys. Rev. B* **65**, 245420 (2002).
25. T. Ando, Y. Zheng, and H. Suzuura, Dynamical conductivity and zero-mode anomaly in honeycomb lattices, *J. Phys. Soc. Jpn.* **71**, 1318 (2002).
26. T. Ando and H. Suzuura, Presence of perfectly conducting channel in metallic carbon nanotubes, *J. Phys. Soc. Jpn.* **71**, 2753 (2002).
27. T. Ando, Aharonov-Bohm effect and symmetry crossover in carbon nanotubes, *J. Phys. Soc. Jpn.* **75**, 054701 (2006).
28. T. Ando, Effects of symmetry crossover in quantum transport in graphene and nanotube, *Phil. Trans. Roy. Soc. A* **366**, 221 (2008).
29. H. Suzuura and T. Ando, Crossover from symplectic to orthogonal class in a two-dimensional honeycomb lattice, *Phys. Rev. Lett.* **89**, 266603 (2002).
30. E. McCann, K. Kechedzhi, V. I. Falko, H. Suzuura, T. Ando, and B. L. Altshuler, Weak localisation magnetoresistance in graphene, *Phys. Rev. Lett.* **97**, 146805 (2006).
31. See, for example, A. Kobayashi, S. Katayama, Y. Suzumura, and H. Fukuyama, Massless fermions in organic conductor, *J. Phys. Soc. Jpn.* **76**, 034711 (2007).
32. E. McCann and V. I. Falko, Landau-level degeneracy and quantum Hall effect in a graphite bilayer, *Phys. Rev. Lett.* **96**, 086805 (2006).

33. M. Koshino and T. Ando, Transport in bilayer graphene: Calculation within a self-consistent Born approximation, *Phys. Rev. B* **73**, 245403 (2006).
34. M. I. Katsnelson, Minimal conductivity in bilayer graphene, *Euro. Phys. J. B* **52**, 151 (2006).
35. E. McCann, Asymmetry gap in the electronic band structure of bilayer graphene, *Phys. Rev. B* **74**, 161403 (2006).
36. J. Nilsson, A. H. Castro Neto, N. M. R. Peres, and F. Guinea, Electron-electron interactions and the phase diagram of a graphene bilayer, *Phys. Rev. B* **73**, 214418 (2006).
37. F. Guinea, A. H. Castro Neto, and N. M. R. Peres, Electronic states and Landau levels in graphene stacks, *Phys. Rev. B* **73**, 245426 (2006).
38. E. V. Castro, K. S. Novoselov, S. V. Morozov, N. M. R. Peres, J. M. B. Lopes dos Santos, J. Nilsson, F. Guinea, A. K. Geim, and A. H. Castro Neto, Biased bilayer graphene: Semiconductor with a gap tunable by the electric field effect, *Phys. Rev. Lett.* **99**, 216802 (2007).
39. M. Koshino, Electronic transport in bilayer graphene, *New J. Phys.* **11**, 095010 (2009).
40. M. Koshino and T. Ando, Orbital diamagnetism in multilayer graphenes: Systematic study with the effective mass approximation, *Phys. Rev. B* **76**, 085425 (2007).
41. M. Koshino and T. Ando, Magneto-optical properties of multilayer graphenes, *Phys. Rev. B* **77**, 115313 (2008).
42. M. Koshino and T. Ando, Electronic structures and optical absorption of multilayer graphenes, *Solid State Commun.* **149**, 1123 (2009).
43. M. V. Berry, Quantum phase factors accompanying adiabatic changes, *Proc. Roy. Soc. London* **A392**, 45 (1984).
44. B. Simon, Holonomy, the quantum adiabatic theorem, and Berry's phase, *Phys. Rev. Lett.* **51**, 2167 (1983).
45. T. Ando, Screening effect and impurity scattering in monolayer graphene, *J. Phys. Soc. Jpn.* **75**, 074716 (2006).
46. S. Y. Zhou, G.-H. Gweon, A. V. Fedorov, P. N. First, W. A. de Heer, D.-H. Lee, F. Guinea, A. H. Castro Neto, and A. Lanzara, Substrate-induced bandgap opening in epitaxial graphene, *Nat. Mat.* **6**, 770 (2007).
47. S. Y. Zhou, D. A. Siegel, A. V. Fedorov, F. E. Gabaly, A. K. Schmid, A. H. Castro Neto, D.-H. Lee, and A. Lanzara, Origin of the energy bandgap in epitaxial graphene, *Nat. Mat.* **7**, 259 (2008).

48. A. W. W. Ludwig, M. P. A. Fisher, R. Shankar, and G. Grinstein, Integer quantum Hall transition: An alternative approach and exact results, *Phys. Rev. B* **50**, 7526 (1994).
49. J. W. McClure, Theory of diamagnetism of graphite, *Phys. Rev.* **119**, 606 (1960).
50. M. P. Sharma, L. G. Johnson, and J. W. McClure, Diamagnetism of graphite, *Phys. Rev. B* **9**, 2467 (1974).
51. S. A. Safran and F. J. DiSalvo, Theory of magnetic susceptibility of graphite intercalation compounds, *Phys. Rev. B* **20**, 4889 (1979).
52. J. Blinowski and C. Rigaux, Theory of magnetic susceptibility in acceptor and donor graphite intercalation compounds, *J. Phys. (Paris)* **45**, 545 (1984).
53. R. Saito and H. Kamimura, Orbital susceptibility of higher-stage graphite intercalation compounds, *Phys. Rev. B* **33**, 7218 (1986).
54. M.-C. Chang and Q. Niu, Berry phase, hyperorbits, and the Hofstadter spectrum: Semiclassical dynamics in magnetic Bloch bands, *Phys. Rev. B* **53**, 7010 (1996).
55. D. Xiao, W. Yao, and Q. Niu, Valley-contrasting physics in graphene: Magnetic moment and topological transport, *Phys. Rev. Lett.* **99**, 236809 (2007).
56. H. Ajiki and T. Ando, Magnetic properties of carbon nanotubes, *J. Phys. Soc. Jpn.* **62**, 2470 (1993).
57. M. Yamamoto, M. Koshino, and T. Ando, Electric and magnetic response of multi-wall carbon nanotubes, *J. Phys. Soc. Jpn.* **77**, 084705 (2008).
58. T. Ando, Theory of cyclotron resonance line shape in a two-dimensional electron system., *J. Phys. Soc. Jpn.* **38**, 989 (1975).
59. R. R. Nair, P. Blake, A. N. Grigorenko, K. S. Novoselov, T. J. Booth, T. Stauber, N. M. R. Peres, and A. K. Geim, Fine structure constant defines visual transparency of graphene, *Science* **320**, 1308 (2008).
60. Z. Q. Li, E. A. Henriksen, Z. Jiang, Z. Hao, M. C. Martin, P. Kim, H. L. Stormer, and D. N. Basov, Dirac charge dynamics in graphene by infrared spectroscopy, *Nat. Phys.* **4**, 532 (2008).
61. T. Ando, Effects of valley mixing and exchange on excitons in carbon nanotubes with Aharonov–Bohm flux, *J. Phys. Soc. Jpn.* **75**, 024707 (2006).
62. T. Ando, A. B. Fowler, and F. Stern, Electronic properties of two-dimensional systems, *Rev. Mod. Phys.* **54**, 437 (1982).
63. E. A. Taft and H. R. Philipp, Optical properties of graphite, *Phys. Rev.* **138**, A197 (1965).

64. K. Nomura and A. H. MacDonald, Quantum Hall ferromagnetism in graphene, *Phys. Rev. Lett.* **96**, 256602 (2006).
65. T. Fukuzawa, M. Koshino, and T. Ando, Weak-field Hall effect in graphene calculated within self-consistent Born approximation, *J. Phys. Soc. Jpn.* **78**, 094714 (2009).
66. T. Ando and Y. Uemura, Theory of quantum transport in a two-dimensional electron system under magnetic fields. I. Characteristics of level broadening and transport under strong fields, *J. Phys. Soc. Jpn.* **36**, 959 (1974).
67. J. Martin, N. Akerman, G. Ulbricht, T. Lohmann, J. H. Smet, K. von Klitzing, and A. Yacoby, Observation of electron-hole puddles in graphene using a scanning single-electron transistor, *Nat. Phys.* **4**, 144 (2008).
68. M. Noro, M. Koshino, and T. Ando, Theory of transport in graphene with long-range scatterers, *J. Phys. Soc. Jpn.* **79**, 094713 (2010).
69. E. Fradkin, Critical behavior of disordered degenerate semiconductors. II. Spectrum and transport properties in mean-field theory, *Phys. Rev. B* **33**, 3263 (1986).
70. P. A. Lee, Localized states in a d-wave superconductor, *Phys. Rev. Lett.* **71**, 1887 (1993).
71. A. K. Geim and K. S. Novoselov, The rise of graphene, *Nat. Mater.* **6**, 183 (2007).
72. Y.-W. Tan, Y. Zhang, K. Bolotin, Y. Zhao, S. Adam, E. H. Hwang, S. Das Sarma, H. L. Stormer, and P. Kim, Measurement of scattering rate and minimum conductivity in graphene, *Phys. Rev. Lett.* **99**, 246803 (2007).
73. K. I. Bolotin, K. J. Sikes, Z. Jiang, G. Fundenberg, J. Hone, P. Kim, and H. L. Stormer, Ultrahigh electron mobility in suspended graphene, *Solid State Commun.* **146**, 351 (2008).
74. H. Kumazaki and D. S. Hirashima, Effects of impurities in two-dimensional graphite, *J. Phys. Soc. Jpn.* **75**, 053707 (2006).
75. I. L. Aleiner and K. B. Efetov, Effect of disorder on transport in graphene, *Phys. Rev. Lett.* **97**, 236801 (2006).
76. K. Ziegler, Robust transport properties in graphene, *Phys. Rev. Lett.* **97**, 266802 (2006).
77. K. Nomura and A. H. MacDonald, Quantum transport of massless Dirac fermions, *Phys. Rev. Lett.* **98**, 076602 (2007).
78. J. H. Bardarson, J. Tworzydo, P. W. Brouwer, and C. W. J. Beenakker, One-parameter scaling at the Dirac point in graphene, *Phys. Rev. Lett.* **99**, 106801 (2007).

79. S. Adam, E. H. Hwang, V. M. Galitski, and S. Das Sarma, A self-consistent theory for graphene transport, *Proc. Nat. Acad. Sci.* **104**, 18392 (2007).
80. K. Ziegler, Long-range correlations in disordered graphene, *Phys. Rev. B* **78**, 125401 (2008).
81. S. Adam, P. W. Brouwer, and S. Das Sarma, Crossover from quantum to Boltzmann transport in graphene, *Phys. Rev. B* **79**, 201404 (2009).
82. T. Ando, Charged impurity scattering in graphenes: Effects of environmental screening, band gap, and AA stacking, *J. Phys.: Conf. Ser.* **302**, 012015 (2011).
83. W. W. Toy, M. S. Dresselhaus, and G. Dresselhaus, Minority carriers in graphite and the H-point magnetoreflexion spectra, *Phys. Rev. B* **15**, 4077 (1977).
84. M. Monteverde, C. Ojeda-Aristizabal, R. Weil, K. Bennaceur, M. Ferrier, S. Gueron, C. Glattli, H. Bouchiat, J. N. Fuchs, and D. L. Maslov, Transport and elastic scattering times as probes of the nature of impurity scattering in single-layer and bilayer graphene, *Phys. Rev. Lett.* **104**, 126801 (2010).
85. C. Jang, S. Adam, J.-H. Chen, E. D. Williams, S. Das Sarma, and M. S. Fuhrer, Tuning the effective fine structure constant in graphene: Opposing effects of dielectric screening on short- and long-range potential scattering, *Phys. Rev. Lett.* **101**, 146805 (2008).
86. L. A. Ponomarenko, R. Yang, T. M. Mohiuddin, M. I. Katsnelson, K. S. Novoselov, S. V. Morozov, A. A. Zhukov, F. Schedin, E. W. Hill, and A. K. Geim, Effect of a high- κ environment on charge carrier mobility in graphene, *Phys. Rev. Lett.* **102**, 206603 (2009).
87. F. Chen, J. Xia, D. K. Ferry, and N. Tao, Dielectric screening enhanced performance in graphene FET, *Nano Lett.* **9**, 2574 (2009).
88. A. Hashimoto, K. Suenaga, A. Gloter, K. Urita, and S. Iijima, Direct evidence for atomic defects in graphene layers, *Nature* **430**, 870 (2004).
89. J. H. Warner, M. H. Rummeli, L. Ge, T. Gemming, B. Montanari, N. M. Harrison, B. Buchner, and G. A. D. Briggs, Structural transformations in graphene studied with high spatial and temporal resolution, *Nat. Nano.* **4**, 500 (2009).
90. S. Y. Zhou, D. A. Siegel, A. V. Fedorov, and A. Lanzara¹, Metal to insulator transition in epitaxial graphene induced by molecular doping, *Phys. Rev. Lett.* **101**, 086402 (2008).

91. F. Schedin, A. K. Geim, S. V. Morozov, E. W. Hill, P. Blake, M. I. Katsnelson, K. S. Novoselov, Detection of individual gas molecules adsorbed on graphene, *Nat. Mat.* **6**, 652 (2007).
92. See, for example, C. Coletti, C. Riedl, D. S. Lee, B. Krauss, L. Patthey, K. von Klitzing, J. H. Smet, and U. Starke, Charge neutrality and band-gap tuning of epitaxial graphene on SiC by molecular doping, *Phys. Rev. B* **81**, 235401 (2010).
93. T. Ando, T. Nakanishi, and M. Igami, Effective-mass theory of carbon nanotubes with a vacancy, *J. Phys. Soc. Jpn.* **68**, 3994 (1999).
94. M. Igami, T. Nakanishi, and T. Ando, Conductance of carbon nanotube with a vacancy, *J. Phys. Soc. Jpn.* **68**, 716 (1999).
95. M. Igami, T. Nakanishi, and T. Ando, Numerical study of transport in carbon nanotubes with lattice vacancy, *J. Phys. Soc. Jpn.* **68**, 3146 (1999).
96. M. Igami, T. Nakanishi, and T. Ando, Effect of lattice vacancy on conductance of carbon nanotubes, *Physica B* **284–288**, 1746 (2000).
97. M. Igami, T. Nakanishi, and T. Ando, Effect of lattice vacancy on carbon nanotubes: Conductance quantization, *Mol. Cryst. Liq. Cryst.* **340**, 719 (2000).
98. M. Igami, T. Nakanishi, and T. Ando, Effective-mass theory of carbon nanotubes with vacancies in magnetic fields., *J. Phys. Soc. Jpn.* **70**, 481 (2001).
99. O. Zhou, R. M. Fleming, D. W. Murphy, R. C. Haddon, A. P. Ramirez, and S. H. Glarum, Carbon nanotube with defects, *Science* **263**, 1744 (1994).
100. M. Bockrath, W. J. Liang, D. Bozovic, J. H. Hafner, C. M. Lieber, M. Tinkham, and H. K. Park, Resonant electron scattering by defects in single-walled carbon nanotubes, *Science* **291**, 283 (2001).
101. J. W. Park, J. Kim, J.-O. Lee, K. C. Kang, J.-J. Kim, and K.-H. Yoo, Effects of artificial defects on the electrical transport of single-walled carbon nanotubes, *Appl. Phys. Lett.* **80**, 133 (2002).
102. J.-C. Charlier, T. W. Ebbesen, and Ph. Lambin, Structural and electronic properties of pentagon–heptagon pair defects in carbon nanotubes, *Phys. Rev. B* **53**, 11108 (1996).
103. L. Chico, L. X. Benedict, S. G. Louie, and M. L. Cohen, Quantum conductance of carbon nanotubes with defects, *Phys. Rev. B* **54**, 2600 (1996).
104. H. J. Choi, J.-S. Ihm, S. G. Louie, and M. L. Cohen, Defects, quasibound states, and quantum conductance in metallic carbon nanotubes, *Phys. Rev. Lett.* **84**, 2917 (2000).

105. B. C. Pan, W. S. Yang, and Jinlong Yang, Formation energies of topological defects in carbon nanotubes, *Phys. Rev. B* **62**, 12652 (2000).
106. T. Kostyrko, M. Bartkowiak, and G. D. Mahan, Reflection by defects in a tight-binding model of nanotubes, *Phys. Rev. B* **59**, 3241 (1999).
107. H. Matsumura and T. Ando, Conductance of carbon nanotube with a Stone–Wales defect, *J. Phys. Soc. Jpn.* **70**, 2657 (2001).
108. A. Toyoda and T. Ando, Theory of electron scattering by lattice defects in monolayer graphene, *J. Phys. Soc. Jpn.* **79**, 094708 (2010).
109. F. J. Dyson, Statistical theory of the energy levels of complex systems. I, *J. Math. Phys.* **3**, 140 (1962).
110. T. Ando and K. Akimoto, Effects of short-range scatterers on perfect channel in metallic carbon nanotubes, *J. Phys. Soc. Jpn.* **73**, 1895 (2004).
111. H. Ajiki and T. Ando, Energy bands of carbon nanotubes in magnetic fields, *J. Phys. Soc. Jpn.* **65**, 505 (1996).
112. K. Akimoto and T. Ando, Effects of trigonal warping on perfect channel in metallic carbon nanotubes, *J. Phys. Soc. Jpn.* **73**, 2194 (2004).
113. T. Ando, Spin–orbit interaction in carbon nanotubes, *J. Phys. Soc. Jpn.* **69**, 1757 (2000).
114. S. V. Morozov, K. S. Novoselov, M. I. Katsnelson, F. Schedin, L. A. Ponomarenko, D. Jiang, and A. K. Geim, Strong suppression of weak localization in graphene, *Phys. Rev. Lett.* **97**, 016801 (2006).
115. X.-S. Wu, X.-B. Li, Z.-M. Song, C. Berger, and W. A. de Heer, Weak antilocalization in epitaxial graphene: Evidence for chiral electrons, *Phys. Rev. Lett.* **98**, 136801 (2007).
116. F. V. Tikhonenko, D. W. Horsell, R. V. Gorbachev, and A. K. Savchenko, Weak localization in graphene flakes, *Phys. Rev. Lett.* **100**, 056802 (2008).
117. D.-K. Ki, D.-C. Jeong, J.-H. Choi, H.-J. Lee, and K.-S. Park, Inelastic scattering in a monolayer graphene sheet: A weak-localization study, *Phys. Rev. B* **78**, 125409 (2008).
118. F. V. Tikhonenko, A. A. Kozikov, A. K. Savchenko, and R. V. Gorbachev, Transition between electron localization and antilocalization in graphene, *Phys. Rev. Lett.* **103**, 226801 (2009).
119. H. Suzuura and T. Ando, Phonons and electron–phonon scattering in carbon nanotubes, *Phys. Rev. B* **65**, 235412 (2002).
120. A. C. Ferrari, J. C. Meyer, V. Scardaci, C. Casiraghi, M. Lazzeri, F. Mauri, S. Piscanec, D. Jiang, K. S. Novoselov, S. Roth, and A. K. Geim, Raman spectrum of graphene and graphene layers, *Phys. Rev. Lett.* **97**, 187401 (2006).

121. A. Gupta, G. Chen, P. Joshi, S. Tadigadapa, and P.C. Eklund, Raman scattering from high-frequency phonons in supported n-graphene layer films, *Nano Lett.* **6**, 2667 (2006).
122. C. N. R. Rao, A. K. Sood, K. S. Subrahmanyam, and A. Govindaraj, Graphene: The new two-dimensional nanomaterial, *Angew. Chem.* **48**, 7752 (2009).
123. K. Ishikawa and T. Ando, Optical phonon interacting with electrons in carbon nanotubes, *J. Phys. Soc. Jpn.* **75**, 084713 (2006).
124. T. Ando, Anomaly of optical phonon in monolayer graphene, *J. Phys. Soc. Jpn.* **75**, 124701 (2006).
125. T. Ando, Magnetic oscillation of optical phonon in graphene, *J. Phys. Soc. Jpn.* **76**, 024712 (2007).
126. J. Maultzsch, S. Reich, C. Thomsen, H. Requardt, and P. Ordejon, Phonon dispersion in graphite, *Phys. Rev. Lett.* **92**, 075501 (2004).
127. N. A. Viet, H. Ajiki, and T. Ando, Lattice instability in metallic carbon nanotubes, *J. Phys. Soc. Jpn.* **63**, 3036 (1994).
128. M. Lazzeri and F. Mauri, Nonadiabatic Kohn anomaly in a doped graphene monolayer, *Phys. Rev. Lett.* **97**, 266407 (2006).
129. S. Pisana, M. Lazzeri, C. Casiraghi, K. S. Novoselov, A. K. Geim, A. C. Ferrari, and F. Mauri, Breakdown of the adiabatic Born-Oppenheimer approximation in graphene, *Nat. Mat.* **6**, 198 (2007).
130. J. Yan, Y. Zhang, P. Kim, and A. Pinczuk, Electric field effect tuning of electron-phonon coupling in graphene, *Phys. Rev. Lett.* **98**, 166802 (2007).
131. A. Das, S. Pisana, B. Chakraborty, S. Piscanec, S. K. Saha, U. V. Waghmare, K. S. Novoselov, H. R. Krishnamurthy, A. K. Geim, A. C. Ferrari, and A. K. Sood, Monitoring dopants by Raman scattering in an electrochemically top-gated graphene transistor, *Nat. Nanotech.* **3**, 210 (2008).
132. M. O. Goerbig, J.-N. Fuchs, K. Kechedzhi, and V. I. Fal'ko, Filling-factor-dependent magnetophonon resonance in graphene, *Phys. Rev. Lett.* **99**, 087402 (2007).
133. C. Faugeras, M. Amado, P. Kossacki, M. Orlita, M. Sprinkle, C. Berger, W. A. de Heer, and M. Potemski, Tuning the electron-phonon coupling in multilayer graphene with magnetic fields, *Phys. Rev. Lett.* **103**, 186803 (2009).
134. H. Suzuura and T. Ando, Zone-boundary phonon in graphene and nanotube, *J. Phys. Soc. Jpn.* **77**, 044703 (2008).
135. N. Mori and T. Ando, Magnetophonon resonance in monolayer graphene, *J. Phys. Soc. Jpn.* **80**, 044706 (2011).

136. A. Misu, E. Mendez, and M. S. Dresselhaus, Near infrared reflectivity of graphite under hydrostatic pressure. I. experiment, *J. Phys. Soc. Jpn.* **47**, 199 (1979).
137. H. Min, B. Sahu, S. K. Banerjee, and A. H. MacDonald, *Ab initio* theory of gate induced gaps in graphene bilayers, *Phys. Rev. B* **75**, 155115 (2007).
138. T. Ando and M. Koshino, Field effects on optical phonons in bilayer graphene, *J. Phys. Soc. Jpn.* **78**, 034709 (2009).
139. D. S. L. Abergel and V. I. Falko, Optical and magneto-optical far-infrared properties of bilayer graphene, *Phys. Rev. B* **75**, 155430 (2007).
140. T. Ando and M. Koshino, Optical absorption by interlayer density excitations in bilayer graphene, *J. Phys. Soc. Jpn.* **78**, 104716 (2009).
141. T. Ando, Bilayer graphene with long-range scatterers studied in a self-consistent Born approximation, *J. Phys. Soc. Jpn.* **80**, 014707 (2011).
142. T. Ando, Anomaly of optical phonons in bilayer graphene, *J. Phys. Soc. Jpn.* **76**, 104711 (2007).
143. L. M. Malard, D. C. Elias, E. S. Alves, and M. A. Pimenta, Observation of distinct electron-phonon couplings in gated bilayer graphene, *Phys. Rev. Lett.* **101**, 257401 (2008).
144. J. Yan, T. Villarsen, E. A. Henriksen, P. Kim, and A. Pinczuk, Optical phonon mixing in bilayer graphene with a broken inversion symmetry, *Phys. Rev. B* **80**, 241417 (2009).
145. M. Bruna and S. Borini, Observation of Raman G-band splitting in top-doped few-layer graphene, *Phys. Rev. B* **81**, 125421 (2010).
146. J. M. Garcia, R. He, M. P. Jiang, J. Yan, A. Pinczuk, Y. M. Zuev, K. S. Kim, P. Kim, K. Baldwin, K. W. West, and L. N. Pfeiffer, Multilayer graphene films grown by molecular beam deposition, *Solid State Commun.* **150**, 809 (2010).
147. A. B. Kuzmenko, L. Benfatto, E. Cappelluti, I. Crassee, D. van der Marel, P. Blake, K. S. Novoselov, and A. K. Geim, Gate tunable infrared phonon anomalies in bilayer graphene, *Phys. Rev. Lett.* **103**, 116804 (2009).
148. T.-T. Tang, Y. Zhang, C.-H. Park, B. Geng, C. Girit, Z. Hao, M. C. Martin, A. Zettl, M. F. Crommie, S. G. Louie, Y. R. Shen, and F. Wang, A tunable phonon-exciton Fano system in bilayer graphene, *Nat. Nano.* **5**, 32 (2010).

This page intentionally left blank

Chapter 3

Experimental Approaches to Graphene Electron Transport for Device Applications

Akinobu Kanda

*Institute of Physics and Tsukuba Research Center for Interdisciplinary Materials
Science (TIMS), University of Tsukuba,
Tsukuba, Ibaraki 305-8571, Japan
kanda@lt.px.tsukuba.ac.jp*

3.1 Introduction

This chapter reviews several experimental aspects of graphene research, focusing, in particular, on experimental methods and important results regarding graphene electron transport, and some possible applications.

Graphene is a gapless semiconductor with a linear dispersion relation near the K and K' points, which are the corners of the hexagonal Brillouin zone. This makes the conduction electrons behave as massless Dirac fermions, as discussed theoretically in Chapter 2. Because of this exotic property, electron transport in graphene has attracted much attention from the viewpoint of

Physics and Chemistry of Graphene: Graphene to Nanographene

Edited by Toshiaki Enoki and Tsuneya Ando

Copyright © 2013 Pan Stanford Publishing Pte. Ltd.

ISBN 978-981-4241-48-9 (Hardcover), 978-981-4241-49-6 (eBook)

www.panstanford.com

fundamental sciences; graphene exhibits many novel and exciting “relativistic” phenomena in solid-state systems.

Furthermore, graphene has created high expectations for its use in electronics applications from the very beginning: The first experiment on graphene electron transport [1] reported excellent electron conduction, with a typical mobility^a of more than ten times that of silicon ($\sim 10^3$ cm²/Vs), and strong ability to modulate conductivity by changing gate voltage. These properties are ideal for applications in the creation of field-effect transistors (FETs).

In fact, novel useful materials are urgently needed by the electronics industry. The miniaturization of the electronic circuits has proceeded for the last 40 years following Moore’s law: “The density of transistors in silicon integrated logic circuits doubles in 36 to 48 months”; however, we have approached a limit. Present miniaturized devices suffer from difficulties such as leakage current due to the quantum-mechanical tunneling effect and the scattering of the device properties due to fluctuations in the density of dopants. One possible method of overcoming these limitations is the so-called “beyond CMOS” approach, which aims to develop novel electronic devices based on novel operational principles, with performance exceeding that of present CMOS (complementary metal-oxide-semiconductor) devices. Graphitic materials such as carbon nanotubes and graphene are among the promising candidates for use in “beyond CMOS” technology.

In exploring fundamental sciences and future applications of graphene, it would be helpful to summarize the basic experimental techniques and important results regarding electron transport in graphene. However, it should be noted that the field of graphene research is too vast to be summarized in a compact way. Furthermore, this field is developing so rapidly that a notion that is believed to be true today might be revealed to be false tomorrow. Thus, this chapter is intended to deliver basic information on the present status of experimental research on graphene and to clarify the urgent issues to be solved.

^aMobility refers to the mean velocity of carriers (electrons and/or holes) along an electric field with unit strength. This characterizes how quickly a carrier can move in metals or semiconductors.

This chapter is divided into two parts. In the first section, basic experimental techniques are summarized, which include the formation of graphene, the determination of graphene thickness, and several basic methods used for characterizing graphene electron transport. This information will be helpful in interpreting the experimental results, as well as in elucidating the problems in present graphene research. In the second section, experiments regarding graphene electron transport are reviewed. Basic transport properties that are important for certain applications are selected, including the gate electric field effect, mobility improvement, spin transport, and Cooper pair transport via the superconducting proximity effect. Theoretical interpretations of these topics are briefly reviewed. Gaps between the (theoretical) expectations for ideal graphene and experimental results for graphene are stressed; possible methods for improving the characteristics of graphene are discussed.

This chapter is organized as follows. In Section 3.2, several methods of obtaining graphene films, as well as experimental techniques for characterizing graphene, are summarized. Section 3.3 is devoted to the transport properties of graphene: gate voltage dependence of conductance (3.3.2), quantum Hall effect (3.3.3), Klein tunneling (3.3.4), mobility improvement (3.3.5), bandgap engineering (3.3.6), graphene quantum effect devices (3.3.7), use in chemical sensors (3.3.8), possible applications in spintronics (3.3.9), and superconducting proximity effect (3.3.10). Most of the graphene films introduced in these subsections were obtained from graphene formed by the mechanical exfoliation of high-quality graphite. Throughout these subsections, experimental efforts to bridge the gap between theoretical expectations and observations are stressed. Finally, a summary is presented in Section 3.4.

3.2 Formation of Graphene

Before the proliferation of graphene research, it was long believed that single-layer graphene did not exist in nature. According to the Mermin–Wagner theorem [2], long-range fluctuations in the position of atoms can be created with little energy cost in

dimensions $d \leq 2$. In other words, thermally activated low-energy (long-wavelength) phonons result in the displacement of atoms from their equilibrium positions, an effect that increases logarithmically with the size of the system. This leads to the instability of two-dimensional crystals [3]. As a result, graphene, a perfect two-dimensional crystal, can easily be crumpled, decomposed, or segregated; in practice, it changes into amorphous carbon. However, it was the micromechanical cleavage of graphite developed by the Manchester group [4] that verified the stability of graphene in nature.^b Fragments of single-layer graphene were successfully isolated from bulk graphite in different forms such as being attached to a substrate [4] and even suspended in a space [6, 7]. This stability of graphene in space is attributed to the intrinsic thermally activated ripples with ~ 1 nm-high corrugations normal to the graphene surface, which appear over a characteristic lateral scale of 10–25 nm [6, 8].^c

Before either the Manchester team's micromechanical cleavage of graphite [4] or the Scotch tape method [5] developed for the isolation of graphene became widespread, many people had attempted to obtain thin graphite films and single-layer graphene using various methods. For example, Jang *et al.* [10] obtained nanometer-size single-layer and multilayer graphene by carbonizing a variety of precursor polymers (such as polyacrylonitrile (PAN) fibers), or heat-treating petroleum or coal tar pitch, and subsequently subjecting the resulting polymeric carbon to a mechanical attrition treatment (e.g.,

^bThe micromechanical cleavage method reported in Ref. [4] differs from the so-called Scotch tape method [5] described in Section 3.2.1. However, they are often confused. In Ref. [4], a fresh surface of a layered crystal (graphite, boron nitride, NbSe₂, Bi₂Sr₂CaCu₂O_x, and so on) was rubbed against another surface (substrate) to obtain flakes with a variety of thicknesses, including a single layer, whereas the Scotch tape method uses a sticky tape to cleave the graphite. Note that the critical process for obtaining a single layer is how to find and identify a single layer efficiently, rather than how to isolate a single layer. In both techniques, the preliminary identification of single layers among thicker films is performed using optical microscope images. Details are discussed in the main text.

^cWhen attached to the substrate, the graphene film is *meta*-stabilized by deposition on a substrate, rather than by thermally activated ripples. Actually, when the atomically flat terraces of cleaved mica surfaces are used as a substrate, single-layer graphene becomes flat down to the atomic level [9].

ball milling). Viculus *et al.* [11] chemically exfoliated potassium-intercalated carbon using its highly exothermic interaction with aqueous solvents, and obtained scrolled graphene. Mechanical exfoliation was also carried out: Bunch *et al.* [12] sonicated natural graphite flakes in a dichlorobenzene solution. They placed a drop of the solution on a Si substrate and dried it to obtain graphene pieces with thicknesses ranging from several hundred nanometers to a few nanometers. Zhang *et al.* [13] made graphite micropillars on HOPG (highly oriented pyrolytic graphite) using optical lithography followed by oxygen plasma etching. They attached a pillar on the top of a cantilever of an atomic force microscopy (AFM) system and rubbed it against a substrate to shear off thin graphite films with thicknesses ranging from 10 to 100 nm. Both Bunch *et al.* and Zhang *et al.* succeeded in measuring the electrical conductance of their samples, which depended on the gate electric field.

Despite significant efforts to obtain single-layer and multilayer graphene, the decisive formation of single-layer graphene had never been reported before 2004 [1]. This is because of the difficulty in finding and identifying a single-layer graphene film. Novoselov *et al.* summarized the reasons for this difficulty as follows [4]:

- Single layers are in a great minority among accompanying (that is, thicker) flakes.
- Single layers have no clear signature in transmission electron microscopy (TEM).
- Single layers are completely transparent to visible light and cannot be seen under an optical microscope on most substrates.
- Atomic force microscope (AFM) observation has a very low throughput, although it can identify single layers.

A breakthrough in finding and identifying single-layer graphene was made by Novoselov *et al.*, [1] who used a silicon substrate with a 300 nm SiO₂ layer on top, which enabled them to identify single-layer graphene easily and efficiently using an optical microscope.

In the following subsections, several techniques for obtaining and identifying graphene are described.

3.2.1 Scotch Tape Method

The Scotch tape method is very common in the fabrication of graphene devices, which are mainly used in research into the fundamental properties of graphene. It can produce high-quality graphene with lateral sizes ≤ 0.1 mm; however, controlling the size and position of the graphene is almost impossible. The following is the typical procedure of the Scotch tape method:

- (i) Place a few flakes of graphite (≈ 1 mm) on the adhesive side of a plastic sticky tape with tweezers (Fig. 3.1(a)). Scotch tape

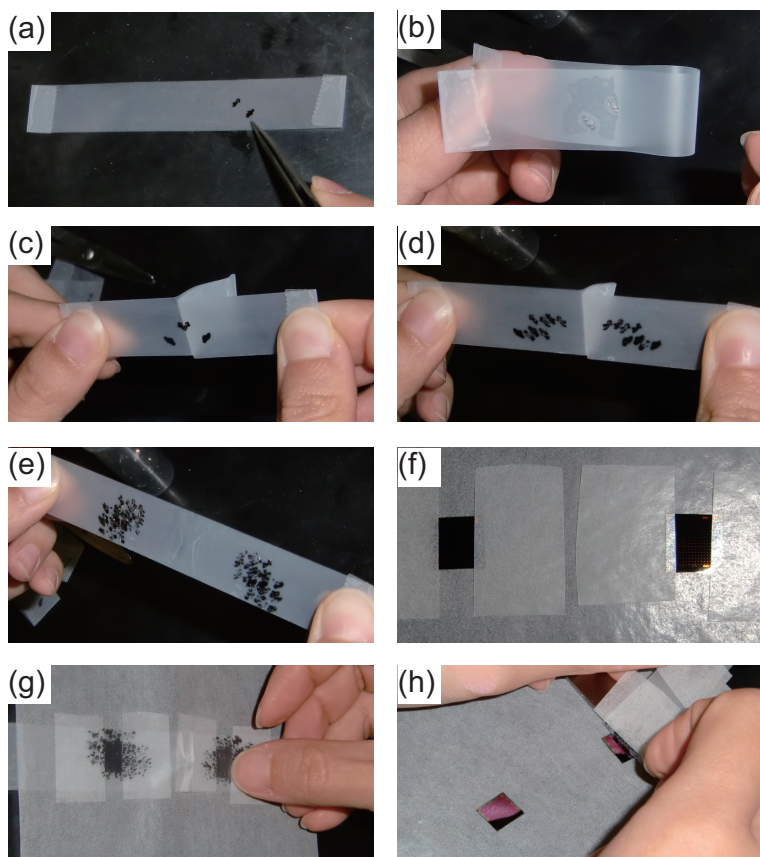


Figure 3.1 The typical procedure of the Scotch tape method.

(3M) and Nitto tape are commonly used. Natural graphite, Kish graphite, or HOPG (highly oriented pyrolytic graphite) is usually used for the starting material.

- (ii) Fold the adhesive side to sandwich the graphite flakes and press the tape firmly (Fig. 3.1(b)).
- (iii) Peel the tape apart slowly, so that the graphite flakes are cleaved and attached on both sides of the tape (Fig. 3.1(c)).
- (iv) Repeat the second and the third steps with slightly shifting the fold line, so that the graphite flakes do not overlap (Fig. 3.1(d)).
- (v) Stop repeating the cleavage when graphite flakes spread over the sticky tape (Fig. 3.1(e)).
- (vi) Prepare a silicon substrate with a silicon dioxide layer on the top surface (Fig. 3.1(f)). Place address markers on the surface in advance using photolithography so that one can easily locate the position of a graphene flake in an image. These markers are indispensable for further microfabrication on graphene. An example of the address markers is shown in Fig. 3.2
- (vii) Attach the adhesive side of the tape with the graphite flakes to a silicon substrate, and gently rub the surface to remove any air between the substrate and the tape (Fig. 3.1(g)).
- (viii) Slowly peel the tape off the substrate (for example, more than 2 min for a 1 cm substrate) (Fig. 3.1(h)). Not only graphite flakes but also some adhesive remains on the substrate. The latter can be removed by submerging the substrate in acetone for a few seconds.

In optical microscope images, thin graphite flakes have different colors that depend on their thickness. An example is shown in Fig. 3.3. A thick graphite film has a metallic luster and appears white or yellow (not shown in Fig. 3.3). As a graphite film becomes thinner, its color changes to blue, then violet-blue, and finally, approaches the color of the substrate. When a substrate with a SiO_2 layer of the appropriate thickness is used, films with the most subtle color correspond to single-layer graphene, as shown in Fig 3.3. Although the confirmation of the thickness needs more sophisticated techniques, such as Raman spectroscopy, AFM, and

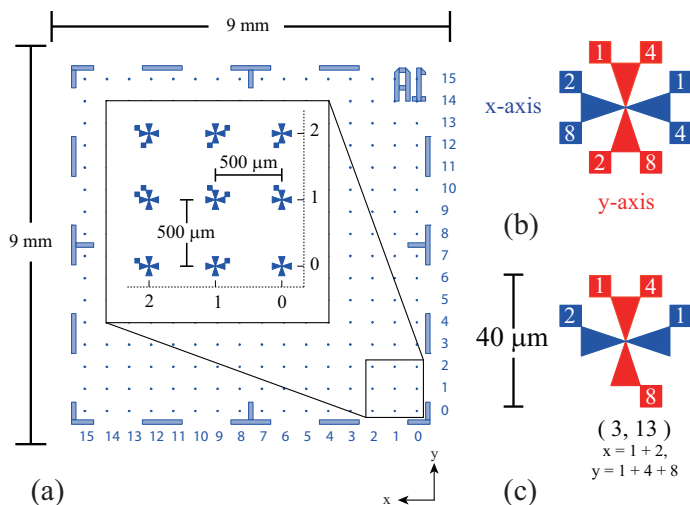


Figure 3.2 An example of address markers used by the University of Tsukuba group. (a) Location of address markers in a substrate (9 mm \times 9 mm). Separation of adjacent address markers is 500 μm and each address marker has different shape so that one can know its position from the shape. (b) In each address marker, the horizontal (x) and vertical (y) coordinates of its position are known from the position of dots. Each dot indicates 1, 2, 4, or 8 in the x or y axis, depending on its position. The sum of the numbers corresponds to the coordinate. An example is shown in (c). This address marker indicates the position (3,13).

quantum Hall effect measurement, the present optical technique allows one to find a candidate for single-layer graphene rapidly and efficiently. Detailed techniques for thickness determination are discussed in Section 3.2.2.

Despite such harsh formation methods, the quality of the resulting graphene is quite high. In a scanning tunneling microscope (STM) image, a symmetrical honeycomb structure was observed; it was without any lattice defects, point-like interaction with the underlying substrate, or folding of the graphene sheet [14].

Usually in the Scotch tape method, not only graphene flakes but also a large amount of adhesive is attached to the substrate. The latter can be removed by immersing the substrate in acetone.

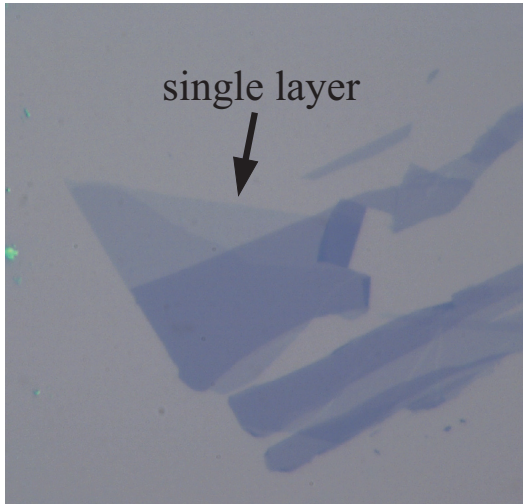


Figure 3.3 An optical image of graphene placed on a Si substrate covered with a 300 nm SiO₂ layer.

Alternatively, one can use the following method, which prevents the adhesives from sticking to the substrate [15]:

- (i) Peel a thin foil of HOPG from the bulk material using Scotch tape and transfer it onto a substrate with a fine pair of tweezers.
- (ii) Apply pressure to the graphite foil using high-pressure nitrogen gas for ~5 seconds.
- (iii) Remove the foil from the substrate and look for graphene using an optical microscope.
- (iv) Repeat the above procedure until a sufficient number of graphene flakes have been obtained.

3.2.2 Determination of the Number of Layers

The success of the Manchester group [1, 4] in forming graphene was allowed by the efficient estimation of the graphene thickness based on the contrast in optical images. The estimation can be confirmed by other methods such as Raman spectroscopy, the quantum Hall effect, and direct thickness measurements using AFM.

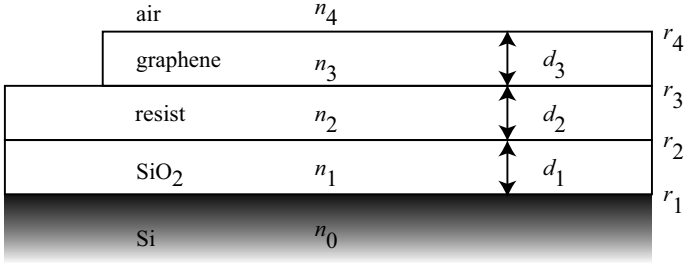


Figure 3.4 A model of graphene placed on a Si/SiO₂ substrate.

Optical microscopy In their first graphene experiment, the Manchester group [1] used a Si substrate with a 300 nm SiO₂ layer on the surface. They found that on this substrate, even single-layer graphene with a thickness of only 0.34 nm was discernible by optical microscopy. This finding was a critical step in the development of graphene research.

The visibility of graphene on a Si substrate can be explained quantitatively using a Fresnel-law-based model in which the reflection of light at the boundary of different materials is taken into account [16–18]. Here, we consider a three-layer system (Fig. 3.4) in which graphene (thickness $d_3 = k \times 0.34$ nm, for k -layer graphene) is placed on a Si/SiO₂ substrate (the thickness of the SiO₂ layer is d_1) covered by another layer (resist, etc., thickness d_2). For light incident perpendicular to the surface, the reflected light intensity is given by [19].

$$I = \left| \frac{r_1 + r_2 e^{-i\Delta_1} + r_3 e^{-i(\Delta_1 + \Delta_2)} + r_4 e^{-i(\Delta_1 + \Delta_2 + \Delta_3)} + r_1 r_2 r_3 e^{-i\Delta_2}}{1 + r_1 r_2 e^{-i\Delta_1} + r_1 r_3 e^{-i(\Delta_1 + \Delta_2)} + r_1 r_4 e^{-i(\Delta_1 + \Delta_2 + \Delta_3)} + r_2 r_3 e^{-i\Delta_2}} \right. \\ \left. \frac{+ r_1 r_3 r_4 e^{-i\Delta_3} + r_1 r_2 r_4 e^{-i(\Delta_2 + \Delta_3)} + r_2 r_3 r_4 e^{-i(\Delta_1 + \Delta_3)}}{+ r_3 r_4 e^{-i\Delta_3} + r_2 r_4 e^{-i(\Delta_2 + \Delta_3)} + r_1 r_2 r_3 r_4 e^{-i(\Delta_1 + \Delta_3)}} \right|^2. \quad (3.1)$$

Here, using the (complex) refractive indices of Si, SiO₂, resist, graphene, and air (n_0, n_1, n_2, n_3 , and $n_4 = 1$, respectively [16]), the relative index of refraction, r_i , for the boundary of the materials with refractive indices n_{i-1} and n_i becomes

$$r_i = \frac{n_{i-1} - n_i}{n_{i-1} + n_i} \quad (i = 1, 2, 3, 4). \quad (3.2)$$

Note that the refractive indices depend on the wavelength λ of the light. The refractive index values are given, for example, in Ref. [20].

In Ref. [16], it was shown that the experimental contrasts were well reproduced when using the refractive index of bulk graphite, $n_3 = 2.6 - 1.3i$, which is independent of the wavelength. $\Delta_i = 4\pi n_i d_i / \lambda$ ($i = 1, 2, 3, 4$) is the phase shift of light of wavelength λ due to the change in the optical path, $2d_i$. The expression for a double-layer system (without resist) is obtained for $r_2 = 0$ and $d_2 = 0$.

The contrast is defined as the relative intensity of the reflected light in the presence ($n_3 = 2.6 - 1.3i$) and absence ($n_3 = 1$) of graphene,

$$C = I(n_3 = 1) - I(n_3 = 2.6 - 1.3i). \quad (3.3)$$

The normalized intensity

$$C_n = \frac{I(n_3 = 1) - I(n_3 = 2.6 - 1.3i)}{I(n_3 = 1)} \quad (3.4)$$

was also calculated [16].

Figures 3.5 and 3.6 show the contrast defined in Eq. (3.3) and the normalized contrast defined in Eq. (3.4), respectively, plotted in the wavelength–SiO₂ thickness plane. It is obvious that the contrast strongly depends on the light wavelength and the thickness of the SiO₂ layer; a contrast peak exists for most SiO₂ thicknesses, except for $\lambda < 30$ nm and $\lambda \approx 150$ nm. Although the peak contrast becomes larger for smaller wavelengths in Fig. 3.5, it is notable that the optical contrast is also affected by the spectral sensitivity of the human eye, which has peaks around 450 nm (blue) and 560 nm (green), and that blue light rapidly makes human eyes tired. For

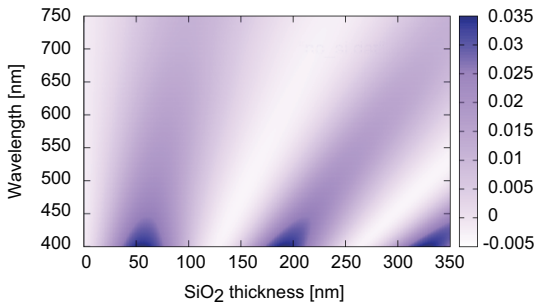


Figure 3.5 Contrast of graphene placed on a Si/SiO₂ substrate, defined in Eq. (3.3), plotted in the wavelength–SiO₂ thickness plane.

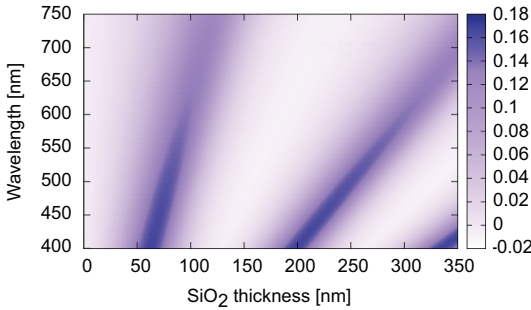


Figure 3.6 Normalized contrast of graphene placed on a Si/SiO₂ substrate, defined in Eq. (3.4), plotted in the wavelength-SiO₂ thickness plane.

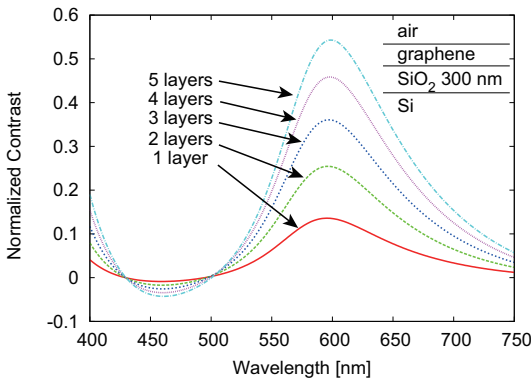


Figure 3.7 Normalized contrast of single-layer to five-layer graphene placed on a Si/SiO₂ (300 nm) substrate.

these reasons, a SiO₂ thickness of ~ 90 nm or ~ 290 nm, which yield a contrast peak around 560 nm (green), is commonly used for naked-eye observation.

It is also notable that the contrast peak wavelength is almost independent of the graphene thickness. Figure 3.7 shows the normalized contrast for single-layer to five-layer graphene, placed on a Si/SiO₂ substrate (thickness of SiO₂ = 300 nm). For all layers, the peak is situated at $\lambda \approx 600$ nm, where the difference in the contrast of graphene with different thicknesses becomes large,

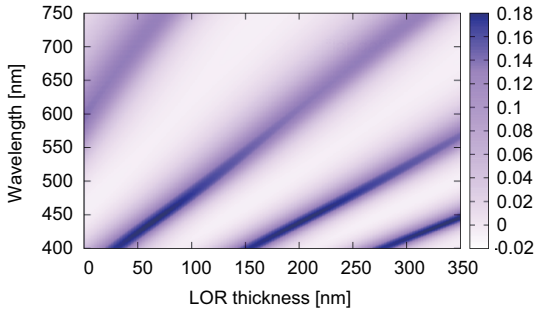


Figure 3.8 Normalized contrast of graphene placed on a Si/SiO₂ (300 nm)/LOR substrate, plotted in wavelength-LOR thickness plane. (LOR is an electron-beam resist.)

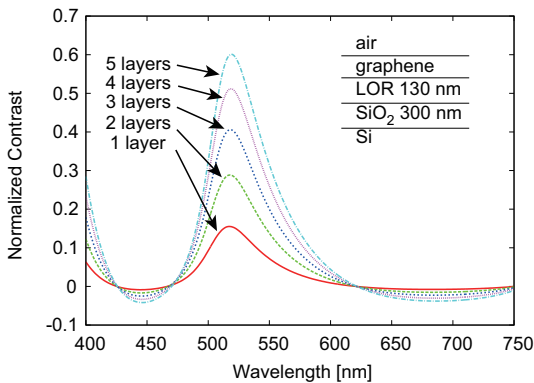


Figure 3.9 Normalized contrast of single-layer to five-layer graphene placed on a Si/SiO₂ (300 nm)/LOR (130 nm) substrate.

indicating that the selection of thickness is also effectively carried out at the contrast peak.

The contrast pattern drastically changes when an additional layer is involved. An example is shown in Figs. 3.8 and 3.9, in which an electron-beam resist layer, LOR, is inserted between the graphene and the SiO₂ layer. (This kind of inserted resist layer is often needed when a graphene film is transferred from one substrate to another [21]). In Fig. 3.8, the normalized contrast of single-layer graphene is shown for a substrate Si/SiO₂ (300 nm)/LOR. The LOR

thickness strongly influences the contrast, and more than one peak is seen for all LOR thickness. In Fig. 3.9, the normalized contrast is shown for single-layer to five-layer graphene placed on a Si/SiO₂ (300 nm)/LOR (130 nm) substrate. As is the case in Fig. 3.7, the peak is situated at the same wavelength ($\lambda = 520$ nm) for single-layer to five-layer graphene, indicating easier thickness separation at the contrast peak.

In practical thickness determination using optical microscopy, it is convenient to quantify the observed contrast [22]. This can be performed by extracting the green component of the RGB (red-green-blue) colors from photographs, which are taken using a digital camera with fixed shooting conditions. The green shift, defined as the difference between the green contrast of the graphene and that of the substrate, takes discrete values, corresponding to single-, double-, triple-, ... layer graphene.

Raman spectroscopy Raman spectroscopy is a widely used method for the determination of graphene thickness.

When a material is illuminated with monochromatic light with frequency ν_0 , the scattered light includes not only the frequency ν_0 but also $\nu_0 \pm \nu$. The former process is called Rayleigh scattering and the latter is called Raman scattering. The frequency shift ν includes information about the phonon modes (rotation, vibration, and so on) in the material. Raman spectroscopy is a powerful tool for the characterization of materials, including graphene [17, 23–25]. Figure 3.10 is an example of the Raman spectra of a graphene film placed on a Si/SiO₂ (300 nm)/LOR (130 nm) substrate for a 514.5 nm (2.41 eV) laser line. (LOR is an electron beam resist.) The horizontal axis is the Raman shift, defined as the difference in wavenumber between the incident and scattered light in units of inverse centimeters (cm^{-1}). There are three characteristic peaks, called the D band (~ 1350 cm^{-1}), the G band (~ 1580 cm^{-1}), and the 2D band (~ 2700 cm^{-1}). The 2D band is also called the G' or D' band.

The G band is due to the LO and TO modes of the graphite honeycomb lattice vibration, which degenerate at the center (the Γ point) of the Brillouin zone (see Fig. 3.11(a)). The G peak is characteristic of sp²-hybridized carbon-carbon bonds and is commonly observed in graphitic materials; however, the peak

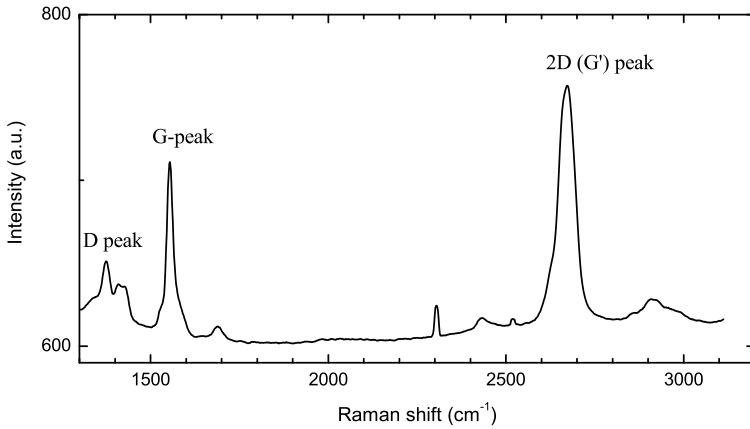


Figure 3.10 Raman spectra at 514.5 nm (2.41 eV) laser line for graphene placed on a Si/SiO₂ (300 nm)/LOR (130 nm) substrate.

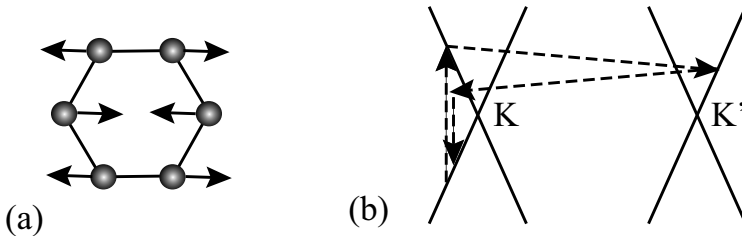


Figure 3.11 (a) Vibration mode of the G band. (b) Double resonance process of the 2D band.

position slightly depends on the detailed structure of the material. The D and 2D bands are double resonance processes. For the 2D band, the incident laser light excites an electron-hole pair, and after two inelastic electron-phonon scattering events involving phonons with opposite momenta, electron-hole recombination occurs (Fig. 3.11(b)) [23]. When there is a defect, one of the electron-phonon scattering events occurs elastically, leading to the creation of a D band. Thus, the strength of the D peak strongly depends on the amount of disorder in the graphitic material. A D peak is also seen at the edges of graphene, locations at which the translational

symmetry breaks down. The 2D band is Raman-active, even in defect-free graphene.

The Raman spectra of graphene have the following thickness dependence [17, 23–25]:

- (i) The G-band peak is situated at $1584 - 1587 \text{ cm}^{-1}$ for single-layer graphene. By increasing the number of layers (n), the G-band peak position ω_G downshifts for small n . The G peak position exhibits an approximately linear dependence on $1/n$, i.e., $\omega_G(n) = \omega_G(\infty) + \beta/n$, where $\beta \approx 5.5 \text{ cm}^{-1}$ [24]. Thus, when one compares the G-peak position for different n 's, the $n = 1$ peak position is different from that of other peaks (see Fig. 3.12).
- (ii) The 2D peak of single-layer graphene can be fitted to a single Lorentzian, whereas $n \geq 2$ graphene has a much broader 2D

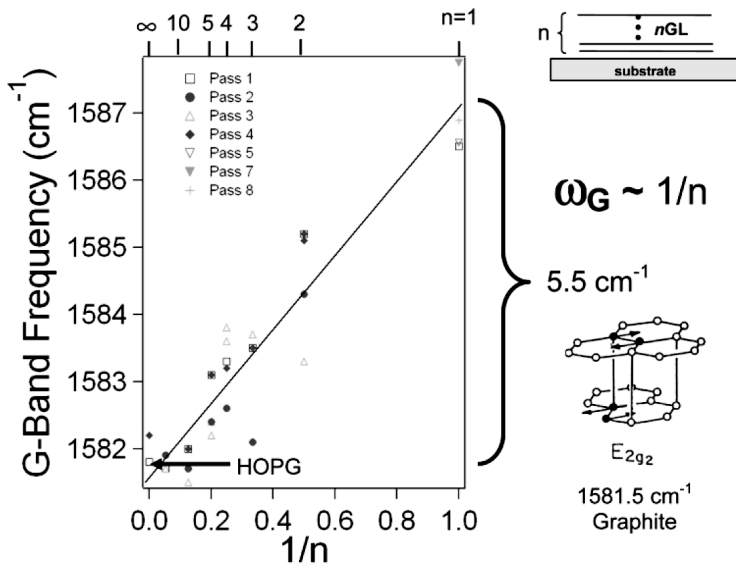


Figure 3.12 G-band frequency vs the inverse of the number of layers, $1/n$. Each pass represents a data set collected under identical optical conditions. The solid line represents the results of a least-squares fit to the data: $\omega_G(\infty) = 1581.6 \text{ cm}^{-1}$ and $d\omega/d(1/n) = 5.5 \text{ cm}^{-1}$. The average of five values found for supported graphene ($n = 1$) is $\omega_G = 1587.1 \text{ cm}^{-1}$. After Ref. [24].

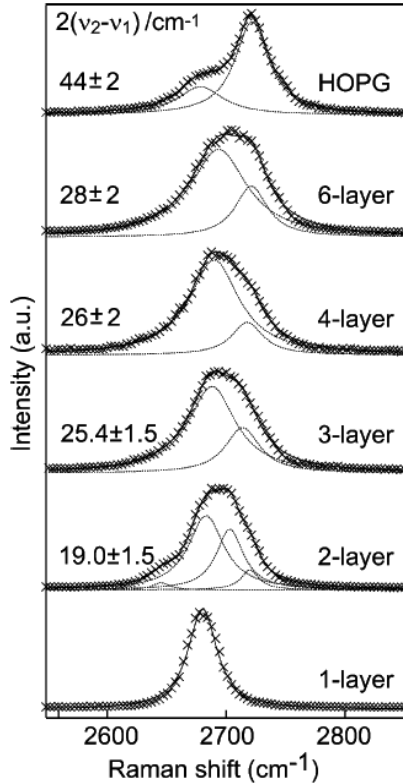


Figure 3.13 2D peaks for an increasing number of graphene layers along with HOPG as a bulk reference. The dashed lines show the Lorentzian peaks used to fit the data; the solid lines are the fitted results. The single peak position for the single-layer graphene is at $2678.8 \pm 1.0 \text{ cm}^{-1}$. The peak positions of the two innermost peaks for double-layer graphene are 2683.0 ± 1.5 and $2701.8 \pm 1.0 \text{ cm}^{-1}$. On the left, the value for the splitting from double-layer graphene up to HOPG is presented. All peaks are normalized in amplitude and vertically offset. After Ref. [25].

band because of the splitting of the electronic bands. Thus, at high resolutions, the 2D band of $n \geq 2$ graphene splits into different subpeaks, e.g., into four Lorentzians for double-layer graphene (see Fig. 3.13). The typical full-width at half maximum (FWHM) of the 2D band for single-layer graphene is $\sim 30 \text{ cm}^{-1}$, while that for $n \geq 2$ graphene is $\sim 60 \text{ cm}^{-1}$ [25].

- (iii) The integrated intensity of the G-band monotonically increases with increasing n , whereas that of the 2D band stays almost constant. The ratio of the integrated intensity of the G band to that of the 2D band is approximately 0.3 for single-layer graphene; this ratio increases almost linearly as one adds layers (from one to four), and saturates for $n \geq 5$.

The influence of laser irradiation on the structure of graphene has previously been studied [26]. Under 1 mW laser irradiation, on a short time scale ($t < 2$ h), laser-induced heating causes the removal of doping adsorbates such as oxygen and water. Thus, usual Raman spectroscopy does not cause the graphene to deteriorate. On the other hand, at long time scales ($t > 3 - 4$ h), laser light induces local decomposition of the graphene crystal into a network of interconnected nanocrystallites with a characteristic length scale of 10 nm. The effect is substantially weaker in thicker graphene.

Similar modification of graphene occurs under electron-beam irradiation [27] and ion-beam irradiation [28]. Ref. [27] reports that e-beam (20 keV) exposure of $4 \times 10^3 \mu\text{C}/\text{cm}^2$ leads to a significant increase in the D-band intensity.

Transport measurement Single-layer and double-layer graphene can be identified by their integer quantum Hall effect seen in transport measurements. This effect will be discussed in detail in Section 3.3.3.

3.2.3 Other Techniques for Formation of Graphene

Although mechanical exfoliation (i.e., the Scotch tape method) produces high-quality graphene flakes, it is almost impossible to adjust the size and position of the flakes being produced. However, this kind of adjustment is indispensable in industrial applications of graphene. Thus, considerable effort has been devoted to growing large-scale, high-quality graphene films.

In this chapter, the two main methods of graphene growth, thermal decomposition of SiC and chemical vapor deposition on metals, are briefly introduced. The advantages and disadvantages of these methods are summarized in Table 3.1.

Table 3.1 Various graphene production methods.

Methods	Advantages	Disadvantages
Mechanical exfoliation (Scotch tape method)	High quality Easy to obtain	Small size Uncontrollable positions and sizes
Thermal decomposition of SiC	Wafer-size possible High quality	High temperature needed SiC substrate expensive
CVD on metallic substrate	Thickness controllable Roll-to-roll production possible Relatively-low-temperature process	Transfer of graphene needed

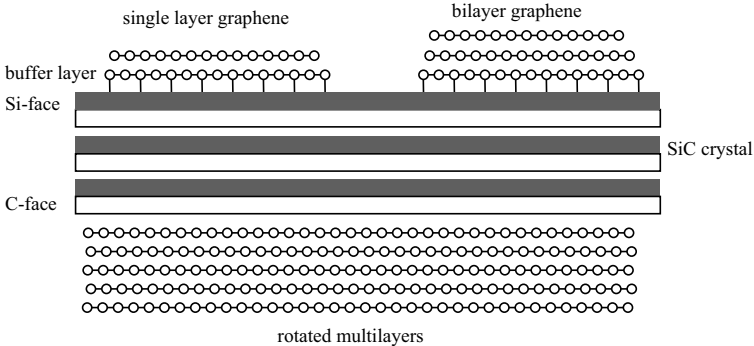


Figure 3.14 Schematic view of graphene grown on the Si-face and C-face of an SiC crystal.

3.2.3.1 Thermal decomposition of SiC

Single-layer and multilayer graphene can be obtained by annealing hexagonal 4H- and 6H-SiC crystals [29]. SiC is a wide-gap semiconductor and 4H- and 6H-SiC are formed by stacking basal planes of bilayers of Si and C atoms, as shown in Fig. 3.14. By annealing SiC substrates (typically at 1200°C to 1900°C) in ultra-high vacuum (UHV) [30] or in an Ar atmosphere [31], Si atoms desorb from the substrate and the remaining carbon atoms rearrange to form graphene sheets. Because the density of carbon atoms in the Si/C bilayer is one third of that in graphene, in the recession of the SiC

surface by Si desorption, three bilayers of Si and C atoms correspond to a single graphene layer.

The growth of graphene layers on the silicon-terminated SiC(0001) surface (Si-face) is slow and terminates after short times in comparison with the growth on the carbon-terminated SiC(000 $\bar{1}$) surface (C-face), in which thick layers ($\sim 5\text{--}100$ layers) can be produced. Graphene layers close to the SiC interface are electron-doped ($\sim 10^{16} \text{ m}^{-2}$) because of the difference in their work functions. The decay length of the charge density is equivalent to several layers [32].

The structure of graphene sheets in silicon-terminated faces (SiC(0001)) is different from that in carbon-terminated faces (SiC(000 $\bar{1}$)). On the Si-face, the first layer is called the buffer layer, a layer in which the structure is similar to that of graphene, but a strong interaction with the SiC substrate makes this layer semiconducting with a bandgap of ≥ 0.3 eV. The upper layers are isolated from the SiC substrate by the buffer layer, so that their electronic states are almost identical to those of single-layer and multilayer graphene.

Typically, high density of steps and pits are observed on the surface of SiC crystals. It is known that the growth of graphene starts at the step edges and that graphene grows continuously over steps. However, the grain size is limited to 30–200 nm for graphene grown in UHV, presumably because of the morphological changes of the surface over the course of high-temperature annealing. Moreover, regions of different thicknesses coexist. These regions are not desirable in device applications. The film quality can be significantly improved by annealing in an Ar atmosphere [31].

On the C-face, the surface structure depends crucially on the growth conditions. For UHV growth, 3D structures (including rotational domains and even nanotubes) are observed [33], whereas when graphene is grown in a graphitic furnace (the radio-frequency (RF) furnace method), successive layers are flat, and most graphene layers are at an angle of $\approx 30^\circ$ relative to adjacent layers. As a consequence, in the latter case, n -layer graphene grown on the C-face behaves as n independent freestanding single graphene layers in which the charge carriers exhibit Dirac fermion properties [34]. The formation of single-layer graphene has also been reported [35].

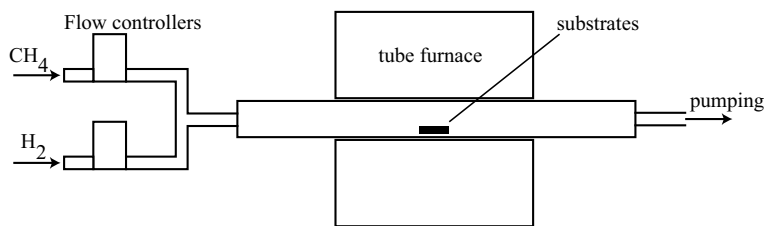


Figure 3.15 Typical apparatus for graphene CVD.

3.2.3.2 Chemical vapor deposition on metallic substrates

It has been known since the 1970s that chemical vapor deposition (CVD) of hydrocarbons on catalytic metals (Ni, Pt, Pd, Co, Ru, etc.) produces thin graphitic layers and even single-layer graphene [36–39]. A typical CVD apparatus is shown in Fig. 3.15. In the case of Ru, for example, carbon is absorbed in the Ru bulk at high temperatures ($\sim 1000^\circ\text{C}$). Because the solubility strongly depends on temperature, one can drive a significant amount of C to the surface by lowering the temperature. Adjusting conditions such as the cooling rate and the target temperature allows one to control the size and thickness of the resulting graphene layers [39, 40].

In early attempts to produce graphene films, ultra-high-vacuum CVD on single crystals of catalytic metals was used. However, the use of both ultra high vacuum and single crystals resulted in high costs; therefore, such processes are not preferable for industrial (large)-scale graphene applications. Moreover, because the catalytic substrate is metallic, one needs to isolate and remove the produced graphene from the metal substrate for practical use.

For low-cost, large-scale production of graphene films, ambient pressure CVD with polycrystalline catalytic metals is suitable. This was first achieved using Ni as a catalyst [40–43].

In Ref. [41], for example, Ni films were electron-beam (e-beam) evaporated onto SiO₂/Si substrates. To limit the amount of carbon atoms dissolving into the Ni in the CVD process and to grow thinner graphene films, the thickness of the Ni catalyst was relatively small ($< 500\text{ nm}$). After Ni single-crystals with grain sizes of 1 to 20 μm were formed by thermal annealing, graphene CVD was carried out at 900–1000 $^\circ\text{C}$ under ambient pressure with a highly

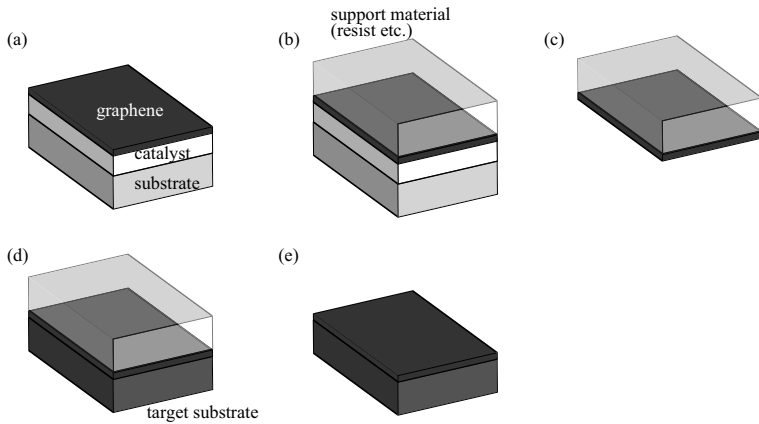


Figure 3.16 Transfer of CVD-grown graphene to a nonspecific substrate. (a) Graphene is formed on metal catalyst by CVD process, (b) graphene is covered by a supporting material such as an e-beam resist PMMA (poly(methyl methacrylate)), (c) catalyst is etched away, (d) the resulting graphene with the supporting material is placed on a target substrate, and (e) the supporting material is removed by a remover such as acetone.

diluted hydrocarbon flow. The produced graphene covered the entire substrate; the thickness ranged from 1 to 12 graphene layers. It was found that the morphologies of the graphene films correlated qualitatively with the microstructure of the Ni films, indicating that individual Ni grains independently affected the thickness of the graphene film during CVD and that the nucleation of the multilayer occurred at the grain boundaries.

The transfer of the CVD-derived graphene films to a nonspecific substrate can be carried out by wet-etching the catalyst layers. The following is an example of the transfer process (Fig. 3.16): First, cover the CVD-grown graphene with a supporting material such as a resist layer. Next, soak the substrate in the etchant of the catalyst (FeCl_3 or acids for Ni) to separate the graphene film from the substrate. After placing the graphene (with the supporting material) on the target substrate, chemically remove the supporting material.

Larger graphene films have been produced using copper as the catalyst [44, 45]. Copper is more suitable than nickel for the following reasons:

- The solubility of carbon in copper is $\sim 0.001\%$ at 900°C , which is much smaller than that of nickel ($\sim 0.1\%$ at 900°C). Thus, the CVD growth of graphene on Cu occurs by a surface adsorption process, whereas graphene on Ni grows via a carbon segregation process [46]. As a result, the growth on Cu is self-limiting, so that one can easily obtain single-layer films.
- Because of the above property, one can use thick Cu “foil” (thickness: $25\ \mu\text{m}$) as a substrate.
- Annealing of Cu leads to a large grain size of $\sim 100\ \mu\text{m}$.

Roll-to-roll production of 30 inch graphene film has been achieved and a graphene-based touchscreen panel has been demonstrated [45].

3.3 Experiments on Transport Properties of Graphene for Device Applications

In this section, we discuss the basic properties of charge transport in graphene from a primarily experimental perspective.

3.3.1 Sample Geometries

Before examining the details of the transport properties of graphene, we first consider several sample geometries used in transport measurement, which are later applied to the graphene transport measurement.

Two- and four-terminal measurements The simplest sample geometry is the two-terminal configuration (Fig. 3.17(a)), in which two electrodes are attached to the sample (in our case, a graphene sample). Each electrode is connected to the current source through a current lead. A voltmeter measures the voltage difference between the current leads. The current I from the current source results in a voltage drop in the sample, current/voltage leads, and contacts. The voltage V recorded by the voltmeter becomes

$$V = (I - i)(R_{\text{sample}} + 2R_{\text{contact}} + 2R_{\text{lead}}) - i(2r_{\text{lead}}), \quad (3.5)$$

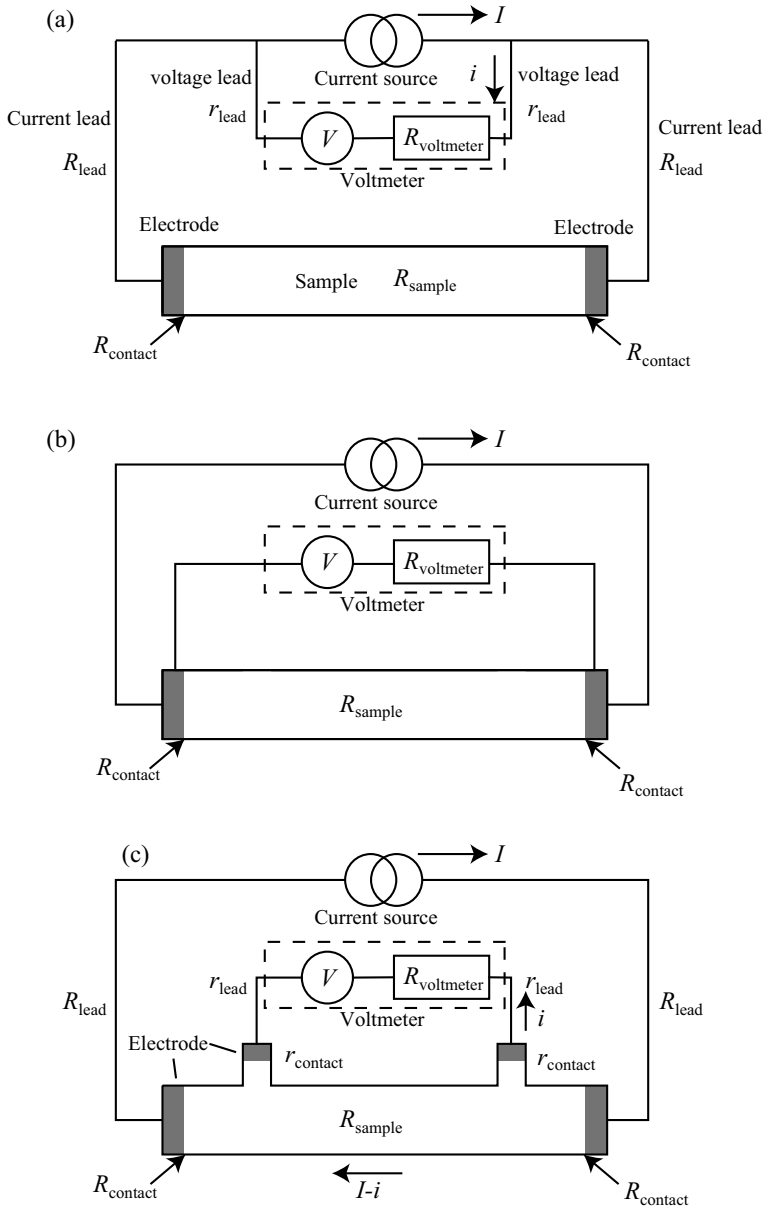


Figure 3.17 Two-terminal configurations (a) and (b), and four-terminal configuration (c) used for transport measurements.

where R_{sample} is the sample resistance, R_{contact} is the interface resistance between the electrode and the sample (contact resistance), R_{lead} (r_{lead}) is the resistance of each voltage (current) lead, and i is the current flowing through the voltmeter. Because the input resistance $R_{\text{voltmeter}}$ of a voltmeter is usually much higher than the sample (lead) resistances (typically $R_{\text{voltmeter}} > \text{several G}\Omega$ for a preamplifier), we can neglect the current i flowing in the voltage leads. Thus, we obtain

$$V \cong I(R_{\text{sample}} + 2R_{\text{contact}} + 2R_{\text{lead}}). \quad (3.6)$$

This means that the measured resistance V/I is increased by the contact and the lead resistances. Thus, the two-terminal resistance is reliable only when the expected value of R_{sample} is much higher than the contact and lead resistances.

The situation is slightly improved when we connect the voltage leads to the sample electrodes, as shown in Fig. 3.17(b). However, in this case, the measured resistance includes the contribution from the contacts,

$$V \cong I(R_{\text{sample}} + 2R_{\text{contact}}). \quad (3.7)$$

This structure is inevitably used, e.g., in transistors and junctions (see Sections 3.3.6, 3.3.9, and 3.3.10).

When the four-terminal configuration is used, the situation is significantly improved (Fig. 3.17(c)). In the four-terminal configuration, the voltage leads are connected to the central section of the sample through additional electrodes. Ideally, as shown in Fig. 3.17(c), the sample has a rectangular shape with additional side arms for voltage electrodes. The side arms are narrow so that the current flow and the potential distribution in the sample are not disturbed by the arms. However, a simplified geometry in which the voltage leads are directly connected to the rectangular sample is often used. The measured voltage in the ideal case is

$$V = (I - i)R_{\text{sample}} - i(2r_{\text{contact}} + 2r_{\text{lead}}) \quad (3.8)$$

$$\cong IR_{\text{sample}}, \quad (3.9)$$

where r_{contact} is the contact resistance of each voltage electrode, and

$$R_{\text{sample}} = (L/S)\rho_{xx} \quad (3.10)$$

is the sample resistance between the voltage electrodes (L = separation of the voltage electrodes, S = cross section of the sample).^d

The resistivity tensor is defined as

$$E_x = \rho_{xx}J_x + \rho_{xy}J_y, \quad (3.11)$$

$$E_y = \rho_{yx}J_x + \rho_{yy}J_y. \quad (3.12)$$

Here, $E_{x(y)}$ and $J_{x(y)}$ are the electric field and the current density in the longitudinal (transverse) direction of the sample, respectively.

In an isotropic sample, $\rho_{xx} = \rho_{yy}$ and $\rho_{xy} = -\rho_{yx}$ are satisfied. In this case, the resistivity tensor $\hat{\rho}$ and the conductivity tensor $\hat{\sigma}$ satisfy the following relationships:

$$\sigma_{xx} = \frac{\rho_{xx}}{\rho_{xx}^2 + \rho_{xy}^2}, \quad \sigma_{xy} = \frac{-\rho_{xy}}{\rho_{xx}^2 + \rho_{xy}^2}, \quad (3.13)$$

$$\rho_{xx} = \frac{\sigma_{xx}}{\sigma_{xx}^2 + \sigma_{xy}^2}, \quad \rho_{xy} = \frac{-\sigma_{xy}}{\sigma_{xx}^2 + \sigma_{xy}^2}. \quad (3.14)$$

Hall bar geometry For the Hall effect measurement, the Hall bar geometry is commonly used. The sample structure is shown in Fig. 3.18, in which narrow arms A, B, C, and D are attached to the rectangular sample. Here, the transverse voltage, V_H , (called the Hall voltage) is measured using a pair of electrodes (A, B) or (C, D), which are placed symmetrically with respect to the longitudinal (x) axis of the sample.

When a magnetic field is applied perpendicular to the sample plane, the Lorentz force exerted on a moving charge causes an accumulation of charges at the longitudinal edges of the sample, producing an electric field perpendicular to the current flow (the Hall effect). The total electric field in the sample is the sum of the electric field produced by the current source (parallel to the x axis) and that due to the Hall effect (parallel to the y axis). The resulting equipotential lines are not perpendicular to the current flow (from P to Q), as depicted in Fig. 3.18. It is notable that close to the source and drain electrodes (P and Q), the equipotential lines are parallel to the boundary of the metallic electrodes, so that the electric field

^dFor graphene samples, the thickness of the graphene is commonly defined as $0.34 \text{ nm} \times n$, where 0.34 nm is the layer separation of a graphite crystal, and n is the number of layers in the sample.

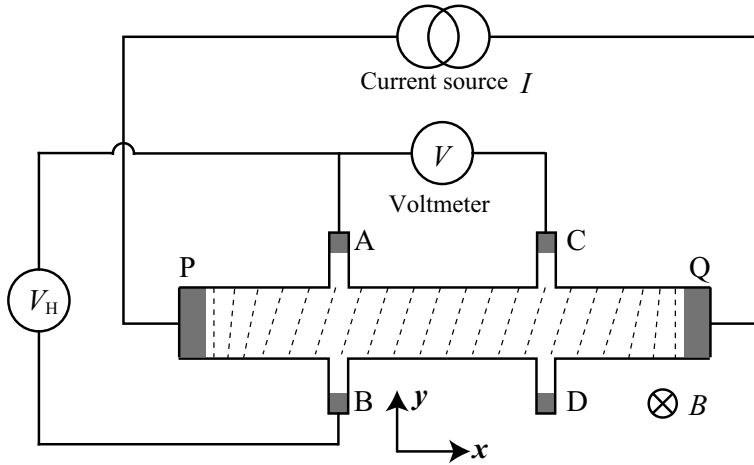


Figure 3.18 Hall bar geometry for the Hall-voltage measurement. The dashed lines in the sample represent the equipotential lines under a perpendicular magnetic field.

distribution near the electrodes is disturbed. As a result, the current flow near the electrodes becomes non-uniform, causing errors in ρ_{xx} and ρ_{xy} . To have an accurate measurement of the Hall voltage, the distance between P and A (or, C and Q) should be much longer than the sample width.

Corbino geometry The longitudinal conductivity in a magnetic field, $\sigma_{xx}(B)$, is accurately determined in the Corbino geometry, in which two coaxial electrodes with the cylindrical symmetry are attached to the sample, as depicted in Fig. 3.19. When a voltage difference V is applied across the inner and outer electrodes, the resulting electric field E points outwards radially from the center. The angle between E and the local current density j is constant, as shown in Fig. 3.19(b). The radial component of the current density, $j_r(r)$, at distance r from the center is related to the electric field $E(r)$ as $j_r(r) = \sigma_{xx}E(r)$. The source–drain current I is given by

$$I = 2\pi r d j_r(r) \quad (3.15)$$

$$= 2\pi r d \sigma_{xx} E(r), \quad (3.16)$$

where d is the thickness of the sample. Note that the circular (azimuth) current component does not contribute to the source–

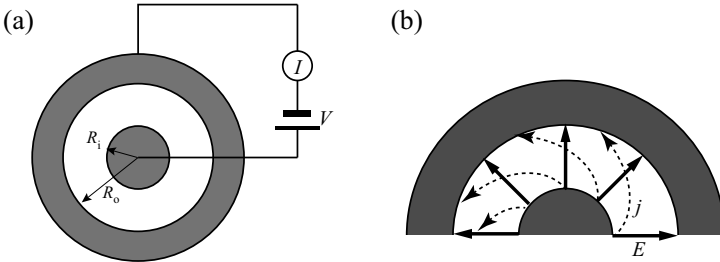


Figure 3.19 (a) Corbino geometry for the accurate measurement of σ_{xx} . (b) Local current density and electric field distributions in the Corbino disk under a perpendicular magnetic field.

drain current I . The electric field $E(r)$ is given by

$$E(r) = \frac{V}{r \ln(R_o/R_i)}, \quad (3.17)$$

where R_o and R_i are the outer and inner radius of the sample. Here, we neglect the contact resistances. From Eqs. (3.16) and (3.17), we obtain

$$\sigma_{xx} = \frac{I}{V} \frac{1}{2\pi d} \ln \frac{R_o}{R_i}. \quad (3.18)$$

van der Pauw method The van der Pauw method [47] is used when well-defined Hall bar samples are not available. This is the case for nanoscale materials such as graphene, in which microfabrication processes for forming the Hall bar geometry might reduce the sample quality. The van der Pauw method can determine the resistivity of flat samples with arbitrary shape if the contacts are placed at the sample edge and the sample is hole-free. Figure 3.20(a) is an example of the sample geometry with four contacts, A, B, C, and D. The measured resistance satisfies the following relation,

$$\exp\left(\frac{-\pi R_{AB,CD}d}{\rho_{xx}}\right) + \exp\left(\frac{-\pi R_{BC,DA}d}{\rho_{xx}}\right) = 1. \quad (3.19)$$

where d is the sample thickness. $R_{AB,CD}$ denotes the resistance defined as V_{CD}/I_{AB} , i.e., the potential difference between C and D

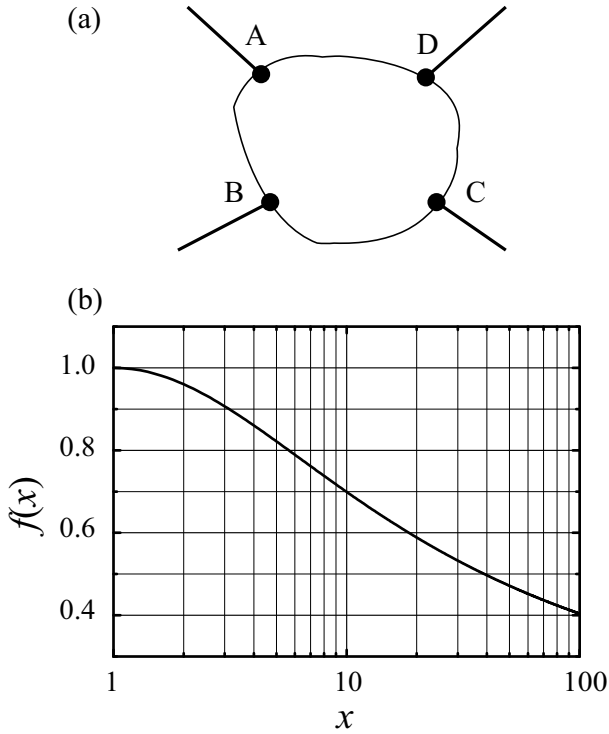


Figure 3.20 (a) An example of the sample geometry in van der Pauw measurement. (b) Function $f(x)$ used in the resistivity calculation.

(V_{CD}) as a result of the current flow I_{AB} from contact A to B is divided by I_{AB} .

From this equation, one can obtain

$$\rho_{xx} = \frac{\pi}{\ln 2} d \frac{R_{AB,CD} + R_{BC,DA}}{2} f\left(\frac{R_{AB,CD}}{R_{BC,DA}}\right), \quad (3.20)$$

where the function $f(x)$ depicted in Fig. 3.20 (b) is the solution to the following equation:

$$\frac{x-1}{x+1} = \frac{f}{\ln 2} \operatorname{arccosh} \left[\frac{1}{2} \exp\left(\frac{\ln 2}{f}\right) \right]. \quad (3.21)$$

The Hall resistivity ρ_{xy} is also obtained from the van der Pauw measurement. When a magnetic field B is applied perpendicular to the sample plane, the voltage $V_{BD}(B)$ between contacts B and

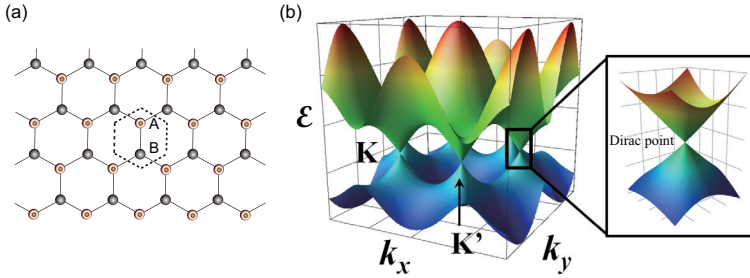


Figure 3.21 (a) The lattice structure of single-layer graphene. A unit cell, indicated by the dotted hexagon, includes two carbon atoms, each of which belongs to the A- or B-sublattice. (b) Electronic band structure of single-layer graphene. Right: close up of the band structure around $\epsilon = 0$, called the Dirac point, which is located at the K and K' points at the corners of the Brillouin zone. Without charge doping, the Fermi level (energy) is situated at the Dirac point.

D for the current I_{AC} from contact A to C experiences a resistance $R_{AC,BD}(B) = V_{BD}(B)/I_{AC}$. The Hall resistance is given by

$$\rho_{xy}(B) = \frac{R_{AC,BD}(B) - R_{AC,BD}(0) + R_{BD,CA}(B) - R_{BD,CA}(0)}{2}. \quad (3.22)$$

3.3.2 Gate Voltage Dependence of Conductance

In the rest of this chapter, we consider previous experiments on the electron transport properties of graphene.

As discussed in Chapter 2, the unit cell of single-layer graphene consists of two carbon atoms, each of which belongs to A- or B- sublattices, as shown in Fig. 3.21(a). Owing to the presence of these two independent sublattices, there are two different sites K and K' at the corners of the Brillouin zone. Single-layer graphene has a linear band structure around the energy $\epsilon = 0$, called the Dirac point (see Fig. 3.21), which is situated at K and K' points. For this reason, the conducting electrons and holes in single-layer graphene behave as massless Dirac fermions, obeying the relativistic Dirac equation. This is in contrast to the carriers in conventional metals and semiconductors, which obey

the (nonrelativistic) Schrödinger equation. Thus, the electrons and holes in graphene correspond to the electrons and positrons in quantum electrodynamics, and phenomena treated in high-energy physics, particle physics, and cosmology are, in principle, observable in graphene. This outstanding property of graphene leads to many unusual phenomena that are not only interesting from the viewpoint of fundamental sciences but also important for applications.

The most important phenomenon observed in graphene electron transport is the large electric field effect: Because of the steep change in the density of states around the Dirac point, the conductivity of graphene strongly depends on the position of the Fermi level at low energies. The position of the Fermi level (Fermi energy) is controlled, for example, by the gate voltage in graphene FET devices. The typical structure of a graphene FET device is shown in Fig. 3.22(a). Here, a graphene film with two metal electrodes (called source and drain) is placed on a highly doped Si substrate covered by an insulating layer. Carriers (electrons or holes) flow from the source to the drain (however, there is no structural difference between the source and drain). By changing the electric potential of the Si substrate (used as a back gate), one can control the carrier density and the position of the Fermi level. An example is shown in Fig. 3.22(b–d). In this case, the sample is a graphene film with four-terminal geometry placed on a Si substrate covered by a 300 nm SiO₂ layer. The gate voltage (V_G) dependence of the conductance shows a V-shaped curve with a minimum corresponding to the Dirac point.^e

From the Drude model [48], the conductivity σ is given by

$$\sigma = ne\mu, \quad (3.23)$$

where n is the carrier density, e is the electron charge, and μ is the carrier mobility. From the gate voltage dependence of the

^eIt is now known that at the gate voltage corresponding to the minimum conductivity, the carrier density does not exactly vanish, because of the existence of charged impurities, as explained in the following subsection.

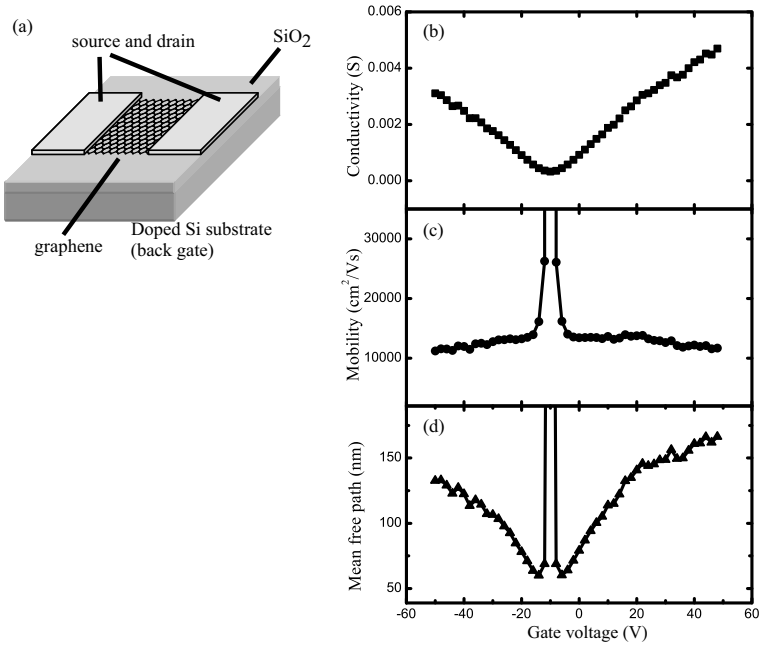


Figure 3.22 (a) Typical structure of a graphene FET device. (b–d) Typical gate voltage dependence of conductance (a), mobility (b), and mean free path (c) in single-layer graphene produced by mechanical exfoliation (the Scotch tape method).

conductivity, one obtains the field-effect mobility^f

$$\mu_{\text{FE}} = \frac{1}{e} \frac{d\sigma}{dn} = \frac{1}{c_G} \frac{d\sigma}{dV_G} \quad (3.24)$$

where $c_G = ne/V_G$ is the gate capacitance per unit area, which is given by $c_G = \epsilon\epsilon_0/d$. Here, ϵ_0 and $\epsilon \sim 4$ are the dielectric constant

^fThe carrier mobility can also be obtained from the Hall effect. The Hall coefficient R_H is defined as

$$R_H = E_y/j_x B_z,$$

where j_x is the current density, E_y the induced Hall electric field, and B_z is the applied magnetic flux density. R_H takes a negative (positive) value when the carriers are electrons (holes). In the free electron model, one can calculate the carrier density n from the relationship $R_H = 1/ne$. Thus, one can define the Hall mobility as

$$\mu_H = \sigma R_H.$$

(permittivity) of the free space and the relative dielectric constant of SiO_2 , respectively, and $d = 300$ nm is the thickness of the SiO_2 layer. Figure 3.22(c) shows the gate voltage dependence of μ_{FE} . The almost linear dependence of the conductivity gives a nearly constant mobility around $1 \text{ m}^2/\text{Vs}$.

The electron mean free path l can be derived from the conductivity as follows: The Einstein relation is

$$\sigma = e^2 D(\varepsilon_{\text{F}}) D_{\text{d}}, \quad (3.25)$$

where $D(\varepsilon_{\text{F}})$ is the density of states at the Fermi level ε_{F} , and D_{d} is the diffusion constant for d -dimensional systems. For $d = 2$,

$$D_2 = \frac{1}{2} v_{\text{F}}^2 \tau = \frac{1}{2} v_{\text{F}} l. \quad (3.26)$$

Here, v_{F} is the Fermi velocity and $\tau = l/v_{\text{F}}$ is the mean scattering time. For single-layer graphene, the Fermi energy is

$$\varepsilon_{\text{F}} = \hbar v_{\text{F}} k_{\text{F}} \quad (3.27)$$

where $\hbar = h/2\pi$ is the Planck constant divided by 2π and k_{F} is the Fermi wavenumber. The carrier density n is given by

$$n = g_{\text{s}} g_{\text{v}} \frac{\pi k_{\text{F}}^2}{(2\pi)^2} = \frac{k_{\text{F}}^2}{\pi} = \frac{\varepsilon_{\text{F}}^2}{\pi (\hbar v_{\text{F}})^2}. \quad (3.28)$$

Here g_{s} and g_{v} are the spin and valley degeneracies, respectively, and $g_{\text{s}} = g_{\text{v}} = 2$ for single-layer graphene, as discussed in Chapter 2. The graphene's density of states becomes

$$D(\varepsilon_{\text{F}}) = \frac{dn}{d\varepsilon} = \frac{2\varepsilon_{\text{F}}}{\pi (\hbar v_{\text{F}})^2} = \frac{4k_{\text{F}}}{\hbar v_{\text{F}}} \quad (3.29)$$

$$= \frac{2}{\hbar v_{\text{F}}} \sqrt{\frac{n}{\pi}}. \quad (3.30)$$

Substitution of the expressions for D_2 and $D(E_{\text{F}})$ into the Einstein relation gives

$$\sigma = \frac{2e^2}{h} k_{\text{F}} l. \quad (3.31)$$

Thus, the mean free path is given by

$$l = \frac{h}{2e^2} \frac{\sigma}{\sqrt{n\pi}}. \quad (3.32)$$

Far from the Dirac point, one expects that the random potentials due to charges in the substrate, the adsorbates, and so on are well screened, and that the net carrier density n approaches the gate-induced carrier density, $n = c_g |V_g - V_D|/e = \alpha |V_g - V_D|$, where V_D is the gate voltage corresponding to the Dirac point. For Si substrates with a 300 nm SiO₂ layer, $\alpha \approx 7.2 \times 10^{14}/\text{m}^2\text{V}$. Figure 3.22(d) shows the mean free path calculated from the conductivity in Fig. 3.22(b) using Eq. (3.32).^g The value far from the Dirac point is around 100 nm, which is common for single-layer graphene placed on a Si/SiO₂ substrate.

The experimental results regarding the gate voltage dependence of the conductivity of graphene were a surprise to the scientific community. The unusual conductivity properties (Fig. 3.22(a)) include (i) a nonvanishing minimum conductivity at the Dirac point, where the carrier concentration (density of states) is zero, (ii) the almost linear dependence of the conductivity on the gate voltage away from the Dirac point, and (iii) the temperature independence of the mobility. A theoretical treatment of the conductivity can be found in Chapter 2.

The first study into electron transport in graphene [49], reported by A. K. Geim's group at the University of Manchester, pointed out that all samples exhibited the same minimum conductivity $\sigma_{\min} \approx 4e^2/h \approx 1.6 \times 10^{-4} \text{ S} (\approx (6.4 \text{ k}\Omega)^{-1})$ within an experimental error of $\sim 15\%$, which remains the same even when varying the mobility by a factor of 10. On the other hand, many theories, dealing with short-range scattering [50–52],^h and based on the Landauer formula [53], predicted a universal value of $4e^2/\pi h$ for σ_{\min} . This discrepancy between theory and experiment was called the “missing π ”.

Later, another active experiment group (led by P. Kim at Columbia University) reported that in their samples the values of σ_{\min} lay in the range of $2 - 12e^2/h$ with most samples having $\sigma_{\min} > 4e^2/h$ [54], in contrast to the earlier report. The result shown in Fig. 3.22(b) also has $\sigma_{\min} \approx 8.3e^2/h$.

^gWe assumed that V_D equals the gate voltage that gives the minimum conductivity, $V_{G,\min}$. However, strictly speaking, it is not exact, as discussed below.

^hShort-range scattering may arise from defects and dislocations in the lattice.

In addition to the gate voltage dependence of the conductivity, studies have also shown a discrepancy between theory and experiment: Theories predicted that away from the Dirac point, either the conductivity steeply increased and approached a constant value or the conductivity is proportional to \sqrt{n} [50–52], whereas in experiments, the conductivity exhibited a broad minimum around the Dirac point and increased almost linearly with the gate voltage.

Such discrepancies between theory and experiment are attributed to the effect of long-range scattering from charged impurities. According to a theory based on a self-consistent random phase approximation (RPA) — Boltzmann formalism, in which the impurity scattering by the charged carriers is treated self-consistently with RPA, and the DC conductivity is treated with Boltzmann theory, the conductivity of graphene dominated by long-range scattering due to charged impurities is given by [55]

$$\sigma(n - \bar{n}) = \begin{cases} C \frac{e^2 n^*}{h n_{\text{imp}}} & \text{for } |n - \bar{n}| < n^* \\ C \frac{e^2 n - \bar{n}}{h n_{\text{imp}}} & \text{for } |n - \bar{n}| > n^* \end{cases}, \quad (3.33)$$

where the residual carrier density n^* , which is determined self-consistently in the theory,ⁱ manifests itself in experiments in the form of a residual conductivity plateau that is shifted by an offset carrier density $\bar{n} = \alpha V_{G,\text{min}}$, as shown in Fig. 3.23(a),^j and n_{imp} is the concentration of the charged impurities.

The constant C depends on the substrate material and is given by

$$C = \frac{2}{G [2r_s]}, \quad (3.34)$$

where

$$G [x] = x^2 \left(\frac{\pi}{4} + 3x - \frac{3\pi x^2}{2} + \frac{x(3x^2 - 2) \arccos[1/x]}{\sqrt{x^2 - 1}} \right). \quad (3.35)$$

ⁱ Because the average carrier density vanishes around the Dirac point, n^* is related to the spatial variation (fluctuation) of the carrier density caused by the formation of electron and hole puddles, as discussed later in this subsection.

^j $V_{G,\text{min}}$ is the gate voltage that gives the minimum conductivity. In general, $V_{G,\text{min}}$ is different from the gate voltage V_D , at which the gate-induced carrier density neutralizes the charged impurity density, as discussed later in this subsection. See Eqs. (3.39) and (3.40).

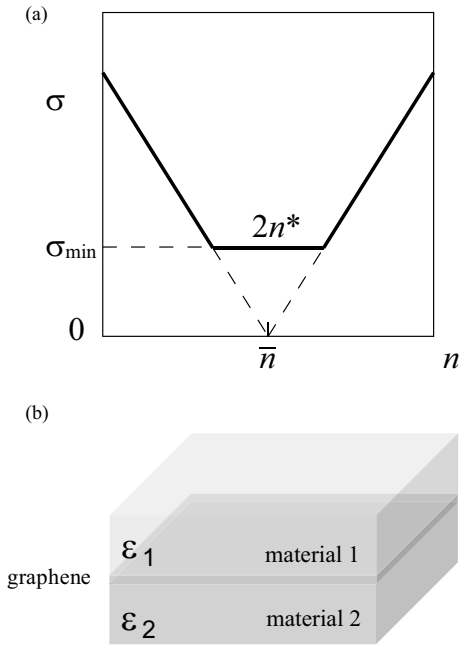


Figure 3.23 (a) Gate voltage dependence of the conductivity calculated from Eq. (3.33). (b) A graphene film sandwiched between two dielectric slabs (materials 1 and 2) with dielectric constants ϵ_1 and ϵ_2 .

r_s is the fine structure constant of graphene sandwiched between two dielectric slabs (materials 1 and 2) with the dielectric constants ϵ_1 and ϵ_2 ,^k respectively, as shown in Fig.3.23(b):

$$r_s = \frac{1}{4\pi\epsilon_0} \frac{e^2}{\hbar v_F} \frac{2}{\epsilon_1 + \epsilon_2}. \quad (3.36)$$

Here $v_F = 1.1 \times 10^6$ m/s is the Fermi velocity [56].^l

For graphene placed on a SiO_2 substrate, $\epsilon_1 = 1$ and $\epsilon_2 \approx 4$, giving $C \approx 20$. The dependence of the constant C on the average dielectric constant $(\epsilon_1 + \epsilon_2)/2$ is shown in Fig. 3.24. Additionally, the constant C for several material combinations is given in Table 3.2.

^kThe relative dielectric constant is sometimes denoted by κ .

^lThe Fermi velocity $v_F = 1.1 \times 10^6$ m/s is slightly larger than the band calculation result of $v_F = 1 \times 10^6$ m/s, which is attributed to electron–electron correlations.

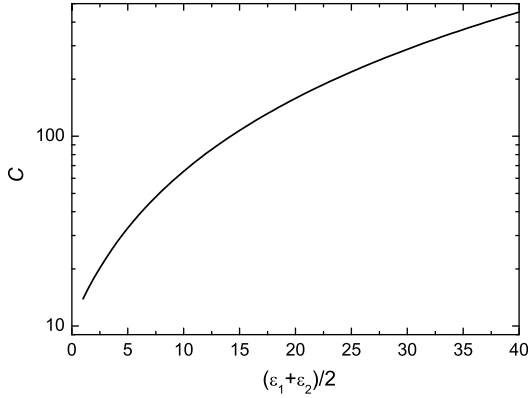


Figure 3.24 Dependence of the constant C on the average dielectric constant $(\epsilon_1 + \epsilon_2)/2$.

Table 3.2 The constant C for several material combinations

Material 1	Material 2	ϵ_1	ϵ_2	r_s	C
Air (vacuum)	SiO ₂	1	4	0.8	20
Air (vacuum)	Air (vacuum)	1	1	2.0	14
Air (vacuum)	PMMA ^a	1	3.5–4.5	0.72–0.89	19–21
PMMA	PMMA	3.5–4.5	3.5–4.5	0.44–0.57	25–30
Air (vacuum)	HfO ₂	1	25	0.15	89
PMMA	HfO ₂	3.5–4.5	25	0.13–0.14	100–105
Air (vacuum)	Al ₂ O ₃	1	10	0.36	36
PMMA	Al ₂ O ₃	3.5–4.5	10	0.27–0.29	43–46

^aPoly(methyl methacrylate).

From Eq. (3.33), the minimum conductivity is given by

$$\sigma_{\min} = C \frac{e^2 n^*}{h n_{\text{imp}}}. \quad (3.37)$$

The ratio n^*/n_{imp} , as determined in the self-consistent procedure in the theory [55], is a monotonically decreasing function of n_{imp} and the dependence is weaker for larger values of n_{imp} . For graphene placed on SiO₂, $\sigma_{\min} \approx 8e^2/h$ for clean samples (e.g., $n_{\text{imp}} \approx 2 \times 10^{11} \text{ cm}^{-2}$), and dirty samples (e.g., $n_{\text{imp}} \approx 3.5 \times 10^{12} \text{ cm}^{-2}$) have $\sigma_{\min} = 4e^2/h$ over a wide range of impurity concentrations, successfully explaining the experimental results reported in Refs. [49] and [54].

From Eqs. (3.33), the mobility has the form^m

$$\mu = C \frac{e}{h} \frac{1}{n_{\text{imp}}}, \quad (3.38)$$

indicating that the only way to increase the mobility for a given substrate is to decrease n_{imp} , i.e., to remove the charged impurities. Another method of increasing the mobility is to change the materials surrounding the graphene. For example, from Table 3.2, changing the substrate from SiO_2 to HfO_2 leads to an increase in the mobility by a factor of 4.5.

Next, we consider several experimental results. Ponomarenko *et al.* [57] reported no significant changes in the carrier mobility either for different substrates (SiO_2 , poly(methyl methacrylate) (PMMA), spin-on glass (SOG), bismuth strontium calcium copper oxide (BSCCO), mica, and boron nitride) or when using glycerol, ethanol, or water as the top dielectric layer, suggesting that charged impurities are not related to the scattering mechanism that limits mobility in graphene.

Nukui *et al.* [58] argued that n_{imp} strongly depends on the materials to which the graphene film attaches, concealing the dependence of the mobility on the dielectric constants of the materials. They used dual-gated multilayer graphene (MLG) devices with a contactless top gate to estimate the mobilities of the top and bottom surfaces (μ_t and μ_b , respectively) of single MLG films placed on a SiO_2 substrate (See Fig. 3.25). Note that the film qualities are the same for the top and bottom surfaces, except that the top surface faces the vacuum while the bottom surface faces SiO_2 . This implies that the strength of the short-range scattering, which is presumably caused by defects and dislocations in the lattice, is the same for the top and bottom surfaces. The experimental result is that the ratio of the mobilities, $r = \mu_b/\mu_t \approx 0.3$ for thick MLG films. Because the dielectric constant of SiO_2 is larger than that of the vacuum, from Eq.

^mEq. (3.38) is used to estimate the value of n_{imp} . For a graphene film placed on a Si/ SiO_2 substrate,

$$\mu[\text{m}^2/\text{Vs}] = \frac{5 \times 10^{15}[\text{Vs}]}{n_{\text{imp}}[\text{m}^{-2}]}.$$

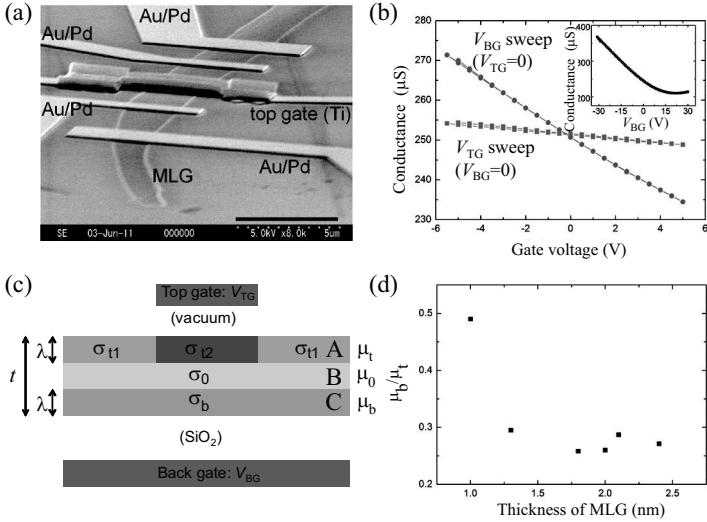


Figure 3.25 (a) SEM image of a dual-gated multilayer graphene (MLG) device. (b) Top and back gate dependences of the conductance. (Inset) Back gate dependence of the conductance for large gate voltages. (c) Model for the calculation of the mobility of the top surface (μ_t) and that of the bottom surface (μ_b) of MLG. (d) Thickness dependence of the mobility ratio, μ_b/μ_t .

(3.38), one can infer that the value of n_{imp} of the bottom surface is larger than that of the top surface.¹¹

¹¹One can estimate the mobility of the top surface (μ_t), and that of the bottom surface (μ_b) of MLG, based on the following model (see also Fig. 3.25(c)). In this model, the layers in the MLG are divided into three parts: the layers including the top (bottom) surface with thickness λ (layer A (C)) and the remaining central part (layer B), as shown in Fig. 3.25(c). Two assumptions are made: 1) the mobilities of layers A to C (μ_t , μ_0 , and μ_b , respectively) are constant over the layers, and 2) the distribution of carrier density in each layer in the direction perpendicular to the surfaces is constant. These assumptions mean that the effect of both the charged impurities and the gate electric fields reaches a distance λ from the surface, so that λ is on the order of the interlayer screening length of MLG, $\lambda_s \approx 1.2$ nm [32]. Under these assumptions, the slope of the conductance for the back gate is given by

$$\frac{dG}{dV_{\text{BG}}} = \frac{d\sigma_b}{dV_{\text{BG}}} \frac{w\lambda}{L} = \frac{dn_b}{dV_{\text{BG}}} \lambda e \mu_b \frac{w}{L} = C_{\text{BG}} \mu_b \frac{w}{L}.$$

Here, $\sigma_b = n_b e \mu_b$ is the conductivity in layer C (n_b is the carrier density of layer C), w is the width of the MLG, and L is the separation of the voltage leads. $C_{\text{BG}} = \epsilon_r \epsilon_0 / t_b$ is the back gate capacitance for unit area, where $\epsilon_r = 4$ is the relative dielectric constant of SiO₂, ϵ_0 the dielectric constant of the vacuum, and t_b is the thickness of

The influence of the charged impurities on graphene conductivity was clearly demonstrated by Chen *et al.* [59] They monitored changes in the gate voltage dependence of the conductivity $\sigma(V_G)$ of initially clean graphene,^o as the density of charged impurities (n_{imp}) was increased by depositing potassium atoms onto its surface in UHV. The following phenomena were observed upon potassium (K) dosing (see also Fig. 3.26):

- (i) The mobility μ decreases as the amount of potassium n_{imp} increases. μ was inversely proportional to n_{imp} .
- (ii) At the lowest K-dosing, $\sigma(V_G)$ is sublinear for large $|V_G - V_D|$. $\sigma(V_G)$ becomes more linear as K-dosing increases.
- (iii) The electron mobility μ_e is smaller than the hole mobility μ_h : $\mu_e/\mu_h = 0.83$.
- (iv) The gate voltage corresponding to the Dirac point V_D shifts to more negative.
- (v) The width of the minimum conductivity region in V_G broadens with K-dosing.
- (vi) The minimum conductivity σ_{min} initially decreases with K-dosing.
- (vii) The linear $\sigma(V_G)$ curves extrapolate to a finite positive value, σ_{res} .

Effects (i), (ii), (iv–vi) agree well with the theoretical prediction made by Adam *et al.* [55] The asymmetry of the electron and hole mobilities (iii) can be attributed to an intrinsic property of graphene, namely, that massless carriers are scattered more strongly when they are attracted to a charged impurity than when they are repelled

SiO₂. In the same way, the slope of the conductance for the top gate around $V_{\text{TG}} = 0$ becomes

$$\frac{dG}{dV_{\text{TG}}} = C_{\text{TG}} \mu_t \frac{wL_t}{L^2},$$

where L_t is the length of the top gate along the current flow, and $C_{\text{TG}} = \epsilon_0/t_t$ is the top gate capacitance per unit area with t_t the height of the top gate. From the experimental results (Fig. 3.25(b)) and the sample geometry, one can obtain μ_t and μ_b .

^oTo obtain clean graphene, the device was annealed in a Ar/H₂ flow at 300°C for 1 h to remove resist residues. After being mounted on a liquid-helium-cooled cold finger in a UHV chamber, the device was annealed in UHV at 490 K overnight to remove residual adsorbed gases.

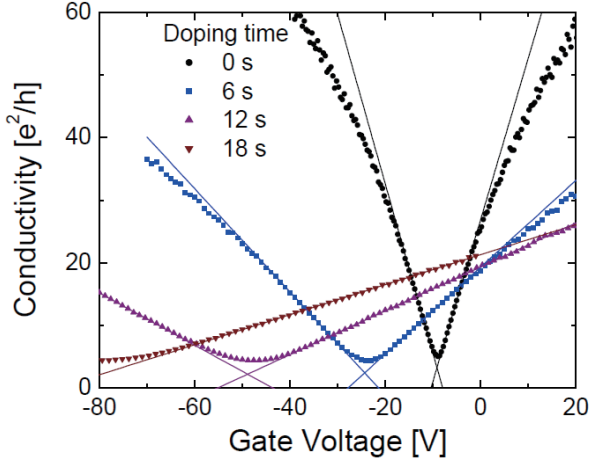


Figure 3.26 The conductivity vs. gate voltage curves for the pristine sample and three different doping concentrations taken at 20 K in ultra high vacuum are shown. The concentration of potassium increases with the doping time. The crossing of the lines defines the points of the residual conductivity and the gate voltage at minimum conductivity ($\sigma_{\text{res}}, V_{G,\text{min}}$) for each data set. After Ref. [59].

by it [60]. The positive σ_{res} value in (vii) is not fully theoretically understood [61, 62].

An additional important finding of Chen *et al.* [59] is that the minimum conductivity does not occur at the induced carrier density that precisely neutralizes the charged impurity density:

$$V_{G,\text{min}} = -n_{\text{imp}} Z e / c_g (\equiv V_D), \quad (3.39)$$

but rather at the induced carrier density at which the average impurity potential is zero,

$$V_{G,\text{min}} = -\bar{n} e / c_g \propto (n_{\text{imp}})^b, \quad (3.40)$$

where $Z e$ is the charge of the potassium ion and \bar{n} is a function of n_{imp} , the impurity spacing from the graphene plane, and the dielectric constant of the substrate. The theoretical value for the constant b is 1.2–1.3, which agrees well with experiment [59].

Electron and hole puddles What is going on at the gate voltage close to $V_{G,\text{min}}$? In an ideal graphene film (free from impurities

and disorder), $V_{G,\min}$ corresponds to the Dirac point, where the density of states vanishes; thus, there are no free carriers in the graphene plane. However, charged impurities create a spatially inhomogeneous potential distribution in the graphene plane, causing the formation of electron and hole puddles at low carrier densities. This was first theoretically predicted [63, 64] and then experimentally verified [65].

Martin *et al.* [65] used a scanning single-electron transistor (SET) to detect the spatial distribution of the local Dirac point in graphene. An SET consists of a metallic grain (called an island) connected to source and drain electrodes through highly resistive small-tunnel junctions [66]. The electron transport in SETs is determined by the change in the charging energy; therefore, the conductance of an SET is sensitive to the electrostatic potential of the island. Thus, the SET tip is capable of measuring the local electrostatic potential with a high sensitivity and a high spatial resolution (close to the island size, ~ 100 nm).

The change in the local electrostatic potential, Φ_{total} , under the modulation of the carrier density n by the gate voltage is related to the change in the local chemical potential in graphene, ε_F , as

$$e \frac{\partial \Phi_{\text{total}}}{\partial n} = - \frac{\partial \varepsilon_F}{\partial n} = - \frac{\hbar v_F}{2} \sqrt{\frac{\pi}{|n|}}, \quad (3.41)$$

exhibiting a steep peak at the local Dirac point ($n \approx 0$). Thus one can identify the local Dirac point with high accuracy.^P

The observed spatial density fluctuations are shown in Fig. 3.27(a). Even when the average carrier density is zero at the charge neutrality point, the graphene plane is divided into electron and hole puddles, areas in which the charge density is negative and positive, respectively. The amplitude of the density fluctuations is $\sim 10^{15}$ m⁻², corresponding to a gate voltage change of ~ 1.5 V for graphene placed on a Si substrate covered with 300 nm SiO₂ layer. Electron

^PIn real-world measurements, the scanning SET picks up not only the spatial variations in the chemical potential but also the potential directly caused by both the charges above the graphene layer and their image charges in the layer. The latter is subtracted from the data based on the potential measured at high carrier densities, where the potential landscape in graphene is expected to be nearly constant because of the screening effect [65].

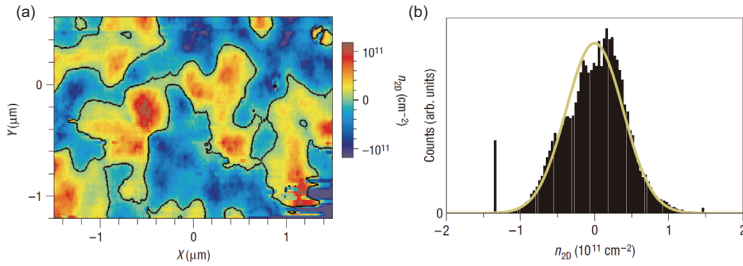


Figure 3.27 (a) Grayscale map of the spatial density variations in the graphene flake extracted from surface potential measurements at high density and when the average carrier density is zero. The black contour marks the zero density contour. (b) Histogram of the density distribution in (a). After Ref. [65].

(hole) puddles are formed because the local Dirac point is below (above) the Fermi level.

A scanning tunneling microscopy (STM) study [67] showed that the spatial charge inhomogeneity (and the resulting formation of electron and hole puddles) is caused not by topographic corrugations in the graphene sample, but rather, is caused by charge-donating impurities within the graphene (Fig. 3.28). A puddle density of $n^* \sim 10^{15} \text{ m}^{-2}$ with a correlation length of $\sim 20 \text{ nm}$ was obtained.

It should be emphasized that all experimental graphene samples inevitably have some free carriers because of the presence of charged impurities, resulting in the formation of electron and hole puddles at the charge neutrality point. Thus, in bulk samples, Dirac physics, which is related to the absence of carriers at the Dirac point, is inaccessible. One always needs to take into account the influence of charged impurities when looking at experimental data.

3.3.3 Quantum Hall Effect

When a strong perpendicular magnetic field is applied to conventional two-dimensional electron systems formed in, for example, Si MOSFETs (metal-oxide-semiconductor field-effect transistor) or GaAs-AlGaAs heterostructures, the Hall conductivity σ_{xy} takes

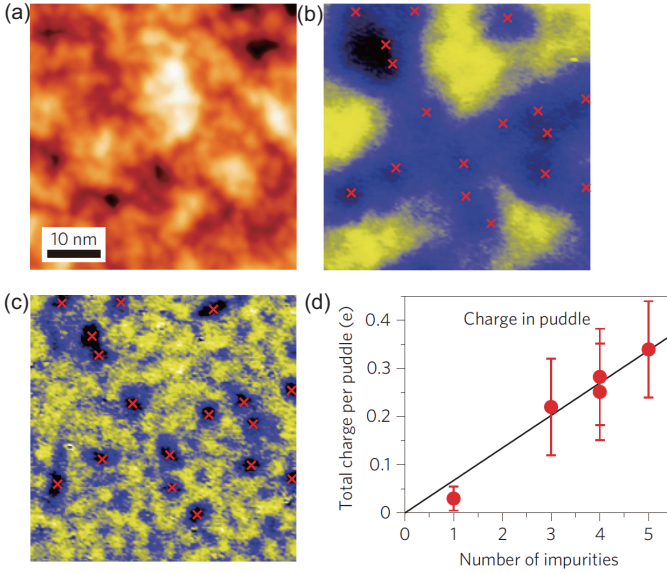


Figure 3.28 (a) STM topography of $50 \times 50 \text{ nm}^2$ area of graphene. (b) dI/dV map at bias near Dirac point showing electron puddles caused by charge fluctuations over the same region of graphene as shown in (a). Crosses indicate the locations of quasiparticle scattering-centre impurities observed in (c). (c) dI/dV map of the same area at larger bias revealing impurity scattering centers in electron-rich charge-density puddles (crosses). (d) Integrated charge per electron puddle plotted as a function of the number of observed impurities in each puddle (puddles are defined as the electron-rich regions left after subtracting the average background charge density). A linear fit to the data (black line) gives the charge associated with each impurity as $0.07 \pm 0.03e$ (e is the charge of an electron). After Ref. [67].

quantized values,

$$\sigma_{xy} = N \frac{e^2}{h}, \quad (3.42)$$

at low temperatures. Here, N is an integer and h is Planck's constant. This property is caused by the cyclotron motion of electrons, which results in a Landau quantization of the energy levels,

$$\varepsilon_N = \hbar\omega_c, \quad (3.43)$$

where $\omega_c = eB/m^*$ is the cyclotron frequency, m^* is the effective mass, and B is the magnetic field. In the case of single-layer

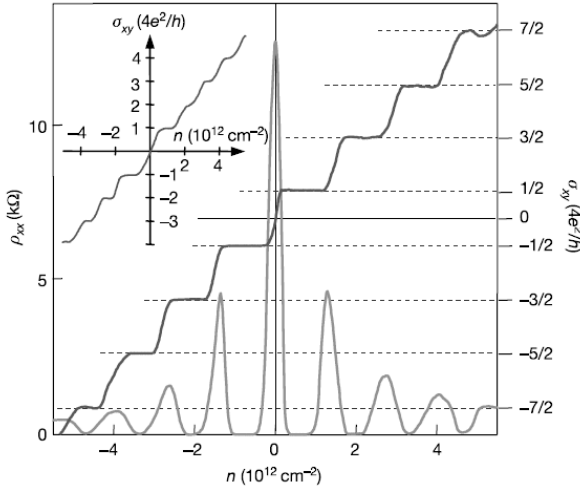


Figure 3.29 Hall conductivity σ_{xy} and longitudinal resistivity ρ_{xx} of single-layer graphene as a function of their concentration at $B = 14$ T and $T = 4$ K. Inset: σ_{xy} in bilayer graphene where the quantization sequence is different from that of the single-layer graphene. After Ref. [49].

graphene, as discussed in Sec 2.2.3, because of its characteristic energy dispersion relation $\varepsilon = v\hbar_F k$, the Landau levels are

$$\varepsilon_N = \sqrt{2e\hbar v_F^2 B} \sqrt{N}. \quad (3.44)$$

This leads to a distinct quantum Hall effect. The Hall conductivity is given by

$$\sigma_{xy} = \pm 4(N + 1/2) \frac{e^2}{h}, \quad (3.45)$$

which is associated with Berry's phase^q π . Here, the factor 4 comes from the double valley and double spin degeneracy. This anomalous quantum Hall effect was reported independently by two groups simultaneously [49, 68]. An example is shown in Fig. 3.29.

For bilayer graphene, Berry's phase 2π leads to the Landau levels

$$\varepsilon_N = \pm \hbar \omega_c \sqrt{N(N-1)}. \quad (3.46)$$

^qDue to the linear dispersion relation of graphene at low energies, when moving around the K (K') point in momentum space, the wavefunction acquires a phase change of π . This is called Berry's phase. This kind of circular path is realized by a cyclotron motion of carriers under a magnetic field.

Here, the standard quantum Hall effect with

$$\sigma_{xy} = 4N \frac{e^2}{h}, \quad (3.47)$$

is seen. However, the first plateau ($N = 0$) is absent.

These distinct quantum Hall effects in single-layer and bilayer graphene are used to identify the number of layers present.

3.3.4 Klein Tunneling

One of the manifestations of the Dirac fermion nature of electrons that obeys quantum electrodynamics is so-called Klein tunneling, an effect that is also discussed in terms of the Klein paradox [69]. This effect states that the transmission coefficient of a Dirac fermion impinging normally on a sharp potential barrier becomes larger as the potential increases and approaches perfect transparency. This is in clear contrast to the tunneling effect seen in nonrelativistic particles obeying the Schrödinger equation, in which the transmission coefficient decreases exponentially as the potential increases. This relativistic effect is attributed to the fact that an electron–positron pair is created at the barrier interface, and that the positron, which is attracted to the barrier, penetrates the barrier.

Although this effect has never been observed in high-energy physics experiments, it was pointed out that confirmation might be possible in graphene, in which an electron (a hole) is converted into a hole (an electron) at the barrier interface corresponding to an np (pn) junction [70]. (n (p) refers to the region in which the carriers are electrons (holes).) This kind of potential barrier can be formed using dual-gated devices (Fig. 3.30(a)), in which the carrier density in regions I and III, which is only affected by the back gate, is different from the carrier density in region II, which is modulated by both top and back gates. In dual-gated devices, the combination of the carrier types in regions I, II, and III are divided into four categories, ppp , nnn , pnp , and nnp , depending on the top and back gate voltages, as shown in Fig. 3.30(b). (The central character refers to the carrier type of region II.) In the measurements of Young and Kim [71], conductance oscillations are observed in the pnp and nnp samples (Fig. 3.31), which can be successfully explained by the occurrence of perfect transmission of carriers normally incident on the junction.

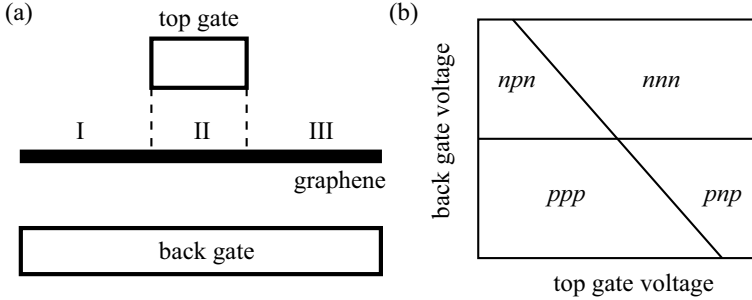


Figure 3.30 (a) Schematic side view of a dual-gated graphene device. In regions I and III, the carrier density is only affected by the back gate, whereas in region II, the carrier density is modulated by both top and back gates. (b) Combination of carrier types in regions I, II, and III are shown for different top and back gate voltages.

3.3.5 Improving Mobility of Graphene

In Section 3.3.2, we looked at the mobility of the experimental samples, which was governed by the influence of charged impurities. For the successful application of graphene to electronic devices such as high-speed FETs, one must enhance the mobility.

3.3.5.1 Effect of phonon scattering

In most previous experiments, the graphene devices under test were placed on a Si/SiO₂ substrate. Thus, it is important to know the limit of the mobility of graphene placed on Si/SiO₂ (and other) substrates. Chen *et al.* [72] derived the upper limit of the mobility of graphene placed on a Si/SiO₂ substrate. They measured the gate voltage V_G dependence and the temperature T dependence of the resistivity ρ of several graphene devices. Their data are shown in Fig. 3.32. These data show that at low temperatures ($20 \text{ K} < T < 100 \text{ K}$), the $\rho(V_G, T)$ curves are linear in temperature with a constant slope of $(4.0 \pm 0.5) \times 10^{-6} h/e^2 \text{ K}$ and are well modeled by

$$\rho(V_G, T) = \rho_0(V_G) + \rho_A(T) \quad (3.48)$$

with

$$\rho_A(T) = \frac{h}{e^2} \frac{\pi^2 D_A^2 k_B T}{2h^2 \rho_s v_s^2 v_F^2}, \quad (3.49)$$

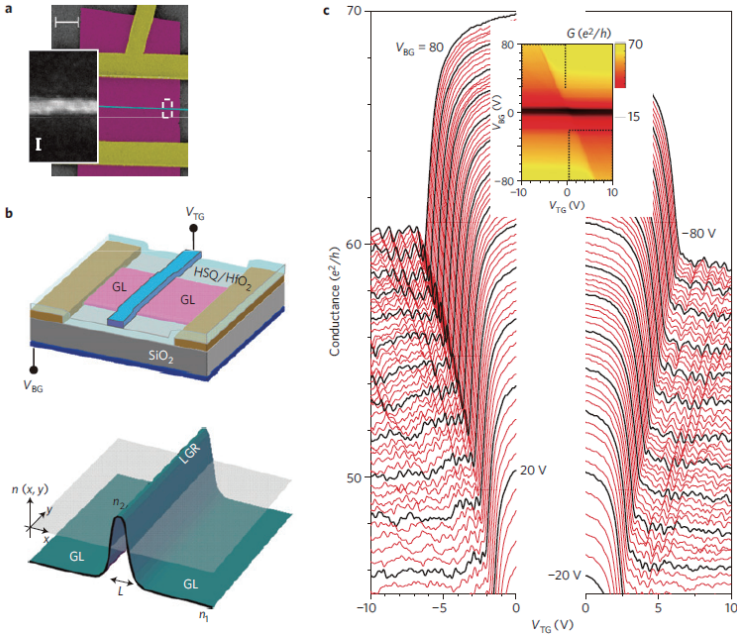


Figure 3.31 (a) Scanning electron microscope image of a typical dual-gated graphene device. The scale bar is 2 μm . Inset: High-magnification view of top gate. The scale bar is 20 nm. (b) Schematic diagram of the device geometry. The electrostatic potential created by the applied gate voltages, V_{BG} and V_{TG} , can create a graphene heterojunction of width L bounded by two pn junctions. GL: “graphene leads.” (c) The inset shows the conductance as a function of V_{BG} and V_{TG} . The main panels show cuts through this map in the regions indicated by the dotted lines in the inset, showing the conductance as a function of V_{TG} at fixed V_{BG} . Traces are separated by a step in V_{BG} of 1 V, starting from ± 80 . After Ref. [71].

where $\rho_0(V_G)$ is the residual resistivity at low temperature, mainly originating from scattering by charged impurities, $\rho_A(T)$ is the portion of the resistivity due to longitudinal acoustic (LA) phonon scattering in graphene, $\rho_s = 7.6 \times 10^{-7} \text{ kg m}^{-2}$ is the two-dimensional mass density of graphene, $v_F = 1.0 \times 10^6 \text{ m/s}$ is the Fermi velocity, $v_s = 2.1 \times 10^4 \text{ m/s}$ is the velocity of sound (LA phonons), and $D_A = 18 \pm 1 \text{ eV}$ is the acoustic deformation potential.

On the other hand, at higher temperatures, the resistivity steeply increases with increasing temperature. The data are successfully

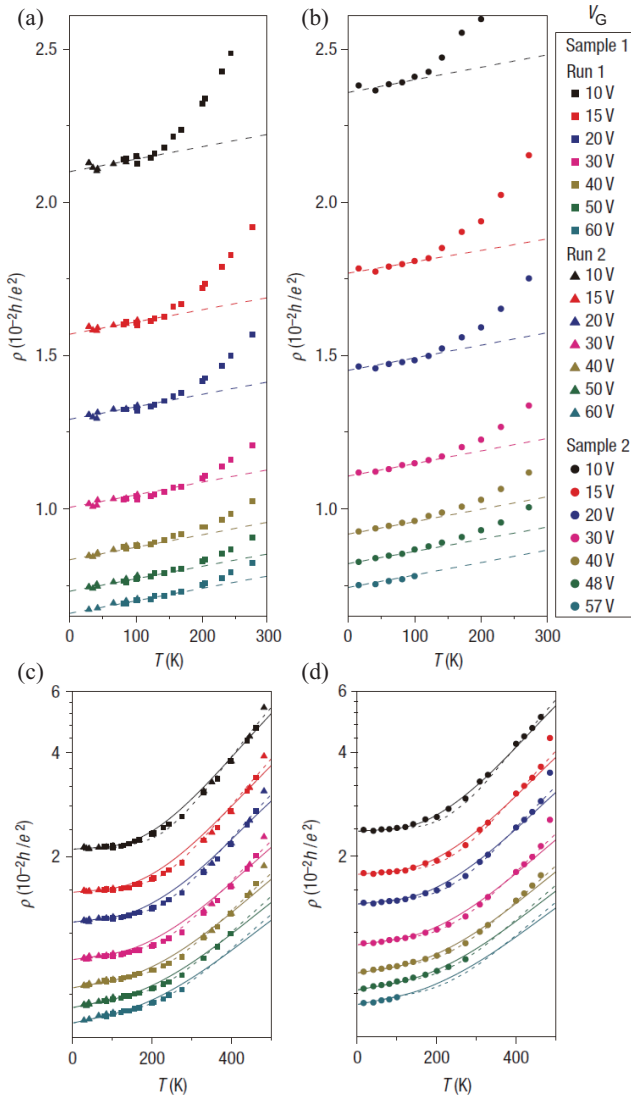


Figure 3.32 (a,b) Resistivity of two graphene samples ((a) sample 1, (b) sample 2) as a function of temperature for gate voltages from 10 to 60 V. Dashed lines are fits to the linear T -dependence (Eq. (3.48)). (c,d) Same data as in (a,b) on a logarithmic scale. The solid lines are fits to Eq. (3.50) (acoustic phonon scattering in graphene plus optical phonon scattering due to the SiO_2 substrate). After Ref. [72].

fitted by

$$\rho(V_G, T) = \rho_0(V_G) + \rho_A(T) + \rho_B(V_G, T) \quad (3.50)$$

with

$$\rho_B(V_G, T) = B_1 V_G^{-\alpha_1} \left(\frac{1}{\exp(59\text{meV}/k_B T) - 1} + \frac{6.5}{\exp(155\text{meV}/k_B T) - 1} \right) \quad (3.51)$$

where $B_1 = 0.607(h/e^2) V^{\alpha_1}$ and $\alpha_1 = 1.04$ are the parameters used to fit the experimental data. The term $\rho_B(V_G, T)$ corresponds to remote interfacial scattering by polar surface phonons in the SiO_2 substrate [73]. The two strongest surface optical phonon modes in SiO_2 are calculated to have energies of 59 meV and 155 meV with a ratio of coupling to the electrons of 1 : 6.5 [73, 74]. These values are used in the expression for $\rho_B(V_G, T)$.

Using Eq. (3.50), one can examine the contributions of the acoustic phonons in graphene and the SiO_2 remote interfacial phonons to the graphene mobility, separately. Figure 3.33 shows the temperature dependence of the mobility, defined as $\mu = 1/ne\rho$, for graphene placed on a Si/SiO_2 substrate (denoted by “with SiO_2 ”) and for graphene without the influence of the SiO_2 remote interfacial phonons (denoted by “without SiO_2 .” Here, the resistivity is given by

$$\rho_{\text{with SiO}_2}(n, T) = \rho_0(n) + \rho_A(T) + \rho_B(n, T), \quad (3.52)$$

and

$$\rho_{\text{without SiO}_2}(n, T) = \rho_0(n) + \rho_A(T), \quad (3.53)$$

respectively (n = carrier density). The latter corresponds to graphene without the SiO_2 substrate. Here, the residual resistivity $\rho_0(n)$ is assumed to have the form $\rho_0(n) = 1/ne\mu_0$, with some low-temperature mobility μ_0 , which depends on the amount of charged impurities and the materials surrounding the graphene (see Eq. (3.38)). In Figs. 3.33(a), (b), and (c), the value of μ_0 is 100, 10, 1 m^2/Vs , respectively. As expected, the difference between $\rho_{\text{with SiO}_2}$ and $\rho_{\text{without SiO}_2}$ is significant at higher temperatures, indicating the stronger influence of the remote interfacial phonons. Note that the temperature dependence of the mobility is weaker for graphene with lower values of μ_0 . This is the experimental situation that was

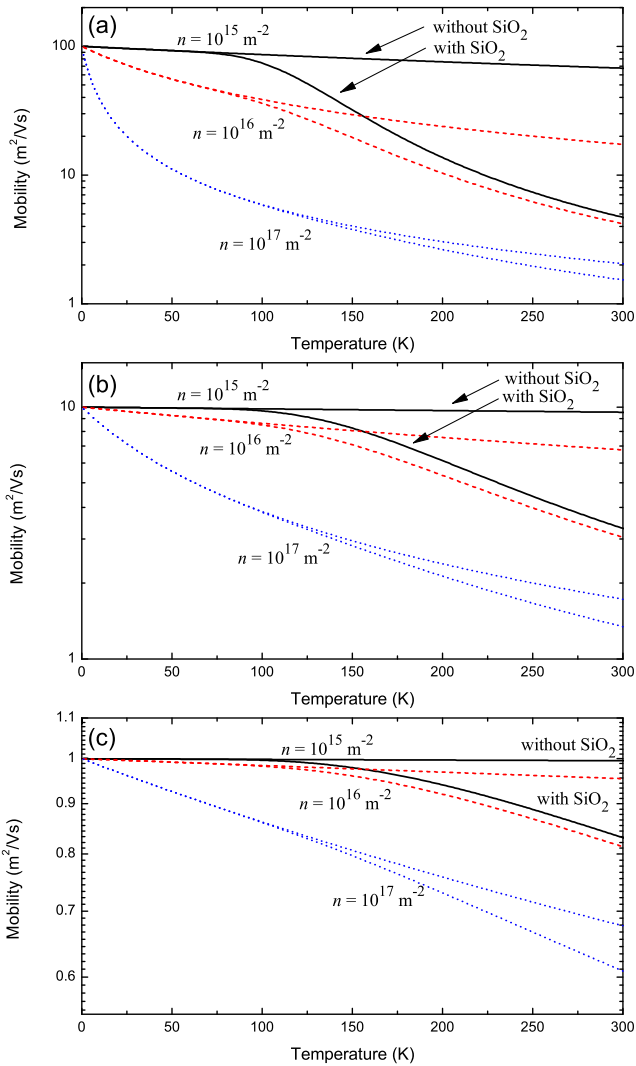


Figure 3.33 Temperature dependence of the mobility calculated for graphene under an influence of SiO_2 remote interfacial phonons (indicated by “with SiO_2 ”) and without it (indicated by “without SiO_2 ”) for several values of carrier density, $n = 10^{15}$, 10^{16} , and 10^{17} m^{-2} , which correspond to gate voltage values of 1.4, 14, and 140 V for 300 nm SiO_2 layer, respectively. The low-temperature mobility is $\mu_0 =$ (a) 100, (b) 10, and (c) $1 \text{ m}^2/\text{Vs}$. For each carrier density, the upper (lower) curve corresponds to the graphene without (with) SiO_2 .

observed in early experiments [49], as discussed in Section 3.3.2. Also notice that the difference between the graphene with SiO₂ and that without SiO₂ is smaller for graphene with a lower mobility. (For example, for a carrier density of $n = 1 \times 10^{16} \text{ m}^{-2}$ at 300 K, the ratio of the mobility $\mu_{\text{with SiO}_2} / \mu_{\text{without SiO}_2} = 4.6, 2.1, \text{ and } 1.2$ for $\mu_0 = 100, 10, \text{ and } 1 \text{ m}^2/\text{Vs}$, respectively.)^r This means that the enhancement of the mobility created by removing the substrate is more effective for graphene with a higher value of μ_0 , i.e., with fewer charged impurities and defects. This was demonstrated by Bolotin *et al.*, [75] as explained later in this subsection.

In Eqs. (3.50) and (3.51), the influence of the phonon scattering on the gate voltage dependence of the conductivity is quantified. Figure 3.34 shows the carrier density dependence of the conductivity at several temperatures for graphene with (a) $\mu_0 = 100 \text{ m}^2/\text{Vs}$ and (b) $\mu_0 = 5 \text{ m}^2/\text{Vs}$, based on Eqs. (3.33) and (3.50). Here, for simplicity, the effect of the minimum conductivity is ignored; therefore, at $T = 0$, $\rho = 1/ne\mu_0$, and the conductivity is zero at the Dirac point. For both $\mu_0 = 100$ and $5 \text{ m}^2/\text{Vs}$ cases, the conductivity-density (σ - n) curve becomes less linear (sublinear) at higher temperatures, and the nonlinearity is more significant in graphene with a higher mobility. Sublinear σ - n curves are also expected both in graphene under the short-range scatterers [52] and in graphene with ultrahigh mobility [75]. The above discussion shows that the sublinear behavior can be seen even in graphene with low mobilities if the temperature is sufficiently high.

Performance of ideal graphene: mobility limit at finite temperatures

The performance of graphene devices with ultimate graphene quality can be estimated from Eq. (3.50) [72].

For graphene with ideal qualities, we may take the low-temperature mobility $\mu_0 \rightarrow \infty$, so that the residual resistivity ρ_0 can be ignored. The resulting temperature dependence of mobility is shown in Fig. 3.35(a) for a carrier density of $n = 10^{16} \text{ m}^{-2}$.

^rWhen the substrate is removed to form “suspended graphene,” the influence of the remote interfacial phonons disappears and the amount of charged impurities decreases. The latter effect corresponds to an increase in the low-temperature mobility μ_0 .

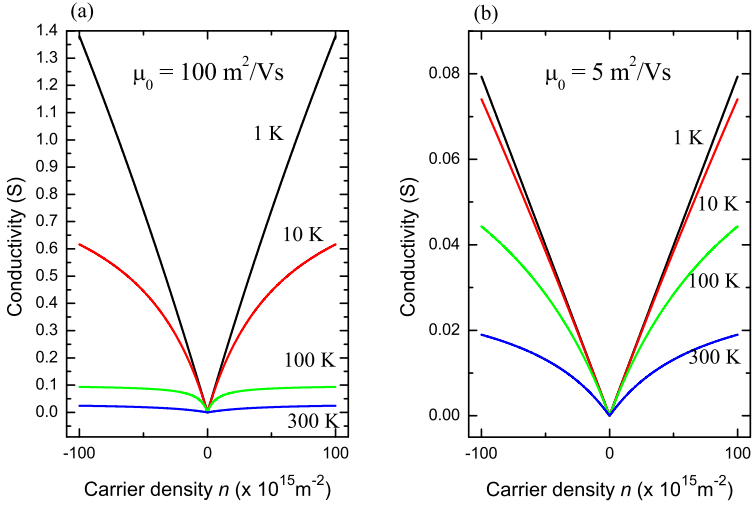


Figure 3.34 Carrier density dependence of the conductivity for graphene with $\mu_0 =$ (a) $100 \text{ m}^2/\text{Vs}$ and (b) $5 \text{ m}^2/\text{Vs}$ for several temperatures, calculated based on Eqs. (3.33) and (3.50); however, the effect of the minimum conductivity is ignored. The negative carrier density corresponds to hole transport.

$(n\rho_A)^{-1}$ corresponds to the mobility limit of graphene without any substrate (only including the influence of the LA phonons), and takes a value of $20 \text{ m}^2/\text{Vs}$ at room temperature (300 K). $(n(\rho_A + \rho_B))^{-1}$ is the mobility limit of the graphene placed on a Si/SiO₂ substrate, excluding the influence of charged impurities. It takes a value of $4 \text{ m}^2/\text{Vs}$ at 300 K. These values are known as the mobility limit for graphene at room temperature.

In graphene with ultimate quality, the shape of the σ - n curve is quite different from that for graphene transport dominated by long-range Coulomb scattering. The carrier density dependence of the conductivity $(\rho_A + \rho_B)^{-1}$ is shown in Fig. 3.35(b). At low temperatures, the conductivity is dominated by LA phonon scattering, and is independent of the carrier density. As the temperature increases beyond 100 K, carrier-density dependent remote interfacial phonon scattering begins to occur, and a dip appears at density $n = 0$.

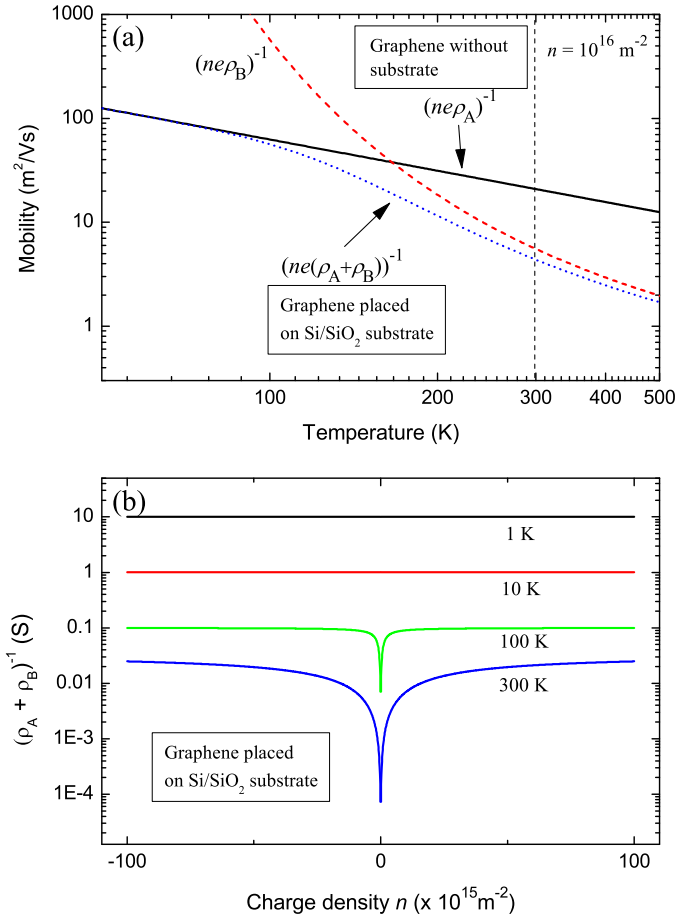


Figure 3.35 Characteristics of graphene with ideal quality. (a) The temperature dependence of the mobility $(ne\rho_A)^{-1}$, $(ne\rho_B)^{-1}$, and $(ne(\rho_A + \rho_B))^{-1}$ for the carrier density $n = 10^{16} \text{ m}^{-2}$. $(ne\rho_A)^{-1}$ corresponds to the mobility limit of graphene without any substrate. $(ne(\rho_A + \rho_B))^{-1}$ corresponds to the mobility limit of the graphene placed on a Si/SiO_2 substrate but without the influence of the charged impurities. (b) The carrier density dependence of the conductivity $(\rho_A + \rho_B)^{-1}$ for several temperatures, which corresponds to graphene placed on a Si/SiO_2 substrate (excluding the influence of the charged impurities). The negative carrier density corresponds to hole transport. The presence of the term ρ_B means that the conductivity vanishes at the Dirac point ($n = 0$), which is not shown in the figure.

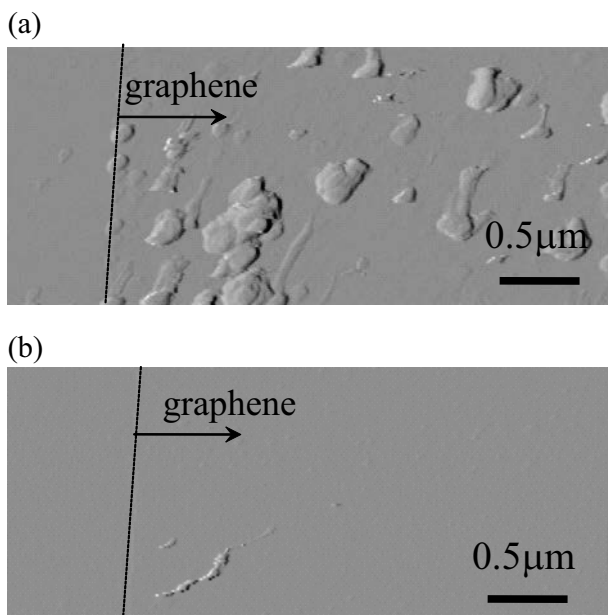


Figure 3.36 AFM images of a graphene surface before (a), and after (b), hydrogen annealing at 300°C in Ar/H₂ atmosphere.

3.3.5.2 Experimental techniques to improve mobility

Several techniques are commonly used to improve the mobility of graphene.

Hydrogen annealing In experiments of potassium doping into graphene, Chen *et al.* [59] removed the resist residue (present on the surface of graphene after electron beam lithography) by annealing the device at 300°C in Ar/H₂ atmosphere for 1 h. This so-called “hydrogen annealing” is quite effective for cleaning the surface of graphene.⁵ Figure 3.36 compares the AFM images at the same position on a graphene sample’s surface before and after hydrogen annealing. After the lift-off step of the electron beam lithography process (Fig. 3.36(a)), resist residues with a height of several tens of nanometers often cover the graphene surface; these residues can

⁵Forming gas (a mixture of hydrogen and nitrogen) is also used.

be successfully removed by the hydrogen annealing process (Fig. 3.36(b)).

Suspended graphene and current annealing The most effective method of removing charged impurities and the influence of remote interface phonons in SiO_2 is to remove the substrate after the device fabrication. This was first attempted by Bolotin *et al.* [75, 76]. They etched the SiO_2 substrate underneath the graphene by immersing the device in a strong acid (buffered hydrofluoric acid, HF).

Buffered HF, also known as buffered oxide etch (BOE), is a mixture of HF and a buffering agent, NH_4F . It is known that a 6 : 1 volume ratio of 40% NH_4F in water to 49% HF in water is capable of etching thermally grown SiO_2 at a rate of ~ 2 nm/s at 25°C . The ratio should be optimized so that the extent of the etching is precisely controllable.

The typical procedure is as follows [77]:

- (i) After the electron beam lithography and metal deposition for the formation of metallic contacts (e.g., 5 nm of chromium and 100 nm of gold) onto graphene placed on a Si/ SiO_2 substrate, immerse the substrate in buffered HF.
- (ii) Transfer the substrate into 2-propanol and then dry with nitrogen blow.

An example of the suspended graphene is shown in Fig. 3.37. In this process, a wide gold contact works as a mask, so that it remains

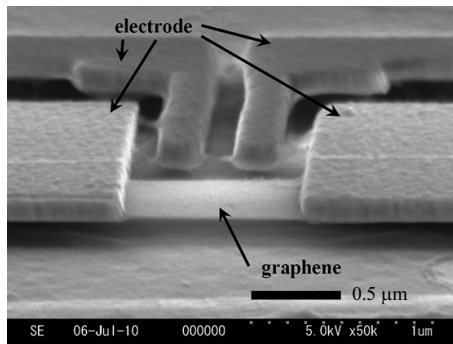


Figure 3.37 A suspended graphene device.

stable on top of the SiO_2 , while the SiO_2 even below a wide graphene flake is etched, owing to the rapid propagation of buffered HF along the SiO_2 /graphene interface [75]. Because the etching is isotropic, a narrow gold contact becomes suspended, as shown in Fig. 3.37; this contact sometimes sags.

The mobility of graphene after the above procedure is not much improved, presumably because charged impurities are still attached to the surface of the graphene. One can enhance the mobility of the suspended graphene by sending a large current across the graphene device with current a density of $\sim 10^8$ A/cm² at low temperatures (below 4 K) [78]. (In the calculation of the current density, the thickness of single-layer graphene is assumed to be 0.34 nm). The large current density heats the graphene locally to $T > 600^\circ\text{C}$ or higher [75, 79], and removes impurities. This process is called “current annealing.” Low-temperature mobilities as large as 10^2 m²/Vs have been reported after current annealing [79].[†]

It is known that excess current annealing easily damages the graphene device. A narrowing of the graphene just before breakage (due to the current annealing) has also been reported; this method was successfully used to observe quantized conductance in graphene [80].

During the annealing process, the resistance at the gate voltage $V_G = 0$ usually increases, presumably both because the charge neutrality point approaches the zero gate voltage and because the temperature increases. This resistance increase is used as a criterion for the cleaning of graphene.

For a graphene film placed on a Si/SiO₂ substrate, the effect of current annealing is not predictable. The mobility of graphene is sometimes even decreased during current annealing. Tanaka *et al.* found contamination on the graphene surface left by the current annealing process when the mobility decreases [81]. This effect occurs when the electrical power density exceeds a certain value, e.g., 2×10^5 W/cm².

[†]In Ref. [79], the mobility was estimated not only from the gate voltage dependence of the conductance but also from the Shubnikov–de Haas oscillations. The observation of the Shubnikov–de Haas oscillations requires $B\mu \sim 1$.

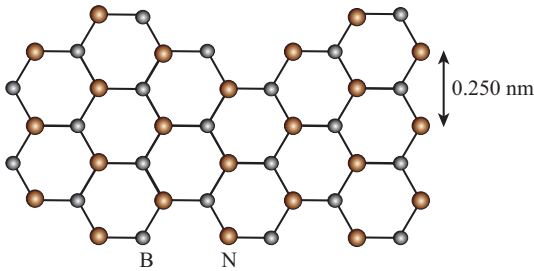


Figure 3.38 Crystal structure of single layer hexagonal BN.

Graphene on hexagonal boron-nitride substrates Although the suspension of graphene significantly improves mobility, it imposes several limitations on device operation, i.e., it is quite difficult to fabricate four-terminal devices, and the application of gate voltages causes an electrostatic force between the gate and the graphene film, leading to strain in the graphene and possible collapse at gate voltages as small as 10 V.

Graphene on a hexagonal boron nitride (h-BN) substrate is an attractive alternative to suspended graphene. h-BN has a crystal structure similar to that of graphene, as shown in Fig. 3.38 h-BN has the following advantages:

- The lattice constant (0.250 nm) is slightly different (2%) from that of graphite (0.246 nm).
- The surface is smooth and relatively free of dangling bonds and charge traps.
- The optical phonon mode (> 100 meV) is larger than that of SiO_2 (59 meV).
- The bandgap is 5.8 eV, which is comparable to that of SiO_2 (8.9 eV).
- The dielectric constant $\sim 3\text{--}4$ is comparable to that of SiO_2 (~ 4).

In experiments, a thin h-BN film can be obtained by the mechanical exfoliation of a single h-BN crystal. Graphene is separately prepared on a substrate covered by a thin, water-soluble layer and PMMA. Next, a PMMA membrane with graphene is obtained by dissolution of the water-soluble layer in water. The resulting

graphene on the PMMA membrane is transferred to the thin h-BN film using a micromanipulator [21].

For graphene placed on h-BN, a typical mobility of $\mu_0 \approx 6 \text{ m}^2/\text{Vs}$ can be obtained at low temperatures, a value that is approximately three times larger than that of graphene on SiO_2 . AFM studies show that the surface roughness of graphene on h-BN is indistinguishable from that of bare h-BN and is approximately three times smaller than that of SiO_2 , even though the h-BN is placed on a SiO_2 substrate. Also, the electron–hole charge fluctuations close to the charge neutrality point are reduced by two orders of magnitude relative to graphene on SiO_2 , which are as small as those in suspended graphene [21, 82].

Here, the upper limit of the electron–hole charge fluctuation δn at low density was obtained from the transport measurement via two methods: One method is to analyze the full-width at half maximum (FWHM) of the resistivity–gate voltage ($\rho(V_G)$) curve, corresponding to $\delta n/\alpha$, the other is the temperature dependence of the minimum conductivity σ_{\min} . σ_{\min} is expected to vary with temperature for $k_B T > E_{\text{puddle}}$, where $E_{\text{puddle}} \approx \hbar v_F \sqrt{\pi \delta n}$ for single-layer graphene [21].

3.3.6 Bandgap Engineering

In modern electronics, bandgap formation is a key concept for switching current, and thus, for processing electric signals [83].

Although graphene has great advantages for use in electronics applications, including atomically thin channels, high mobility, and large electric field effects, its semimetallic electronic band structure makes the creation of a graphene transistor quite challenging.

So far, several methods have been proposed for the introduction of bandgaps into graphene. Among them, the most promising methods are graphene nanoribbons and bilayer graphene under perpendicular electric fields. In this section, we briefly review theoretical predictions, experimental results, and the major challenges of the formation of bandgaps in graphene. Issues regarding graphene nanostructures such as nanoribbons, nanoislands, and nanodots will be discussed in more detail in Chapters 4, 5, and 6.

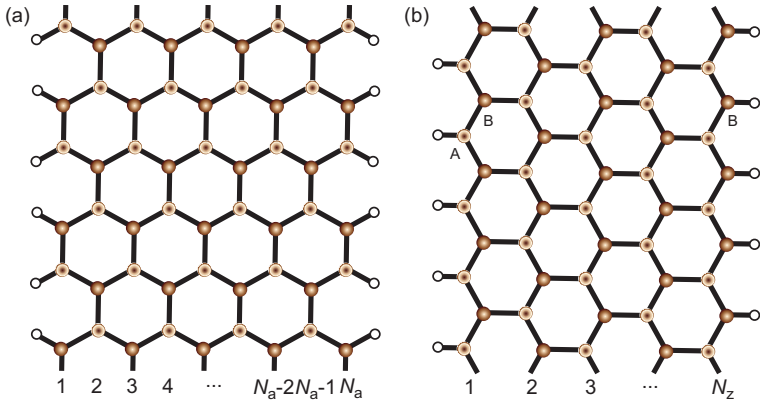


Figure 3.39 Two kinds of graphene nanoribbons: (a) armchair and (b) zigzag. N_a and N_z denote the number of carbon atoms in the ribbon width in armchair and zigzag nanoribbons, respectively. White circles indicate hydrogen atoms passivating the graphene edges.

3.3.6.1 Graphene nanoribbons

In quantum mechanical systems, the confinement of carriers leads to discrete energy levels. This is also the case in graphene; however, some differences are seen because of its peculiar lattice structure.

Thin graphene wires are called graphene nanoribbons. Two common structures, armchair and zigzag nanoribbons (Fig. 3.39), have been intensely studied theoretically. In this section, we first summarize theoretical predictions made regarding the electronic structures of armchair and zigzag nanoribbons, and then review the available experimental data. Other kinds of nanoribbons will be discussed in Chapters 4, 5, and 6.

Theoretical predictions In the following theoretical treatment of graphene nanoribbons, the graphene edges are assumed to be passivated by hydrogen, as illustrated in Fig. 3.39.

As will be discussed in Chapter 4, in the tight-binding (TB) approximation for π -electrons in graphene [84–87], armchair graphene nanoribbons are metallic when the number of the carbon atoms in the ribbon width, N_a (see Fig. 3.39(a) for the definition of N_a), satisfies the relation, $N_a = 3p + 2$ (where p is a positive

integer), and are semiconducting otherwise. The energy gap Δ_{N_a} is inversely proportional to the width in each group, $N_a = 3p$ or $N_a = 3p + 1$. For a particular value of p ,

$$\Delta_{3p} \geq \Delta_{3p+1} > \Delta_{3p+2} = 0 \quad (3.54)$$

is satisfied.

Zigzag nanoribbons in the TB approximation are metallic and have flat bands at $\varepsilon = 0$. In the flat band at $\varepsilon = 0$ for very wide nanoribbons, the wave function is localized near each zigzag edge in a sublattice (A or B) that includes the edge sites; its amplitude decays into the center of the nanoribbon with a decay length depending on the wave vector [84]. The localized edge states at a zigzag edge were confirmed by scanning tunneling microscopy (STM) observation [88]. Here, we note that the sublattice that includes the edge site is different for the two edges of the nanoribbon. (For example, when the left edge belongs to the A sublattice, the right belongs to the B sublattice, as shown in Fig. 3.39(b)). The flat band leads to a very large density of states at $\varepsilon = 0$, which makes the zigzag nanoribbon magnetic under an infinitesimally small on-site repulsion [84].

In the first-principles calculation using the local (spin) density approximation (LSDA), the result is significantly different from that discussed above [89]. Specifically, all of the armchair and zigzag nanoribbons are semiconducting, with gaps depending on the ribbon width.

For armchair nanoribbons, the LSDA shows that the size of the gap obeys the relationship:

$$\Delta_{3p+1} > \Delta_{3p} > \Delta_{3p+2} (\neq 0). \quad (3.55)$$

The difference from the TB results is caused by deformation of the graphene lattice at the edges due to the hydrogen passivation. The bond length at the edges (parallel to the edge) is shortened by $\sim 3.5\%$, leading to the increase in the hopping integral between π orbitals by 12%.

The gaps obtained via the LSDA calculation agree with the analytical results based on the TB approximation when one takes the

modulation of the hopping integral at the edges into account [89]:

$$\Delta_{a,3p} \cong \Delta_{a,3p}^0 - \frac{8\delta\gamma_0}{3p+1} \sin^2 \frac{p\pi}{3p+1}, \quad (3.56)$$

$$\Delta_{a,3p+1} \cong \Delta_{a,3p+1}^0 + \frac{8\delta\gamma_0}{3p+2} \sin^2 \frac{(p+1)\pi}{3p+2}, \quad (3.57)$$

$$\Delta_{a,p+2} \cong \Delta_{a,3p+2}^0 + \frac{2|\delta|\gamma_0}{p+1}, \quad (3.58)$$

where $\gamma_0 = 2.7$ eV [90] is the original hopping integral of graphene; $\delta = 0.12$ is the amount of the modulation in the hopping integral at the edges; and $\Delta_{a,3p}^0$, $\Delta_{a,3p+1}^0$, $\Delta_{a,3p+2}^0$ are the gaps without the hopping integral modification, which are given by

$$\Delta_{a,3p}^0 = \gamma_0 \left(4 \cos \frac{p\pi}{3p+1} - 2 \right), \quad (3.59)$$

$$\Delta_{a,3p+1}^0 = \gamma_0 \left(2 - 4 \cos \frac{(p+1)\pi}{3p+2} \right), \quad (3.60)$$

$$\Delta_{a,3p+2}^0 = 0. \quad (3.61)$$

The energy gap of the zigzag nanoribbons in the LSDA calculation, Δ_z , is well fitted by

$$\Delta_z[\text{eV}] = \frac{0.933}{w[\text{nm}] + 1.5}, \quad (3.62)$$

for ribbon widths $w > 1$ nm. This gap originates from the inclusion of the spin degree of freedom, which leads to a magnetic insulating ground state with ferromagnetic ordering at each zigzag edge and antiparallel spin orientation between the two edges. The details of this phenomenon will be discussed in Chapter 4.

The magnitude of the gaps is presented in Fig. 3.40.

Experiments Graphene nanoribbons have been made by various methods, including electron beam lithography followed by oxygen plasma etching [91–94], and chemical derivation [96–99]. Nanoribbon fabrication will be discussed in Chapter 6. The main challenge in gap formation in graphene nanoribbons is the suppression of structural disorder. Structural disorder causes weak localization and the Coulomb blockade effect, and suppresses the mobility.

Lithographically defined graphene nanoribbons were first reported by Han *et al.* in 2007 [91]. After contacting a graphene

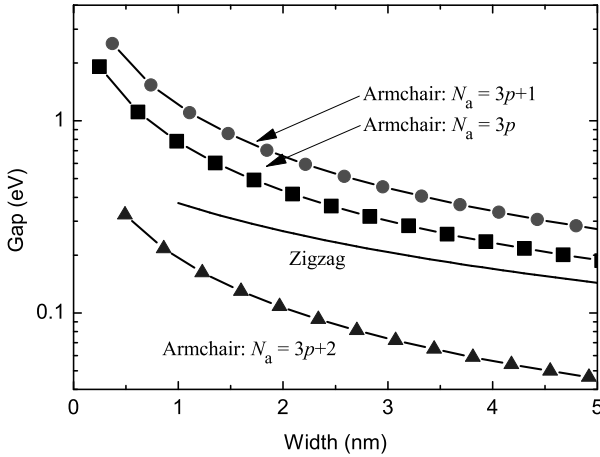


Figure 3.40 Energy gaps in graphene nanoribbons, as calculated from Eqs. (3.56)–(3.62).

flake with Cr/Au (3/50 nm) electrodes, they produced a graphene nanoribbon from the flake by oxygen plasma etching, using a negative tone electron beam resist (hydrogen silsesquioxane, HSQ) as a mask. In the gate voltage dependence of the conductance, they observed suppression of the conductance near the charge neutrality point, which was enhanced at lower temperatures and in narrower ribbons, indicating the existence of an energy gap, as shown in Fig. 3.41. They estimated the magnitude of the energy gap from the nonlinear current–voltage characteristics at the charge neutrality point, and found that the energy gap ε_g is well fitted by

$$\varepsilon_g = \frac{a}{w - w^*}, \quad (3.63)$$

where w is the ribbon width, $a = 0.2$ eVnm and $w^* = 16$ nm. Han *et al.* attributed the inactive width w^* to contributions from localized edge states near the ribbon edges caused by structural disorder from the etching process, combined with inaccurate width determination caused by over-etching underneath the HSQ etch mask. They also examined the dependence of the energy gap on the nanoribbon orientation; no dependence was seen. This result does not agree with the theoretical prediction (see Fig. 3.40).

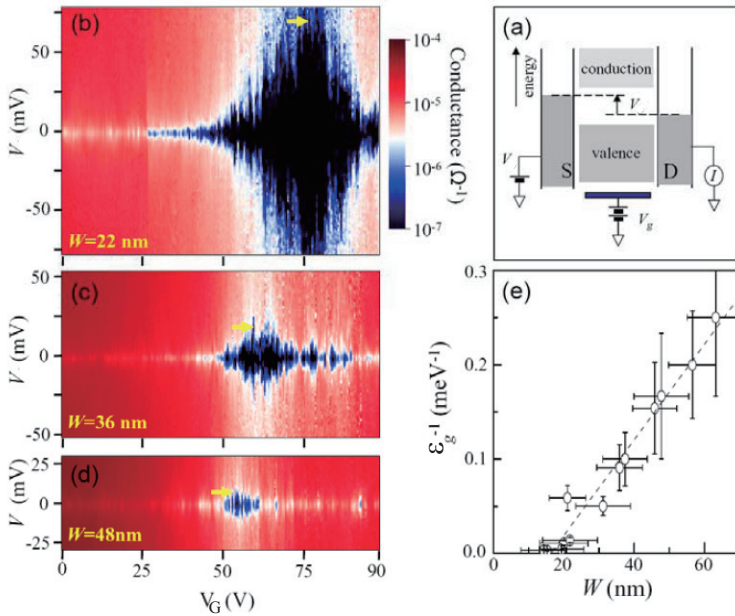


Figure 3.41 (a) Schematic energy band diagram of a graphene nanoribbon with an applied bias voltage. The current I is controlled by both source–drain bias V and gate voltage V_G . (b–d) The differential conductance (dI/dV) of three representative graphene nanoribbons of width $W = 22$, 36 , and 48 nm as a function of V and V_G measured at $T = 1.6$ K. The light (dark) color indicates high (low) conductance as indicated in the color map. The horizontal (dark) arrows represent $V = \varepsilon_g/e$. (e) Inverse of energy gap ε_g^{-1} versus W obtained from similar a analysis as in (b–d), with a linear fit of the data. After Ref. [91].

Later, Sols *et al.* [100] showed theoretically that the data obtained by Han *et al.* can be quantitatively explained by the Coulomb blockade effect caused by the roughness at the edges of nanoribbons. Edge roughness inevitably occurs in lithographically defined nanoribbons, mainly because of the grain size of the electron beam resist used as the etching mask. The edge roughness may lead to the localization of charge near the edges [88] and the formation of charge puddles. Furthermore, as depicted in Fig. 3.42, constrictions (or necks) formed by the edge roughness can cause a reduction

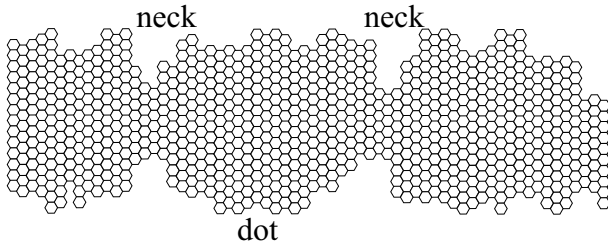


Figure 3.42 Graphene nanoribbon with structural disorder at the edges, forming a quantum dot, as suggested by Sols *et al.* [100].

in the size of conduction channels, forming quantum dots between adjacent constrictions.

The existence of the Coulomb blockade effect in graphene nanoribbons was experimentally confirmed by several groups. Miyazaki *et al.* [101] and Todd *et al.* [93] observed an irregular Coulomb diamond structure (with gate voltage modulation of the current-voltage characteristics around the origin), which was caused by electron conduction through multiple quantum dots [102]. An example is shown in Fig. 3.43 [93]. Han *et al.* [94] investigated the temperature dependence of the conductance minimum of lithographically defined nanoribbons with different geometrical capacitances. They observed that thermal activation energy heavily depends upon the capacitance at high temperatures (Fig. 3.44), indicating that the Coulomb blockade effect provided a substantial portion of the observed energy gap.

Additionally, the effect of the randomly distributed charge puddles, which leads to a percolation-driven 2D metal-insulator transition in graphene nanoribbons, was discussed and experimentally verified by Adam *et al.* [95].

Graphene nanoribbons have also been made by chemical exfoliation. Li *et al.* [96] obtained graphene nanoribbons with edges that appeared smoother than those obtained lithographically. They exfoliated expandable graphite by brief heating to 1000°C in forming gas (3% hydrogen in argon) and dispersed the resulting graphite flakes in a solution. Graphene nanoribbons with various widths ranging from ~50 nm down to sub-10 nm scale were obtained via this method. The room temperature on-off current ratio $I_{\text{on}}/I_{\text{off}}$

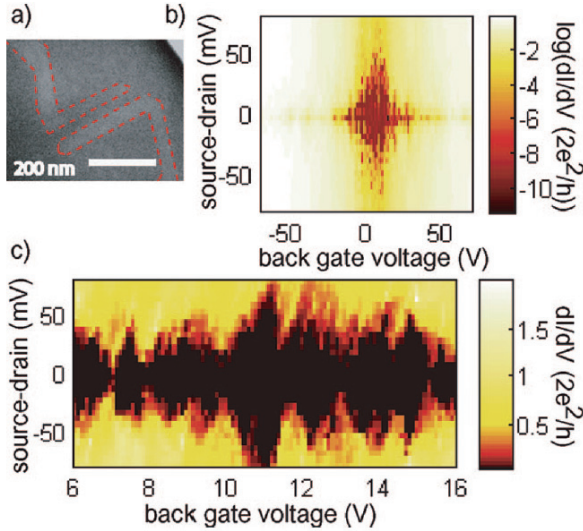


Figure 3.43 (a) SEM micrograph of a long graphene nanoribbon 250 nm in length and 40 nm in width. Lighter areas are where graphene has been removed by an oxygen plasma etch to define the constriction. Dashed lines are guides to the eye, indicating the boundary of the etched area. (b) Logarithmic map of the differential conductance dI/dV vs. back gate voltage and source–drain bias acquired at 4.2 K showing conduction gap. (c) dI/dV over a smaller range, showing Coulomb blockade behavior suggesting the presence of several quantum dots in series. After Ref. [93].

induced by the back gate voltage increased exponentially with decreasing ribbon width; it reached 10^7 in sub-10 nm ribbons. Here, the on (off) current I_{on} (I_{off}) is defined as the maximum (minimum) value of the source–drain current I for a fixed bias (source–drain) voltage V within a measured gate voltage range. For example, in Fig. 3.45(a) and (c), $I_{\text{on}}/I_{\text{off}}$ is ~ 100 and $\sim 10^5$, respectively, at room temperature. The energy gap ε_g estimated from the relationship

$$I_{\text{on}}/I_{\text{off}} \propto \exp\left(\frac{\varepsilon_g}{k_B T}\right) \quad (3.64)$$

was converted into an empirical form

$$\varepsilon_g[\text{eV}] = \frac{0.8}{w[\text{nm}]} \quad (3.65)$$

and falls between the limits of theoretical results (Fig. 3.40).

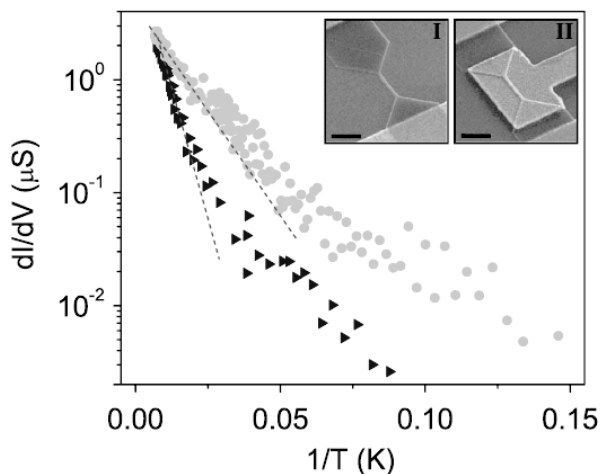


Figure 3.44 Temperature dependence of the conductance minimum for dual-gated (circles) and back-gated (triangles) graphene nanoribbons with a similar width and length. The dashed lines are Arrhenius fits in the high-temperature regime. The inset shows SEM images of back-gated (left) and dual-gated (right) devices. The scale bar represents 500 nm. In device I, 60% of the activation energy comes from the Coulomb charging energy. After Ref. [94].

Wang *et al.* [98] reported that even in smooth, chemically derived graphene nanoribbons with widths \sim sub-10 nm (which were expected to exhibit energy gaps large enough for room-temperature transistor operation), the mobility was limited to ~ 200 cm²/Vs and the mean free path was limited to ~ 10 nm. These values are significantly smaller than those for wider graphene devices (see, e.g., Fig. 3.22). These values were attributed to backscattering at the edges caused by edge roughness. (Note that the influence of the edge roughness on electron transport is stronger for narrower nanoribbons.) The importance of edge disorder has been also studied theoretically by several researchers [103–105].

There are several techniques other than electron beam lithography and chemical exfoliation for the fabrication of graphene nanoribbons, as shown in the following short list (see also Chapter 6):

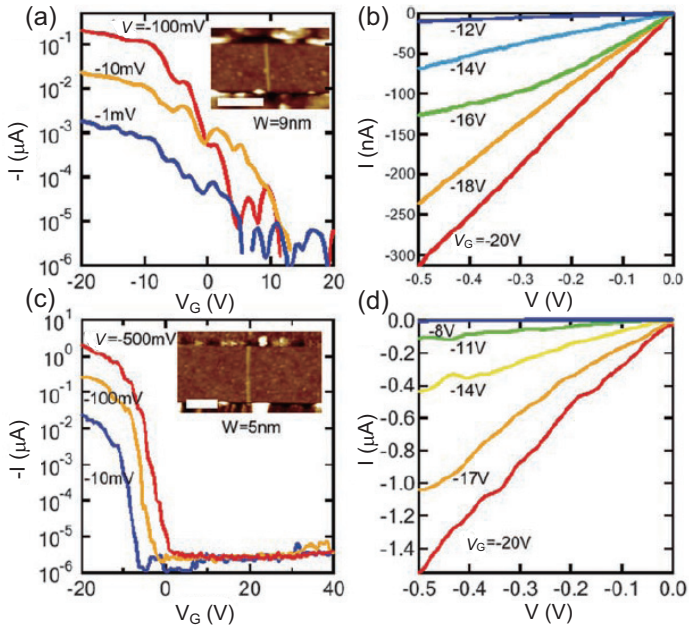


Figure 3.45 Room-temperature graphene nanoribbon FET with high on-off ratios. (a) Transfer characteristics (current versus gate voltage $I-V_G$) for a $w \sim 9$ nm (thickness ~ 1.5 nm, \sim two layers) and channel length $L \sim 130$ nm graphene nanoribbon with palladium contacts and Si back gate. (Inset) Atomic force microscope (AFM) image of the device. The scale bar is 100 nm. (b) Current-voltage ($I-V$) curves recorded for different values of V_G for the device in (a). (c) Transfer characteristics for a $w \sim 5$ nm (~ 1.5 nm, \sim two layers) and channel length $L \sim 210$ nm graphene nanoribbon with palladium contacts. (Inset) An AFM image of this device. The scale bar is 100 nm. (d) $I-V$ characteristics recorded under various V_G for the device in (c). After Ref. [96].

- (i) Multiwall carbon nanotubes are unzipped (cut lengthwise and unraveled) by the Ar plasma etching of nanotubes that are partly embedded in a polymer film (PMMA) [106], by the mild gas-phase oxidation of nanotubes and subsequent mechanical sonication in an organic solvent [107], or by solution-based chemical oxidation of nanotubes followed by reduction of nanoribbons [108]. The width of the resulting nanoribbons is constant.

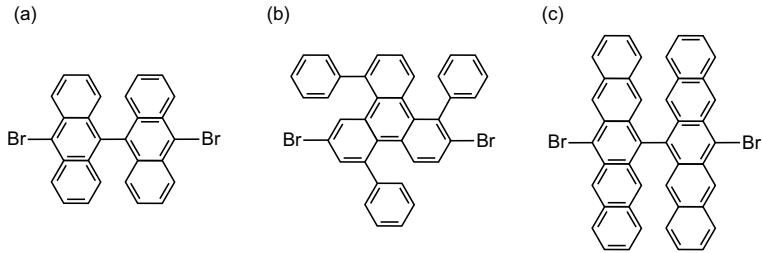


Figure 3.46 Precursor molecules used for the formation of atomically precise armchair nanoribbons with widths $N_a =$ (a) 7, (b) 9, and (c) 11 [110].

- (ii) The width of lithographically defined nanoribbons is reduced by gas-phase chemical etching from the ribbon edges, without damaging the basal plane. This effect is achieved by high-temperature oxidation of graphene in a slightly reducing environment in the presence of ammonia and with a controlled etch rate (≤ 1 nm/min) [109].
- (iii) Atomically precise graphene nanoribbons are produced by surface-assisted coupling of molecular precursors (such as 10,10'-dibromo-9,9'-bianthryl monomers (Fig. 3.46(a)) into linear polyphenylenes followed by cyclodehydrogenation [110]. The structure of the synthesized nanoribbons is determined by the precursor molecules, as shown in Fig. 3.46. Metallic substrates such as Au(111) and Ag(111) are used. Nanographene can also be made using a similar method [111].
- (iv) Self-organized graphene nanoribbons are formed on a $(1\bar{1}0n)$ facet of a SiC substrate by the thermal decomposition of SiC. Controlled $(1\bar{1}0n)$ facets are produced using fluorine-based reactive ion etching (RIE) of SiC with photolithographically defined Ni masks, and subsequent heating to 1200–1300°C in vacuum [112].

3.3.6.2 Bilayer graphene under perpendicular electric fields

As discussed in Section 2.7, in bilayer graphene with AB (Bernal) stacking, a bandgap can open between the conduction and valence

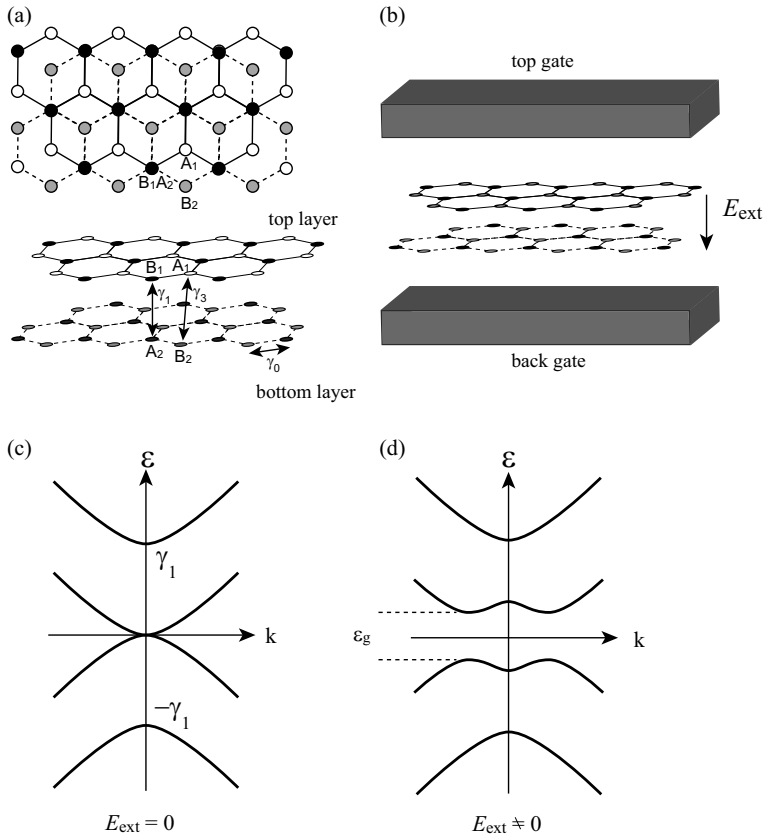


Figure 3.47 (a) Structure of bilayer graphene. (b) Dual-gated bilayer graphene sandwiched between top and bottom gates. Bilayer graphene band structure around the K point without (with) an electric field E_{ext} is schematically shown in (c) ((d)) for $\gamma_3 = 0$.

bands, even without any structural confinement. This is due to the breaking of the inversion symmetry between the two layers.

Here, we briefly summarize some of theoretical predictions [113–115]. The structure of bilayer graphene with AB stacking is shown in Fig. 3.47(a); the B-sublattice (B_1) of the top layer sits on top of the A-sublattice (A_2) in the bottom layer. (A different definition is also used in some of the literature.)

In the TB model for bilayer graphene, we take into account the following hopping integrals (see Fig. 3.47(a)): γ_0 (≈ 2.7 eV [90]) for intralayer nearest neighbor hopping, γ_1 (≈ 0.4 eV in graphite [113]) for vertical hopping between carbon atoms in B_1 and A_2 sublattices, and γ_3 (≈ 0.3 eV in graphite [113]) for hopping between the nearest A_1 - and B_2 - carbon atoms. Note that the values of the hopping integrals for bilayer graphene can be different from those for graphite; therefore, they should be determined independently.

For $\gamma_3 = 0$ without an electric field, two parabolic bands

$$\varepsilon = \pm \hbar^2 v_F^2 k^2 / \gamma_1, \quad (3.66)$$

appear around $\varepsilon = 0$ near K points, and two additional bands appear at $\varepsilon = \pm \gamma_1$, as shown in Fig. 3.47(c).

In the presence of γ_3 , the band structure undergoes a significant change: instead of the parabolic bands touching at $\varepsilon = 0$, there appear four sets of Dirac cones at $\varepsilon = 0$ which are similar to that of single-layer graphene. One is at the K point; the other three lie at three equivalent points with a finite momentum around the K point. This is called trigonal warping [116].

One can break the inversion symmetry in bilayer graphene by applying a finite bias U between the two layers, or equivalently, placing bilayer graphene in a perpendicular electric field $E_{\text{ext}} = U/d$, where $d = 0.335$ nm is the interlayer spacing of bilayer graphene (Fig. 3.47). As a result, we find two Mexican hat structures in the dispersion relation with an energy gap between them (Fig. 3.47(d)). Here, we note that, in general, E_{ext} is not equal to the potential difference between the top and bottom gates divided by their separation, because of the distribution of charge in bilayer graphene.

For $\gamma_3 = 0$, the energy gap is given as

$$\varepsilon_g \approx |U| \frac{\gamma_1}{\sqrt{\gamma_1^2 + U^2}}. \quad (3.67)$$

The bias (U) dependence of the energy gap is plotted in Fig. 3.48 for the interlayer nearest neighbor hopping integral $\gamma_3 = 0$ [115]. For small biases, the gap increases almost linearly with U , saturating at γ_1 for large U because of the Mexican hat structure in the bands (Fig. 3.47(d)). This means that the magnitude of the energy gap is controllable externally. Thus, bilayer graphene in a perpendicular

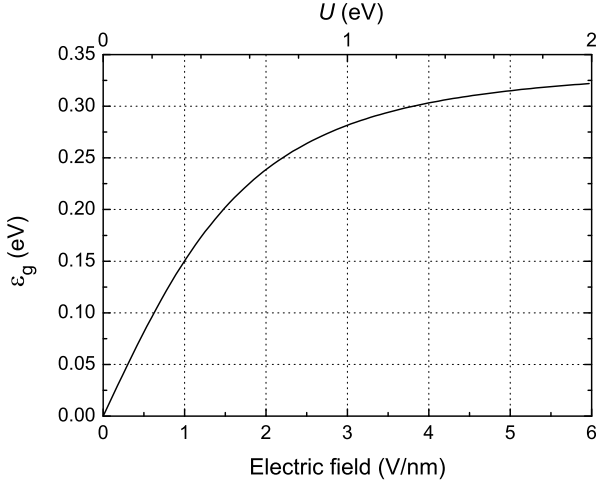


Figure 3.48 Bias voltage and electric field dependence of the energy gap in bilayer graphene with the interlayer nearest neighbor hopping integral $\gamma_3 = 0$ eV [115].

electric field is a tunable-gap semiconductor [115, 117]. When γ_3 is taken into account, the energy gap is reduced slightly; however, its overall dependence on the bias is the same as that for $\gamma_3 = 0$. The saturation value of the bandgap when taking γ_3 into account is around 0.26 eV. This value agrees well with the value from the *ab initio* density functional theory (DFT) calculation [115].

Experimentally, an electric field perpendicular to the bilayer graphene plane can be achieved by chemical doping on graphene [117, 118] and/or by gate electric fields [22, 119–122]. Here, we note that for the confirmation of the bandgap, the Fermi level ϵ_F and the gate electric field E_{ext} should be controlled independently; for example, if only the back gate is used, the Fermi level strays from $\epsilon = 0$ (the point around which the energy gap is formed) as the gate voltage (and the gate electric field) increases. If there is another electric field source, one can move the Fermi level back to $\epsilon = 0$.

In chemical doping, ammonia [117] and potassium [118] have been used as the dopants adsorbed on graphene. In other cases, the dual-gate structure, as shown in Fig. 3.47(b), is employed. So far, deposited SiO_2 [22], Al_2O_3 [119], and HfO_2 [121], self-organized

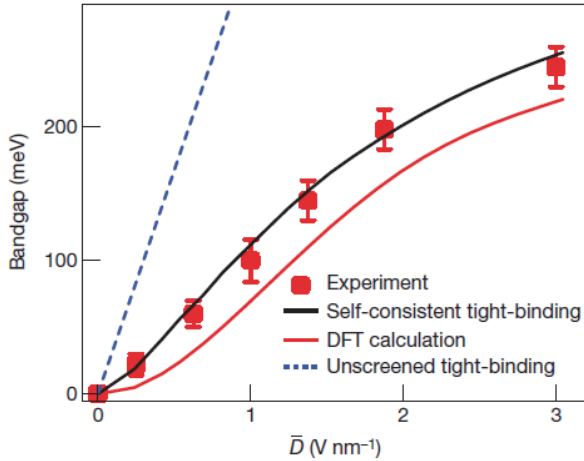


Figure 3.49 Electric field dependence of tunable energy bandgap in graphene bilayer. Experimental data (squares) are compared to theoretical predictions based on self-consistent TB (black trace), *ab initio* density functional (gray trace), and unscreened TB calculations (dashed trace). The error bar is estimated from the uncertainty in determining the absorption peaks in the spectra. After Ref. [119].

AlO_x thin films [122], and a polymer electrolyte (poly(ethylene oxide): LiClO_4) [120] have been used as the top gate dielectric.

Using optical spectroscopic measurements such as angle-resolved photoemission spectroscopy (ARPES) [118] and infrared spectroscopy [119, 120], bandgap formation has been successfully confirmed; the observed dependence of the bandgap on the gate electric field was consistent with theoretical predictions [114, 115]. An example is shown in Fig. 3.49.

On the other hand, the first paper on transport measurement [22] reported that although insulating behavior was observed with the increase of resistance while lowering temperature, the observed temperature dependence of conductance at low temperatures (below 50 K) was not of the thermal activation type,

$$G \propto \exp\left(-\frac{\varepsilon_a}{k_B T}\right), \quad (3.68)$$

which is regarded as direct evidence of bandgap opening with a magnitude of $\varepsilon_g = 2\varepsilon_a$, but of the variable-range-hopping type,

$$G \propto \exp\left(-\left(\frac{T_h}{T}\right)^{1/3}\right), \quad (3.69)$$

which is typically observed in strongly disordered two-dimensional systems. In the above expression, k_B is Boltzmann constant, T is temperature, and T_h is a constant. It was claimed that the experimentally obtained bandgap was below 10 meV, in spite of the fact that the device structure was similar to those used in Ref. [119], in which a bandgap of over 200 meV was measured using optical spectroscopy.

Later, Miyazaki *et al.* [122] showed that the temperature dependence of the conductance between 77 K and 200 K was successfully explained as being a function of the sum of the thermally activated conduction and the two-dimensional variable range hopping conduction (Fig. 3.50):

$$G = C_1 \exp\left(-\frac{\varepsilon_a}{k_B T}\right) + C_2 \exp\left(-\left(\frac{T_h}{T}\right)^{1/3}\right), \quad (3.70)$$

where C_1 and C_2 are constants. They found that the energy gaps extracted from the above temperature dependence (Eq. (3.70)), $\varepsilon_g = 2\varepsilon_a$, agreed with the theoretical bandgaps from DFT calculations [115] for electric field values ranging 0–1.3 V/nm and were unrelated to the mobility of bilayer graphene. Furthermore, from the mobility dependence of parameter T_h , they demonstrated that the contribution of variable-range hopping, which causes degradation of the insulating state inside the bandgap and allows leakage current to flow, becomes smaller in bilayer graphene that has a higher mobility. These results indicate that the improvement of mobility is crucial for the successful application of bilayer graphene to FET devices. The effect of disorder is also theoretically discussed in Refs. [123–125].

3.3.6.3 Other methods for bandgap formation

Techniques for the formation of graphene bandgaps other than in nanoribbons and bilayer graphene under perpendicular electric fields have been proposed. These techniques are based on spacial

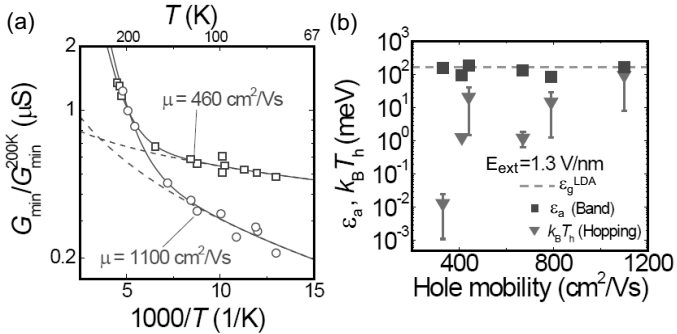


Figure 3.50 (a) Arrhenius plot of the minimum conductance for samples with a field-effect hole mobilities of 460 and 1100 cm^2/Vs . The conductance is normalized by its value at 200 K. Results of the fitting by Eq. (3.69) (solid curve) and the contribution of the variable range hopping conduction (dashed curve) are also shown. (b) Thermal activation energy ε_a extracted from the thermal activation type conduction seen at high temperatures (square) and characteristic energy $k_B T_h$ for variable range hopping conduction (triangle) for six samples as a function of the hole mobility with an electric field of $E_{\text{ext}} = 1.3 \text{ V/nm}$. A bandgap calculated via the local density approximation is also shown (dashed line). Note that larger $k_B T_h$ corresponds to a smaller contribution of the variable range hopping conduction to the conductivity. After Ref. [122].

modulation of the graphene electronic properties (superlattices) by placing antidots (holes) [126], by making bonds with hydrogen atoms (hydrogenation) [127], or by inducing strain [128].

Uniform bonding of another element or molecule also significantly modifies the graphene band structure: uniform hydrogenation [129] leads to an insulating state (called graphane, Fig. 3.51) [130] and uniform fluorination (bonding of F atoms) leads to a wide-gap semiconducting state [131].

3.3.7 Graphene Quantum Effect Devices: Mesoscopic Electron Transport in Graphene

From the 1980s onward, owing to the development of semiconductor microfabrication techniques, electron transport in metals and semiconductors with submicron-to-nanometer size has been intensively investigated. In such small systems, the quantum-mechanical

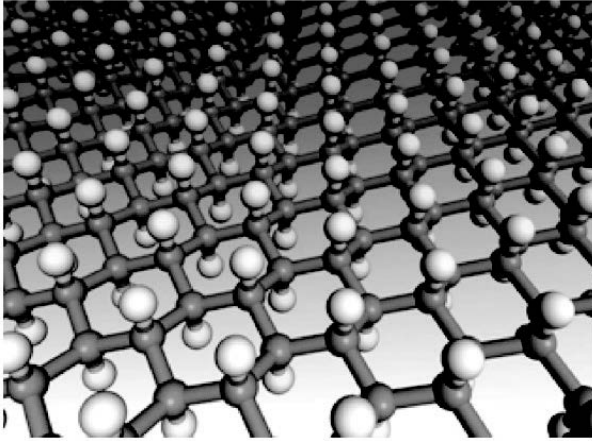


Figure 3.51 Structure of graphane in the chair conformation. Carbon atoms are shown in gray. Hydrogen atoms are shown in white. The figure shows the hexagonal network with carbon in the sp^3 hybridization. After Ref. [129].

nature of electrons manifests itself, leading to the emergence of so-called *mesoscopic* phenomena in electron transport [135]. Mesoscopic quantum transport can be divided into two categories, depending on which nature of electrons is emphasized, *wave* or *particle*. The first category includes the electron interference effect in conductors whose size is smaller than the phase coherence length and/or mean free path. The second category includes the single-electron tunneling effect in quantum dots. Both effects influence the operation of nanoscale electronic devices, which work on the basis of novel operational principles (“beyond CMOS” technology, see Section 3.1).

Graphene is among the promising materials for use in quantum effect devices, mainly because of its large mean free path and ease of microfabrication by oxygen plasma etching.

Many mesoscopic phenomena have been realized in graphene devices, including the Aharonov–Bohm (quantum interference) effect in a ring [136, 137], conductance quantization in a constriction [80], Fabry–Perot interference in a short channel [138], and a variety of Coulomb blockade effects [139–142]. The graphene

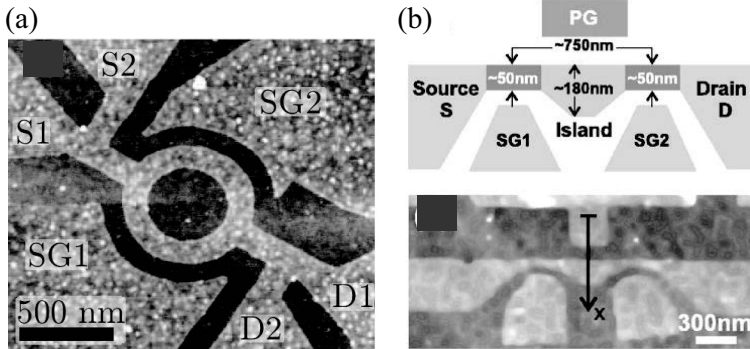


Figure 3.52 Graphene quantum effect devices. (a) Aharonov-Bohm ring with source (S1 and S2), drain (D1 and D2), and side gates (SG1 and SG2) (made from the same piece of graphene). After Ref. [137]. (b) Graphene quantum dot device with source, drain, side gates (SG1 and SG2), and plunger gate (PG) (made from the same piece of graphene). After Ref. [140].

devices have an advantage that most of the important components (the nanostructures under study, measurement leads, and tunnel barriers) in a device can be made from a single crystal of graphene. Examples are shown in Fig. 3.52.

3.3.8 Application to Chemical Sensors

As discussed in Section 3.3.2, graphene electron transport is strongly influenced by the presence of charged impurities. This implies the possibility of using graphene as a chemical sensor, a device in which the conductivity is changed by the gas molecules adsorbed on a surface that act as donors or acceptors. Although similar chemical sensors made from semiconductor nanowires and carbon nanotubes [132] have been intensively studied, graphene possesses new advantages in terms of sensitivity, due to its large surface area, large surface-area-to-volume ratio, and strong electric field effects.

Schedin *et al.* [133] reported the detection of individual gas molecules adsorbed on a graphene surface. They used a graphene FET with Hall bar geometry (see Section 3.3.1), which was fabricated using electron beam lithography on micromechanically exfoliated graphene (Section 3.2) followed by oxygen plasma etching. As

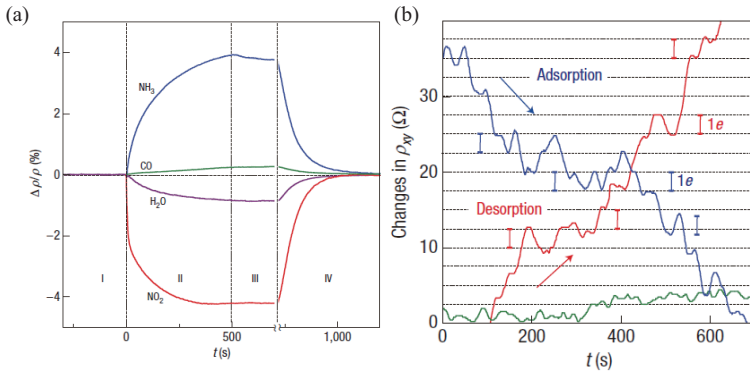


Figure 3.53 Sensitivity of graphene to chemical doping. (a) Changes in resistivity ρ at zero magnetic field caused by graphene exposed to various gases diluted in concentrations of 1 p.p.m. The positive (negative) sign of the change indicates electron (hole) doping. Region I: the device is in vacuum before exposure. Region II: exposure to a 5 L volume of a diluted chemical. Region III: evacuation of the experimental setup. Region IV: annealing at 150°C . Note that the annealing caused an initial spike-like response in ρ that lasted for a few minutes and was generally irreproducible. For clarity, this transient region between III and IV is omitted. (b) Examples of changes in Hall resistivity ρ_{xy} observed near the neutrality point ($|n| < 10^{11} \text{ cm}^{-2}$) during adsorption of strongly diluted NO_2 and its desorption in vacuum at 50°C . The bottom curve is a reference; it is the same device thoroughly annealed and then exposed to pure He. The curves are for a three-layer device in a magnetic field $B = 10 \text{ T}$. The grid lines correspond to changes in ρ_{xy} caused by adding one electron charge e ($\delta R \approx 2.5 \Omega$), as calibrated using independent measurements by varying the gate voltage. For adsorption, the device was exposed to 1 p.p.m. NO_2 leaking at a rate of $\approx 10^{-3} \text{ mbar L s}^{-1}$. After Ref. [133].

shown in Fig. 3.53(a), the resistivity of the device is sensitive to the introduction (and the concentration) of chemicals. The adsorbed molecules are strongly attached to the graphene at room temperature (region III in Fig. 3.53(a)). Nevertheless, the initial, undoped state can be recovered by annealing the device at 150°C (region IV), indicating the suitability of this configuration for use in reusable chemical sensors. From the typical noise level in Fig. 3.53(a), $\Delta\rho/\rho \approx 10^{-4}$, the detection limit of the graphene gas sensor was estimated to be on the order of 1 p.p.b., which was comparable to that of gas sensors made from other materials [132].

Further improvement of the sensitivity was achieved by optimizing the device parameters and measurements [133]. An example in which the chemically induced changes in ρ_{xy} are no longer smooth, but instead occurred in a step-like manner, is shown in Fig. 3.53(b). The typical step height corresponds to one electron charge e being removed from or added to the area of the Hall cross (the central part of the hall bar), indicating the detection of individual molecules.

In Ref. [133], the mobility of the graphene device did not show any noticeable degradation after the introduction of gas molecules. Extra scattering of carriers was expected to occur via the adsorption of charged molecules, based on the model described in Section 3.3.2. It was speculated that a several-nanometer-thick layer of absorbed water would provide sufficient dielectric screening to explain the suppressed scattering on charged impurities [133]. This speculation was supported by the observation that cleaning of the graphene surface significantly reduced the sensitivity [134]. However, the detailed origin of the discrepancy is not clear at this moment.

3.3.9 Graphene Spintronics

Graphitic materials such as graphite, graphene, and carbon nanotubes are among the most promising materials for use in spintronics. Spintronics (also called spin electronics) is the research field that adds new functionality to charge-based electronics by exploiting the spin degree of freedom.

In this section, we review the topic of spin transport in graphene, with an emphasis on spintronics applications.

3.3.9.1 Spintronics

First, we examine what region within the field of spintronics graphene can be applied to.

LSI logic circuits, which form the basis of modern electronics, have been continually miniaturized since their invention. Their progress follows Moore's law, which states that the density of the CMOS (complementary metal-oxide-semiconductor) components on a chip doubles every 18–24 months. The gate length of the present (typical) CMOS device has reached the order of 10 nm.

With such small circuits, conventional electronics encounters unprecedented and inevitable (but intrinsic) problems such as quantum-mechanical leakage currents and quality variations, which, in a sense, make manifest the physical limits of modern electronics. Under these circumstances, new research that seeks “the next stage of modern silicon electronics” has been widely conducted; spintronics is one such research field. In particular, spintronics can be categorized as “beyond CMOS.”

By making use of ferromagnetic metals as electrodes, spintronics does not merely store information in the magnetization direction but also processes data using spin-polarized currents.¹⁴ Spintronic data processing is based on the so-called magnetoresistance effect, which utilizes the fact that electrical resistance depends on the direction of the magnetization in an electrical circuit (including ferromagnetic materials). Although this effect has already been used in some commercial products, including the read heads of hard drives and nonvolatile high-speed MRAM (magnetoresistive random access memory), we do not consider these topics here. Instead, we focus on the application of the magnetoresistance effect in the production of spin transistors, which will become the key component in spintronics logic circuits.

The two kinds of leading spin transistor structures that have been developed are the spin FET proposed by Datta and Das in 1990 [143], and the spin MOSFET (metal-oxide-semiconductor FET) proposed by Sugahara and Tanaka in 2004 [144]. The structures of these spin transistors are schematically shown in Fig. 3.54 In this section, for simplicity, we assume that both structures use half-metals as ferromagnetic source and drain electrodes. Half-metals have a metallic band for one spin orientation and a semiconducting band for the other spin orientation, so that the current flow is fully spin-polarized. Examples include Heusler alloy and CrO_2 .

In spin FETs (Fig. 3.54(a)), two-dimensional electron gases (2DEGs) formed at the interface of semiconducting heterostructures is used as a channel that connects the source and drain. The

¹⁴In ferromagnets, the density of states at the Fermi level for spins parallel to the magnetization (majority spins) is different from that for spins antiparallel to the magnetization (minority spins), so that the current flowing in a circuit including a ferromagnet is generally spin-polarized.

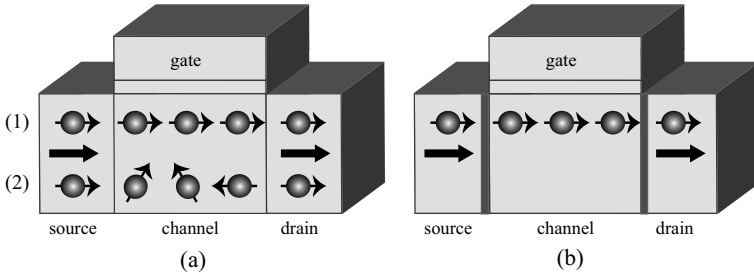


Figure 3.54 Schematics of two kinds of spin transistor, (a) spin SET, and (b) spin MOSFET. Thick arrows in the source and drain electrodes indicate the magnetization direction.

spin orientation of the conducting electrons is controlled by the application of a gate electric field via the spin-orbit interaction, as explained below [145]. In general, the Hamiltonian of the spin-orbit interaction is given in the following form:

$$H_{\text{so}} = -\frac{e\hbar}{4m^2c^2}\vec{\sigma} \cdot (\vec{E} \times \vec{p}) \quad (3.71)$$

$$= -\mu_{\text{B}}\vec{\sigma} \cdot \left(\frac{\vec{E} \times \vec{p}}{2mc^2} \right), \quad (3.72)$$

where m is the mass of a free electron, c is the speed of light, $\vec{\sigma}$ is the set of Pauli matrices, \vec{p} is the electron momentum, $\mu_{\text{B}} = e\hbar/2m$ is the Bohr magneton, and \vec{E} is the electric field. This form is similar to the expression for an electron in magnetic fields, $\frac{1}{2}\mu_{\text{B}}\vec{\sigma} \cdot \vec{B}$, indicating that for a moving electron an electric field is effectively a magnetic field under the effect of the spin-orbit interaction. This effect leads to spin precession, a change of the spin orientation. There are two kinds of electric field in crystal lattices that are caused by symmetry breaking. The first kind of electric field is caused by the lack of an inversion center (bulk inversion asymmetry), leading to the so-called Dresselhaus spin-orbit interaction [146]; the second is caused by structure inversion asymmetry, leading to the Rashba spin-orbit interaction [147]. In semiconductor heterostructures, the latter effect is dominant. The Rashba spin-orbit interaction can be further tuned by introducing a gate electric field. The gate electric field can play an important role in the operation of spin FETs.

As a result of spin precession, when the electrons injected by the source ferromagnet have a spin orientation parallel to the direction of the magnetization in the drain at the channel/drain interface, the output current is maximized (for example, see Fig. 3.54(a)(1)), because the spin-resolved density of states in the drain is larger for spins parallel to the magnetization. Similarly, antiparallel orientation produces a zero output current for a half-metallic drain (for example, Fig. 3.54(a)(2)). Because the magnitude of the effective magnetic field is tuned by the gate electric field, the gate voltage modulates the output current.

In the spin MOSFETs shown in Fig. 3.54(b), a semiconductor such as silicon is used as the channel. While a Schottky barrier that is formed at the interface between the source (drain) and the semiconducting channel blocks the current flow for zero gate voltage, the application of the gate voltage makes the barrier width narrower, allowing current to flow. This operation principle itself is the same as that of conventional Schottky MOSFETs; however, the difference is that the current flowing in spin MOSFETs is spin-polarized.

Because the magnitude of the output current both in spin FETs and in spin MOSFETs depends crucially on whether the magnetization of the source electrode is parallel or antiparallel to that of the drain electrode, these spin transistors can be used as nonvolatile memory in which the magnetization is detected by the output current. Additionally, reconfigurable logic circuits can be realized using two kinds of transistor operations, corresponding to parallel and antiparallel magnetizations. For the realization of this kind of spin transistor, the following conditions must be satisfied:

- (i) Effective spin injection is allowed between the ferromagnet and the channel.
- (ii) The spin relaxation length of the channel is longer than the channel length, such that no spin-flip scattering occurs in the channel.

The main reason why graphitic materials are suitable for use in spintronics is that the spin relaxation length is expected to be relatively long. This property holds both because of the small scale of the spin-orbit interaction, which generally becomes smaller in

atoms with smaller atomic number, and because of the negligible hyperfine interaction in natural carbon atoms, most of which (about 99%) are carbon-12, which has no nuclear spins. Accordingly, for graphitic materials, one cannot expect a strong Rashba spin-orbit interaction, which is required for the operation of spin FETs [143]. However, the semiconducting channel needed for spin MOSFETs can be obtained by making the graphene semiconducting. Additionally, spin qubits using graphene nanoribbons have been proposed; they also employ the long spin relaxation length [148].

3.3.9.2 Experimental techniques for determining spin relaxation length of graphene

Next, we consider the magnitude of graphene's spin relaxation length, λ_s . Similar to the case of graphene mobility discussed in Section 3.3.5, the experimental values of λ_s are significantly lower than theoretical expectations. We will discuss the possible origins of the short spin relaxation length. Before discussing in more depth, we consider experimental techniques for deriving λ_s .

In spin transport experiments, the two kinds of device structures shown in Fig. 3.55 are used. Measurement using the devices shown in Fig. 3.55(a) is called "local measurement" and that using the devices shown in Fig. 3.55(b) is called "nonlocal measurement." In local measurement, two ferromagnets are connected to the graphene sample and the magnetic-field dependence of the resistance between the ferromagnets is measured. The ferromagnets are long and narrow, so that the long axis becomes the axis most easily magnetized (easy magnetization axis). The ferromagnets have different widths (or aspect ratios) so as to have different coercive forces, which leads to parallel and antiparallel configurations of magnetization when a magnetic field is swept along the long axis. For this configuration, the resistance between the ferromagnets becomes large for antiparallel magnetization configuration. The difference in the resistance between parallel and antiparallel magnetizations is called the "spin signal"; it is a measure of the amount of spin injected into the graphene. Note that in the local measurement, the resistance is also influenced by background resistances such as anisotropic magnetoresistance (AMR) in ferromagnets.

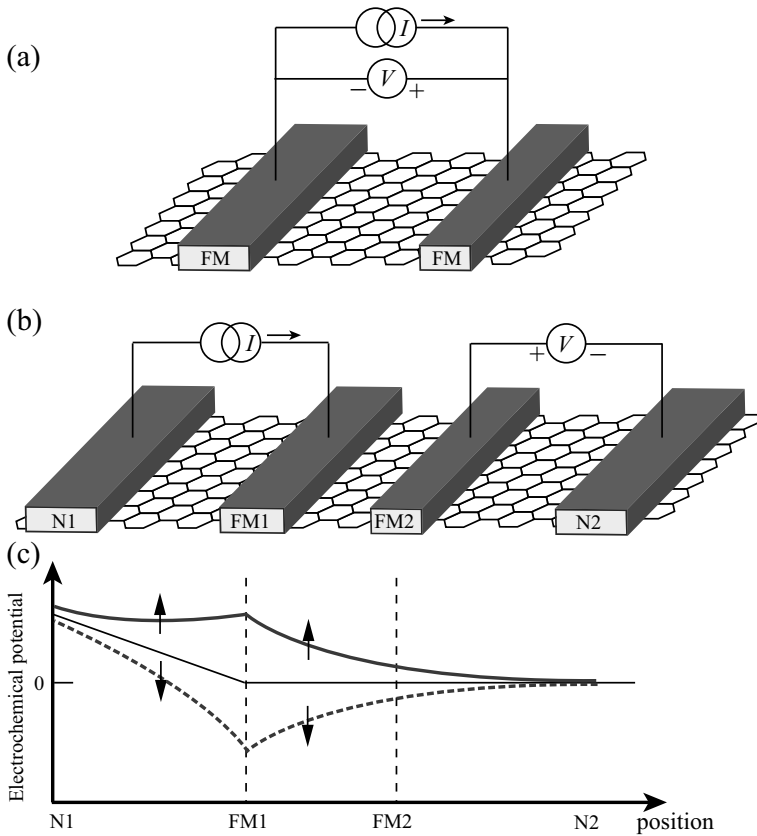


Figure 3.55 Device structures for local measurement (a), and nonlocal measurement (b). FM, FM1, and FM2 denote ferromagnets, and N1 and N2 denote nonmagnets. (c) Spatial variation of electrochemical potentials of up-spins and down-spins in the nonlocal measurement.

This kind of extrinsic magnetoresistance is excluded in the nonlocal measurement (in which a pair of nonmagnets are placed outside of the ferromagnet pair, so that the current path is separated from the pair of the voltage contacts, as shown in Fig. 3.55(b)) [149, 150].

The spin-polarized current injected by ferromagnet FM1 causes a difference in the densities (and consequently, the electrochemical potentials) of up-spins and down-spins in the graphene underneath

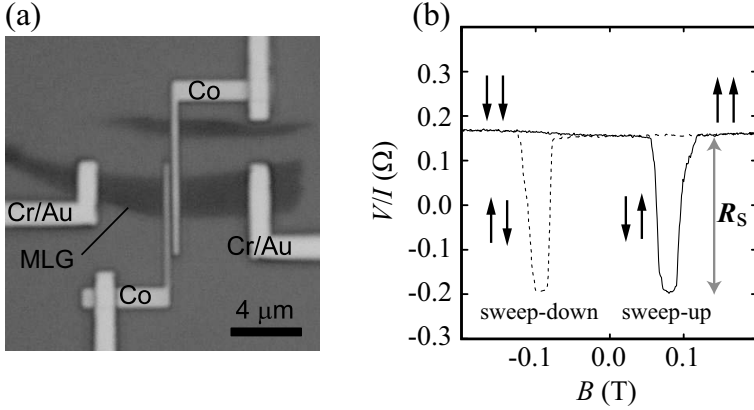


Figure 3.56 (a) An SEM image of multilayer graphene (MLG) used for nonlocal measurement. Ferromagnets (Co) and nonmagnets (Cr/Au) are connected to the MLG. (b) Magnetic field dependence of the voltage divided by the current, V/I , for increasing and decreasing magnetic fields. Arrows indicate the magnetization configuration (parallel or antiparallel).

FM1. The spins injected by FM1 diffuse into the other ferromagnet, FM2, via spin relaxation. The electrochemical potentials at FM2 are detected as a voltage between FM2 and N2. Here, the voltage is positive when the magnetizations of FM1 and FM2 are parallel; it is negative for the antiparallel configuration. For nonlocal measurement, the difference in voltage between the parallel and antiparallel configurations is called the spin signal R_s .

Figure 3.56 shows both an example of a device structure used for nonlocal measurement, and the magnetic field dependence of the voltage for increasing and decreasing magnetic fields.

The theoretical expression for the spin signal is given by [151]

$$R_s = \frac{4p_F^2}{(1-p_F^2)^2} R_N \left(\frac{R_F}{R_N} \right)^2 \frac{e^{-L/\lambda_N}}{1-e^{-2L/\lambda_N}}, \quad (3.73)$$

for transparent contacts ($R_1, R_2 \ll R_F$), and by

$$R_s = P_j^2 R_N e^{-L/\lambda_N}, \quad (3.74)$$

for tunnel contacts ($R_1, R_2 \gg R_F$). Here, $R_F = \lambda_F/\sigma_F A_F$ and $R_N = \lambda_s/\sigma_N A_N$ are the so-called spin resistances of ferromagnetic and nonmagnetic (graphene) electrodes with cross section A_F and

A_N , spin relaxation length λ_F and λ_s , and conductivity σ_F and σ_N , respectively. R_1 (R_2) is the interface resistance between FM1 (FM2) and graphene, and L is the separation between FM1 and FM2.

$$p_F = \frac{\sigma_F^\uparrow - \sigma_F^\downarrow}{\sigma_F^\uparrow + \sigma_F^\downarrow} \quad (3.75)$$

is the current polarization of FM1 and FM2, where σ_F^\uparrow and σ_F^\downarrow are the conductivity of the ferromagnet due to carriers with up-spins and down-spins, respectively, satisfying $\sigma_F = \sigma_F^\uparrow + \sigma_F^\downarrow$ and $\sigma_F^\uparrow \neq \sigma_F^\downarrow$. Similarly,

$$P_J = \frac{|G_i^\uparrow - G_i^\downarrow|}{G_i} \quad (3.76)$$

is the interfacial current polarization, where G_i^\uparrow and G_i^\downarrow are the conductance of the interface between FM*i* ($i = 1, 2$) and graphene due to carriers with up-spins and down-spins, respectively, and $G_i = G_i^\uparrow + G_i^\downarrow$.

The magnitude of R_s for a transparent contact is usually several orders smaller than that of a tunnel contact, because, typically, $R_F/R_N \sim 0.01$ ($\sigma_F/\sigma_N \sim 0.1$, $\lambda_F/\lambda_s \sim 0.01$, and $A_F/A_N \sim 10$).

From the length L dependence of the spin signal, one can derive λ_s . A typical length dependence of a spin signal is shown in Fig. 3.57.

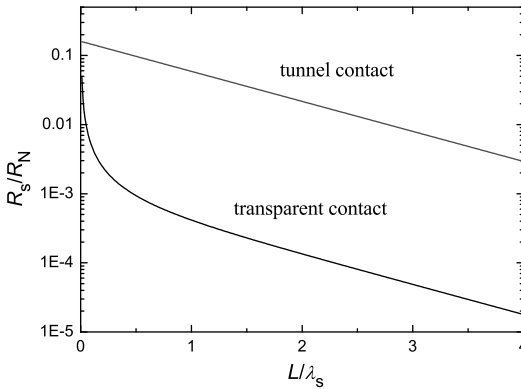


Figure 3.57 Junction length L dependence of the spin signal for transparent and tunnel contacts, calculated from Eqs. (3.73) and (3.74). $R_F/R_N = 0.01$, $p_F = 0.73$, and $P_J = 0.4$ are used [151].

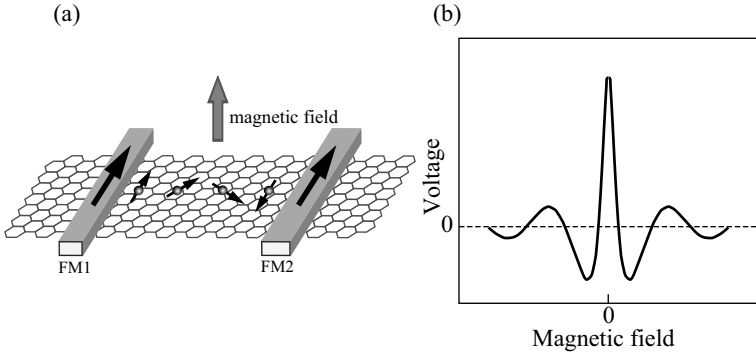


Figure 3.58 (a) Experimental setup around the ferromagnets for Hanle spin precession measurement. The magnetization in ferromagnets and the spin precession are indicated by large and small arrows, respectively. (b) The shape of Eq. (3.78) for parallel magnetization configuration in the Hanle spin precession measurement.

Another method commonly used for the estimation of the spin relaxation length of graphene is called the Hanle spin precession method [149, 150]. In this method, a magnetic field perpendicular to the graphene plane is applied after the magnetization of the ferromagnets (FM1 and FM2) are set to parallel or antiparallel.

As shown in Fig. 3.58, when a magnetic field is applied perpendicular to the graphene, the spins injected by the ferromagnet FM1 precess in the graphene plane at the Larmor frequency

$$\omega_L = g\mu_B B/\hbar, \quad (3.77)$$

where g is the Landé factor (~ 2 for graphene) and μ_B is the Bohr magneton. Because the voltage between FM2 and N2 is proportional to the projection of the spin direction with angle $\varphi = \omega_L t$ (t : diffusion time) in the magnetization direction of FM2, it oscillates as $\cos \varphi(t)$. Taking into account the spin relaxation, the voltage between FM2 and N2 can be given by [150]

$$V(B) \propto \pm \int_0^\infty P(t) \cos(\omega_L t) \exp\left(-\frac{t}{\tau_s}\right) dt, \quad (3.78)$$

where the $+$ ($-$) sign corresponds to a parallel (antiparallel) magnetization configuration of the ferromagnets, D is the diffusion constant, $\tau_s = \lambda_s^2/D$ is the spin relaxation time, and

$$P(t) = \frac{1}{\sqrt{4\pi Dt}} \exp\left(-\frac{L^2}{4Dt}\right) \quad (3.79)$$

describes the distribution of the diffusion time t for an electron to travel from FM1 to FM2. Figure 3.58(b) shows an example of the shape of the magnetic field dependence of the voltage (Eq. (3.78)) for a parallel magnetization configuration.

Fitting of the experimental magnetic field dependence of the voltage to Eq. (3.78) gives the spin relaxation time τ_s , the diffusion constant D , and consequently, the spin relaxation length $\lambda_s = \sqrt{D\tau_s}$.

3.3.9.3 Experimental values vs. theoretical expectations of the spin relaxation length

Ertler *et al.* [152] have calculated the spin relaxation time of graphene, taking into account the spin-orbit interaction originating from the charged impurities, the remote polar phonons in the substrate, and the acoustic phonons in graphene. They concluded that the effect of charged impurities is the dominant source of spin relaxation, and that τ_s is $10^{-4} - 10^{-3}$ s for an impurity density $n_{\text{imp}} = 4 \times 10^{15} \text{ m}^{-2}$ and $10^{-6} - 10^{-5}$ s for $n_{\text{imp}} = 4 \times 10^{16} \text{ m}^{-2}$, corresponding to $\lambda_s = 1 - 3$ mm and $0.1 - 0.3$ mm, respectively, for the typical diffusion constant $D = 0.01 \text{ m}^2/\text{s}$. On the other hand, the experimentally obtained value of λ_s is $1 - 2 \text{ }\mu\text{m}$, [153–156], which is several orders of magnitude smaller than the theoretical value. An example in which the spin relaxation length was derived from the Hanle measurement is shown in Fig. 3.59.

The origin of the discrepancy between the theoretical and experimental spin relaxation lengths is not clear at this stage. We can, however, list some possible causes for the small value of λ_s :

- (i) Strain and ripples in the graphene produce an effective gauge field and a corresponding random pseudo-magnetic field. Ripples of ~ 100 nm in size can make the theoretical value of λ_s comparable to experimental values [157].
- (ii) At the zigzag edges of graphene boundaries, the local density of states localizes, and local magnetism is induced [84]. A zigzag section longer than $3a$ (a : lattice constant) is sufficient for the formation of local magnetic moments in disordered graphene edges [158].
- (iii) A local magnetic moment is induced also by vacancies [158] or by adatoms [159].

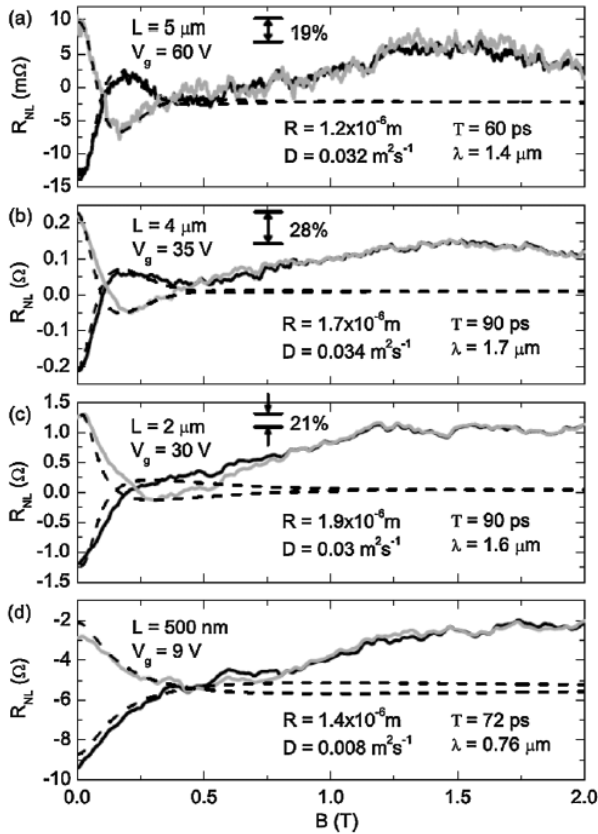


Figure 3.59 Anisotropic spin relaxation at high electron density $n = 2.1 \times 10^{12} \text{ cm}^{-2}$ (a). Initially, spins are injected parallel to the graphene plane. The magnetization of the spin injector is set parallel (gray line) or antiparallel (black line) to the detector (at a distance $L = 5 \mu\text{m}$). The diffusion constant D and the relaxation time T_{\parallel} can be extracted from the fits to Eq. (3.78) (dashed line). A magnetic field of $\sim 1.4 \text{ T}$ is needed to align the magnetization of the ferromagnetic electrodes out of their easy-magnetization axis. In this case, the spins are injected perpendicular to the graphene layer with a spin relaxation time T_{\perp} . T_{\perp} is 19% smaller than T_{\parallel} . The small decrease in the nonlocal signal found between 1.5 and 2 T is attributed to a background caused by orbital magnetoresistance effects. The same experiment was performed for (b) $L = 4 \mu\text{m}$ ($n = 3.5 \times 10^{12} \text{ cm}^{-2}$), (c) $L = 2 \mu\text{m}$ ($n = 2.8 \times 10^{12} \text{ cm}^{-2}$), and (d) $L = 500 \text{ nm}$ ($n = 3.5 \times 10^{12} \text{ cm}^{-2}$). After Ref. [155].

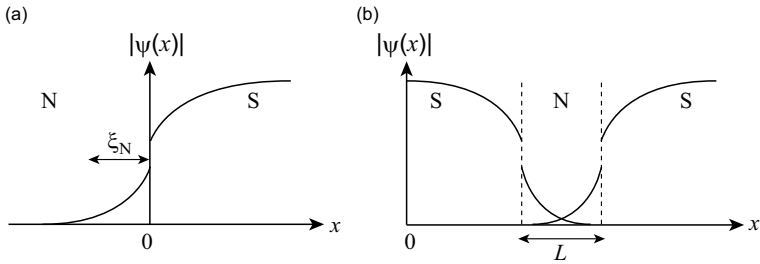


Figure 3.60 Spatial variation of the amplitude of the superconducting wave function, $|\Psi(x)|$ in a superconductor/normal metal (SN) junction (a) and in an SNS junction (b).

Thus, whereas ideal (clean) graphene does not have ferromagnetic or ferrimagnetic order, real-world graphene with disordered edges, vacancies, and adatoms tends to have a local magnetic moment, which might reduce the spin relaxation length in graphene.

3.3.10 Cooper-Pair Transport

3.3.10.1 Superconducting proximity effect

When a superconductor (S) is placed in clean contact with a normal (conventional) metal (N), the superconductivity in the vicinity of the S/N interface is weakened on the superconductor side and some superconductivity is induced in the normal metal side. This phenomenon, which has been studied since the late 1950s [160, 161], is called the superconducting proximity effect and is described either as the penetration of the superconducting wave function (or the superconducting order parameter) from the superconductor into the normal metal (Fig. 3.60(a)) [162], or as the Andreev reflection [163]. The penetration length of the superconducting order parameter is characterized by the so-called coherence length, ξ_N ; its magnitude depends on the properties of the normal metal, such as the electron mean free path and the Fermi velocity.

In an SNS structure, in which a normal metal is sandwiched by two superconductors, when the separation of the superconductors, L , is comparable to or smaller than ξ_N , the penetrating superconducting wave functions from both superconductors overlap,

and a dissipationless supercurrent flows in the normal metal (Fig. 3.60(b)). This SNS junction behaves as a kind of Josephson junction. (Note that in conventional Josephson junctions, a thin insulator, instead of a normal metal, is sandwiched between two superconductors.)

In this device, if one can adjust the coherence length ξ_N by modulating the properties of the normal metal, one can control the magnitude of the supercurrent accordingly. Specifically, a three-terminal superconducting FET can be formed if the carrier density of the normal metal is modulated by an electric field [164, 165]. This so-called superconducting transistor rapidly developed in 1980s and 90s, because of theoretical progress and advances in crystal growth and nanofabrication techniques.

Graphene provides new possibilities for research into superconducting proximity effects and also superconducting electronics. Although no one has ever succeeded in making graphene superconducting, one can induce superconductivity using the proximity effect. When considering this method, we note that superconductivity itself is a nonrelativistic effect, but that one can expect the “relativistic Josephson effect” when Cooper-pairs travel through the graphene. Also, because of the considerable variation of the carrier density from positive to negative values, one can expect a large modulation of the supercurrents. Besides, in multilayer graphene, the density of the gate-induced carriers varies spatially from layer to layer because of gate-field screening, leading to a new type of inhomogeneous proximity system.

In this section, we briefly review the theoretical and experimental aspects of the superconducting proximity effect in graphene.

3.3.10.2 Josephson effect in single-layer graphene: theoretical aspects

Relevant length scales First, we consider the coherence length of SN junctions. The coherence length separates so-called long and short junctions. In clean junctions (mean free path $l \gg \hbar v_F / \Delta$), the coherence length is

$$\xi_{N0,c} = \frac{\hbar v_F}{\Delta}, \quad (3.80)$$

where Δ is the energy gap in the superconductor and v_F is the Fermi velocity in the normal metal. The subscript “N” and “0” denote the normal metal and zero-temperature, respectively. In dirty junctions ($l \ll \hbar v_F / \Delta$), it is

$$\xi_{\text{N0,d}} = \sqrt{\frac{\hbar D}{\Delta}}, \quad (3.81)$$

where D is the diffusion constant in the normal metal. When the junction length L is shorter (longer) than the coherence length, the junction is called a short (long) junction.

At finite temperatures, thermal smearing affects the coherence of the Cooper pairs in the normal metal. The thermal coherence length is expressed by

$$\xi_{\text{NT,c}} = \frac{\hbar v_F}{k_B T}, \quad (3.82)$$

for clean junctions, and

$$\xi_{\text{NT,d}} = \sqrt{\frac{\hbar D}{k_B T}}, \quad (3.83)$$

for dirty junctions.

Andreev reflections Andreev reflection is the microscopic mechanism of the superconducting proximity effect. It describes the conversion of an incoming electron with a charge e from the normal metal into a Cooper pair $2e$ in the superconductor. Simultaneously, the conservation of electrical charge requires the reflection of a hole into the normal metal. This process occurs commonly when the energy of the incident electron is smaller than the superconducting energy gap, Δ , such that the excitation of a single quasiparticle state is forbidden at low temperatures [166].

In the case of a conventional normal metal, the incident electron and the reflected hole are both in the conduction band (*intragap* process), and a retroreflection occurs, i.e., the incident electron and the reflected hole follow the same path (Fig. 3.61(a)). Note, however, that strictly speaking, the Andreev reflection is a perfect retroreflection only when the excitation energy, ε_e , of the incident electron is zero (i.e., the electron incident at the Fermi energy). When $\varepsilon_e \neq 0$, the incident electron with energy $\varepsilon_F + \varepsilon_e$ has a wave

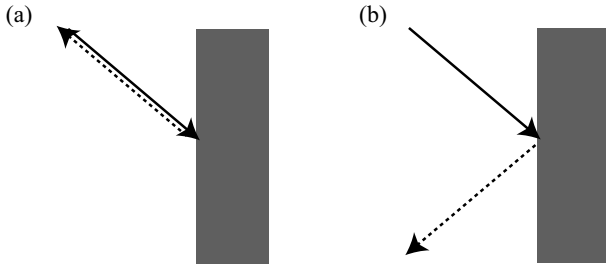


Figure 3.61 (a) Retroreflection and (b) specular reflection.

vector $k_F + \delta k/2$; the reflected hole with energy $\varepsilon_F - \varepsilon_e$ has a wave vector $k_F - \delta k/2$, with $\delta k = 2\varepsilon_e/\hbar v_F$.

The Andreev reflection is dominant when the S/N interface is transparent. For a perfect contact, all of the charge transfer is via the Andreev reflection; therefore, the subgap conductance becomes twice the normal state conductance.

For superconductor–graphene interfaces, in addition to the Andreev retroreflection, specular Andreev reflection occurs [167]. Specular Andreev reflection dominates in weakly doped graphene, in which the incident electron in the conduction band is reflected as a hole in the valence band (*interband* process). In other words, the excitation energy ε_e of the incident electron is larger than the Fermi energy ε_F , as shown in Fig. 3.62 [168].

The specular Andreev reflection can be distinguished from the Andreev retroreflection in the differential conductance [167]. The differential conductance decreases with increasing bias voltage for the specular Andreev reflection ($\varepsilon_e \gg \varepsilon_F$), while it increases for the Andreev reflection ($\varepsilon_e \ll \varepsilon_F$).

Supercurrent and current–phase relationship Titov *et al.* derived the critical supercurrent of S/graphene/S junctions in the clean and short junction limit^v in the framework of the Dirac–Bogoliubov–de Gennes (BdG) equation [169]. They made three assumptions:

- (I) The Fermi wavelength of the superconductor is much smaller than both the Fermi wavelength of graphene and the coherence length ($\xi_{N0,c}$).

^vThis condition implies that the junction is ballistic ($l \gg L$).

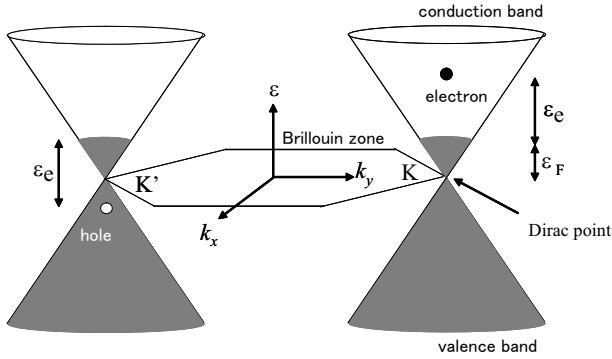


Figure 3.62 The specular Andreev reflection occurs when the excitation energy ϵ_e of the incident electron is smaller than the Fermi energy ϵ_F (interband process).

- (II) The S/graphene interface is smooth and impurity-free on the scale of $\xi_{N0,c}$.
- (III) No lattice mismatch exists at the interface. This can be satisfied by depositing the superconductor on top of a heavily doped region of the graphene.

They obtained the critical supercurrent I_c for a short and wide junction ($L \ll W$, $\xi_{N0,c}$, where L and W are the junction length and width, respectively). The current–phase relation around the Dirac point ($\epsilon \ll \hbar v_F/L$) is given by

$$I(\phi) = \frac{e\Delta}{\hbar} \frac{2W}{\pi L} \cos(\phi/2) \operatorname{arctanh}[\sin(\phi/2)], \quad (3.84)$$

where ϕ is the phase difference between two superconductors. The corresponding critical supercurrent I_c is

$$I_c = 1.33 \frac{e\Delta}{\hbar} \frac{W}{\pi L}. \quad (3.85)$$

For the opposite limit $\epsilon \gg \hbar v_F/L$,

$$I_c = 1.22 \frac{e\Delta}{\hbar} \frac{\epsilon W}{\pi \hbar v_F}, \quad (3.86)$$

is obtained.

Here, we note that, even for the Dirac point, where the density of states vanishes, a finite supercurrent flows in the system. The critical supercurrent at the Dirac point is inversely proportional to the

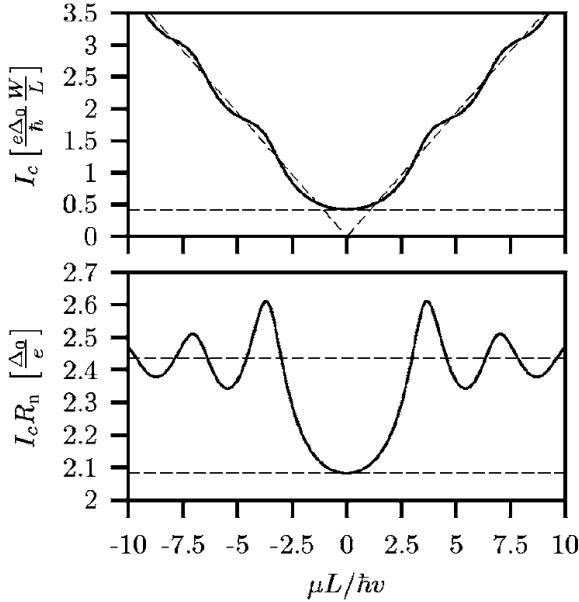


Figure 3.63 Critical current I_c and $I_c R_n$ (R_n : normal state resistance) product of a ballistic Josephson junction (length L is short compared to either width W or superconducting coherence length ξ_N), as a function of the Fermi energy μ in the normal region. The asymptotes (3.85), (3.86), (3.88), and (3.89) are indicated by dashed lines. After Ref. [169].

junction length L , which is quite different from the L -independent I_c in conventional SNS junctions in the clean and short limit,

$$I_c = N \frac{e\Delta}{\hbar}, \quad (3.87)$$

(N = the number of transverse modes at the Fermi level), and is similar to the expression for the short and dirty junctions. The current-phase relation, Eq. (3.84), is identical to that of a disordered normal metal upon substitution $k_{Fl} \rightarrow 1$. This is called *pseudodiffusive* behavior.

Also note that the $I_c R_n$ product (R_n : normal state resistance) remains on the same order as Δ/e for all ε [169];

$$I_c R_n = 2.08 \frac{\Delta}{e}, \quad (3.88)$$

for the Dirac point, and

$$I_c R_n = 2.44 \frac{\Delta}{e}, \quad (3.89)$$

for $\varepsilon \gg \hbar v_F/L$. An analysis based on a self-consistent TB BdG formalism [170] showed that the functional form of the current-phase relation (Eq. (3.84)),

$$I(\phi) \propto \cos(\phi/2) \operatorname{arctanh}[\sin(\phi/2)], \quad (3.90)$$

is valid not only for a short junction at the Dirac point but also for a long junction at the Dirac point and moderately doped short or long junctions ($\varepsilon \gg \hbar v_F/L$). It was shown that the critical supercurrent has an L -dependence of

$$I_c \propto L^{-1.3} \quad (3.91)$$

for the Dirac point, and

$$I_c \propto L^{-0.4} \quad (3.92)$$

for moderate doping.

Curvas and Yeyati discussed the current-voltage characteristics and the excess current $I_{exc} = I(V) - V/R_n$ in similar devices. These properties showed a gate voltage dependence similar to that of the critical supercurrent [171].

3.3.10.3 Josephson effect in single-layer graphene: experiments

Experimental verification of the “relativistic Josephson effect” in graphene seems to be challenging; no one has yet succeeded in observing this phenomenon. Here, we summarize the present state of the art and difficulties encountered in experiments.

Figure 3.64 shows an SEM image and a schematic side view of a conventional S/graphene/S Josephson junction fabricated using electron beam lithography. A graphene film is connected to two superconducting electrodes, thus forming a Josephson junction. The length of the junction L is typically larger than $0.2 \mu\text{m}$ for lithographically defined S/graphene/S junctions (the conventional type). As the superconductor, Pd/Al (Ti/Al) is commonly used, where Pd (Ti) is an adhesion layer. The Fermi energy of the graphene can be controlled by the back gate voltage. At temperatures well below

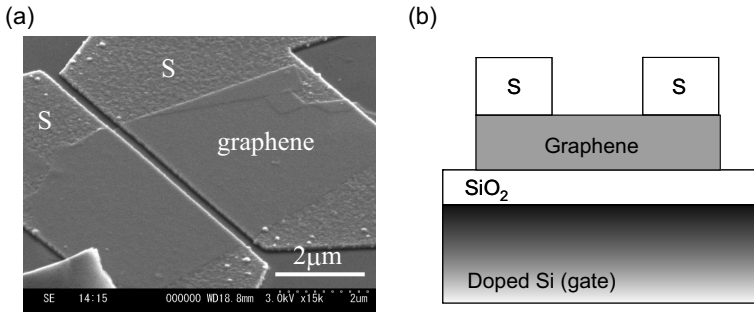


Figure 3.64 An SEM image (a) and a schematic side view of a lithographically defined S/graphene/S Josephson junction.

the superconducting transition temperature of the superconducting electrodes (≈ 1.0 K for Ti/Al electrodes), a supercurrent flows in the graphene Josephson junctions.

The Josephson supercurrent in S/graphene/S junctions was first reported by Heersche *et al* [172, 173]. They observed not only the zero-voltage supercurrent but also dips in the differential resistance caused by multiple Andreev reflection, the Fraunhofer pattern of the critical supercurrent as a function of the magnetic field, and the A.C. Josephson effect [174]. These observations confirmed the formation of Josephson junctions. They observed a finite supercurrent at the charge neutrality point, and were able to modulate the critical supercurrent by changing the gate voltage. A similar example is shown in Fig. 3.65. The $I_c R_N$ product was on the order of Δ/e and exhibited a dip at the charge neutrality point. These results appeared to be consistent with theoretical predictions regarding relativistic Josephson effects.

Later, Du *et al.* [175] pointed out that the gate voltage dependence of both the proximity-induced sub-gap features (multiple Andreev reflections) and the critical supercurrent cannot be explained by the ballistic S/graphene/S model; they can, however, be explained by the diffusive junction model. Du *et al.* concluded that the data reported by Heersche *et al.* [172, 173] were also consistent with the diffusive junction model. In practice, as is shown in Fig. 3.22, the typical mean free path of graphene placed on a Si/SiO₂ substrate is around 100 nm. The lithographically defined graphene

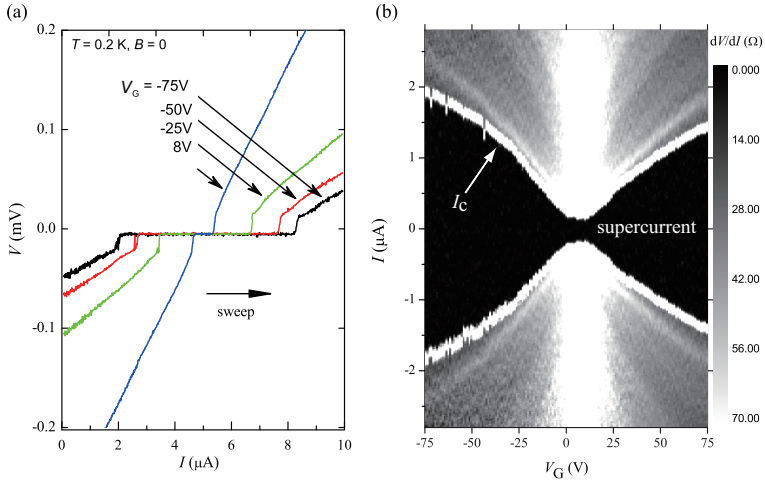


Figure 3.65 (a) Current–voltage (I – V) characteristics of a lithographically defined S/graphene/S junction at 0.2 K for several gate voltages. The separation of the superconductors (S) is $L = 0.22 \mu\text{m}$. (b) Gray scale plot of the differential resistance of the same junction in the bias current–gate voltage plane, measured at 0.2 K. Bright (dark) regions correspond to high (low) differential resistance. The black region around the bias current $I = 0$ corresponds to supercurrent. The upper boundary of the black region is the critical supercurrent.

Josephson junctions have a length of $\geq 200 \text{ nm}$, indicating that electrons traveling through a junction experience scattering.

One can infer whether the electron transport is ballistic or diffusive from the temperature dependence of the critical supercurrent I_c . Theoretically, the supercurrent of clean and short (ballistic) Josephson junctions follows so-called Kulik–Omel’yanchuk (KO)-2 theory [176], which gives the current–phase relation

$$I(\phi) = \frac{\pi \Delta(T)}{eR_N} \sin(\phi/2) \tanh \frac{\Delta(T) \cos(\phi/2)}{2k_B T}, \quad (3.93)$$

whereas the supercurrent of dirty and short (diffusive) Josephson junctions is given by KO-1 theory [177],

$$I(\phi) = \frac{2\Delta(T)}{eR_N} \cos(\phi/2) \pi k_B T \sum_{\omega} \frac{1}{\sqrt{\omega^2 + \Delta^2(T) \cos^2(\phi/2)}} \times \arctan \frac{\Delta(T) \sin(\phi/2)}{\sqrt{\omega^2 + \Delta^2(T) \cos^2(\phi/2)}}, \quad (3.94)$$

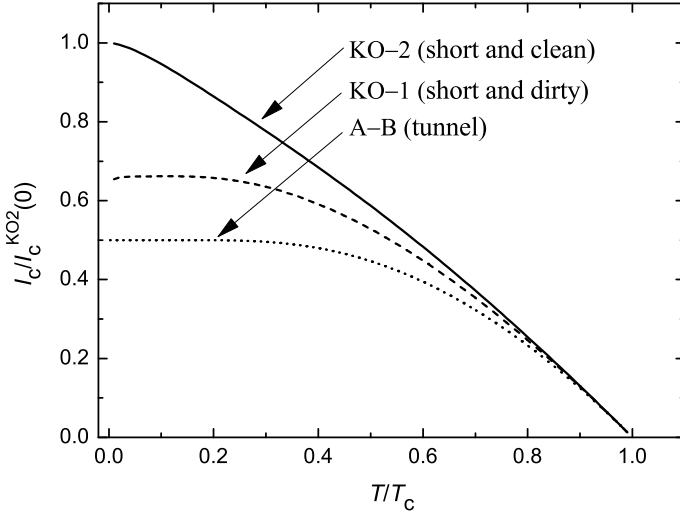


Figure 3.66 Temperature dependence of the critical supercurrent, $I_c(T)$, in the Kulik–Omel’yanchuk theories for ballistic (KO-2) and diffusive (KO-1) junctions, normalized by $I_c^{KO2}(0) = \pi \Delta(0)/eR_N$. $I_c(T)$ in Ambegaokar–Baratoff theory (A-B) is also plotted.

where $\Delta(T)$ is the temperature-dependent superconducting energy gap of the electrodes, and $\omega = (2n+1)\pi k_B T/\hbar$. The resulting critical supercurrent is shown in Fig. 3.66 together with the Ambegaokar–Baratoff result for Josephson tunnel junctions [178],

$$I_c(T) = \frac{\pi \Delta(T)}{2eR_N} \tanh \frac{\Delta(T)}{2k_B T}. \quad (3.95)$$

Figure 3.67 shows the temperature dependence of I_c for a graphene Josephson junction with $L = 0.22 \mu\text{m}$. For all gate voltages, the data are well fitted by KO-1 theory, indicating that the junction is diffusive. Similar results were reported in Ref. [179].

As mentioned above, to observe the relativistic Josephson effect, one needs to prepare ballistic graphene Josephson junctions. For the realization of a ballistic junction, two approaches are possible: one is to make the junction shorter, and the other is to make the mean free path longer.

Tomori *et al.* [180] have developed a technique to fabricate ultrashort graphene Josephson junctions with lengths as short as several tens of nanometers, lengths that are not attainable by

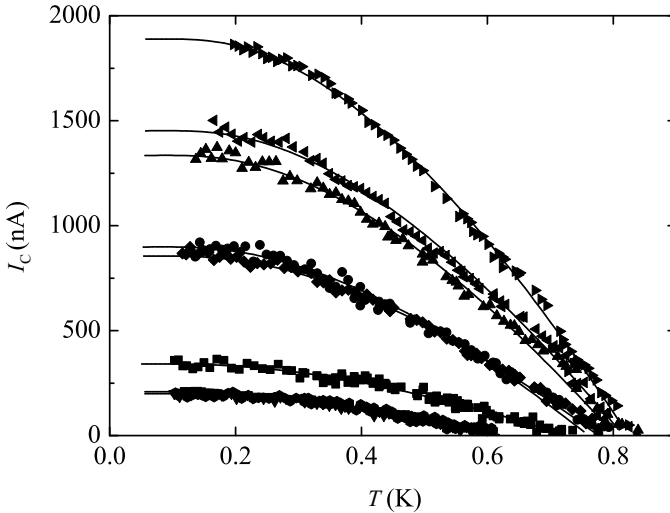


Figure 3.67 Temperature dependence of the critical supercurrent, $I_c(T)$ for a lithographically defined graphene Josephson junction for several gate voltages. The gate voltage values are -75 V, -50 V, 75 V, 50 V, -25 V, 25 V, 0 V, and 8 V from the top to bottom. The solid curves are the results of fits to KO-1 theory for short and diffusive junctions. The sample is the same as that in Figs. 3.64 (a) and 3.65. The junction length is $L = 0.22$ μm .

conventional e-beam lithography and lift-off. They used electron beam lithography followed by double-angle deposition of metal films and lift-off. In this method, the first deposited film acts as a mask for the second deposition, which is applied from a different angle. A similar technique is commonly used for the fabrication of small metallic tunnel junctions [181, 182] and nanogaps [183]. Figure 3.68(a) is an SEM image of an ultrashort graphene Josephson junction with a length of 50 nm.

In the current-voltage characteristics of the 50 nm Josephson junction at low temperatures, a supercurrent was observed, as shown in Fig. 3.69(a). The temperature dependence of I_c is better fitted by KO-2 theory for ballistic Josephson junctions than by KO-1 theory for diffusive junctions, as shown in Fig. 3.69(b), indicating that the electron transport is ballistic. Here, we note that the gate

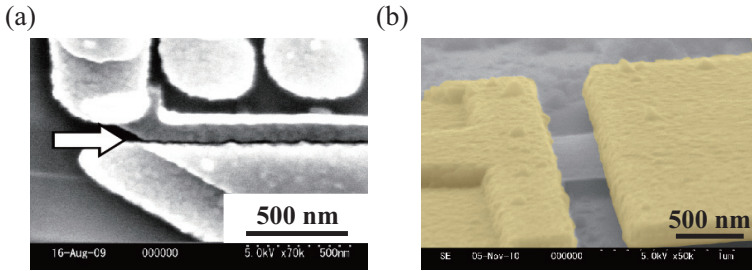


Figure 3.68 (a) Ultrashort graphene Josephson junction with a junction length of 50 nm. The arrow indicates the gap between the two superconductors (aluminum), the location at which the graphene junction is formed. (b) Suspended graphene Josephson junction with superconducting electrodes (aluminum).

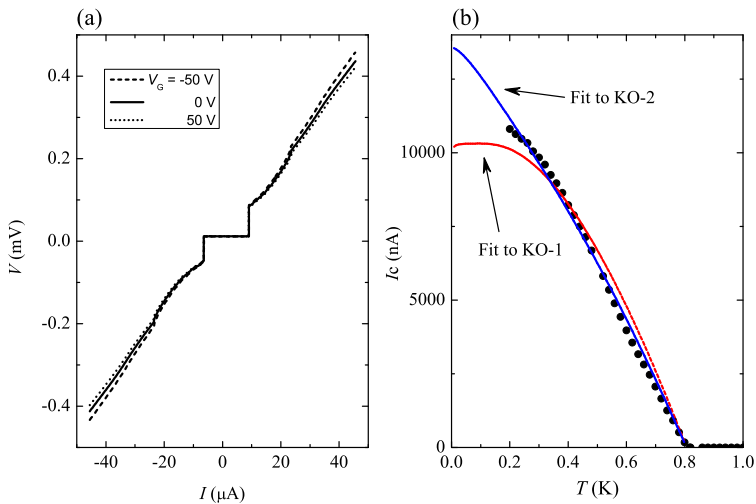


Figure 3.69 (a) Current-voltage characteristics of a 50 nm graphene Josephson junction for several gate voltages, measured at 0.2 K. (b) Temperature dependence of I_c is compared to results of KO-1 and KO-2 theory.

modulation of the conductivity is weakened relative to that of conventional graphene devices, and that no gate voltage dependence was seen in I_c , as shown in Fig. 3.69(a).

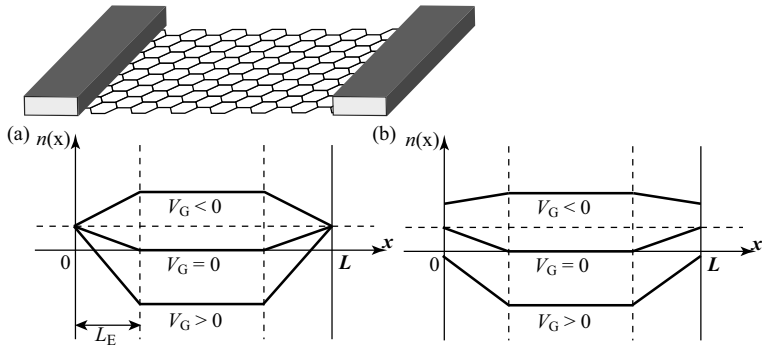


Figure 3.70 Spatial variation of the local carrier density in a metal/graphene/metal junction with perfect Fermi level pinning (a), and imperfect pinning (b). The metal/graphene interfaces are at $x = 0$ and $x = L$.

One possible origin of the small field effect is the influence of Fermi level pinning; when graphene is in contact with a metal, because of the difference in work functions, the graphene portion near the interface is locally doped by the metal. This situation is depicted in Fig. 3.70(a); even in the absence of the gate electric field ($V_G = 0$), the local carrier density $n(x)$ increases as the position x approaches the interfaces at $x = 0$ and $x = L$ because of carrier injection from the electrodes, whereas $n(x) = 0$ at the graphene portion away from the interfaces. The carrier doping by the contact metal is reported to extend a length $L_E \sim 0.2\text{--}0.3 \mu\text{m}$ [184]. When the gate voltage is changed by δV_G , the corresponding change in the local carrier density $\delta n(x)$ decreases as one approaches the interfaces. When the Fermi level pinning is perfect, $\delta n(0) = \delta n(L) = 0$, as shown in Fig. 3.70(a).

When the Fermi level pinning is strong enough, one cannot bring the Fermi level of the interface to the Dirac point. Thus, the observation of relativistic phenomena that occur at the Dirac point is not possible. If one can remove or reduce the Fermi level pinning in some way, as depicted in Fig. 3.70(b), one might reach the Dirac point at the interface; however, even in this case, the carrier density slopes near the interface. These situations are not taken into account

in theories of relativistic Josephson effects, and might be the reason why the effects have not yet been confirmed experimentally.

In the second approach to the ballistic Josephson junctions, one could remove the substrate (thus making the graphene suspended), as explained in Section 3.3.5. Conventional suspended graphene devices are fabricated by etching the SiO_2 substrate using a strong acid such as buffered HF; however, strong acid damages most superconductors. Instead, Tomori *et al.* developed a technique to make a graphene film suspended, without removing a substrate, using multiple e-beam lithography with two kinds of resists that have different properties [185]. An SEM image of a suspended graphene Josephson junction is shown in Fig. 3.64(b). In this kind of suspended Josephson junction, one can both decrease the normal state resistance R_N and clean the graphene film by current annealing (see Section 3.3.5), which may be favorable for the observation of the Josephson effect.

3.4 Summary

In this chapter, some experimental aspects of graphene research were reviewed. It should be emphasized that presumably because graphene is a perfect two-dimensional crystal, its electronic properties are strongly influenced by its environment. For example, the electric field effect is significantly changed by the existence of charged impurities in the substrate, and the corresponding mobility is significantly reduced. For spin transport, the observed spin relaxation length is several orders of magnitude smaller than the theoretical expectation, possibly because there are ripples, strain effects, edges, vacancies, and adatoms in graphene samples. Additionally, in Cooper-pair transport, the effect of the contact metals may hinder the observation of relativistic Josephson effects. Thus, for the observation of special phenomena in graphene and successful application of graphene to electronic devices, a deeper understanding of its interaction with its environment and the control of environmental parameters are indispensable.

References

1. K. S. Novoselov, A. K. Geim, S. V. Morozov, D. Jiang, Y. Zhang, S. V. Dubonos, I. V. Grigorieva, and A. A. Firsov, Electric field effect in atomically thin carbon films, *Science*, **306**, 666–669 (2004).
2. N. D. Mermin and H. Wagner, Absence of ferromagnetism or antiferromagnetism in one- or two-dimensional isotropic Heisenberg models, *Phys. Rev. Lett.*, **17**, 1133–1136 (1966).
3. R. E. Peierls, Bemerkung ueber Umwandlungstemperaturen, *Helv. Phys. Acta.*, **7**, 81–83 (1934).
4. K. S. Novoselov, D. Jiang, F. Schedin, T. J. Booth, V. V. Khotkevich, S. V. Morozov, and A. K. Geim, Two-dimensional atomic crystals, *Proc. Nat. Acad. Sci. USA*, **102**, 10451–10453 (2005).
5. A. K. Geim and P. Kim, Carbon wonderland, *Scientific American*, **298**, 90–97 (2007).
6. J. C. Meyer, A. K. Geim, M. I. Katsnelson, T. Booth, K. S. Novoselov, and S. Roth, The structure of suspended graphene sheets, *Nature*, **446**, 60–63 (2007).
7. T. J. Booth, P. Blake, R. R. Nair, D. Jiang, E. W. Hill, U. Bangert, A. Bleloch, M. Gass, K. S. Novoselov, M. I. Katsnelson, and A. K. Geim, Macroscopic graphene membranes and their extraordinary stiffness, *Nano Lett.*, **8**, 2442–2446 (2008).
8. A. Fasolino, J. H. Los, and M. I. Katsnelson, Intrinsic ripples in graphene, *Nat. Mater.*, **6**, 858–861 (2007).
9. C. H. Lui, L. Liu, K. F. Mak, G. W. Flynn, and T. F. Heinz, Ultraflat graphene, *Nature*, **462**, 339–341 (2009).
10. B. Z. Jang and W. C. Huang, Nano-scaled graphene plates, U. S. Pat. No. 7,071,258 (submitted on 10/21/2002, and issued on 07/04/2006).
11. L. M. Viculus, J. J. Mack, R. B. Kaner, A chemical route to carbon nanoscrolls, *Science*, **299**, 1361 (2003).
12. J. S. Bunch, Y. Yaish, M. Brink, K. Bolotin, P. L. McEuen, Coulomb oscillations and Hall effect in quasi-2D graphite quantum dots, *Nano Lett.*, **5**, 287–290 (2005).
13. Y. Zhang, J. P. Small, W. V. Pontius, and P. Kim, Electric field modulation of galvanomagnetic properties of mesoscopic graphite, *Appl. Phys. Lett.*, **86**, 073104–1–3 (2005).
14. E. Stolyarova, K. T. Rim, S. Ryu, J. Maultzsch, P. Kim, L. E. Brus, T. F. Heinz, M. S. Hybertsen, and G. W. Flynn, High-resolution scanning tunneling

- microscopy imaging of mesoscopic graphene sheets on an insulating surface, *Proc. Nat. Acad. Sci. USA*, **104**, 9209–9212 (2007).
15. Xu Du, I. Skachko, A. Barker, E. Y. Andrei, Approaching ballistic transport in suspended graphene, *Nat. Nanotechnol.*, **3**, 491–495 (2008).
 16. P. Blake, E. W. Hill, A. H. Castro Neto, K. S. Novoselov, D. Jiang, R. Yang, T. J. Booth, and A. K. Geim, Making graphene visible, *Appl. Phys. Lett.*, **91**, 063124–1–3 (2007).
 17. Z. H. Ni, H. M. Wang, J. Kasim, H. M. Fan, T. Yu, Y. H. Wu, Y. P. Feng, and Z. X. Shen, Graphene thickness determination using reflection and contrast spectroscopy, *Nano Lett.*, **7**, 2758–2763 (2007).
 18. I. Jung, M. Pelton, R. Piner, D. A. Dikin, S. Stankovich, S. Watcharotone, M. Hausner, and R. S. Ruoff, Simple approach for high-contrast optical imaging and characterization of graphene-based sheets, *Nano Lett.*, **7**, 3569–3575 (2007).
 19. H. Anders, *Thin Films in Optics* (Focal, London, 1967), Pt. 1.
 20. *Handbook of Optical Constants of Solids* edited by E. Palik (Academic, New York, 1991).
 21. C. R. Dean, A. F. Young, I. Meric, C. Lee, L. Wang, S. Sorgenfrei, K. Watanabe, T. Taniguchi, P. Kim, K. L. Shepard, and J. Hone, Boron nitride substrates for high-quality graphene electronics, *Nat. Nanotechnol.*, **5**, 722–726 (2010).
 22. J. B. Oostinga, H. B. Heersche, L. Liu, A. F. Morpurgo, and L. M. K. Vandersypen, Gate-induced insulating state in bilayer graphene devices, *Nat. Mater.*, **7**, 151–157 (2008).
 23. A. C. Ferrari, J. C. Meyer, V. Scardaci, C. Casiraghi, M. Lazzeri, F. Mauri, S. Piscanec, D. Jiang, K. S. Novoselov, S. Roth, and A. K. Geim, Raman spectrum of graphene and graphene layers, *Phys. Rev. Lett.*, **97**, 187401–1–4 (2007).
 24. A. Gupta, G. Chen, P. Joshi, S. Tadigadapa, and P. C. Eklund, Raman scattering from high-frequency phonons in supported n-graphene layer films, *Nano Lett.*, **6**, 2667–2673 (2006).
 25. D. Graf, F. Molitor, K. Ensslin, C. Stampfer, A. Jungen, C. Hierold and L. Wirtz, Spatially resolved Raman spectroscopy of single- and few-layer graphene, *Nano Lett.*, **7**, 238–242 (2007).
 26. B. Krauss, T. Lohmann, D.-H. Chae, M. Haluska, K. von Klitzing, J. H. Smet, Laser-induced disassembly of a graphene single crystal into a nanocrystalline network, *Phys. Rev. B.*, **79**, 165428–1–9 (2009).

27. D. Teweldebrhan and A. A. Balandin, Modification of graphene properties due to electron-beam irradiation, *Appl. Phys. Lett.*, **94**, 013101-1-3 (2009).
28. T. Moriki, A. Kanda, T. Sato, H. Miyazaki, S. Odaka, Y. Ootuka, Y. Aoyagi, and K. Tsukagoshi, Electron transport in thin graphite films: Influence of microfabrication processes, *Physica E*, **40**, 241-244 (2007).
29. A. J. van Bommel, J. E. Crombeen, and A. van Tooren, LEED and Auger electron observations of the SiC(0001) surface, *Surf. Sci.*, **48**, 463-472 (1975).
30. T. Ohta, F. E. Gabaly, A. Bostwick, J. L. McChesney, K. V. Emtsev, A. K. Schmid, Th. Seyller, K. Horn, and E. Rotenberg, Morphology of graphene thin film growth on SiC(0001), *New J. Phys.*, **10**, 023034-1-8 (2008).
31. K. V. Emtsev, A. Bostwick, K. Horn, J. Jobst, G. L. Kellogg, L. Ley, J. L. McChesney, T. Ohta, S. A. Reshanov, J. Rohrl, E. Rotenberg, A. K. Schmid, D. Waldmann, H. B. Weber, and Th. Seyller, Towards wafer-size graphene layers by atmospheric pressure graphitization of silicon carbide, *Nat. Mater.*, **8**, 203-207 (2009).
32. H. Miyazaki, S. Odaka, T. Sato, S. Tanaka, H. Goto, A. Kanda, K. Tsukagoshi, Y. Ootuka, and Y. Aoyagi, Inter-layer screening length to electric field in thin graphite film, *Appl. Phys. Express.*, **1**, 034007-1-3 (2008).
33. S. Irle, Z. Wang, G. S. Zheng, K. Morokuma, and M. Kusunoki, Theory and experiment agree: Single-walled carbon nanotube caps grow catalyst-free with chirality preference on a SiC surface, *J. Chem. Phys.*, **125**, 044702-1-5 (2006).
34. W. A. de Heer, C. Berger, X. Wu, P. N. First, E. H. Conrad, X. Li, T. Li, M. Sprinkle, J. Hass, M. L. Sadowski, M. Potemski, and G. Martinez, Epitaxial graphene, *Solid State Commun.*, **143**, 92-100 (2007).
35. X. Wu, Y. Hu, M. Ruan, N. K. Madiomanana, J. Hankinson, M. Sprinkle, C. Berger, and W.A. de Heer, Half integer quantum Hall effect in high mobility single layer epitaxial graphene, *Appl. Phys. Lett.*, **95**, 223108-1-3 (2009).
36. C. Shelton, H. R. Patil, and J. M. Blakely, Equilibrium segregation of carbon to a nickel (111) surface: A surface phase transition, *Surf. Sci.*, **43**, 493-520 (1974).
37. C. Oshima, E. Bannai, T. Tanaka, and S. Kawai, Carbon layer on lanthanum hexaboride (100) surface, *Jpn. J. Appl. Phys.*, **16**, 965-969 (1977).

38. J. C. Hamilton and J. M. Blakely, Carbon segregation to single crystal surfaces of Pt, Pd and Co, *Surf. Sci.*, **91**, 199–217 (1980).
39. P. Sutter, J. I. Flege, and E. Sutter, Epitaxial graphene on ruthenium, *Nature Mater.*, **7**, 406–411 (2008).
40. Q. K. Yu, J. Lian, S. Siripongert, H. Li, Y. P. Chen, and S. S. Pei, Graphene segregated on Ni surfaces and transferred to insulators, *Appl. Phys. Lett.*, **93**, 113103–1–3 (2008).
41. A. Reina, X. T. Jia, J. Ho, D. Nezich, H. Son, V. Bulovic, M. S. Dresselhaus, and J. Kong, Large area, few-layer graphene films on arbitrary substrates by chemical vapor deposition, *Nano Lett.*, **9**, 30–35 (2009).
42. K. S. Kim, Y. Zhao, H. Jang, S. Y. Lee, J. M. Kim, K. S. Kim, J. H. Ahn, P. Kim, J. Choi, and B. H. Hong, Large-scale pattern growth of graphene films for stretchable transparent electrodes, *Nature*, **457**, 706–710 (2009).
43. H. Cao, Q. K. Yu, D. Pandey, D. Zemlianov, R. Colby, I. Childres, V. Drachev, E. Stach, J. Lian, H. Li, S. S. Pei, and Y. P. Chen, Large-scale graphitic thin films synthesized on Ni and transferred to insulators: Structural and electronic properties, *J. Appl. Phys.*, **107**, 044310–1–7 (2010).
44. X. Li, W. Cai, J. An, S. Kim, J. Nah, D. Yang, R. Piner, A. Velamakanni, I. Jung, E. Tutuc, S. K. Banerjee, L. Colombo, and R. S. Ruoff, Large-area synthesis of high-quality and uniform graphene films on copper foils, *Science*, **324**, 1312–1314 (2009).
45. S. Bae, H. Kim, Y. Lee, X. Xu, J. -S. Park, Y. Zheng, J. Balakrishnan, T. Lei, H. R. Kim, Y. I. Song, Y. -J. Kim, K. S. Kim, B. Özyilmaz, J. -H. Ahn, B. H. Hong, and S. Iijima, Roll-to-roll production of 30-inch graphene films for transparent electrodes, *Nat. Nanotechnol.*, **5**, 574–578 (2010).
46. X. S. Li, W. W. Cai, L. Colombo, and R. S. Ruoff, Evolution of graphene growth on Ni and Cu by carbon isotope labeling, *Nano Lett.*, **9**, 4268–4272 (2009).
47. L. J. van der Pauw, A method of measuring the resistivity and Hall coefficient on lamellae of arbitrary shape, *Philips Tech. Rev.*, **20**, 220–224 (1958).
48. N. M. Ashcroft and N. D. Mermin, *Solid State Physics* (Holt, Rinehart and Winston, New York, 1976).
49. K. S. Novoselov, A. K. Geim, S. V. Morozov, D. Jiang, M. I. Katsnelson, I. V. Grigorieva, S. V. Dubonos, and A. A. Firsov, Two-dimensional gas of massless Dirac fermions in graphene, *Nature*, **438**, 197–200 (2005).
50. N. H. Shon and T. Ando, Quantum transport in two-dimensional graphite system, *J. Phys. Soc. Jpn*, **67**, 2421–2429 (1998).

51. K. Ziegler, Robust transport properties in graphene, *Phys. Rev. Lett.*, **97**, 266802-1-4 (2006).
52. K. Nomura and A. H. MacDonald, Quantum transport of massless Dirac fermions, *Phys. Rev. Lett.*, **98**, 076602-1-4 (2007).
53. J. Tworzydło, B. Trauzettel, M. Titov, A. Rycerz, and C. W. J. Beenakker, Sub-Poissonian shot noise in graphene, *Phys. Rev. Lett.*, **96**, 246802-1-4 (2006).
54. Y.-W. Tan, Y. Zhang, K. Bolotin, Y. Zhao, S. Adam, E. H. Hwang, S. Das Sarma, H. L. Stormer, and P. Kim, Measurement of scattering rate and minimum conductivity in graphene, *Phys. Rev. Lett.*, **99**, 246803-1-4 (2007).
55. S. Adam, E. H. Hwang, V. M. Galitski, and S. Das Sarma, A self-consistent theory for graphene transport, *Proc. Nat. Acad. Sci. USA*, **104**, 18392-18397 (2007).
56. Z. Jiang, E. A. Henriksen, L. -C. Tung, Y. -J. Wang, M. E. Schwartz, M. Y. Han, P. Kim, and H. L. Stormer, Infrared Spectroscopy of Landau Levels of Graphene, *Phys. Rev. Lett.*, **98**, 197403-1-4 (2007).
57. L. A. Ponomarenko, R. yang, T. M. Mohiuddin, M. I. Katsnelson, K. S. Novoselov, S. V. Morozov, A. A. Zhkov, F. Schedin, E. W. Hill, and A. K. Geim, Effect of a High- κ environment on charge carrier mobility in graphene, *Phys. Rev. Lett.*, **102**, 206603-1-4 (2009).
58. Y. Nukui, H. Tomori, H. Goto, Y. Ootuka, K. Tsukagoshi, and A. Kanda, unpublished.
59. J. H. Chen, C. Jang, S. Adam, M. S. Fuhrer, E. D. Williams, and M. Ishigami, Charged-impurity scattering in graphene, *Nat. Phys.*, **4**, 377-381 (2008).
60. D. S. Novikov, Numbers of donors and acceptors from transport measurements in graphene, *Appl. Phys. Lett.*, **91**, 102102-1-3 (2007).
61. M. Trushin and J. Schliemann, Minimum electrical and thermal conductivity of graphene: A quasiclassical approach, *Phys. Rev. Lett.*, **99**, 216602-1-4 (2007).
62. X. -Z. Yan, Y. Romiah, and C. S. Ting, Electric transport theory of Dirac fermions in graphene, *Phys. Rev. B*, **77**, 125409-1-6 (2008).
63. E. H. Hwang, S. Adam, and S. Das Sarma, Carrier transport in two-dimensional graphene layers, *Phys. Rev. Lett.*, **98**, 186806-1-4 (2007).
64. V. M. Galitski, S. Adam, and S. Das Sarma, Statistics of random voltage fluctuations and the low-density residual conductivity of graphene, *Phys. Rev. B*, **76**, 245405-1-7 (2007).

65. J. Martin, N. Akerman, G. Ulbricht, T. Lohmann, J. H. Smet, K. von Klitzing, A. Yacoby, Observation of electron–hole puddles in graphene using a scanning single-electron transistor, *Nat. Phys.*, **4**, 144–148 (2008).
66. D. V. Averin and K. K. Likharev, in *Mesoscopic Phenomena in Solids*, edited by B. L. Altshuler, P. A. Lee, and R. A. Webb (Elsevier, Amsterdam, 1991).
67. Y. Zhang, V. W. Brar, C. Girit, A. Zettl, and M. F. Crommie, Origin of spatial charge inhomogeneity in graphene, *Nat. Phys.*, **5**, 722–726 (2009).
68. Y. Zhang, Y.-W. Tan, H. L. Stormer and P. Kim, Experimental observation of the quantum Hall effect and Berry’s phase in graphene, *Nature*, **438**, 201–204 (2005).
69. O. Klein, Die Reflexion von Elektronen an einem Potentialsprung nach der relativistischen Dynamik von Dirac, *Zeitschrift für Physik*, **53**, 157–165 (1929).
70. M. I. Katsnelson, K. S. Novoselov, A. K. Geim, Chiral tunneling and the Klein paradox in graphene, *Nat. Phys.*, **2**, 620–625 (2006).
71. A. F. Young and P. Kim, Quantum interference and Klein tunneling in graphene heterojunctions, *Nat. Phys.*, **5**, 222–226 (2009).
72. J. H. Chen, C. Jang, S. Xiao, M. Ishigami, M. S. Fuhrer, Intrinsic and extrinsic performance limits of graphene devices on SiO₂, *Nat. Nanotechnol.*, **3**, 206–209 (2008).
73. S. Fratini and F. Guinea, Substrate-limited electron dynamics in graphene, *Phys. Rev. B*, **77**, 195415–1–6 (2008).
74. M. V. Fischetti, D. A. Neumayer, and E. A. Cartier, Effective electron mobility in Si inversion layers in metal–oxide–semiconductor systems with a high- κ insulator: The role of remote phonon scattering, *J. Appl. Phys.*, **90**, 4587–4608 (2001).
75. K. I. Bolotin, K. J. Sikes, Z. Jiang, M. Klima, G. Fudenberg, J. Hone, P. Kim, and H. L. Stormer, Ultrahigh electron mobility in suspended graphene, *Solid State Commun.*, **146**, 351–355 (2008).
76. K. I. Bolotin, K. J. Sikes, J. Hone, H. L. Stormer, and P. Kim, Temperature-dependent transport in suspended graphene, *Phys. Rev. Lett.*, **101**, 096802–1–4 (2008).
77. K. I. Bolotin, Ghahari, M. D. Shulman, H. L. Stormer, P. Kim, Observation of the fractional quantum Hall effect in graphene, *Nature*, **462**, 196–199 (2009).
78. J. Moser, A. Barreiro, and A. Bachtold, Current-induced cleaning of graphene, *Appl. Phys. Lett.*, **91**, 163513–1–3 (2007).

79. D. C. Elias, R. V. Gorbachev, A. S. Mayorov, S. V. Morozov, A. A. Zhukov, P. Blake, L. A. Ponomarenko, I. V. Grigorieva, K. S. Novoselov, F. Guinea and A. K. Geim, Dirac cones reshaped by interaction effects in suspended graphene, *Nat. Phys.*, **7**, 701–704 (2011).
80. N. Tombros, A. Veligura, J. Junesch, M. H. D. Guimaraes, I. J. Vera-Marun, H. T. Jonkman and B. J. vanWees, Quantized conductance of a suspended graphene nanoconstriction, *Nat. Phys.*, **7**, 697–700 (2011).
81. S. Tanaka, H. Goto, H. Tomori, Y. Ootuka, K. Tsukagoshi and A. Kanda, Effect of current annealing on electronic properties of multilayer graphene, *J. Phy., Conf. Ser.*, **232**, 012015–1–4 (2010).
82. J. Xue, J. Sanchez-Yamagishi, D. Bulmash, P. Jacquod, A. Deshpande, K. Watanabe, T. Taniguchi, P. Jarillo-Herrero and B. J. LeRoy, Scanning tunnelling microscopy and spectroscopy of ultra-flat graphene on hexagonal boron nitride, *Nat. Mater.*, **10**, 282–285 (2011).
83. S. M. Sze, and K. K. Ng, *Physics of Semiconductor Devices*, 3rd ed. (Wiley-Interscience, 2006).
84. M. Fujita, K. Wakabayashi, K. Nakada, and K. Kusakabe, Peculiar localized state at zigzag graphite edge, *J. Phys. Soc. Jpn.*, **65**, 1920–1923 (1996).
85. K. Nakada, M. Fujita, G. Dresselhaus, and M. S. Dresselhaus, Edge state in graphene ribbons: Nanometer size effect and edge shape dependence, *Phys. Rev. B*, **54**, 17954–17961 (1996).
86. K. Wakabayashi, M. Fujita, H. Ajiki, and M. Sigrist, Electronic and magnetic properties of nanographite ribbons, *Phys. Rev. B*, **59**, 8271–8282 (1999).
87. M. Ezawa, Peculiar width dependence of the electronic properties of carbon nanoribbons, *Phys. Rev. B*, **73**, 045432–1–8 (2006).
88. Y. Kobayashi, K.-I. Fukui, T. Enoki, K. Kusakabe, and Y. Kaburagi, Observation of zigzag and armchair edges of graphite using scanning tunneling microscopy and spectroscopy, *Phys. Rev. B*, **71**, 193406–1–4 (2005).
89. Y.-W. Son, M. L. Cohen, and S. G. Louie, Energy gaps in graphene nanoribbons, *Phys. Rev. Lett.*, **97**, 216803–1–4 (2006).
90. S. Reich, J. Maultzsch, C. Thomsen, and P. Ordejón, Tight-binding description of graphene, *Phys. Rev. B*, **66**, 035412–1–5 (2002).
91. M. Y. Han, B. Ozyilmaz, Y. Zhang, and P. Kim, Energy band-gap engineering of graphene nanoribbons, *Phys. Rev. Lett.*, **98**, 206805–1–4 (2007).

92. Z. Chen, Y.-M. Lin, M. J. Rooks and Ph. Avouris, Graphene nano-ribbon electronics, *Physica E*, **40**, 228–232 (2007).
93. K. Todd, H.-T. Chou, S. Amasha and D. Goldhaber-Gordon, Quantum dot behavior in graphene nanoconstrictions, *Nano Lett*, **9**, 416–421 (2009).
94. M. Y. Han, J. C. Brant, and P. Kim, Electron transport in disordered graphene nanoribbons, *Phys. Rev. Lett.*, **104**, 056801–1–4 (2010).
95. S. Adam, S. Cho, M. S. Fuhrer, and S. Das Sarma, Density inhomogeneity driven percolation metal–insulator transition and dimensional crossover in graphene nanoribbons, *Phys. Rev. Lett.*, **101**, 046404–1–4 (2008).
96. X. Li, X. Wang, L. Zhang, S. Lee, H. Dai, Chemically derived, ultrasmooth graphene nanoribbon semiconductors, *Science*, **319**, 1229–1232 (2008).
97. Y. Ouyang, X. Wang, H. Dai, and J. Guo, Carrier scattering in graphene nanoribbon field-effect transistors, *Appl. Phys. Lett.*, **92**, 243124–1–4 (2008).
98. X. Wang, Y. Ouyang, X. Li, H. Wang, J. Guo, and H. Dai, Room-temperature all-semiconducting sub-10 nm graphene nanoribbon field-effect transistors, *Phys. Rev. Lett.*, **100**, 206803–1–4 (2008).
99. J.-M. Poumirol, A. Cresti, S. Roche, W. Escoffier, M. Goiran, X. Wang, X. Li, H. Dai, and B. Raquet, Edge magnetotransport fingerprints in disordered graphene nanoribbons, *Phys. Rev. B*, **82**, 041413(R)–1–4 (2010).
100. F. Sols, F. Guinea, and A. H. Castro Neto, Coulomb blockade in graphene nanoribbons, *Phys. Rev. Lett.*, **99**, 166803–1–4 (2007).
101. H. Miyazaki, S. Odaka, T. Sato, S. Tanaka, H. Goto, A. Kanda, K. Tsukagoshi, Y. Ootuka, and Y. Aoyagi, Coulomb blockade oscillations in narrow corrugated graphite ribbons, *App. Phys. Express*, **1**, 024001–1–3 (2008).
102. Y. Nazarov and Y. M. Blanter, *Quantum Transport: Introduction to Nanoscience* (Cambridge Univ. Press, Cambridge, 2009), p. 228.
103. D. Gunlycke, D. Areshkin, and C. T. White, Semiconducting graphene nanostrips with edge disorder, *Appl. Phys. Lett.*, **90**, 142104–1–3 (2007).
104. D. Areshkin, D. Gunlycke, and C. T. White, Ballistic transport in graphene nanostrips in the presence of disorder: Importance of edge effects, *Nano Lett.*, **7**, 204–210 (2007).

105. I. Martin and Y. M. Blanter, Transport in disordered graphene nanoribbons, *Phys. Rev. B*, **79**, 235132–1–5 (2009).
106. L. Jiao, L. Zhang, X. Wang, G. Diankov, and H. Dai, Narrow graphene nanoribbons from carbon nanotubes, *Nature*, **458**, 877–880 (2009).
107. L. Jiao, X. Wang, G. Diankov, H. Wang, and H. Dai, Facile synthesis of high-quality graphene nanoribbons, *Nat. Nanotechnol.*, **5**, 321–325 (2010).
108. D. V. Kosynkin, A. L. Higginbotham, A. Sinitiskii, J. R. Lomeda, A. Dimiev, B. K. Price, and J. M. Tour, Longitudinal unzipping of carbon nanotubes to form graphene nanoribbons, *Nature*, **458**, 872–876 (2009).
109. X. Wang and H. Dai, Etching and narrowing of graphene from the edges, *Nat. Chem.*, **2**, 661–665 (2010).
110. J. Cai, P. Ruffieux, R. Jaafar, M. Bieri, T. Braun, S. Blankenburg, M. Muoth, A. P. Seitsonen, M. Saleh, X. Feng, K. Muellen, and R. Fasel, Atomically precise bottom-up fabrication of graphene nanoribbons, *Nature*, **466**, 470–473 (2010).
111. M. Treier, C. A. Pignedoli, T. Laino, R. Rieger, K. Müllen, D. Passerone, and R. Fasel, Surface-assisted cyclodehydrogenation provides a synthetic route towards easily processable and chemically tailored nanographenes, *Nat. Chem.*, **3**, 61–67 (2011).
112. M. Sprinkle, M. Ruan, X. Wu, Y. Hu, M. Rubio-Roy, J. Hankinson, C. Berger, and W. A. de Heer, Scalable templated growth of graphene nanoribbons on SiC, *Nat. Nanotechnol.*, **5**, 727–731 (2010).
113. A. H. C. Neto, F. Guinea, N. M. R. Peres, K. S. Novoselov, and A. K. Geim, The electronic properties of graphene, *Rev. Mod. Phys.*, **81**, 109–162 (2009).
114. E. McCann, Asymmetry gap in the electronic band structure of bilayer graphene, *Phys. Rev. B*, **74**, 161403(R)–1–4 (2006).
115. H. K. Min, B. Sahu, S. K. Banerjee, and A. H. MacDonald, *Ab initio* theory of gate induced gaps in graphene bilayers, *Phys. Rev. B*, **75**, 155115–1–7 (2007).
116. E. McCann and V. Fal’ko, Landau-level degeneracy and quantum Hall effect in a graphite bilayer, *Phys. Rev. Lett.*, **96**, 086805–1–4 (2006).
117. E. V. Castro, K. S. Novoselov, S. V. Norozov, N. M. R. Peres, J. M. B. Lopes dos Santos, J. Nilsson, F. Guinea, A. K. Geim, and A. H. Castro Neto, Biased Bilayer Graphene: Semiconductor with a gap tunable by the electric field effect, *Phys. Rev. Lett.*, **99**, 216802–1–4 (2007).

118. T. Ohta, A. Bostwick, T. Seyller, K. Horn, and E. Rotenberg, Controlling the electronic structure of bilayer graphene, *Science*, **313**, 951–954 (2006).
119. Y. Zhang, T. Tang, C. Girit, Z. Hao, M. C. Martin, A. Zettl, M. F. Crommie, Y. R. Shen, and F. Wang, Direct observation of a widely tunable bandgap in bilayer graphene, *Nature*, **459**, 820–823 (2009).
120. K. F. Mak, C. H. Lui, J. Shan, and T. F. Heinz, Observation of an electric-field-induced band gap in bilayer graphene by infrared spectroscopy, *Phys. Rev. Lett.*, **102**, 256405–1–4 (2009).
121. F. Xia, D. B. Farmer, Y.-M. Lin, and Ph. Avouris, Graphene field-effect transistors with high on/off current ratio and large transport band gap at room temperature, *Nano Lett.*, **10**, 715–718 (2010).
122. H. Miyazaki, K. Tsukagoshi, A. Kanda, M. Otani, and S. Okada, Influence of disorder on conductance in bilayer graphene under perpendicular electric field, *Nano Lett.*, **10**, 3888–3892 (2010).
123. J. Nilsson and A. H. C. Neto, Impurities in a biased graphene bilayer, *Phys. Rev. Lett.*, **98**, 126801–1–4 (2007).
124. V. V. Mkhitarian and M. E. Raikh, Disorder-induced tail states in gapped bilayer graphene, *Phys. Rev. B*, **78**, 195409–1–7 (2008).
125. J. Nilsson, A. H. C. Neto, F. Guinea, and N. M. R. Peres, Electronic properties of bilayer and multilayer graphene, *Phys. Rev. B*, **78**, 045405–1–34 (2008).
126. J. Bai, X. Zhong, S. Jiang, Y. Huang, and X. Duan, Graphene nanomesh, *Nat. Nanotechnol.*, **5**, 190–194 (2010).
127. R. Balog, B. Jørgensen, L. Nilsson, M. Andersen, E. Rienks, M. Bianchi, M. Fanetti, E. Lægsgaard, A. Baraldi, S. Lizzit, Z. Slijivancanin, F. Besenbacher, B. Hammer, T. G. Pedersen, P. Hofmann, L. Hornekær, Bandgap opening in graphene induced by patterned hydrogen adsorption, *Nat. Mater.*, **9**, 315–319 (2010).
128. F. Guinea, M. I. Katsnelson, and A. K. Geim, Energy gaps and a zero-field quantum Hall effect in graphene by strain engineering, *Nat. Phys.*, **6**, 30–33 (2010).
129. J. O. Sofo, A. S. Chaudhari, and G. D. Barber, Graphane: A two-dimensional hydrocarbon, *Phys. Rev. B*, **75**, 135401–1–4 (2007).
130. D. C. Elias, R. R. Nair, T. M. G. Mohiuddin, S. V. Morozov, P. Blake, M. P. Halsall, A. C. Ferrari, D. W. Boukhvalov, M. I. Katsnelson, A. K. Geim, and K. S. Novoselov, Control of graphene's properties by reversible hydrogenation: evidence for graphane, *Science*, **323**, 610–613 (2009).

131. S. Cheng, K. Zou, F. Okino, H. R. Gutierrez, A. Gupta, N. Shen, P. C. Eklund, J. O. Sofo and J. Zhu, Reversible fluorination of graphene: Evidence of a two-dimensional wide bandgap semiconductor, *Phys. Rev. B*, **81**, 205435–1–5 (2010).
132. J. Kong, N. R. Franklin, C. Zhou, M. G. Chapline, S. Peng, K. Cho, and H. Dai, Nanotube molecular wires as chemical sensors, *Science*, **287**, 622–625 (2000).
133. F. Schedin, A. K. Geim, S. V. Morozov, E. W. Hill, P. Blake, M. I. Katsnelson, and K.S. Novoselov, Detection of individual gas molecules adsorbed on graphene, *Nat. Mater.*, **6**, 652–655 (2007).
134. Y. P. Dan, Y. Lu, N. J. Kybert, Z. T. Luo, and A. T. C. Johnson, Intrinsic response of graphene vapor sensors, *Nano Lett.*, **9**, 1472–1475 (2009).
135. For example, D. K. Ferry, S. M. Goodnick, and J. Bird, *Transport in Nanostructures* (Cambridge University Press, Cambridge, 2009).
136. S. Russo, J. B. Oostinga, D. Wehenkel, H. B. Heersche, S. Shams Sobhani, L. M. K. Vandersypen, and A. F. Morpurgo, Observation of Aharonov–Bohm conductance oscillations in a graphene ring, *Phys. Rev. B*, **77**, 085413–1–5 (2008).
137. M. Huefner, F. Molitor, A. Jacobsen, A. Pioda, K. Ensslin, C. Stampfer and T. Ihn, The Aharonov–Bohm effect in a side-gated graphene ring, *New J. Phys.*, **12**, 043054–1–10 (2010).
138. F. Miao, S. Wijeratne, U. Coskun, Y. Zhang W. Bao and C. N. Lau, Phase coherent charge transport in graphene quantum billiards, *Science*, **317**, 1530–1533 (2007).
139. L. A. Ponomarenko, F. Schedin, M. I. Katsnelson, R. Yang, E. H. Hill, K. S. Novoselov, A. K. Geim, Chaotic Dirac billiard in graphene quantum dots, *Science*, **320**, 356–358 (2008).
140. C. Stampfer, J. Güttinger, F. Molitor, D. Graf, T. Ihn, and K. Ensslin, Tunable Coulomb blockade in nanostructured graphene, *Appl. Phys. Lett.*, **92**, 012102–1–3 (2008).
141. C. Stampfer, E. Schurtenberger, F. Molitor, J. Güttinger, T. Ihn, and K. Ensslin, Tunable graphene single electron transistor, *Nano Lett.* **8**, 2378–2383 (2008).
142. J. Güttinger, T. Frey, C. Stampfer, T. Ihn, and K. Ensslin, Spin states in graphene quantum dots, *Phys. Rev. Lett.*, **105**, 116801–1–4 (2010).
143. S. Datta and B. Das, Electronic analog of the electro-optic modulator, *Appl. Phys. Lett.*, **56**, 665–667 (1990).

144. S. Sugahara and M. Tanaka, A spin metal–oxide–semiconductor field-effect transistor using half-metallic-ferromagnet contacts for the source and drain, *Appl. Phys. Lett.*, **84**, 2307–2309 (2004).
145. J. Nitta, T. Akazaki, H. Takayanagi and T. Enoki, Gate control of spin-orbit interaction in an inverted $\text{In}_{0.53}\text{Ga}_{0.47}\text{As}/\text{In}_{0.52}\text{Al}_{0.48}\text{As}$ heterostructure, *Phys. Rev. Lett.*, **78**, 1335–1338 (1997).
146. G. Dresselhaus, Spin-orbit coupling effects in zinc blende structures, *Phys. Rev.* **100**, 580–586 (1955).
147. Y. A. Bychkov and E. I. Rashba, Oscillatory effects and the magnetic susceptibility of carriers in inversion layers, *J. Phys. C*, **17**, 6039–6045 (1984).
148. B. Trauzettel, D. V. Bulaev, D. Loss, G. Burkard, Spin qubits in graphene quantum dots, *Nat. Phys.*, **3**, 192–196 (2007).
149. M. Johnson and R. H. Silsbee, Interfacial charge-spin coupling: Injection and detection of spin magnetization in metals, *Phys. Rev. Lett.*, **55**, 1790–1793 (1985).
150. F. J. Jedema, H. B. Heersche, A. T. Filip, J. J. A. Baselmans, and B. J. van Wees, Electrical detection of spin precession in a metallic mesoscopic spin valve, *Nature*, **416**, 713–716 (2002).
151. S. Takahashi and S. Maekawa, Spin injection and detection in magnetic nanostructures, *Phys. Rev. B*, **67**, 052409–1–4 (2003).
152. C. Ertler, S. Konschuh, M. Gmitra, and J. Fabian, Electron spin relaxation in graphene: The role of the substrate, *Phys. Rev. B*, **80**, 041405(R)–1–4 (2009).
153. N. Tombros, C. Jozsa, M. Popinciuc, H. T. Jonkman, and B. J. van Wees, Electronic spin transport and spin precession in single graphene layers at room temperature, *Nature*, **448**, 571–574 (2007).
154. W. Han, K. Pi, W. Bao, K. M. McCreary, Yan Li, W. H. Wang, C. N. Lau, and R. K. Kawakami, Electrical detection of spin precession in single layer graphene spin valves with transparent contacts, *Appl. Phys. Lett.*, **94**, 222109–1–3 (2009).
155. N. Tombros, S. Tanabe, A. Veligura, C. Józsa, M. Popinciuc, H. T. Jonkman, and B. J. van Wees, Anisotropic spin relaxation in graphene, *Phys. Rev. Lett.*, **101**, 046601–1–4 (2008).
156. M. Popinciuc, C. Józsa, P. J. Zomer, N. Tombros, A. Veligura, H. T. Jonkman and B. J. van Wees, Electronic spin transport in graphene field-effect transistors, *Phys. Rev. B*, **80**, 214427–1–13 (2009).
157. D. Huertas-Hernando, F. Guinea, and A. Brataas, Spin-orbit-mediated spin relaxation in graphene, *Phys. Rev. Lett.*, **103**, 146801–1–4 (2009).

158. H. Kumazaki and D. S. Hirashima, Tight-binding study of nonmagnetic-defect-induced magnetism in graphene, *Low Temp. Phys.*, **34**, 805–811 (2008) [*Fiz. Nizk. Temp.*, **34**, 1025–1032 (2008)].
159. D. Soriano, F. Munoz-Rojas, J. Fernandez-Rossier, and J. J. Palacios, Hydrogenated graphene nanoribbons for spintronics, *Phys. Rev. B*, **81**, 165409–1–7 (2010).
160. H. Meissner, Measurements on superconducting contacts, *Phys. Rev.*, **109**, 686–694 (1958).
161. H. Meissner, Range of order of superconducting electrons, *Phys. Rev. Lett.*, **2**, 458–459 (1959).
162. P. G. de Gennes, *Superconductivity of Metals and Alloys* (Benjamin, 1966).
163. A. F. Andreev, Thermal conductivity of the intermediate state of superconductors, *Sov. Phys. LETP*, **19**, 1228–1231 (1964).
164. T. Akazaki, J. Nitta, H. Takayanagi, T. Enoki and K. Arai, Improving the mobility of an $\text{In}_{0.52}\text{Al}_{0.48}\text{As}/\text{In}_{0.53}\text{Ga}_{0.47}\text{As}$ inverted modulation-doped structure by inserting a strained InAs quantum well, *Appl. Phys. Lett.*, **65**, 1263–1265 (1994).
165. A. F. Morpurgo, T. M. Klapwijk, and B. J. van Wees, Hot electron tunable supercurrent, *Appl. Phys. Lett.*, **72**, 966–968 (1998).
166. G. E. Blonder, M. Tinkham, and T. M. Klapwijk, Transition from metallic to tunneling regimes in superconducting microconstrictions: Excess current, charge imbalance, and supercurrent conversion, *Phys. Rev. B*, **25**, 4515–4532 (1982).
167. C. W. J. Beenakker, Specular Andreev reflection in graphene, *Phys. Rev. Lett.*, **97**, 067007–1–4 (2006).
168. C. W. J. Beenakker, Colloquium: Andreev reflection and Klein tunneling in graphene, *Rev. Mod. Phys.*, **80**, 1337–1354 (2008).
169. M. Titov and C. W. J. Beenakker, Josephson effect in ballistic graphene, *Phys. Rev. B*, **74**, 041401(R)–1–4 (2006).
170. A. M. Black-Schaffer and S. Doniach, Self-consistent solution for proximity effect and Josephson current in ballistic graphene SNS Josephson junctions, *Phys. Rev. B*, **78**, 024504–1–7 (2008).
171. J. C. Cuevas and A. L. Yeyati, Subharmonic gap structure in short ballistic graphene junctions, *Phys. Rev. B*, **74**, 180501(R)–1–4 (2006).
172. H. B. Heersche, P. Jarillo-Herrero, J. B. Oostinga, L. M. K. Vandersypen, and A. F. Morpurgo, Bipolar supercurrent in graphene, *Nature*, **446**, 56–59 (2007).

173. H. B. Heersche, P. Jarillo-Herrero, J. B. Oostinga, L. M. K. Vandersypen, and A. F. Morpurgo, Induced superconductivity in graphene, *Solid State Commun.*, **143**, 72–76 (2007).
174. A. Barone and G. Paterno, *Physics and Applications of the Josephson Effect* (Wiley-VCH).
175. X. Du, I. Skachko, and E. Y. Andrei, Josephson current and multiple Andreev reflections in graphene SNS junctions, *Phys. Rev. B*, **77**, 184507–1–5 (2008).
176. I. O. Kulik and A. N. Omel'yanchuk, Properties of superconducting microbridges in the pure limit, *Sov. J. Low Temp. Phys.*, **3**, 459–461 (1977) [*Fiz. Nizk. Temp.*, **3**, 945–948 (1977)].
177. I. O. Kulik and A. N. Omel'yanchuk, Contribution to the microscopic theory of the Josephson effect in superconducting bridges, *JETP Lett.*, **21**, 96–97 (1975) [*Zh. Eksp. Teor. Fiz. Pis'ma*, **21**, 216–219 (1975)].
178. V. Ambegaokar and A. Baratoff, Tunneling between superconductors, *Phys. Rev. Lett.*, **10**, 486–489 (1963); erratum, **11**, 104 (1963).
179. C. Ojeda-Aristizabal, M. Ferrier, S. Guéron, and H. Bouchiat, Tuning the proximity effect in a superconductor–graphene–superconductor junction, *Phys. Rev. B*, **79**, 165436–1–5 (2009).
180. H. Tomori, A. Kanda, H. Goto, S. Takana, Y. Ootuka, and K. Tsukagoshi, Fabrication of ultrashort graphene Josephson junctions, *Physica C*, **470**, 1492–1495 (2010).
181. G. J. Dolan, Offset masks for lift-off photoprocessing, *Appl. Phys. Lett.*, **31**, 337–339 (1977).
182. A. Kanda, B. J. Baelus, F. M. Peeters, K. Kadowaki, and Y. Ootuka, Experimental evidence for giant vortex states in a mesoscopic superconducting disk, *Phys. Rev. Lett.*, **93**, 257002–1–4 (2004).
183. A. Kanda, M. Wada, Y. Hamamoto, and Y. Ootuka, Simple and controlled fabrication of nanoscale gaps using double-angle evaporation, *Physica E*, **29**, 707–711 (2005).
184. T. Mueller, F. Xia, M. Freitag, J. Tsang, and P. Avouris, Role of contacts in graphene transistors: A scanning photocurrent study, *Phys. Rev. B*, **79**, 245430–1–6 (2009).
185. H. Tomori, A. Kanda, H. Goto, Y. Ootuka, and k. Tsukagoshi, unpublished.

This page intentionally left blank

Chapter 4

Electronic Properties of Nanographene

Katsunori Wakabayashi

International Center for Materials Nanoarchitectonics (WPI-MANA),

National Institute for Materials Science (NIMS),

Namiki 1-1, Tsukuba 305-0044, Japan

WAKABAYASHI.Katsunori@nims.go.jp

4.1 Introduction

Graphene, a single-layer hexagonal lattice of carbon atoms, has emerged recently as a fascinating system for fundamental studies in condensed matter physics, as well as a promising candidate material for future applications in carbon-based nanoelectronics and molecular devices [1, 2]. Since the honeycomb crystal structure of graphene consists of two nonequivalent sublattices, graphene has a unique band structure for the itinerant π -electrons near the Fermi energy. In particular, as we have seen in Chapter 2, the motion of electrons in graphene near the Fermi energy is well described by the massless Dirac equation. The valence and conduction bands conically touch at two nonequivalent Dirac points, which are called the K and K' points. Because of the peculiar linear energy spectrum, graphene provides an environment for highly unconventional and

Physics and Chemistry of Graphene: Graphene to Nanographene

Edited by Toshiaki Enoki and Tsuneya Ando

Copyright © 2013 Pan Stanford Publishing Pte. Ltd.

ISBN 978-981-4241-48-9 (Hardcover), 978-981-4241-49-6 (eBook)

www.panstanford.com

fascinating two-dimensional (2D) electronic properties [3–5] such as the half-integer quantum Hall effect [6, 7], the absence of backward scattering [4, 8, 9], Klein tunneling [10], and the π -phase shift of Shubnikov–de Haas oscillations [11]. Owing to its high electronic mobility [12] and thermal conductivity [13], graphene is recognized as one of the key materials for realizing next-generation electronic devices.

The successive miniaturization of graphene-based electronic devices will require clarification of the effect of edges on the electronic structure and electronic transport properties of nanometer-size graphene. The presence of edges in graphene has strong implications for the low-energy spectrum of the π -electrons [14–16]. There are two basic edge shapes, *armchair* and *zigzag*, which determine the properties of graphene ribbons. It has been shown that nanoribbons with zigzag edges (zigzag nanoribbons) possess localized edge states with energies close to the Fermi level [14–18]. In contrast, edge states are absent for ribbons with armchair edges. Because zigzag edges can induce a strong magnetic response [14, 16, 17, 19, 20], considerable effort has been devoted to studying the effect of edges in graphitic nanomaterials. Recent experiments using scanning tunneling microscopy [21–23] and high-resolution angle-resolved photoemission spectroscopy (ARPES) [24] have provided evidence of edge-localized states.

The presence of graphene edge states results in a relatively large contribution to the density of states (DOS) near the Fermi energy in a nanoscale graphene system. Thus, these edge states play an important role in the magnetic properties of nanosize graphitic systems. Even weak electron–electron interactions make the edge states magnetic, and the ferrimagnetic spin alignment along the zigzag edge is favored [14, 17]. The existence of such magnetic states has been confirmed using mean-field theory [14, 17, 25–29], the density matrix renormalization group for the Hubbard model [30] and density functional theory (DFT) [20, 31]. Recent studies have shown the robustness of edge states to changes in their size and geometry [32–34]. Since the structural or chemical modification of graphene edges affects the electronic states near the Fermi energy [31, 35–38], they can be used to design the functionality of nanocarbon systems.

Recently, several routes have been reported for the synthesis of graphene nanoribbons. The lithographic patterning of graphene samples [39, 40] can yield graphene nanoribbons; however, the reported ribbons had large widths of 15–100 nm with a small electronic bandgap of up to 200 meV due to the significant edge roughness. Another route [41], which utilizes chemical methods such as solution dispersion and sonication, has demonstrated that graphene sheets spontaneously break into narrow ribbons with smooth edges. Recently, carbon nanotubes have been successfully cut along their axis and flattened out to form graphene nanoribbons [42, 43]. A bottom-up approach can also yield linear 2D graphene nanoribbons with lengths of up to 12 nm [44]. However, control of the edge structure, which is necessary for the application of nanographene to nanoelectronic devices, is still unsatisfactory. Transport measurements carried out by several groups show the existence of a transport gap near the Dirac point at low temperatures due to the edge roughness and/or conduction through electron-hole puddles [39, 45–49]. Experimental trials on controlling edge structures using Joule heating [50], anisotropic etching [51], and a bottom-up chemical approach [52] have been reported recently. A combination of these new methods may lead to the design of graphene nanoribbons and nanostructures with controlled edge orientation and electronic properties. Details of experimental approaches to nanographene will be discussed in Chapter 6.

In this chapter, we introduce the theoretical aspects of nanographene and graphene nanoribbons. Here we attempt to elucidate the electronic states of graphene nanoribbons in detail by using analytic and/or numerical techniques, and clarify how the electronic states depend on the graphene edge structures and graphene size. In Section 4.2, the electronic states of graphene are briefly overviewed. The minimal theoretical background for studying the electronic states of nanographene is given. In Section 4.3, the electronic structures of graphene nanoribbons analyzed by the tight-binding model are summarized. In Section 4.4, analytic expressions for the energy spectrum and the corresponding wave function on the basis of the tight-binding model are pedagogically derived. The relation between the electronic structures of bulk graphene and graphene nanoribbons is clarified. In Section 4.6,

it is shown how to construct the electronic states of graphene nanoribbons using the massless Dirac equation. In Section 4.8, we study the electronic states of nanographene in a magnetic field. We will see that because of the presence of edge states, nanographenes exhibits a crossover from diamagnetic behavior at room temperature to strong paramagnetic behavior at low temperatures in spite of the fact that bulk graphene is known to exhibit a strong diamagnetic response. In Section 4.10, the effect of the electron–electron Coulomb interaction is studied. Because the presence of edge states indicates strong Fermi instability, peculiar magnetic polarization is expected. Also, the mechanism of electric-field-induced half-metallicity is introduced. In Section 4.11, the electronic transport properties of graphene nanoribbons are briefly introduced. It will be shown that graphene nanoribbons have a single perfectly conducting channel, i.e., the absence of Anderson localization, due to the channel imbalance between left- and right-going channels.

4.2 Electronic States of Graphene

We start our discussion by reviewing the π -band structure of a graphene sheet [53]. More theoretical details are given in Chapter 2. Figures 4.1(a) and (b) show the lattice structure and the first Brillouin zone (BZ) of graphene, respectively. Graphene has a honeycomb lattice structure, and thus its first BZ is hexagonal. The corners of the first BZ are called K or K' points, which are also referred to as Dirac points because the energy spectrum at these corners can be described by the massless Dirac equation (Weyl equation).

In this chapter, we employ a single-orbital nearest-neighbor tight-binding model for the π -electron network to describe the electronic states of graphene. This model has been successfully applied to nanocarbon materials such as carbon nanotubes and fullerenes. Let us define the wave functions at \mathbf{R}_A of a lattice site A and \mathbf{R}_B of a lattice site B as $\psi_A(\mathbf{R}_A)$ and $\psi_B(\mathbf{R}_B)$, respectively. As already introduced in Chapter 2, these wave functions can be related

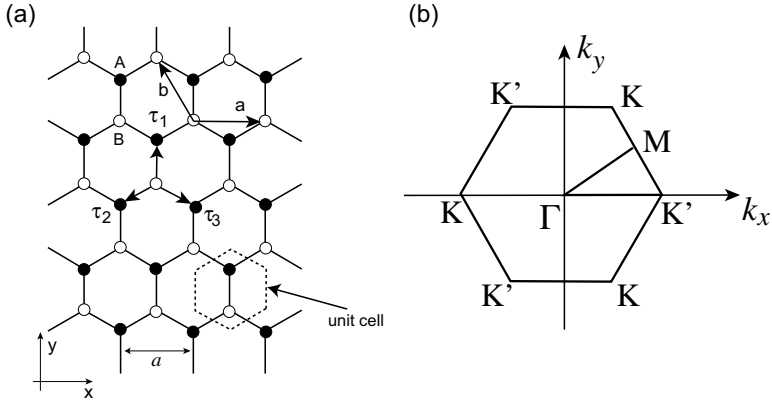


Figure 4.1 (a) Graphene sheet in real space, where the black (white) circles denote A(B)-sublattice sites; a is the lattice constant and $\mathbf{a} = (a, 0)$ and $\mathbf{b} = (-a/2, \sqrt{3}a/2)$ are the primitive vectors. Here $\boldsymbol{\tau}_1 = (0, a/\sqrt{3})$, $\boldsymbol{\tau}_2 = (-a/2, -a/2\sqrt{3})$ and $\boldsymbol{\tau}_3 = (a/2, -a/2\sqrt{3})$. (b) First BZ of graphene. $\mathbf{K} = \frac{2\pi}{a}(\frac{1}{3}, \frac{1}{\sqrt{3}})$, $\mathbf{K}' = \frac{2\pi}{a}(\frac{2}{3}, 0)$, $\Gamma = (0, 0)$. Note that there are three \mathbf{K} and \mathbf{K}' points, which can be connected by the reciprocal lattice vectors.

by the following equations of motion:

$$\varepsilon \psi_A(\mathbf{R}_A) = -\gamma_0 \sum_{l=1}^3 \psi_B(\mathbf{R}_A - \boldsymbol{\tau}_l), \quad (4.1)$$

$$\varepsilon \psi_B(\mathbf{R}_B) = -\gamma_0 \sum_{l=1}^3 \psi_A(\mathbf{R}_B + \boldsymbol{\tau}_l). \quad (4.2)$$

Here $\mathbf{R}_A = n_a \mathbf{a} + n_b \mathbf{b} + \boldsymbol{\tau}_3$ and $\mathbf{R}_B = n_a \mathbf{a} + n_b \mathbf{b}$, where integers n_a and n_b represent the locations of sites A and B, respectively. γ_0 is the transfer integral between nearest-neighbor carbon sites, which has been estimated to be about 2.75 eV in a graphene system [3].

If we assume a plane wave form of the wave function, i.e., $\psi_A(\mathbf{R}_A) \propto f_A(\mathbf{k}) \exp(i\mathbf{k} \cdot \mathbf{R}_A)$ and $\psi_B(\mathbf{R}_B) \propto f_B(\mathbf{k}) \exp(i\mathbf{k} \cdot \mathbf{R}_B)$, we obtain the eigenvalue equation as a 2×2 matrix,

$$\begin{pmatrix} 0 & h_{AB}^*(\mathbf{k}) \\ h_{AB}(\mathbf{k}) & 0 \end{pmatrix} \begin{pmatrix} f_A(\mathbf{k}) \\ f_B(\mathbf{k}) \end{pmatrix} = \varepsilon \begin{pmatrix} f_A(\mathbf{k}) \\ f_B(\mathbf{k}) \end{pmatrix} \quad (4.3)$$

with

$$h_{AB}(\mathbf{k}) = -\gamma_0 \sum_{l=1}^3 \exp(-i\mathbf{k} \cdot \boldsymbol{\tau}_l). \quad (4.4)$$

Thus, the energy bands are given by $\varepsilon_s = s|h_{AB}(\mathbf{k})|$, namely,

$$\varepsilon_s(\mathbf{k}) = s\gamma_0 \sqrt{1 + 4 \cos \frac{k_x a}{2} \cos \frac{\sqrt{3} k_y a}{2} + 4 \cos^2 \frac{k_x a}{2}} \quad (4.5)$$

with $s = \pm 1$. Because one carbon site has one π -electron on average, only the $\varepsilon_-(\mathbf{k})$ band is completely occupied. Thus, $s = +1$ and $s = -1$ correspond to the conduction and valence bands, respectively. The wave function can be written as

$$\begin{pmatrix} f_A(\mathbf{k}) \\ f_B(\mathbf{k}) \end{pmatrix} = \frac{1}{\sqrt{2}} \begin{pmatrix} 1 \\ -s \frac{h_{AB}(\mathbf{k})}{|h_{AB}(\mathbf{k})|} \end{pmatrix}. \quad (4.6)$$

Thus, the Bloch wave function of graphene has a relative phase between A and B sublattice sites. This intrinsic phase structure determines many properties of graphene; it is the origin of the π -Berry phase around the Dirac points [4, 9] and chiral-dependent Klein tunneling [10]. As shown in the next section, this relative phase structure is preserved in the presence of an armchair edge; however, the presence of a zigzag edge has a detrimental effect. The DOS is calculated as

$$D(\varepsilon) = -\frac{1}{\pi} \Im \int_{\text{1st BZ}} d\mathbf{k} \frac{1}{\varepsilon - \varepsilon(\mathbf{k}) + i\eta}, \quad (4.7)$$

where the \mathbf{k} -integration is over the first BZ and η is an infinitesimally small real number.

Figures 4.2(a) and (b) depict the energy band structures of graphene for π -electrons. Figure 4.2(c) shows the corresponding

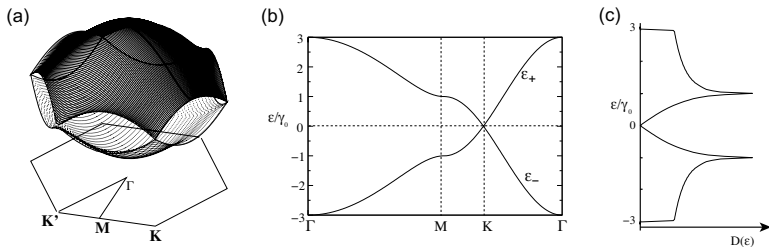


Figure 4.2 (a) 3D plot of the energy band structure for π -electrons. The valence and conduction bands are in contact at the degeneracy points, \mathbf{K} and \mathbf{K}' . (b) Energy band structure of graphene within the irreducible BZ. (c) DOS of a graphene sheet.

DOS. Near the Γ point, both valence and conduction bands can be expressed as quadratic functions of k_x and k_y , i.e., $\varepsilon_k = \pm\gamma_0(3 - 3|\mathbf{k}|^2/4)$. At the M points, which are the midpoints of the sides of the hexagonal first BZ, a saddle point appears in the energy dispersion in the vicinity of $\varepsilon = \pm\gamma_0$, resulting in logarithmic divergence of the DOS as can be seen in Fig. 4.2(c). Near the K point at the corner of the hexagonal first BZ, the energy dispersion is a linear function of the magnitude of the wave vector, $\varepsilon_k = \pm\sqrt{3}\gamma_0 a|\mathbf{k}|/2$, where the DOS linearly depends on energy. Here $a(= \sqrt{3}|\tau_i|(i = 1, 2, 3))$ is the lattice constant. The Fermi energy is located at the K points, and there is no energy gap at these points because ε_k vanishes there owing to the hexagonal symmetry.

The electronic state in the vicinity of a K point can be described by the massless Dirac equation. For a K point, we have

$$\gamma \begin{pmatrix} 0 & \hat{k}_x - i\hat{k}_y \\ \hat{k}_x + i\hat{k}_y & 0 \end{pmatrix} \mathbf{F}^K(\mathbf{r}) = \varepsilon \mathbf{F}^K(\mathbf{r}), \quad (4.8)$$

and for a K' point, we have

$$\gamma \begin{pmatrix} 0 & \hat{k}_x + i\hat{k}_y \\ \hat{k}_x - i\hat{k}_y & 0 \end{pmatrix} \mathbf{F}^{K'}(\mathbf{r}) = \varepsilon \mathbf{F}^{K'}(\mathbf{r}), \quad (4.9)$$

where $\mathbf{F}^K(\mathbf{r})$ and $\mathbf{F}^{K'}(\mathbf{r})$ are the two-component envelope functions

$$\mathbf{F}^K(\mathbf{r}) = \begin{pmatrix} F_A^K(\mathbf{r}) \\ F_B^K(\mathbf{r}) \end{pmatrix}, \quad \mathbf{F}^{K'}(\mathbf{r}) = \begin{pmatrix} F_A^{K'}(\mathbf{r}) \\ F_B^{K'}(\mathbf{r}) \end{pmatrix}. \quad (4.10)$$

\hat{k}_x and \hat{k}_y are wave number operators and are replaced with the differential operators of the coordinates $\hat{k}_x \rightarrow -i\frac{\partial}{\partial x}$ and $\hat{k}_y \rightarrow -i\frac{\partial}{\partial y}$. The band parameter γ is given by

$$\gamma = \frac{\sqrt{3}a}{2}\gamma_0. \quad (4.11)$$

The real space wave function, $(\psi_A(\mathbf{r}), \psi_B(\mathbf{r}))$, can be obtained from the envelope functions as

$$\begin{cases} \psi_A(\mathbf{r}) = e^{i\mathbf{K}\cdot\mathbf{r}}F_A^K(\mathbf{r}) + e^{i\mathbf{K}'\cdot\mathbf{r}}F_A^{K'}(\mathbf{r}), \\ \psi_B(\mathbf{r}) = -\omega e^{i\mathbf{K}\cdot\mathbf{r}}F_B^K(\mathbf{r}) + e^{i\mathbf{K}'\cdot\mathbf{r}}F_B^{K'}(\mathbf{r}). \end{cases} \quad (4.12)$$

Here $\omega = \exp(i2\pi/3)$, which is introduced to absorb the extra phase factor [8].

The energy spectrum and eigenfunction of bulk graphene can be obtained by assuming the plane wave form as a solution of the envelope function, namely,

$$\mathbf{F}^K(\mathbf{r}) \propto \begin{pmatrix} f_A \\ f_B \end{pmatrix} \exp(i\mathbf{k} \cdot \mathbf{r}), \quad (4.13)$$

from which we can immediately obtain the linear spectrum of energy as

$$\varepsilon_s(\mathbf{k}) = s\gamma|\mathbf{k}|, \quad \text{with } s = \pm 1. \quad (4.14)$$

The wave function can be written as

$$\mathbf{F}_{sk}^K(\mathbf{r}) = \frac{1}{\sqrt{L_x L_y}} \exp(i\mathbf{k} \cdot \mathbf{r}) \mathbf{F}_{sk}^K, \quad (4.15)$$

with the “spin” sector

$$\mathbf{F}_{sk}^K = \frac{1}{\sqrt{2}} \begin{pmatrix} s \exp(i\theta(\mathbf{k})) \\ 1 \end{pmatrix}. \quad (4.16)$$

Here $\theta(\mathbf{k})$ is defined as the angle between wave vector \mathbf{k} and the k_x -axis, i.e., $k_x + ik_y = |\mathbf{k}|e^{i\theta(\mathbf{k})}$. The sign of the eigenfunction for the “spin” sector does not change after the 2π rotation of $\theta(\mathbf{k}) \rightarrow \theta(\mathbf{k}) + 2\pi$. However, the wave function changes the sign when we consider the Berry phase. See Chapter 2 for details. Note that the term “spin” appearing here does not mean the real spin of the electron, since the eigenfunction for the “spin” sector describes the amplitude of the wave function on A and B sublattices. Thus, it is normally called “pseudo-spin” to distinguish it from the real electron spin.

4.3 Graphene Nanoribbons and Edge States

The presence of a graphene edge has a strong impact on the electronic states of Dirac electrons. In this section, we will see that graphene exhibits a significant nanoscale edge effect by studying the electronic structures of the graphene nanoribbon using the tight-binding model.

There are two types of graphene edge: *armchair* and *zigzag* edges. These two edges have a 30° difference in their orientation within the graphene sheet. A large difference in the π -electronic

structures is induced by the two types of graphene edges [14]. In particular, a zigzag edge exhibits localized states, whereas an armchair edge does not exhibit such localized states. The appearance of graphene edge states may be a source of the peculiar magnetic and transport properties of nanoscale graphene, as will be discussed in the following section.

The graphene nanoribbon model is useful for analyzing the electronic states of nanographene. Because of the periodicity along the longitudinal direction of nanoribbons, we can define the crystal momentum (wave number k) so as to apply the ordinal approach of solid state physics to these systems. The lattice structures of graphene nanoribbons are shown in Figs. 4.3(a) and (b). Figure 4.3(a) shows a graphene nanoribbon with armchair edges (armchair nanoribbon). The primitive vector for armchair nanoribbons is $\mathbf{a} = (0, a_T)$, where $a_T = \sqrt{3}a$; a is the lattice constant of graphene. Figure 4.3(b) shows a graphene nanoribbon with zigzag edges (zigzag nanoribbon). Similarly, the primitive vector for this system is given by $\mathbf{a} = (a, 0)$.

We define the width of a graphene ribbon as N , where N is the number of dimer (two carbon sites) lines for an armchair nanoribbon and the number of zigzag lines for an zigzag nanoribbon.

Note that the same number N for both zigzag and armchair ribbons does not give the same ribbon width when the ribbons are measured by the same unit of length. Therefore, when we compare the physical quantities of zigzag and armchair ribbons with the same width W , we will use the following definition:

$$W = \begin{cases} (N + 1)\frac{1}{2}a \equiv W_a & \text{armchair ribbons} \\ \frac{\sqrt{3}}{2}Na + \frac{a}{\sqrt{3}} \equiv W_z & \text{zigzag ribbons} \end{cases} \quad (4.17)$$

where a is the lattice constant of graphene. Several values of ribbon width for both type of ribbon are summarized in Table 4.1.

It is assumed that all dangling bonds at graphene edges are terminated by hydrogen atoms and thus do not contribute to the electronic states near the Fermi level. We employ a single-orbital tight-binding model for the π -electron network similarly to in the previous section. The Hamiltonian is written as

$$H = \sum_{i,j} \gamma_{i,j} c_i^\dagger c_j, \quad (4.18)$$

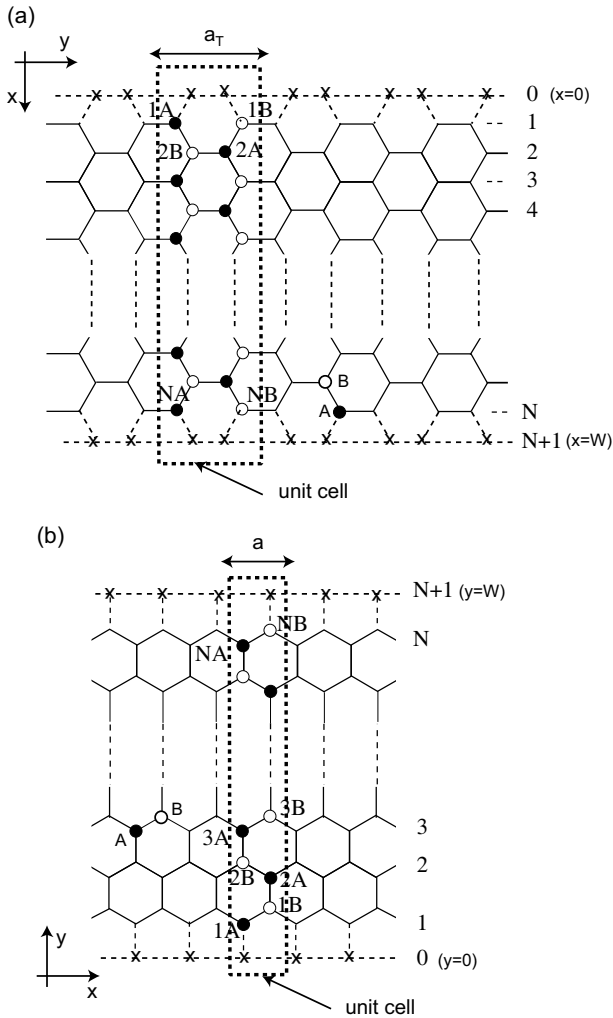


Figure 4.3 Structure of graphene nanoribbons with (a) armchair edges (armchair ribbon) and (b) zigzag edges (zigzag ribbon). The dashed rectangles define the unit cells; a_T and a are the respective unit cell widths for armchair and zigzag nanoribbons; N defines the ribbon width. The \times marks indicate the missing carbon atoms for the edge boundary condition. The nanoribbon width is defined as $W = \frac{1}{2}(N + 1)a$ for armchair nanoribbons and $W = \frac{\sqrt{3}}{2}Na + \frac{a}{\sqrt{3}}$ for zigzag nanoribbons.

Table 4.1 Some examples of graphene ribbon width

N	Armchair nanoribbon	Zigzag nanoribbon
10	5.5a (1.35[nm])	9.238a (2.27[nm])
20	10.5a (2.58[nm])	17.898a (4.40[nm])
50	25.5a (6.27[nm])	43.879 a (10.79[nm])
100	50.5a (12.42[nm])	87.180a (21.45[nm])
200	100.5a (24.72[nm])	173.782a (42.75[nm])
300	150.5a (37.02[nm])	260.385a (64.06[nm])
500	250.5a (61.62[nm])	433.590a (106.66[nm])

where $\gamma_{i,j}$ is the transfer integer and c_i^\dagger and c_i are the electron creation and annihilation operators at the i -site, respectively. $\gamma_{i,j} = -\gamma_0$ if the i -site is a nearest-neighbor site of the j -site, and vice versa. Otherwise, $\gamma_{i,j} = 0$. Details of the calculation of the eigenenergy spectrum and eigenfunctions are described in the next section. Here we briefly overview the electronic states of graphene nanoribbons.

Figures 4.4(a–c) show the DOS and energy band structures of armchair ribbons for three different ribbon widths. The top of the valence band and the bottom of the conduction band are located at $ka = 0$. Note that the ribbon width determines whether the system is metallic or semiconducting. As shown in Fig. 4.4(b), the system is metallic when $N = 3m - 1$, where $m = 1, 2, 3, \dots$. For semiconducting ribbons, the direct bandgap decreases with increasing ribbon width and approaches zero in the limit of very large N . For narrow undoped metallic armchair nanoribbons, an energy gap can be formed by Peierls instabilities at low temperatures [54], which is consistent with DFT calculations [20, 32, 55].

For zigzag ribbons, however, a remarkable feature arises in the band structure, as shown in Figs. 4.5(a–c). The top of the valence band and the bottom of the conduction band are always degenerate at $ka = \pi$, and the degeneracy of the center bands at $ka = \pi$ does not originate from the intrinsic band structure of the graphene sheet. These two special center bands flatten with increasing ribbon width. A pair of partial flat bands appears within the region $2\pi/3 \leq |ka| \leq \pi$, where the bands are located in the vicinity of the Fermi level.

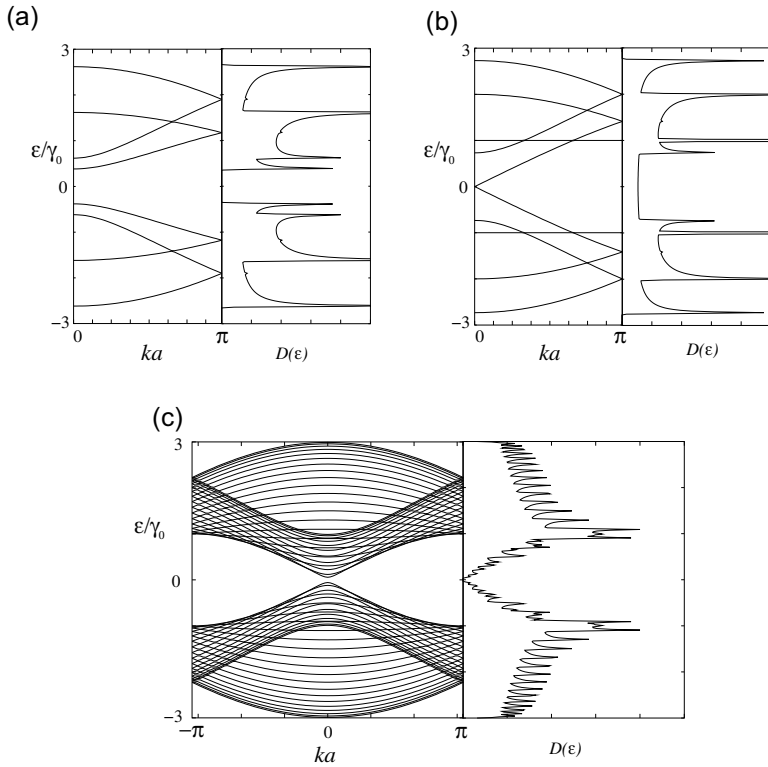


Figure 4.4 Energy band structure $\varepsilon(k)$ and DOS $D(\varepsilon)$ of armchair ribbons of various widths: (a) $N = 4$, (b) $N = 5$ and (c) $N = 30$.

The electronic states in the partial flat bands of the zigzag ribbons can be understood as localized states near the zigzag edge by examining the charge density distribution [14–16, 21–23]. Here we show that the puzzling emergence of the edge states can be explained by considering a semi-infinite graphene sheet with a zigzag edge. First, we show the distribution of charge density in flat band states for different wave numbers in Figs. 4.6(a–d), where the amplitude is proportional to the circle radius. The wave function has a non-bonding character, i.e., it only has a finite amplitude on one of the two sublattices that include the edge sites. It is completely localized at the edge site when $ka = \pi$ and starts to gradually

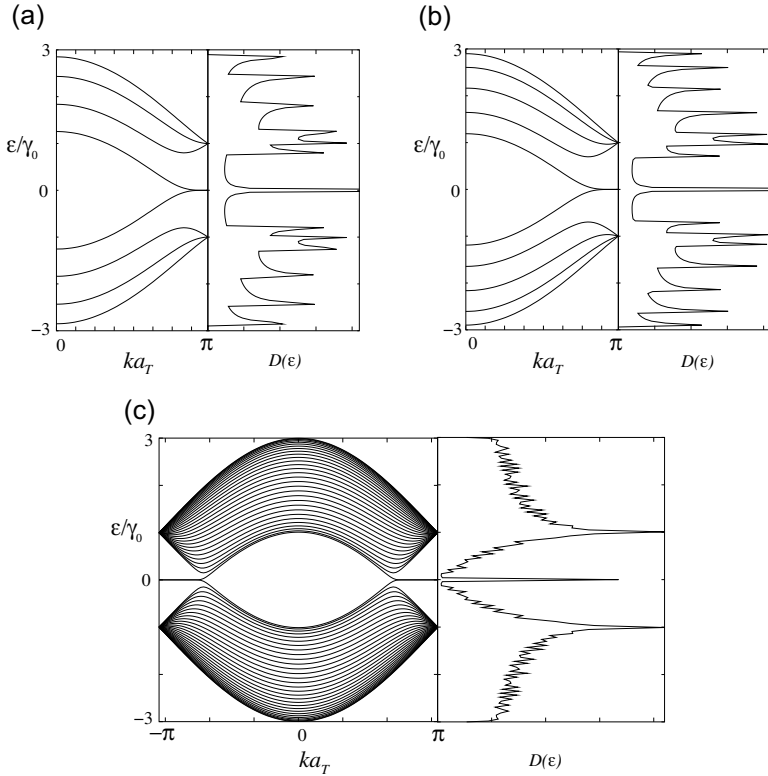


Figure 4.5 Energy band structure $\varepsilon(k)$ and DOS $D(\varepsilon)$ of zigzag ribbons of various widths: (a) $N = 4$, (b) $N = 5$ and (c) $N = 30$.

penetrate into the inner sites when ka deviates from π , reaching an extended state at $ka = 2\pi/3$.

Considering the translational symmetry, we can start constructing the analytical solution for the edge state by letting the Bloch components of the linear combination of atomic orbitals (LCAO) wave function be $\dots, e^{ika(n-1)}, e^{ikan}, e^{ika(n+1)}, \dots$ on successive edge sites, where n denotes a site located on the edge. Then, the mathematical condition necessary for the wave function to be exact for $\varepsilon = 0$ is that the sum of the components of the complex wave function over the nearest-neighbor sites becomes zero. In Fig. 4.6(e), the above condition implies that $e^{ika(n+1)} + e^{ikan} + x = 0, e^{ikan} +$

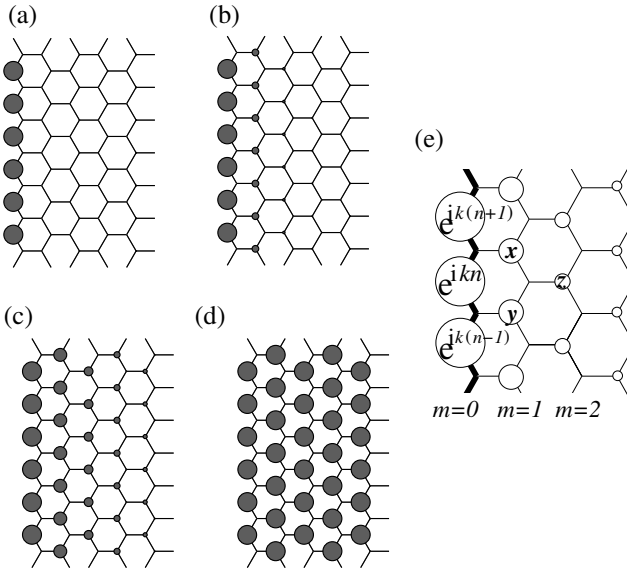


Figure 4.6 Charge density plot for analytical solution of the edge states in a semi-infinite graphene sheet for various wave numbers: (a) $ka = \pi$, (b) $ka = 8\pi/9$, (c) $ka = 7\pi/9$ and (d) $ka = 2\pi/3$. (e) Analytical form of the edge state for a semi-infinite graphene sheet with a zigzag edge, shown by the bold lines. Each carbon site is specified by a location index n on the zigzag chain and by a chain order index m , which increases from the edge. The magnitude of the charge density at each site, such as x , y and z , is obtained analytically (see text). The radius of each circle is proportional to the charge density on each site, and the drawing corresponds to $ka = 7\pi/9$.

$e^{ika(n-1)} + y = 0$ and $x + y + z = 0$. Therefore, the wave function components x , y and z are found to be $D_k e^{ika(n+1/2)}$, $D_k e^{ika(n-1/2)}$ and $D_k^2 e^{ikan}$, respectively. Here, $D_k = -2 \cos(ka/2)$. Thus, the charge density is proportional to $D_k^{2(m-1)}$ at each non-nodal site of the m -th zigzag chain from the edge. Then the convergence condition $|D_k| \leq 1$ is required, for otherwise the wave function would diverge in a semi-infinite graphene sheet. This convergence condition defines the region $2\pi/3 \leq |ka| \leq \pi$, where the flat bands appear.

From this analytic expression for the edge state, we can derive an analytic expression for the DOS near the Fermi energy. As we have seen, the edge state penetrates to inner sites when the wave number

changes from π/a to $2\pi/3a$. If we consider graphene ribbons with width N , two edge states that originate from both sides of an edge will overlap each other and develop bonding and anti-bonding interactions. Since the magnitude of the overlap becomes larger when the wave number approaches $2\pi/3a$, the bandgap between the bonding and anti-bonding states formed by the two edge states increases toward $ka = 2\pi/3$. Therefore, the partly flat bands acquire a slight dispersion whose magnitude depends on the ribbon width N . The energy dispersion is calculated from the overlap of the two edge states. The amplitude of the edge state that penetrates from the first zigzag line is given by $\psi_n = D_k^{n-1} \equiv \psi_A$; this edge state is located only on the A-sublattice. On the other hand, the amplitude of the edge state that penetrates from the N th zigzag line is given by $\psi_{N-n} = D_k^{n-1} \equiv \psi_B$; this edge state is located only on the B-sublattice. Using the tight-binding Hamiltonian, the overlap of the two edge states is easily calculated to be

$$\langle \psi_A | H | \psi_B \rangle = -2\gamma_0 N D_k^{N-1} (1 + D_k/2) \equiv \eta_k. \quad (4.19)$$

Therefore, the energy spectrum of the edge states in the lowest-order perturbation in the overlap is given by the following eigenvalue problem:

$$\begin{pmatrix} 0 & \eta_k \\ \eta_k & 0 \end{pmatrix} \begin{pmatrix} \psi_A \\ \psi_B \end{pmatrix} = \varepsilon \begin{pmatrix} \psi_A \\ \psi_B \end{pmatrix}. \quad (4.20)$$

The energy spectrum is $\varepsilon = \pm\eta_k$, which gives the form $\varepsilon \sim (ka)^N$ around $ka = \pi$. Therefore, the DOS related to the edge states has the form

$$\rho(\varepsilon) = \frac{\partial k}{\partial \varepsilon} \sim \frac{1}{N} \varepsilon^\alpha, \quad (4.21)$$

where $\alpha = \frac{1}{N} - 1$. Note that this DOS has a power-law dependence, which is different from the ordinary van Hove singularity of $\rho \sim 1/\sqrt{\varepsilon}$ observed in a one-dimensional (1D) system. It has also been found that the renormalized DOS is inversely proportional to the ribbon width, which has been confirmed by numerical calculation [15].

The edge states are reasonably robust even if the graphene edge does not have a clear zigzag edge. Actually, a general edge structure that is not parallel to the armchair edge can have a zero-energy edge

state, which was shown by analogy to the condition of the zero-energy Andreev bound state in an unconventional superconductor [56]. Even for an armchair edge, a localized state and a completely flat band can be obtained in the case of a strong imbalance of the on-site potential energy between sublattice sites A and B [36]. The existence of edge states crucially affects the physical properties of nanographene systems.

4.4 Energy Spectrum and Wave Functions: Tight-Binding Model

The entire energy spectrum, shown in the previous section, and the wave function can be obtained by solving the equations of motion for the nearest-neighbor tight-binding model. More details can be found in Ref. [57].

4.4.1 Armchair Nanoribbons

The set of equations of motion for armchair nanoribbons based on the nearest-neighbor tight-binding model is described by

$$(\varepsilon/\gamma_0)\psi_{m,A} = -e^{-ik/2}\psi_{m,B} - \psi_{m-1,B} - \psi_{m+1,B}, \quad (4.22)$$

$$(\varepsilon/\gamma_0)\psi_{m,B} = -e^{+ik/2}\psi_{m,A} - \psi_{m-1,A} - \psi_{m+1,A}, \quad (4.23)$$

where $m = 1, 2, 3, \dots, N$. $\psi_{m,A}$ and $\psi_{m,B}$ are the wave function at the mA and mB -sites, respectively. The site indices are given in Fig. 4.3(a). In the following, we set the absolute value of the primitive vector to unity, i.e., $|\mathbf{a}| = a_T = 1$, for simplicity, since the generality of the discussion is not lost. Because the Fourier transformation along the longitudinal y -direction has already been taken, the Bloch phase factor, $e^{\pm k/2}$, appears. The range of the wave number is $-\pi \leq k \leq \pi$. The boundary condition for armchair nanoribbons is

$$\psi_{0,A} = \psi_{0,B} = \psi_{N+1,A} = \psi_{N+1,B} = 0. \quad (4.24)$$

Equations (4.22) and (4.23) can be written as the eigenvalue equation in the form of a $2N \times 2N$ matrix as

$$\hat{H}(k)\Psi(k) = \varepsilon(k)\Psi(k). \quad (4.25)$$

Here $\varepsilon(k)$ is the energy; $\Psi(k)$ is the corresponding wave function,

$$\Psi(k) = (\psi_{1A}, \psi_{2A}, \dots, \psi_{NA}, \psi_{1B}, \psi_{2B}, \dots, \psi_{NB})^T, \quad (4.26)$$

where $(\dots)^T$ denotes the transpose operator. $\hat{H}(k)$ is a $2N \times 2N$ matrix and is decomposed into four submatrices with dimensions of $N \times N$ as

$$\hat{H}(k) = \begin{pmatrix} \hat{h}_{AA}(k) & \hat{h}_{AB}(k) \\ \hat{h}_{BA}(k) & \hat{h}_{BB}(k) \end{pmatrix}. \quad (4.27)$$

Since graphene armchair nanoribbons are AB-bipartite, there is no electron hopping between the same sublattices. Thus, $\hat{h}_{AA} = \hat{h}_{BB} = 0$. On the other hand, Eq. (4.22) leads to the tridiagonal matrix $\hat{h}_{AB}(k)$ given by

$$\hat{h}_{AB}(k) = -\gamma_0 \begin{pmatrix} e^{-ik/2} & 1 & 0 & \dots & \dots & 0 \\ 1 & e^{-ik/2} & 1 & 0 & \dots & 0 \\ 0 & 1 & e^{-ik/2} & 1 & \dots & 0 \\ \vdots & & \ddots & \ddots & \ddots & \vdots \\ \vdots & & 0 & 1 & e^{-ik/2} & 1 \\ 0 & \dots & \dots & 0 & 1 & e^{-ik/2} \end{pmatrix}. \quad (4.28)$$

$\hat{h}_{BA}(k)$ is the Hermite conjugate of $\hat{h}_{AB}(k)$, i.e., $\hat{h}_{BA}(k) = \hat{h}_{AB}^\dagger(k)$. The energy band structures shown in Figs. 4.4(a-c) were obtained by numerically diagonalizing the above $2N \times 2N$ Hermite matrix. The DOS can be obtained from

$$D(\varepsilon) = -\frac{1}{\pi} \int_{-\pi}^{\pi} dk \text{Tr} [(\varepsilon + i\eta)\hat{I} - \hat{H}(k)]^{-1}, \quad (4.29)$$

where \hat{I} is a unit matrix and η is an infinitesimally small real number. $\text{Tr}[\hat{M}]^{-1}$ indicates the trace of the inverse matrix of \hat{M} .

In the rest of this section, we will derive the analytic expressions for the energy spectrum and wave function by solving the above equations of motion analytically. We assume that the generic solutions for $\psi_{m,A}$ and $\psi_{m,B}$ have the form

$$\psi_{m,A} = Ae^{ipm} + Be^{-ipm}, \quad (4.30)$$

$$\psi_{m,B} = Ce^{ipm} + De^{-ipm}. \quad (4.31)$$

Here A , B , C , and D are arbitrary coefficients, which will be determined under the boundary condition (Eq. (4.24)); p is the

wave number in the transverse direction, which is also determined under the boundary condition. The boundary condition leads to the following relations:

$$\psi_{0,A} = A + B = 0, \tag{4.32}$$

$$\psi_{0,B} = C + D = 0, \tag{4.33}$$

$$\psi_{N+1,A} = Az + Bz^{-1} = 0, \tag{4.34}$$

$$\psi_{N+1,B} = Cz + Dz^{-1} = 0, \tag{4.35}$$

where $z = e^{ip(N+1)}$. Thus, we have

$$\psi_{m,A} = A (e^{ipm} - e^{-ipm}), \tag{4.36}$$

$$\psi_{m,B} = C (e^{ipm} - e^{-ipm}). \tag{4.37}$$

Substituting these functions into the equations of motion, we obtain the relation

$$\begin{pmatrix} \varepsilon & \varepsilon_p + e^{ik/2} \\ \varepsilon_p + e^{-ik/2} & \varepsilon \end{pmatrix} \begin{pmatrix} A \\ C \end{pmatrix} = 0, \tag{4.38}$$

where $\varepsilon_p = 2 \cos(p)$. The condition for a nontrivial solution for A and C , i.e.,

$$\begin{pmatrix} A \\ C \end{pmatrix} \neq 0, \tag{4.39}$$

is

$$\det \begin{pmatrix} \varepsilon & \varepsilon_p + e^{ik/2} \\ \varepsilon_p + e^{-ik/2} & \varepsilon \end{pmatrix} = 0. \tag{4.40}$$

Then, we immediately obtain the solution for the energy as

$$\varepsilon_s = s\gamma_0 \sqrt{1 + 2\varepsilon_p \cos\left(\frac{k}{2}\right) + \varepsilon_p^2}. \tag{4.41}$$

Here, $s = \pm 1$; $s = +1$ ($s = -1$) corresponds to the conduction (valence) energy band. Note that ε_s becomes zero at $k = 0$ and $p = 2\pi/3$, which corresponds to a Dirac point.

We can set the condition for the transverse wave number p as follows. Since the boundary condition yields $z^{-1}B = -zA$ and $B = -A$, we have $B = -z^2A = z^2B$, i.e., $z^2 = e^{i2p(N+1)} = 1$. Therefore,

$$p = \frac{r}{N+1}\pi, \quad r = 1, 2, 3, \dots, N. \tag{4.42}$$

Note that $\varepsilon_s = 0$ at $k = 0$ whenever $N = 3m - 1$ ($m = 1, 2, 3, \dots$), which is simply the condition for metallic armchair nanoribbons.

Figure 4.7(a) shows the energy surfaces given by Eq. (4.41) for $N = 5$ and discrete wave number p . Figure 4.7(b) shows the corresponding projected energy band structure of a graphene nanoribbon with $N = 5$. In this case, since the cutting line of $r = 4$ gives $p = 2\pi/3$, the corresponding subband passes through the Dirac point, i.e., the nanoribbon has a metallic band structure with linear dispersion. Thus, the energy band structures of armchair nanoribbons can be obtained by slicing the band structure of graphene, as in the case of carbon nanotubes [58, 59].

The wave function is written as

$$\begin{pmatrix} \psi_{m,A} \\ \psi_{m,B} \end{pmatrix} = N_c \begin{pmatrix} -s\sqrt{\varepsilon_p + e^{-ik/2}} \\ \sqrt{\varepsilon_p + e^{+ik/2}} \end{pmatrix} \sin(mp). \quad (4.43)$$

Here N_c is the normalization constant, which is given by

$$N_c = \frac{1}{\sqrt{|\varepsilon|}} \left(N - \frac{\sin(Np)}{\sin(p)} \cos[(N+1)p] \right)^{-\frac{1}{2}}. \quad (4.44)$$

The real-space wave function $(\Psi_{m,A}(y_{l,mA}), \Psi_{m,B}(y_{l,mB}))$ in the l -th unit cell ($l = 1, 2, \dots, L_y$) can be obtained by the Fourier transform of $(\psi_{m,A}, \psi_{m,B})$, defined in a similar manner to Eq. (4.43). Thus,

$$\begin{pmatrix} \Psi_{m,A}(y_{l,mA}) \\ \Psi_{m,B}(y_{l,mB}) \end{pmatrix} = N_c \frac{1}{\sqrt{L_y}} \sum_k \begin{pmatrix} -s\sqrt{\varepsilon_p + e^{-ik/2}} e^{iky_{l,mA}} \\ \sqrt{\varepsilon_p + e^{+ik/2}} e^{iky_{l,mB}} \end{pmatrix} \sin(mp). \quad (4.45)$$

4.4.2 Zigzag Nanoribbons

Now we turn to zigzag nanoribbons. Although the existence of edge states makes the problem more complicated, in principle we can take the same strategy as that used for armchair nanoribbons. The set of equations of motion for zigzag nanoribbons is given by

$$(\varepsilon/\gamma_0)\psi_{m,A} = -\psi_{m-1,B} - g_k\psi_{m,B}, \quad (4.46)$$

$$(\varepsilon/\gamma_0)\psi_{m,B} = -\psi_{m+1,A} - g_k\psi_{m,A}. \quad (4.47)$$

Here $g_k = 2 \cos(k/2)$, and the site index is $m = 0, 1, 2, \dots, N+1$. $\psi_{m,A}$ and $\psi_{m,B}$ describe the wave functions at the mA - and mB -sites,

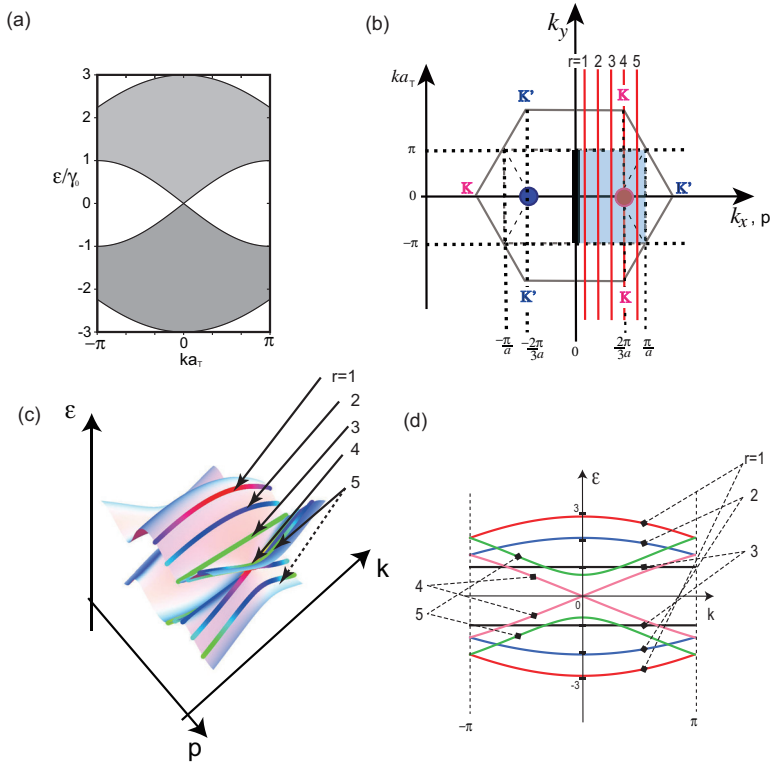


Figure 4.7 (a) Energy band structure of graphene mapped onto the BZ of armchair nanoribbons (Eq. (4.41)), where transverse wave number p is taken as the continuum in the range $0 \leq p \leq \pi$. (b) Relation between the BZ of graphene and that of armchair nanoribbons. The hexagonal BZ of graphene is mapped onto the bold black line on the k_y -axis ($-\pi \leq k_y \leq \pi$) as the BZ of armchair nanoribbons. The shaded rectangle (light blue) corresponds to the phase space of variables k and p of Eq. (4.41). Note the range of p is $0 \leq p \leq \pi$. The five red lines parallel to the k_y -axis correspond to the cutting lines of the case for the armchair nanoribbon of $N = 5$ (metallic). The cutting line of $r = 4$ clearly passes through the Dirac point, i.e., the nanoribbon is metallic. (c) 3D plot of bulk graphene band structure of (a) in the region $|k| \leq \pi$ and $|p| \leq \pi$. The bold lines correspond to the ribbon width with $N = 5$ and discrete transverse wave number p . Note that a Dirac point appears at $k = 0$ and $p = 2\pi/3$. (d) Energy band structure of armchair nanoribbon ($N = 5$) with subband indices, which is equivalent to the projection of the 3D plot onto the $\epsilon - k$ plane; γ_0 and a_τ are set to unity.

respectively. The site indices are given in Fig. 4.3(b). Since we have already done the Fourier transformation along the longitudinal x -direction, the wave number appearing in g_k is due to the Bloch phase. We also have set $a = 1$ for simplicity. The boundary condition for zigzag nanoribbons is given by $\psi_{0,B} = \psi_{N+1,A} = 0$. As we have shown in the previous subsection, the above set of equations of motion forms a $2N \times 2N$ matrix. The only difference from the case of armchair nanoribbons appears in the matrix elements of $N \times N$ submatrix \hat{h}_{AB} , which can be written for the zigzag nanoribbons as

$$\hat{h}_{AB}(k) = -\gamma_0 \begin{pmatrix} g_k & 0 & 0 & \cdots & \cdots & 0 \\ 1 & g_k & 0 & 0 & \cdots & 0 \\ 0 & 1 & g_k & 0 & \cdots & 0 \\ \vdots & & \ddots & \ddots & \ddots & \vdots \\ \vdots & & 0 & 1 & g_k & 0 \\ 0 & \cdots & \cdots & 0 & 1 & g_k \end{pmatrix}. \quad (4.48)$$

$\hat{h}_{BA}(k)$ is the Hermite conjugate of $\hat{h}_{AB}(k)$, i.e., $\hat{h}_{BA}(k) = \hat{h}_{AB}^\dagger(k)$. The energy band structures in Figs. 4.5(a)-(c) were obtained by numerically diagonalizing the above $2N \times 2N$ Hermite matrix of Eq. (4.27) with the above matrix elements.

In the remainder of this subsection, we attempt to deduce an analytic expression for the energy and wave functions. First, we assume the generic solution for $\psi_{m,A}$ and $\psi_{m,B}$ to be

$$\psi_{m,A} = A e^{ipm} + B e^{-ipm}, \quad (4.49)$$

$$\psi_{m,B} = C e^{ipm} + D e^{-ipm}. \quad (4.50)$$

Here A , B , C , and D are arbitrary coefficients, which will be determined under the above boundary condition; p is the wave number in the transverse direction, which is also given under the boundary condition.

From the boundary condition, we have the following relations:

$$\psi_{0,B} = C + D = 0, \quad (4.51)$$

$$\psi_{N+1,A} = Az + Bz^{-1} = 0, \quad (4.52)$$

where $z = e^{ip(N+1)}$. Thus, we have

$$\psi_{m,A} = A (e^{ipm} - z^2 e^{-ipm}), \quad (4.53)$$

$$\psi_{m,B} = C (e^{ipm} - e^{-ipm}). \quad (4.54)$$

Substituting these functions into the equations of motion, we obtain the relation

$$\mathbf{M} \begin{pmatrix} A \\ C \end{pmatrix} = 0 \quad (4.55)$$

with

$$\mathbf{M} = \begin{pmatrix} \varepsilon (e^{ipm} - z^2 e^{-ipm}) & (g_k + e^{-ip})e^{ipm} - (g_k + e^{ip})e^{-ipm} \\ (g_k + e^{ip})e^{ipm} - (g_k + e^{-ip})e^{-ipm} z^2 & \varepsilon (e^{ipm} - e^{-ipm}) \end{pmatrix}. \quad (4.56)$$

The condition for a nontrivial solution for A and C , i.e., $(A, C)^T \neq 0$, is $\det \mathbf{M} = 0$. However, note that the solutions of $p = 0$ and $\pm\pi$ should be excluded as unphysical because matrix \mathbf{M} becomes zero for these values of p . In other words, such values yield $\psi_{m,A} = \psi_{m,B} = 0$ for arbitrary m , i.e., electrons are absent in the system. Therefore, we can find solutions that satisfy $\det \mathbf{M} = 0$ for arbitrary m except when $p = 0$ and $\pm\pi$. After some arithmetic, we can show that $\det \mathbf{M} = 0$ has the following form:

$$v e^{i2pm} + w e^{-i2pm} + x = 0, \quad (4.57)$$

where v , w and x are functions of ε , g_k and z . Thus, all the coefficients of $e^{\pm i2pm}$ terms and the constant term should be equal to zero. From the coefficient of $e^{\pm i2pm}$, we obtain the energy spectrum

$$\varepsilon^2 = (g_k + e^{ip})(g_k + e^{-ip}) = 1 + g_k^2 + 2g_k \cos(p). \quad (4.58)$$

Thus, the energy is

$$\varepsilon_s = s \sqrt{1 + g_k^2 + 2g_k \cos(p)}, \quad (4.59)$$

where $s = \pm 1$, and $s = +1$ ($s = -1$) corresponds to the conduction (valence) energy band. Similarly, from the condition that the constant term should also be equal to zero,

$$(1 + z^2)\varepsilon^2 = (g_k + e^{-ip})^2 z^2 + (g_k + e^{ip})^2, \quad (4.60)$$

which leads to the condition for the transverse wave number p . Substituting Eq. (4.58) into Eq. (4.60) to eliminate ε^2 , we obtain

$$F(p, N) \equiv \sin[pN] + g_k \sin[p(N+1)] = 0. \quad (4.61)$$

This equation yields the transverse wave number $p = p(k, N)$, which is, however, not a simple form as in the case of armchair

nanoribbons. The transverse wave number depends not only on the width N but also on the longitudinal wave number k .

We can obtain the relation $C = -Az$ from the parity of the zigzag nanoribbon, i.e., $\psi_{N+1-m,A} = \psi_{m,B}$, and thus the generic form of the wave function can be written as

$$\begin{pmatrix} \psi_{m,A} \\ \psi_{m,B} \end{pmatrix} = N'_c \begin{pmatrix} e^{-ipm}z - e^{ipm}z^{-1} \\ e^{-ipm} - e^{ipm} \end{pmatrix} = N_c \begin{pmatrix} \sin(p(N+1-m)) \\ \sin(pm) \end{pmatrix} \quad (4.62)$$

with the normalization constant N_c .

We now closely investigate the analytic properties for the condition $F(p, N) = 0$, which determines the transverse wave number p for a given g_k . As $F(p, N)$ is a periodic odd function, i.e., $F(p+2\pi, N) = F(p, N)$ and $F(-p, N) = -F(p, N)$, it is sufficient to search for the solutions within the range $0 < p < \pi$.

(i) *Extended states*

Figure 4.8 schematically shows $F(p, N)$ for (a) $|g_k| \geq g_k^c$ and (b) $|g_k| < g_k^c$ when $N = 4$. Let us define the solutions $F(p, N) = 0$ for fixed N as p_i ($i = 1, 2, \dots, p_n$) within $0 < p < \pi$, i.e., excluding $p = 0$ and π . All these p_i solutions give the extended states. The number of p_i , i.e., p_n , depends on the value of g_k ,

$$p_n = \begin{cases} N, & |g_k| \geq g_k^c, \\ N-1, & |g_k| < g_k^c. \end{cases} \quad (4.63)$$

As shown below, g_k^c depends on the ribbon width N and becomes $g_k^c \sim 1$ for $N \gg 1$; g_k^c is analytically given as

$$\left. \frac{\partial}{\partial p} F(p, N) \right|_{p=\pi} = 0 \quad (4.64)$$

and can be written explicitly as

$$g_k^c = \pm \frac{1}{1 + 1/N}. \quad (4.65)$$

Using the relation $g_k = 2 \cos(k/2)$, we can obtain the critical k_c that yields g_k^c as

$$k_c = \pm 2 \arccos \left(\frac{1}{1 + 1/N} \right). \quad (4.66)$$

In general, there are two solutions $k_c (= k_c^L, k_c^R)$ within $0 \leq k \leq \pi$ as shown in Fig. 4.9 In the limit of large N , $g_c = \pm 1$, and $k_c^L = 2\pi/3$ and $k_c^R = 4\pi/3$, which correspond to the Dirac K and K' points.

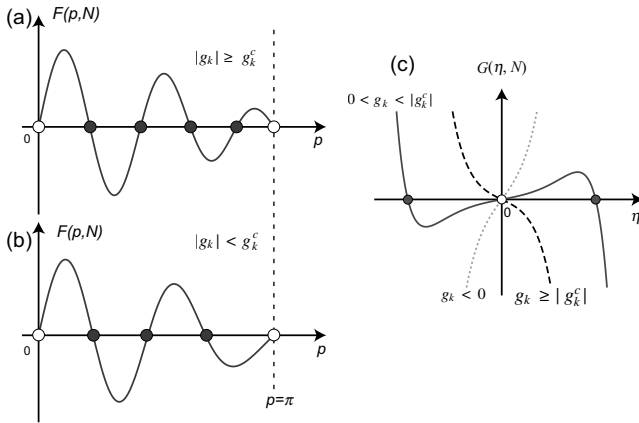


Figure 4.8 Schematic figure of $F(p, N)$ for (a) $|g_k| \geq g_k^c$ and (b) $|g_k| < g_k^c$ when $N = 4$. Note that $p = 0$ and π (empty circles) are unphysical solutions. There are N (4 filled circles) solutions corresponding to extended states for $|g_k| \geq g_k^c$, but only $N - 1$ (3 filled circles) solutions corresponding to extended states (filled circles) for $|g_k| < g_k^c$. The missing state corresponds to edge states, which can be found as the nonzero η -solution of $G(\eta, N) = 0$ shown in (c). Note that the $\eta = 0$ solution (open circle) is unphysical. Nonzero η -solutions (filled circles) can appear for $0 < g_k < |g_k^c|$. After Ref. [57].

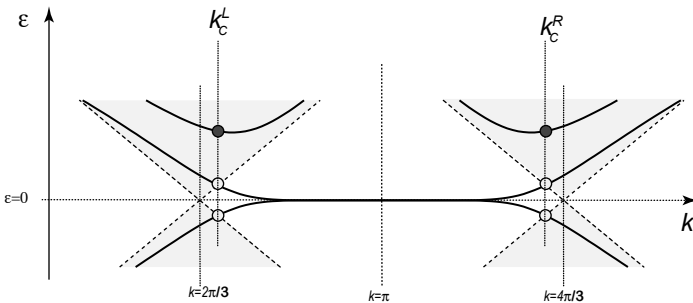


Figure 4.9 Schematic energy band dispersion near $\epsilon = 0$ for zigzag nanoribbons. The bold lines indicate the energy subband of zigzag nanoribbons. The shaded area indicates the bulk graphene spectrum. Here γ_0 and a are set to unity. After Ref. [57].

The wave function for extended states is written as

$$\begin{pmatrix} \psi_{m,A} \\ \psi_{m,B} \end{pmatrix} = N_c \begin{pmatrix} s(-1)^r \sin(p(N+1-m)) \\ \sin(pm) \end{pmatrix}, \quad (4.67)$$

where $r = 1, 2, 3, \dots, N$ and the normalization constant N_c

$$N_c = \left(N - \frac{\sin(Np)}{\sin(p)} \cos((N+1)p) \right)^{-\frac{1}{2}}. \quad (4.68)$$

The real-space wave function $(\Psi_{m,A}(x_{l,mA}), \Psi_{m,B}(x_{l,mB}))$ can be obtained by the Fourier transform of $(\psi_{m,A}, \psi_{m,B})$, which is defined in a similar manner to Eq. (4.67). Thus,

$$\begin{pmatrix} \Psi_{m,A}(x_{l,mA}) \\ \Psi_{m,B}(x_{l,mB}) \end{pmatrix} = N_c \frac{1}{\sqrt{L_x}} \sum_k \begin{pmatrix} s(-1)^r \sin(p(N+1-m)) \\ \sin(pm) \end{pmatrix} e^{ikx_{l,mA}} e^{ikx_{l,mB}}. \quad (4.69)$$

(ii) *Edge states*

As can be seen from Eq. (4.63), one solution is missing for $|g_k| \geq g_k^c$. This solution can be obtained by analytical continuation as

$$p \rightarrow \pi \pm i\eta \equiv p_\pi, \quad k_c^L < |k| < \pi, \quad (4.70)$$

$$\varepsilon_s = s \sqrt{1 + g_k^2 - 2g_k \cosh \eta}, \quad (4.71)$$

The transverse imaginary wave number that damps the wave function toward the inner sites is given by the following relation:

$$\sinh(\eta N) - g_k \sinh(\eta(N+1)) = 0, \quad \text{for } p_\pi, \quad (4.72)$$

Each of relation yields a single η solution corresponding to the edge state.

$$G(\eta, N) \equiv \sinh(\eta N) - g_k \sinh(\eta(N+1)) = 0 \quad (4.73)$$

Figure 4.8(c) schematically shows $G(\eta, N)$ when $N = 4$. One can see that $G(\eta, N)$ has a nonzero η solution if $0 < g_k < |g_k^c|$.

After analytical continuation, we can obtain the wave function for the edge states as

$$\begin{pmatrix} \psi_{m,A} \\ \psi_{m,B} \end{pmatrix} = N_c \begin{pmatrix} s(-1)^r \sinh(\eta(N+1-m)) \\ \sinh(\eta m) \end{pmatrix}, \quad (4.74)$$

where $r = 1, 2, 3, \dots, N$ and a normalization constant N_c ,

$$N_c = \left(\frac{\sin(Np)}{\sin(p)} \cos((N+1)p) - N \right)^{-\frac{1}{2}}. \quad (4.75)$$

The real-space wave function $(\Psi_{m,A}(x_{l,mA}), \Psi_{m,B}(x_{l,mB}))$ in the l -th unit cell ($l = 1, 2, \dots, L_x$) can be given by

$$\begin{pmatrix} \Psi_{m,A}(x_{l,mA}) \\ \Psi_{m,B}(x_{l,mB}) \end{pmatrix} = N_c \frac{1}{\sqrt{L_x}} \sum_k \begin{pmatrix} s(-1)^r \sinh(\eta(N+1-m)) e^{ikx_{l,mA}} \\ \sinh(\eta m) e^{ikx_{l,mB}} \end{pmatrix} \quad (4.76)$$

Note that the wave function for armchair nanoribbons given by Eq. (4.43) has a phase difference between sublattice sites A and B due to the chiral nature of graphene. On the other hand, the wave function for zigzag nanoribbons is always real and thus has no phase, irrespective of whether the state is extended or localized. This difference in wave functions between armchair and zigzag nanoribbons is related to the nature of pseudospin in graphene [60] and to some physical properties such as Kohn anomalies [61] and their effect on Raman scattering [62].

4.5 Energy Bandgap

Next, we analytically show that both the energy gap Δ_a at $k = 0$ for armchair ribbons and the energy gap Δ_z at $k = 2\pi/3$ for zigzag ribbons are inversely proportional to the width of the graphene ribbon. This result indicates that the physical quantities related to the energy gap can be scaled by the ribbon width. A quantitative estimate of the energy bandgap using the DFT can be found in Ref. [20].

4.5.1 Armchair Nanoribbons

Since a direct gap always appears at $k = 0$, we obtain $\varepsilon_{\pm} = \pm\gamma_0(1 + \varepsilon_p)$ from the analytical solution of the energy spectrum, Eq. (4.41), by substituting in $k = 0$. Here $\varepsilon_p = 2 \cos(p)$ with $p = \frac{r}{N+1}\pi$. Thus,

the energy gap $\Delta_a = 2\varepsilon_+$ is given by

$$\Delta_a = \begin{cases} 0 & N = 3m - 1 \\ 2\gamma_0 \left[1 + 2 \cos \left(\frac{2m+1}{3m+1} \pi \right) \right] & N = 3m, \\ 2\gamma_0 \left[1 + 2 \cos \left(\frac{2m+1}{3m+2} \pi \right) \right] & N = 3m + 1, \end{cases} \quad (4.77)$$

where $m = 1, 2, 3, \dots$. After expressing N in terms of $W (= (N + 1)\frac{a}{2})$, which is the ribbon width in the unit of the lattice constant a , we perform the Taylor expansion under the condition $1/W \ll 1$. The leading order of Δ_a/γ_0 for $N \neq 3m - 1$ behaves as

$$\frac{\Delta_a}{\gamma_0} \sim \frac{\pi}{W/a}. \quad (4.78)$$

Thus, Δ_a is inversely proportional to the ribbon width.

For the case of armchair nanoribbons with $N = 3m - 1$, the energy gap closes in the tight-binding scheme. However, the incorporation of the electron-phonon interaction opens a small gap accompanied with the Peierls distortion. [54] This behavior can also be confirmed by using the DFT with the local density approximation (LDA). [20]

4.5.2 Zigzag Nanoribbons

Since in zigzag nanoribbons the two edge states are degenerate at $k = \pi$, the gap of the zigzag ribbons is always zero and the system is always metallic. However, the energy bands have a gap at $k = 2\pi/3$ because the bonding and anti-bonding configurations between the two edge states originating from both edges develop toward $k = 2\pi/3$ from $k = \pi$. According to the projection of the band structure of a graphene sheet onto the first BZ of zigzag ribbons, the degenerate points of the valence and conduction bands of a graphene sheet meet at $k = 2\pi/3$. Thus, in the limit of infinite ribbon width, the energy gap Δ_z at $k = 2\pi/3$ is zero. The Hamiltonian of zigzag ribbons at $k = 2\pi/3$ is rewritten as

$$H = -\gamma_0 \sum_{i=1}^{2N} (a_i^\dagger a_{i+1} + H.c.), \quad (4.79)$$

which is equivalent to the tight-binding model for a 1D lattice having $2N$ sites. The site index i corresponds to iA if i is an odd number

and to iB if i is an even number. The eigenvalues are evaluated as $\epsilon = -2\gamma_0 \cos\left(\frac{n\pi}{2N+1}\right)$ ($n = 1, 2, \dots, 2N$), and the corresponding wave function at the j th site, Ψ_j , is $\Psi_j = B \sin\left(\frac{nj\pi}{2N+1}\right)$, where B is the normalization factor. Therefore, Δ_z is given as

$$\Delta_z = 4\gamma_0 \cos\left(\frac{N}{2N+1}\pi\right). \quad (4.80)$$

A Taylor expansion under the condition $1/N \ll 1$ yields

$$\frac{\Delta_z}{\gamma_0} \sim \frac{\pi}{N} = \frac{\pi}{\frac{2}{\sqrt{3}}\frac{W}{a} - \frac{2}{3}}. \quad (4.81)$$

Here $W = \frac{\sqrt{3}}{2}Na + \frac{a}{\sqrt{3}}$ is the ribbon width in the unit of the lattice constant. Thus, Δ_a is also inversely proportional to the ribbon width.

Figure 4.10(a) shows the width dependence of the energy gap for armchair and zigzag ribbons and Fig. 4.10(b) shows a plot of $N\Delta$ versus N . $N\Delta$ becomes constant for values greater than about $N = 30$ ($N = 60$) for zigzag (armchair) ribbons.

4.6 Energy Spectrum and Wave Function: Massless Dirac Equation

As we have seen in Section 4.2 and Chapter 2, the electronic state of graphene in the vicinity of the K - or K' point can be described by the

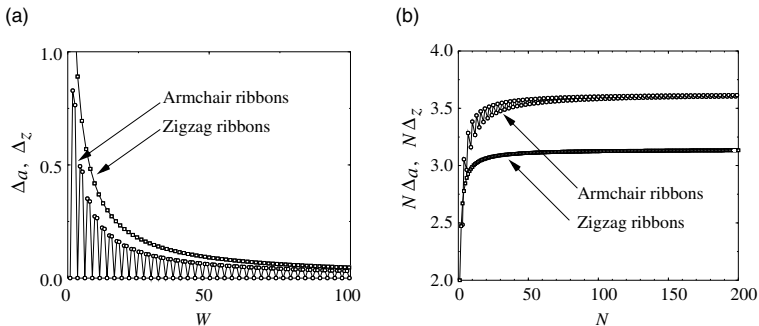


Figure 4.10 (a) Width dependence of the energy gap of armchair ribbons at $k = 0$ (Δ_a) and zigzag ribbons at $k = 2\pi/3$ (Δ_z). (b) Plot of $N\Delta_a$ and $N\Delta_z$ versus N .

massless Dirac equation. In this section, we will discuss the relation between the massless Dirac equation and edge boundary condition, and also show how the electronic states of graphene nanoribbons can be described in this scheme step by step.

4.6.1 Semi-Infinite Graphene Sheet with a Zigzag Edge

Let us start by considering the electronic states of a semi-infinite graphene sheet with a zigzag edge on the basis of the massless Dirac equation. The lattice structure is shown in Fig. 4.11(a), where carbon atoms only exist in the $y > 0$ region, i.e., the upper half-plane. The region below the dashed line, $y < 0$, indicates the lattice network of missing carbon atoms, i.e., a vacuum. The boundary condition for semi-infinite graphene with a zigzag edge is $f_B(y = 0) = 0$, which corresponds to the amplitude of sites marked with “x” being equal to zero. The shaded semi-infinite rectangular box is the unit cell. Since, as can be seen in Fig. 4.11(b), the BZ of this system corresponds to the region $-\pi \leq k_x a \leq \pi$ of the original graphene BZ, the two Dirac cones K and K' are mapped onto at $k_x a = 2\pi/3$ and $k_x a = -2\pi/3$, respectively. Also, the two Dirac points are well separated in momentum space. Thus, we can assume that K and K' are independent, and treat them separately.

The translational invariance is maintained along the x -direction. Thus, we assume that the wave function of the Dirac equation has a plane wave form along this direction, i.e.

$$\mathbf{F}^K(\mathbf{r}) \propto \begin{pmatrix} f_A(y) \\ f_B(y) \end{pmatrix} e^{ikx}. \quad (4.82)$$

Here k is the wave number measured from the K point ($k_x a = 2\pi/3$), i.e., $k = k_x - 2\pi/3a$. By substituting this form into the Dirac equation, Eq. (4.8), we obtain two differential equations:

$$\begin{aligned} \left(k - \frac{\partial}{\partial y}\right) f_B &= (\varepsilon/\gamma) f_A, \\ \left(k + \frac{\partial}{\partial y}\right) f_A &= (\varepsilon/\gamma) f_B. \end{aligned} \quad (4.83)$$

When we merge these two equations by eliminating the variable f_B , we obtain a second-order differential equation:

$$\frac{\partial^2}{\partial y^2} f_A = \left(k^2 - \frac{\varepsilon^2}{\gamma^2}\right) f_A. \quad (4.84)$$

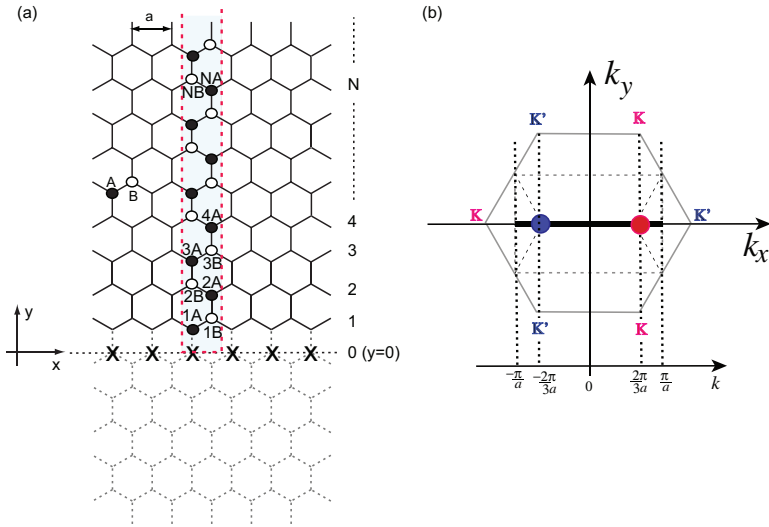


Figure 4.11 (a) Lattice structure of semi-infinite graphene sheet with a zigzag edge, where carbon atoms only exist $y > 0$ region, i.e., the upper half-plane. The region with the dashed line, $y < 0$, indicates region with missing carbon sites. The boundary condition for this system is $f_B(y = 0) = 0$, which corresponds to the amplitude of sites marked with “x” being equal to zero. The shaded semi-infinite rectangular box is the unit cell. (b) Because the semi-infinite graphene sheet has translational symmetry only along the x -axis, the hexagonal BZ of graphene is mapped to the 1D BZ (bold line in the region $-\pi < k_x < \pi$). Thus, the K and K' points are mapped onto $k = 2\pi/3$ (red circle) and $k = -2\pi/3$ (blue circle), respectively.

Assuming the exponential form $e^{\eta y}$ as a solution to this second-order differential equation, we obtain the condition for η as

$$\eta^2 = k^2 - (\varepsilon/\gamma)^2 \implies \eta = \pm \sqrt{k^2 - (\varepsilon/\gamma)^2}. \quad (4.85)$$

Since η becomes purely imaginary for $|\varepsilon| \geq \gamma|k|$, the wave function has a plane wave feature such as $e^{\pm iy\sqrt{(\varepsilon/\gamma)^2 - k^2}}$, which corresponds to the extended bulk states; $e^{+iy\sqrt{(\varepsilon/\gamma)^2 - k^2}}$ is the propagating plane wave mode from the edge toward the inner region $y > 0$. $e^{+iy\sqrt{(\varepsilon/\gamma)^2 - k^2}}$ propagates in the opposite direction. Meanwhile, since η becomes real when $|\varepsilon| < \gamma|k|$, the wave function has a damping or diverging feature toward the inner region from the edge ($y > 0$), i.e., $e^{\pm y\sqrt{k^2 - (\varepsilon/\gamma)^2}}$, which means that the in-gap states are similar to edge

states. Actually, the edge states can be obtained from this damping solution.

As we have already seen in the previous section, the edge states appearing near a zigzag edge correspond to the localized wave function of $\varepsilon = 0$. Since the wave function of B -sublattice sites should be identically zero, the boundary condition for a zigzag edge can be expressed as $f_B(y > 0) = 0$. Thus, Eq. (4.83) can be simplified to

$$\left(k_x + \frac{\partial}{\partial y}\right) f_A(y) = 0. \quad (4.86)$$

Immediately, we obtain $f_A(y) = C \exp(-ky)$, where C is a constant determined by normalization. At $k = 0$, $f_A(y)$ is independent of y and becomes uniform in the space because the wave function corresponds to that of a Dirac point, i.e., a bulk state. However, when $k_x > 0$, $f_A(y) = C \exp(-|k|y)$ becomes a damping solution toward the $y > 0$ region from the graphene edge of $y = 0$; this wave function actually corresponds to the edge states of a zigzag edge. Thus, the wave function of the edge state can be described as

$$\mathbf{F}^K(\mathbf{r}) = C \theta(y) \theta(k) \begin{pmatrix} e^{-ky} \\ 0 \end{pmatrix} e^{ikx}. \quad (4.87)$$

Here $\theta(z)$ denotes a step function, i.e., $\theta(z) = 1$ if $z \geq 0$, and $\theta(z) = 0$ if $z < 0$.

Some readers may also notice that, even if $k < 0$, $f_A(y) = C \exp(|k|y)$ becomes a damping solution in the $y < 0$ region. Actually, this solution corresponds to the edge state of Klein's edge (bearded edge). The tight-binding description for the edge state of Klein's edge will be discussed in Section 4.7. Because this solution is identical to the edge state solution for $y \geq 0$ with $f_A(y) = 0$, the edge state wave function for Klein's bearded edge can be written as

$$\mathbf{F}^K(\mathbf{r})_{\text{bearded edge}} = C \theta(y) \theta(-k) \begin{pmatrix} 0 \\ e^{ky} \end{pmatrix} e^{ikx}. \quad (4.88)$$

Now we shall focus on the zigzag edge state again. Here we combine two edge states originating from the K and K' points. As can be seen in Eqs. (4.8) and (4.9), the Hamiltonian of the K' point is obtained by replacing \hat{k}_y with $-\hat{k}_y$ in that of the K point. Thus, the zigzag edge state for the K' point is written as

$$\mathbf{F}^{K'}(\mathbf{r}) = C \theta(y)\theta(-k') \begin{pmatrix} e^{k'y} \\ 0 \end{pmatrix} e^{ik'x}, \quad (4.89)$$

where k' is the wave number measured from the K' point.

4.6.2 Zigzag Nanoribbons

Next we construct the wave function for zigzag nanoribbons. In the nanoribbon geometry, two edge states originating from the upper and lower zigzag edges interfere, and generate bonding and anti-bonding states. Initially, we focus only on the states near the K point. First we assume the generic form for $f_A^K(y)$ to be

$$f_A^K(y) = C_1 e^{\eta y} + C_2 e^{-\eta y}, \quad (4.90)$$

where $\eta = \sqrt{k^2 - (\epsilon/\gamma)^2}$ and $C_1(C_2)$ is an arbitrary coefficient. This form is a generic solution of the differential Eq. (4.84). Similarly, we can obtain the generic form for $f_B^K(y)$ from Eq. (4.83) as

$$\begin{aligned} f_B^K(y) &= \frac{\gamma}{\epsilon} \left(k + \frac{\partial}{\partial y} \right) f_A^K \\ &= C_1 \frac{\gamma(k+\eta)}{\epsilon} e^{\eta y} + C_2 \frac{\gamma(k-\eta)}{\epsilon} e^{-\eta y}. \end{aligned} \quad (4.91)$$

Therefore, we shall assume the following generic form for the wave function:

$$\begin{pmatrix} f_A^K(y) \\ f_B^K(y) \end{pmatrix} = C_1 \begin{pmatrix} 1 \\ \gamma(k+\eta)/\epsilon \end{pmatrix} e^{\eta y} + C_2 \begin{pmatrix} 1 \\ \gamma(k-\eta)/\epsilon \end{pmatrix} e^{-\eta y}. \quad (4.92)$$

The above wave function should satisfy the following open boundary conditions [18, 63]:

$$f_B^K(0) = 0 \quad f_A^K(W) = 0. \quad (4.93)$$

These conditions give rise to

$$\begin{aligned} f_A^K(W) &= C_1 e^{\eta W} + C_2 e^{-\eta W} = 0, \\ f_B^K(0) &= C_1 \frac{\gamma(k+\eta)}{\epsilon} + C_2 \frac{\gamma(k-\eta)}{\epsilon} = 0. \end{aligned} \quad (4.94)$$

Since the coefficients should satisfy the condition

$$\begin{pmatrix} C_1 \\ C_2 \end{pmatrix} \neq 0, \quad (4.95)$$

we obtain the relation between η and k as

$$\frac{(k + \eta)}{\epsilon} e^{-\eta W} - \frac{(k - \eta)}{\epsilon} e^{\eta W} = 0, \quad (4.96)$$

which gives

$$1 = \frac{k - \eta}{k + \eta} e^{2\eta W} = \frac{(k - \eta)^2}{(\epsilon/\gamma)^2} e^{2\eta W} \implies \epsilon = \pm \gamma(k - \eta) e^{\eta W}. \quad (4.97)$$

Therefore, the wave vector k and energy ϵ have to be self-consistently connected by the equation

$$\epsilon_s = s(k - \eta) e^{\eta W}, \quad (4.98)$$

where $s = \pm$. Using the relation between C_1 and C_2 given by Eq. (4.94), we can rewrite the wave function as

$$\begin{pmatrix} f_A^K(y) \\ f_B^K(y) \end{pmatrix} = C \begin{pmatrix} \sinh(\eta(y - W)) \\ s \cdot \sinh(\eta y) \end{pmatrix} \quad (4.99)$$

with the normalization constant

$$C = \sqrt{\frac{1}{4} \sqrt{\frac{\eta}{\sinh(2\eta W) - 2W\eta}}}, \quad (4.100)$$

which was determined by the condition

$$\int_0^W \{|f_A^K(y)|^2 + |f_B^K(y)|^2\} dy = \frac{1}{2}. \quad (4.101)$$

Here 1/2 originates from the fact that we are now considering one of two K points.

Meanwhile, the wave function for the extended bulk state, which satisfies the condition $|\epsilon| \geq \gamma|k|$, can be obtained by the analytic continuation of $\eta \rightarrow ip$, where $p = \sqrt{(\epsilon/\gamma)^2 - k^2}$, i.e.,

$$\begin{pmatrix} f_A^K(y) \\ f_B^K(y) \end{pmatrix} = C' \begin{pmatrix} \sin(p(y - W)) \\ s \cdot \sin(py) \end{pmatrix} \quad (4.102)$$

with the normalization constant

$$C' = \sqrt{\frac{1}{4} \sqrt{\frac{p}{\sin(2pW) - 2Wp}}}. \quad (4.103)$$

The condition that relates the transverse wave number p and energy ϵ becomes

$$\epsilon_s = s\gamma(k - ip) e^{ipW}. \quad (4.104)$$

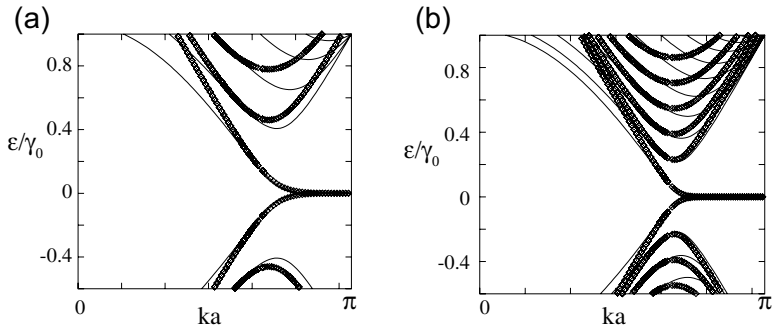


Figure 4.12 Comparison of the energy band structures between the tight-binding model and massless Dirac model. The bold (diamond) lines represent the band structures based on the tight binding model (massless Dirac equation) for zigzag nanoribbons with (a) $N = 10$ and (b) $N = 20$. After Ref. [18].

The whole envelope function including the longitudinal direction for each case can be obtained by multiplying the plane wave along the x -axis, i.e.,

$$F^K(\mathbf{r}) = \frac{1}{\sqrt{L_x}} \begin{pmatrix} f_A^K(y) \\ f_B^K(y) \end{pmatrix} e^{ikx}, \quad (4.105)$$

where L_x is the length of the nanoribbon. Figures 4.12(a) and (b) show a comparison of the energy band structures between the tight-binding model and massless Dirac model. The bold (diamond) lines represent the band structures based on the tight-binding model (massless Dirac equation) for zigzag nanoribbons with different ribbon widths. The energy spectrum for the massless Dirac model was obtained through the conditions given by Eqs. (4.98) and (4.104). We confirm that the massless Dirac equation can accurately describe the low-energy band structures of the tight-binding model.

4.6.3 Armchair Nanoribbons

Now we derive the energy spectrum and wave function for armchair nanoribbons on the basis of the massless Dirac equation. The boundary condition of armchair nanoribbons projects the K and K' states onto the Γ point in the first BZ as can be seen in

Fig. 4.7(b). Thus, the low-energy states for armchair nanoribbons are the superposition of the K and K' states. We take the K' point at $\mathbf{K}' = \frac{2\pi}{a}(\frac{2}{3}, 0)$ and the K point at $\mathbf{K} = \frac{2\pi}{a}(-\frac{2}{3}, 0)$. For simplicity, let us define $K_0 = 4\pi/3a$ and $\mathbf{K}_0 = (K_0, 0)$. Then, \mathbf{K} and \mathbf{K}' can be expressed as $\mathbf{K}' = \mathbf{K}_0$ and $\mathbf{K} = -\mathbf{K}_0$, respectively.

Let us write the wave function in real space using the envelope functions at the K and K' points as

$$\begin{cases} \psi_A(\mathbf{r}) = e^{i\mathbf{K}\cdot\mathbf{r}}F_A^K(\mathbf{r}) + e^{i\mathbf{K}'\cdot\mathbf{r}}F_A^{K'}(\mathbf{r}), \\ \psi_B(\mathbf{r}) = -e^{i\mathbf{K}\cdot\mathbf{r}}F_B^K(\mathbf{r}) + e^{i\mathbf{K}'\cdot\mathbf{r}}F_B^{K'}(\mathbf{r}), \end{cases} \quad (4.106)$$

where the minus sign in the equation for $\psi_B(\mathbf{r})$ was introduced to absorb the extra phase factor. If we expand the equations of motion for the tight-binding model, i.e., Eqs. (4.1) and (4.2), using the above form of the wave function, we obtain the massless Dirac equation in the vicinity of \mathbf{K} as Eq. (4.8). In the vicinity of \mathbf{K}' , the massless Dirac equation is the same as before, i.e., Eq. (4.9).

The boundary condition for armchair nanoribbons can be written as

$$\Psi_A(0, y) = \Psi_B(0, y) = \Psi_A(W, y) = \Psi_B(W, y) = 0, \quad (4.107)$$

where the ribbon width is $W = \frac{N+1}{2}a$. Thus, the envelope functions should satisfy [3, 63]

$$\begin{aligned} \Psi_A(0, y) &= F_A^K(0, y) + F_A^{K'}(0, y) = 0, \\ \Psi_B(0, y) &= -F_B^K(0, y) + F_B^{K'}(0, y) = 0, \\ \Psi_A(W, y) &= e^{-iK_0W}F_A^K(W, y) + e^{iK_0W}F_A^{K'}(W, y) = 0, \\ \Psi_B(W, y) &= -e^{-iK_0W}F_B^K(W, y) + e^{iK_0W}F_B^{K'}(W, y) = 0. \end{aligned} \quad (4.108)$$

Since armchair nanoribbons have translational invariance along the y -axis, the envelope function can be expressed as

$$\mathbf{F}^{K, K'}(\mathbf{r}) \propto \begin{pmatrix} f_A^{K, K'}(x) \\ f_B^{K, K'}(x) \end{pmatrix} e^{iky}. \quad (4.109)$$

Thus, the boundary condition can be simplified to

$$\begin{aligned} \pm f_\mu^K(0) + f_\mu^{K'}(0) &= 0, \\ \pm e^{-iK_0W}f_\mu^K(W) + e^{iK_0W}f_\mu^{K'}(W) &= 0, \end{aligned} \quad (4.110)$$

where $\mu = A, B$. The upper (lower) sign is for $\mu = A$ (B). By substituting the above form of the envelope function into the Dirac

equation, given by Eqs. (4.9) and (4.8), we obtain two differential equations,

$$\begin{aligned} (-i \frac{d}{dx} \pm ik) f_A^{K,K'}(x) &= \frac{\varepsilon}{\gamma} f_B^{K,K'}(x), \\ (-i \frac{d}{dx} \mp ik) f_B^{K,K'}(x) &= \frac{\varepsilon}{\gamma} f_A^{K,K'}(x), \end{aligned} \quad (4.111)$$

where the upper (lower) sign corresponds to the K (K') point. When we merge the two equations by the elimination of either f_A or f_B , we obtain the following second-order differential equation similarly to before:

$$\frac{\partial^2}{\partial x^2} f_{\mu}^{K,K'}(x) = \left(k^2 - \frac{\varepsilon^2}{\gamma^2} \right) f_{\mu}^{K,K'}(x). \quad (4.112)$$

Let us assume that $f_A^{K,K'}(x)$ has the generic form

$$\begin{cases} f_A^{K'}(x) = A e^{ipx} + B e^{-ipx}, \\ f_A^K(x) = C e^{ipx} + D e^{-ipx}, \end{cases} \quad (4.113)$$

then we impose the boundary conditions

$$\begin{cases} A + B + C + D = 0, \\ A e^{i(p+K_0)W} + B e^{-i(p-K_0)W} + C e^{i(p-K_0)W} + D e^{-i(p+K_0)W} = 0. \end{cases} \quad (4.114)$$

We choose the following relations to satisfy the boundary conditions:

$$A = D = 0, \quad B = -C. \quad (4.115)$$

Since these conditions lead to

$$B \sin((p + K_0)W) = 0, \quad (4.116)$$

the condition for transverse wave number p is given by

$$p_n = \frac{n}{W} \pi - K_0, \quad (4.117)$$

for integers $n = 0, \pm 1, \pm 2, \dots$. The energy spectrum becomes

$$\epsilon_n = s\gamma \sqrt{k^2 + p_n^2}. \quad (4.118)$$

According to the tight-binding model, armchair nanoribbons with a ribbon width of $N = 3m - 1$ have a linear dispersion originating from the Dirac cone. Actually, Eq. (4.116) is simplified to $B \sin(pW) = 0$ when $N = 3m - 1$. Thus,

$$p_n = \frac{n}{W} \pi \quad \text{for} \quad N = 3m - 1 \quad (4.119)$$

In this case, $n = 0$ gives the linear dispersion

$$\varepsilon_{n=0} = s\gamma|k|. \quad (4.120)$$

Thus, the massless Dirac equation accurately reproduces the low-energy electronic states of armchair nanoribbons.

The envelope function can be obtained as

$$\begin{pmatrix} f_A^K(x) \\ f_B^K(x) \\ f_A^{K'}(x) \\ f_B^{K'}(x) \end{pmatrix} = \frac{1}{\sqrt{4W}} \begin{pmatrix} s \\ -e^{-i\theta(p,k)} \\ s \\ e^{i\theta(p,k)} \end{pmatrix} \begin{pmatrix} e^{-ipx} \\ e^{ipx} \end{pmatrix}, \quad (4.121)$$

where the phase factor is defined as

$$e^{\pm i\theta(p,k)} = \frac{p \pm ik}{\sqrt{p^2 + k^2}}. \quad (4.122)$$

The whole envelope function including the longitudinal direction for each case can be obtained by multiplying the plane wave along the y -axis, i.e.,

$$F(\mathbf{r}) = \frac{1}{\sqrt{L_y}} \begin{pmatrix} f_A^K(x) \\ f_B^K(x) \\ f_A^{K'}(x) \\ f_B^{K'}(x) \end{pmatrix} e^{iky}, \quad (4.123)$$

where L_y is the length of the armchair nanoribbon.

4.7 Bearded Edges and Cove Edges

In this section, we discuss two other important edge shapes having translational symmetry of the zigzag axis, called *bearded* and *cove* edges. Although these two edges look more artificial than a pristine zigzag edge, they are interesting because they also exhibit non-bonding edge localization.

A bearded edge is a zigzag edge with additional π -electron hopping bonds as shown in Fig. 4.13(a). This type of edge was first studied by Klein [64]. In Fig. 4.13(b), the band structure of a semi-infinite graphene sheet with a bearded edge is shown. Interestingly, a partial flat band appears in the region $|ka| \leq 2\pi/3$, which is the opposite condition to that for a the semi-infinite graphene sheet

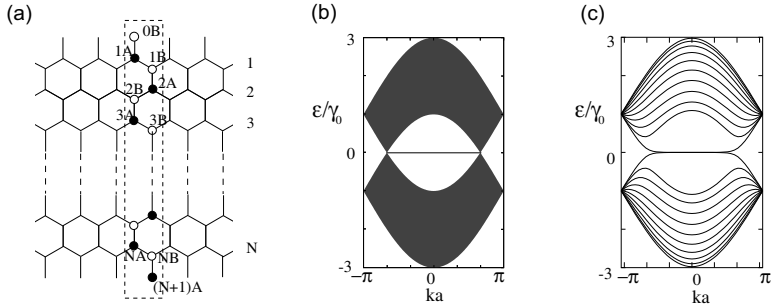


Figure 4.13 (a) Structure of a graphene ribbon with two bearded edges. (b) Energy band structure of a semi-infinite graphene sheet with a bearded edge. (c) Energy band structure of a bearded ribbon for $N = 10$.

with a zigzag edge. The analytic form of this edge state can be derived in a similar manner, used to derive the edge state for zigzag edges described in the previous section. If we consider the case of infinite N (Fig. 4.13(a)), the analytic solution can be written as

$$\psi_{nB} = (1/D_k)^n \quad \text{and} \quad \psi_{nA} = 0, \quad (4.124)$$

where $D_k = -2 \cos(ka/2)$. The convergence condition of the wave function, $|1/D_k| \leq 1$, gives the region of the edge state as $|ka| \leq 2\pi/3$. Since the penetration depth of the edge states increases toward $ka = \pm 2\pi/3$, small energy gaps appear near $ka = \pm 2\pi/3$ in the case of finite width ribbons owing to the bonding and anti-bonding interactions between the two edge states. The wave function of edge states for a bearded edge can also be described on the basis of the massless Dirac equation. As we have seen in Section 4.6.1, the wave function can be obtained as the counterpart of the edge state wave function for a zigzag edge.

Next we show a ribbon having a zigzag edge and a bearded edge as shown in Fig. 4.14(a). Since in this ribbon $|N_A - N_B| = 1$, where $N_A(N_B)$ is the number of sites belonging to the A(B) sublattice, there is a flat band at $\varepsilon = 0$ throughout the first BZ as shown in Fig. 4.14(b). The analytic solution of this flat band can be easily understood as the combination of two edge states for zigzag and bearded edges. In the region $|ka| < 2\pi/3$, the electrons are localized at the bearded edge, and in the region $|ka| > 2\pi/3$, the electrons are localized at the zigzag edge. At $ka = \pm 2\pi/3$, the electrons are

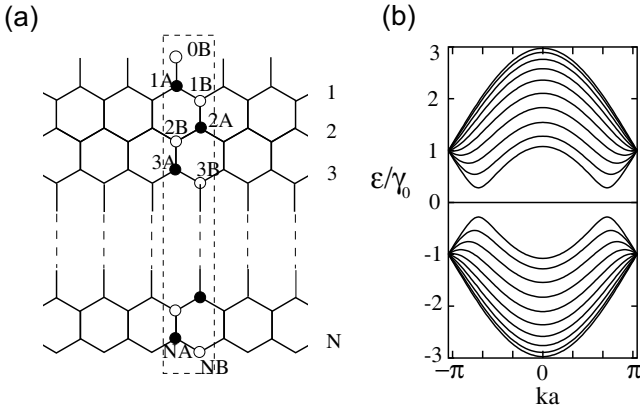


Figure 4.14 (a) Structure of a graphene ribbon with a zigzag edge and a bearded edge and (b) energy band structure for $N = 10$.

delocalized. Note that this ribbon is insulating because the flat band does not carry current and there are energy gaps between the flat band and next subbands.

A cove edge is a zigzag edge with additional attached hexagon rings. A semi-infinite graphene with a cove edge is shown in Fig. 4.15(a). For convenience, we divide the lattice structure into four sub-lattices called α , β , γ , and δ -sublattices as shown in Fig. 4.15(a). Figure 4.15(b) shows the schematic structure of a graphene nanoribbon with cove edges. The energy band structure of a graphene nanoribbon with cove edges for $N = 30$ is shown in Fig. 4.15(c). This case also has a partly flat band in the region $|kd| \leq 2\pi/3$, where $d = 2a$. Because the unit cell is double the size of the other two ribbons with zigzag or bearded edges, the analytic solution of the wave function for the cove edge state is more complicated than that for the zigzag and bearded edges. However, we can obtain the wave function of zero-energy edge states for a cove edge, which can be described using the transfer matrix method as [36]

$$\psi_{m\beta} = \frac{1}{2} \left[\frac{(-1)^m}{(\eta + \eta^*)^{m-1}} - \frac{1}{(\eta - \eta^*)^{m-1}} \right], \quad (4.125)$$

$$\psi_{m\delta} = \frac{1}{2} \left[\frac{(-1)^m}{(\eta + \eta^*)^{m-1}} + \frac{1}{(\eta - \eta^*)^{m-1}} \right]. \quad (4.126)$$

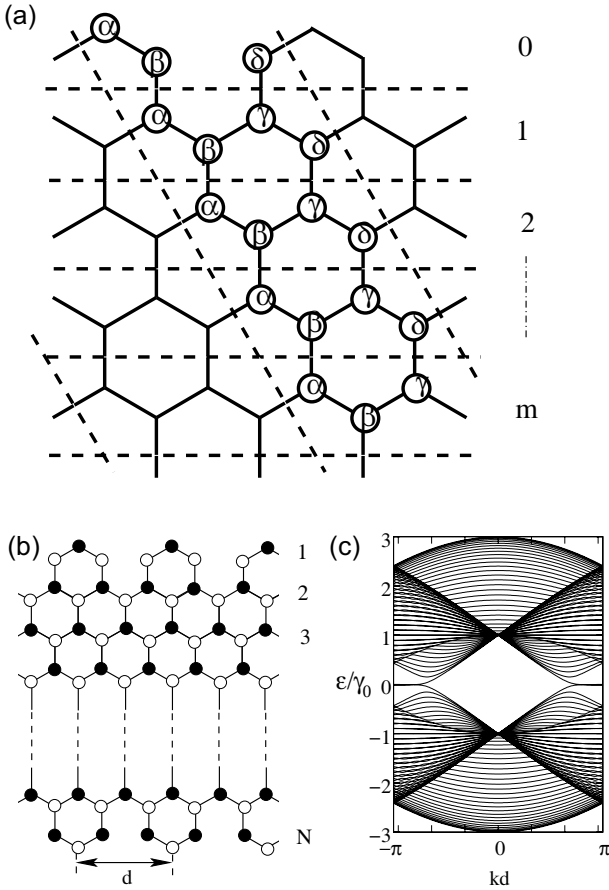


Figure 4.15 (a) Schematic figure of semi-infinite graphene sheet with a cove edge. (b) Structure of nanoribbon with cove edges and (c) corresponding energy band structure for $N = 30$. After Ref. [36].

$\psi_{m\alpha}$ and $\psi_{m\gamma}$ are identically zero for arbitrary m , i.e., they are nodal sites. Here $\eta = \exp(ikd/4)$ is the Bloch phase. The above wave function also converges in the region $2\pi/3 \leq |kd| \leq \pi$. This convergence condition corresponds to the region of the zero energy flat band shown in Fig. 4.15(c).

In general, an edge that is not parallel to an armchair axis has edge states. Actually, graphene ribbons with mixed armchair edges and zigzag edges also exhibit localized states [15, 56].

4.8 Electronic States in a Magnetic Field

In this section we consider the electronic states of graphene nanoribbons in a magnetic field. A magnetic field \mathbf{B} perpendicular to the graphene plane is incorporated in the transfer integral γ_{ij} by means of the Peierls phase, where γ_{ij} is defined as

$$\gamma_{ij} \longrightarrow \gamma_{ij} \exp \left[i 2\pi \frac{e}{ch} \int_i^j \mathbf{dl} \cdot \mathbf{A} \right], \quad (4.127)$$

\mathbf{A} is the vector potential and the integral is along the hopping path. This hopping integral with the Peierls phase is incorporated into the Hamiltonian of the tight-binding model given in Eq. (4.18). γ_{ij} is taken as $-\gamma_0$ only between nearest-neighbor sites as in the previous section. Otherwise, $\gamma_{ij} = 0$.

We define the magnitude of the magnetic flux passing through a single benzene ring of a graphene sheet in the unit of quantum flux ($\phi_0 = ch/e$) as ϕ . Since a single benzene ring has area $S_{\text{hex}} = \sqrt{3}a^2/2$, where $a = 0.246$ nm is the lattice constant of graphene, ϕ is given as $\phi = BS_{\text{hex}}/\phi_0$. Here $B = |\mathbf{B}|$ and $\phi = 1$ corresponds to 7.9×10^4 T. In this section, we consider the weak-magnetic-field limit, i.e., $\phi \ll 1$. Several values of magnetic flux with the corresponding magnetic field and magnetic length are summarized in Table 4.2. The magnetic length, l , is given by $l = \sqrt{ch/eB}$. We use a Landau gauge with $\mathbf{A} = (0, Bx, 0)$ for armchair nanoribbons and $\mathbf{A} = (-By, 0, 0)$ for zigzag nanoribbons to maintain the translational invariance. The coordination axis is the same as that in Fig. 4.3(a) and (b). Both vector potentials give a magnetic field perpendicular to the graphene nanoribbon plane, i.e., $\mathbf{B} = \nabla \times \mathbf{A} = (0, 0, B)$.

In ribbon-shaped systems, the ratio between the width of a ribbon and the magnetic length effectively characterizes the electronic states of the ribbon in a magnetic field. Therefore, we define the ratio between the ribbon width and the cyclotron diameter as the effective magnetic field \tilde{B} for convenience, which

Table 4.2 Several values of magnetic flux, magnetic field and magnetic length

Magnetic flux ϕ	Magnetic field B [T]	Magnetic length
1/100000	0.78	406.7a
1/10000	7.8	128.6a
1/1000	78	40.7a
1/100	780	12.8a

is given by $\tilde{B} = (W/d)^2$, where $d = 2l$. In the case of $\tilde{B} < 1$, since the cyclotron diameter is larger than the ribbon width the cyclotron motion of electrons is impeded and the Landau levels are not formed. Secondly, in the case of $\tilde{B} > 1$, since the cyclotron diameter is smaller than the ribbon width, the cyclotron motion of electrons is not disturbed except in the vicinity of ribbon edges and the Landau levels appear. Finally, in the case of $\tilde{B} \gg 1$, where the cyclotron diameter is much smaller than the ribbon width and is on the order of the lattice constant, the topology of the lattice becomes important.

4.8.1 Tight-Binding Model with Peierls Phase

Let us adapt the tight-binding Hamiltonian with the Peierls phase to graphene nanoribbons. The presence of a magnetic field modifies the hopping integral by appending the phase factor, which depends on the magnetic flux.

For armchair nanoribbons, the equations of motion for the tight-binding model for sites mA and mB can be written as

$$\begin{aligned} (\varepsilon/\gamma_0)\psi_{m,A} &= -\exp[-i(\frac{k}{2} + m\pi\phi)]\psi_{m,B} - \psi_{(m-1),B} - \psi_{(m+1),B}, \\ (\varepsilon/\gamma_0)\psi_{m,B} &= -\exp[+i(\frac{k}{2} + m\pi\phi)]\psi_{m,A} - \psi_{(m-1),A} - \psi_{(m+1),A}, \end{aligned} \quad (4.128)$$

where $m = 1, 2, 3, \dots, N$. The range of the wave number is $-\pi \leq k \leq \pi$. Note that these equations become Eq. (4.22) if we take the limit of $\phi = 0$. The boundary condition for armchair nanoribbons is the same as that in the case of zero magnetic field, i.e.,

$$\psi_{0,A} = \psi_{0,B} = \psi_{N+1,A} = \psi_{N+1,B} = 0. \quad (4.129)$$

Therefore, Eq. (4.128) can be written in a $2N \times 2N$ matrix form as

$$\hat{H}(k, \phi)\Psi(k, \phi) = \varepsilon(k, \phi)\Psi(k, \phi). \quad (4.130)$$

Here $\Psi(k, \phi)$ is the wave function

$$\Psi(k, \phi) = (\psi_{1A}, \psi_{2A}, \dots, \psi_{NA}, \psi_{1B}, \psi_{2B}, \dots, \psi_{NB})^T \quad (4.131)$$

and $^T(\dots)$ denotes the transpose operator. $\hat{H}(k, \phi)$ is a $2N \times 2N$ Hermite matrix and is decomposed into four submatrices of dimension $N \times N$ as

$$\hat{H}(k, \phi) = \begin{pmatrix} \hat{h}_{AA}(k, \phi) & \hat{h}_{AB}(k, \phi) \\ \hat{h}_{BA}(k, \phi) & \hat{h}_{BB}(k, \phi) \end{pmatrix}. \quad (4.132)$$

Because there is no electron hopping within the same sublattices, $\hat{h}_{AA} = \hat{h}_{BB} = 0$. On the other hand, Eq. (4.128) leads to the following tridiagonal matrix $\hat{h}_{AB}(k)$, whose matrix elements depend on magnetic flux ϕ :

$$\hat{h}_{AB}(k, \phi) = -\gamma_0 \begin{pmatrix} \xi^*(k, \phi; 1) & 1 & 0 & \dots & \dots & 0 \\ 1 & \xi^*(k, \phi; 2) & 1 & 0 & \dots & 0 \\ 0 & 1 & \xi^*(k, \phi; 3) & 1 & \dots & 0 \\ \vdots & & \ddots & \ddots & \ddots & \vdots \\ \vdots & & & 0 & 1 & \xi^*(k, \phi; N-1) & 1 \\ 0 & \dots & \dots & 0 & 1 & \xi^*(k, \phi; N) \end{pmatrix}. \quad (4.133)$$

Here we have defined $\xi(k, \phi; m)$ as

$$\xi(k, \phi; m) = \exp \left[+i \left(\frac{k}{2} + m\pi\phi \right) \right]. \quad (4.134)$$

Also, $(\dots)^*$ is the complex conjugate of (\dots) . $\hat{h}_{BA}(k)$ is the Hermite conjugate of $\hat{h}_{AB}(k)$, i.e., $\hat{h}_{BA}(k) = \hat{h}_{AB}^\dagger(k)$. We obtain the energy band structures for armchair nanoribbons in a magnetic field by numerically diagonalizing the above $2N \times 2N$ Hermite matrix for each fixed k and ϕ . In the numerical calculations, the factor $m\pi\phi$ in $\xi(k, \phi; m)$ is replaced as

$$m\pi\phi \rightarrow \left(m - 1 - \frac{N-1}{2} \right) \pi\phi, \quad (4.135)$$

to keep the energy band structures symmetric with respect to $k = 0$ for arbitrary magnetic flux. This replacement means that the origin of the x -axis is shifted to the center of the ribbon width.

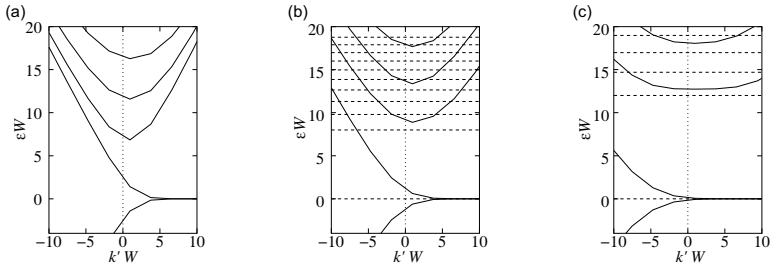


Figure 4.16 Scaled energy band structures of zigzag ribbons near $k = 2\pi/3$ for (a) $\tilde{B} = 0$, (b) $\tilde{B} = 4$ and (c) $\tilde{B} = 16$. Bold lines show the dispersions of zigzag ribbons. Here k' is the wave number measured from $k = 2\pi/3$. Dotted lines show the corresponding Landau levels of a graphene sheet for comparison.

Next we turn to the case of zigzag nanoribbons. The equations of motion for zigzag nanoribbons in a magnetic field can be derived as

$$(\varepsilon/\gamma_0)\psi_{m,A} = -\psi_{m-1,B} - g_k(\phi; m)\psi_{m,B}, \quad (4.136)$$

$$(\varepsilon/\gamma_0)\psi_{m,B} = -\psi_{m+1,A} - g_k(\phi; m)\psi_{m,A}. \quad (4.137)$$

Here $g_k(\phi; m) = 2 \cos(k/2 - m\pi\phi)$ for site index $m = 0, 1, 2, \dots, N + 1$. $\psi_{m,A}$ and $\psi_{m,B}$ describe the wave functions at mA and mB -sites, respectively. Since we have already performed the Fourier transformation along the longitudinal x -direction, the wave number appears in g_k owing to the Bloch phase. Also we have set $a = 1$ for simplicity. The boundary condition for zigzag nanoribbons is given by $\psi_{0,B} = \psi_{N+1,A} = 0$. Similarly to the case of armchair nanoribbons, the equations of motion form a $2N \times 2N$ matrix. The energy band structures in a magnetic field can be obtained by numerically diagonalizing the above $2N \times 2N$ Hermitic matrix. In the numerical calculations, the same replacement given by Eq. (4.135) is performed to keep the energy band structures symmetric with respect to $k = 0$ for arbitrary magnetic flux. This replacement means that the origin of the y -axis is shifted to the center of the ribbon width.

We now show that the band dispersions near $\varepsilon = 0$ can be scaled by the ribbon width W for sufficiently wide ribbons. In

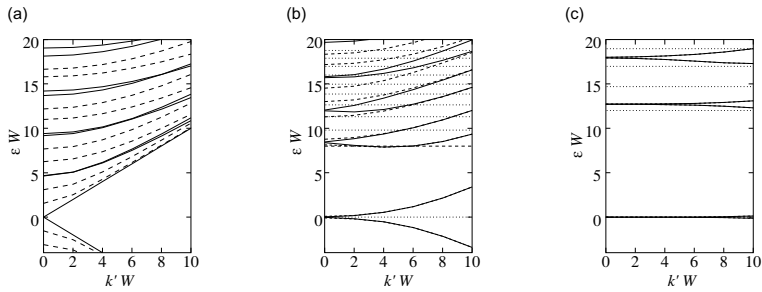


Figure 4.17 Scaled energy band structures of armchair ribbons near $k = 0$ for (a) $\tilde{B} = 0$, (b) $\tilde{B} = 4$ and (c) $\tilde{B} = 16$. Bold lines show the dispersions of metallic armchair ribbons ($N = 3m - 1$) and dashed lines show the dispersions of semiconducting armchair ribbons ($N \neq 3m - 1$). Dotted lines show the corresponding Landau levels of a graphene sheet for comparison.

Fig. 4.16, the scaled band structures are shown for (a) $\tilde{B} = 0$, (b) $\tilde{B} = 4$ and (c) $\tilde{B} = 16$. Here the energy and the wave number k' are scaled by W , where k' is the wave number measured from $k = 2\pi/3$. In the figures, the bold lines show the dispersions of zigzag ribbons and the dotted lines show the corresponding Landau levels of a graphene sheet for comparison. Similarly, the band dispersions of the armchair ribbons can be scaled. In Fig. 4.17, the scaled band structures are shown for (a) $\tilde{B} = 0$, (b) $\tilde{B} = 4$ and (c) $\tilde{B} = 16$. Bold lines show the dispersions of metallic armchair ribbons ($N = 3m - 1$) and dashed lines show those of semiconducting armchair ribbons ($N \neq 3m - 1$). The dotted lines show the corresponding Landau levels of a graphene sheet for comparison.

In Fig. 4.18, the magnetic field dependence of the energy gap for armchair and zigzag ribbons is shown. The energy gap of semiconducting armchair ribbons becomes negligible when the effective magnetic field \tilde{B} is much larger than 2. This condition is the same for a conventional quantum wire. However, we need a stronger magnetic field to collapse the energy gap (at $k = 2\pi/3$) of zigzag ribbons. This is due to the non-bonding character of the edge states. In the zero-field limit, $(1 - \Delta_{a(z)}(\tilde{B})/\Delta_{a(z)}(0))$ depends on \tilde{B}^4 for armchair ribbons and \tilde{B}^2 for zigzag ribbons.

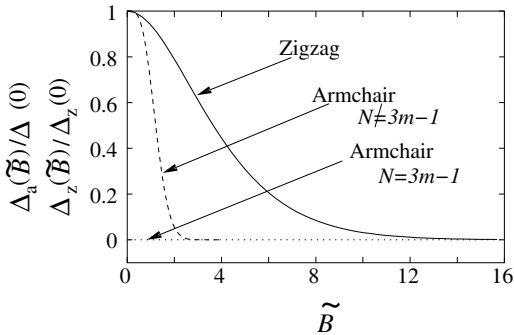


Figure 4.18 Magnetic field dependence of the energy gap of armchair (zigzag) ribbons at $k = 0$ ($k = 2\pi/3$), $\Delta_a(\tilde{B})$ ($\Delta_z(\tilde{B})$). The energy gaps are normalized by the energy gap, $\Delta_a(0)$ ($\Delta_z(0)$), at $\tilde{B} = 0$.

4.9 Orbital Diamagnetism and Pauli Paramagnetism

In the following two sections, the magnetic properties of nanographenes are discussed in the absence and presence of electron–electron interactions. It is well known that bulk graphene exhibits a large anisotropic diamagnetic susceptibility, while aromatic molecules have only weak diamagnetism. This means that the orbital diamagnetic susceptibility is sensitive to the size of graphene fragments. On the other hand, the sharp peak in the DOS due to the edge states gives a rather strong Pauli paramagnetic response; thus, the competition between these two components occurs in nanographene systems. Since the edge states also give the possibility of spin polarization at low temperatures due to the electron–electron interaction, we discuss the possibility of the appearance of localized spins at the edges.

4.9.1 Orbital Magnetization and Susceptibility

The observed magnetic susceptibility χ is the sum of four components: (1) localized spin susceptibility χ_{spin} , (2) diamagnetic susceptibility due to the core electrons χ_{core} , (3) Pauli paramagnetic susceptibility χ_P and (4) orbital diamagnetic susceptibility χ_{orb} due to the cyclotron motion of the itinerant electrons. Since we

neglect electron–electron interactions for the moment, χ_{spin} can be neglected. Furthermore, χ_{core} is unimportant here because it is small and basically temperature-independent. On the other hand, the Pauli paramagnetic susceptibility is related to the DOS at the Fermi level, which is an important component in zigzag graphene nanoribbons, where an enhanced DOS appears at the Fermi level. Note that χ_{P} is negligible in armchair ribbons, aromatic molecules and graphene sheets because their DOS is suppressed at the Fermi level. We will see below that since the DOS introduced by the edge states has a sharp peak at the Fermi energy, χ_{P} introduces a very pronounced temperature dependence that is nearly Curie-like. The diamagnetic contribution to the susceptibility is very familiar from the magnetic properties of graphene (see also Chapter 2). It is due to the orbital cyclotron motion of electrons in a field with a finite component perpendicular to the plane. Naturally, this diamagnetic response is highly anisotropic and only weakly temperature-dependent. From this we can conclude that in nanographenes with zigzag edges the susceptibility should mainly consist of these two competing contributions, χ_{P} and χ_{orb} . Hence, a crossover occurs from a high-temperature diamagnetic regime to a low-temperature paramagnetic regime, where the characteristic temperature depends on the width of the ribbon and on the orientation of the external field. Note that the field direction is an important physical quantity in distinguishing the magnitude of the two components.

In this section, we briefly summarize how to calculate the orbital diamagnetic susceptibility χ_{orb} for graphene ribbons using the tight-binding model. The free energy $F(H, T)$ including the magnetic field is given by

$$F(H, T) = \mu N - \frac{1}{\beta\pi} \int_{\text{BZ}} dk \sum_n \ln(1 + e^{-\beta(\epsilon_{k,n}(H) - \mu)}) \quad (4.138)$$

where $\beta = 1/k_{\text{B}}T$, μ is the chemical potential and $\epsilon_{k,n}(H)$ (n is the band index) is the energy spectrum of the graphene ribbon in the magnetic field calculated on the basis of the tight-binding model. Then the magnetic moment $M(H)$ and the magnetic susceptibility $\chi(H)$ per site for a finite temperature and arbitrary magnetic field H are given by the first and second derivatives of the free energy

with respect to H , respectively.

$$M(H) = -\frac{1}{N_e} \frac{\partial F}{\partial H}, \quad \text{and} \quad \chi(H) = \frac{1}{N_e} \frac{\partial M}{\partial H}. \quad (4.139)$$

Here let us briefly summarize the properties of large orbital diamagnetism in graphene. The origin of the large diamagnetism in graphene is due to the appearance of the Landau level at $\varepsilon = 0$. This was first shown by McClure [65]. Details of the derivation can be found in Chapter 2. When the energy dispersion is linear in k near the K or K' points, the Landau levels ε_n in the first BZ of the graphene sheet are expressed as

$$\varepsilon_n = \text{sgn}(n) \sqrt{|n|} \hbar \omega_B \quad (4.140)$$

with

$$\hbar \omega_B = \frac{\sqrt{2}}{l} \gamma, \quad (4.141)$$

where n is the index of the Landau levels and γ is the band parameter of the massless Dirac equation. Each Landau level has a characteristic feature and is very different from the Landau levels of an ordinary three-dimensional (3D) free electron gas, as shown in Fig. 4.19. Note that the zeroth Landau level is always located at $\varepsilon = 0$, and is not shifted by a magnetic field. We can easily show that all the Landau levels with zero and negative Landau indices that are occupied by the valence electrons act to increase the free energy in a magnetic field, and thus orbital diamagnetism appears. When the Fermi energy is located at zero energy, the oscillation of the free energy, which is known to cause the de Haas-van Alphen effect at low temperatures, has a cusp at $\varepsilon_F = 0$ and yields large orbital diamagnetism as shown in Fig. 4.20(a). In Fig. 4.20(b), we also show the free energy as a function of ε_F in the case of a 3D electron gas. As can be seen in this figure, there are no sharp cusp in the oscillation in contrast to the results in Fig. 4.20(a) for a graphene sheet. The expression for the orbital susceptibility of a graphene sheet at finite temperatures has been derived by McClure [65] using the massless Dirac equation is

$$\chi_{orb} = \int_{-\infty}^{\infty} \left(-\frac{\partial f(\varepsilon)}{\partial \varepsilon} \right) \chi(\varepsilon) d\varepsilon \quad (4.142)$$

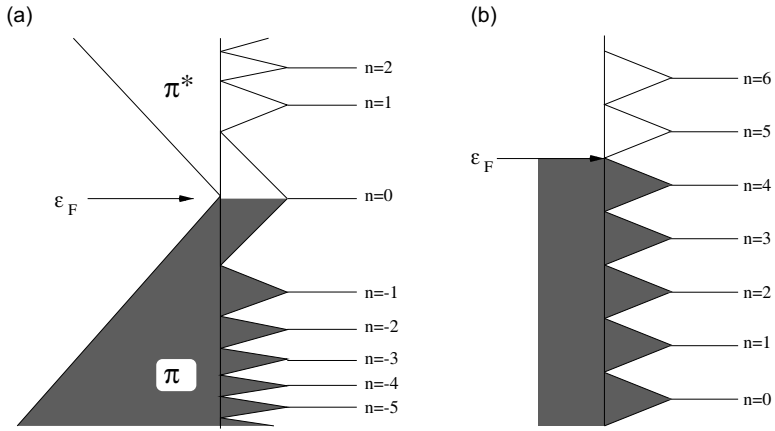


Figure 4.19 (a) Landau levels of graphene sheet near K point. (b) Landau levels of 3D free electron gas.

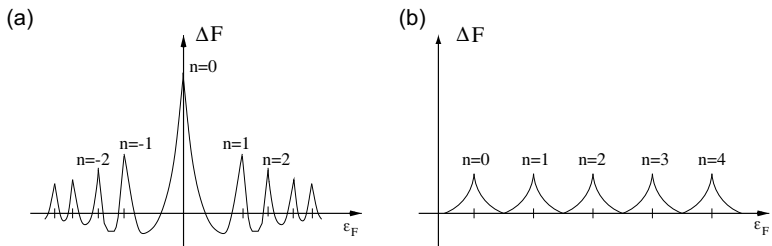


Figure 4.20 (a) Oscillation of free energy of graphene sheet as a function of ϵ_F . When the Fermi energy is located at zero, this oscillation has sharp cusps; however (b) a simple 3D metal does not exhibit such sharp cusps. The existence of this cusp is the origin of the large diamagnetism in graphenes.

with

$$\chi(\epsilon) = -\frac{g_v g_s \gamma^2}{6\pi} \left(\frac{e}{c\hbar}\right)^2 \delta(\epsilon), \quad (4.143)$$

where $f(\epsilon)$ is the Fermi–Dirac distribution function and $\delta(\epsilon)$ is Dirac’s delta function. $g_s (= 2)$ and $g_v (= 2)$ are the degeneracy of the spin and valley, respectively. Thus, the orbital susceptibility exhibits negatively diverging behavior with decreasing temperature, i.e., giant diamagnetism. A typical value of χ_{orb} for graphene at room temperature is 21.0×10^{-6} emu/g.

The orbital magnetism is affected by the system geometry and size. Here we show the Fermi energy dependence of χ_{orb} . In actual in real graphene materials, a small change in the carrier density from half-filling is possible and can even be controlled by the properties of the substrate on which the graphene sheet is placed. The calculated Fermi energy dependence is shown in Fig. 4.21(a), where it is found that χ_{orb}/W is a universal function of $\varepsilon_F W$ for the ribbon width W and Fermi energy ε_F . We normalize χ_{orb} by dividing it by W , since it is proportional to W . Furthermore, we multiply ε_F by W because the direct gap at $k = 0$ is proportional to $1/W$ at $k = 0$ for armchair ribbons and at $k = 2\pi/3$ for zigzag ribbons for large W .

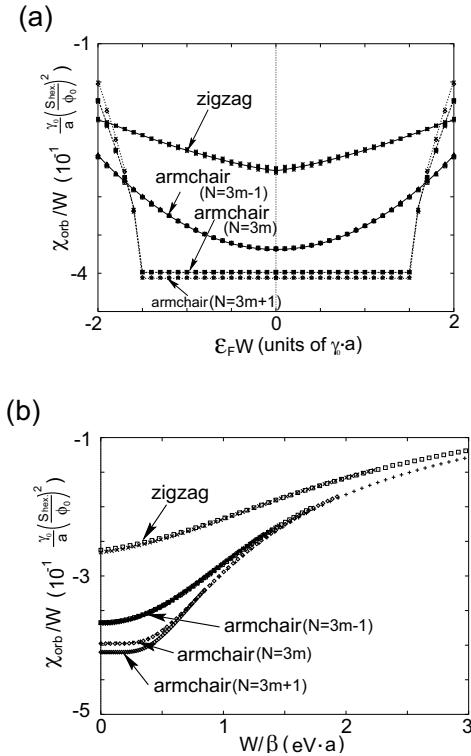


Figure 4.21 (a) Fermi energy dependence of the orbital magnetic moment χ_{orb} of graphene ribbons at $T = 0$. (b) Temperature dependence of χ_{orb} , where χ_{orb} is scaled by $1/W$ and β is scaled by W .

Figure 4.21(b) shows temperature dependence of χ_{orb} . In all cases the magnitude of χ_{orb} decreases with increasing temperature. It is also found that the temperature dependence of χ_{orb}/W scales as a function of βW because the energy gap is proportional to $1/W$. Our calculation also demonstrates that the edge effect becomes more significant at lower temperatures. Similar scaling properties can also be found in carbon nanotubes [66, 67].

4.9.2 Pauli Paramagnetism

In the previous section, we have seen that the orbital diamagnetic susceptibility depends on the edge shape in nanographene ribbons. Here we discuss another important component of the magnetic susceptibility, Pauli paramagnetic susceptibility χ_{P} , because zigzag ribbons have a sharp peak of the DOS at the Fermi level. The width of this peak has the meV order, which is comparable to the temperature scale at room temperature. Therefore, we expect that the Pauli susceptibility of zigzag ribbons will be sensitive to temperature, although the Pauli susceptibility of conventional metals is temperature independent. On the other hand, since the DOS of armchair ribbons at $\varepsilon = 0$ is zero or very small, we can neglect the effect of Pauli paramagnetism in armchair ribbons.

The magnetic moment due to the Zeeman effect is $M = \mu_{\text{B}} (n_{\uparrow} - n_{\downarrow})$, where μ_{B} is the Bohr magneton and n_{\uparrow} (n_{\downarrow}) denotes the electron density with up-spin (down-spin). The electron density at an arbitrary temperature for each spin is given by

$$n_{\sigma} = \frac{1}{\pi} \int_{1\text{stBZ}} dk \sum_n \frac{1}{1 + e^{\beta(\varepsilon_{n,k} - \sigma\mu_{\text{B}}H)}}, \quad (4.144)$$

where σ ($=\uparrow, \downarrow$) denotes the spin index. Therefore, the Pauli susceptibility χ_{P} per site is given by

$$\chi_{\text{P}} = \lim_{H \rightarrow 0} \frac{\partial M}{\partial H} = \frac{\beta\mu_{\text{B}}^2}{\pi N_e} \sum_n \int dk \frac{1}{\cosh(\beta\varepsilon_{n,k})}. \quad (4.145)$$

We numerically calculate the finite temperature Pauli susceptibility of graphene ribbons up to room temperature using this equation.

It is possible to determine the contribution of the edge states to χ_{P} . As we have seen in Section 4.3, the DOS due to the edge states is given by Eq. (4.21). After the substitution of Eq. (4.21) into

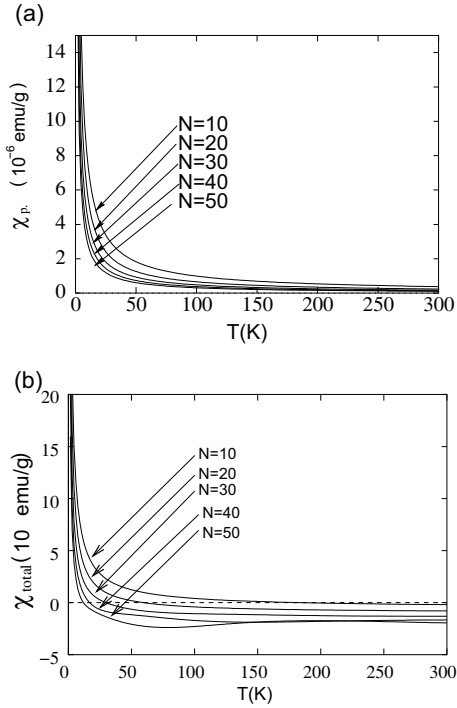


Figure 4.22 (a) Temperature dependence of χ_P for $N = 10, 20, \dots, 50$ up to room temperature. (b) Temperature dependence of total susceptibility χ , which is $\chi_{\text{orb}} + \chi_P$, shown for $N = 10, 20, \dots, 50$.

Eq. (4.145), we replace the k -integration by the energy integration. Then we can obtain the χ_P contribution due to the edge states as

$$\chi_P = \frac{1}{N_e N \beta^\alpha} \int dx \frac{x^\alpha}{\cosh x + 1} \sim \frac{1}{N} T^\alpha, \quad (4.146)$$

where $x = \beta \varepsilon_k$ and $\alpha = \frac{1}{N} - 1$. Interestingly, χ_P has a Curie-like temperature dependence. The exponent of χ_P depends on the ribbon width through α . When N becomes infinite, the exponent α approaches -1 and χ_P obeys the Curie law. However, in this limit, the contribution of χ_P is diminished by the factor $1/N$ in Eq. (4.146). Numerical results for the Pauli susceptibility χ_P of zigzag ribbons up to room temperature are shown in Fig. 4.22(a) for various values of N . As expected, because of the edge states, χ_P exhibits a Curie-like temperature dependence.

The observed susceptibility χ is essentially the sum of the contributions of the orbital χ_{orb} and the Pauli susceptibility χ_{P} . The temperature dependence of the total susceptibility χ is shown in Fig. 4.22(b). The total susceptibility χ exhibits diamagnetic behavior at high temperatures regime and paramagnetic behavior at low temperatures.

Here we remind readers that both aromatic molecules and bulk graphene exhibit diamagnetic behavior; however, nanographenes with zigzag edges exhibit strong paramagnetic behavior because of the edge states. If this paramagnetic behavior is experimentally detected, it will be indirect evidence of the existence of edge states.

4.10 Magnetic Instability

The presence of a sharp peak in the DOS near the Fermi energy should induce lattice distortion via the electron–phonon interaction and/or magnetic polarization via the electron–electron interaction. Because of the non-bonding character of the edge states, lattice distortion in the vicinity of zigzag edges is unlikely with the expected strength of the electron–phonon coupling [54]. The absence of lattice distortion was also confirmed by a DFT [20, 55]. Here, we examine the effect of the electron–electron interaction on the basis of the Hubbard model. The Hamiltonian is written as

$$H_{\text{Hubbard}} = -\gamma_0 \sum_{(i,j),\sigma} c_{i,\sigma}^\dagger c_{j,\sigma} + U \sum_i n_{i,\uparrow} n_{i,\downarrow}, \quad (4.147)$$

where the operator $c_{i,\sigma}^\dagger$ creates an electron with spin σ on site i , and $n_{i,\sigma} = c_{i,\sigma}^\dagger c_{i,\sigma}$. The indices of the sites in graphene ribbons are the same as those in Figs. 4.3(a) and (b). The first term of the Hamiltonian is simply the nearest-neighbor tight-binding model we have studied, but the electron spin degree of freedom is introduced. The second term describes the on-site Coulomb repulsion. Although two electrons with same spin cannot occupy a single site because of the Pauli exclusion principle, two electrons with opposite spin moment, however, can occupy a single site with the loss of some amount of Coulomb energy $U > 0$.

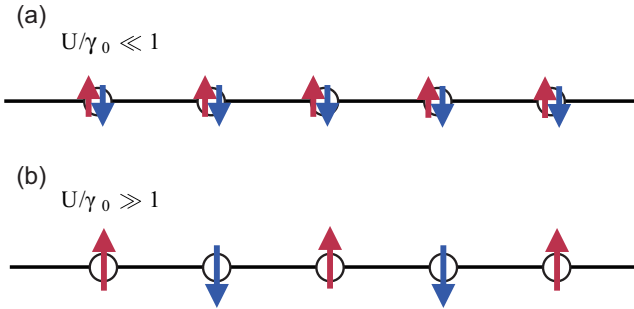


Figure 4.23 Schematic picture of mean field solution for Hubbard model in a 1D chain. Here we assume that the electron density is half-filling, i.e., the total number of electrons is equal to the total number of lattice sites. In this situation, $\langle n_{i\uparrow} \rangle + \langle n_{i\downarrow} \rangle = 1.0$ holds for each site. The red and blue arrows represent the electron density of up- and down-spins, respectively. The length of each arrow schematically represents the magnitude of the electron density. (a) Since the Coulomb repulsion is weak in the weak-coupling region of $U/\gamma_0 \ll 1$, the same amount of up- and down-spin electrons can co-exist in the same lattice site, i.e., $\langle n_{i\uparrow} \rangle - \langle n_{i\downarrow} \rangle \sim 0$ for each site i . Then the system becomes metallic. (b) On the other hand, in the strong-coupling region of $U/\gamma_0 \gg 1$, two electrons cannot remain on the same site because of the strong Coulomb repulsion. Then, the electron spin fully polarizes at each site, resulting in the antiferromagnetic order, $|\langle n_{i\uparrow} \rangle - \langle n_{i\downarrow} \rangle| \sim 1$.

The Hubbard model is an excellent model for describing two electronic phases in terms of the parameter of Coulomb interaction. When $U/\gamma_0 \ll 1$, since the electron hopping term dominates the energy loss due to the Coulomb interaction, the system becomes metallic (see Fig. 4.23(a)). On the other hand, for $U/\gamma_0 \gg 1$, the electrons need to have a large amount of energy hopping from sites to sites in the system to overwhelm the Coulomb interaction energy. Thus, the motion of electrons is frozen owing to the strong Coulomb interaction, hence the system enters a Mott insulating phase. Also, in this phase, two adjacent sites have an anti-ferromagnetic spin-spin correlation (see Fig. 4.23(b)).

Since the Coulomb interaction term gives rise to a product of four fermion operators, $n_{i,\uparrow}n_{i,\downarrow} \approx c_{i,\uparrow}^\dagger c_{i,\uparrow} c_{i,\downarrow}^\dagger c_{i,\downarrow}$, we cannot simply diagonalize the Hamiltonian to obtain the eigenstates. Thus, we introduce the unrestricted Hartree–Fock (HF) approximation, or the

mean-field approximation, which reduces the above four-fermion-operator term to a bilinear form. Let us now rewrite the electron density operator as

$$n_{i,\sigma} = \langle n_{i,\sigma} \rangle + (n_{i,\sigma} - \langle n_{i,\sigma} \rangle) \equiv \langle n_{i,\sigma} \rangle + \delta n_{i,\sigma}, \quad (4.148)$$

where $\langle n_{i,\sigma} \rangle$ denotes the statistical expectation value, self-consistently determined using the HF eigenstates. The final term, $\delta n_{i,\sigma}$, denotes the fluctuation from the expectation value. After we substitute Eq. (4.148) into Eq. (4.147), we take an approximation by neglecting the terms of the square of the fluctuation, $\delta^2 n_{i,\sigma}$. This is the essence of the mean field approximation. Now the Hamiltonian is rewritten as

$$H_{HF} = -\gamma_0 \sum_{\langle i,j \rangle, \sigma} c_{i,\sigma}^\dagger c_{j,\sigma} + U \sum_{i,\sigma} \left(\langle n_{i,-\sigma} \rangle - \frac{1}{2} \right) n_{i,\sigma}. \quad (4.149)$$

Here we have introduced $1/2$ as an offset to shift the band center to $\varepsilon = 0$. Note that the two sectors of up-spin and down-spin are now decoupled. Thus, the Hamiltonian can be further simplified to

$$H_{HF} = \sum_{\sigma} H_{\sigma} \quad (4.150)$$

with

$$H_{\sigma} = -\gamma_0 \sum_{\langle i,j \rangle} c_{i,\sigma}^\dagger c_{j,\sigma} + U \sum_i \left(\langle n_{i,-\sigma} \rangle - \frac{1}{2} \right) n_{i,\sigma}. \quad (4.151)$$

Readers might notice that this is simply the tight-binding model with on-site potential. However, there are two important points: (1) The on-site potential energy for an up-spin electron is given by the mean field of the down-spin electron density, and vice versa. (2) We have to self-consistently obtain the expectation value of the spin dependent electron density, $\langle n_{i,-\sigma} \rangle$, by using the eigenwave function of H_{HF} .

The Hamiltonian H_{σ} can be reduced to an eigenvalue problem of $2N \times 2N$ dimensions as before;

$$\hat{H}_{\sigma}(k)\Psi_{\sigma}(k) = \varepsilon_{\sigma}(k)\Psi_{\sigma}(k). \quad (4.152)$$

The $2N \times 2N$ matrix is decomposed into four $N \times N$ matrices as

$$\hat{H}_{\sigma}(k) = \begin{pmatrix} \hat{h}_{\sigma}^{AA}(k) & \hat{h}_{\sigma}^{AB}(k) \\ \hat{h}_{\sigma}^{BA}(k) & \hat{h}_{\sigma}^{BB}(k) \end{pmatrix}, \quad (4.153)$$

and

$$\Psi_\sigma(k) = (\psi_\sigma^{1A}, \psi_\sigma^{2A}, \dots, \psi_\sigma^{NA}, \psi_\sigma^{1B}, \psi_\sigma^{2B}, \dots, \psi_\sigma^{NB})^T. \quad (4.154)$$

Since the hopping term does not depend on the spin, $\hat{h}_\sigma^{AB}(k)$ is identically given by Eq. (4.48) for zigzag nanoribbons and Eq. (4.28) for armchair nanoribbons. Similarly, $\hat{h}_\sigma^{BA}(k)$ is the Hermite conjugate of $\hat{h}_\sigma^{AB}(k)$, i.e. $\hat{h}_\sigma^{BA}(k) = [\hat{h}_\sigma^{AB}(k)]^\dagger$. In addition, we have finite matrix elements in the submatrices $\hat{h}_\sigma^{AA}(k)$ and $\hat{h}_\sigma^{BB}(k)$ as

$$\hat{h}_\sigma^{AA}(k) = U \text{diag}[\langle n_{1A,-\sigma} \rangle, \langle n_{2A,-\sigma} \rangle, \langle n_{3A,-\sigma} \rangle, \dots, \langle n_{NA,-\sigma} \rangle] - \frac{1}{2} U \hat{I}, \quad (4.155)$$

and

$$\hat{h}_\sigma^{BB}(k) = U \text{diag}[\langle n_{1B,-\sigma} \rangle, \langle n_{2B,-\sigma} \rangle, \langle n_{3B,-\sigma} \rangle, \dots, \langle n_{NB,-\sigma} \rangle] - \frac{1}{2} U \hat{I}, \quad (4.156)$$

where diag denotes a diagonal matrix element. \hat{I} is the unit matrix of $N \times N$ dimensions, i.e.,

$$\hat{I} = \text{diag}(1, 1, 1, \dots, 1). \quad (4.157)$$

Now let us define the eigenvalues and eigenvectors that are obtained after the diagonalization of the above eigenvalue equation as $\varepsilon_{\nu,\sigma}(k)$ and

$$\Phi_{\nu,\sigma}(k) = (\phi_{\nu,\sigma}^{1A}, \phi_{\nu,\sigma}^{2A}, \dots, \phi_{\nu,\sigma}^{NA}, \phi_{\nu,\sigma}^{1B}, \phi_{\nu,\sigma}^{2B}, \dots, \phi_{\nu,\sigma}^{NB})^T, \quad (4.158)$$

respectively. Here $\nu = 1, 2, 3, \dots, 2N$ is the band index. The expectation value $\langle n_{mA,-\sigma} \rangle$ is self-consistently determined by

$$\langle n_{m\mu,-\sigma} \rangle = \sum_{\nu=1}^{2N} f(\varepsilon_\nu) \frac{1}{2\pi} \int_{-\pi}^{\pi} dk [\phi_{\nu,-\sigma}^{m\mu}(k)]^* \phi_{\nu,-\sigma}^{m\mu}(k), \quad \mu = A, B, \quad (4.159)$$

where $f(\varepsilon)$ is the Fermi–Dirac distribution function. In the following calculation, we maintain the chemical potential (Fermi energy; ε_F) of the system as $\varepsilon_F = 0$. This condition involves the assumption that the system is half-filled. In the limit of $U/\gamma_0 = 0$, there is no imbalance of charge densities between up- and down spins, i.e., $\langle n_{m\mu,\sigma} \rangle = \langle n_{m\mu,-\sigma} \rangle$ for an arbitrary site. However, with increasing U , an imbalance may occur, leading to finite spin density. Thus, we define the spin density, $M_{m\mu}$ ($\mu = A, \text{ or } B$), for each site as

$$M_{m\mu} = \frac{1}{2}\mu_B (\langle n_{m\mu,\uparrow} \rangle - \langle n_{m\mu,\downarrow} \rangle), \quad (4.160)$$

where μ_B is the Bohr magneton.

Figure 4.24 shows the U dependence of magnetization M/μ_B for several sites in zigzag nanoribbons with (a) $N = 2$, (b) $N = 3$ and (c) $N = 10$. The site index is defined in Fig. 4.3(b). The dashed lines are mean-field solutions for a graphene sheet. A peculiar feature of the zigzag nanoribbons is that large magnetic moments emerge on the edge carbon atoms, even for a small U , which is explained as follows: 2D graphene is a zero-gap metal with DOS equal to zero at the Fermi level, and thus the slope of the broken line rapidly increases at $U=U_c \sim 2.2\gamma_0$. This is consistent with the fact that graphene is nonmagnetic; thus, U is expected to be much smaller than U_c . On the other hand, the zigzag ribbons have a large DOS at the Fermi level originating from the edge states. Thus, nonzero magnetic solutions can emerge for infinitesimally small U as indicated by the present mean-field result. However, special emphasis should be placed on the behavior of the magnetization at edge site 1A. As shown in Fig. 4.24, the magnetization at site 1A rapidly increases with the ribbon width and reaches about 0.1, even at a small U/γ_0 of ≈ 0.1 .

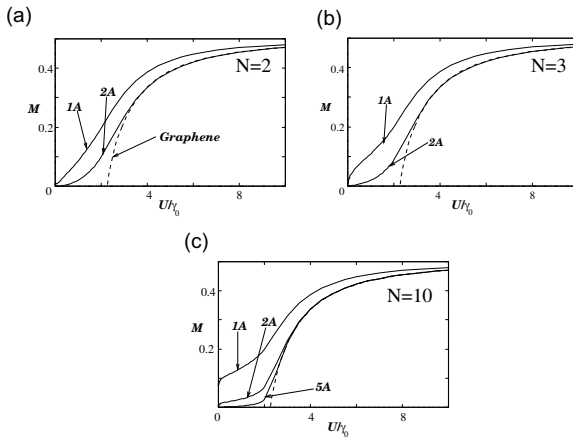


Figure 4.24 U dependence of the magnetization M (in the unit of μ_B) for zigzag ribbons with (a) $N = 2$, (b) $N = 3$ and (c) $N = 10$. The dashed lines correspond to the mean-field solutions for a graphene sheet.

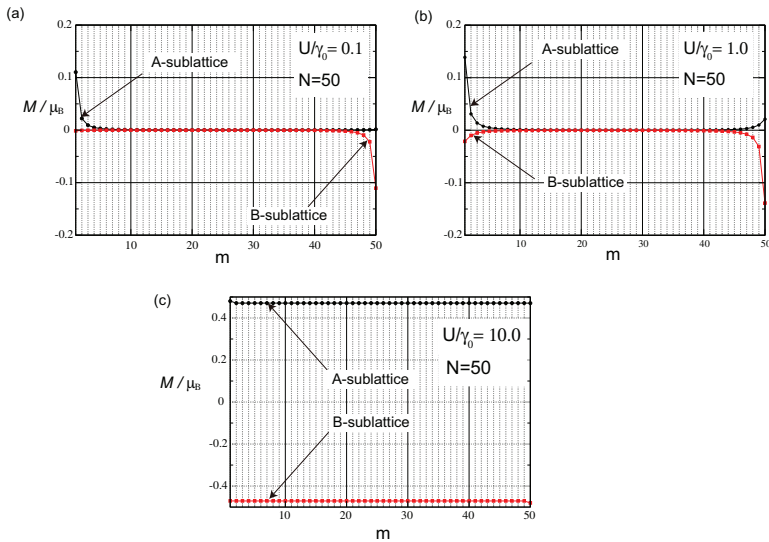


Figure 4.25 Distribution of magnetic moment at each carbon site for a zigzag nanoribbon of $N = 50$. The black (red) lines show the magnetic moment of A(B)-sublattice site on the m -th zigzag line of the nanoribbon. (a) $U/\gamma_0 = 0.1$, (b) $U/\gamma_0 = 1.0$, and (c) $U/\gamma_0 = 10.0$.

Figures 4.25(a) and (b) show the distribution of the magnetic moment at each carbon site for the case of zigzag nanoribbons with $N = 50$ for (a) $U/\gamma_0 = 0.1$, (b) $U/\gamma_0 = 1.0$ and (c) $U/\gamma_0 = 10$. It can be clearly seen that the spin polarization is developed only near the zigzag edge site in the weak Coulomb interaction in the regime of $U < U_c$. There is no spin polarization in the middle of nanoribbons. On the other, in the strong Coulomb interaction region, each electron is fully polarized at each site with developing anti-ferromagnetic order even in the middle of nanoribbons. Note that the mirror symmetry of magnetization, i.e., $M_{m,A} = -M_{N-m+1,B}$ ($m = 1, 2, 3, \dots, N$), is always preserved irrespective of the magnitude of U/γ_0 . Thus, the net magnetization of the system is always zero. Fig. 4.26(a) shows a schematic picture of the spin structure in real space for $U/\gamma = 0.1$. It can be seen that the electron magnetic moments align along a zigzag edge with a ferrimagnetic correlation. The total net magnetic moment is zero, however, because at the opposite edge the magnetic moments align in the opposite direction.

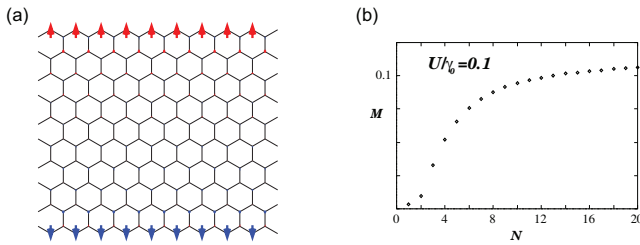


Figure 4.26 (a) Schematic magnetic structure of a zigzag ribbon with $N = 10$ at $U/t = 0.1$. (b) Dependence of the magnetization at the outermost site (1A) on the ribbon width N . The magnetization at site NB has the same magnitude but the opposite sign to that at site 1A.

The origin of this structure can also be explained from the nature of the edge states, which are responsible for the magnetization. The amplitude of the edge states is nonzero on only one of the two sublattices at an edge and decreases in the inward direction. Thus, the magnetic moment selectively increases on this sublattice forming a local ferrimagnetic spin configuration, whereas it rapidly decreases at the inner sites. The opposite edge sites, however, belong to different sublattices, and the total magnetization of the zigzag graphene ribbon is zero, although the vanishing total spin for the ground state is consistent with the exact statement of the half-filled Hubbard model [68]. Fig. 4.26(b) shows the dependence of magnetization at the outermost site (1A or NB) on the ribbon width N . The magnetization rapidly increases with the ribbon width and then saturates at approximately $N = 10$.

The energy band structures are shown in Fig. 4.27 for $U/\gamma_0 = 0.1$ and 1.0 with $N = 10$ (a) and $N = 50$ (b). Since a finite U opens the bandgap at $E = 0$ accompanying with the spin polarization, the peak in the DOS at $E = 0$ splits into two smaller peaks as can be seen in Fig. 4.27. Since the edge states are responsible for the edge spin polarization in the weak- U regime, the energy bandgap does not uniformly open in the region $2\pi/3 \leq |ka| \leq \pi$, i.e., the bandgap is larger near $ka = \pi$ than near $ka = 2\pi/3$. The U -dependence of the energy bandgap at $ka = \pi$ and $2\pi/3$ is shown Figs. 4.27 (c) and (d). It is clear that the bandgap opens at $ka = \pi$ even in the region $U \leq U_c$; however, a larger $U \geq U_c$ is necessary to open the

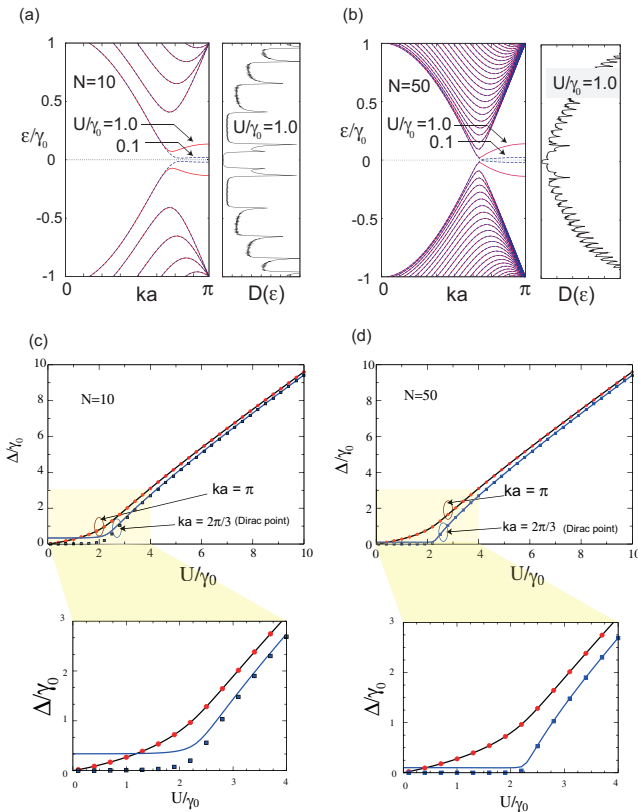


Figure 4.27 Energy band structures for zigzag nanoribbons with (a) $N = 10$ and (b) $N = 50$ when $U/\gamma_0 = 0.1$ and 1.0 , together with the DOS for $U/\gamma_0 = 1.0$. Since the edge states are responsible for the magnetic instability, the opening of energy bandgap increases toward $ka = \pi$ from the Dirac point ($ka = 2\pi/3$). U/γ_0 dependence of the energy bandgap at $ka = \pi$ and $ka = 2\pi/3$ (Dirac point) for (c) $N = 10$ and (d) $N = 50$. Each bottom panel is a magnified drawing in the small- U region. The bandgap at $ka = \pi$ opens even for an infinitesimal U ; however, a larger $U \geq U_c$ is necessary to open a bandgap around the Dirac point ($ka = 2\pi/3$). The closed red circles and closed blue squares are plots of the value of $2UM/\gamma_0$. The value of M is taken from the value at the $1A$ site (edge site) for $ka = \pi$ and from that at the $(N/2)A$ -site (in the middle of the nanoribbon) for $ka = 2\pi/3$.

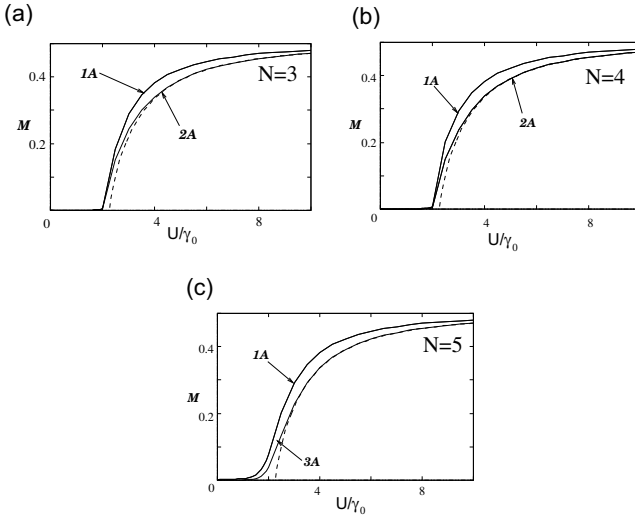


Figure 4.28 U dependence of the magnetization M (in the unit of μ_B) for armchair ribbons with (a) $N = 3$, (b) $N = 4$ and (c) $N = 5$. The dashed lines correspond to the mean-field solutions for a graphene sheet.

bandgap at $ka = 2\pi/3$ (Dirac point). The energy bandgap at $ka = \pi$ is well fitted by $2UM/\gamma_0$. Consequently, the corresponding spin wave modes become unconventional [17] because of this peculiar charge excitation spectrum.

Figure 4.28 shows the corresponding results for armchair ribbons with (a) $N = 3$, (b) $N = 4$ and (c) $N = 5$. Note that the armchair ribbons do not exhibit the singular magnetic behavior seen in zigzag nanoribbons.

The above scheme of the mean field approximation can even be applied in the presence of the second nearest neighbor interaction (γ_{2nd}) (see Fig. 4.29) by rewriting Eq. (4.151) as

$$\begin{aligned}
 H_\sigma = & -\gamma_0 \sum_{\langle i,j \rangle} c_{i,\sigma}^\dagger c_{j,\sigma} - \gamma_{2nd} \sum_{\langle\langle i,j \rangle\rangle} c_{i,\sigma}^\dagger c_{j,\sigma} \\
 & + U \sum_i \left(\langle n_{i,-\sigma} \rangle - \frac{1}{2} \right) n_{i,\sigma} - 3\gamma_{2nd} \sum_i n_{i,\sigma}, \quad (4.161)
 \end{aligned}$$

where $\langle\langle i, j \rangle\rangle$ means that the summation is taken if i and j are the second nearest neighbors. The offset of $-3\gamma_{2nd}$ is introduced

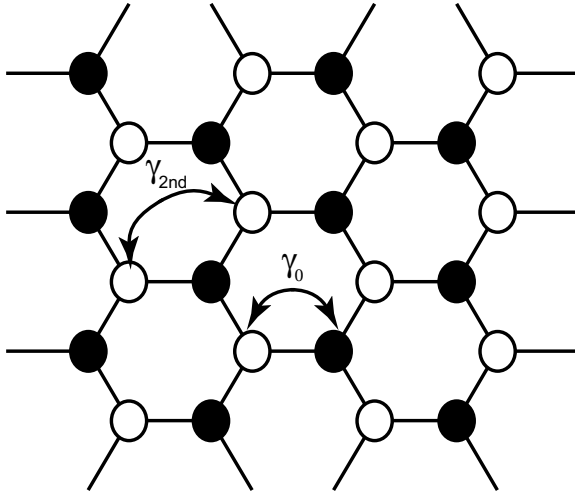


Figure 4.29 Definition of second-nearest-neighbor hopping γ_{2nd} .

to remove the uniform energy shift due to the occurrence of second-nearest-neighbor hopping. The inclusion of γ_{2nd} does not change the physical pictures obtained here; the only difference appears in the energy spectrum, which does not have particle-hole symmetry. However, the mirror symmetry of the magnetization, i.e., $M_{m,A} = -M_{N-m+1,B}$ ($m = 1, 2, 3, \dots, N$), is preserved. Although the second-nearest-neighbor hopping only has a weak effect, the inclusion of γ_{2nd} in the mean-field Hubbard model helps to reproduce the energy band structures calculated by DFT with the local spin density approximation (LSDA).¹

The ferrimagnetic spin polarization along a zigzag edge is interesting from the viewpoint of the magnetic properties of nanographenes. Nevertheless, the long-range order derived from the mean-field calculation is spurious because no finite-momentum long-range spin order is expected in a 1D system with full spin-rotation symmetry [69]. We may even argue that a quasi-long-range order, similar to that of the spin-1/2 Heisenberg chain, is not realized

¹The energy band structures based on the mean field Hubbard model with finite $\gamma_{2nd}/\gamma_0 = 0.1$ and $U/\gamma_0 = 1.0$ can be found in Fig. 4.31(b) in the following subsection. They are in qualitatively agreement with the band structure obtained by DFT-LSDA [20].

in zigzag ribbons of finite width because the unit cell of the ribbons contains an even number of sites; thus, Haldane's conjecture applies, i.e., the system should exhibit a spin gap [70]. This is very similar to the case of ladder systems with an even number of legs, which display a resonating valence bond ground state, i.e., a short range correlated spin-liquid state. With increasing ribbon width, however, random phase approximation analysis shows that the spin gap Δ_s decreases exponentially owing to the diminished overlap between the two edges [17, 30]. The absence of the spin excitation gap for zigzag nanoribbons with odd N is shown by mapping the effective Hamiltonian onto the nonlinear sigma model [28]. This means that zigzag edges favor spin polarization with the ferrimagnetic alignment. Thus, a systematic analysis of the topological networks in nanographenes will provide helpful guidelines for designing new magnetic carbon materials [25, 31] Also note that similar magnetic behavior is expected around a lattice vacancy or rough edges [29, 71].

4.10.1 Electric Field-Induced Half-Metallicity

Ferrimagnetic spin polarization appears along a zigzag edge as the solution of the mean-field approximation. However, as can be seen in Fig. 4.26(a), since two zigzag edges have magnetic moments with opposite directions total magnetization is zero in a zigzag nanoribbon. Thus, the energy bands for the up- and down-spins are degenerate.

The application of a transverse electric field to a zigzag nanoribbon can lift the spin degeneracy and induce a half-metallic state [19]. Half-metallic materials are crucial for the application of spintronics devices because they can be used as the source of spin-polarized current or as a spin-filtering device. A schematic figure of the DOS for half-metallic materials is drawn in Fig. 4.30 In half-metallic materials, the spin degeneracy near the Fermi energy is lifted, and one of the two spin states becomes absent. Thus, only one spin component contributes to the electronic conduction as a spin-polarized current.

The conceptual setup for an electric-field-induced half-metallic device is shown in Fig. 4.31(a). The electric voltage V is applied

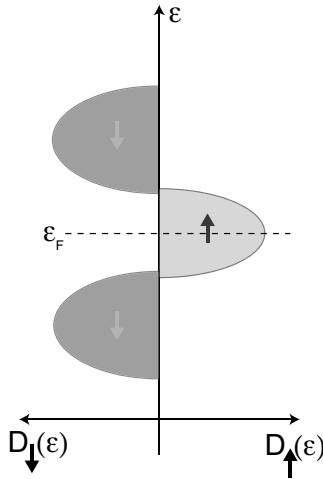


Figure 4.30 Schematic figure of DOS for half-metallic materials. The left (right) side shows the DOS for *down-* (*up-*) spins. The degeneracy between two spins is lifted. Since only one of the two spin states has a finite DOS near the Fermi energy (ϵ_F), only up spin states (in this case) contributes to electronic conduction. Thus, half-metallic materials can be a source of spin-polarized current or spin-filtering materials because the other spin states (in this case, down-spin) do not allow conduction.

along the transverse y direction of zigzag nanoribbons; thus, the electric field E is given by

$$E = \frac{V}{W}. \tag{4.162}$$

The transverse electric field is modeled here as the slope of the scalar potential. Thus, the potential at the i -th carbon site is written as

$$V(y_i) = V \left(\frac{1}{2} - \frac{y_i}{W} \right), \tag{4.163}$$

where y_i is the y -coordinate of i -th carbon site², and $W = \frac{\sqrt{3}}{2}Na + \frac{a}{\sqrt{3}}$ is the width of each zigzag nanoribbon. Here the potential term due to the transverse electric field is included in Eq. (4.161) as

²The y -coordinates for the mA - and mB -sites are written as $y_{mA} = \frac{a}{\sqrt{3}} + (m-1)\frac{\sqrt{3}}{2}a$ and $y_{mB} = \frac{\sqrt{3}}{2}ma$, respectively.

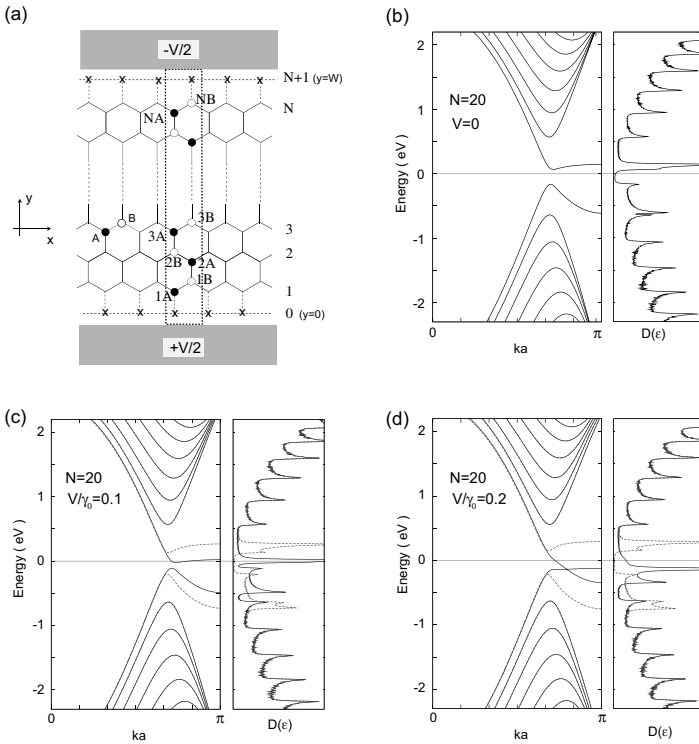


Figure 4.31 (a) Schematic figure of zigzag nanoribbons with the application of a transverse electric field. (b) Energy band structures and corresponding DOS for zigzag nanoribbons with $N = 20$. Here the hopping between next nearest neighbor sites is included. The applied electric field is (b) $V/\gamma_0 = 0$, (c) $V/\gamma_0 = 0.1$ and (d) $V/\gamma_0 = 0.2$. In Figs. (c) and (d), the blue lines and red dashed lines denote down- and up-spin states. In Fig. (b), the energy bands for up and down spin are degenerate. Here we set the Coulomb interaction to $U/\gamma_0 = 1$ and the second nearest neighbor hopping to $\gamma_{2nd}/\gamma_0 = 0.1$.

$$H_{V,\sigma}(V) = H_\sigma + \sum_i V_i n_{i,\sigma}, \quad (4.164)$$

where $V_i = V(y_i)$.

Figure 4.31(b) shows the energy band structure in the absence of an electric field. The two bands for up- and down spins are degenerate. The gradual application of a transverse electric field lifts the spin degeneracy as shown in Figs. 4.31(c) and (d). Here, the

energy gap for the up-spin starts closing with increasing electric field, while that for the down-spin remains open. In this situation, only up-spins become metallic in the vicinity of $\varepsilon = 0$ under the application of transverse electric field, i.e., the system becomes half-metallic. The control of half-metallicity using chemical edge modification or doping has been studied by several authors [37, 38, 72, 73].

4.11 Electronic Transport Properties

In this section we study the electronic transport properties of graphene nanoribbons using the Landauer approach. From the theoretical viewpoint, electronic transport through graphene nanoribbons exhibits a number of intriguing phenomena owing to their peculiar electronic properties. As one example, we show that zigzag nanoribbons with long-range impurities possess a perfectly conducting channel [56, 74], i.e., the absence of Anderson localization, even though that graphene nanoribbons can be viewed as quantum wires. This property is in strong contrast to the behavior of quantum wires composed of massive free electrons, in which conductance decays exponentially with increasing system length L and eventually vanishes in the limit of $L \rightarrow \infty$. Graphene nanojunction structures can provide zero-conductance Fano resonances in their low-energy electronic transport [75–78], which can be used for current control and on/off switching in graphene devices [75–78]. It has been suggested that the same type of geometrical configuration can be used as a filtering device to distinguish the valley states of the graphene wave function [79]. Furthermore, the ferrimagnetic spin-polarized state of a zigzag edge can be used for half-metallic conduction by applying an electric field in the transverse direction of a nanoribbon [19] as we have seen in the previous section. Interestingly, the electronic states of zigzag nanoribbons with the explicit inclusion of the spin-orbit interaction can be an initial minimum model for studying the spin Hall effect [80] or topological insulators [81, 82]. Recent theoretical studies have demonstrated a strong even-odd parity effect in p-n junctions [83, 84], the large fluctuation of conductance near the Dirac point due to the presence

of zero-conductance Fano resonances [85] and specular Andreev reflection at the interface between a normal metal superconductor and graphene [86].

In general, electron scattering in a quantum wire is described by the scattering matrix [87]. Through the scattering matrix \mathbf{S} , the amplitudes of the scattered waves \mathbf{O} are related to the incident waves \mathbf{I} as follows:

$$\begin{pmatrix} \mathbf{O}_L \\ \mathbf{O}_R \end{pmatrix} = \mathbf{S} \begin{pmatrix} \mathbf{I}_L \\ \mathbf{I}_R \end{pmatrix} = \begin{pmatrix} \mathbf{r} & \mathbf{t}' \\ \mathbf{t} & \mathbf{r}' \end{pmatrix} \begin{pmatrix} \mathbf{I}_L \\ \mathbf{I}_R \end{pmatrix}. \quad (4.165)$$

Here, \mathbf{r} and \mathbf{r}' are reflection matrices, \mathbf{t} and \mathbf{t}' are transmission matrices, and L and R denote the left and right lead lines, respectively. The Landauer-Büttiker formula [88] relates the scattering matrix to the conductance of a sample. The electric conductance is calculated using the Landauer-Büttiker formula

$$G(\varepsilon) = \frac{e^2}{\pi\hbar} \text{Tr}(\mathbf{t}\mathbf{t}^\dagger) = \frac{e^2}{\pi\hbar} g(\varepsilon). \quad (4.166)$$

Here the transmission matrix $\mathbf{t}(\varepsilon)$ is calculated by the recursive Green function method [89, 90]. For simplicity, throughout this section, we evaluate electric conductance in the unit of quantum conductance ($e^2/\pi\hbar$), i.e., dimensionless conductance $g(\varepsilon)$.

Since the transmission probability is unity in the clean limit, the dimensionless conductance at zero temperature is equal to the number of channels, i.e., the number of subbands across the Fermi energy. Thus, the dimensionless conductance is given as

$$g(E) = \begin{cases} n & \text{semiconducting armchair nanoribbon} \\ n + 1 & \text{metallic armchair nanoribbon} \\ 2n + 1 & \text{zigzag nanoribbon,} \end{cases} \quad (4.167)$$

where $n = 0, 1, 2, \dots$.

4.11.1 One-Way Excess Channel System

In this subsection, we consider the conductance of zigzag nanoribbons in the clean limit, which is simply given by the number of conducting channels. As can be seen in Fig. 4.32(a), there is always one excess left-going channel in the right valley (K) within the energy window $0 \leq \varepsilon/\gamma_0 \leq 1$. Analogously, there is one excess right-going channel in the left valley (K') within the same energy window.

Although the numbers of left-going and right-going channels are balanced in the whole system, if we focus on one of the two valleys, there is always one excess channel in one direction, i.e., a chiral mode.

Now let us consider the injection of electrons from the left side to the right side through the sample. When the chemical potential is changed from $\varepsilon = 0$, the quantization rule of the dimensionless conductance (g_K) in valley K is given as

$$g_K = n, \quad (4.168)$$

where $n = 0, 1, 2, \dots$. The quantization rule in valley K' is

$$g_{K'} = n + 1. \quad (4.169)$$

Thus, the conductance quantization of the zigzag nanoribbon in the clean limit near $\varepsilon = 0$ has the following odd-number quantization:

$$g = g_K + g_{K'} = 2n + 1. \quad (4.170)$$

Since we have an excess mode in each valley, the scattering matrix has some peculiar features that can be seen when we explicitly write the valley dependence in the scattering matrix. By denoting the contribution of the right valley (K) as $+$ and that of the left valley (K') as $-$, the scattering matrix can be rewritten as

$$\begin{pmatrix} \mathbf{O}_L^+ \\ \mathbf{O}_L^- \\ \mathbf{O}_R^+ \\ \mathbf{O}_R^- \end{pmatrix} = \begin{pmatrix} r & t' \\ t & r' \end{pmatrix} \begin{pmatrix} \mathbf{I}_L^+ \\ \mathbf{I}_L^- \\ \mathbf{I}_R^+ \\ \mathbf{I}_R^- \end{pmatrix}. \quad (4.171)$$

Note that the dimension of each column vector is not identical. Let us denote the number of right-going channels in valley K and the left-going channels in valley K' as n_c . For example, $n_c = 1$ at $\varepsilon = E_0$ in Fig. 4.32(a). Fig. 4.32(b) shows a schematic figure of the scattering geometry for the K and K' points. According to the figure, the dimensions of the column vectors are given as follows:

$$\begin{cases} \dim(\mathbf{I}_L^+) = n_c, & \dim(\mathbf{I}_R^+) = n_c + 1, \\ \dim(\mathbf{I}_L^-) = n_c + 1, & \dim(\mathbf{I}_R^-) = n_c, \end{cases} \quad (4.172)$$

and

$$\begin{cases} \dim(\mathbf{O}_L^+) = n_c + 1, & \dim(\mathbf{O}_R^+) = n_c, \\ \dim(\mathbf{O}_L^-) = n_c, & \dim(\mathbf{O}_R^-) = n_c + 1. \end{cases} \quad (4.173)$$

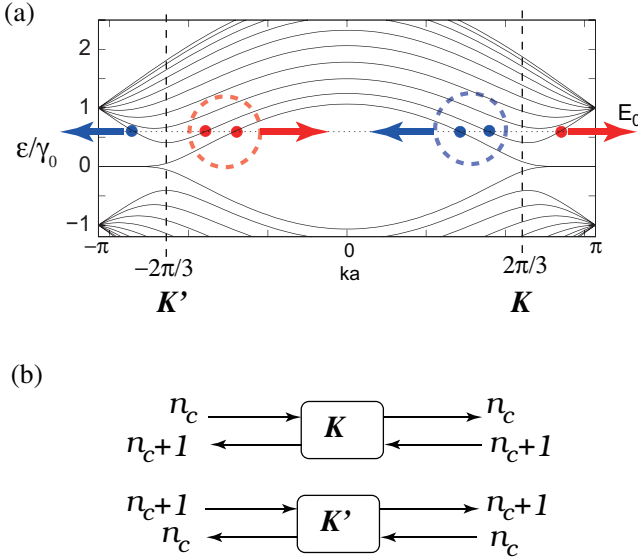


Figure 4.32 (a) Energy dispersion of zigzag ribbon with $N = 10$. The valleys in the energy dispersion near $k = 2\pi/3a$ ($k = -2\pi/3a$) originate from the Dirac K (K')-point of graphene. The red filled (blue unfilled) circles denote the right (left)-moving open channel at energy E_0 (dashed horizontal line). In the left (right) valley, the degeneracy between right and left moving channels is missing owing to one excess right (left)-going mode. The time-reversal symmetry under intra-valley scattering is also broken. (b) Schematic figure of scattering geometry at K and K' points in zigzag nanoribbons, where a single excess right-going mode exists for the K' point, and a single excess left-going mode exists for the K point. Here $n_c = 0, 1, 2, \dots$.

Subsequently, the reflection matrices have the following matrix structures:

$$\mathbf{r} = \begin{matrix} n_c & n_c + 1 \\ n_c + 1 & n_c \end{matrix} \begin{pmatrix} r_{++} & r_{+-} \\ r_{-+} & r_{--} \end{pmatrix}, \quad (4.174)$$

$$\mathbf{r}' = \begin{matrix} n_c + 1 & n_c \\ n_c & n_c + 1 \end{matrix} \begin{pmatrix} r'_{++} & r'_{+-} \\ r'_{-+} & r'_{--} \end{pmatrix}. \quad (4.175)$$

The reflection matrices become nonsquare when the intervalley scattering is suppressed, i.e., the off-diagonal submatrices (\mathbf{r}_{+-} , \mathbf{r}_{-+} and so forth) are zero.

When the electrons are injected from the left lead of the sample and the intervalley scattering is suppressed, a system with an excess channel is realized in valley K' . Thus, for single valley transport, \mathbf{r}_{--} and \mathbf{r}'_{--} are $n_c \times (n_c + 1)$ and $(n_c + 1) \times n_c$ matrices, and \mathbf{t}_{--} and \mathbf{t}'_{--} are $(n_c + 1) \times (n_c + 1)$ and $n_c \times n_c$ matrices, respectively. Noting the dimensions of \mathbf{r}_{--} and \mathbf{r}'_{--} , we find that $\mathbf{r}'_{--}\mathbf{r}_{--}$ and $\mathbf{r}'_{--}\mathbf{r}'_{--}$ have a single zero eigenvalue. Combining this property with the flux conservation relation ($\mathbf{S}^\dagger\mathbf{S} = \mathbf{S}\mathbf{S}^\dagger = \mathbf{1}$), we arrive at the conclusion that $\mathbf{t}_{--}\mathbf{t}'_{--}$ has an eigenvalue equal to unity, which indicates the presence of a perfectly conducting channel (PCC) only in the right-moving channels. Note that $\mathbf{t}'_{--}\mathbf{t}'_{--}$ does not have such an anomalous eigenvalue. If the set of eigenvalues for $\mathbf{t}'_{--}\mathbf{t}'_{--}$ is expressed as $\{T_1, T_2, \dots, T_{n_c}\}$, then that for $\mathbf{t}_{--}\mathbf{t}_{--}$ is expressed as $\{T_1, T_2, \dots, T_{n_c}, 1\}$. Thus, one of the transmission eigenvalues is identically one, which indicates that at least one of the conducting channels becomes perfectly transmission, i.e., the presence of a PCC. Thus, the dimensionless conductance g for the right-moving channels is given as

$$g_{K'} = \sum_{i=1}^{n_c+1} T_i = 1 + \sum_{i=1}^{n_c} T_i, \quad (4.176)$$

while that for the left-moving channels is

$$g'_{K'} = \sum_{i=1}^{n_c} T_i. \quad (4.177)$$

We see that $g_{K'} = g'_{K'} + 1$. Since the overall time reversal symmetry (TRS) of the system guarantees the relation

$$\begin{aligned} g'_K &= g_{K'}, \\ g'_{K'} &= g_K, \end{aligned} \quad (4.178)$$

the conductances $g = g_K + g_{K'}$ (right-moving) and $g' = g'_K + g'_{K'}$ (left-moving) are equivalent. If the probability distribution of $\{T_i\}$ is obtained as a function of L , we can describe the statistical properties of both g and g' . The evolution of the distribution function with increasing L is described by the DMPK (Dorokhov–Mello–Pereyra–Kumar) equation for transmission eigenvalues [91].

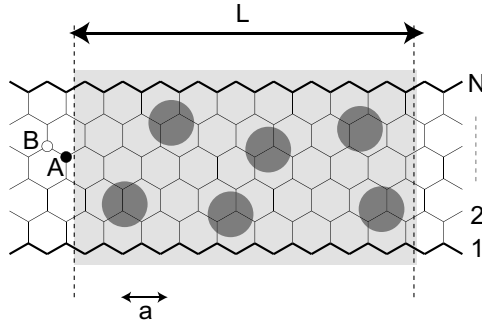


Figure 4.33 Schematic figure of zigzag nanoribbons with impurity potential. The shaded rectangle with length L indicates the disordered region. The shaded circles indicate randomly distributed impurities.

In the following, the presence of a PCC in disordered graphene nanoribbons will be demonstrated by numerical calculation. Recently Hirose *et al.* pointed out that the Chalker–Coddington model, which contains nonsquare reflection matrices with unitary symmetry, gives rise to a PCC [92]. However, systems with an excess channel in one direction have been considered difficult to realize. Therefore disordered graphene zigzag nanoribbons with long-range impurities might constitute the first realistic example of such systems. It is possible to extend the discussion to a generic multiple-excess channel model, where m -PCCs ($m = 2, 3, \dots$) appear [91]. Such systems can be realized by stacking zigzag nanographene ribbons [55]. The electronic transport due to a PCC resembles the electronic transport due to a chiral mode in a quantum Hall system.

4.11.2 Perfectly Conducting Channel: Absence of Anderson Localization

Here we give the numerical calculation result for the conductance of graphene nanoribbons with impurities on the basis of the tight-binding model. Figure 4.33 shows a schematic configuration of zigzag nanoribbons with long-range impurities. Here, the impurities are randomly distributed with density n_{imp} in the nanoribbons. In the numerical calculation, it is assumed that the each impurity potential has a Gaussian form of a range d . Thus, the on-site potential

energy at site i is written as

$$V(\mathbf{r}_i) = \sum_{\mathbf{r}_0(\text{random})} u \exp\left(-\frac{|\mathbf{r}_i - \mathbf{r}_0|^2}{d^2}\right), \quad (4.179)$$

where the strength u is uniformly distributed within the range $|u| \leq u_M$, \mathbf{r}_i is the coordinate of carbon site i and \mathbf{r}_0 is the center of the impurity. Here u_M satisfies the normalization condition

$$u_M \sum_{\mathbf{r}_i}^{(\text{full space})} \exp(-\mathbf{r}_i^2 d^2) / (\sqrt{3}/2) = u_0. \quad (4.180)$$

Thus, the total Hamiltonian can be written as

$$H = \sum_{i,j} \gamma_{i,j} c_i^\dagger c_j + \sum_i V_i c_i^\dagger c_i, \quad (4.181)$$

where $V_i = V(\mathbf{r}_i)$. The first term is simply the tight-binding Hamiltonian with nearest-neighbor hopping. In the following, we will see that the electronic transport properties of graphene nanoribbons crucially depend on the range of impurities (d). When the range of impurities is much larger than the lattice constant, i.e., $d \gg a$, a PCC appears, even in the dirty limit of disordered zigzag graphene nanoribbons, owing to the imbalance between left- and right-going modes as seen in the previous section. Thus, the absence of Anderson localization is confirmed. On the other hand, ordinal localization is induced when $d \ll a$. Hereafter, we call an impurity with $d \gg a$ long-range impurity (LRI), and one with $d \ll a$ short-range impurity (SRI).

We first focus on the case of LRIs using the potential with $d/a = 1.5$, which is sufficient to avoid inter-valley scattering. Fig. 4.34(a) shows the averaged dimensionless conductance as a function of L for different incident energies (Fermi energies), averaging over an ensemble of 40000 samples with different impurity configurations for ribbons of width $N = 10$. The potential strength and impurity density are chosen to be $u_0 = 1.0$ and $n_{imp.} = 0.1$, respectively. As a typical localization effect we observe that $\langle g \rangle$ gradually decreases with increasing length L (Fig. 4.34). However, $\langle g \rangle$ converges to 1 for LRIs (Fig. 4.34(a)), indicating the presence of a single PCC. It can be seen that $\langle g \rangle(L)$ has exponential behavior as

$$\langle g \rangle - 1 \sim \exp(-L/\xi) \quad (4.182)$$

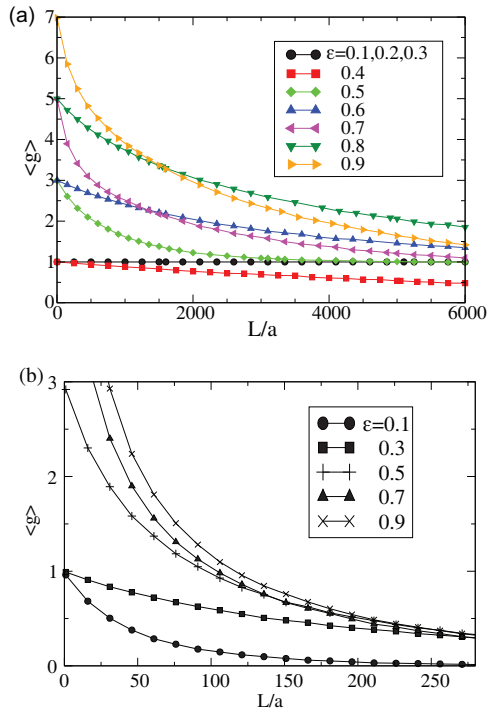


Figure 4.34 L -dependence of the average dimensionless conductance $\langle g \rangle$ for zigzag nanoribbon with $N = 10$; (a) $d/a = 1.5$ (no inter-valley scattering), (b) $d/a = 0.1$ (inter-valley scattering). Here $u_0 = 1.0$ and $n_{imp.} = 0.1$. More than 40000 samples with different impurity configurations are included in the ensemble average. After Ref. [74].

with ξ as the localization length. As the effect is connected to the subtle features of an excess mode in the band structure, it is natural that the result can only be valid for sufficiently weak potentials. For potential strengths comparable to the energy scale of the band structure, for example, the energy difference between the transverse modes, the result should be qualitatively altered [93]. Deviations from the limit $\langle g \rangle \rightarrow 1$ also occur if the incident energy lies at a value close to the change between $g = 2n - 1$ and $g = 2n + 1$ for a ribbon without disorder. This is visible in the above calculations for $E = 0.4$, where the limiting value is less than one (Fig. 4.34(a)).

Turning to the case of SRIs the inter-valley scattering becomes sufficiently large to ensure TRS, such that the perfect transport supported by the effective chiral mode in a single valley ceases to exist. In Fig. 4.34(b), the nanoribbon length dependence of the average conductance for SRIs is shown. Since SRIs cause the inter-valley scattering for any incident energy, the electrons tend to be localized and the averaged conductance decays exponentially, $\langle g \rangle \sim \exp(-L/\xi)$, without developing a PCC.

4.12 Summary

In this chapter, we have studied nanoscale effects on the electronic properties of graphene. The presence of a graphene edge crucially affects the electronic states of nanoscale graphene (nanographene). Two typical types of graphene edges, namely, *armchair* and *zigzag* edges exhibit completely different electronic properties. Although the presence of an armchair edge tends to preserve the properties of Dirac fermions of graphene, the presence of a zigzag edge is detrimental to Dirac fermions and induces localized edge states at the Fermi energy.

We also studied the electronic states of graphene nanoribbons in detail by analytically solving the eigenvalue problem for the tight-binding model for graphene nanoribbons. We have also shown how to construct the wave functions of graphene nanoribbons starting from the massless Dirac equation.

Since the presence of edge states produces a non-negligible large peak in the DOS at the Fermi energy of nanographene, the magnetic properties of nanographene are considerably different from those of graphene. In this chapter, we have seen that the presence of edge states indicates a crossover from diamagnetic behavior at room temperature to strong paramagnetic behavior at low temperatures in spite of the fact that bulk graphene is known to exhibit a strong diamagnetic response.

We have also seen that the strong Fermi instability of the edge states may induce the ferrimagnetic spin polarization even for very weak electron–electron interactions. The presence of zigzag edge states might be the source of the exotic magnetic response observed

in the experiment on nanographenes (see Chapter 6). The careful control and theoretical designing of such magnetic states will serve to realize carbon-based spintronic devices.

We have also discussed the role of edge states in the transport properties. In zigzag nanoribbons, the propagating modes in each valley contain a single chiral mode originating from a partially flat band at the band center due to the edge state. This feature gives rise to a PCC in the disordered system if impurity scattering does not connect the two valleys, i.e., for long-range impurity potentials. The presence of a PCC makes results in a clear difference between graphene nanoribbon systems and quantum wires with massive electrons.

The recent rapid progress in graphene research has revealed the unconventional electronic properties of massless Dirac fermion systems. However, we have seen that graphene can exhibit a strong nanoscale edge effect. Such an effect might be the origin of the diverse of physical and chemical properties of aromatic molecules. Further exploration of the physics of nanoscale graphene will be demanded for the realization of carbon-based devices.

Finally, since the discovery of graphene, more than a few thousands of papers have been published every year on graphene nanoribbons and nanographenes. In this chapter, since we have tried to explain the theoretical aspects of nanographenes and graphene nanoribbons using only minimal knowledge, all the relevant references may not be included. However, we hope that this chapter is a helpful introduction to the field for researchers of other fields and students.

References

1. K. S. Novoselov, A. K. Geim, S. V. Morozov, D. Jiang, Y. Zhang, S. V. Dubonos, I. V. Grigorieva, and A. A. Firsov, Electric field effect in atomically thin carbon films, *Science*. **306**(5296), 666–669, (2004).
2. A. K. Geim and K. S. Novoselov, The rise of graphene, *Nature Materials*. **6** (3), 183–191, (2007).
3. A. H. Castro Neto, F. Guinea, N. M. R. Peres, K. S. Novoselov, and A. K. Geim, The electronic properties of graphene, *Reviews of Modern Physics*. **81**(1), 109–162, (2009).

4. T. Ando, Theory of electronic states and transport in carbon nanotubes, *Journal of the Physical Society of Japan*. **74**(3), 777–817, (2005).
5. T. Ando, Physics of graphene - zero-mode anomalies and roles of symmetry, *Progress of Theoretical Physics Supplement*. (176), 203–226, (2008).
6. K. S. Novoselov, A. K. Geim, S. V. Morozov, D. Jiang, M. I. Katsnelson, I. V. Grigorieva, S. V. Dubonos, and A. A. Firsov, Two-dimensional gas of massless dirac fermions in graphene, *Nature*. **438**(7065), 197–200, (2005).
7. Y. B. Zhang, Y. W. Tan, H. L. Stormer, and P. Kim, Experimental observation of the quantum hall effect and berry's phase in graphene, *Nature*. **438**(7065), 201–204, (2005).
8. T. Ando and T. Nakanishi, Impurity scattering in carbon nanotubes - absence of back scattering, *Journal of the Physical Society of Japan*. **67**(5), 1704–1713, (1998).
9. T. Ando, T. Nakanishi, and R. Saito, Berry's phase and absence of back scattering in carbon nanotubes, *Journal of the Physical Society of Japan*. **67**(8), 2857–2862, (1998).
10. M. I. Katsnelson, K. S. Novoselov, and A. K. Geim, Chiral tunnelling and the klein paradox in graphene, *Nature Physics*. **2**(9), 620–625, (2006).
11. I. A. Luk'yanchuk and Y. Kopelevich, Phase analysis of quantum oscillations in graphite, *Physical Review Letters*. **93**(16), 166402, (2004).
12. K. I. Bolotin, K. J. Sikes, Z. Jiang, M. Klima, G. Fudenberg, J. Hone, P. Kim, and H. L. Stormer, Ultrahigh electron mobility in suspended graphene, *Solid State Communications*. **146**(9-10), 351–355, (2008).
13. A. A. Balandin, S. Ghosh, W. Z. Bao, I. Calizo, D. Teweldebrhan, F. Miao, and C. N. Lau, Superior thermal conductivity of single-layer graphene, *Nano Letters*. **8**(3), 902–907, (2008).
14. M. Fujita, K. Wakabayashi, K. Nakada, and K. Kusakabe, Peculiar localized state at zigzag graphite edge, *Journal of the Physical Society of Japan*. **65**(7), 1920–1923, (1996).
15. K. Nakada, M. Fujita, G. Dresselhaus, and M. S. Dresselhaus, Edge state in graphene ribbons: Nanometer size effect and edge shape dependence, *Physical Review B*. **54**(24), 17954–17961, (1996).
16. K. Wakabayashi, M. Fujita, H. Ajiki, and M. Sgrist, Electronic and magnetic properties of nanographite ribbons, *Physical Review B*. **59**(12), 8271–8282, (1999).

17. K. Wakabayashi, M. Sigrist, and M. Fujita, Spin wave mode of edge-localized magnetic states in nanographite zigzag ribbons, *Journal of the Physical Society of Japan*. **67**(6), 2089–2093, (1998).
18. K. Wakabayashi. *Low-Energy Physical Properties of Edge States in Nano-Graphites*. PhD thesis, University of Tsukuba, (2000). URL <http://hdl.handle.net/2241/2592>.
19. Y. W. Son, M. L. Cohen, and S. G. Louie, Half-metallic graphene nanoribbons, *Nature*. **444**(7117), 347–349, (2006).
20. Y. W. Son, M. L. Cohen, and S. G. Louie, Energy gaps in graphene nanoribbons, *Physical Review Letters*. **97**(21), 216803, (2006).
21. Y. Kobayashi, K. Fukui, T. Enoki, K. Kusakabe, and Y. Kaburagi, Observation of zigzag and armchair edges of graphite using scanning tunneling microscopy and spectroscopy, *Physical Review B*. **71**(19), 193406, (2005).
22. Y. Kobayashi, K. Fukui, T. Enoki, and K. Kusakabe, Edge state on hydrogen-terminated graphite edges investigated by scanning tunneling microscopy, *Physical Review B*. **73**(12), 125415, (2006).
23. Y. Niimi, T. Matsui, H. Kambara, K. Tagami, M. Tsukada, and H. Fukuyama, Scanning tunneling microscopy and spectroscopy studies of graphite edges, *Applied Surface Science*. **241**(1-2), 43–48, (2005).
24. K. Sugawara, T. Sato, S. Souma, T. Takahashi, and H. Suematsu, Fermi surface and edge-localized states in graphite studied by high-resolution angle-resolved photoemission spectroscopy, *Physical Review B*. **73**(4), 045124, (2006).
25. K. Wakabayashi and K. Harigaya, Magnetic structure of nano-graphite mobius ribbon, *Journal of the Physical Society of Japan*. **72**(5), 998–1001, (2003).
26. A. Yamashiro, Y. Shimoji, K. Harigaya, and K. Wakabayashi, Spin- and charge-polarized states in nanographene ribbons with zigzag edges, *Physical Review B*. **68**(19), 193410, (2003).
27. K. Harigaya and T. Enoki, Mechanism of magnetism in stacked nanographite with open shell electrons, *Chemical Physics Letters*. **351**(1-2), 128–134, (2002).
28. H. Yoshioka, Spin excitation in nano-graphite ribbons with zigzag edges, *Journal of the Physical Society of Japan*. **72**(9), 2145–2148, (2003).
29. H. Kumazaki and D. S. Hirashima, Local magnetic moment formation on edges of graphene, *Journal of the Physical Society of Japan*. **77**(4), 044705, (2008).

30. T. Hikiyara, X. Hu, H. H. Lin, and C. Y. Mou, Ground-state properties of nanographite systems with zigzag edges, *Physical Review B*. **68**(3), 035432, (2003).
31. K. Kusakabe and M. Maruyama, Magnetic nanographite, *Physical Review B*. **67**(9), 092406, (2003).
32. O. Hod, J. E. Peralta, and G. E. Scuseria, Edge effects in finite elongated graphene nanoribbons, *Physical Review B*. **76**(23), 233401, (2007).
33. M. Ezawa, Metallic graphene nanodisks: Electronic and magnetic properties, *Physical Review B*. **76**(24), 245415, (2007).
34. K. N. Kudin, Zigzag graphene nanoribbons with saturated edges, *Acs Nano*. **2**(3), 516–522, (2008).
35. T. Wassmann, A. P. Seitsonen, A. M. Saitta, M. Lazzeri, and F. Mauri, Structure, stability, edge states, and aromaticity of graphene ribbons, *Physical Review Letters*. **101**(9), 096402, (2008).
36. K. Wakabayashi, S. Okada, R. Tomita, S. Fujimoto, and Y. Natsume, Edge states and flat bands of graphene nanoribbons with edge modification, *Journal of the Physical Society of Japan*. **79**(3), 034706, (2010).
37. S. Dutta, A. K. Manna, and S. K. Pati, Intrinsic half-metallicity in modified graphene nanoribbons, *Physical Review Letters*. **102**(9), 096601, (2009).
38. E. J. Kan, Z. Y. Li, J. L. Yang, and J. G. Hou, Half-metallicity in edge-modified zigzag graphene nanoribbons, *Journal of the American Chemical Society*. **130**(13), 4224, (2008).
39. M. Y. Han, B. Ozyilmaz, Y. B. Zhang, and P. Kim, Energy band-gap engineering of graphene nanoribbons, *Physical Review Letters*. **98** (20), 206805, (2007).
40. Z. H. Chen, Y. M. Lin, M. J. Rooks, and P. Avouris, Graphene nano-ribbon electronics, *Physica E*. **40**(2), 228–232, (2007).
41. X. L. Li, X. R. Wang, L. Zhang, S. W. Lee, and H. J. Dai, Chemically derived, ultrasmooth graphene nanoribbon semiconductors, *Science*. **319**(5867), 1229–1232, (2008).
42. D. V. Kosynkin, A. L. Higginbotham, A. Sinitskii, J. R. Lomeda, A. Dimiev, B. K. Price, and J. M. Tour, Longitudinal unzipping of carbon nanotubes to form graphene nanoribbons, *Nature*. **458**(7240), 872–U5, (2009).
43. L. Y. Jiao, L. Zhang, X. R. Wang, G. Diankov, and H. J. Dai, Narrow graphene nanoribbons from carbon nanotubes, *Nature*. **458**(7240), 877–880, (2009).

44. X. Y. Yang, X. Dou, A. Rouhanipour, L. J. Zhi, H. J. Rader, and K. Mullen, Two-dimensional graphene nanoribbons, *Journal of the American Chemical Society*. **130**(13), 4216, (2008).
45. F. Molitor, J. Guttinger, C. Stampfer, D. Graf, T. Ihn, and K. Ensslin, Local gating of a graphene hall bar by graphene side gates, *Physical Review B*. **76**(24), 245426, (2007).
46. X. R. Wang, Y. J. Ouyang, X. L. Li, H. L. Wang, J. Guo, and H. J. Dai, Room-temperature all-semiconducting sub-10-nm graphene nanoribbon field-effect transistors, *Physical Review Letters*. **100**(20), 206803, (2008).
47. L. Tapasztó, G. Dobrik, P. Lambin, and L. P. Biro, Tailoring the atomic structure of graphene nanoribbons by scanning tunnelling microscope lithography, *Nature Nanotechnology*. **3**(7), 397–401, (2008).
48. C. Stampfer, J. Guttinger, S. Hellmueller, F. Molitor, K. Ensslin, and T. Ihn, Energy gaps in etched graphene nanoribbons, *Physical Review Letters*. **102**(5), 056403, (2009).
49. H. Miyazaki, S. Odaka, T. Sato, S. Tanaka, H. Goto, A. Kanda, K. Tsukagoshi, Y. Ootuka, and Y. Aoyagi, Coulomb blockade oscillations in narrow corrugated graphite ribbons, *Applied Physics Express*. **1**(2), 024001, (2008).
50. X. T. Jia, M. Hofmann, V. Meunier, B. G. Sumpter, J. Campos-Delgado, J. M. Romo-Herrera, H. B. Son, Y. P. Hsieh, A. Reina, J. Kong, M. Terrones, and M. S. Dresselhaus, Controlled formation of sharp zigzag and armchair edges in graphitic nanoribbons, *Science*. **323**(5922), 1701–1705, (2009).
51. L. C. Campos, V. R. Manfrinato, J. D. Sanchez-Yamagishi, J. Kong, and P. Jarillo-Herrero, Anisotropic etching and nanoribbon formation in single-layer graphene, *Nano Letters*. **9**(7), 2600–2604, (2009).
52. J. M. Cai, P. Ruffieux, R. Jaafar, M. Bieri, T. Braun, S. Blankenburg, M. Muoth, A. P. Seitsonen, M. Saleh, X. L. Feng, K. Mullen, and R. Fasel, Atomically precise bottom-up fabrication of graphene nanoribbons, *Nature*. **466**(7305), 470–473, (2010).
53. P. R. Wallace, The band theory of graphite, *Physical Review*. **71**(9), 622–634, (1947).
54. M. Fujita, M. Igami, and K. Nakada, Lattice distortion in nanographite ribbons, *Journal of the Physical Society of Japan*. **66**(7), 1864–1867, (1997).
55. Y. Miyamoto, K. Nakada, and M. Fujita, First-principles study of edge states of h-terminated graphitic ribbons, *Physical Review B*. **59** (15), 9858–9861, (1999).

56. K. Wakabayashi, Y. Takane, M. Yamamoto, and M. Sigrist, Edge effect on electronic transport properties of graphene nanoribbons and presence of perfectly conducting channel, *Carbon*. **47**(1), 124–137, (2009).
57. K. Wakabayashi, Electronic states of graphene nanoribbons and analytical solutions, *Science and Technology of Advanced Materials*. **11**, 054504, (2010).
58. R. Saito, M. Fujita, G. Dresselhaus, and M. S. Dresselhaus, Electronic-structure of graphene tubules based on c-60, *Physical Review B*. **46**(3), 1804–1811, (1992).
59. R. Saito, M. Fujita, G. Dresselhaus, and M. S. Dresselhaus, Electronic-structure of chiral graphene tubules, *Applied Physics Letters*. **60**(18), 2204–2206, (1992).
60. K. Sasaki and K. Wakabayashi, Chiral gauge theory for the graphene edge, *Physical Review B*. **82**(3), 035421, (2010).
61. K. Sasaki, M. Yamamoto, S. Murakami, R. Saito, M. S. Dresselhaus, K. Takai, T. Mori, T. Enoki, and K. Wakabayashi, Kohn anomalies in graphene nanoribbons, *Physical Review B*. **80**(15), 155450, (2009).
62. K. Sasaki, R. Saito, K. Wakabayashi, and T. Enoki, Identifying the orientation of edge of graphene using g band raman spectra, *Journal of the Physical Society of Japan*. **79**(4), 044603, (2010).
63. L. Brey and H. A. Fertig, Electronic states of graphene nanoribbons studied with the dirac equation, *Physical Review B*. **73**(23),–(2006).
64. D. J. Klein, Graphitic polymer strips with edge states, *Chemical Physics Letters*. **217**(3), 261–265, (1994).
65. J. W. McClure, Diamagnetism of graphite, *Physical Review*. **104**(3), 666–671, (1956).
66. H. Ajiki and T. Ando, Magnetic-properties of carbon nanotubes, *Journal of the Physical Society of Japan*. **62**(7), 2470–2480, (1993).
67. J. P. Lu, Novel magnetic-properties of carbon nanotubes, *Physical Review Letters*. **74**(7), 1123–1126, (1995).
68. E. H. Lieb, 2 theorems on the hubbard-model, *Physical Review Letters*. **62**(10), 1201–1204, (1989).
69. L. Pitaevskii and S. Stringari, Uncertainty principle, quantum fluctuations, and broken symmetries, *Journal of Low Temperature Physics*. **85** (5-6), 377–388, (1991).
70. S. Gopalan, T. M. Rice, and M. Sigrist, Spin ladders with spin gaps - a description of a class of cuprates, *Physical Review B*. **49**(13), 8901–8910, (1994).

71. O. V. Yazyev, Magnetism in disordered graphene and irradiated graphite, *Physical Review Letters*. **101**(3), 037203, (2008). PRL.
72. O. Hod, V. Barone, J. E. Peralta, and G. E. Scuseria, Enhanced half-metallicity in edge-oxidized zigzag graphene nanoribbons, *Nano Letters*. **7**(8), 2295–2299, (2007).
73. O. Hod, V. Barone, and G. E. Scuseria, Half-metallic graphene nanodots: A comprehensive first-principles theoretical study, *Physical Review B*. **77**(3), 035411, (2008).
74. K. Wakabayashi, Y. Takane, and M. Sigrist, Perfectly conducting channel and universality crossover in disordered graphene nanoribbons, *Physical Review Letters*. **99**(3), 036601, (2007).
75. K. Wakabayashi and M. Sigrist, Zero-conductance resonances due to flux states in nanographite ribbon junctions, *Physical Review Letters*. **84**(15), 3390–3393, (2000).
76. K. Wakabayashi, Electronic transport properties of nanographite ribbon junctions, *Physical Review B*. **64**12(12), 125428, (2001).
77. K. Wakabayashi and T. Aoki, Electrical conductance of zigzag nanographite ribbons with locally applied gate voltage, *International Journal of Modern Physics B*. **16**(32), 4897–4909, (2002).
78. M. Yamamoto and K. Wakabayashi, Control of electric current by graphene edge structure engineering, *Applied Physics Letters*. **95**(8), 082109, (2009).
79. A. Rycerz, J. Tworzydło, and C. W. J. Beenakker, Valley filter and valley valve in graphene, *Nature Physics*. **3**(3), 172–175, (2007).
80. C. L. Kane and E. J. Mele, $Z(2)$ topological order and the quantum spin hall effect, *Physical Review Letters*. **95**(14), 146802, (2005).
81. M. Z. Hasan and C. L. Kane, Colloquium: Topological insulators, *Reviews of Modern Physics*. **82**(4), 3045–3067, (2010).
82. S. Murakami, Quantum spin hall phases, *Progress of Theoretical Physics Supplement*. (176), 279–301, (2008). 407FD Times Cited:3 Cited References Count:37.
83. A. R. Akhmerov, J. H. Bardarson, A. Rycerz, and C. W. J. Beenakker, Theory of the valley-valve effect in graphene nanoribbons, *Physical Review B*. **77**(20), 205416, (2008).
84. J. Nakabayashi, J. Nakabayashi, D. Yamamoto, and S. Kurihara, Band-selective filter in a zigzag graphene nanoribbon, *Physical Review Letters*. **102**(6), 066803, (2009).
85. K. Wakabayashi and M. Sigrist, Enhanced conductance fluctuation due to the zero-conductance Fano resonances in the quantum point contact

- on graphene, *Journal of the Physical Society of Japan*. **77**(11), 113708, (2008).
86. C. W. J. Beenakker, Specular andreev reflection in graphene, *Physical Review Letters*. **97**(6), 067007, (2006).
87. C. W. J. Beenakker, Random-matrix theory of quantum transport, *Reviews of Modern Physics*. **69**(3), 731–808, (1997).
88. M. Buttiker, Y. Imry, R. Landauer, and S. Pinhas, Generalized many-channel conductance formula with application to small rings, *Physical Review B*. **31**(10), 6207–6215, (1985).
89. A. Mackinnon, The calculation of transport-properties and density of states of disordered solids, *Zeitschrift Fur Physik B-Condensed Matter*. **59**(4), 385–390, (1985).
90. T. Ando, Quantum point contacts in magnetic-fields, *Physical Review B*. **44**(15), 8017–8027, (1991).
91. Y. Takane and K. Wakabayashi, Conductance of disordered wires with unitary symmetry: Role of perfectly conducting channels, *Journal of the Physical Society of Japan*. **76**(5), 053701, (2007).
92. K. Hirose, T. Ohtsuki, and K. Slevin, Quantum transport in novel chalker-coddington model, *Physica E*. **40**(5), 1677–1680, (2008).
93. K. Wakabayashi, Numerical study of the lattice vacancy effects on the single-channel electron transport of graphite ribbons, *Journal of the Physical Society of Japan*. **71**(10), 2500–2504, (2002).

Chapter 5

Spin Structure of Polycyclic Aromatic Hydrocarbons

Akihito Konishi and Takashi Kubo

*Department of Chemistry, Graduate School of Science, Osaka University,
Machikaneyama 1-1, Toyonaka, Osaka 560-0043, Japan
kubo@chem.sci.osaka-u.ac.jp*

5.1 Introduction

In Chapter 2, graphene is discussed from the viewpoint of physics. When a graphene sheet is cut into nano-size fragments, nano-size graphene, which is called nanographene, is created.

Nanographene is a two-dimensional material with a hexagonal network of sp^2 -carbons. In nanographene, one can see the structures of many polycyclic aromatic hydrocarbons (PAHs) such as hexabenzocoronene, perylene, anthracene, and naphthalene, and ultimately benzene. This means that the property of PAHs would be related to that of nanographene. Accordingly, in this chapter, we discuss nanographene from the viewpoint of PAHs.

The electronic structure of nanographene is strongly influenced by the shape of its edge, and a large spin density originating from non-bonding π -state appears on zigzag edges, as discussed

Physics and Chemistry of Graphene: Graphene to Nanographene

Edited by Toshiaki Enoki and Tsuneya Ando

Copyright © 2013 Pan Stanford Publishing Pte. Ltd.

ISBN 978-981-4241-48-9 (Hardcover), 978-981-4241-49-6 (eBook)

www.panstanford.com

in Chapters 4 and 6. This so-called *edge state* might be the term that is usually used for nanographene and graphene. However, some PAHs would also possess similar spin state at their molecular edges, because PAHs are the structural component of nanographene. If so, what is the origin of the edge state of PAHs?

PAHs naturally have distinct edge structures. Therefore, it is expected that PAHs become a good model for examining the edge state of nanographene if a proper molecular design is given.

This chapter first describes a brief introduction of category of PAHs and then presents the concept of *Clar's aromatic sextet*, which is simple but important (and useful) for understanding the electronic structure of PAHs. Next, we focus on the topological effect of six-membered rings on the spin state using the Ovchinnikov rule and the Borden–Davidson rule. In the later sections, we present the recent theoretical and experimental studies on the edge state of relatively large PAHs.

5.2 A Brief Introduction of PAHs

5.2.1 Categories of Polycyclic Aromatic Hydrocarbons

PAHs are composed of fused rings, and unlimited possibilities of a ring-fusion manner lead to the diversity of molecular structures. Therefore, the compounds in this chapter are limited to the structures containing mostly six-membered ring. The simplest-fused aromatic hydrocarbon is naphthalene, which has two adjacent rings. The next larger system has three rings and there are three structural isomers: anthracene, phenanthrene, and phenalene. Anthracene and phenanthrene are derived from *ortho-fusion* of the third ring with naphthalene, and phenalenylyl from *ortho- and peri-fusion*. In *ortho-fusion*, two adjacent rings share one bond, whereas in *ortho- and peri-fusion*, the ring to be connected shares two or more bonds in contiguous series of *ortho-fused* rings (Fig. 5.1) [1, 2].

ortho-Fusion in a linear arrangement leads to the *acene* family, whose examples are anthracene, tetracene, pentacene, and hexacene. On the other hand, *ortho-fusion* in an alternating angular arrangement gives the *phenacene* family, whose examples are

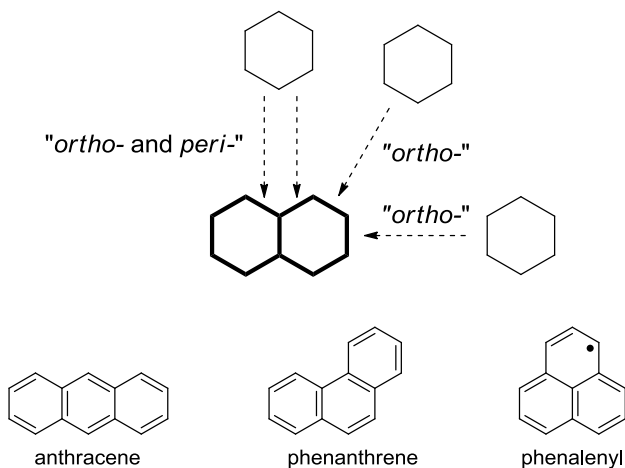
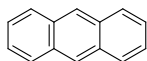


Figure 5.1 Ring fusion nomenclature of PAHs.

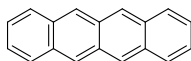
chrysene and picene (Fig. 5.2). The third category is the *phen* family, which includes the bent *ortho*-fused structure; examples are phenanthrene, tetraphene, pentaphene, and hexaphene. It is noted that acenes and phenacenes possess zigzag- and armchair-edged structures in their periphery, respectively, and that phens have both edges.

Another major class of PAHs includes *ortho*- and *peri*-fused structures. The representatives are phenalenyl, pyrene, perylene, bisantehene, ovalene, and hexabenzocoronene (Fig. 5.3). This fusion affords an internal carbon that is shared by three rings.

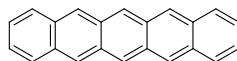
Most PAHs with even carbon atoms have a closed-shell electronic structure (i.e., all electrons in a molecule are paired), whereas some PAHs have an open-shell electronic structure (i.e., some electrons are unpaired) due to the topology of π -electron array, even if they have even carbon atoms. The representative is triangulene, whose electron spin state is closely related to the edge state of nanographene. The fully conjugated compounds for which at least one classical structure (Kekulé structure) can be written are referred to as *Kekulé compounds*. In contrast, *non-Kekulé compounds* have no classical structure without leaving two unpaired electrons on nonadjacent carbons (Fig. 5.4).

Acenes

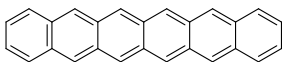
anthracene



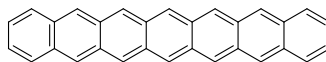
tetracene



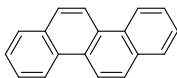
pentacene



hexacene



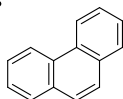
heptacene

Phenacenes

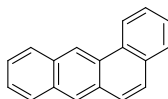
chrysene



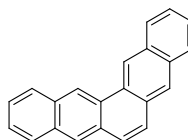
picene

Phenes

phenanthrene



tetraphene



pentaphene

Figure 5.2 *ortho*-Fused PAHs.**5.2.2** *Brief History of Aromatic Sextet*

The minimum repeating unit of rings in nanographene is benzene, whose now familiar hexagon formula with alternate single and double bonds was first proposed by August Kekulé in 1865 [3–5]. Benzene is an unsaturated compound having the characteristic properties such as high thermal stability, remarkable resistance to oxidation, and electrophilic substitution rather than addition. Its peculiar stability has been a long-standing mystery, and was first explained with the significance of the sextet of electrons by Armit and Robinson [6]. Their idea, so-called *aromatic sextet*, also explains the aromatic character of other monocyclic conjugative compounds including heterocycles (i.e., pyridine, furan, thiophene, etc.) and ionic species with six π -electrons (i.e., cyclopentadienyl anion, cycloheptatrienyl cation, etc.). Writing the circle inside the

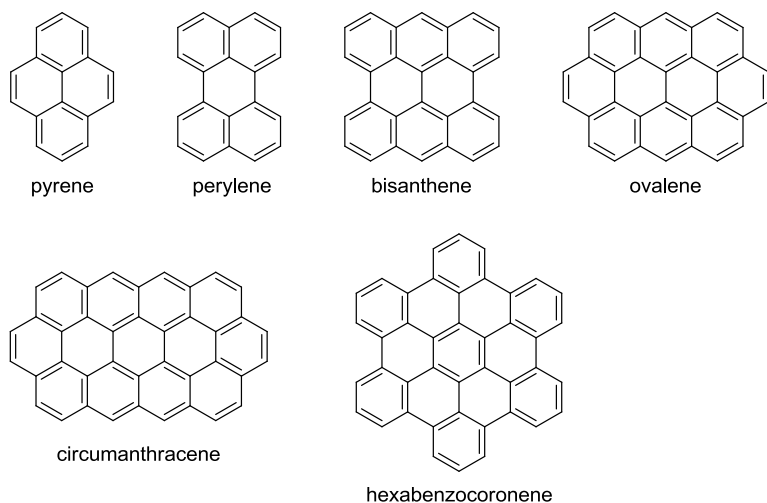


Figure 5.3 *ortho*- and *peri*-Fused PAHs.

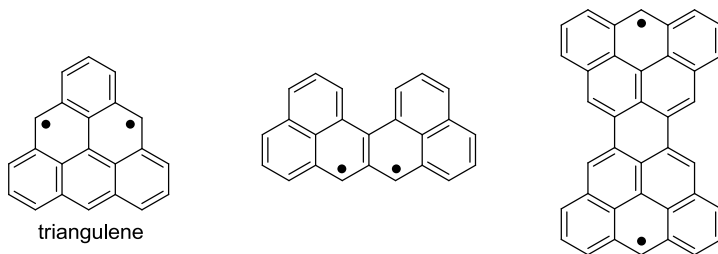


Figure 5.4 non-Kekulé PAHs.

benzene skeleton to symbolize the aromatic sextet is also their idea. Robinson's idea is not based on theoretical formulation, whereas quantum chemical treatment for the special stability due to cyclic six π -electrons was first conducted by Hückel, who concluded that the monocyclic system with $(4n + 2)$ π -electrons are blessed with particular electronic stability. Inversely, those with $4n$ π -electrons are quite unstable because of open-shell configurations with electrons in non-bonding molecular orbitals. This *Hückel rule*

is the most fundamental concept for understanding aromaticity and anti-aromaticity [7–10].

The synthesis and characterization of PAHs were extensively studied by Clar and Scholl in the first half of the 20th century. Clar summarized the numerous studies on PAHs in his two books [11]. He put forward the idea *Clar's aromatic sextet* (*Clar sextet*) in extension of Robinson's aromatic sextet in order to explain the physical and chemical properties of many kinds of polycyclic compounds [12]. In Clar's idea, for a given PAH, three π -bonds in a ring are substituted by a circle, and the circle can migrate from one ring to the other. Although this idea is also from an empirical basis, Clar's aromatic sextet well explains the molecular geometry and the chemical reactivity at the specific atoms of PAHs.

5.2.3 Clar Sextet in Relation to the Property of PAHs

There is a simple but strict rule in the notation of Clar sextet, that is, avoid circles in adjacent rings. In the example of naphthalene, both of the two rings can hold the circle, but only one does so at a time (Fig. 5.5).

Another rule may be notable. Many PAHs possess more than one Clar structure. For example, pyrene has two Clar structures **1a** and **1b** (Fig. 5.6). The more important formula should be chosen, and in this case, **1b** is preferable to **1a** because **1b** is blessed with more aromatic stabilization energy. Thus the formula **1b** contributes more largely to the ground state; consistent with the short C–C bond length at the double bond site of **1b** (0.1352 nm) [13]. For this reason, we should choose the formula **1b'** rather than **1a'** when the chemical formula of pyrene is written with the Kekulé structure.

Using the Clar structure, the electronic structure of PAHs can be easily predicted. For example, kekulene **2** has two possible Kekulé



Figure 5.5 (a) Correct and (b) incorrect representations of Clar sextet for naphthalene.

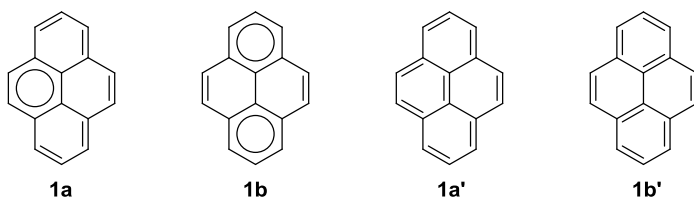


Figure 5.6 Clar and Kekulé structures of pyrene.

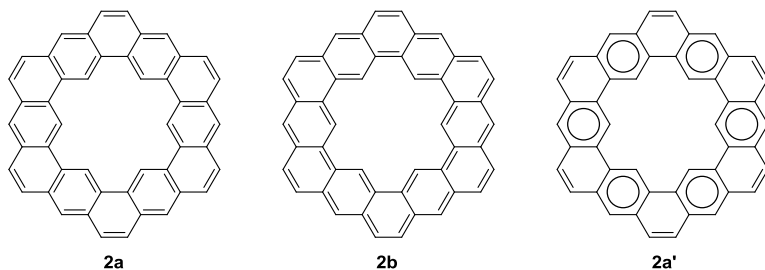


Figure 5.7 Kekulé and Clar structures of kekulene.

structures **2a** and **2b**, and the former can be rewritten with the Clar structure **2a'** (Fig. 5.7). This indicates the more important Kekulé structure is **2a**. The $^1\text{H-NMR}$ signal of the inner protons appears at a down-field region, suggesting that there is no or small effect of the ring current due to the macrocyclic π -array ([18]annulene) [14]. The UV spectrum of **2** gives absorptions at the higher-energy region than 388 nm, and the X-ray structure agrees with the benzenoid formula like **2a** (or **2a'**) [15]. All these experimental results strongly support the dominant contribution of **2a** (or **2a'**) to the ground state.

Clar's idea also accounts for the chemical reactivity of PAHs. The both terminal six-membered rings in phenanthrene are more stabilized than the central one, because the most important Clar structure consists of two Clar sextets and one double bond (Fig. 5.8). Bromine attacks the 9,10-double bond to give a relatively stable dibromide **3** instead of the substitution reaction that usually occurs in aromatic compounds [16]. Thus, the 9,10-double bond in phenanthrene actually has strong double bond character, not

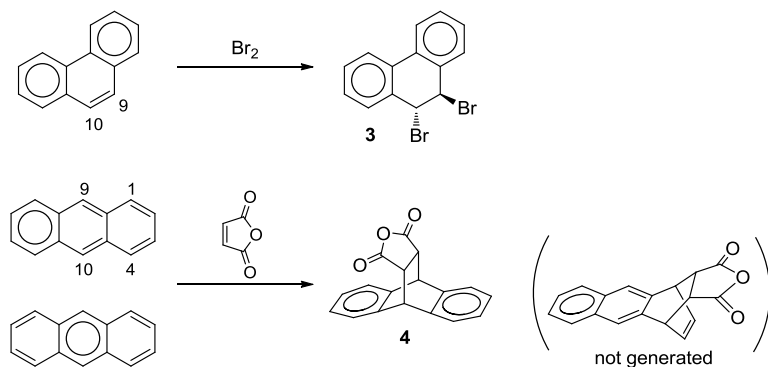


Figure 5.8 Reactivity of phenanthrene and anthracene.

aromatic one, as depicted by the Clar structure. On the other hand, anthracene possesses two Clar structures. The relative stability (i.e., relative reactivity) of the terminal and central rings seems not to be distinguished, but the reaction of anthracene with maleic anhydride exclusively gives the Diels–Alder adduct **4** at the 9,10-position [17]. In this case, the stability of the products would affect the selectivity. The reaction at the 9,10-position affords two aromatic sextets instead of only one sextet by the 1,4-position attack.

Phenanthrene is more stable than anthracene, which is easily predicted by the number of Clar sextet. This prediction based on Clar’s idea holds true for the relative stability of longer acenes and phenacenes. In acenes, only one circle can be written and furthermore the migration of the circle into adjacent rings “dilutes” the stabilization effect of the aromatic sextet. The stability of acenes drastically decreases with increasing number of rings. Pentacene is subjected to rapid oxidation in air [18], and unsubstituted acenes larger than hexacene can long survive only in a polymer matrix [19]. On the other hand, phenacenes are very stable compounds with a high melting point [20, 21]. The reason comes from that the number of the circle in phenacenes increases with increasing molecular size. In addition to the relative stabilities, there is also a difference in the colors between acenes and phenacenes. Acenes show a drastic red-shift in a HOMO–LUMO transition with increasing molecular size, whereas phenacenes show no appreciable shift (Fig. 5.9).

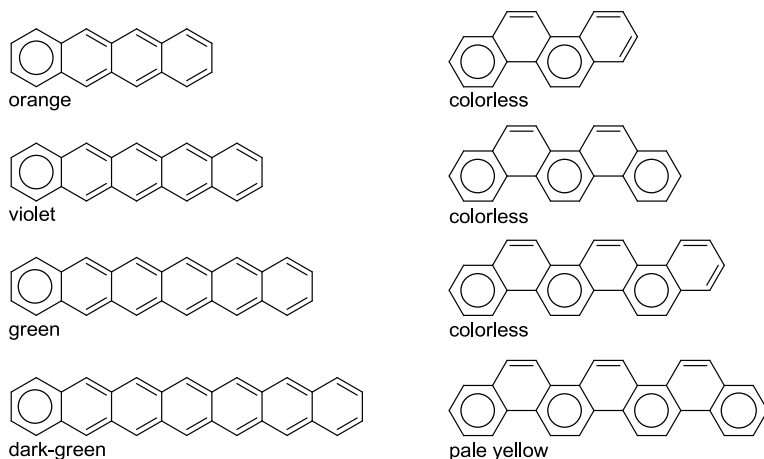


Figure 5.9 Color of acenes (left) and phenacenes (right).

The additively increasing aromatic sextets in phenacenes keep the HOMO–LUMO gap wide.

The Clar structure of triphenylene **5**, dibenzo[*fg,op*]tetracene **6**, and hexa-*peri*-benzocoronene (HBC) **7** includes no double bond, and therefore these compounds are extraordinarily stable. In their Clar structures, the circle cannot migrate anywhere, and consequently these compounds possess benzenoid and non-benzenoid rings. The benzenoid rings actually have aromatic character, which can be assessed by the nucleus-independent-chemical shifts (NICS) calculation developed by Schleyer [22, 23]. The NICS value is a simple index of aromaticity, and its negative, zero, and positive values denote aromatic, non-aromatic, and anti-aromatic character, respectively. Benzene has a large negative values of -11.2 for NICS(1). In the case of **7**, the NICS(1) value of the benzenoid rings (*A* and *C* in Fig. 5.10) is comparable to that of benzene, whereas the non-benzenoid ring (*B* in Fig. 5.10) has the value close to zero. The molecular geometry determined by X-ray crystallography [24] is thoroughly consistent with the aromatic character on the each ring, because the bond lengths connecting the benzenoid rings (0.1459 nm for *A–A*, 0.1448 nm for *A–C*) are close to that of the $C(sp^2)–C(sp^2)$ single bond (0.1467 nm).

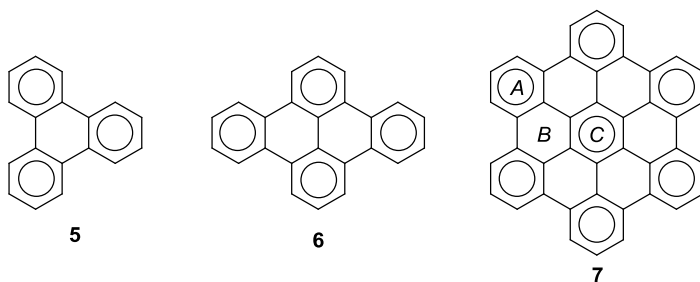


Figure 5.10 Clar structure of **5**, **6**, and **7**. The NICS(1) values of **7** are -11.5 (ring *A*), -3.2 (*B*), and -15.1 (*C*).

5.3 Recent Advanced Studies on PAHs: Synthesis, Property, and Application

PAHs have been expected as materials applicable to semiconductors and light-emitting diodes, because their planar and rigid molecular structures are suitable for electron and hole transfers between molecules. Pioneering work on organic semiconductor was conducted by Akamatsu and Inokuchi, who measured electroconductivity of various PAHs [25–28]. They considered PAHs a small piece of a carbon sheet in graphite. In 1954, the same authors discovered a prominent feature on electroconductivity with perylene–bromine charge transfer complex. The complex showed metallic behavior down to 90 K [29]. After the discovery, many researchers have developed various organic metals [30], and recently, organic semiconductors based on PAHs have been used as active elements in optoelectronic devices such as organic light-emitting diodes (OLED) [31], organic solar cells [32], and organic field-effect transistors (OFET) [33].

Although PAHs are a good potential candidate for organic devices, large PAHs actually have difficulty in preparation and solubility. Classical synthetic methods require harsh conditions such as thermo-pyrolysis, oxidation in a melting salt, and flash vacuum pyrolysis (FVP), and poor solubility makes it difficult to purify and to characterize PAHs. However, recent advances in scanning tunneling microscopy (STM) and atomic force microscopy (AFM) enable to investigate directly PAH molecules (or aggregates) on

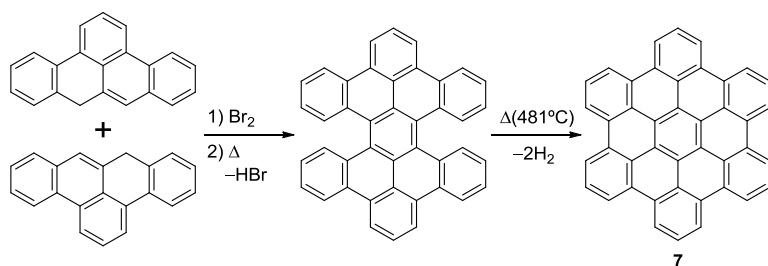


Figure 5.11 Clar's route to HBC 7.

surfaces. The technical development of the microscopies pushes forward nanoscience and nanotechnology for large PAHs instead of bulk-material science.

The PAH molecule that is most used as a nanomaterial so far would be HBC 7 and its derivatives, which have been attracting intensive interests of researchers due to their strong aggregation character. The first synthesis of parent HBC was achieved by Clar in 1958 (Fig. 5.11) [34]. Another synthetic method was also reported by Halleux and co-workers [35]. However, both methods involved complicated experimental treatments and gave the desired HBC only in very low yield.

Müllen and co-workers has developed an efficient synthetic method to prepare HBC by oxidative cyclodehydrogenation of branched oligophenylene precursors with Cu(II) salts catalyzed with AlCl_3 , or FeCl_3 (Fig. 5.12). This method is performed under milder condition and affords HBC in very high yield [36, 37]. These methods are also effective in synthesizing HBC derivatives substituted with several groups.

Müllen and co-workers also found that HBCs substituted peripherally with long alkyl chains aggregate self-assembly into one-dimensional column. In the column, the aromatic core of HBCs stacks face to face due to a large dispersion force. Depending on the temperature and on the length of alkyl chains, the solid state of HBCs changes from a crystalline phase to a discotic liquid crystal phase. In this assembly, the alkyl side chains fill the inter-column space, which turns the arrangement into a two-dimensional array (Fig. 5.13) [38, 39]. High charge carrier mobility is observed in the

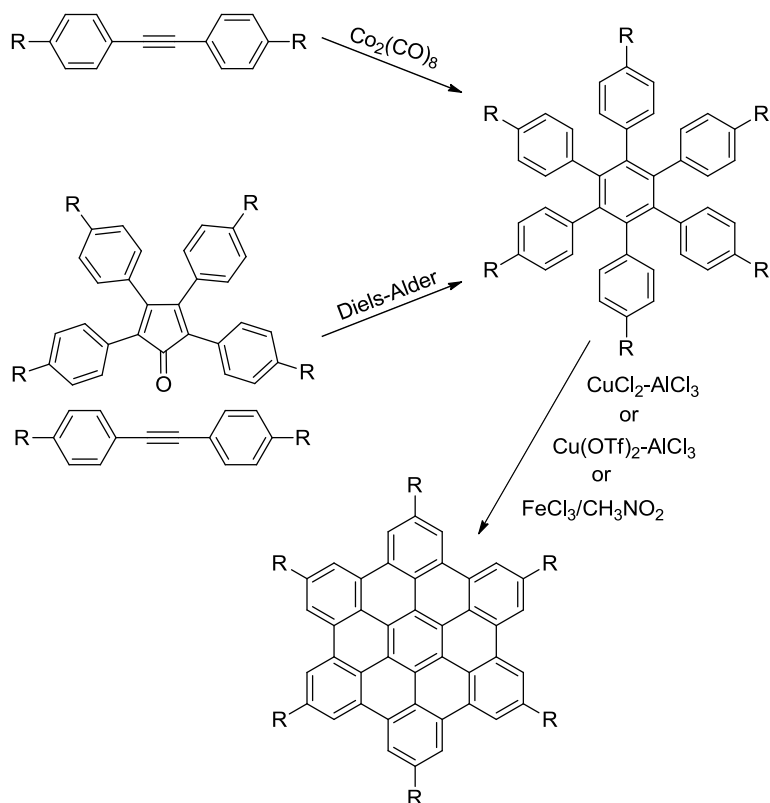


Figure 5.12 Efficient syntheses of HBCs developed by Müllen and co-workers.

columnar direction, and the peculiar solid phase property qualifies them as a semiconductor in organic molecular devices [40, 41].

PAHs larger than HBC have also been synthesized by using a similar synthetic method (Fig. 5.14) [42–45]. It is interesting that how close these large PAHs can be to graphene with respect to properties. To date, the compound **11** composed of 222 carbon atoms is a largest PAH molecule with a characterized structure. This PAH shows an absorption band at 765 nm with a tail band in a near-IR region, indicating a very small HOMO–LUMO gap. One-dimensional polymeric graphite ribbon **12** has also been synthesized. The electronic and vibrational properties of **12** were characterized by

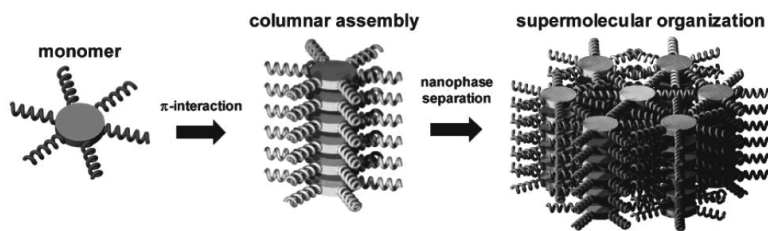


Figure 5.13 Schematic illustration of aggregations of HBC derivatives. After ref. 39.

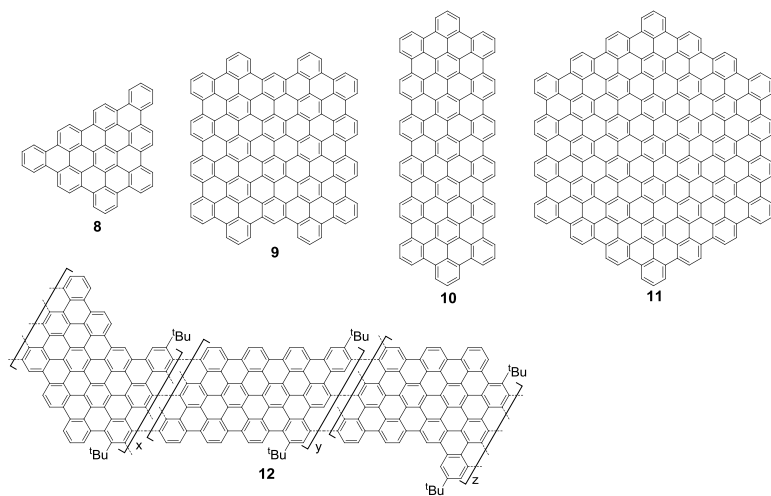


Figure 5.14 Giant PAHs **8–11** and graphene nanoribbon (GNR) **12** prepared by chemical syntheses.

solid state UV-Vis, Raman, and infrared spectroscopies. The longest absorption band of **12** was observed around 800 nm. The profile of the Raman spectrum of **12** is characterized by two strong bands (1603 cm^{-1} , 1322 cm^{-1}), which corresponds to the G and D bands of graphite. High-resolution transmission electron microscopy (HR-TEM) showed that **12** was ordered as a layer structure with a layer distance of 0.38 nm [44].

Atomically precise preparation of graphene nanoribbon (GNR) was achieved by Cai and co-workers. Biradical species generated

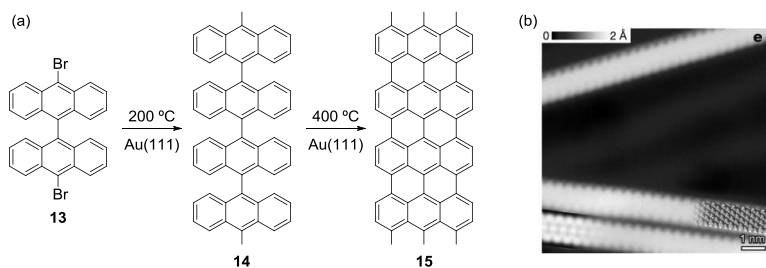


Figure 5.15 (a) Reaction scheme from **13** to GNR **15** on a Au(111) surface. (b) High-resolution STM image of **15**. After ref. 46.

from **13** by heating at 200°C on a Au(111) surface formed a polymeric compound **14**, and subsequent heating at higher temperature led to cyclodehydrogenation, giving a width-controlled GNR **15** (Fig. 5.15) [46]. The width and the edge-shape of **15** are defined by the structure of the molecular precursor **13**, and this means that GNR might be fabricated in response to the intended use.

5.4 Electronic Structure of PAHs

5.4.1 Effects of Edge Shapes on the Electronic Structure of PAHs

As described in Section 5.2.3, the stability of acenes decreases with increasing ring annelation, whereas phenacenes show very high stability even for the [11]phenacene derivative [21]. In this one-dimensional system, the difference in the shape of molecular periphery is directly related to the difference in the stability. Ring annelation in a zigzag-edged manner results in quinoidal π -conjugation, whereas that in an armchair-edged manner benzenoid one. The quinoidal conjugation is known to lead to high reactivity for a given molecule. The simplest quinoid compound, *o*-quinodimethane shows rapid ring cyclization or dimerization, and the high reactivity is derived from its biradical character [47]. In a similar way, the *o*-quinoid structure in acenes endows them with biradical character, which causes a rapid oxidation reaction for

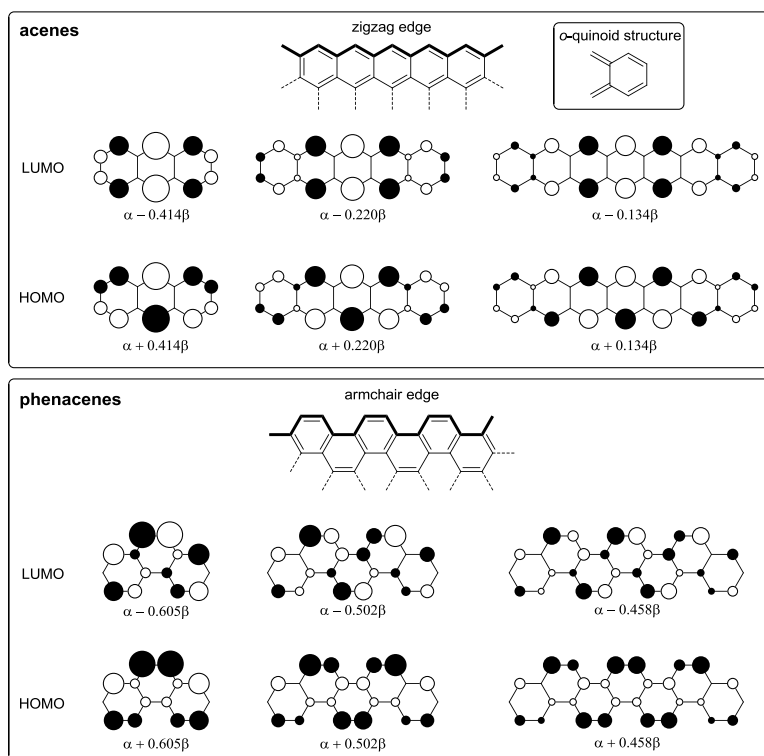


Figure 5.16 Frontier orbitals of acenes (top) and phenacenes (bottom), which are a structural piece of zigzag and armchair edges of graphene, respectively.

longer acenes [48]. The Hückel molecular orbital (HMO) calculation reveals that frontier orbitals of acenes bear more non-bonding character and the HOMO–LUMO energy gap rapidly decreases, with increasing ring annelation (Fig. 5.16). The non-bonding frontier orbitals with a small gap are closely related to the biradical character [49], and a more sophisticated calculation reveals higher anti-ferromagnetic spin-state (i.e., polyradical character) for longer acenes [50, 51]. Unpaired electrons reside mostly on the *peri*-positions at the zigzag edge region. The peculiar electronic structure of acenes and the properties derived from it will be described in

Section 5.4.4 in more detail. On the other hand, phenacenes keep their frontier orbitals bonding and anti-bonding, and the energy gap between them converges into a large value (3.60 eV at the B3LYP/6-31G* level) for the infinite system [52], probably due to the aromatic sextets formation. The large HOMO–LUMO gap leads to the non-magnetic ground state for phenacenes. It is notable that the bandgap of acenes is predicted to be much smaller than that of polyphenacene [53] and that 1.2 eV is the extrapolated experimental value [54].

Fujita and co-workers studied the electronic structure of one-dimensional zigzag- and armchair-edged GNRs with large width, by performing tight binding band calculations [55–57]. They found that GNR with zigzag edges shows a remarkably sharp peak in density of states and a non-bonding π -state at the Fermi level, whereas GNR with armchair edges does not (Fig. 5.17). The wave function of the zigzag-edged GNR completely localizes at its edges in the case of $k = \pi$, with a quite similar distribution pattern seen at the edge of longer acenes. The non-bonding π -state arising from the localization of the wave functions on the zigzag edge is referred to as *edge state*. Unpaired electrons also localize at the zigzag edge [58, 59].

The electronic structure of a two-dimensional system is also affected by the shape of edge. Stein and co-workers studied the electronic structure of giant PAHs with a well-defined edge structure consisting of more than 200 carbon atoms, by using the HMO theory [60]. The electronic populations of the HOMO are almost uniformly distributed in the entire region for the armchair-edged PAH (Fig. 5.18 left), whereas the HOMO of the zigzag-edged PAH possesses the largest populations in the zigzag edge region (Fig. 5.18 right). The distribution pattern at the zigzag edge resembles that of longer acenes and the zigzag-edged GNR and indicates the non-bonding character of the molecular orbital. The calculation results imply that a large PAH with zigzag edges has edge state, which is a characteristic electronic structure of graphene and GNR. Stein and co-workers also conclude that the difference of the electronic density distributions influences reactivity of molecules, that is, PAHs with zigzag edges are more reactive than armchair-edged ones.

In this way, the shape of edge influences the stability and property of PAH and GNR. This is because a non-bonding wave

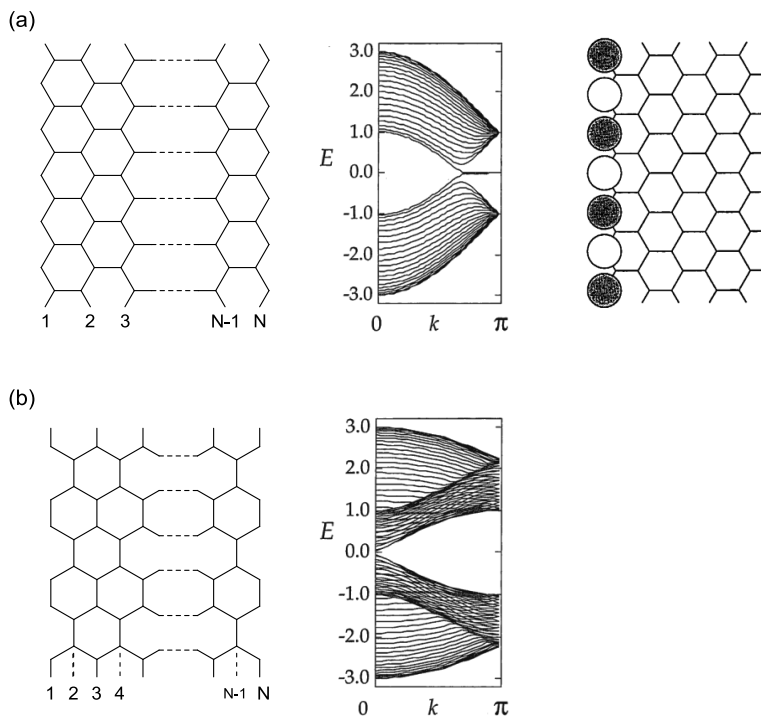


Figure 5.17 (a) The band structure ($N = 20$) and the wave function ($k = \pi$) of GNR with zigzag edges. (b) The band structure ($N = 20$) of GNR with armchair edges. After ref. 55.

function at the HOMO or Fermi level localizes at the zigzag edges. In the following sections, we will discuss the ground state spin multiplicity of zigzag-edged PAHs.

5.4.2 Prediction of the Spin Multiplicity in the Ground State: Ovchinnikov Rule

In this section, we focus on the spin state only for PAHs whose periphery is solely decorated by zigzag edges. PAHs consisting only of the six-membered ring are categorized into *alternate hydrocarbon*, in which its sp^2 carbon atoms can be divided into two sets. As illustrated in Fig. 5.19, naphthalene has the carbon atoms of one

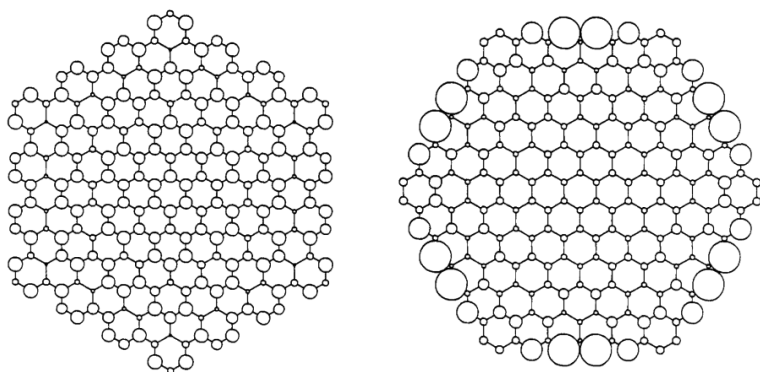


Figure 5.18 The electronic density distributions of the HOMO for PAHs with armchair (right) and zigzag (left) edges. After ref. 60.

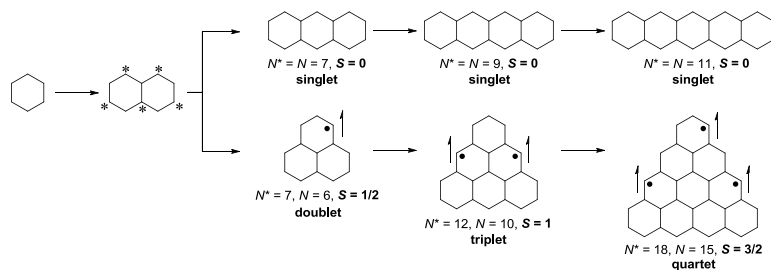


Figure 5.19 Prediction of spin quantum number S and spin multiplicity in the ground state of PAHs with zigzag edges.

set marked with “star” and those of the other set non-marked. Any atoms belonging to the same set are not nearest neighbors. This traditional starred and unstarred classification is closely related to the valence bond model, because one spin (for example α -spin) is put on the starred atoms and opposite spin (β -spin) is put on the unstarred atoms, and then the anti-parallel spins in the nearest neighbor atoms can be paired to form π -bonds. If the number of the starred atoms (N^*) is equal to that of the unstarred atoms (N), the system has no unpaired electron and consequently the ground state is singlet. Generally N^*-N represents excess spins, and Ovchinnikov found that the spin quantum number S in the ground state of a

given PAH molecule can be predicted by the following equation; $S = (N^* - N)/2$ [61]. According to Ovchinnikov's rule, one can predict the spin multiplicity in the ground state by simply counting the N^* and N , and the results for linear and triangular ring-annulated PAHs with zigzag edges are shown in Fig. 5.19.

For the linear system, i.e., acenes, N^* is always equal to N , and consequently their ground state is singlet even for an infinite system. However, as mentioned in Section 5.4.1 longer acenes have biradical or polyradical character in the ground state. Actually, the ground state of acenes is predicted to be strictly singlet, but the strength of the electron pairing becomes weaker with increasing ring annelation [49–51]. Each electron, which is almost unpaired, resides on the zigzag edge region and behaves like an isolated spin with holding anti-parallel correlation. Thus the electronic structure of the linear system is the open-shell singlet (i.e., antiferromagnetic) ground state [62].

On the other hand, triangular PAHs have a non-zero value for $N^* - N$, and S increases with increasing molecular size. Thus Ovchinnikov's rule predicts that the ground state of the triangular PAHs is always high spin state. The spin multiplicity predicted by Ovchinnikov's rule is consistent with the prediction by use of the molecular orbital theory. Longuet-Higgins found that alternate hydrocarbons have at least $n - 2t$ non-bonding molecular orbitals (NBMO) at the HMO level, where n is the number of sp^2 carbon atoms and t is the number of π -bonds, and that just one electron accommodated in each NBMO aligns in a spin-parallel manner according to Hund's rule [63] to give highest spin multiplicity [64]. Longuet-Higgins's rule cannot be applied to an alternate hydrocarbon molecule that violation of Hund's rule occurs, whereas Borden and Davidson developed a new rule that correctly predicts the ground state multiplicity of an alternate hydrocarbon biradical by taking consideration of the Coulomb repulsion between two electrons in NBMOs (see Section 5.4.3).

A DFT calculation reveals that a large spin density appears in the zigzag edge region for both the linear and triangular PAHs (Fig. 5.20). This spin-localizing nature at the zigzag edge would be intrinsically responsible for edge state of graphene.

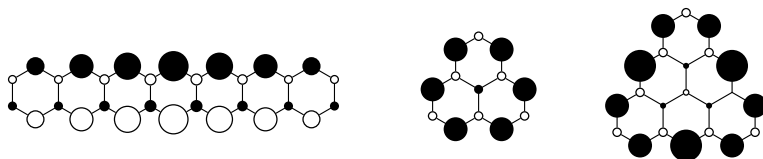


Figure 5.20 Spin density distribution of linear and triangular PAHs. Filled and open circles denote α - and β -spin, respectively.

5.4.3 Non Kekulé-Type PAHs

In 1977, Borden and Davidson reported that the spin multiplicity of the ground state for a given π -conjugated biradical can be estimated from a distribution pattern of non-bonding molecular orbitals [65]. For example, trimethylenemethane (TMM) and tetramethylenemethane (TME) are given considerations [66]. Each NBMO is represented in Fig. 5.21.

The NBMOs of TMM have atoms in common, and NBMOs with such distribution is referred to as *non-disjoint*. The spin multiplicity of a π -conjugated biradical with non-disjoint NBMOs is triplet ground state by considering the Pauli principle, which gives zero probability for parallel electrons to share a same region of space simultaneously. The smaller Coulomb repulsion between two electrons due to the Pauli principle leads to a triplet ground state. In fact, the spin state of TMM is experimentally determined to be the triplet ground state [67, 68].

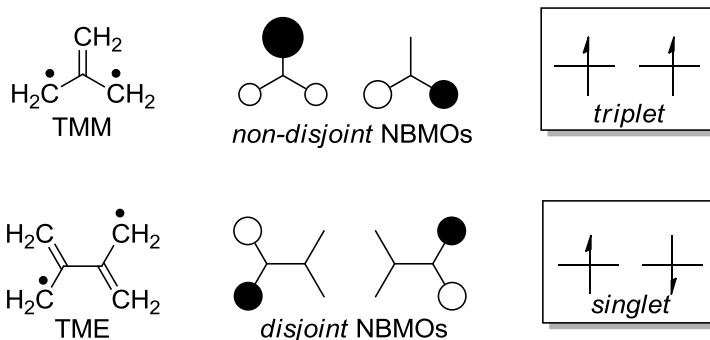


Figure 5.21 Distribution of the NBMOs of TMM (above) and TME (below).

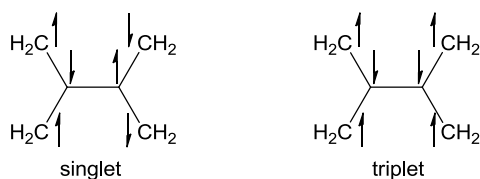


Figure 5.22 Valence bond description of the singlet and triplet states of TME.

On the other hand, the NBMOs of TME do not coincide with each other and is categorized into *disjoint* type. No orbital overlap between the NBMOs leads to zero or very small energy gap between singlet and triplet states. However, a valence bond (VB) model gives a preference for a singlet state over a triplet state as a result of more pairings of electrons (Fig. 5.22). The combination of the MO and VB models predicts the singlet ground state for TME, but an actual molecule is subject to more complicated interactions such as a long-range bonding (i.e., a non-nearest neighbor interaction) and dynamic spin polarization. Because of the intrinsic small energy gap between singlet and triplet states, the spin multiplicity of TME is difficult to determine. Dowd demonstrated by using ESR measurements that the ground state of TME is triplet or that singlet and triplet are degenerate [69], whereas computational works reveal that the ground state multiplicity is very sensitive to the torsional angle of two allyl radical moieties [70].

These results estimated by the Borden–Davidson rule agree with those estimated by the Ovchinnikov rule. According to the Ovchinnikov rule, TMM has $N^* = 3$ and $N = 1$, and consequently gives $S = (N^* - N)/2 = 1$. Therefore, the spin multiplicity of TMM is certainly triplet in the ground state. On the other hand, TME has $N^* = 3$ and $N = 3$, and consequently gives $S = (N^* - N)/2 = 0$, resulting in the singlet ground state for TME. In this way, the spin state of non-Kekulé molecules in the ground state can be easily estimated by using the Ovchinnikov rule and the Borden–Davidson rule, and this simple way to estimate the ground state spin multiplicity holds true for π -extended biradicals.

m-Quinodimethane **16** is a non-Kekulé molecule with two unpaired electrons (Fig. 5.23 (a)). According to the Ovchinnikov

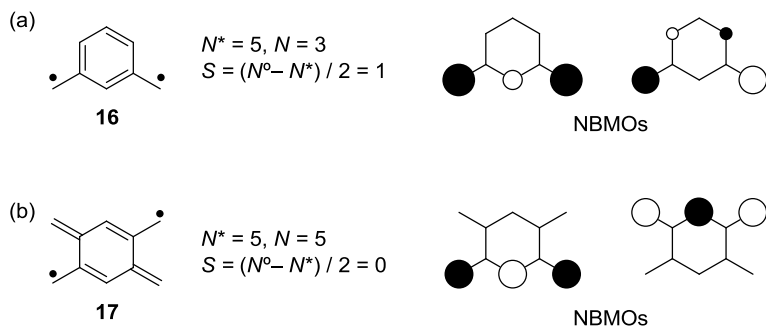


Figure 5.23 Ground state spin multiplicity predicted by the Ovchinnikov rule and NBMO distributions of (a) *m*-quinodimethane **16** and (b) 1,2,4,5-tetramethylenebenzene **17**.

($S = 1$) and the Borden–Davidson (non-disjoint NBMOs) rules, the spin multiplicity of *m*-quinodimethane is predicted to be triplet in the ground state and is actually determined to be triplet by a Curie plot of the ESR signal intensity [71]. On the other hand, 1,2,4,5-tetramethylenebenzene **17** has $S = 0$ and disjoint NBMOs, and consequently the singlet state is preferable or is nearly degenerate with the triplet state (Fig. 5.23 (b)). The ground state of **17** was initially determined to be triplet by ESR and UV-Vis measurements [72]. However, later careful experiments and sophisticated quantum chemical calculations demonstrated that the species had actually the singlet ground state [73–76].

According to the Ovchinnikov rule, triangular zigzag-edged PAHs possess the increasing spin multiplicity with increasing their molecular size (Fig. 5.24). The non-disjoint NBMOs of triangulene **18** would support this prediction. Experimental determination of the multiplicity has not been done so far, except for **18**. Tri-*tert*-butyl derivative of **18** gives an ESR signal typical for triplet species with three-fold symmetry, and a Curie plot of the signal intensity supports the triplet ground state [77].

On the other hand, a goblet-shaped biradical (Clar goblet) **19** is predicted to possess a low-spin ground state by the Ovchinnikov rule and the disjoint NBMOs, being supported by a quantum chemical calculation (Fig. 5.25) [78].

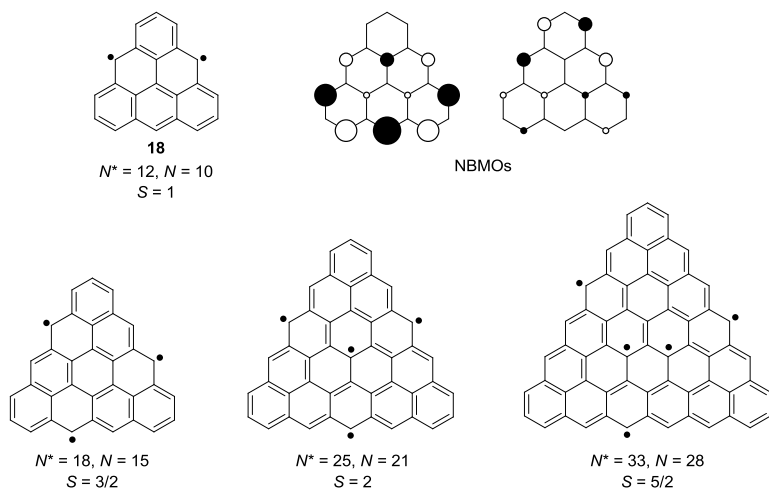


Figure 5.24 Spin quantum number S of triangular PAHs and distributions of the NBMOs of **18**.

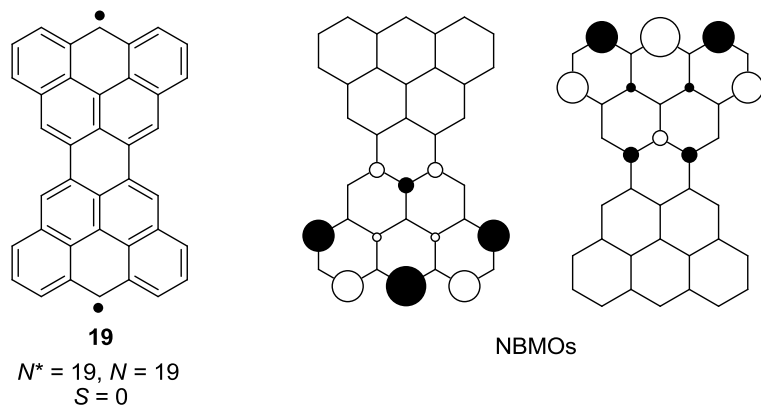


Figure 5.25 Spin quantum number S and distributions of the NBMOs of **19**.

It should be noted that non-Kekulé PAHs are divided into two groups: One is antiferromagnetic, whose spin multiplicity is singlet in the ground state, and the other is ferromagnetic, whose spin multiplicity is a high-spin state in the ground state. The difference

of the multiplicity depends on how their NBMOs are populated. However, in both cases, the spin density is mostly distributed on their zigzag edges. This means that the electronic structure of these non-Kekulé type PAHs would be closely related to the edge state of graphene.

5.4.4 Kekulé-Type PAHs

5.4.4.1 Theoretical treatment of singlet biradical character

Unlike non-Kekulé compounds, it is difficult to intuitively recognize the spin structure of Kekulé compounds because they have no unpaired electron in their chemical formula. Kekulé compounds that show a chemical reactivity like biradical species have been long studied by spectroscopic and products analysis methods as well as theoretical calculations, and from their behaviors, the compounds are referred to as *biradicaloid*, whose terminology was defined by Michl [79]. The common feature of biradicaloids comes from nearly degenerated molecular orbitals that are occupied with two electrons [80]. The near degeneracy in the frontier orbitals, that is a small HOMO–LUMO gap, leads to the preference for the promotion of electrons from HOMO to LUMO, and therefore, advances the admixture of a doubly excited configuration ${}^1\Phi_{H,H\rightarrow L,L}$ into a ground configuration ${}^1\Phi_0$ (see below). As a result of the configuration mixing, the repulsion between the two electrons is taken into consideration, and the two electrons with anti-parallel spins are permitted to correlate at separated spaces. Thus, biradicaloids possess more or less singlet biradical character and consequently show a high reactivity. Another aspect in the electronic structure of biradicaloids would be a small singlet–triplet energy gap due to the small HOMO–LUMO gap. Thermal excitation to the triplet state is also responsible for a high reactivity.

Biradicaloids encounter the difficulty in the experimental elucidation of how much amounts of biradical character they have. Instead, a theoretical study gives an obvious criterion [80], and the amount of biradical character is estimated by natural orbital occupation number (NOON) [81]. In the multi-configurational scheme, the admixture of the ${}^1\Phi_{H,H\rightarrow L,L}$ into the ${}^1\Phi_0$ represents

uncoupling of electron pair, and hence the occupation number of LUMO is a direct computational measure of the amount of biradical character. A perfect biradical is characterized by occupation numbers of 1.0 in HOMO and LUMO, whereas a perfect closed-shell molecule possesses occupation numbers of 2.0 and 0.0 in HOMO and LUMO, respectively. A UHF-based (or UDFT-based) broken symmetry method gives another quantitative guidance for the biradical character [82, 83]. The amount of biradical character (y_i) is expressed as $y_i = 1 - 2T_i / (1 + T_i^2)$ by using the spin-projected UHF (PUHF) theory, where T_i is defined by $T_i = (n_{\text{HOMO}-i} - n_{\text{LUMO}+i}) / 2$ using the occupation numbers (n_i) of UHF natural orbitals and is closely related to the spatial orbital overlap between the corresponding orbital pairs [84, 85]. In the broken symmetry formalism, α - and β -electrons occupy a different part of space in a biradicaloid molecule, and consequently a spin distribution pattern can be easily recognized by visualization of spin density using a drawing software package.

5.4.4.2 Linear system: quantum chemical prediction of spin structure in the ground state

Houk and co-workers performed a (U)B3LYP/6-31G* calculation for polyacenes, which predicted that octacene would exhibit a triplet ground state on the basis of extrapolation from the singlet–triplet energy difference of benzene through hexacene [86]. However, Bendikov, Houk, and co-workers later revised this result by using a broken symmetry UB3LYP/6-31G* method, and estimated that the open-shell singlet is the lowest state in acenes larger than hexacene, and they behave as singlet biradicals, whose singly occupied molecular orbital (SOMO) is populated on their zigzag edges (Fig. 5.26) [49].

Much larger acenes might have polyradical character in the ground state. Hachmann [51] and Jiang [50] demonstrated that polyacenes have the singlet ground state with multi-spin polarized, by performing density matrix renormalization group (DMRG) calculation and DFT calculation, respectively. Figure 5.27 shows the three highest occupied spin orbitals (HOSOs) of 20-acenes. The contribution of these spin orbitals to the total magnetization is

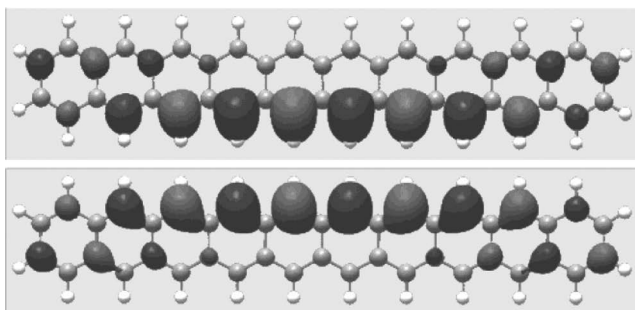


Figure 5.26 SOMOs of decacene calculated by Bendikov and co-workers. After ref. 49.

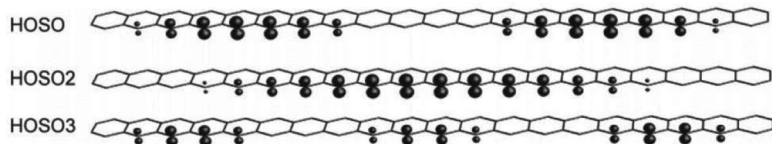


Figure 5.27 Charge density for α -spin electrons of 20-acene. Only the three highest occupied spin orbitals (HOSOs) are shown. After ref. 50.

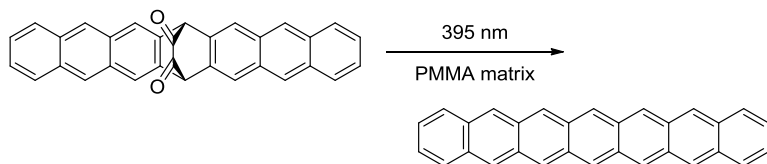
0.909, 0.739, and 0.456 for HOSO, HOSO2, and HOSO3, respectively. This result clearly demonstrates that the biradical description is inaccurate for higher acenes.

5.4.4.3 Linear system: isolation and characterization of large acenes

Not only the theoretical works but also the experimental works of acenes have been intense study. The synthesis of larger acenes is a difficult and challenging task due to their very low solubility, poor stability to light and oxygen, and tendency to dimerize, as well as a tedious long-step synthesis. Therefore, successful experimental studies on larger acenes are very limited.

Neckers and co-workers obtained unsubstituted heptacene in a poly(methyl methacrylate) (PMMA) matrix by photo-decarbonylation of a dione precursor (Scheme 5.1) [87]. The irradiation at 395 nm gave the longest wavelength absorption centered at 760 nm,

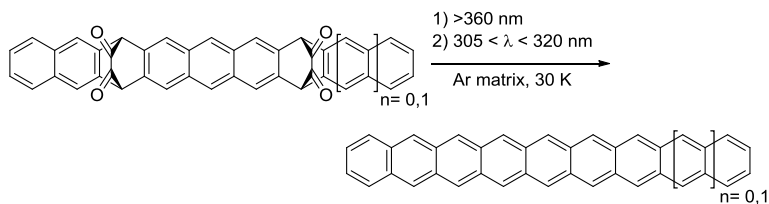
and from the decay of the absorption band, heptacene was found to be stable up to 4 h in a PMMA matrix.



Scheme 5.1 Synthetic route for parent heptacene by photodecarbonylation.

Full characterization of heptacene was made by the introduction of substituents to the core rings. Because unsubstituted heptacene is immediately oxidized and is decomposed in solution at room temperature, some protecting groups are required for the stabilization. Many research groups synthesized heptacene derivatives substituted with bulky groups (Fig. 5.28) and measured electronic and solid state properties [88–91].

Larger acenes have also been studied. Bettinger and co-workers reported the synthesis and spectroscopic detection of unsubstituted octacene and nonacene under the condition of matrix isolation (Scheme 5.2) [54]. UV-Vis-NIR spectra gave the longest wavelength absorption centered at 806 nm and 865 nm for octacene and nonacene, respectively, and preserved an absorption peak profile characteristic for acenes (i.e., weak long-wavelength bands and intense short-wavelength bands).



Scheme 5.2 Synthetic route for octacene and nonacene by photodecarbonylation.

The isolation of nonacene was achieved by introducing many substituent groups into the core rings [92]. The molecular structure

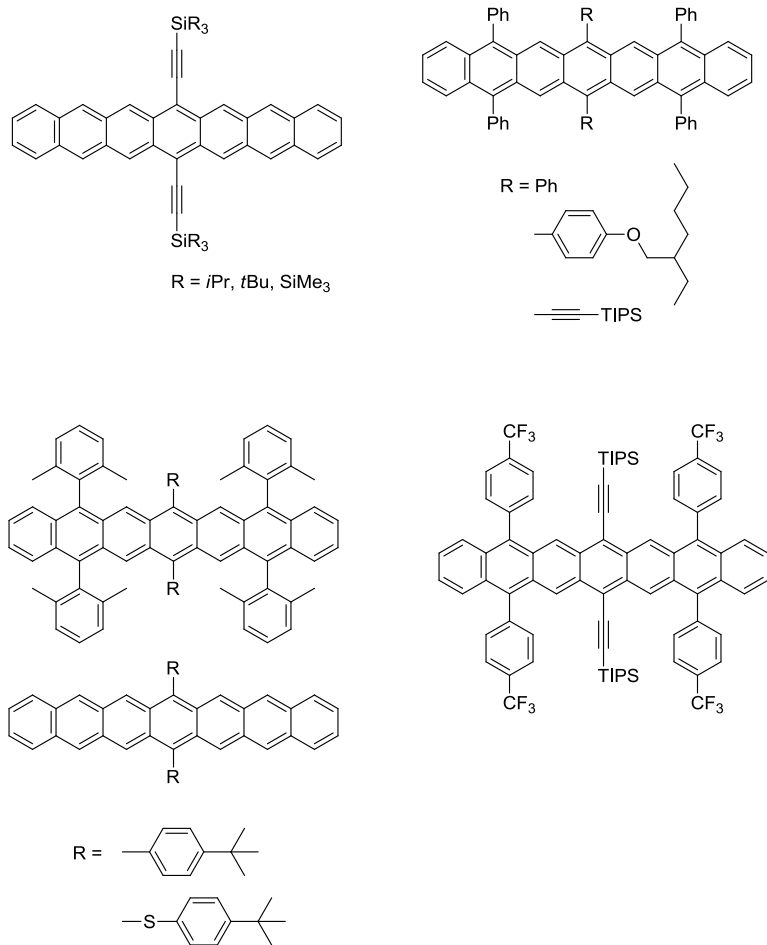


Figure 5.28 Substituted heptacenes.

of **20** was determined by X-ray single crystal crystallographic analysis. Nonacenes **20** showed a prominent HOMO–LUMO transition at 1014 nm, which was located at lower-energy region than that of non-substituted nonacene [54]. The optical HOMO–LUMO gap is determined to be 1.2 eV, which was almost the same as the electrochemical HOMO–LUMO gap (1.19 eV). These small HOMO–LUMO gaps suggest some extent of singlet biradical character of

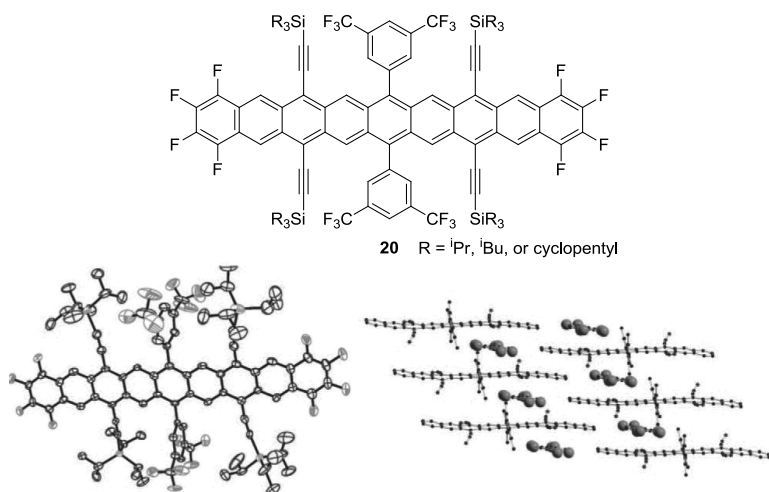


Figure 5.29 Anthony's nonacenes **20** and crystal structure of the R = ⁱPr derivative. After ref. 92.

nonacene. Actually, ¹H-NMR spectrum of **20** gave no signal due to the existence of magnetic species, probably thermally excited triplet species.

5.4.4.4 Two-dimensional system: quantum chemical prediction of spin structure in the ground state

peri-Condensation of acenes leads to rectangular PAHs, which are referred to as periacenes. Periacenes possess both zigzag and armchair edges in their periphery, and therefore would be a good model for a study of nanographene. In this chapter, the number of six-membered rings in each direction of the linear and the angular ring-fusion is indicated in brackets as [m.n] in the order of the linear and the angular ring-fusion (Fig. 5.30).

Jiang and co-workers performed B3LYP and PBE0/6-311G** calculations for estimating the ground state of periacenes, giving that the ground state of [4.3]periacene and larger ones are an open-shell singlet state along with spin polarization on zigzag edges, while [3.3]periacene has a closed-shell singlet ground state (Fig. 5.31) [93]. On the other hand, the calculation with a HSE06/6-31G**

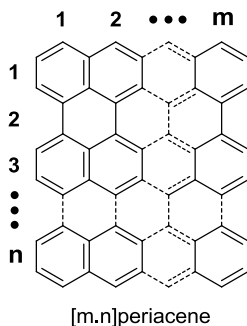


Figure 5.30 Nomenclature of periacenes.

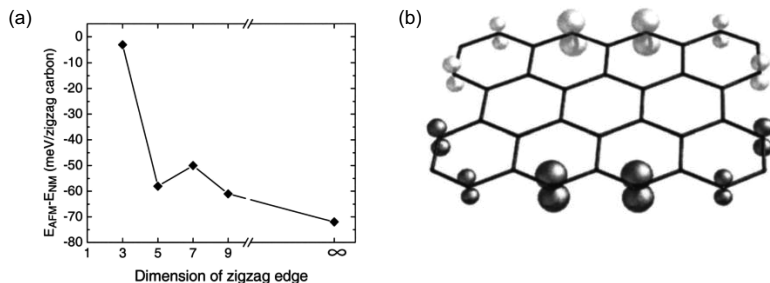


Figure 5.31 (a) Energy difference ($E_{AFM} - E_{NM}$) between antiferromagnetic and non-magnetic states of periacenes, and (b) spin density distributions of [4.3]periacene. After ref. 93.

method by Hod and co-workers indicated the spin polarized state on zigzag edges even in [3.3]periacene [94]. The authors concluded that [3.3]periacene would be the smallest nanographene to present a spin polarized ground state.

The difference between these calculation results on open-shell character of the small periacene derives from the evaluation method of electron correlation effect in the DFT calculation. Moscardo and San-Fabián performed UHF, UDFT, and post-SCF (MPn and CISD) calculations for [4.n]periacens [95]. Although UHF and UDFT calculations showed that the ground state is changing from a closed-shell to an open-shell singlet state with increasing ring annelation, post-SCF calculations gave opposite results: any periacene has a

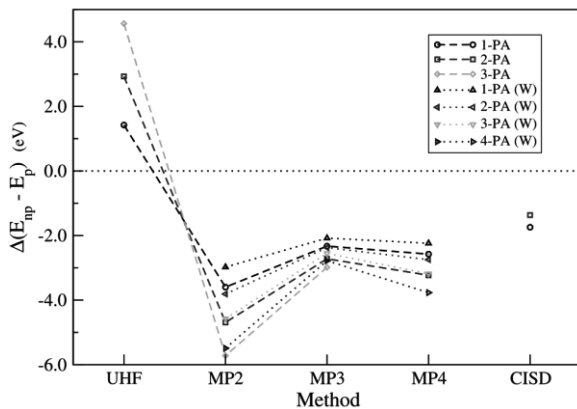


Figure 5.32 Energy differences between antiferromagnetic and non-magnetic states of [4.n]periacenes, calculated by Moscardo and San-Fabián. After ref. 95.

closed-shell singlet ground state (Fig. 5.32). Thus, the electronic structure of nanographene in the ground state would be varied depending on the degree of the evaluation of electron correlation effect.

Circumarenes (*circumacenes* is used in ref [96]), which are decorated with ethene bridges at the armchair edges of periacenes, are also reported to show a spin polarized state on zigzag edges [96]. Although the change in open-shell character is more gradual than that of periacenes, it is estimated that the ground state of circumarenes also approaches an open-shell singlet state, and the spin would be polarized on their zigzag edges, with increasing molecular size (Figs. 5.33 and 5.34).

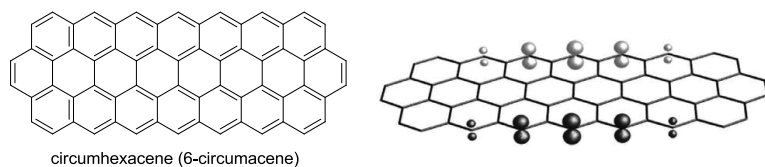


Figure 5.33 Spin density distribution of circumhexacene. After ref. 96.

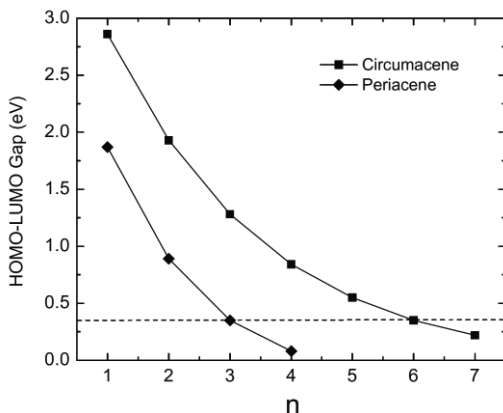


Figure 5.34 HOMO–LUMO gaps of circumarenes and periacenes. After ref. 96.

5.4.5 Detailed Discussion on Spin-Polarized State at Zigzag Edges of Kekulé-Type PAHs

Valence bond model is helpful for understanding the spin polarized state at the zigzag edge of acenes and periacenes. As mentioned in Section 5.4.1 acenes contain *o*-quinodimethane structures. The molecular structure of *o*-quinodimethane should be drawn as a resonance hybrid of Kekulé and biradical forms, in contrast to that most Kekulé compounds have negligible contribution of a biradical form in the ground state. The reason of the non-negligible biradical contribution is that upon transforming from the Kekulé form to the biradical form, the large destabilization energy due to the π -bond cleavage is partially compensated by the aromatic stabilization energy. The aromatic stabilization energy of benzene based on the homodesmotic stabilization energy is ca. 90 kJ/mol [97, 98], whereas the destabilization energy due to C–C π -bond cleavage is ca. 270 kJ/mol (Fig. 5.35) [99].

Based on this valence bond consideration on the biradicaloid nature of *o*-quinodimethane, we will consider biradical character of periacenes. For simplicity, we focus on [3.*n*]periacenes (i.e., *pericondensed anthracenes*, so-called *anthenes*), because all anthenes are subjected to loss of only one double bond when the structure is

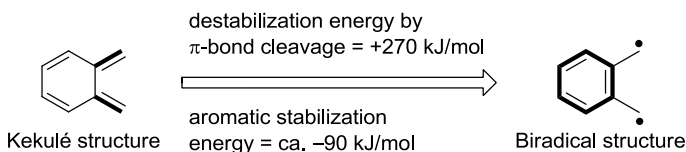


Figure 5.35 Energy balance between from Kekulé to biradical form.

written with a maximum number of Clar sextets (Fig. 5.36). In these biradical forms, Clar sextets, the isolated double bonds, and the unpaired electrons have fixed positions, i.e., the influence of sextet migration or spin delocalization is limited. Therefore, the discussion of the biradical character can be concentrated on the energy balance between the formal loss of the double bond and the aromatic sextet formation.

Anthracene ([3.1]periacene) has one aromatic sextet in the Kekulé form, whereas two sextets in the biradical form. Destabilization energy during the transformation from the Kekulé form to the biradical form is very large. Therefore the Kekulé form has dominant contribution to the ground state in anthracene. The energy difference in bisanthene ([3.3]periacene) between the Kekulé and biradical forms is smaller than that of anthracene, since the unpairing in bisanthene generates additional two sextets. For larger periacenes such as teranthene ([3.5]periacene) and quarteranthene ([3.7]periacene), the difference of the sextets increases with increasing molecular size; three for teranthene and four for quarteranthene. More sextets in the biradical forms result in more dominant contribution of the biradical form to the ground state.

For more quantitative discussions, singlet open-shell character was estimated using the index defined by Yamaguchi [84, 85] coupled to the symmetry-broken UBHandHLYP/6-31G* calculation. The amount of singlet open-shell character, y_i , can be determined from the following equations: $y_i = 1 - 2T_i / (1 + T_i^2)$, $T_i = (n_{\text{HOMO}-i} - n_{\text{LUMO}+i}) / 2$, where $n_{\text{HOMO}-i}$ and $n_{\text{LUMO}+i}$ represent natural orbital occupation numbers of HOMO- i and LUMO+ i , respectively. The y_0 and y_1 , which are determined from the HOMO-LUMO pair and the HOMO-1-LUMO+1 pair, are related to first and second π -bond cleavages, respectively, and vary continuously from zero to unity.

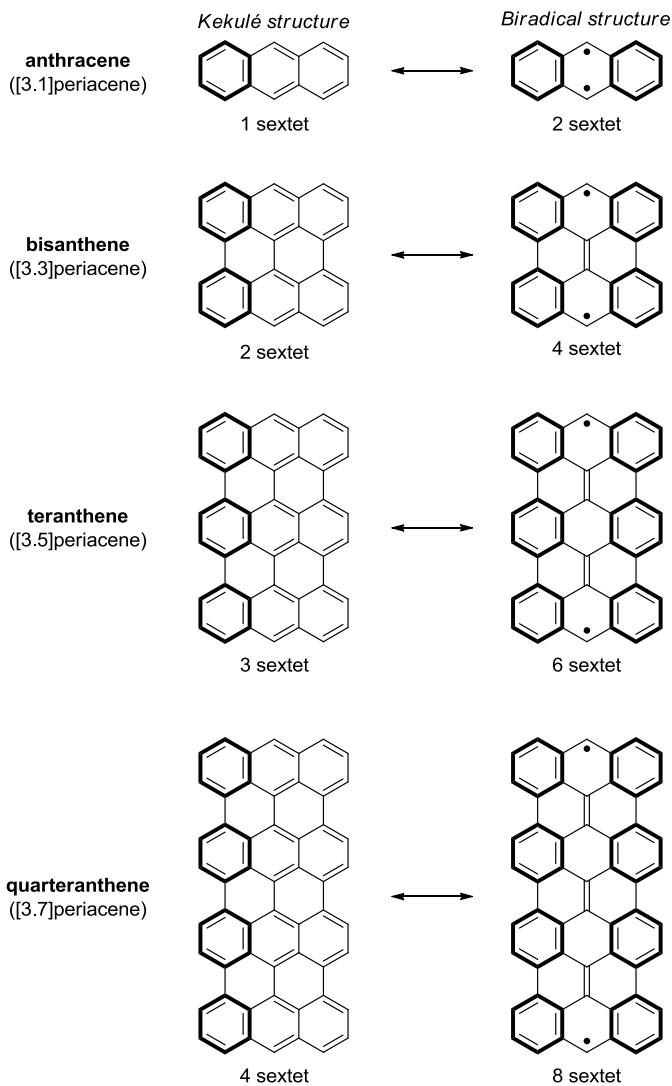


Figure 5.36 Resonance Structures of [3.n]periacenes (anthenes). The six-membered rings depicted by bold lines represent the Clar aromatic sextets.

Table 5.1 Amounts of open-shell character y_0 and y_1 of $[m.n]$ periacenes

y_0	m = 2	3	4	5	6	7
n = 1	0.00	0.00	0.01	0.07	0.20	0.40
3	0.00	0.12	0.60	0.84	0.94	0.98
5	0.01	0.59	0.91	0.98	0.99	1.00
7	0.05	0.84	0.98	1.00	1.00	1.00
y_1	m = 2	3	4	5	6	7
n = 1	0.00	0.00	0.00	0.00	0.01	0.02
3	0.00	0.00	0.01	0.02	0.07	0.20
5	0.00	0.00	0.01	0.05	0.23	0.54
7	0.00	0.00	0.01	0.10	0.44	0.77

A perfect biradical molecule has y_0 of unity and y_1 of zero, but for the molecule with large y_1 , the biradical description is inaccurate and tetradical character should be taken into account. Table 5.1 lists the y_0 and y_1 values of polyacenes and polyperiacenes.

Bisanthene ([3.3]periacene) [100–104] has a small y_0 (12%), suggesting that the molecule is basically classified into a closed-shell molecule. However, high reactivity toward oxygen of bisanthene might imply potential biradicaloid nature. A larger homolog, teranthene ([3.5]periacene), gives a large value of y_0 (59%), clearly indicating its appreciable biradical character. The biradical ground states are also supported by the spin density distribution as shown in Fig. 5.37, which indicates anti-parallel spins residing on the zigzag edges of these periacenes. It is noted that molecules larger than [6.5]periacene possess a sizable y_1 value, suggesting an appreciable contribution of a tetradical form to the ground state. The largest polyperiacene [7.7]periacene in Table 5.1 has very large y_0 (1.00) and y_1 (0.77), indicating the singlet tetradical ground state.

5.4.5.1 Synthesis of bisanthene and teranthene

Unsubstituted bisanthene has been isolated as an air-sensitive crystalline powder [105]. UV-Vis [105, 106], photoelectron [107], fluorescence [108], and vibrational spectra [109] of this labile compound have also been measured. Although X-ray crystal struc-

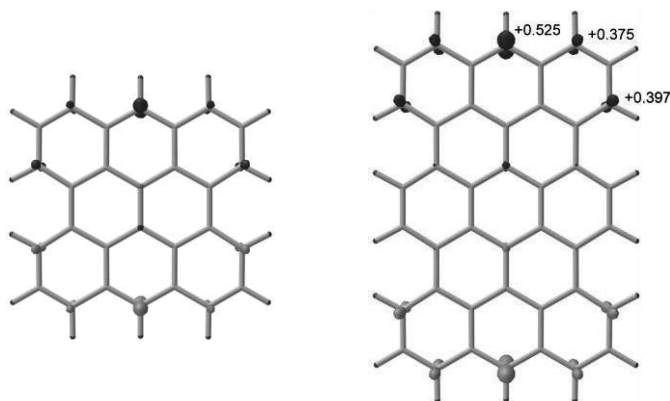
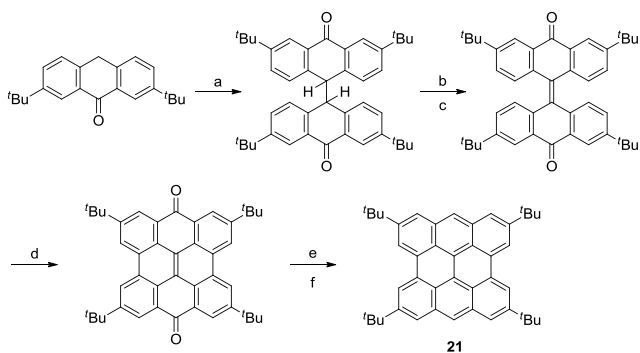


Figure 5.37 The spin density distributions of bisanthene (left) and teranthene (right).

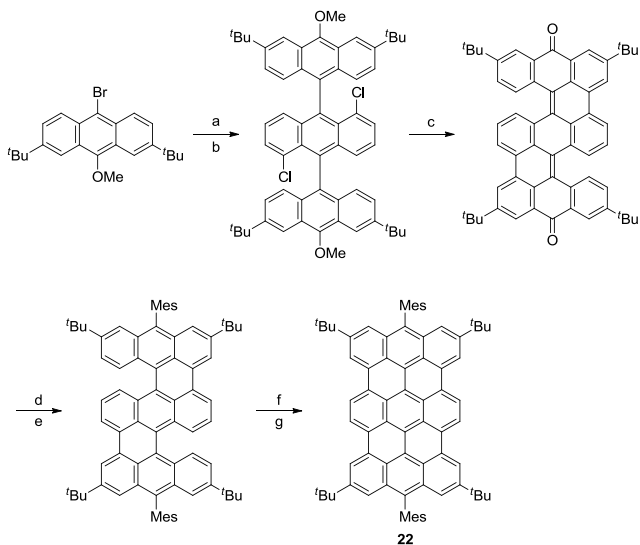
ture of unsubstituted bisanthene has not yet been determined, Wu and co-workers recently reported the crystal structure of a bis(4-(trifluoromethyl)phenyl) derivative [104]. They also investigated the stability and electrochemical properties of some derivatives. An important study on the reactivity of bisanthene comes from Scott and co-workers, who found that the Diels–Alder cycloaddition of acetylene to a bay region could be a suitable method to form cylindrical hydrocarbons [103].

Kubo and co-workers also prepared a tetra-*tert*-butyl derivative (**21**) of bisanthene for investigating biradical character experimentally. The synthetic procedure for **21** is basically the same as that of unsubstituted bisanthene (Scheme 5.3). The final compound **21** was obtained as a deeply blue solid and was found to be moderately stable. Its half-life in a toluene solution is 19 days at room temperature open to air under room light. Recrystallization of **21** from a CH_2Cl_2 –hexane solution gave single crystals suitable for X-ray crystallographic structure analysis.

In contrast to bisanthene, teranthene has not been explored experimentally before Kubo and co-workers report the synthesis and characterization of a derivative of **3–5** [110]. They designed the teranthene derivative **22** having mesityl and *tert*-butyl groups, because of improvement of solubility and stability. Scheme 5.4



Scheme 5.3 Synthetic procedure for **21**. Reagents and conditions: (a) FeCl_3 , AcONa , AcOH/water (3:1), reflux, 1 h, 73%; (b) KOH , EtOH , reflux, 0.5 h; (c) $\text{K}_2\text{S}_2\text{O}_8$, rt, 2 h, quant. (2 steps); (d) $h\nu$ (>350 nm), $\text{acetone}/\text{benzene}$ (7:1), rt, 2 h, 51%; (e) NaBH_4 , AlCl_3 , THF , reflux, 2 h; (f) *p*-chloranil, toluene , reflux, 0.25 h 49% (2 steps).



Scheme 5.4 Synthetic procedure for **22**. Reagents and conditions: (a) $n\text{BuLi}$, ether, 0°C , then 1,5-dichloroanthraquinone, 0°C to RT; (b) NaI , $\text{NaH}_2\text{PO}_2 \cdot \text{H}_2\text{O}$, AcOH , 150°C , 90% (2 steps); (c) KOH , quinoline , 190°C , 78%; (d) Mestylceriumbromide, THF/ether (4:1), -30°C ; (e) NaI , $\text{NaH}_2\text{PO}_2 \cdot \text{H}_2\text{O}$, AcOH , 150°C , 75% (2 steps); (f) DDQ , $\text{Sc}(\text{OTf})_3$, toluene , reflux; (g) $\text{N}_2\text{H}_4 \cdot \text{H}_2\text{O}$, toluene , RT, 72% (2 steps).

displays the synthetic procedure for **22**. The final product **22** was obtained as a dark green solid. Single crystals suitable for X-ray crystallographic analysis were obtained by recrystallization from a CH_2Cl_2 -hexane solution under argon flow. A toluene solution of **22** showed gradual decomposition with a half-life period of three days open to air under room light at room temperature.

5.4.5.2 Geometrical consideration of singlet biradical character

Figure 5.38 shows the crystal structures of **21** and **22**, and bond lengths of them are summarized in Fig. 5.39. The molecular geometry of **22** reflects its prominent biradical character. As shown in Fig. 5.40, the biradical resonance contribution enforces shortening of the *a* bonds due to their double bond character. The length of the *a* bond in **22** (C8-C18 in Fig. 5.38) is found to be 0.1424(4) nm, which is considerably short compared to the general $\text{C}(\text{sp}^2)\text{-C}(\text{sp}^2)$ single bond length (0.1467 nm) [111], whereas the correcting bond of **21** (0.1451(2) nm) is closer in length to the

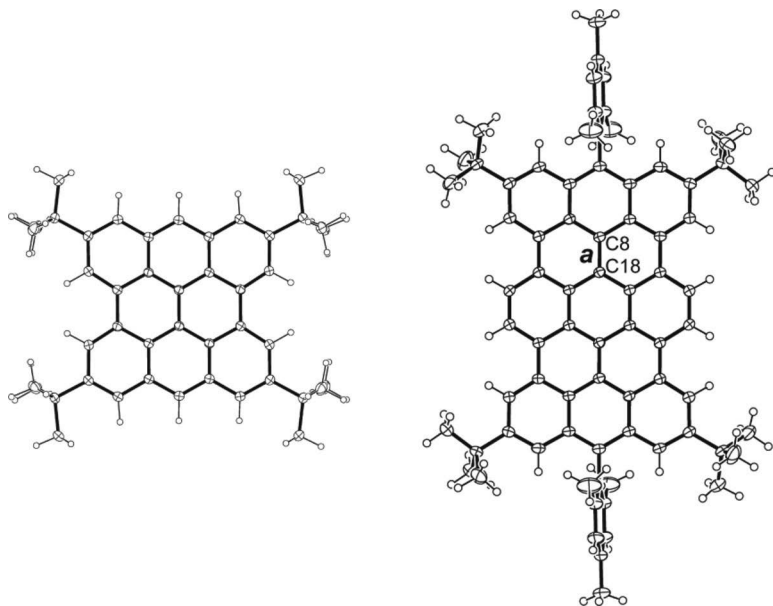


Figure 5.38 The crystal structures of **21** (left) and **22** (right).

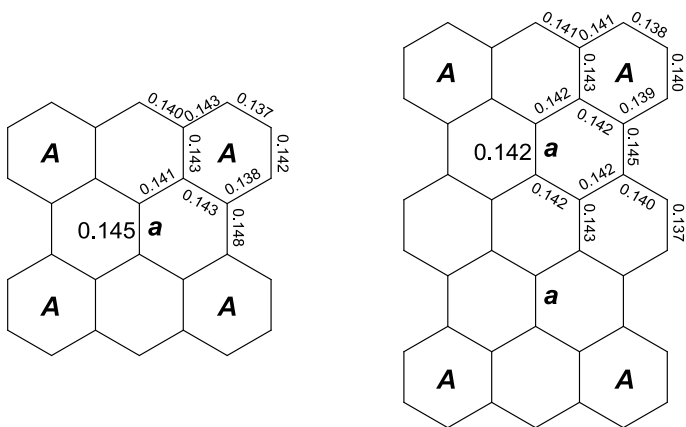


Figure 5.39 The bond lengths in nanometers of **21** (left) and **22** (right).

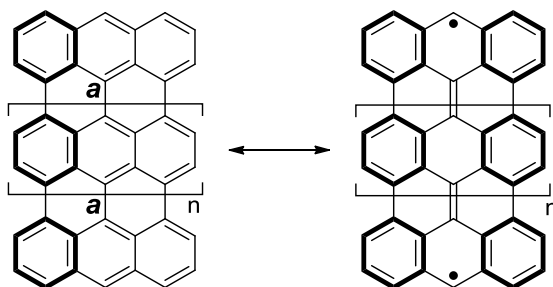


Figure 5.40 The resonance formula of [3.n]pericene.

general $C(sp^2)-C(sp^2)$ single bond. Additionally, the four corner six-membered rings (denoted by *A* in Fig. 5.39) show a considerable decrease of bond length alternation, in other words, the corner rings of **22** bears more benzene character than those of **21**.

These geometrical findings are in line with the extent of the biradical character estimated at the UBHandHLYP level of theory, which predicts a large LUMO occupation number of only 0.12 for **21**, whereas 0.59 for **22** (Table 5.1).

Upon transforming into the biradical form, **21** contains only two additional sextets and therefore the destabilization energy due to the π -bond cleavage cannot be fully compensated, and therefore

21 favors electron pairing. In contrast, **22** includes three additional sextets in its biradical form, and therefore both the Kekulé and the biradical forms contribute similarly to the ground state.

5.4.5.3 Singlet–triplet energy gap

Magnetic properties of singlet biradical species cannot be investigated directly by the method of ESR and SQUID. Instead, the presence of thermally accessible triplet species would be a good criterion for the singlet biradical ground state. The CD_2Cl_2 solution of **22** showed no $^1\text{H-NMR}$ signals from the teranthene core at room temperature, while upon cooling, progressive line sharpening was observed (Fig. 5.41). This behavior is associated with the presence of thermally excited triplet species at elevated temperatures.

The small singlet–triplet energy gap (ΔE_{S-T}) of **22** was confirmed by SQUID measurements of a powdered sample (Fig. 5.42), which showed an increasing susceptibility above 220 K. Careful curve fitting based on the Bleaney–Bowers equation for the singlet–triplet model [112] gave the ΔE_{S-T} of 1920 K (16.0 kJ/mol). The

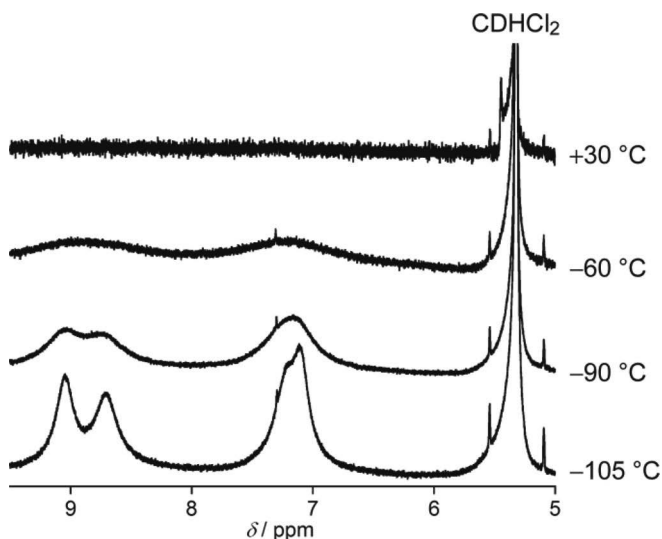


Figure 5.41 Variable temperature $^1\text{H-NMR}$ spectra of **22** in CD_2Cl_2 in the aromatic region.

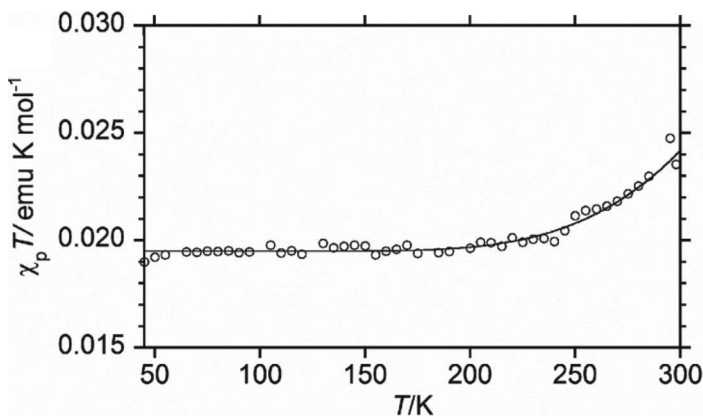


Figure 5.42 χT - T plot of the powdered **22**. The measured data are plotted as open circles. The theoretical curve is drawn using the Bleaney-Bowers equation for the singlet-triplet model [112], with the parameters of $2 J/k_B = 1920$ K, impurity spin contamination = 5.2%, $g = 2.00$, diamagnetic susceptibility = -771×10^{-6} emu/mol.

determined ΔE_{S-T} value was in good agreement with the theoretical value of 2590 K calculated for **22** at the B3LYP/6-31G** level. Thus, the two unpaired electrons in **22** couple very weakly compared to most Kekulé compounds ($\Delta E_{S-T} \sim 10^4$ K). In contrast, **21** gave sharp $^1\text{H-NMR}$ signals even at 383 K, indicating a negligible influence of the triplet species due to a larger ΔE_{S-T} . The value of ΔE_{S-T} for **1** was estimated to be 6300 K at the B3LYP/6-31G** level.

5.4.5.4 HOMO-LUMO energy gap

The HOMO-LUMO energy gap is closely related to the singlet biradical character, because the electronic structure of singlet biradical species can be described by a double excitation of electrons from HOMO to LUMO in a two-electron-two-orbital model. A smaller HOMO-LUMO gap leads to a larger extent of an admixture of a doubly excited configuration $^1\Phi_{H,H \rightarrow L,L}$ into the ground configuration $^1\Phi_0$. In addition, a small HOMO-LUMO gap is also relevant to promotion to an energetically low-lying triplet excited state.

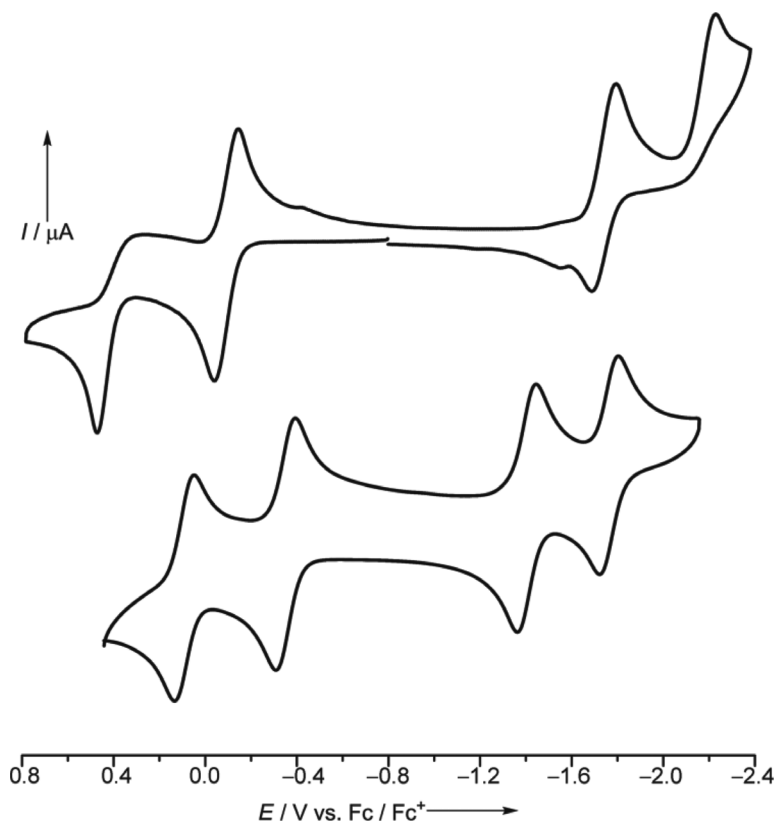


Figure 5.43 Cyclic voltammogram of **21** (upper) and **22** (lower).

The cyclic voltammogram of **22** shows four reversible redox waves; $E_2^{\text{ox}} = +0.09$, $E_1^{\text{ox}} = -0.35$, $E_1^{\text{red}} = -1.40$, $E_2^{\text{red}} = -1.76$ (V vs. Fc/Fc⁺, Fig. 5.43). From the difference between the first oxidation and reduction potentials, the electrochemical HOMO–LUMO gap amounts to 1.05 eV, which is 0.63 eV smaller than that of **21**.

The electronic absorption spectrum of **22** in a CH₂Cl₂ solution gave a low-energy band at 1054 nm ($\epsilon = 8000$ cm/M) as shown in Fig. 5.44, from which the optical HOMO–LUMO gap was determined to be 1.18 eV. This value is 0.70 eV smaller than that of **21**. The smaller HOMO–LUMO gap of **22** is consistent with its larger biradical character.

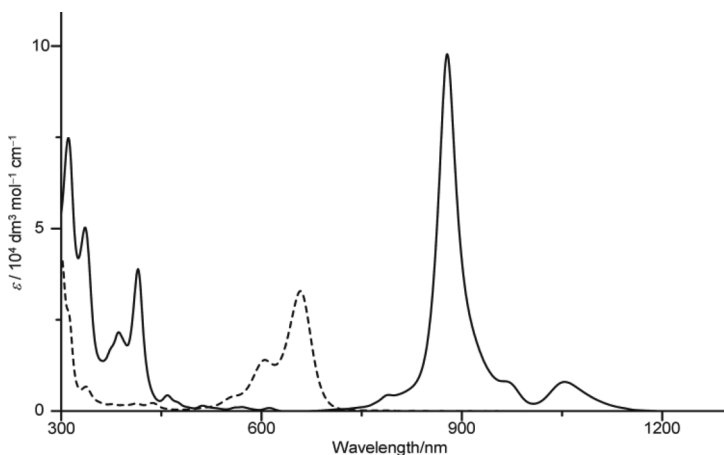


Figure 5.44 Electronic absorption spectra of **21** (---) and **22** (—).

5.4.5.5 Transition probability from S_0 to S_1 state

One signature of the biradicaloid character is the presence of a low-lying excited singlet state dominated by the doubly excited configuration. Negri and co-workers reported that a weak low-energy band was observed for the thienoquinoid compound with large biradical character [113]. Computational analysis indicated that this weak band is assignable to a doubly excited band.

As shown in Fig. 5.44, teranthene **22** also affords a weak low-energy band centered at 1054 nm, whereas non-magnetic **21** gives an intense band at 658 nm. The band profile observed in **21** is quite similar to that of [2.n]periacene (so called *rylenes*) (Fig. 5.45) [114]. Basically, [2.n]periacene has small singlet biradical character, as shown in Table 5.1. The feature of the lowest-energy bands is the similarity of the shape among them, that is, well-structured vibrational bands. It is interesting that all of these non-magnetic PAHs, including **21**, have a common feature of the band shape. However, antiferromagnetic **22** is not the case. Small absorption coefficient of the lowest-energy band in **22** probably originates from a small transition probability due to the localization of unpaired electrons at the zigzag edges.

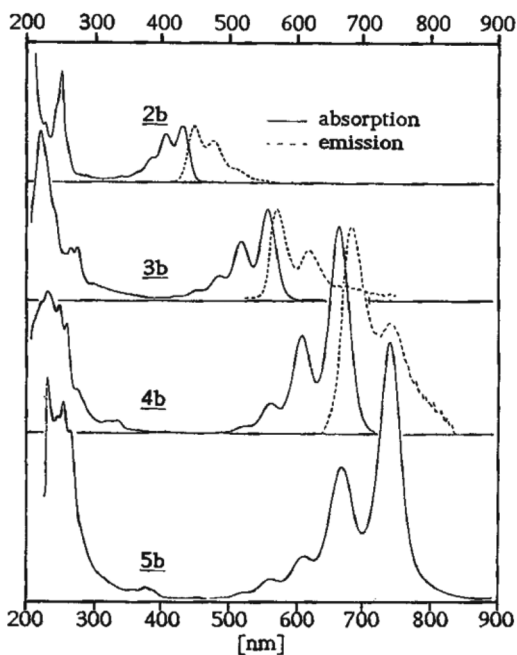


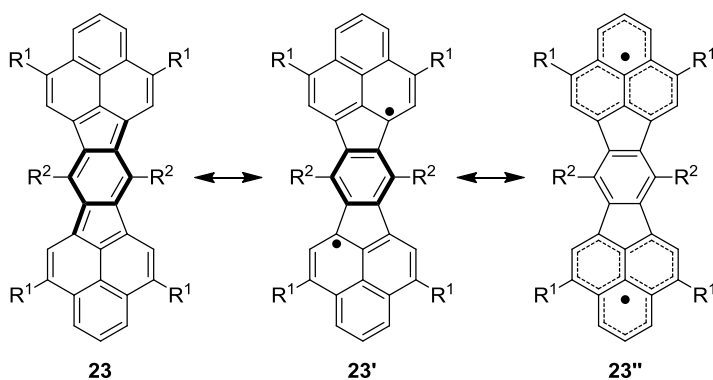
Figure 5.45 Electronic absorption and fluorescence spectra of [2.*n*]periacene. After ref. 114. **2b**, perylene ([2.3]periacene), **3b**, terrylene ([2.5]periacene), **4b**, quarterrylene ([2.7]periacene), and **5b**, pentarylene ([2.9]periacene).

5.5 Highly Stable Antiferromagnetic PAHs

5.5.1 Molecular Design for Thermodynamically Stabilized Antiferromagnetic Molecules

Stability is a very important factor for exploring the feature of antiferromagnetic PAHs and would be inevitable for the use as functional materials. Intrinsic stability of open-shell species can be attained by the delocalization of unpaired electrons. On the basis of ROMP2 calculation, the delocalization of one electron to one double bond leads to a thermodynamic stabilization amounting to 77.5 kJ/mol [115].

As mentioned above, a quinoidal π -conjugation confers singlet biradical (i.e., antiferromagnetic) character on a molecule, and the



23a, $R^1 = R^2 = H$; **23b**, $R^1 = \text{tert-Bu}$, $R^2 = H$; **23c**, $R^1 = H$, $R^2 = \text{Ph}$

Figure 5.46 Resonance forms of a *p*-quinodimethane-linked bisphenalenyl **23**.

delocalization of unpaired electrons appearing in the biradical canonical form would lead to thermodynamic stabilization of the molecule of interest. Following this design concept, Kubo and co-workers designed a molecule (**23**) that consists of *p*-quinodimethane and two phenalenyl rings (Fig. 5.46). In the resonance formula, the phenalenyl ring acts as a spin-delocalizing unit, because its highly symmetric structure (D_{3h}) enables an unpaired electron to delocalize on the entire molecule [116, 117]. The quinoid Kekulé form **23** would resonate well with the biradical form **23'** as a result of gaining the aromatization energy of the central six-membered ring, and then the unpaired electrons emerging on the terminal carbons of the *p*-quinodimethane moiety can delocalize on the phenalenyl rings (the form **23''**). This resonance consideration leads to the conclusion that **23** should be a thermodynamically stabilized singlet biradical.

5.5.2 Theoretical Assessment of Singlet Biradical Character

A CASSCF(2,2)/6-31G//RB3LYP/6-31G** calculation for **23a** gave the LUMO occupation number of 0.30, and consequently the amount of the biradical character was estimated to be 30%. Together, a broken-symmetry UB3LYP/6-31G** calculation of **23a** gave the

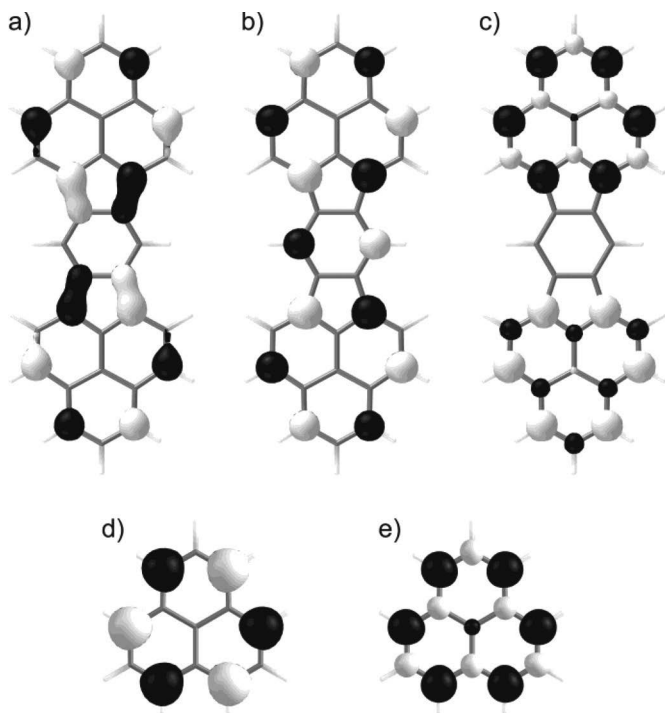


Figure 5.47 (a) HOMO, (b) LUMO, and (c) spin density of **23a**. (d) SOMO and (e) spin density of phenalenyl radical. The calculations were performed at RB3LYP/6-31G** [(a) and (b)] and UB3LYP/6-31G** [(c), (d), and (e)] levels of theory. Bright and dark surfaces of the spin density maps represent α and β spin densities drawn at 0.004 e/au³ level, respectively.

LUMO occupation number of 0.37 with spin contaminations $\langle S^2 \rangle = 0.65$. The spin density map of **23a** is shown in Fig. 5.47.

The relatively large biradical character of **23** is associated with a weak coupling of two unpaired electrons on the phenalenyl rings through the benzene linker. With the help of a perturbation MO analysis [118], the SOMO of phenalenyl radical is weakly perturbed by the MOs of benzene, because the aromatic character of benzene serves a wide energy gap between the bonding and anti-bonding orbitals and hence the MOs of both fragments differ considerably in energy. Thus, the mixing of the phenalenyl's SOMO with the benzene's MOs is not effective, and the HOMO and LUMO of **23**

retain the character of the SOMO of phenalenyl radical as shown in Fig. 5.47. For this reason, **23** has a small energy gap as well as a large spatial overlap between the HOMO and LUMO, which are favorable for the mixing of $^1\Phi_{\text{H,H}\rightarrow\text{L,L}}$ with $^1\Phi_{\text{H,H}}$.

5.5.3 Antiferromagnetic Couplings of Two Unpaired Electrons

The intramolecular antiferromagnetic coupling of two unpaired electrons of interest in **23** was assessed with a tetra-*tert*-butyl derivative **23b** [119]. The solution $^1\text{H-NMR}$ spectrum of **23b** gave very broad signals in the aromatic region at room temperature, and upon cooling, progressive line sharpening was observed. Weak coupling of unpaired electrons within the molecule leads to a small energy gap between the singlet ground state and the excited triplet state ($\Delta E_{\text{S-T}}$), and the thermally excited triplet species would cause the signal broadening at elevated temperatures. Actually, the triplet species was detected by a solid-state ESR measurement, which gave signals with a zero-field parameter of $D = 9.6$ mT and $E \leq 0.2$ mT. Least-square curve fitting of the signal intensities at various temperatures gave the $\Delta E_{\text{S-T}}$ value of 20.4 kJ/mol, from which we could determine the intramolecular coupling of 20.4 kJ/mol. It is noted that the value is almost 8% of the rotational barrier of the ethylene C–C double bond (270 kJ/mol).

Inadequate coupling of two unpaired electrons within the molecule would give an opportunity for unpaired electrons to experience an antiferromagnetic coupling between molecules. The intermolecular antiferromagnetic coupling in **23** could be assessed with a diphenyl derivative **23c**, which had no substituents on the phenalenyl rings [120]. As shown in Fig. 5.48 (a), **23c** formed a one-dimensional (1D) chain in a slipped stacking arrangement with an average π – π distance of 0.3137 nm, which was substantially shorter than the sum of the van der Waals radius of carbon atom (0.34 nm). The π – π overlap was found only on the phenalenyl ring (Fig. 5.48 (b)) in the same arrangement as that of a π -dimer of phenalenyl radical itself [117]. In the π -dimer of phenalenyl radical, a staggered stacking maximizes a SOMO–SOMO interaction (Fig. 5.48 (c)), and the very effective overlap of SOMOs is one of the crucial attractive

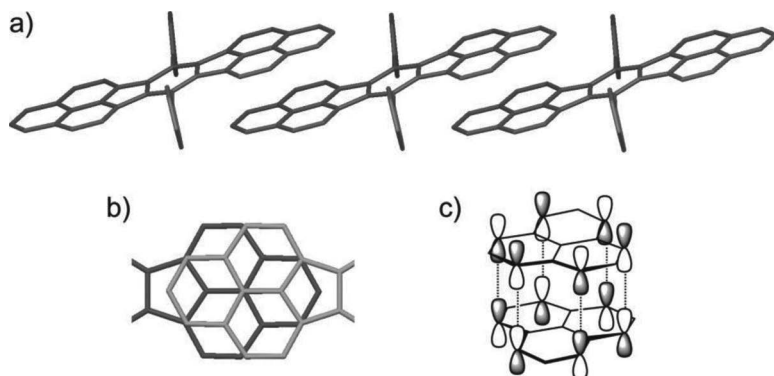


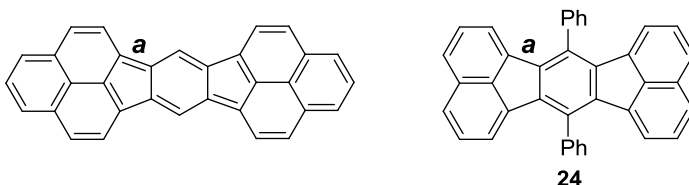
Figure 5.48 One-dimensional stack of **23c**. (b) Top view of overlapping phenalenyl rings. (c) SOMO-SOMO overlap of the π -dimer of phenalenyl radical.

bonding interactions [121]. Therefore, the attractive force in the 1D-stack of **23c** would originate from the intermolecular coupling of unpaired electrons, in addition to a conventional dispersion force.

5.5.4 Coexistence of Intra- and Intermolecular Antiferromagnetic Couplings

In the 1D-stack of **23c**, the length of the bonds (denoted by a) connecting the phenalenyl rings and the benzene ring is longer than that of **23b** but is still shorter than that of the corresponding bonds of 7,14-diphenylacenaphtho[1,2- k]fluoranthene **24** [122]; 0.1470 nm (**23c**), 0.1450 nm (**23b**), 0.1479 nm (**24**). The length of the bond a in **24** is sensitive to the extent of the intramolecular coupling of two unpaired electrons, because the bond a has both single- and double-bond character in the quinoid Kekulé form but only single-bond character in the biradical forms. On the other hand, only single-bond can be drawn in **24**, and consequently, the length of the bond a in **24** would be equivalent to that of a perfect biradical state of **23**. Therefore, the intermediate bond length of **23c** implies that the antiferromagnetic coupling would be operative not only between molecules but also within a molecule.

The optical spectrum of **23c** in a solid state showed a drastic red-shift of the lowest-energy band with respect to the solution



band (Fig. 5.49), due to the long-range π -conjugation through the intra- and intermolecular couplings of electrons. The shift amounts to $\sim 6600\text{ cm}^{-1}$. The large red-shift due to the coexistence of the couplings implies that the 1D chain of **23c** mimics the electronic structure of an infinite polyene, although the magnitude of the coupling of unpaired electrons is quite different.

The strength of the antiferromagnetic couplings is quantum-chemically estimated by Huang and Kertesz [123]. They interpreted the electronic structure of the 1D chain using an alternating Heisenberg chain model, and interestingly, found that the *inter* molecular coupling (3400 K , $= 28\text{ kJ/mol}$) is stronger than the *intra* molecular one (2300 K , $= 19\text{ kJ/mol}$).

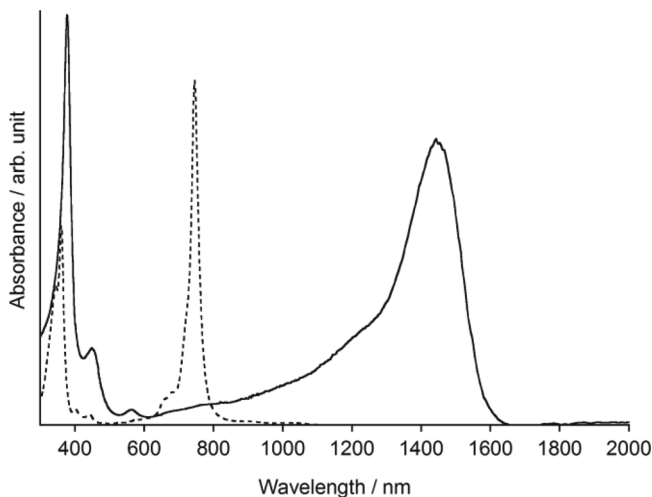


Figure 5.49 Optical spectra of **23c**. Absorption spectrum (---) in CH_2Cl_2 , and optical conductivity (—) obtained with light polarized along the stacking direction.

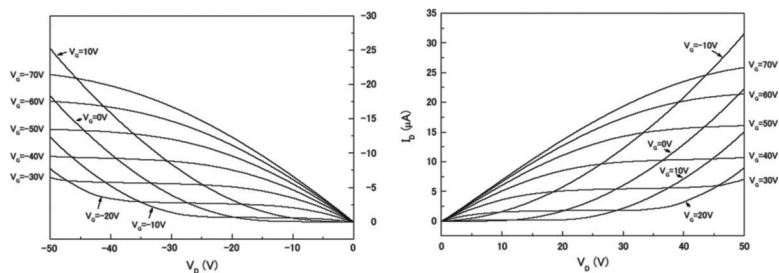


Figure 5.50 Output characteristics of the ambipolar OFET based on **23c** for negative (left) and positive gate (right).

Through the long-range antiferromagnetic coupling (i.e., a weak π -conjugation), the solid **23c** is invested with an electro-conductive property. The electro-conductivity of a compressed pellet of **23c** at room temperature was $1.0 \times 10^{-5} \text{ Scm}^{-1}$, with an activation energy of 0.3 eV at 200–300 K. It is noted that the conductivity is obtained in a single component state, not a charge transfer complex or salt, and is substantially large among structurally well-defined hydrocarbon molecules. An extended Hückel theory band structure calculation gave a very large dispersion in the valence and conduction bands along the stacking direction, fully supporting the conductive behavior. Thin-film properties and ambipolar transport are also investigated. The organic field-effect transistors (OFETs) based on **23c** exhibited ambipolar transport with balanced hole and electron mobilities in the order of $10^{-3} \text{ cm}^2/\text{V s}$ (Fig. 5.50) [124].

5.5.5 Non-Linear Optical Property

Weak coupling of two unpaired electrons allows the electronic distribution along the π -conjugated system to distort easily. Nakano and co-workers theoretically found that molecules with an intermediate amount of singlet biradical character feature an enhanced third-order nonlinear optical response, and consequently a large two-photon absorption (TPA) activity [125–128].

Kamada and co-workers actually measured the TPA activity of some singlet biradicals including **23b** and **23c**, and found that these singlet biradicals have much stronger TPA activity than closed-shell

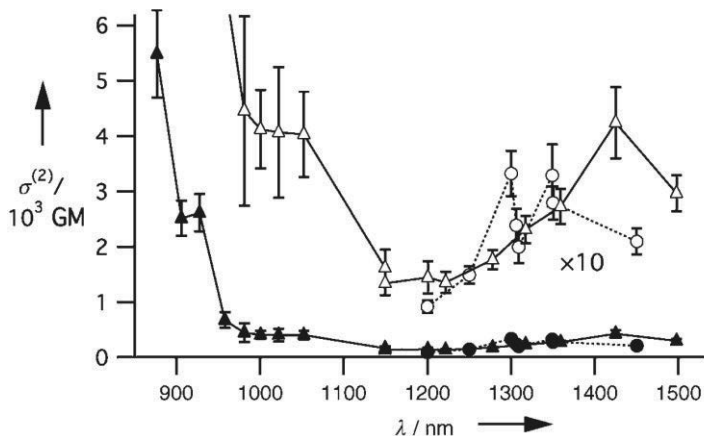


Figure 5.51 Two-photon absorption spectra of **23b** (circles) and **23c** (triangles). After ref. 129.

Table 5.2 Two-photon absorption properties of hydrocarbons

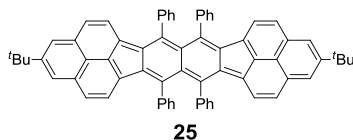
Compounds	$\sigma^{(2)[a]}$ [GM]	$\lambda^{(2)[b]}$ [nm]
23b	330	1300
23c	424	1425
25	890 ^[c]	1500
TIPS-pentacene	27	875
diphenyloctatetraene	61	608
bis(<i>o</i> -methylstyryl)benzene	66	590

^[a] Peak two-photon absorption cross section.

^[b] Wavelength of the two-photon peak.

^[c] Maximum value observed in the one-photon off-resonance region.

π -conjugated hydrocarbons [129]. Fig. 5.51 shows TPA spectra of **23b** and **23c**, and the TPA cross-sectional values determined are listed in Table 5.2.



5.5.6 Experimental Estimation of the Amount of Singlet Biradical Character

Nakano and co-workers demonstrated that the amount of singlet biradical character can be deduced from the equation $y = 1 - 4|t|/(U^2 + 16t^2)^{1/2}$, where U represents the difference between on-site and inter-site Coulomb integrals, and t is a transfer integral, using the localized natural orbital basis [130]. This formula is alternatively expressed as

$$y = 1 - \sqrt{1 - \left(\frac{E_{S1u,S1g} - E_{T1u,S1g}}{E_{S2g,S1g}} \right)^2} \quad (5.1)$$

where $E_{S2g,S1g}$, $E_{S1u,S1g}$, and $E_{T1u,S1g}$ correspond to the excitation energies of the higher singlet state of g symmetry (two-photon allowed excited state), of the lower singlet state with u symmetry (one-photon allowed excited state), and of the triplet state with u symmetry, respectively. These parameters can be determined experimentally from TPA, UV-Vis-NIR, and ESR (or phosphorescence, SQUID) measurements, respectively. The amount of singlet biradical character experimentally estimated for **1b** was 34%, which is in good agreement with the value calculated by the CASSCF(2,2) or broken-symmetry UB3LYP calculations. It is noted that a pentacene derivative was found to have non-negligible singlet biradical character of 15%. High reactivity of pentacene might be related partially to the biradical character in the ground state.

5.6 Concluding Remarks

Aromatic compounds have a long history of being important subjects of research in organic chemistry, physical chemistry, and material science. In the studies, Kekulé, Robinson, and Hückel played a crucial role in understanding the electronic structure relevant to aromaticity, and Clar extended the idea into the PAH chemistry through the extensive synthetic and investigative works. The classical PAH chemistry was almost summed up by Clar and was documented by himself in *Polycyclic Hydrocarbons, Vols. 1 and 2*, 1964. Modern new achievement of PAH chemistry has arisen from Mullen's extensive

work on extraordinary large PAH molecules, and his successive studies reach nanographene chemistry. Another notable progress in PAH chemistry has been recently seen in acenes, which has attracted considerable attention from material scientists as use of OFET.

Acenes have another prominent feature that was first pointed out theoretically by Bendikov and co-workers in 2004, that is, the antiferromagnetic ground state. This peculiar state is also seen in *peri*-condensed acenes, *periacenes*, and is closely related to edge state of graphene and nanographene. The origin of the antiferromagnetic state is associated with the formation of aromatic sextets, being confirmed by our experimental study based on the synthesis and characterization of teranthene. Exploiting electron spin appearing at molecular edges will broaden the scope of PAHs and nanographene, for instance, the application for spintronics and optoelectronic devices.

References

1. Moss, G. P. (1998). Nomenclature of fused and bridged fused ring systems, *Pure Appl. Chem.*, **70**, 143–216.
2. For a classical nomenclature of ring fusion including *peri*- and *kata*-, see Zahradnik, R. (1965). Electronic Structure and Properties of Non-Alternant Hydrocarbons, *Angew. Chem. Int. Ed. Engl.* **4**, 1039–1050.
3. Kekulé, A. (1865). Sur la constitution des substances aromatiques. *Bull. Soc. Chim. Paris* **3**, 98–110.
4. Kekulé, A. (1866). Untersuchungen über Aromatische Verbindungen. *Ann. Chem. Pharm.*, **137**, 129–196.
5. Kekulé, A. (1869). Über die Constitution des Benzols, *Ber. Deutsch. Chem. Ges.*, **2**, 362–365.
6. Armit, J. W., and Robinson, R. (1925). CCXI-Polynuclear heterocyclic aromatic types. Part II. Some anhydronium bases., *J. Chem. Soc.*, 1604–1618.
7. Hückel, E. (1931). Quantentheoretische Beiträge zum Benzolproblem I. Die Elektronenkonfiguration des Benzols und verwandter Verbindungen. *Z. Physik*, **70**, 204–286.
8. Hückel, E. (1931). Quantentheoretische Beiträge zum Benzolproblem II. Quantentheorie der induzierten Polaritäten. *Z. Physik*, **72**, 310–337.

9. Hückel, E. (1932). Quantentheoretische Beiträge zum Problem der aromatischen und ungesättigten Verbindungen. III. *Z. Physik*, **76**, 628–648.
10. Hückel, E. (1933). Die freien Radikale der organischen Chemie Quantentheoretische Beiträge zum Problem der aromatischen und ungesättigten Verbindungen. IV. *Z. Physik*, **83**, 632–668.
11. Clar, E. (1964). *Polycyclic Hydrocarbons*, vol. I and II (Academic Press, London).
12. Clar, E. (1972). *The Aromatic Sextet* (Wiley, London).
13. Kai, Y., Hama, F., Yasuoka N., and Kasai, N. (1978). Structural chemistry of layered cyclophanes. III. Molecular structures of [2.2](2,7)pyrenophane-1,1'-diene and pyrene (redetermined) at -160°C . *Acta Cryst.*, **B34**, 1263–1270.
14. Diederich, F., and Staab, H. A. (1978). Benzenoid versus annulenoid aromaticity: Synthesis and properties of kekulene. *Angew. Chem. Int. Ed. Engl.*, **17**, 372–374.
15. Krieger, C., Diederich, F., Schweitzer, D., and Staab, H. A. (1979). Molecular structure and spectroscopic properties of kekulene. *Angew. Chem. Int. Ed. Engl.*, **18**, 699–701.
16. Van der Linde, J., and Havinga, E. (1965). The addition of bromine to phenanthrene in methanol as a solvent, *Recl. Trav. Chim. Pays-Bas*, **84**, 1047–1057.
17. Diels, O., and Alder K. (1931). Synthesen in der hydroaromatischen Reihe. VIII. Mitteilung: Dien-Synthesen des Anthracens. Anthracen-Formel, *Justus Liebigs Ann. Chem.*, **486**, 191–202.
18. Stevens, B., Perez, S. R., and Ors, J. A. (1976). Photoperoxidation of unsaturated organic molecules. $\text{O}_2^1\Delta_g$ Acceptor properties and reactivity, *J. Am. Chem. Soc.*, **96**, 6846–6850.
19. Mondal, R., Adhikari, R. M., Shah, B. K., and Neckers, D. C. (2007). Revisiting the stability of hexacenes, *Org. Lett.* **9**, 2505–2508.
20. Mallory, F. B., Butler, K. E., and Evans, A. C. (1996). Phenacenes: A family of graphite ribbons. 1. Syntheses of some [7]phenacenes by stilbene-like photocyclizations. *Tetrahedron Lett.* **37**, 7173–7176.
21. Mallory, F. B., Butler, K. E., Evans, A. C., Brondyke, E. J., Mallory, C. W., Yang, C., and Ellenstein, A. (1997). Phenacenes: A family of graphite ribbons. 2. Syntheses of some [7]phenacenes and an [11]phenacene by stilbene-like photocyclizations. *J. Am. Chem. Soc.* **119**, 2119–2124.

22. Schleyer, P. V. R., Maerker, C., Dransfeld, A., Jiao, H., and Hommes, N. J. R. V. E. (1996). Nucleus-Independent Chemical Shifts — A simple and efficient aromaticity probe, *J. Am. Chem. Soc.*, **118**, 6317–6318.
23. Chen, Z., Wannere, C. S., Corminboeuf, C., Puchta, R., and Schleyer, P. V. R. (2005). Nucleus-independent chemical shifts (NICS) as an aromaticity criterion, *Chem. Rev.*, **105**, 3842–3888.
24. Goddard, R., Haenel, M. W., Herndon, W. C., Krueger, C., and Zander, M. (1995). Crystallization of large planar polycyclic aromatic hydrocarbons: The molecular and crystal structures of hexabenzobenzocoronene [bcefhiklnoqr]coronene and benzo[1,2,3-*bc*:4,5,6-*b'c'*]dibenzocoronene, *J. Am. Chem. Soc.*, **117**, 30–41.
25. Akamatsu, H., and Inokuchi, H. (1950). On the electrical conductivity of violanthrone, iso-violanthrone, and pyranthrene, *J. Chem. Phys.*, **18**, 810–811.
26. Akamatsu, H., Inokuchi, H., and Handa, T. (1951). Electrical conductivity and magnetic susceptibility of ovalene, *Nature*, **168**, 520–521.
27. Inokuchi, H. (1951). Electrical conductivity of condensed polynuclear aromatic compounds, *Bull. Chem. Soc. Jpn.*, **24**, 222–226.
28. Inokuchi, H., Matsubara, N., Maruyama, Y., and Clar, E. (1965). Electrical conductivity of circumanthracene, *Nature*, **205**, p. 64.
29. Akamatsu, H., Inokuchi, H., and Matsunaga, Y. (1954). Electrical conductivity of the perylene–bromine complex, *Nature*, **173**, 168–169.
30. Saito, G., and Yoshida, Y. (2007). Development of conductive organic molecular assemblies: Organic metals, superconductors, and exotic functional materials, *Bull. Chem. Soc. Jpn.* **80**, 1–137.
31. Müllen, K., and Scherf, U. (2006). *Organic Light Emitting Devices: Synthesis, Properties and Applications* (Wiley-VCH, Weinheim).
32. Bredas, J.-L., Norton, J. E., Cornil, J., and Coropceanu, V. (2009). Molecular understanding of organic solar cells: The challenges, *Acc. Chem. Res.*, **42**, 1691–1699.
33. Bao, Z., and Locklin, J. (2007). *Organic field-effect transistors (optical science and engineering series)* (CRC Press, Boca Raton, FL).
34. Clar, E., and Ironside, C. T. (1958). hexabenzocoronene, *Proc. Chem. Soc.*, p. 150.
35. Hallux, A., Martin, R. H., and King, G. S. D. (1958) Synthesis of highly condensed aromatic polycyclic derivatives. Hexabenzocoronene, tetrabenzoperopyrene, and tetrabenzobisanthene, *Helv. Chim. Acta.*, **129**, 1177–1183.

36. Müller, M., Kübel, C., and Müllen K. (1998). Giant polycyclic aromatic hydrocarbons, *Chem. Eur. J.*, **4**, 2099–2109.
37. Stabel, A., Herwig, P., Müllen, K., and Rabe, J. P. (1995). Diodelike current–voltage curves for a single molecule–tunneling spectroscopy with submolecular resolution of an alkylated, *pericondensed* hexabenzocoronene, *Angew. Chem. Int. Ed. Engl.*, **34**, 1609–1611.
38. Herwig, P., Kayser, C. W., Müllen, K., and Spiess, H. W. (1996). Columnar mesophases of alkylated hexa-*peri*-hexabenzocoronenes with remarkably large phase widths, *Adv. Mater.*, **8**, 510–513.
39. Wu, J., Pisula, W., and Mullen, K. (2007). Graphenes as potential material for electronics, *Chem. Rev.* **107**, 718–747.
40. van de Craats, A. M., Waraman, J. M., Müllen, K., Geerts, Y., and Brand, J. (1998). The origin of electroluminescence at porous p-silicon layers electrolyte interfaces, *Adv. Matter.*, **10**, 36–38.
41. van de Craats, A. M., Warman, J. M., Fechtenkötter, A., Brand, J. D., Harbison, M. A. and Müllen, K. (1999). Record charge carrier mobility in a room-temperature discotic liquid-crystalline derivative of hexabenzocoronene, *Adv. Matter.*, **11**, 1469–1472.
42. Compound **8**: Müller, M., Mauermann-Düll, H., Wagner, M., Enkelmann, V., and Miillen, K. (1995). A cycloaddition–cyclodehydrogenation route from stilbenoids to extended aromatic hydrocarbons, *Angew. Chem. Int. Ed. Eng.* **35**, 1583–1586.
43. Compound **9**: Morgenroth, F., Reuther, E., and Müllen, K. (1997). Polyphenylene dendrimers: from three-dimensional to two-dimensional structures, *Angew. Chem. Int. Ed. Engl.*, **36**, 631–634.
44. Compound **10**: Wu, J., Gherghel, L., Watson, M. D., Li, J., Wang, Z., Simpson, C. D., Kolb, U., and Müllen, K. (2003). From branched polyphenylenes to graphite ribbons, *Macromolecules*, **36**, 7082–7089.
45. Compound **11**: Simpson, C. D., Brand, J. D., Berresheim, A. J., Przybilla, L., Räder, H. J., and Müllen, K. (2000). Synthesis of a giant 222 carbon graphite sheet, *Chem. Eur. J.*, **8**, 1424–1429.
46. Cai, J., Ruffieux, P., Jaafar, R., Bieri, M., Braun, T., Blankenburg, S., Muoth, M., Seitsonen, A. P., Saleh, M., Feng, X., Müllen, K., and Fasel, R. (2010). Atomically precise bottom-up fabrication of graphene nanoribbons, *Nature*, **466** 470–473.
47. Flynn, C. R., and Michl, J. (1974). $\pi\pi$ -Biradicaloid hydrocarbons. *o*-Xylylene. Photochemical preparation from 1,4-dihydrophthalazine in rigid glass, electric spectroscopy, and calculations, *J. Am. Chem. Soc.*, **96**, 3280–3288.

48. Reddy, A. R., and Bendikov, M. (2006). Diels–Alder reaction of acenes with singlet and triplet oxygen — theoretical study of two-state reactivity, *Chem. Comm.*, 1179–1181.
49. Bendikov, M., Duong, H. M., Starkey, K., Houk, K. N., Carter, E. A., and Wudl, F. (2004). Oligoacenes: Theoretical prediction of open-shell singlet diradical ground state, *J. Am. Chem. Soc.*, **126**, 7416–7417 and p. 10493.
50. Jiang, D., and Dai, S. (2008). Electronic ground state of higher acenes, *J. Phys. Chem. A*, **112**, 332–335.
51. Hachmann, J. Dorando, J. J. Avilés, M., and Chan, G. K.-L. (2007). The radical character of the acenes: A density matrix renormalization, *J. Chem. Phys.*, **127**, 134309-1–9.
52. Tian, Y. -H., Park, G., and Kertesz, M. (2008). Electronic structure of helicenes, C₂S helicenes, and thiaheterohelicenes, *Chem. Mater.*, **20**, 3266–3277.
53. Liegener, C. -M., Bakhshi, A. K., and Ladik, J. (1992). Effects of topology on the electronic properties of fused-ring polymers, *Chem. Phys. Lett.* **199**, 62–64.
54. Tönshoff, C., and Bettinger, H. F. (2010). Photogeneration of octacene and nonacene, *Angew. Chem. Int. Ed.* **49**, 4125–4128.
55. Fujita, M., Wakabayashi, K., Nakada, K., and Kusakabe, K. (1996). Peculiar localized state at zigzag graphite edge, *J. Phys. Soc. Jpn.*, **65**, 1920–1923.
56. Tanaka, K., Yamashita, S., Yamabe, H., and Yamabe, T. (1987). Electronic properties of one-dimensional graphite family, *Synth. Met.*, **17**, 143–148.
57. Nakada, K., Fujita, M., Dresslhaus, G., and Dresslhaus M. (1996). Edge state in graphene ribbons: Nanometer size effect and edge shape dependence, *Phys. Rev. B*, **54**, 17954–17961.
58. Okada, S., and Oshiyama, A. (2001). Magnetic ordering in hexagonally bonded sheets with first-row elements, *Phys. Rev. Lett.* **87**, 146803-1–4.
59. Yamashiro, A., Shimoi, Y., Harigaya, K., and Wakabayashi, K. (2003). Spin- and charge-polarized states in nanographene ribbons with zigzag edges, *Phys. Rev. B*, **68**, 193410-1–4.
60. Stein, S. E., and Brown, R. L. (1987). π -Electron properties of large condensed polyaromatic hydrocarbons, *J. Am. Chem. Soc.*, **109**, 3721–3729.

61. Ovchinnikov, A. (1978). Multiplicity of the ground state of large alternant organic molecules with conjugated bonds, *Theor. Chim. Acta.*, **47**, 297–304.
62. Qu, Z., Zhang, D., Liu, C., and Jiang, Y. (2009). Open-shell ground state of polyacenes: A valence bond study, *J. Phys. Chem. A* **113**, 7909–7914.
63. Hund, F. (1927). *Linienspektren und periodische Systeme der Elemente* (Springer-Verlag, Berlin).
64. Longuet-Higgins, H. C. (1950). Some studies in molecular orbital theory I. Resonance structures and molecular orbitals in unsaturated hydrocarbons, *J. Chem. Phys.* **18**, 265–274.
65. Borden, W. T., and Davidson, E. R. (1977). Effects of electron repulsion in conjugated hydrocarbon diradicals, *J. Am. Chem. Soc.*, **99**, 4587–4594.
66. Experimental studies on TMM and TME by Dowd is well summarized in Cramer, C. J. (1998). Paul Dowd and diradicals, *J. Chem. Soc., Perkin Trans. 2*, 1007–1013.
67. Dowd, P. (1966). Trimethylenemethane, *J. Am. Chem. Soc.*, **88** 2587–2589.
68. Baseman, R. J., Pratt, D. W., Chow, M., and Dowd, P. (1976). Trimethylenemethane. Experimental demonstration that the triplet state is the ground state, *J. Am. Chem. Soc.* **98**, 5726–5727.
69. Dowd, P., Chang, W., and Paik, Y. H. (1986). Tetramethyleneethane, a ground-state triplet, *J. Am. Chem. Soc.* **108**, 7416–7417.
70. Nachtigall, P., and Jordan, K. D. (1993). Theoretical study of the low-lying triplet and singlet states of tetramethyleneethane: Prediction of a triplet below singlet state at the triplet equilibrium geometry, *J. Am. Chem. Soc.*, **115**, 270–271.
71. Wright, B. B., and Platz, M. S. (1983). Electron spin resonance spectroscopy of the triplet state of *m*-xylylene, *J. Am. Chem. Soc.*, **105**, 630–631.
72. Roth, W. R., Langer, R., Bartmann, M., Stevermann, B., Maier, G., Reisenauer, H. P., Sustmann, R., and Müller, W. (1987). The diradical 2,3,5,6-tetramethylene-1,4-cyclohexanediyl (“1,2,4,5-tetramethylenebenzene”), *Angew. Chem. Int. Ed. Engl.*, **26**, 256–258.
73. Reynolds, J. H., Berson, J. A., Kumashiro, K. K., Duchamp, J. C., Zilm, K. W., Rubello, A., and Vogel, P. (1992). A kinetically stable singlet state of 1,2,4,5-tetramethylenebenzen, *J. Am. Chem. Soc.*, **114**, 763–764.

74. Reynolds, J. H., Berson, J. A., Scaiano, J. C., and Berinstain, A. B. (1992). Photochemical generation and preparative capture of 1,2,4,5-tetramethylenebenzene in fluid solution. Nanosecond time-resolved spectroscopic determination of absolute rates of dimerization and oxygen trapping of a disjoint singlet hydrocarbon biradical, *J. Am. Chem. Soc.*, **114**, 5866–5867.
75. Hrovat, D. A., and Borden, W. T. (1994). MCSCF and CASPT2N calculations on the excited states of 1,2,4,5-tetramethylenebenzene. The UV-Vis spectrum observed belongs to the singlet state of the diradical, *J. Am. Chem. Soc.*, **116**, 6327–6331.
76. Reynolds, J. H., Berson, J. A., Kumashiro, K. K., Duchamp, J. C., Zilm, K. W., Scaiano, J. C., Berinstain, A. B., Rubello, A., and Vogel, P. J. (1993). 2,3,5,6-Tetrakis(methylene)-1,4-cyclohexanediyl (1,2,4,5-tetramethylenebenzene), a disjoint non-Kekulé singlet hydrocarbon biradical, *J. Am. Chem. Soc.*, **115**, 8073–8090.
77. Inoue, J., Fukui, K., Kubo, T., Nakazawa, S., Sato, K., Shiomi, D., Morita, Y., Yamamoto, K., Takui, T., and Nakasuji, K. (2001). The first detection of a clar's hydrocarbon, 2,6,10-tri-*tert*-butyltriangulene: A ground-state triplet of non-Kekulé polynuclear benzenoid hydrocarbon, *J. Am. Chem. Soc.*, **123**, 12702–12703.
78. Pogodin, S., and Agranat, I. (2003). Clar goblet and related non-Kekulé benzenoid LPAHs. A theoretical study, *J. Org. Chem.*, **68**, 2720–2727.
79. Kolc, J., and Michl, J. (1973). $\pi\pi$ -Biradicaloid hydrocarbons. The pleiadene family. I. Photochemical preparation from cyclobutene precursors, *J. Am. Chem. Soc.*, **95**, 7391–7401.
80. Salem, L., and Ronland C. (1972). The electronic properties of diradicals, *Angew. Chem. Int. Ed. Engl.*, **11**, 92–111.
81. Döhnert, D., and Koutecký, J. (1980). Occupation numbers of natural orbitals as a criterion for biradical character. different kinds of biradicals, *J. Am. Chem. Soc.*, **102**, 1789–1796.
82. Noodleman, L. (1981). Valence bond description of antiferromagnetic coupling in transition metal dimers, *J. Chem. Phys.*, **74**, 5737–5743.
83. Yamaguchi, K. (1975). The electron structure of biradicals in the unrestricted Hartree–Fock approximation, *Chem. Phys. Lett.*, **33**, 330–335.
84. Yamaguchi, K. (1990) Chapter 7, Instability in chemical bonds, in *Self-Consistent Field: Theory and Applications* (eds. Carbo, R., Klobukowski, M.), Elsevier, Amsterdam, pp. 727–823.

85. Yamanaka, S., Okumura, M., Nakano, M., and Yamaguchi, K. (1994). EHF theory of chemical reactions Part 4. UNO CASSCF, UNO CASPT2 and R(U)HF coupled-cluster (CC) wavefunctions, *J. Mol. Struct. (THEOCHEM)*, **310**, 205–218.
86. Houk, K. N., Lee, P. S., and Nendel, M. (2001). Polyacene and cyclacene geometries and electronic structures: Bond equalization, vanishing band gaps, and triplet ground states contrast with polyacetylene, *J. Org. Chem.*, **66**, 5517–5521.
87. Mondal, R., Shah, B. K., and Neckers, D. C. (2006). Photogeneration of heptacene in a polymer matrix, *J. Am. Chem. Soc.*, **128**, 9612–9613.
88. Payne, M. M., Parkin, S. R., and Anthony, J. E. (2005) Functionalized higher acenes: Hexacene and heptacene, *J. Am. Chem. Soc.*, **127**, 8028–8029.
89. Chun, D., Cheng, Y., and Wudl, F. (2008) The most stable and fully characterized functionalized heptacene, *Angew. Chem. Int. Ed.*, **47**, 8380–8385.
90. Kaur, I., Stein, N. N., Kopreski, R. P., and Miller, G. P. (2009) Exploiting substituent effects for the synthesis of a photooxidatively resistant heptacene derivative, *J. Am. Chem. Soc.*, **131**, 3424–3425.
91. Quad, H., and Chi, C. (2010) A stable heptacene derivative substituted with electron-deficient trifluoromethylphenyl and triisopropylsilylethynyl group, *Org. Lett.* **12**, 3360–3363.
92. Purushothaman, B., Bruzek, M., Parkin, S. R., Miller, A.-F., and Anthony, J. E. (2011). Synthesis and structural characterization of crystalline nonacene, *Angew. Chem. Int. Ed.*, **50**, 7013–7017.
93. Jiang, D.-E., Sumpter, B. G., and Dai, S. (2007). First principles study of magnetism in nanographenes, *J. Chem. Phys.*, **127**, 124703-1–5.
94. Hod, O., Barone, V., and Scuseria G. E. (2008). Half-metallic graphene nanodots: A comprehensive first-principles theoretical study, *Phys. Rev. B*, **77**, 035411-1–6.
95. Moscardo, F., and San-Fabián, E. (2009). On the existence of a spin-polarized state in the n-periacene molecules, *Chem. Phys. Lett.*, **480**, 26–30.
96. Jiang, D.-E., and Dai, S. (2008). Circumacenes versus periacenes: HOMO–LUMO gap and transition from nonmagnetic to magnetic ground state with size, *Chem. Phys. Lett.*, **466**, 72–75.
97. Glukhovtsev, M. N., Bach, R. D., and Laiter, S. (1997). Isodesmic and homodesmotic stabilization energies of [n]annulenes and their

- relevance to aromaticity and antiaromaticity: Is absolute antiaromaticity possible?, *J. Mol. Struct. (THOCHEM)*, **417**, 123–129.
98. Slayden, S. W., and Liebman, J. F. (2001). The energetics of aromatic hydrocarbons: An experimental thermochemical perspective, *Chem. Rev.*, **101**, 1541–1566.
99. Douglas, J. E., Rabinovitch, B. S., and Looney, F. S. (1955). Kinetics of the thermal *cis-trans* isomerization of dideuteroethylene, *J. Chem. Phys.*, **23**, 315–323.
100. Scholl, R., and Meyer, K. (1934). Der blaue aromatische Grundkohlenwasserstoff des meso-Naphtho-dianthrons und seine Überführung durch Maleinsäure-anhydrid in Anthro-dianthren, *Ber. Dtsch. Chem. GES.*, **67**, 1236–1238.
101. Clar, E. (1948). Das Kondensationsprinzip, ein einfaches neues Prinzip im Aufbau der aromatischen Kohlenwasserstoffe (Aromatische Kohlenwasserstoffe XLII. Mitteilung), *Chem. Ber.*, **81**, 52–63.
102. Clar, E. (1949). Synthesen von Benzologen des Perylens und Bisanthens. (Aromatische Kohlenwasserstoffe, XLVIII. Mittel.), *Chem. Ber.*, **82**, 46–60.
103. Fort, E. H. Donovan, P. M., and Scott, L. T. (2009). Diels–Alder reactivity of polycyclic aromatic hydrocarbon bay regions: Implications for metal-free growth of single-chirality carbon nanotubes, *J. Am. Chem. Soc.*, **131**, 16006–16007.
104. Li, J., Zhang, K., Zhang, X., Huang, K.W., Chi, C., and Wu, J. (2010). meso-Substituted bisanthenes as soluble and stable near-infrared dyes, *J. Org. Chem.*, **75**, 856–863.
105. Brockmann, H., and Randebrock, R. (1951). Synthese und Absorptionsspektren einiger meso-Naphthodianthren-Derivate, *Chem. Ber.*, **84**, 533–545.
106. Kuroda, H. (1960). Absorption spectra of photo-oxide of mesonaphthodianthrene, *J. Chem. Phys.*, **33**, 1586–1587.
107. Clar, E., and Schmidt, W. (1977). Correlations between photoelectron and ultraviolet absorption spectra of polycyclic hydrocarbons. The perylene, coronene and bisanthene series, *Tetrahedron*, **33**, 2093–2097.
108. Arabei, S. M., and Pavich, T. A. (2000). Spectral-luminescent properties and photoinduced transformations of bisanthene and bisanthenequinone, *J. Appl. Spectrosc.*, **67**, 236–244.
109. D'yachenko, G. G., Petukhoc, V. A., Arabei, S. M., and Pavich, T. A. (2003) Analysis of the electronic vibrational spectra of bisanthene by calculating normal modes, *J. Appl. Spectrosc.*, **70**, 208–215.

110. Konishi, A., Hirao, Y., Nakano, M., Shimizu, A., Botek, E., Champagne, B., Shiomi, D., Sato, K., Takui, T., Matsumoto, K., Kurata, H., and Kubo, T. (2010). Synthesis and characterization of teranthene: A singlet biradical polycyclic aromatic hydrocarbon having Kekulé structures, *J. Am. Chem. Soc.*, **132**, 11021–11023.
111. Kveseth, K., Seip, R., and Kohl, D. A. (1980). Conformational analysis. The structure and torsional potential of 1,3-butadiene as studied by gas electron diffraction, *Acta Chem. Scand.*, **A34** 31–42.
112. Bleaney, B., and Bowers, K. D. (1952). Anomalous paramagnetism of copper acetate, *Proc. R. Soc. London Ser. A*, **214**, 451–465.
113. Motta, S. D., Negri, F., Fazzi, D., Castiglioni, C., and Canesi, E. V. (2010). Biradicaloid and polyenic character of quinoidal oligothiophenes revealed by the presence of a low-lying double-exciton state, *J. Phys. Chem. Lett.*, **1**, 3334–3339.
114. Koch, K.-H., and Müllen, K. (1991). Synthesis of tetraalkyl-substituted oligo(1,4-naphthylene)s and cyclization to soluble oligoberi-naphthylene)s, *Chem. Ber.*, **124**, 2091–2100.
115. Zipse, H. (2006). Radical stability—A theoretical perspective, *Top Curr. Chem.*, **263**, 163–189.
116. Reid, D. H. (1965). The chemistry of the phenalenes, *Quart. Rev.*, **19**, 274–302.
117. Goto, K., Kubo, T., Yamamoto, K., Nakasuji, K., Sato, K., Shiomi, D., Takui, T., Kubota, M., Kobayashi, T., Yakusi, K., and Ouyang, J. (1999). A stable neutral hydrocarbon radical: Synthesis, crystal structure, and physical properties of 2,5,8-tri-*tert*-butyl-phenalenyl, *J. Am. Chem. Soc.*, **121**, 1619–1620.
118. Dewar, M. J. S., and Dougherty, R. C. (1975). *The PMO Theory of Organic Chemistry* (Plenum Press, New York).
119. Ohashi, K., Kubo, T., Masui, T., Yamamoto, K., Nakasuji, K., Takui, T., Kai, Y., and Murata, I. (1998). 4,8,12,16-Tetra-*tert*-butyl-*s*-indaceno[1,2,3-*cd*:5,6,7-*c'd'*]diphenalene: A four-stage amphoteric redox system, *J. Am. Chem. Soc.*, **120**, 2018–2027.
120. Kubo, T., Shimizu, A., Sakamoto, M., Uruichi, M., Yakushi, K., Nakano, M., Shiomi, D., Sato, K., Takui, T., Morita, Y., and Nakasuji, K. (2005). Synthesis, intermolecular interaction, and semiconductive behavior of a delocalized singlet biradical hydrocarbon, *Angew. Chem. Int. Ed.*, **44**, 6564–6568.
121. Small, D., Zaitsev, V., Jung, Y., Rosokha, S. V., Head-Gordon, M., and Kochi, J. K. (2004). Intermolecular π -to- π bonding between stacked aromatic

- dyads. Experimental and theoretical binding energies and near-IR optical transitions for phenalenyl radical/radical versus radical/cation dimerizations, *J. Am. Chem. Soc.*, **126**, 13850–13858.
122. Watson, W. H., Kashyap, R. P., Plummer B. F., and Reese, W. G. (1991). Structures of 7,10-diphenylfluoranthene and 7,14-diphenylacenaphtho[1,2-*k*]fluoranthene, *Acta Cryst.*, **C47**, 1848–1851.
123. Huang, J., and Kertesz, M. (2007). Intermolecular covalent π - π bonding interaction indicated by bond distances, energy bands, and magnetism in biphenalenyl biradicaloid molecular crystal, *J. Am. Chem. Soc.*, **129**, 1634–1643.
124. Chikamatsu, M., Mikami, T., Chisaka, J., Shimizu, A., Kubo, T., Morita, Y., Nakasuji, K., Yoshida, Y., Azumi, R., and Yase, K. (2007). Ambipolar organic field-effect transistors based on a low band gap semiconductor with balanced hole and electron mobilities, *Appl. Phys. Lett.*, **91**, 043506–1–3.
125. Nakano, M., Kishi, R., Nitta, T., Kubo, T., Nakasuji, K., Kamada, K., Ohta, K., Champagne, B., Botek, E., and Yamaguchi, K. (2005). Second hyperpolarizability (γ) of singlet diradical system: Dependence of γ on the diradical character, *J. Phys. Chem. A*, **109**, 885–891.
126. Nakano, M., Kubo, T., Kamada, K., Ohta, K., Kishi, R., Ohta, S., Nakagawa, N., Takahashi, H., Furukawa, S., Morita, Y., and Nakasuji, K. (2006). Second hyperpolarizabilities of polycyclic aromatic hydrocarbons involving phenalenyl radical units, *Chem. Phys. Lett.*, **418**, 142–147.
127. Nakano, M., Kishi, R., Nakagawa, N., Ohta, S., Takahashi, H., Furukawa, S., Kamada, K., Ohta, K., Champagne, B., Botek, E., Yamada, S., and Yamaguchi, K. (2006). Second hyperpolarizabilities (γ) of bisimidazole and bistriazole benzenes: diradical character, charged state, and spin state dependences, *J. Phys. Chem. A*, **110**, 4238–4243.
128. Ohta, S., Nakano, M., Kubo, T., Kamada, K., Ohta, K., Kishi, R., Nakagawa, N., Champagne, B., Botek, E., Umezaki, S.-y., Takeba, A., Takahashi, H., Furukawa, S., Morita, Y., Nakasuji, K., and Yamaguchi, K., Second hyperpolarizability of phenalenyl radical system involving acetylene π -conjugated bridge, *Chem. Phys. Lett.*, **420**, 432–437.
129. Kamada, K., Ohta, K., Kubo, T., Shimizu, A., Morita, M., Nakasuji, K., Kishi, R., Ohta, S., Furukawa, S., Takahashi, H., and Nakano, M. (2007). Strong two-photon absorption of singlet diradical hydrocarbons, *Angew. Chem. Int. Ed.*, **46**, 3544–3546.
130. Kamada, K., Ohta, K., Shimizu, A., Kubo, T., Kishi, R., Takahashi, H., Botek, E., Champagne, B., and Nakano, M. (2010). Singlet diradical character from experiment, *J. Phys. Chem. Lett.*, **1** 937–940.

This page intentionally left blank

Chapter 6

Experimental Approach to Electronic and Magnetic Properties of Nanographene

Toshiaki Enoki

*Department of Chemistry, Tokyo Institute of Technology,
Ookayama, Meguro-ku, Tokyo 152-8551, Japan*
tenoki@chem.titech.ac.jp

6.1 Introduction

When an infinite graphene sheet is cut into nano-size graphene fragments (nanographene) or semi-infinite graphene sheets, important questions arise regarding the creation of graphene edges. This is evident in early theoretical [1–6] and experimental works [7–13], several of which predate the discovery of graphene in 2004 by many years [14]. Depending on the direction of the line along which a graphene sheet is cut, two distinct types of edge can be created, as shown in Fig. 6.1: armchair and zigzag edges [13]. The electronic structure of nanographene depends crucially on the geometrical shape of the edges. In fact, according to theoretical [1–6] and experimental studies [7–13], a nonbonding π electron state called an edge state is created along zigzag edges, whereas no such state appears in armchair edges. The presence of an edge state can be

Physics and Chemistry of Graphene: Graphene to Nanographene

Edited by Toshiaki Enoki and Tsuneya Ando

Copyright © 2013 Pan Stanford Publishing Pte. Ltd.

ISBN 978-981-4241-48-9 (Hardcover), 978-981-4241-49-6 (eBook)

www.panstanford.com

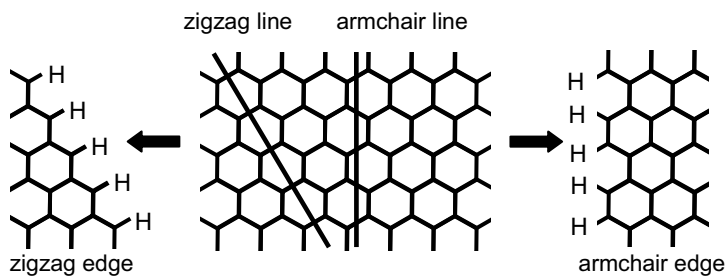


Figure 6.1 Zigzag and armchair lines, and hydrogen-terminated zigzag and armchair edges in a graphene sheet.

physically understood as a consequence of broken symmetry in Dirac fermions at zigzag edges (see Chapters 2 and 4). The presence or absence of edge states is relevant to the discussion in Chapter 5 regarding aromaticity in condensed polycyclic aromatic hydrocarbon molecules [15–22], of which graphene can be considered an indefinitely large version. In these molecules, nonbonding π electron states are created with the same geometrical dependence as in nanographene and graphene edges. Chemists describe the presence of edge states as a result of the degradation of aromaticity.

In addition to edge states, another interesting feature of the electronic structure is that graphene edges participate in electron wave scattering in a manner that depends on their geometrical shape [23, 24]. Electron scattering at armchair edges is accompanied by interference effects due to the participation of two Dirac cones, whereas electron wave interference is absent from scattering at zigzag edges. This difference in scattering appears in the creation of superlattices on a graphene sheet [25] and in the Raman spectral characteristics [26, 27].

The edge state, which is well localized near zigzag edges and works to reduce the stability of the molecule, is therefore a type of surface state that is electronically and chemically active. It plays an important role in producing electronic and chemical features that are specific to nanographene sheets and less aromatic molecules. In the long history of carbon-based materials, their chemical activity has been a central issue. The catalytic activity of carbon-based materials, batteries, and capacitors are important for practical use

[28,29]. Graphene edges, particularly edge states, are considered to be responsible for this activity.

In addition, the edge state, which is singly occupied and strongly spin polarized, contributes to the creation of strong spin magnetism, even ferromagnetism. Accordingly, edge-state spins are responsible for carbon-based magnetism. The magnetism of carbon-based materials has been one of the most important challenges in carbon science and molecule magnetism since the 1950s [30], and it still remains controversial owing to the difficulty of obtaining well-characterized materials [31]. Recent works on nanographene and graphene edges have illuminated this long-standing problem, and edge states have been proposed as a promising candidate for the source of magnetism in π -electron-based carbon materials [8, 32–35]. Edge-state spins, which interact with π electron conduction carriers, are expected to be an important ingredient in promising spintronics and electronic device applications in the future.

In this chapter, we discuss the fabrication of graphene nanostructures, the electronic and magnetic structures of nanographene, and its chemical activity, with a focus on the important role of edges. Section 6.2 discusses the fabrication of graphene nanostructures. Section 6.3 covers issues associated with the electronic structure of edges. Section 6.4 discusses the magnetism of the edge state in nanographene. Section 6.5 covers the stability and chemical activity of nanographene and graphene edges. A summary is presented in Section 6.6.

6.2 Fabrication of Graphene Nanostructures

The fabrication of graphene nanostructures is important not only for investigating the electronic structure of graphene edges and nanographene in terms of basic science but also for electronic device applications. Several techniques can be used to create graphene nanostructures such as graphene nanosheets and graphene nanoribbons [36, 37]: chemical vapor deposition (CVD) on a substrate [38–41], nanofabrication of graphene oxide [42–44], unzipping of carbon nanotubes [45–48], heat-induced conversion of nanodiamond [49], heat-induced fractionalization of graphite [26, 50, 51] and SiC

[52, 53], electron beam lithography [54–57], scanning tunneling microscopy/atomic force microscopy (STM/AFM) lithography [58, 59], chemical reactions with crystallographic selectivity [60–63], bottom-up production from aromatic molecules [64–66], and other methods. In this section, we discuss several techniques for fabricating graphene nanostructures.

6.2.1 *Chemical Vapor Deposition*

Thermal decomposition of hydrocarbon molecules such as acetylene, ethylene, butadiene, or benzene on a metal or metal carbide substrate at high temperature causes the formation of a graphene sheet (see Section 3.2.3.2) [38, 39]. Typical substrates include Ni, Pd, Pt, Ir, Re, Ru, TiC, TaC, HfC, and WC, and CVD is conducted at temperatures of 800–1300°C. These substrates catalyze the decomposition of hydrocarbon molecules and subsequent formation of graphene sheets. Accordingly, a single layer of graphene is easily formed in a rapid process when hydrocarbon molecules are applied to the substrate, but it is rather difficult to form subsequent layers on the first layer because the catalytic substrate is inaccessible to hydrocarbon molecules [38]. The creation of wide, uniform graphene sheets on a Cu substrate was recently reported [39].

Graphene nanostructure can be created by CVD employing a nano-size area on a single crystal surface of the substrate. Single sheets of graphene nanoislands and nanoribbons were formed on a TiC(111)-faceted surface of $\sim 200 \times 200 \text{ nm}^2$ and a TiC(410) surface, respectively [40]. Figure 6.2 shows a stepped surface of TiC(410) with a terrace width of 0.886 nm on which a graphene nanoribbon was created at 1000°C. Angle-resolved photoelectron spectroscopy (ARPES) indicates the formation of single-layer graphene nanoribbons, although low-energy electron diffraction (LEED) shows no indication of a graphene diffraction pattern because the ribbon width predicted from the terrace width, 0.72 nm ($\sim 3 \times$ the unit cell width of 0.246 nm) is too narrow to be detected by LEED. The drawback of this method is that most of the substrates are metallic. Therefore, as-formed graphene nanostructures prepared by CVD cannot be used for electronic devices; they must first be transferred to a dielectric substrate.

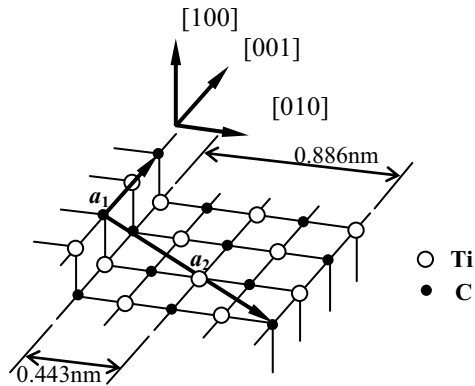


Figure 6.2 Schematic of TiC(410) stepped surface; a_1 and a_2 denote 2D real-lattice unit vectors. After Ref. 40.

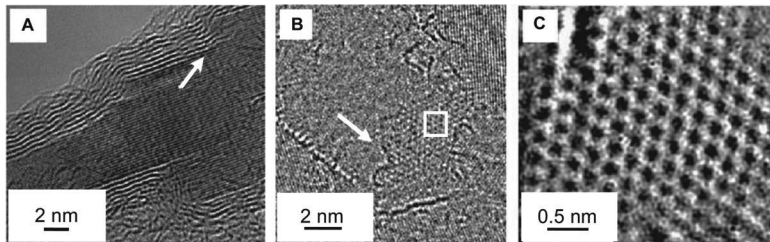


Figure 6.3 (A) Transmission electron microscope (TEM) image of few-layer graphene on a MgO crystal. Note that the graphene layers interface directly with the MgO lattice fringes (arrow). (B) Top view of graphene island (arrow) on the surface of a MgO crystal. (C) Magnified region from the box in panel B highlighting graphene structure. After Ref. 41.

However, a recent report suggests that dielectric insulators may be used as substrates [41]. Indeed, graphene nanosheets can be formed on the surface of MgO nanocrystals. Figure 6.3 shows graphene nanoislands created on high-purity MgO nanocrystals. Thermal decomposition of acetylene at a relatively low temperature of 325°C for 5 min to 1 h yields single-layer to few-layer graphene nanoislands 30–50 nm in size.

6.2.2 Graphene Oxides

Graphene or graphite can be oxidized by reaction with strong oxidants such as KMnO_4 and H_2SO_4 , yielding graphene oxide or graphite oxide. This method is known as Hummers' method [67]. In most of the prepared graphene oxide, oxidation produces a graphene sheet randomly bonded with oxygen-containing functional groups and thus irregularly corrugated, so the electronic structure is converted from a zero-gap semiconductor to an insulator. However, among the graphene oxide samples, regularly wrinkled graphene oxide sheets appear, as shown in Fig. 6.4 [42]. AFM images reveal that this structure exhibits a two-dimensional (2D) regular arrangement of one-dimensional (1D) arrays of triangular epoxy rings running along a zigzag direction. The estimated periodic

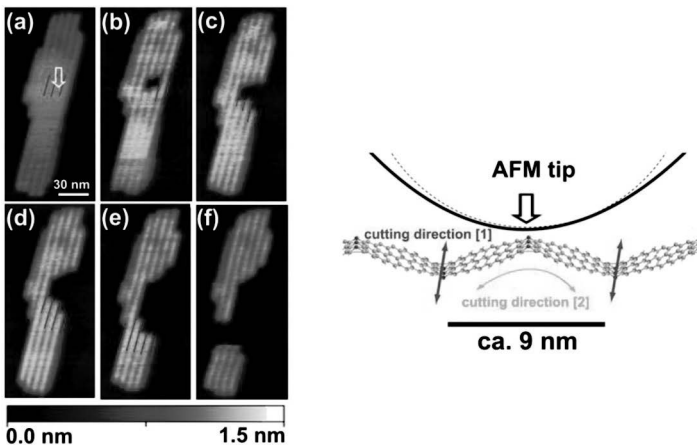


Figure 6.4 (Left) Series of noncontact-AFM images of a graphene oxide sheet with ordered wrinkles during and after AFM manipulation. (a) Point contact between the sheet and the AFM probe is made at the center of the sheet. White arrow indicates contact area. Region indicated by the line is removed during the point contact experiment. (b–f) The sheet then starts spontaneously breaking up, with segmentation of the regions indicated by lines. (Right) Schematic illustration of removal event. The point contact between the wrinkle and the AFM tip, with a typical radius of 10 nm, causes cutting of the graphene nanodomain along two distinct types of directions. The small dark circles at the ridges and valleys denote oxygen atoms constituting epoxy rings with carbon atoms of graphene sheet. After Ref. 42.

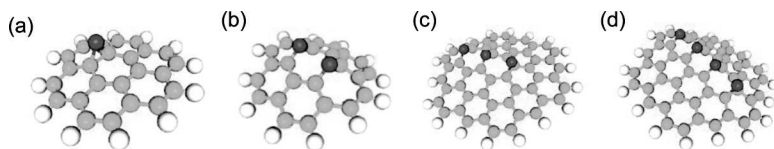


Figure 6.5 (a) One epoxy ring is attached to a coronene molecule, which is a model of graphene sheet. (b) Two epoxy rings are aligned on a coronene molecule, initiating an unzipping process. (c) Three epoxy rings are aligned on a piece of graphene. (d) Four epoxy rings are aligned on a piece of graphene. The graphene platelet shows a crack. After Ref. 43.

inter-wrinkle spacing is 8.6 nm, and the corrugation amplitude is 300 pm. This regular structure can be explained in terms of a 2D arrangement of zigzag-edged graphene nanoribbons having a width of 4.3 nm and mutually bonded through a bridge of oxygen atoms, as shown in Fig. 6.4. As a result, the graphene sheets are unzipped by oxidation. The width of the graphene nanoribbon corresponds to that of 20 unit cells (lattice constant $a = 0.246$ nm). Theoretical analysis confirms this structure, as illustrated in Fig. 6.5 [43, 44]. In the elementary process of oxidation, one oxygen atom attacking a graphene sheet is bonded to a pair of carbon atoms arranged along the armchair direction, forming a triangular epoxy ring. The formation of this ring distorts the local structure of the graphene sheet surrounding the sites bonded to the oxygen atom, facilitating bonding of another oxygen atom to the next carbon pair by reducing the bond formation energy. This process is repeated, forming a 1D array of epoxy rings along the zigzag direction. Eventually, a 2D regular arrangement of 1D epoxy arrays is formed with a periodic inter-array distance.

Zigzag graphene nanoribbons mutually connected to the oxygen bridge can be nanofabricated by cutting them using an AFM tip. The cutting process is schematically illustrated in Fig. 6.4. Manipulation by the AFM tip intentionally creates graphene nanostructures based on zigzag ribbons.

With the employment of AFM lithography, zigzag-edged graphene nanoribbons are selectively obtained from graphene oxide, although zigzag edges are thermodynamically unstable owing to their lower aromaticity [16, 22].

6.2.3 *Unzipping of Carbon Nanotubes*

Unzipping of carbon nanotubes is also an important method of creating graphene nanoribbons [45–48]. Single-wall and multiwall carbon nanotubes are unzipped by oxidation [45] and Ar plasma etching [46]. In the former method, multiwall carbon nanotubes 40–80 nm in diameter are treated with a strong oxidant consisting of H_2SO_4 and KMnO_4 at room temperature to 70°C . The mechanism here is similar to that in the unzipping of graphene oxide discussed in Section 6.2.2. The attacking oxidant, permanganate, forms manganate ester at a pair of carbon atoms in the first step, making the adjacent pair more susceptible to the next attack by permanganate. A sequence of such processes unzips the carbon nanotubes. The oxidation reaction yields graphene nanoribbons >100 nm wide. The nanoribbon samples thus obtained are not very well defined owing to the intensive oxidation.

Ar plasma etching produces narrower nanoribbons having rather well-defined edges. The fabrication process of controlled unzipping is illustrated in Fig. 6.6, where multiwall carbon nanotubes ~ 8 nm in diameter are employed [46]. The carbon nanotubes are embedded in a poly(methyl methacrylate) (PMMA) layer as an etching mask. Pristine multiwall carbon nanotubes dispersed in surfactant solution are deposited on a Si substrate. After the PMMA-nanotube film is peeled off in a KOH solution, carbon nanotubes embedded in the PMMA film have a narrow strip of side wall not covered by PMMA. Then the PMMA-nanotube film is subjected to Ar plasma treatments of various durations. Owing to the protection provided by the PMMA, the top side walls of the carbon nanotubes are etched faster and removed by the plasma. Single-, bi-, and multilayer graphene nanoribbons and graphene nanoribbons with inner carbon nanotube cores are produced depending on the diameter and initial number of layers of nanotubes and the etching time. The obtained nanoribbons have a uniform width of 10–20 nm and smooth edges. The height profiles and Raman spectra confirmed that the nanoribbons are single-, bi-, or trilayered.

6.2.4 *Heat-Induced Structural Changes*

Nanodiamond particles are transformed into graphite by heat treatment at 1600°C [8]. Applying the same heat treatment

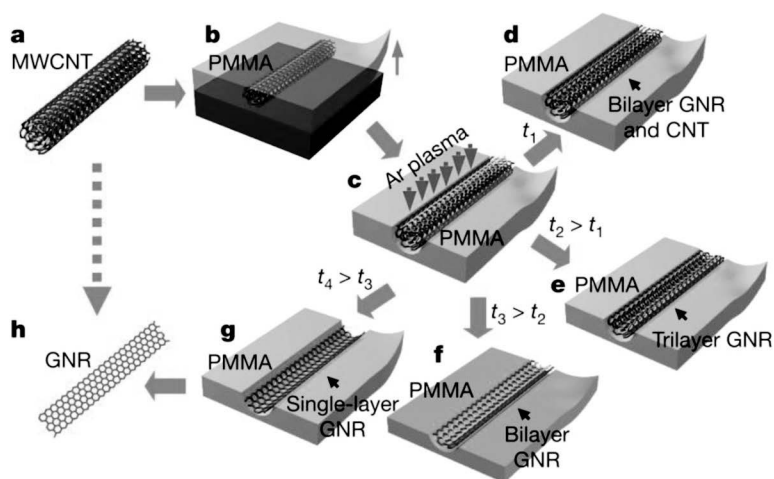


Figure 6.6 Graphene nanoribbons prepared by unzipping carbon nanotubes with Ar plasma etching. (a) A pristine multiwalled carbon nanotube is used as the starting raw material. (b) The multiwall nanotube is deposited on a Si substrate and then coated with a PMMA film. (c) The PMMA-multiwall nanotube film is peeled from the Si substrate, turned over, and then exposed to an Ar plasma. (d–g) Several possible products are generated after etching for different times. Graphene nanoribbons with carbon nanotube cores are obtained after etching for a short time t_1 (d). Tri-, bi-, and single-layer graphene nanoribbons are produced after etching for times t_2 , t_3 , and t_4 , respectively ($t_4 > t_3 > t_2 > t_1$; (e–g)). (h). The PMMA is removed to release the graphene nanoribbons. After Ref. 46.

conditions to nanodiamond particles electrophoretically seeded on a highly oriented pyrolytic graphite (HOPG) substrate [49, 68] yields graphene nanoislands. To avoid fusion of nanodiamond particles, the particle distribution is adjusted by controlling the electrophoretic conditions so that the interparticle distance is great enough to isolate individual particles from each other. The STM image in Fig. 6.7(a) shows an example of isolated graphene nanoislands on an HOPG substrate. The nanoislands are circular and typically have a mean size of ca. 10 nm. An atomically resolved STM image (Fig. 6.7(b)) obtained from the surface of an isolated graphene nanoisland clearly shows a triangular pattern with a lattice constant of 0.25 nm, which is characteristic of graphite. The line-profile analysis in Fig. 6.7(c) shows that the heights of

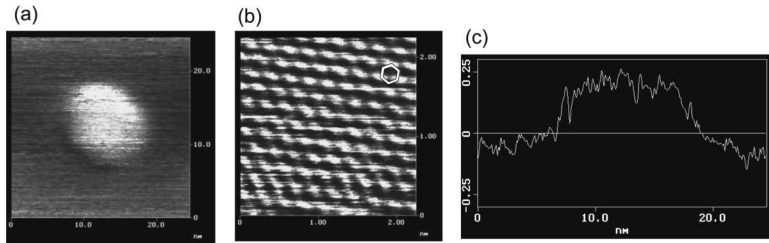


Figure 6.7 (a) STM images of graphene nanoislands obtained after heat treatment of nanodiamond particles at 1600°C. (b) STM lattice image and (c) line profile of a single-sheet graphene nanoisland on an HOPG substrate. The line profile is in the horizontal direction across the center of the graphene nanoisland. The hexagon in (b) represents a benzene ring. After Ref. 49.

the islands range from 0.35 to 0.37 nm, which is considerably larger than the inter-sheet distance of 0.3354 nm in bulk graphite. These findings demonstrate the formation of a single sheet of graphene nanoislands. Nanodiamond particles merely heated at 1600°C yield hollow polyhedral nanographite particles [8]. A trace of oxygen in the argon gas in the graphite furnace might react with the surface of a nanodiamond particle, and consequently part of the particle would be oxidized during heat treatment. In the nanodiamond particles deposited on the HOPG substrate, the surfaces of the particles in contact with the HOPG surface are more stable against oxidation than the free exposed parts. Also, the part in contact with HOPG changes to graphene more rapidly than the free part, which is subjected to easy oxidation with the carbon dioxide produced during the process. The newly converted graphene interacts with the flat HOPG substrate, giving rise to flat single-sheet graphene nanoislands. The observed triangular lattice STM images (Fig. 6.7(b)) is a consequence of the *AB* stacking mode of graphene nanoislands with the HOPG substrate. The observed elongated distance (0.35–0.37 nm) between the graphene nanoisland and the substrate indicates that the inter-layer interaction (the inter-layer resonance integral γ_1) is reduced [69] by 26–50% from that of bulk graphite, where $\gamma_1 = 0.39$ eV for bulk graphite [70].

The same heat treatment at 1600°C happens by chance to create graphene nanoribbons around the step edges on a graphite surface

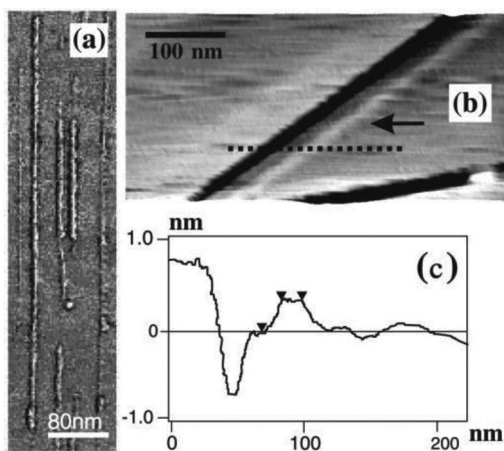


Figure 6.8 (a) AFM image of many graphene nanoribbons parallel to each other near a graphite step edge. (b) Typical AFM image of a graphene nanoribbon. Arrow indicates the position of the ribbon for reference. (c) Height profile obtained along the dotted line in (b). After Ref. 26.

[26]. This is a consequence of heat-induced fractionalization of the uppermost graphene sheet of graphite near the step edge, which is easily affected by heat treatment. Figure 6.8 shows an AFM image of graphene nanoribbons oriented parallel to each other along the direction of the step edge. The average width of the ribbons is 8 nm, and their length can be as large as 1 μm . The height profile (Fig. 6.8[c]) shows a height of 0.35 nm, which corresponds exactly to the inter-sheet distance of bulk graphite, indicating that the ribbon has only one sheet of atoms. The Raman G-band spectra, which are presented in Section 6.3.4, confirm that the graphene nanoribbons are armchair-edged. This proves also that the width of 8 nm corresponds to a length of ~ 30 unit cells (at a lattice constant of 0.246 nm).

A modification of the above heat-treatment method yields graphene nanoribbons, which can be manipulated to fabricate electronic devices such as graphene-nanoribbon-based field effect transistors (FETs) [50, 51]. Graphite intercalated with sulfuric acid is exfoliated at a heat-treatment temperature of 1000°C in a forming gas (3% H_2 in Ar). The resulting exfoliated graphite is

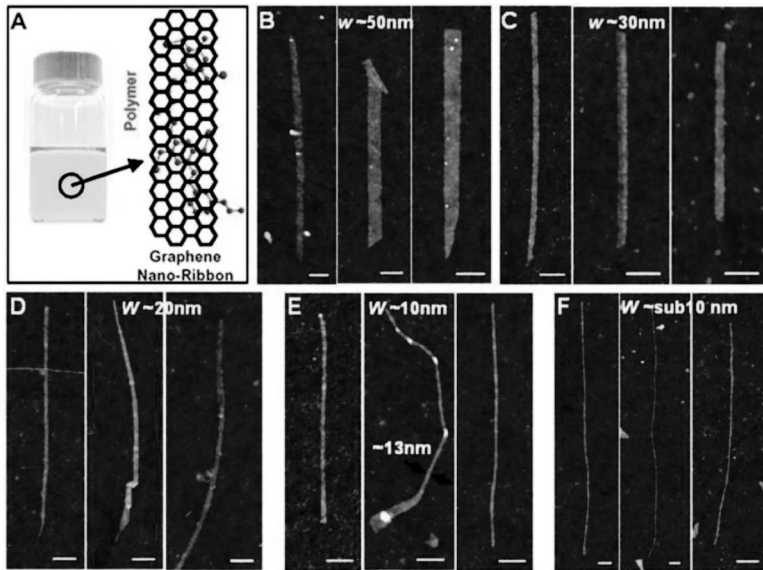


Figure 6.9 Graphene nanoribbons obtained by exfoliation at 1000°C and subsequent chemical treatment. (A) (Left) Photograph of a polymer PmPV/dichloroethene solution containing stably suspended graphene nanoribbons. (Right) Schematic drawing of a graphene nanoribbon with two units of a PmPV polymer chain adsorbed on top of the graphene via π stacking. (B–F) AFM images of graphene nanoribbons with widths in the 50 nm, 30 nm, 20 nm, 10 nm, and sub-10 nm regions, respectively. All scale bars indicate 100 nm. After Ref. 50.

dispersed by sonication in a 1,2-dichloroethane solution of poly(m-phenylenevinylene-co-2,5-dioctoxy-p-phenylenevinylene (PmPV) to form a homogeneous suspension. From this suspension, single-layer and few-layer graphene nanoribbons are formed with various widths ranging from ~ 50 nm to less than 10 nm and an average length of ~ 1 μm . The graphene nanoribbons thus obtained have smooth edges and can be deposited on Si substrates to produce FET devices. Figure 6.9 shows the graphene nanoribbons, the narrowest of which is 2 nm wide. Interestingly, these narrow graphene nanoribbons are semiconducting, and the bandgap is inversely proportional to the ribbon width, as will be discussed in Section 6.3.3.

Thermal annealing of SiC is a popular method of creating graphene sheets [52]. A sheet grows epitaxially on the SiC at

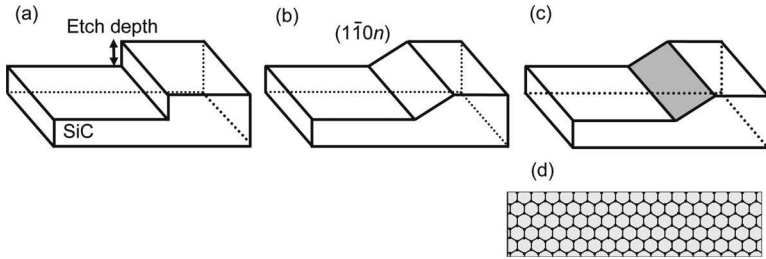


Figure 6.10 Process of tailoring a SiC crystal for epitaxial graphene nanoribbon growth. (a) Nanometer-scale step is etched into SiC crystal by fluorine-based reactive ion etching. (b) Crystal is heated to 1200–1300°C under low vacuum, inducing step flow and relaxation to the $(1\bar{1}0n)$ facet. (c) Upon further heating to $\sim 1450^\circ\text{C}$, a self-organized graphene nanoribbon forms on the facet. (d) Graphene nanoribbon.

annealing temperature of 1250–1450°C in vacuum. This method, combined with the nanofabrication of a SiC crystal, produces high-quality graphene nanoribbons [53]. Figure 6.10 illustrates schematically the fabrication process of epitaxial graphene nanoribbons. A nanometer-scale step is etched into a SiC crystal by fluorine-based reactive ion etching, and the crystal is heated to 1200–1300°C under low vacuum. This induces step flow and relaxation to the $(1\bar{1}0n)$ facet. A graphene nanoribbon grows epitaxially on the facet at 1450°C. Raman and transmission electron microscopy (TEM) observations confirm the creation of high-quality graphene nanoribbon sheets < 40 nm wide.

6.2.5 Electron Beam Lithography and STM/AFM Lithography

Electron beam lithography is commonly used to fabricate nanodevices incorporating not only graphene nanostructures but also other nanostructures. Therefore, electron beam lithography is the conventional method for creating graphene nanostructures [54–57]. A mechanically cleaved graphene sheet is placed on a SiO_2/Si substrate. Electron-beam resist is then spun onto the samples and patterned to form an etch mask defining the widths and lengths of the desired nanostructures. Oxygen plasma processing

is applied to etch away the exposed graphene, forming graphene nanostructures. The typical width and length obtained by this method are 10–100 nm and 1–2 μm , respectively. The width is somewhat larger than that obtained by heat-treatment-assisted nanofabrication (see Section 6.2.4) and STM lithography, the latter of which is discussed below. The drawback of this method is that the edges are disordered and not well defined. In addition, the resist-based treatment degrades the quality of the obtained graphene nanostructures. To avoid this degradation, the quality is improved by using a silicon nanowire deposited on a graphene sheet [56]. A silicon nanowire 20–50 nm wide serves as an etch mask. This method improves the surface cleanness of the resulting nanoribbons by avoiding resist residue, and eases the fabrication process by using one-step electron beam lithography.

STM lithography using an STM tip as a cutting tool is employed for fabricating graphene nanostructures [58]. Etching is realized by electrochemical oxidation of graphene in the water meniscus between the negatively charged tip and the positively charged graphene. Nanostructures smaller than those obtained in electron beam lithography can be fabricated by using this technique. In addition, the cutting direction can be determined with respect to the atomic arrangement by using information obtained by microscope imaging at atomic resolution. Figures 6.11(a) and (b) show examples of fabricated graphene nanostructures consisting of straight and bent junction graphene nanoribbons. Other forms of nanostructure can also be designed as needed. Cutting is conducted by applying a constant bias potential significantly higher than the one used for imaging and simultaneously moving the STM tip with a constant velocity in order to etch the desired geometry fitted to the crystallographic structure, which is known from previous atomic-resolution STM imaging. An atomic-resolution STM image of a graphene nanoribbon 10 nm wide is shown in Fig. 6.11(c); the arrangement of individual atoms is visible. However, the edge regions on both sides of the graphene nanoribbon are irregular, suggesting poor definition even when the cutting direction is accurately determined. Therefore, the quality of nanographene sheets obtained by STM lithography is still not high enough for the investigation of phenomena in which the contribution of the edge is

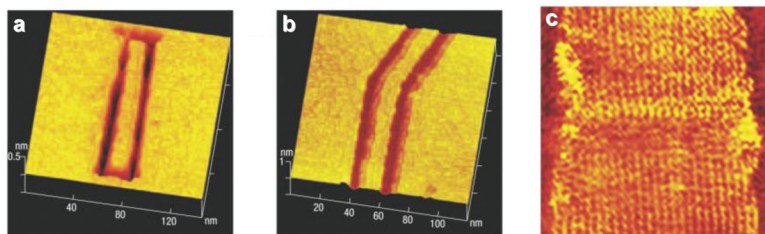


Figure 6.11 Graphene nanostructures patterned by STM lithography. (a) 3D STM image of a 10 nm-wide and 120 nm-long graphene nanoribbon. (b) An 8 nm-wide graphene nanoribbon 30° bent junction connecting an armchair and a zigzag ribbon. (c) Constant current STM image ($12 \times 12 \text{ nm}^2$, 1 nA, 100 mV) of a 10 nm-wide graphene nanoribbon displaying confinement-induced standing wave patterns (stripes parallel to the ribbon's axis). Cutting is performed along the armchair direction. After Ref. 58.

particularly important. Interestingly, stripes of high electron density distribution running parallel to the axis of the ribbon are clearly visible in Fig. 6.11(c). The periodicity of the observed oscillation is 0.4 nm, which clearly differs from the period of the underlying atomic structure (0.246 nm). This feature is a consequence of electron confinement in the finite width of the graphene nanoribbon, as will be discussed in Section 6.3.3.

AFM can also be applied to lithography of graphene nanostructures [59]. The cutting process is similar to that in STM lithography, in which the negatively charged tip oxidizes the graphene. The cutting direction can be determined with respect to the atomic arrangement by using information obtained by microscope imaging, although the resolution is not as high as that of STM lithography. In the etching process, contact-mode AFM is employed with the tip and graphene sheet in electrical contact. Figure 6.12 shows triangle cuts created by AFM lithography. Two etching regimes are separated by a threshold voltage. When a graphene sheet is cut at a high voltage whose absolute value is above the absolute value of the threshold, $V_{\text{thresh}} = -3.5$ to -0.5 V, graphene is truly cut, and the region surrounded by the trench produced by the lithography and the region outside of the trench are electrically isolated from each other. However, if the absolute value of the voltage is smaller than the

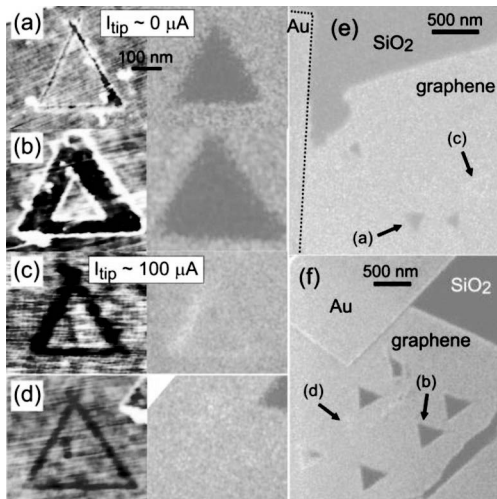


Figure 6.12 Triangular nanographene produced by AFM lithography etching. AFM (left) and SEM images (right) of two triangles cut with the applied voltage $|V_{\text{tip}}| > |V_{\text{thresh}}|$ for (a) and (b), and $|V_{\text{tip}}| < |V_{\text{thresh}}|$ for (c) and (d). The presence of a dark triangular region in the SEM images proves that the triangles are electrically isolated in (a) and (b), whereas those in (c) and (d) are still connected electrically to the surroundings after etching. (e) and (f) SEM images of the areas of graphene flakes from which the triangles were cut. Arrows indicate the locations of the triangles shown in (a–d). After Ref. 59.

threshold voltage, only an indentation (pseudo-cut) is produced, and both regions are still in electrical contact. Therefore, the application of a voltage higher than the threshold voltage is required for the lithography process.

6.2.6 Chemical Reactions with Crystallographic Selectivity

Chemical reactions with metal nanoparticles as the catalyst can be employed for creating graphene nanostructures having well-defined edges [60–63]. Here hydrogenation or oxidation of graphene at the interface between a graphene sheet and a metal nanoparticle in the presence of hydrogen or oxygen, respectively, at elevated temperature produces a sheet etched along the direction commensurate to

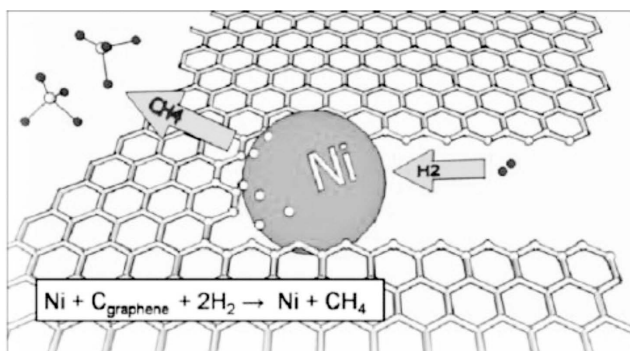


Figure 6.13 Illustration of a Ni nanoparticle etching a graphene sheet. Ni nanoparticles absorb carbon from graphene edges, which then reacts with H_2 to create methane. After Ref. 60.

the graphene lattice. The hydrogenation reaction



occurs in the presence of Fe, Co, or Ni nanoparticles. Metal nanoparticles 4–15 nm in size are seeded on a graphene sheet placed on a SiO_2/Si substrate. The graphene sheet is then subjected to the reaction at a temperature of 900°C (Fe), 600°C (Co), or 700°C (Ni) in a hydrogen atmosphere. The mechanism of the etching process is illustrated in Fig. 6.13 [60]. During the high-temperature etching stage, the metal nanoparticles etch the graphene sheet through catalytic hydrogenation of carbon, where carbon atoms from exposed graphene edges dissociate into the nanoparticle and then react with H_2 at the nanoparticle surface. As a result, carbon from the graphene is hydrogenated into methane by the metal nanoparticle catalyst. The reaction causes the nanoparticle to move, leaving an etch track. The crystallographic orientation of the etching direction is determined by the interfacial interactions of the nanoparticles with the graphene edges due to favorable adhesion and wetting of the metal nanoparticles at the graphene edges along specific crystallographic directions. In this etching process, thermally activated metal nanoparticles act as knives to cut channels along specific crystallographic directions in the graphene. The etching proceeds along specific directions. In few-layer graphene or graphite

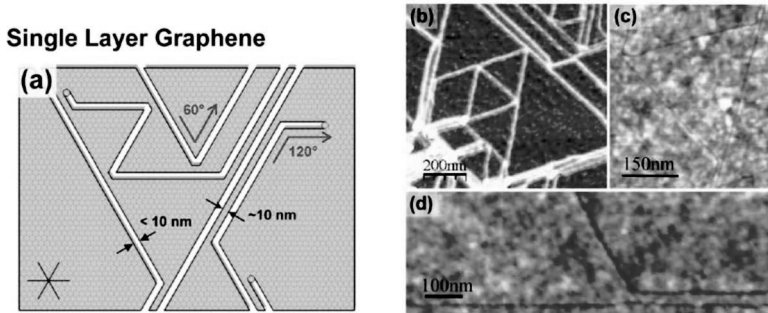


Figure 6.14 Nanoparticle-assisted etching in single-layer graphene. (a) Key features of etching in single-layer graphene are chirality-preserving angles of 60° and 120° , which prevent crossing of etched trenches, leaving ~ 10 nm between adjacent trenches and producing connected nanostructures, and trenches and nanoparticles with uniform width (< 10 nm). (b) AFM phase image of etched single-layer graphene containing geometric nanostructures. (c) AFM height image of equilateral triangle connected to three nanoribbons. (d) AFM height image of a trench running parallel to another trench without crossing it. After Ref. 60.

reacting with Ni nanoparticles, etching along the zigzag edges is most frequent [62]. However, very small Ni nanoparticles (< 10 nm) and Co nanoparticles seem to preferentially form channels along the armchair direction. Figure 6.14 shows the Ni-nanoparticle-assisted cutting of single-layer graphene sheets [60]. The cuts produced in single-layer graphene avoid crossing each other, resulting in continuously connected graphene nanostructures. Interestingly, the deflections and reflections show a regularity, with measured angles between any pair of etched trenches of either 60° or 120° . This proves that the edge chirality (either armchair or zigzag) is conserved in the etching process. Using this method, graphene nanostructures having a width of 10 nm and smooth edges are created.

Oxidation-based etching is also conducted using Ag nanoparticles as a catalyst; oxidation occurs with the evolution of CO and CO₂ [63]. Graphene nanostructures similar to those obtained from the hydrogenation reaction are created, where the edge roughness can be less than 2 nm.

6.2.7 Bottom-Up Fabrication from Aromatic Molecules

Most of the methods for preparing nanographene employ top-down procedures. Bottom-up processes from small aromatic molecules have also been employed in synthetic organic chemistry. Here we have an important issue related to aromaticity, as will be discussed in Section 6.3. Indeed, it is very difficult to prepare zigzag-edged nanographene, which is less aromatic, even if the size is still molecular. For example, in the family of triangular zigzag-edged molecules shown in Figs. 5.1 and 5.4 in Chapter 5, only molecules consisting of three or six hexagon rings have ever been successfully obtained. However, these molecules are extremely unstable, and it is necessary to terminate the carbon atoms at the three apexes with bulky functional group such as the *ter*-butyl group for stabilization. In the 1D zigzag-edged molecules called acene shown in Fig. 5.2, only molecules whose length is up to five hexagon rings are stable. See Chapter 5 and Section 6.3 for more details.

The situation of armchair-edged nanographene is different from that of zigzag-edged nanographene. Many polycyclic aromatic molecules, up to nanographene having armchair edges, have been successfully prepared by systematic organic synthetic methods; the largest such molecule consists of 222 carbon atoms, as shown in Fig. 6.15 [64]. Preparation is difficult because the molecules must be soluble so that they can be placed on an appropriate substrate from a solution. Various armchair-edged long graphene nanoribbons have been prepared on HOPG, Au, and Ag substrates using a polymerization reaction [65, 66]. Graphene nanoribbons 0.738 nm wide were prepared after polymerization of bianthracene monomers on a Au substrate, as shown in the STM atomic images and Raman spectra in Fig. 6.16. The STM image, together with a density functional theory (DFT) calculation, confirms the atomically precise edge structure, which cannot be obtained by top-down methods. The radial-breathing-like mode in the Raman peak at 396 cm^{-1} proves the narrow width, in addition to the Raman G (1600 cm^{-1}) and D bands (1341 cm^{-1}), which also indicate the structural features of graphene nanoribbons.

STM/scanning tunneling spectroscopy (STS) observations and treatments allow us to create nanographene-based molecular electronics [65]. Bottom-up methods can create armchair-edged

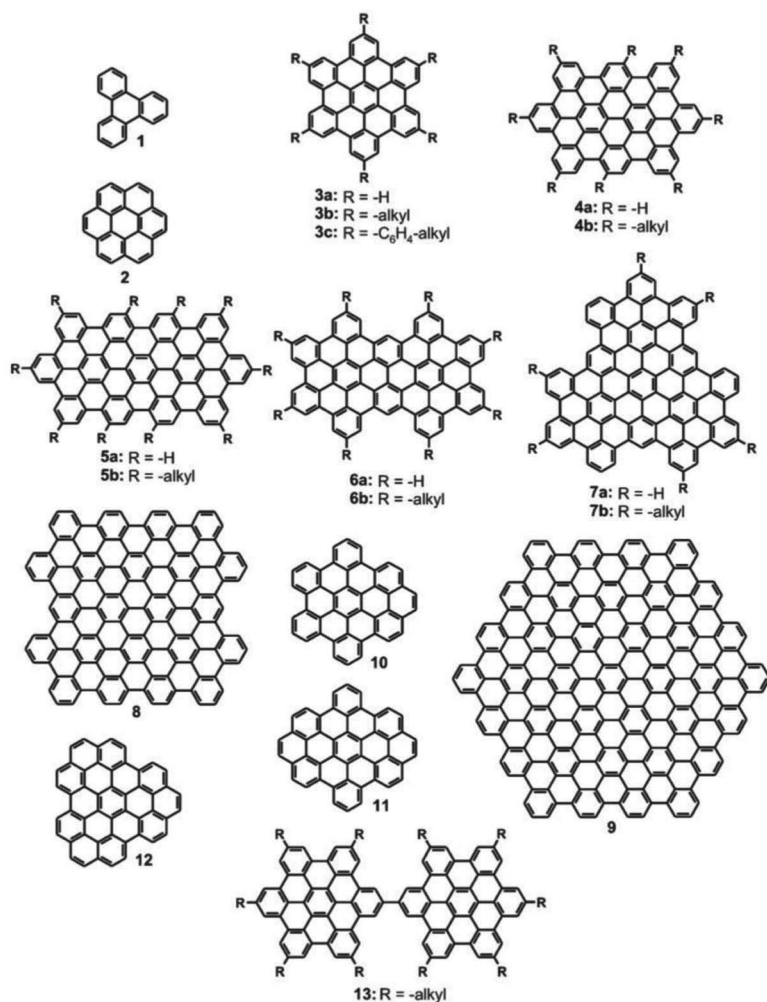


Figure 6.15 Armchair-edged polycyclic aromatic hydrocarbon molecules prepared by bottom-up method. After Ref. 64.

nanographene having a variety of widths, shapes, and lengths [65,66], although further effort is necessary in the future to create zigzag-edged and zigzag/armchair-hybrid edged nanographene sheets, which are expected to perform a variety of electronics/spintronics functions.

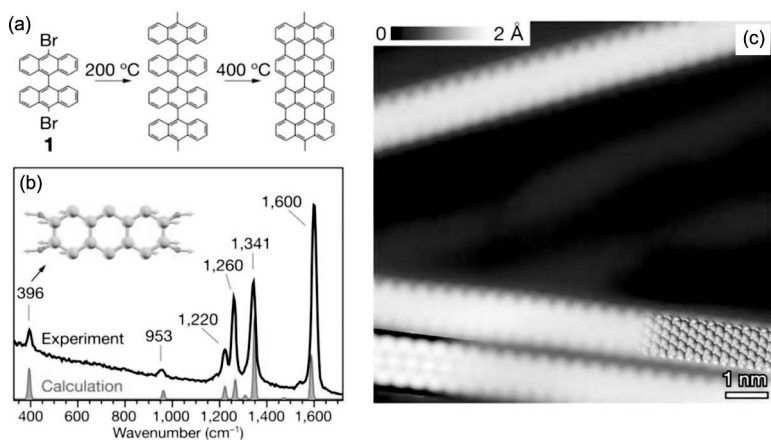


Figure 6.16 Armchair-edged graphene nanoribbons prepared from bianthryl monomers. (a) Reaction scheme from precursor **1** to straight graphene nanoribbons ($N = 7$, width of 0.738 nm). (b) Raman spectrum (incident laser of 532 nm) of a straight graphene nanoribbon. Inset shows the atomic displacements characteristic of the radial-breathing-like mode at 396 cm^{-1} . (c) High-resolution STM image partially overlaid by a molecular model of the ribbon. DFT-based simulation of the nanoribbon is shown at bottom left. After Ref. 66.

6.3 Electronic Structure of Nanographene and Graphene Edges

6.3.1 Theoretical Background of the Edge State

Chapter 5 covers the electronic structure of polycyclic aromatic hydrocarbon molecules, of which graphene can be considered an indefinitely large version, and the electronic structure and related phenomena of nanographene are discussed theoretically in Chapter 4. Here, let us begin by discussing the relationship between aromaticity in small polycyclic aromatic hydrocarbon molecules and the edge state in nanographene/graphene edges. Benzene, which is a typical Kekulé molecule and the primary building block of graphene, consists of three bonding π orbitals and three antibonding π^* orbitals split mutually with a large gap between the highest occupied molecular orbital and the lowest unoccupied molecular orbital (HOMO-LUMO gap) (Fig. 6.17(a)), which is a measure of aromatic

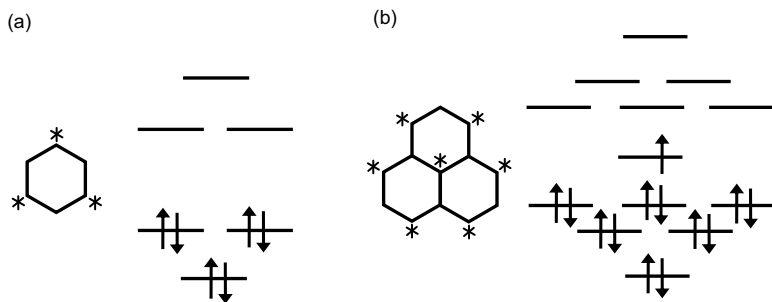


Figure 6.17 π electron states of (a) benzene and (b) phenalene. Starred (unstarred) sites belong to a given subgroup (starred (unstarred)) that is directly bonded to those belonging to another subgroup (unstarred (starred)).

energy stabilization. When benzene rings are fused to each other to form condensed polycyclic aromatic hydrocarbon molecules, the Kekulé structure with a large HOMO-LUMO gap is usually conserved, as evidenced in naphthalene and anthracene. However, as discussed in Section 5.2, in exceptional molecules called non-Kekulé molecules, energy stabilization fails [15–22].

A typical example is phenalene, which consists of three benzene rings fused in a triangle shape, as shown in Fig. 6.17(b) (see Section 5.2.1). In this molecule, a half-filled extra π electron state is present at the Fermi level in the energy gap as a nonbonding π electron state, which destabilizes the molecule. The number of nonbonding states increases upon the increase of the molecule size. As discussed in Section 5.2.3, Clar's aromatic sextet rule [16] allows us to count the number of nonbonding π electron states and eventually discuss comprehensively the aromatic stability of polycyclic condensed aromatic hydrocarbon molecules. According to this rule, the structure of a hydrocarbon molecule is expressed by tiling aromatic sextets, which are defined a benzene ring with six constituent C atoms singly bonded to the surroundings, as shown in Fig. 6.18(a). The aromatic stability is estimated by the number of sextets tiled on the molecule of interest; molecules having more sextets are more stable. For example, graphene, illustrated in Fig. 6.18(b), has sextets located on every three hexagons arranged with a superstructure of $\sqrt{3} \times \sqrt{3}$, which suggests that its aromatic stability

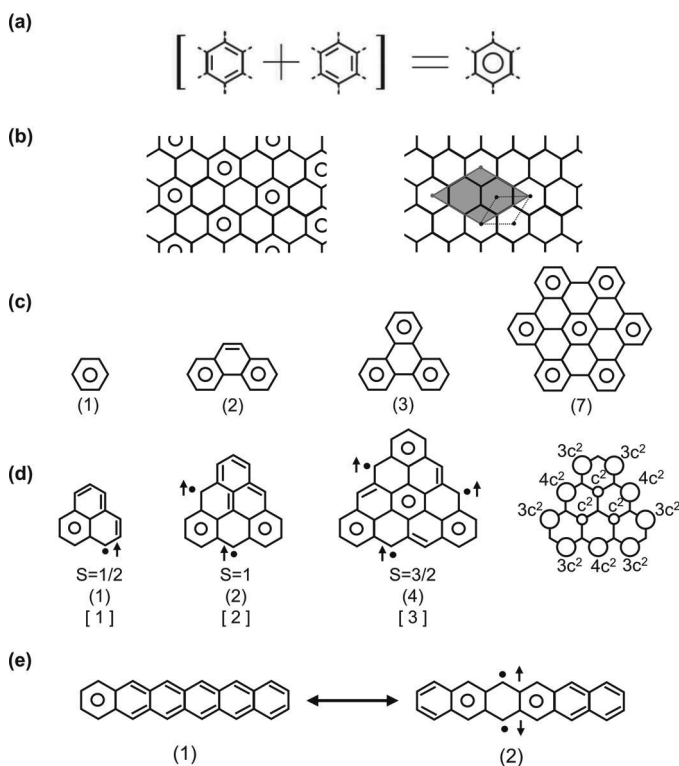


Figure 6.18 (a) Aromatic sextet. (b) (Left) The tiling of aromatic sextets in graphene. (Right) The unit cell (parallelogram with dotted lines) of graphene and a $\sqrt{3} \times \sqrt{3}$ superstructure (shaded parallelogram). (c) Armchair-edged molecules. (d) Triangular zigzag-edged molecules. The population of the edge state in triangulene is shown on the right. (e) Linear zigzag-edged molecules. Number in parentheses is the number of aromatic sextets. Number in brackets is the number of edge states. Arrow indicates the localized edge state spin, and S indicates the spin state.

is one-third that of benzene. The degraded aromaticity of graphene is responsible for its electronic and chemical activity.

Here we focus on edges. Figure 6.18(c) presents the aromaticity of armchair-edged molecules. These molecules have many sextets; molecules consisting of 1, 3, 4, and 13 hexagon rings have 1, 2, 3, and 7 sextets, respectively. Accordingly, these armchair-edged molecules are well stabilized closed shell systems with no nonbonding π

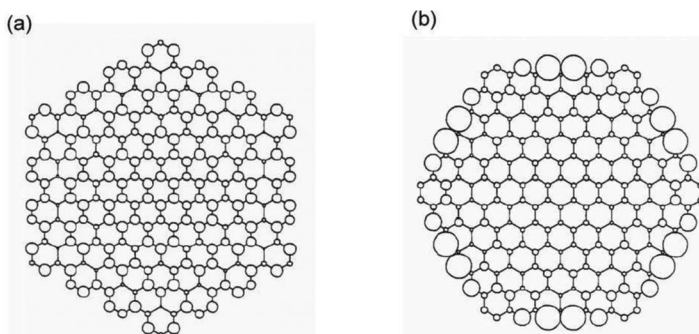


Figure 6.19 Spatial distribution of the HOMO level in (a) armchair-edged and (b) zigzag-edged nanographene sheets. The HOMO level is assigned to the edge state in the zigzag-edged nanographene sheet. After Ref. 1.

electron state in the HOMO-LUMO gap. In contrast, zigzag-edged molecules have a few sextets, as shown in Figs. 6.18(d) and (e) for triangular and linear molecules, respectively. Indeed, triangular molecules consisting of 3, 6, and 10 hexagon rings have only 1, 2, and 4 sextets, respectively, and the linear molecules, referred to as acene, have 1 or 2 sextets irrespective of the number of constituent hexagon rings when the number is larger than 6 [71]. Aromatic sextet tiling also yields the number of radical states, which are assigned to the nonbonding π electron states, as shown in Figs. 6.18(d) and (e): 1, 2, and 3 for triangular molecules consisting of 3, 6, and 10 hexagons, and 2 for acenes. This proves that the zigzag-edged molecules are open-shell systems with nonbonding π electron states existing in the energy gap. Note that the local density of states (LDOS) of the nonbonding π electron state in the zigzag-edged molecule is populated in the zigzag edge region, as shown in Fig. 6.18(d) (see also Section 5.4). This is why the nonbonding π electron state is called the edge state. Also, the edge state, which is singly occupied, is magnetic because it is a radical state with a localized spin. Lieb's theorem [17] can be applied to obtain the spin state, which is given by $S = (1/2)|N^* - N|$. Here, N^* (N) is the number of starred (unstarred) sites, which are those belonging to a given subgroup (starred(unstarred)) directly bonded to those belonging to another subgroup (unstarred(starred)) (see Fig. 6.17). From Lieb's theorem, triangular molecules consisting of 3, 6, and 10 hexagons have spin

states of $S = 1/2$, 1, and $3/2$, respectively, because of Hund's rule, which suggests they are ferromagnetic, whereas linear molecules with the number of constituent hexagon rings being larger than 6 are in the open-shell singlet state with $S = 0$, or antiferromagnetic.

Clar's rule can also be applied to nanographene, which is an extrapolation of polycyclic aromatic molecules to nano-dimensions; it demonstrates the presence of nonbonding edge states when a nanographene sheet is zigzag edged in contrast to their absence in an armchair-edged sheet. Figure 6.19 presents the spatial distribution of the HOMO level for armchair-edged and zigzag-edged nanographene sheets [1]. The HOMO state is uniformly distributed in the armchair-edged nanographene sheet. In contrast, the zigzag-edged nanographene sheet has a large LDOS, which is assigned to the edge state, around the zigzag edge region. Figure 6.20 shows the tiling of aromatic sextets in graphene nanoribbons having armchair and zigzag edges. In the armchair-edged graphene nanoribbon shown in Fig. 6.20(a), the aromatic sextets are tiled on every

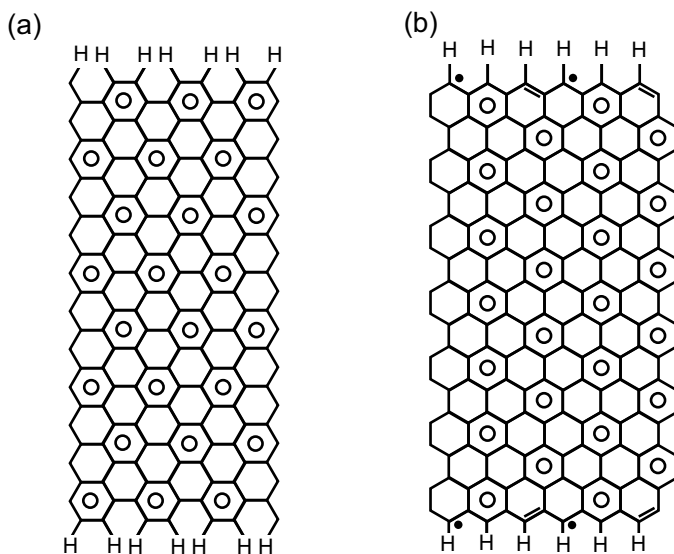


Figure 6.20 Tiling of aromatic sextets in (a) armchair-edged and (b) zigzag-edged graphene nanoribbons with their edge carbon atoms terminated by hydrogen atoms.

three hexagon rings in a $\sqrt{3} \times \sqrt{3}$ superstructure, like the infinite graphene sheet. No additional features appear in the edge region. In sharp contrast, the zigzag-edged graphene nanoribbon shown in Fig. 6.20(b) has a radical state in every three carbon atoms at the edges on both sides. The nonbonding radical state, which is assigned to the edge state at the Fermi level, is the signature of zigzag edges, as in zigzag-edged aromatic molecules.

Let us examine the physics of the edge state. Physicists understand graphene and the edge state in a way different from that of chemists. The electronic structure of graphene is described effectively in terms of the relativistic Weyl equation with massless Dirac fermions (see Chapter 2),

$$i\hbar \frac{\partial}{\partial t} \psi(\mathbf{r}, t) = \begin{pmatrix} \hat{H}^* & 0 \\ 0 & \hat{H} \end{pmatrix} \psi(\mathbf{r}, t), \quad (6.1)$$

$$\hat{H} = v_F \sigma \mathbf{p}, \quad (6.2)$$

where v_F and \mathbf{p} are the Fermi velocity ($v_F = 3\gamma_0 a_{CC}/2\hbar \approx (1/300)c$, c ; light speed) and the momentum, respectively. The intra-sheet transfer integral γ_0 [70], which is responsible for the π electron bond, is estimated as 3.16 eV, and the intra-sheet C-C bond length is $a_{CC} = 0.142$ nm (lattice constant $a = \sqrt{3}a_{CC}$). Here, σ is the 2×2 Pauli matrix,

$$\sigma = (\sigma_x, \sigma_y, \sigma_z), \quad \sigma_x = \begin{pmatrix} 0 & 1 \\ 1 & 0 \end{pmatrix}, \quad \sigma_y = \begin{pmatrix} 0 & -i \\ i & 0 \end{pmatrix}, \quad \sigma_z = \begin{pmatrix} 1 & 0 \\ 0 & -1 \end{pmatrix}, \quad (6.3)$$

for a pseudo-spin (\uparrow, \downarrow), which is not a real spin but is related to the structural degree of freedom specific to the hexagonal network of graphene. The structure of graphene is represented by a bipartite lattice consisting of two independent sublattices (A and B), as shown in Fig. 6.21(a), which suggests that the structural degree of freedom is 2. The pseudo-spin resembling a real spin originates effectively in this structural degree of freedom in the bipartite lattice. In the Brillouin zone of the bipartite lattice, two independent sites, K and K', appear at its corners, as illustrated in Fig. 6.21(b). Equations (6.1) and (6.2) describe cone-shaped conduction and valence bands, which are called Dirac cones, at K and K' as shown in Fig. 6.21(c). The bottom point of the Dirac cone of the conduction band touches

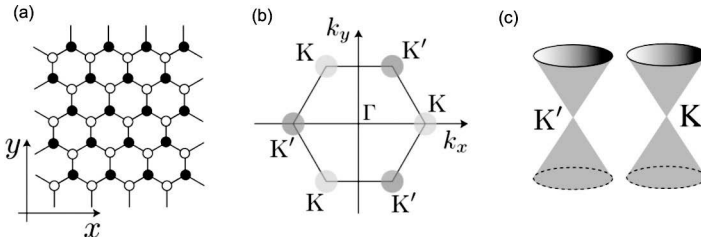


Figure 6.21 (a) Bipartite lattice of graphene consisting of sublattices A (filled circles) and B (open circles). (b) Brillouin zone of graphene with two independent sites K and K'. (c) Dirac cones at K and K'.

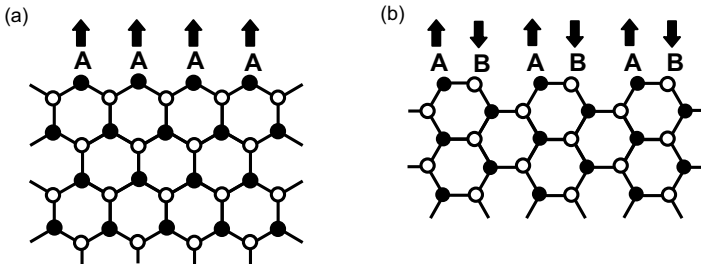


Figure 6.22 (a) Zigzag edge with broken symmetry. (b) Armchair edge with A and B sublattices always paired.

the top point of the valence band at a point called the Dirac point, at which the Fermi level is located in a neutral graphene sheet.

The electronic structure at the graphene edges depends on their geometrical shape. For zigzag edges, only one of the sublattices (A or B) appears, although armchair edges always have paired A and B sites, as exhibited in Figs. 6.22(a) and (b). Thus, the symmetry of the pseudo-spin in the Dirac fermions is broken in the zigzag edge, producing the edge state. Here it should be noted that the momentum \mathbf{p} , which is coupled with the pseudo-spin in Eq. (6.2), is substituted as $\mathbf{p} \rightarrow \mathbf{p} + e\mathbf{A}$ in the magnetic field $\mathbf{B} = \nabla \times \mathbf{A}$, where \mathbf{A} is the gauge field of the magnetic field applied. When the symmetry is broken between sites A and B due to a structural distortion, the distortion induces an additional gauge field \mathbf{A}_{dist} (see 6.3.4.1). Accordingly, in the absence of symmetry between A and B in a graphene lattice, the localized spins are created in the region

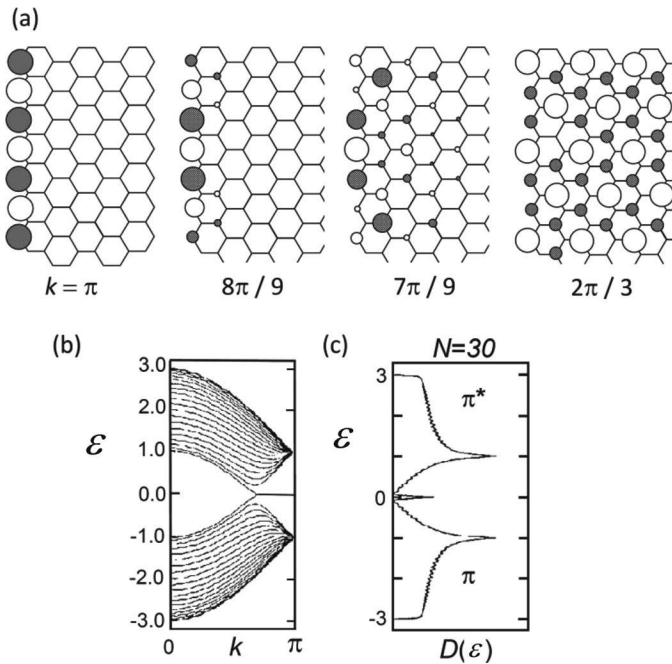


Figure 6.23 Electronic structure of a zigzag-edged graphene nanoribbon (width: 30 unit cells). (a) Population of the edge state depending on the wave number k . The sign of the wave function is + and – for open and shaded circles, respectively. (b) Energy dispersion of the π electron states. The energy is normalized with respect to intra-sheet transfer integral γ_0 . (c) Density of states $D(\mathcal{E})$ as a function of energy with the valence π and conduction π^* bands. After Ref. 3.

where the distortion is generated. The sharp discontinuity in the graphene lattice, accompanied by the broken symmetry between sublattices A and B at the zigzag edge, induces a gauge field, so the edge state is strongly spin polarized. Figure 6.23 exhibits an example of the electronic structure of a zigzag-edged graphene nanoribbon [3]. The edge state is completely localized at the edge carbon atoms in the zigzag edges at the Brillouin zone boundary of $k = \pi$, as shown in Fig. 6.23(a). The edge state becomes less localized as k goes from the Brillouin zone boundary to the zone center, and it is completely delocalized in the entire graphene nanoribbon at $k = 2\pi/3$. The decay length of the wave function of the edge state is given

by $\exp(-r/\xi)$ with

$$\xi = \left(\sqrt{3}a/2 \right) \left| \ln \left(2 \cos \left(\frac{k_c}{2} \right) \right) \right|^{-1} \quad \text{for } \frac{2\pi}{3} \leq k_c \leq \pi, \quad (6.4)$$

where k_c is the wave number along the direction perpendicular to the ribbon's axis. In the energy spectrum of the π electron states (Fig. 6.23(b)), an edge state having a flat band between $k = 2\pi/3$ and $k = \pi$ is located at the Dirac point between the linear conduction π electron state and the linear valence π^* electron state; it contributes to the sharp density-of-states peak at the Dirac point (Fig. 6.23(c)). Details are given in Section 4.3.

6.3.2 Experimental Evidence of Edge States

It is particularly important to provide evidence for the presence of edge states using microprobe techniques such as STM/STS and AFM at atomic resolution [7, 9–13, 72]. Other experimental methods, such as TEM [73–80], ultraviolet photoelectron spectroscopy (UPS) [81, 82], and near-edge x-ray absorption fine structure (NEXAFS) [83–88], can also provide information on the edge state. However, the high-energy electron beam used in TEM observations heats the graphene edges so that they are far from thermal equilibrium, which eventually destroys them. This makes the explanation ambiguous, since unterminated σ -dangling bonds created by electron beam irradiation behave similarly to the edge state of π electron origin [86]. Zigzag edges are generally thermodynamically unstable owing to the presence of edge states at the Fermi level (ε_F), whereas armchair edges are stabilized owing to the enhanced aromaticity [16, 18–22, 89, 90]. However, TEM observations frequently show mainly zigzag edges, in contradiction to the theoretical predictions for the thermodynamically stable state. Meanwhile, the local structure at atomic resolution cannot be observed in UPS and NEXAFS experiments, although these experiments provide information on the energy position of the edge state.

6.3.2.1 STM/STS observations

First, we discuss the experimental evidence for the edge state in terms of STM/STS observations. Let us begin with graphene

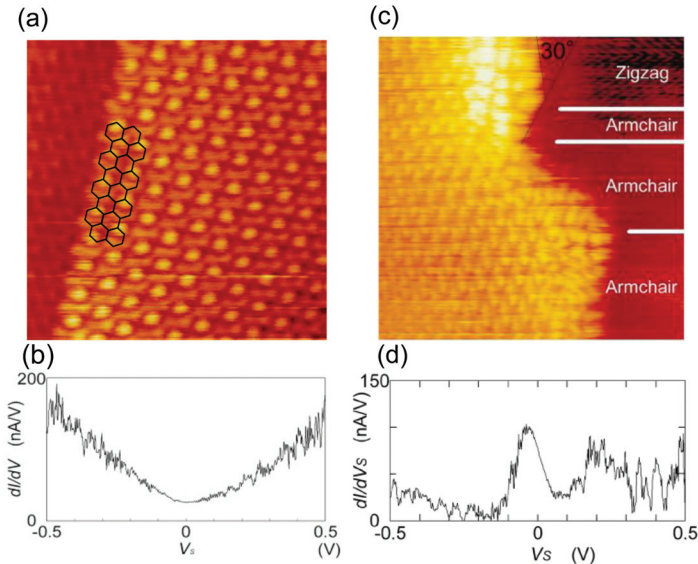


Figure 6.24 (a) Atomically resolved UHV STM image ($5.6 \times 5.6 \text{ nm}^2$) of a homogeneous armchair edge. To clarify the edge structures, a model of the honeycomb lattice is overlaid on the image. (b) dI/dV_s curve from STS measurements taken at the edge in (a). (c) Atomically resolved UHV STM image of zigzag and armchair edges ($9 \times 9 \text{ nm}^2$). (d) dI/dV_s curve from STS data at a zigzag edge in (c). Images were taken in constant-height mode with a bias voltage $V_s = 0.02 \text{ V}$ and current $I = 0.7 \text{ nA}$. After Ref. 9.

edges at graphite step edges. Graphene edges prepared in ambient atmospheric conditions are usually heavily covered with oxygen-containing functional groups owing to the easy oxidation of graphene edges under ambient conditions [91]. STM observations of hydrogen-terminated graphene edges are required in order to examine the electronic structure of the graphene edges. For this reason, the graphene edges are heat-treated at 800°C to remove the oxygen-containing functional groups and then hydrogen terminated in ultra-high vacuum (UHV) [9, 11]. Figure 6.24 shows typical examples of UHV STM lattice images and STS spectra of hydrogen-terminated graphene edges [9]. Figures 6.24(a) and (b) are the STM and STS results, respectively, for a uniform armchair edge. The STS spectrum (dI/dV_s vs. V_s), which corresponds to the density of states,

has linear V_s dependence above and below $V_s = 0$ V, at which the Fermi level is located. This demonstrates that the electronic structure near the Fermi level (ε_F) is the same as that of an infinite graphene sheet with a massless Dirac fermion feature described in terms of linear valence π and conduction π^* bands that touch each other at ε_F (see Fig. 6.21(c) and Chapter 2) [92]. This reflects the lattice image (Fig. 6.24(a)), which shows no extra contribution in the edge region. The observed armchair edges are generally long and less defective, which suggests that they are energetically stable, in accordance with the theoretically predicted aromatic stability, as mentioned above [16, 18–22, 89, 90]. Zigzag edges have different features from armchair edges: Zigzag edges tend to be defective and short. They are frequently observed to be embedded between armchair edges, as shown in Fig. 6.24(c). This is a consequence of the energetically unstable structure of the less-aromatic zigzag edges [16, 18–22, 89, 90]. The important feature in zigzag edges is the presence of the edge state [1–4, 13]. The STS spectrum (Fig. 6.24(d)) at the zigzag edge shows a sharp peak in the density of states at ε_F in addition to the linear π and π^* bands, which provides evidence for the edge state. This is in good agreement with the theoretical results shown in Fig. 6.23(c). The bright spots observed in the zigzag edge region (Fig. 6.24(c)) are ascribed to the edge state. The STM image shown in Fig. 6.24(c) agrees qualitatively with the STM image predicted by calculation, as shown in Fig. 6.25. A large LDOS originating in the edge states appears around the zigzag edge regions, accompanied by a shrinkage of the C–C bond length [22].

The characteristics of the edge states depend on the environment around the zigzag edges [9, 11, 13]. For a monohydrogenated-terminated zigzag edge, the edge state is well localized around the edge region, with a decay length of 1–2 unit cells. However, dihydrogenated edges have a less-localized edge state with a population extending into the interior of the graphene sheet [22]. The way in which the graphene sheets are stacked also affects the distribution of the edge state. In graphite, graphene sheets are stacked in AB fashion, where the carbon atom at one of two independent sites on a sheet is on top of the carbon atom on the sheet beneath, and that at the other site is on the center of the hexagon on the sheet beneath. The former (the α carbon), which interacts directly with

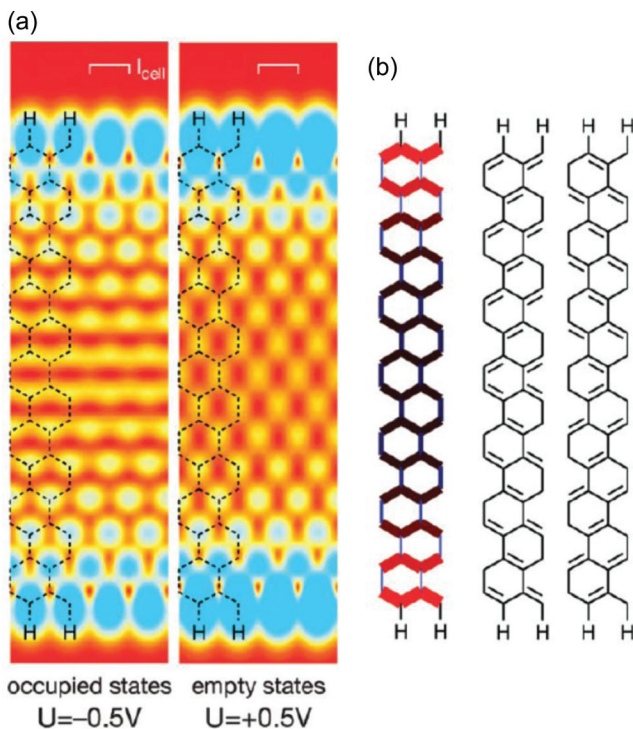


Figure 6.25 (a) Calculated STM images for the spatial distribution of the LDOS for the occupied valence π and unoccupied conduction π^* bands in zigzag-edged graphene nanoribbon. The bias voltage is taken near the Dirac point at -0.5 and $+0.5$ V, respectively. (b) Left: C-C bond lengths; thicker lines represent shorter lengths. Center and right: Clar's formulas, the superposition of which gives the electronic structure of zigzag-edged graphene nanoribbon. (color) After Ref. 22.

the carbon atom beneath, is well localized around the zigzag edge, in comparison with the less-localized latter (the β carbon), which has no carbon atom underneath. When a zigzag edge is embedded between armchair edges, the interaction of the edge state with the wave function in the armchair makes the edge state less localized.

Chemical and structural modifications of edges also change the electronic features of the edge state, which is discussed mainly in Sections 6.4 and 6.5. Here let us comment on the simplest modification, changing a monohydrogenated edge carbon atom to a

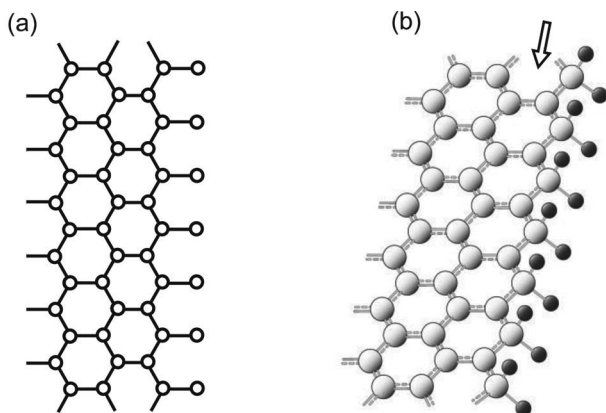


Figure 6.26 (a) Klein edge (zigzag edge in which an extra carbon atom bonded to the edge carbon atom participates in the conjugated π -bond network). (b) Zigzag edge in which each edge carbon atom is dihydrogenated. The large white circle and small black circle represent carbon and hydrogen atoms, respectively. This edge structure corresponds to a Klein edge. Carbon atoms aligned along the direction indicated by the arrow correspond to the extra carbon atoms in (a).

dehydrogenated one by adding an extra hydrogen atom to the edge carbon atom. This change calls to mind the difference between a monohydrogenated zigzag edge and a Klein edge [93, 94], in which an extra carbon atom bonded to an edge carbon atom participates in the conjugated π -bond network, as shown in Fig. 6.26(a). Indeed, dihydrogenation of edge carbon atoms in a zigzag edge, as shown in Fig. 6.26(b), produces a Klein edge. Figure 6.27 presents an example of this modification; the STM image shows a short zigzag edge consisting of three carbon atoms embedded between armchair edges [11]. An array of bright spots, whose brightness decreases monotonically toward the interior of the sheet along a line at an angle of 120° from the direction of the armchair edge, is observed near the center of the zigzag edge in Fig. 6.27.

The image is compared to the spatial distribution of the LDOS calculated by the tight-binding method for the same geometry as that of the experimentally observed lattice, as shown in Fig. 6.27(b). A comparison demonstrates that the LDOS mapping failed to reproduce the direction of the array of bright spots in the observed

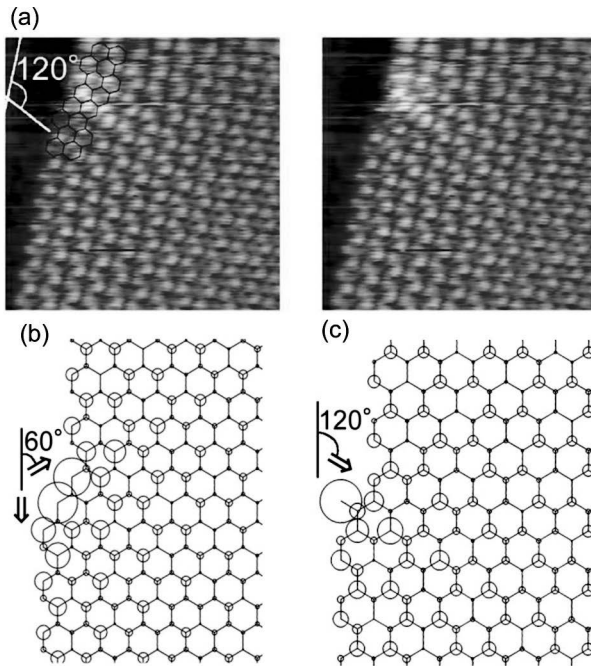


Figure 6.27 (a) STM image ($4.5 \times 4.5 \text{ nm}^2$) of a short zigzag edge consisting of three edge carbon atoms embedded between armchair edges. In the left panel, a honeycomb lattice is overlaid on the original image in the right panel to clarify the location of the zigzag edge. An array of bright spots is observed around the zigzag edge, and its direction and the angle measured from the direction of the armchair edge are drawn in the left panel. (b) Calculated 2D mapping of the LDOS of the edge structure in (a). (c) Calculated 2D mapping of the LDOS of the edge structure in (a) except that an extra carbon atom, shown as a bar, is attached to an edge carbon atom in the center of the zigzag edge. Arrows indicate the direction of the array of large LDOS that extends to the interior of the graphene sheet. After Ref. 11.

STM image. Indeed, the array of the calculated LDOS runs along a line at an angle of 60° from the direction of the armchair edge, which is inconsistent with the observation. The origin of the difference is associated with the presence of an extra carbon atom that is bonded to the edge carbon atom, for example, during sample preparation. The smallest structural difference at the zigzag edge can be produced by the presence or absence of one extra carbon atom

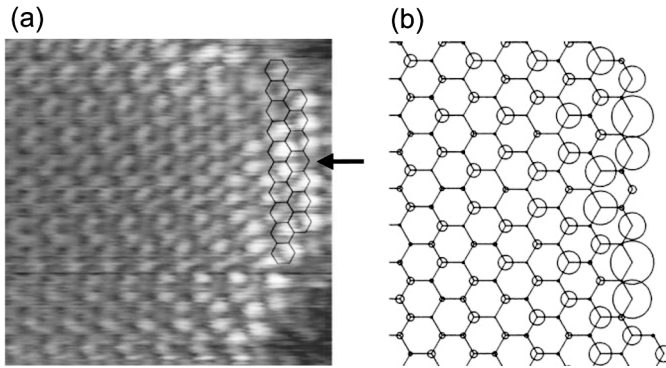


Figure 6.28 (a) STM image ($3.8 \times 3.8 \text{ nm}^2$) of a zigzag edge consisting of seven edge carbon atoms. Arrow indicates a very small LDOS at the center of the zigzag edge. (b) 2D mapping of the LDOS calculated at a zigzag edge having the same structure as that in (a). After Ref. 11.

attached to the edge carbon atom, that is, the presence or absence of a Klein edge at the center of the zigzag edge. Figure 6.27(c) shows the calculated result based on a model that has the same geometric structure as that of Fig. 6.27(b) except that an extra carbon atom is attached to the center of the zigzag edge. Figure 6.27(c) reproduces the array of bright spots in Fig. 6.27(a) well, suggesting the presence of a dihydrogenated carbon site in the zigzag edge.

Here we present an interesting example of the effect of electron confinement in a finite-length zigzag edge [11]. Figure 6.28(a) shows an STM image of a zigzag edge consisting of seven edge carbon atoms. In this image, the bright spot representing the edge state is absent at the center of the zigzag edge, although bright spots at other edge carbon atoms in the zigzag edge prove the presence of the edge state. The absence of bright spots is always detected in a zigzag edge longer than that in Fig. 6.28(a). The calculated result (tight binding calculation) in Fig. 6.28(b) for a zigzag edge structure similar to that in the observed edge reveals that the LDOS in the center of the zigzag edge is very small, although the atomic structure has no vacancies at the edge. This is because the smallest LDOS in the center of the edges corresponds to the node of the wave function of an electron confined in a finite-length zigzag edge having an odd number of edge carbon atoms.

STM/STS investigations have confirmed that graphene nanostructures such as nanoribbons and nanoislands also have edge states at zigzag edges [72]. The edges of nanographene samples obtained by mechanical cleavage of HOPG were experimentally subjected to hydrogen passivation in a UHV chamber. Well-defined lattice images were observed in the STM topographs for nanoisland samples 2–20 nm in size on a Si substrate. Typical lattice patterns are a 0.41 nm hexagonal lattice or 0.25 nm triangular lattice; the former is considered to be a consequence of wave function scattering at the edges. Figure 6.29 shows STM images and the STS spectrum (dI/dV curve) of graphene nanoislands. Around the zigzag edges shown in Figs. 6.29(a) and (d), peaks in the dI/dV spectra appear around bias voltages of -0.33 V and 0.29 V, respectively, just at the edge (0 Å), as shown in Figs. 6.29(b) and (e). These peaks are assigned to the edge state present at the zigzag edges. The edge state peak is theoretically predicted to appear at a bias voltage of $V = 0$ V. The observed deviations from 0 V are understood in terms of charge transfer from the Si substrates. The peak positions of -0.33 eV and 0.29 eV suggest that the charge transfer differs between the two nanoisland samples. The intensity of the edge state peak tends to decrease from the zigzag edge to the interior, confirming that the edge states are well localized around the zigzag edges. Figure 6.29(f) indicates the peak intensity of the edge state as a function of the distance from the zigzag edge for the graphene nanoislands (a) and (d). On the basis of the distance dependence, the decay length of the edge state is estimated as 1.17 ± 0.14 nm to 0.95 ± 0.11 nm, which agrees well with the theoretical results [3]. Unlike the zigzag edges, the armchair edges have no STS peak assigned to an edge state, as shown in Fig. 6.29(c). Only the presence of a minimum at $V = 0$ V is confirmed, suggesting that the electronic structure is described only in terms of linear valence π and conduction π^* bands that touch each other at the Dirac point.

6.3.2.2 Angle-resolved photoemission spectroscopy

Here we examine the edge state using photoemission spectroscopy, which yields information on the electronic structure of the valence bands below ε_F . Angle-resolved photoemission spectroscopy

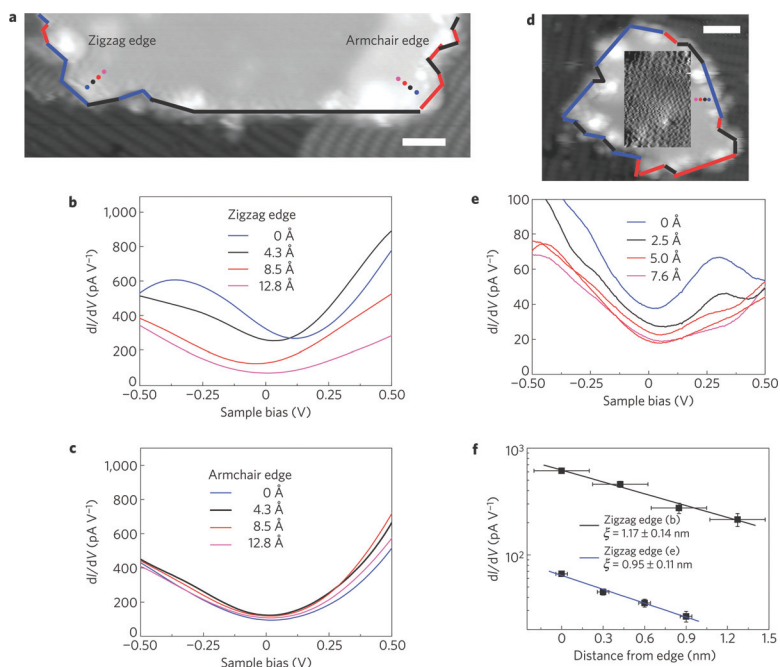


Figure 6.29 STM/STS observations of graphene nanoislands. (a) STM topograph of a ~ 15 nm nanoisland with the edge lattice symmetry labeled zigzag and armchair. (b), (c) Comparison of dI/dV spectra collected near the (b) zigzag edge and (c) armchair edge of sample (a). (d) STM topograph and (e) dI/dV spectrum for another island (~ 8 nm). The topographic spatial derivative image is included to highlight the atomic scale contrast in (d). dI/dV spectrum (e) is measured in the zigzag edge region in (d). (f) dI/dV as a function of distance from the edge. Scale bars in (a) and (d) represent 2 nm. dI/dV spectra are measured along the dotted line in (a) and (d) from the edge (0 Å) to the interior (12.8 Å for (b) and (c), 7.6 Å for (e)). After Ref. 72.

(ARPES) is a powerful tool for investigating the band structure of graphite [95] and graphene [96], as confirmed by previous work. This method was used with high energy and momentum resolution to investigate the edge state located around the Dirac point [81, 82] in a Kish graphite sample, which is a single-crystal-like graphite. Figure 6.30 shows the results of ARPES experiments. The graphite π valence bands, whose top touches the Fermi energy at the K

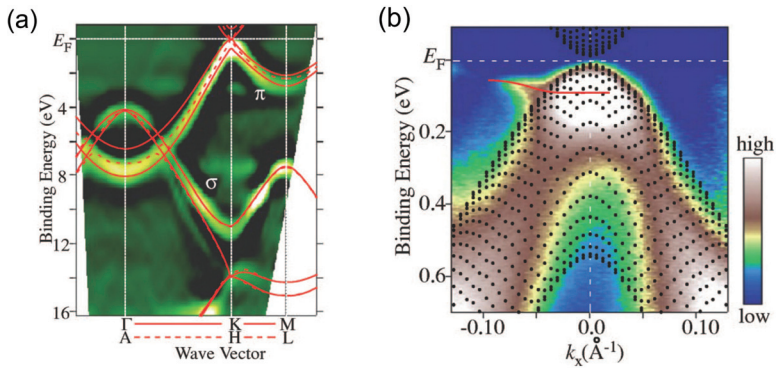


Figure 6.30 (a) Experimental band structure (bright area) of graphite obtained by plotting the second derivative of the angle-resolved photoemission spectral intensity as a function of the wave vector and binding energy, compared with the modified first-principles band structure calculation (solid and dashed lines represent $\Gamma \leftrightarrow K \leftrightarrow M$ and $A \leftrightarrow H \leftrightarrow L$, respectively) [97]. (b) Experimental band structure near ε_F around the K(H) point obtained by the same method as in (a). The experimental result is compared with a projection of the calculated π band onto the (001) plane (small dots) [98]. The line from $k_x \sim 0.0 \text{ \AA}^{-1}$ to -0.10 \AA^{-1} just below ε_F shows the peak position of a weakly dispersed edge state near ε_F . After Ref. 81.

point, are clearly visible in Fig. 6.30(a), in addition to the σ bands well below ε_F . This is in excellent agreement with a first-principles band structure calculation [97] and a previous experiment [95]. Of particular interest is an anomalous electronic feature around the top of the π valence band. In Fig. 6.30(b), this anomalous feature, denoted by a solid line, appears just at the top of the π valence band below ε_F , although the π band is well explained by the projection of the calculated π band onto the (001) plane [98]. This state is almost flat at wave numbers from $k_x \sim 0.0 \text{ \AA}^{-1}$ to -0.05 \AA^{-1} , and it shows a slight upward dispersion toward ε_F at $k_x \sim 0.05 \text{ \AA}^{-1}$ to -0.10 \AA^{-1} . The anomalous state is assigned to the edge state, as we discussed above, and confirmed by STM/STS observations of the zigzag edge. The edge state is considered to originate in the zigzag edges of graphene sheets at the step edges of the Kish graphite sample. The quite weak contribution of the edge state is due to the small contribution of the graphene edges in the well-crystallized Kish graphite sample. To obtain more details, it is necessary to investigate

the edge state using nanographene samples in ARPES experiments. Note that a weak spectral feature of graphene nanoribbons 0.72 nm in width prepared by CVD offers evidence of the edge state [40].

6.3.2.3 X-ray absorption spectroscopy

X-ray absorption spectroscopy (XAS) is an element-specific tool for investigating the electronic structure of states above ε_F , near which the edge state is located; the electronic process used in XAS is the excitation of electrons from a core level to partially filled and empty states. Therefore, we can extract information on the electronic structure of the edge state that is populated around the edge carbon atoms. NEXAFS in the carbon K-edge XAS spectra has been investigated using different nanographene samples such as CVD graphene [83], mechanically cleaved graphene [84], graphene nanoribbons [85], and networked nanographene [86], and also by theoretical methods [87, 88]. In all the samples, an extra peak assigned to the edge state was observed around the Fermi level in addition to the conduction π^* band. Figure 6.31 shows the experimentally observed NEXAFS for nanographene in an activated carbon fiber (ACF), which consists of a three-dimensional (3D) disordered network of nanographene sheets, compared with that for HOPG [86]. The NEXAFS spectra of nanographene and graphite (HOPG) typically have two peaks, at 285.5 eV and 291.9 eV, which correspond to the C1s to π^* and σ^* transitions, respectively, as shown in Fig. 6.31(a). In the nanographene spectrum, an extra small peak around ε_F (284.36 eV) is observed at 284.5 eV, which is assigned to the edge state. The spectral intensity ratio of the edge state to the π^* band is given as 11% in the deconvolution of the two peaks shown in Fig. 6.31(b). The in-plane size of the nanographene sheet constituting the ACF is 2–3 nm. Assuming a hexagonal nanographene sheet 2.5 nm in size as a representative individual nanographene sheet, we can estimate the total number of carbon atoms and the number of carbon atoms at the edge of the sheet, for example, 216 carbon atoms in total and 36 edge carbon atoms. This estimate reveals that 17% of all the carbon atoms are at the edges, which agrees well with the spectral intensity ratio observed in the NEXAFS spectra.

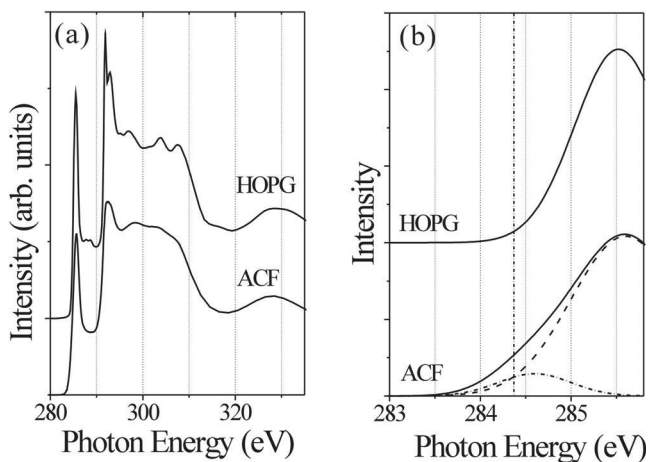


Figure 6.31 (a) Carbon K-edge NEXAFS spectra of nanographene in ACF consisting of networked nanographene sheets and HOPG. (b) Close-up of the pre-edge region of the NEXAFS spectra (solid line) and convoluted curve fit. HOPG spectrum is fitted with a single Gaussian; in the ACF, the deconvolution consists of two Gaussian peaks corresponding to the edge state (dot-dashed line) and the π conduction band (dashed curve). Vertical line indicates the position of the Fermi level of HOPG (284.36 eV). After Ref. 86.

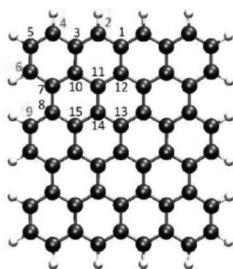
A high-temperature annealing NEXAFS experiment provided information on how the edge state behaves at high temperatures [85]. The edge state contribution survives at temperatures up to $\sim 1000^\circ\text{C}$, tends to decrease at higher temperatures, and disappears completely above 2000°C . This trend tracks the graphitization process of carbon-based materials well. Graphitization occurs above 1500°C . Therefore, the decrease in the contribution of the edge state to the NEXAFS is ascribed to the disappearance of edges upon the fusion of nanographene sheets.

The position of the edge state in energy is sensitive to the detailed structure of the graphene edge [88] arising from the detailed shape of the edges and any chemical modifications. By investigating the peak position of the NEXAFS spectrum (the $1s$ core-level binding energy) of polycyclic aromatic hydrocarbon molecules, which consist of a combination of zigzag and armchair edges, we can learn how the edge state is distributed in the edge region. Table 6.1

Table 6.1 The chemical shifts ($\Delta E_b(1s)$, in eV) of $1s$ core level binding energy ($E_b(1s)$, in eV) of the symmetry-independent C atoms in the graphene nanocluster $C_{54}H_{20}$ [Ref. 88]

Site	Zigzag edge				Armchair edge					
	edge		edge-1		edge		edge-1		interior	
$\Delta E_b(1s)$	C2	C4	C1	C3	C5	C6	C9	C7	C8	C13
	-1.00	-0.72	0.02	0.02	-0.22	-0.71	-0.40	0.02	-0.13	0.00

$\Delta E_b(1s)$ is given with respect to the $E_b(1s)$ of interior C (i.e., C13). The label of C atoms is shown below. Edge and edge-1 denote carbon atoms at the edge and at the site next from the edge.



shows the peak position of the NEXAFS spectrum of the constituent carbon atoms in polycyclic aromatic molecule $C_{54}H_{20}$ obtained theoretically by DFT calculation [88]. A carbon atom having a more negative shift $\Delta E_b(1s)$ than the $\Delta E_b(1s)$ value of the interior carbon atom (C13) (chemical shift) has a larger electron density, which more efficiently screens the core hole and eventually increases the reduction in the attractive potential due to the core hole. Therefore, the fact that the carbon atom (C2) at the center of the zigzag edge has the largest negative chemical shift ($\Delta E_b(1s) = -1.0$ eV) suggests the presence of an edge state at the carbon atom. The contribution of the edge state tends to decrease in the order $C2 > C4 > C6$ ($\Delta E_b(1s) = -1.0$ eV, -0.72 eV, and -0.71 eV for C2, C4, and C6, respectively). Carbon atom C4 is the end of the zigzag edge, which faces the armchair edge. The edge state is partially distributed to carbon atom C6 at the armchair edge in this small aromatic molecule.

The chemical shifts in the NEXAFS spectra of graphene nanoribbons calculated by DFT theory show a systematic trend depending on the edge shape and chemical modifications, as shown in Fig. 6.32 [88], where monohydrogenated or dihydrogenated carbons appear

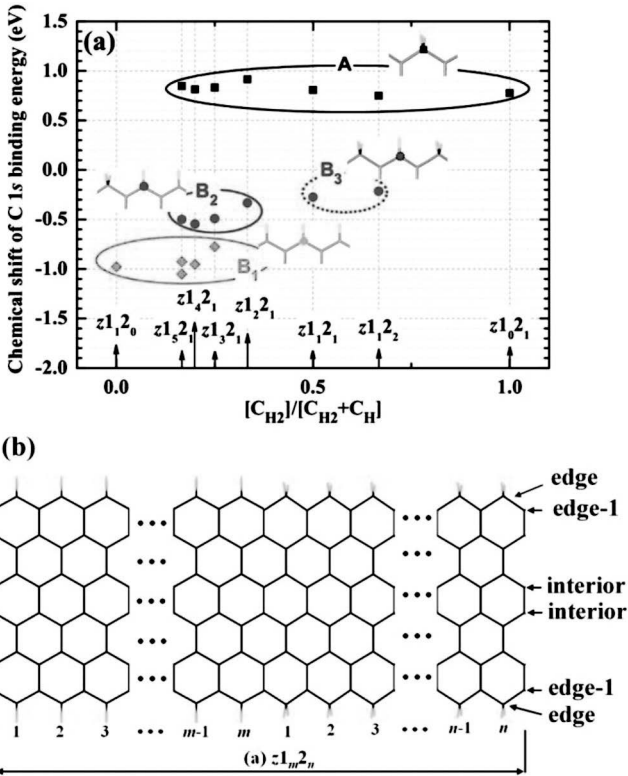


Figure 6.32 (a) Chemical shifts ($\Delta E_b(1s)$) of 1s core-level binding energy of carbon at zigzag edges in zigzag-edged graphene nanoribbons having monohydrogenated edges, dihydrogenated edges, and edges consisting of monohydrogenated and dihydrogenated regions. Insets show the edge structures of the graphene nanoribbons. There are four groups (A, B₁, B₂, B₃) having different chemical shifts in the edge structures. (b) Schematic illustration of geometric structures of graphene nanoribbons with different degrees of hydrogenation at zigzag edge. $z1$ and $z2$ denote the monohydrogenated (H1) and dihydrogenated (H2) zigzag edges, and m and n represent the numbers of H1 and H2 terminations at edges, respectively. Arrows indicate the periodic boundary of the unit cell. After Ref. 88.

at the zigzag edges. Monohydrogenated edges, dihydrogenated edges, and zigzag edges with a mixture of monohydrogenated and dihydrogenated edge carbon atoms are investigated. Here, $z1_mz_n$ denotes a zigzag edge in which the unit cell consists of

a monohydrogenated region with m edge carbon atoms and a dihydrogenated region with n edge carbon atoms. In the edge carbon atom of a pure monohydrogenated zigzag edge or the monohydrogenated edge carbon atom, which is neighbored by monohydrogenated sites on both side, in a zigzag edge having a mixture of monohydrogenated and dehydrogenated sites, the chemical shift shows a large negative value of ~ -1.0 eV, suggesting the presence of an edge state well localized at the edge carbon atom. Note the region encircled with B_1 in Fig. 6.32(a). The edge carbon atom at a site surrounded by dihydrogenated edge carbon site(s) has a less negative chemical shift of ~ -0.2 to -0.5 eV (regions B_2 , B_3), which is in good agreement with the STM observations of a dihydrogenated zigzag edge discussed above. The edge carbon atom having a larger number of dihydrogenated neighboring sites has less a negative chemical shift. In contrast, the dihydrogenated edge carbon atom (region A) has a positive chemical shift of ~ 0.6 to 0.8 eV, and the edge state is absent at the carbon site.

6.3.2.4 Transmission electron microscopy

High-resolution transmission electron microscopy (HRTEM) has been employed to observe graphene edges [73–80]. Interestingly, the electron energy loss spectra obtained by scanning transmission electron microscopy (STEM), together with lattice images, can provide information on the electronic structure. Here, we summarize the investigation of graphene edges using TEM and STEM.

In STM/STS examinations of graphene edges, armchair edges are frequently observed because they are thermodynamically stable, whereas zigzag edges tend to be short and defective, as discussed above [16, 18–22, 89, 90]. However, we observed well-defined zigzag edges as well as armchair edges using TEM [73–78]. We found that zigzag edges are more abundant in TEM observations than in STM observations [76]. Figure 6.33(a) clearly exhibits this trend; both zigzag and armchair edges are observed with similar probability. In the edges of as-prepared graphene nanoribbons, the edges are less regularly formed [75]. Annealing by Joule heating makes the edges more regular and straight, as shown in Fig. 6.33(a). The deviation from thermodynamically stable edge structure originates

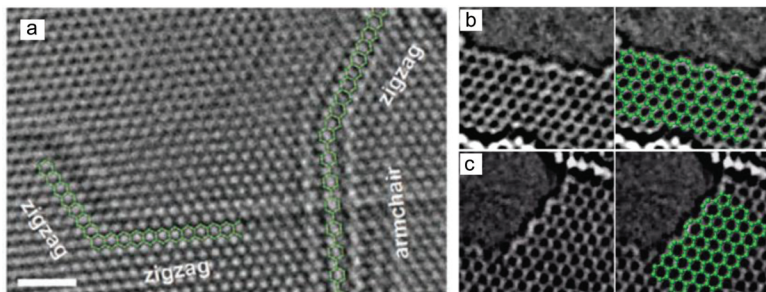


Figure 6.33 Transmission electron microscopy observation of edges. (a) Graphene nanoribbons after annealing by Joule heating. Scale bar; 1 nm. After Ref. 75. (b), (c) Graphene edge reconstruction accompanied by the formation of pentagonal and heptagonal rings. Images on the right side are the same as those on the left side but with the hexagonal network overlaid. After Ref. 76.

in electron beam irradiation, which causes the graphene edges to deviate far from the thermodynamically defined state. The high-energy electron beam activates the motion of carbon atoms at the edges of the graphene, producing kinetically determined edge structures. Accelerated electrons are believed to cause damage and eject doubly coordinated carbon atoms at the edges. Zigzag edges are repaired rapidly by diffusion of single carbon atoms, whereas the repair of armchair edges requires two carbon atoms and hence is slower [76]. In addition, edge reconstruction due to electron beam irradiation occurs. This can be seen in Figs. 6.33(b) and (c) as the formation of pentagonal and heptagonal rings incorporated at the edges of the hexagonal graphene network.

A combination of microscope image observations and electron energy loss carbon K-edge spectroscopy (ELNES) measurements in low acceleration voltage STEM can provide atom-by-atom spectroscopy at graphene edges [80]. Figure 6.34 shows the result of STEM observation at the graphene edge of a graphite flake using an acceleration voltage of 60 kV, which is low enough to avoid knock-on damage to the graphene network. The arrangement of carbon atoms and the edge structure are clearly seen at atomic resolution in Figs. 6.34(a) and (b). Interestingly, two types of edge carbon atom are recognizable in the figure: a carbon atom with

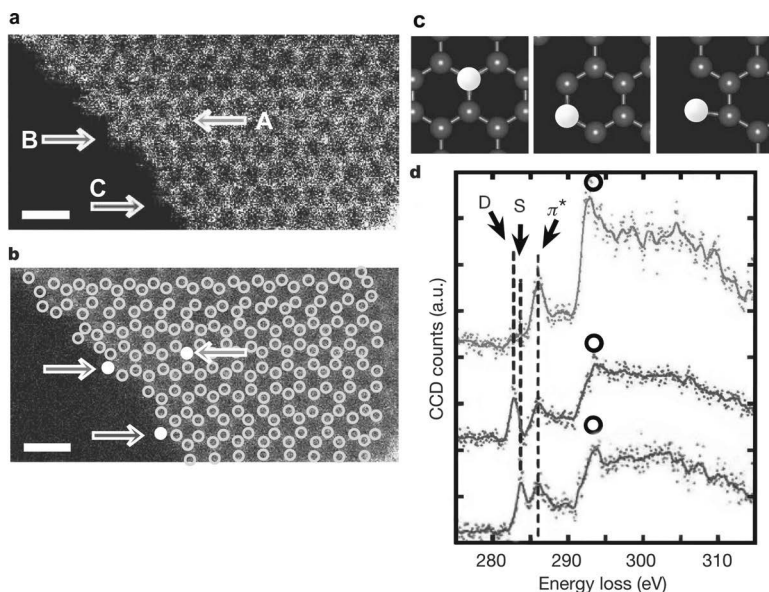


Figure 6.34 (a) TEM image of a graphene edge. (b) Same image as (a) with atomic positions marked by circles. Arrows indicate the positions of a carbon atom in the interior (A), an edge carbon atom with two-coordination (B), and a carbon atom singly bonded to the edge (C). Scale bars are 0.5 nm. (c) Schematic illustrations of the carbon atoms at A, B, and C. (d) Electron energy loss near edge spectra of carbon K-edge (1s) for the atoms at A, B, and C (top, middle, and bottom, respectively). π^* , D and S are assigned to the conduction π^* -band, the extra-states from a carbon atom with two coordination at B and that singly bonded to the edge at C, respectively. After Ref. 80.

two-coordination at a short zigzag edge (B), and a carbon atom singly bonded to the graphene edge (C). ELNES spectra were taken at the individual carbon sites, as shown in Fig. 6.34(d). Carbon atom (A), in the interior of the graphene network, exhibits peaks at 286 eV and 292 eV, which are assigned to the conduction π^* electron band and the σ^* band, respectively, in good agreement with the NEXAFS spectra discussed above [83–88]. Carbon atom (B), at the edge, shows an extra peak at 282.6 eV (D), which is also similar to that observed in the NEXAFS spectra. Accordingly, this extra peak is assigned to the edge state contribution. Near the edge, another

peak appears at 283.6 eV (S) at the carbon site singly bonded to the graphene edge (C). This might be an edge state similar to that in the Klein edge (see Fig. 6.26) [93, 94]. Note that graphene edges are continuously etched under electron beam irradiation even at such a low acceleration voltage. This suggests that the graphene edge observed by TEM is not in thermal equilibrium.

6.3.3 *Electron Confinement and Gap Opening in Nanographene*

In addition to the edge state, the electronic structure of nanographene configurations such as graphene nanoribbons and graphene nanoislands has an additional feature which should be taken into account irrespective of edge geometry (zigzag edge/armchair edge): the electron confinement effect associated with the finite size [52–55, 72, 99–101]. The electron confinement effect appears as the formation of superperiodic spatial oscillation of the electron density distribution. For example, in a graphene nanoribbon, a standing wave is created perpendicular to the ribbon's axis in the interior between the two edges that act as potential walls, although the wave number is continuous along the direction of the ribbon's axis. A clear oscillatory pattern was observed in a 10 nm-wide graphene nanoribbon prepared by STM lithography, as shown in Fig. 6.11(c) in Section 6.2.5. Figures 6.35(a) and (b) show an analysis of the periodic oscillation in Fig. 6.11(c) and the 2D Fourier transformation of the STM image, respectively. The periodicity of the observed oscillation is 0.4 nm, which clearly differs from the period of the underlying atomic arrangement (lattice constant: $a = 0.246$ nm). A theoretical tight binding analysis of the graphene nanoribbon yields an estimated periodicity of 0.37 nm, which is in good quantitative agreement with the observed periodicity, confirming that the oscillation is associated with electron confinement perpendicular to the ribbon's axis [58].

A bandgap is created in conjunction with the electron confinement effect, as discussed theoretically in Section 4.5 [3, 99–101]. The STS spectra taken from the same graphene nanoribbon sample are shown in Fig. 6.35(c) [58]. The spectra demonstrate the presence of an energy gap of 0.18 eV, which is attributed to the electron

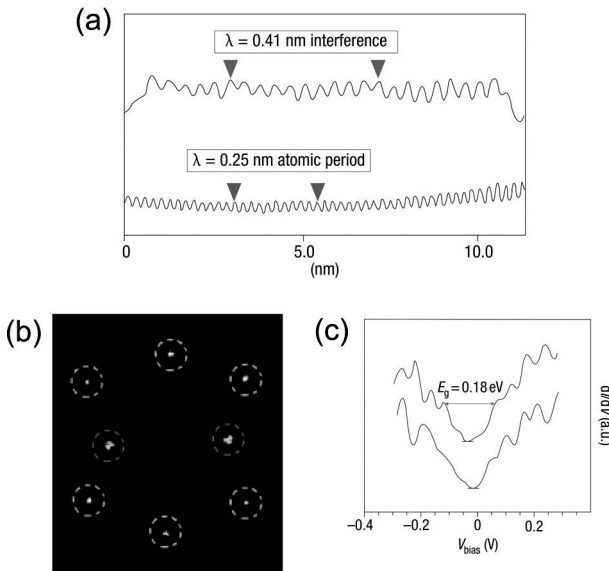


Figure 6.35 (a) Average line cuts revealing the period (0.41 nm) of the observed oscillation of the 10 nm-wide graphene nanoribbon shown in Fig. 6.11(c). The atomic period of 0.25 nm is also shown. (b) 2D Fourier transformation of the STM image. (c) Representative tunneling spectra (STS) taken on the ribbon, revealing an energy gap of 0.18 eV (horizontal line at the bottom of the spectrum indicates zero density of states). After Ref. 58.

confinement effect. Indeed, the gap is expected to be given by the following equation as a function of ribbon width W :

$$\varepsilon_g(W) = \pi \hbar v_F / W \approx (2 \text{ eV}\cdot\text{nm}) / W. \quad (6.5)$$

From Eq. (6.5), for a ribbon width of 10 nm, the gap is estimated to be 0.20 eV, which is in good quantitative agreement with that observed in the STS measurement. Moreover, the electron transport measurement reproduces the energy gap [102, 103].

Graphene nanoislands exhibit a similar size dependence in the energy gaps, as shown in Fig. 6.36, where the island's edge shape is defined using UHV-STM observations. Nanoislands are labeled armchair or zigzag depending on which crystallographic orientation is present in a higher fraction (>0.5). The armchair-edged graphene nanoislands exhibit gaps that are inversely proportional

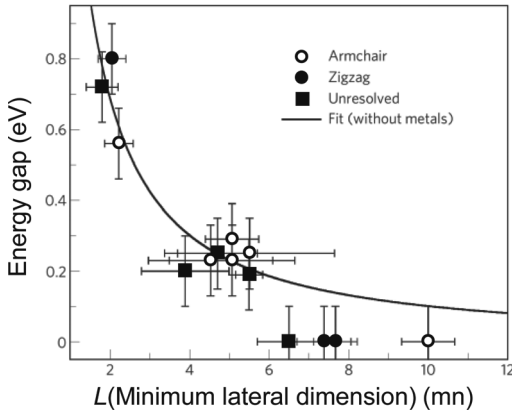


Figure 6.36 Energy gap of graphene nanoislands as a function of lateral dimension L . Nanoislands are labeled as zigzag- or armchair-edged depending on which crystallographic orientation is present in a higher fraction (>0.5). The energy gaps for armchair graphene nanoislands and some of the unresolved nanoislands are inversely proportional to L (solid line). Most of the zigzag nanoislands have negligible gaps. After Ref. 72.

to the lateral size L of the islands, similar to those in graphene nanoribbons; $\varepsilon_g(L) = 1.57 \pm 0.21 \text{ eV} \cdot \text{nm}/L^{1.19 \pm 0.15}$. In contrast, zigzag nanoislands have negligible gaps.

The wider graphene nanoribbons prepared by electron beam lithography exhibited a gap. Figure 6.37 plots the gap as a function of ribbon width for the graphene nanoribbons prepared by electron beam lithography [54]. The bandgap ε_g is inversely proportional to the width W of the ribbon, which is consistent with the behavior predicted by Eq. (6.5), although we should take into account a correction of $W \rightarrow W + W_0$ with a constant of W_0 . Theory suggests that armchair nanoislands and nanoribbons are semiconducting, whereas zigzag ones have non-bonding edge states around the Fermi level, as discussed in Sections 6.3.1 and 6.3.2. However, according to the experimental results, no geometrical dependence (orientation dependence) of the edges is observed. This is a consequence of the less-defined edges and greater width, which is too wide to observe the geometrical effect of edges.

Here we discuss the opening of the gap theoretically with respect to the geometrical dependence of the edges [100, 101]. As we

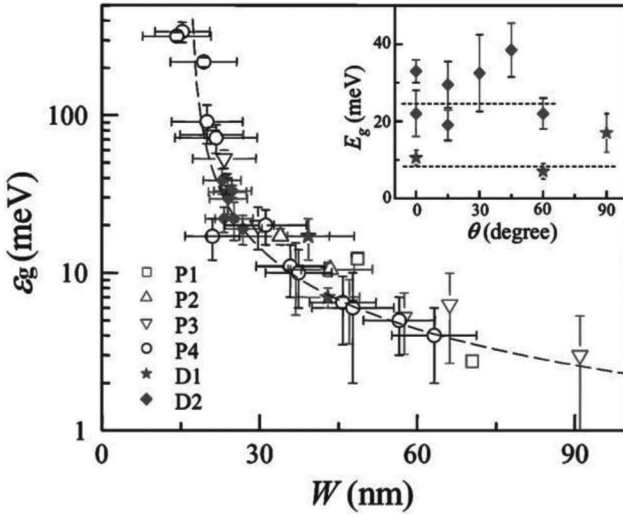


Figure 6.37 Energy gap ϵ_g as a function of ribbon width W for six graphene nanoribbon samples (P1, P2, P3, P4, D1, D2) prepared by electron beam lithography. P1 to P4 are parallel-type samples; D1 and D2 have varying orientation. Inset shows ϵ_g vs. the relative angle for samples D1 and D2. Dashed lines in the inset show the value of ϵ_g predicted by the empirical scaling of ϵ_g vs. W . After Ref. 54.

discussed in Section 4.5, armchair-edged graphene nanoribbons are semiconducting, and the periodic nature of the electronic structure depends on their width. Indeed, there are three families having different features of energy gaps, $\epsilon_g^{3p+1} > \epsilon_g^{3p} > \epsilon_g^{3p+2}$ for widths of $n = 3p + 1$, $n = 3p$, and $n = 3p + 2$, where the ribbon width is spanned by n C-C dimer chains, and p is an integer [99, 101]. Figure 6.38 shows the width dependence of the gap for these three families [101]. Calculations were made using two methods: density functional theory (DFT) and a first-principle many-electron Green's function approach within the GW approximation, in which the electron-electron correlation effect is taken into account [101]. The calculated gap decreases in inverse proportion to the width for widths of 0.4 to 1.6 nm as $\epsilon_g(W) \propto 1/(W + W_0 + \delta)$, which agrees well with the behavior determined by a simple tight binding theoretical treatment and also that observed experimentally [54, 58]. The estimated correction parameter W_0 is 0.24 nm. The

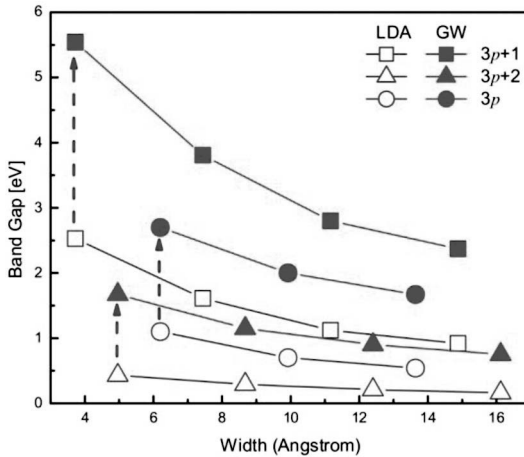


Figure 6.38 Variation in band gap with the width of armchair-edged graphene nanoribbons. Three families of armchair graphene nanoribbons are represented by different symbols. Values for members of the same family of armchair nanographene are connected by solid lines as guides to the eye. Open symbols represent band gaps calculated by LDA; solid symbols represent the corresponding quasiparticle band gaps obtained by the GW method. Dashed arrows indicate the self-energy correction for the narrowest ribbon in each of the three families. After Ref. 101.

parameter δ represents leakage of the electron distribution from the edge boundary. This is due to the non-rigidity of the edge boundary, and it yields an estimate of 0.15–0.29 nm for the GW calculations. Interestingly, the gap obtained by the quasiparticle GW method is larger by 0.5–3 eV than that of DFT. This reveals that the electron correlation has an important effect on gap formation, particularly in narrow graphene nanoribbons, suggesting that the electron correlation effect is enhanced by 1D quantum confinement.

Electron confinement appears differently in zigzag-edged graphene nanoribbons, in which edge states play an important role [101]. The top of the valence band and the bottom of the conduction band are actually composed mainly of edge states. In addition, the spin interaction of the edge states introduces a finite band gap in zigzag-edged graphene nanoribbons. Figure 6.39 shows the band structure and the band gap vs. the ribbon width in zigzag-edged graphene nanoribbons calculated by both DFT and

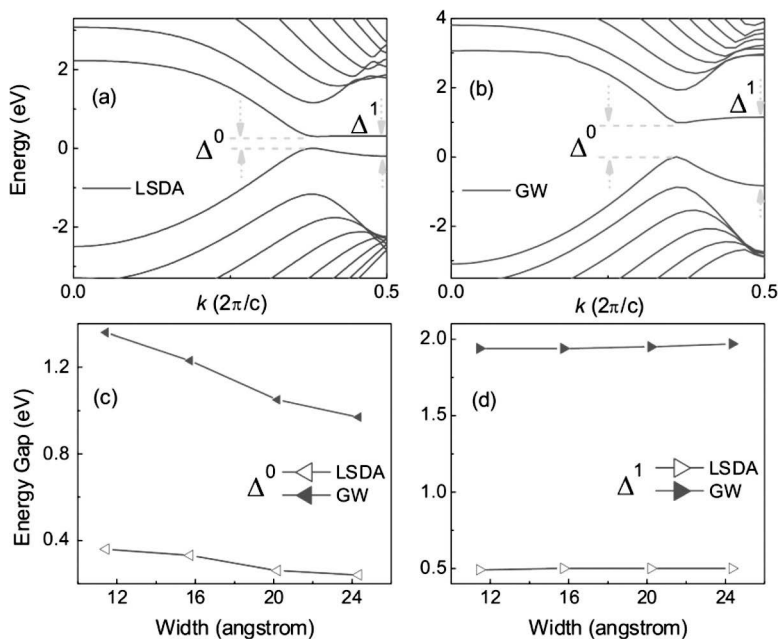


Figure 6.39 Calculated band structure and energy gap of zigzag-edged graphene nanoribbons. (a) Local spin density approximation (LSDA) (LDF) band structure of a zigzag graphene nanoribbon ($n = 12$). Up and down spin states are degenerate in all the bands, and the top of the valence band is set at zero. The symbols Δ^0 and Δ^1 denote the direct band gap and the energy gap at the zone boundary, respectively. (b) GW quasiparticle band structure of a zigzag graphene nanoribbon ($n = 12$). (c) Variation in the direct band gap with the width of zigzag graphene nanoribbons. (d) Variation in the energy gap at the zone boundary with the width of zigzag graphene nanoribbons. Open symbols denote LSDA results; solid symbols represent GW results for (c) and (d). After Ref. 100.

GW quasiparticle calculations [101]. The top of the valence band and the bottom of the conduction band shown in Figs. 6.39(a) and (b) are composed of spin-polarized edge states, and the spin interaction is responsible for the opening of the gap, which is increased by the electron correlation. In the gap formation data in Figs. 6.39(c) and (d), the correction of the electron correlation (0.8–1.5 eV), which is represented by the upward shift of the gap in the GW results relative to those of the local density functional (LDF),

is in a range similar to that of armchair graphene nanoribbons. Note the difference between the direct gap Δ^0 and the gap at the zone boundary Δ^1 . The direct bandgap Δ^0 is located about 3/4 of the way to the Brillouin zone boundary and is rather insensitive to the edge state (see Sections 4.5 and 6.3.1). Its ribbon width dependence is $\Delta^0(W) \propto 1/(W + \delta)$. The correction parameter δ is 1.6 nm in the GW calculation, which is an order of magnitude larger than that of armchair graphene nanoribbons, suggesting the important contribution of spin-polarized edge states around the zigzag edges. Interestingly, the gap at the zone boundary Δ^1 has no width dependence. As we discussed in Section 6.3.1, the edge state is completely localized around the zigzag edges in the zigzag graphene nanoribbon at the Brillouin zone boundary. The contribution of the spin-polarized edge state makes the width dependence disappear in Δ^1 .

6.3.4 Electron Wave Interference: Theory and Experiments

Another important feature of edges is electron wave interference in the scattering process at edges. Figure 6.40 shows how an electron is scattered at zigzag and armchair edges. In scattering at a zigzag edge, the y -component of the electron momentum is converted from

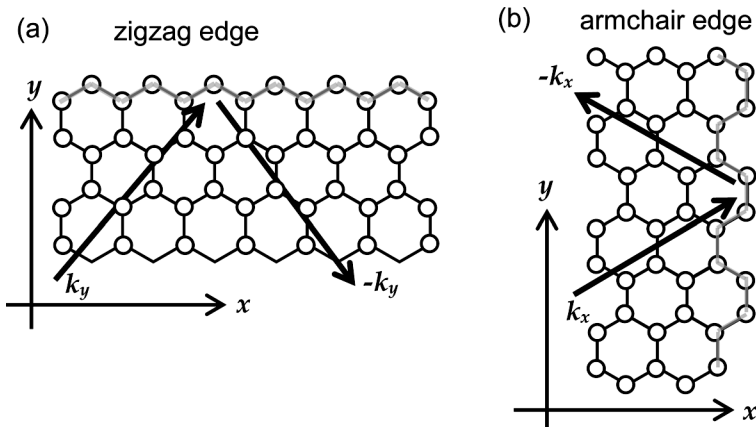


Figure 6.40 Electron wave scattering at (a) zigzag and (b) armchair edges. In scattering at the zigzag (armchair) edge, k_y (k_x) is converted to $-k_y$ ($-k_x$).

k_y to $-k_y$. This process corresponds to the intravalley transition from point K to point K (or from K' to K') in k space (see Fig. 6.21(b)). In contrast, scattering at an armchair edge, which converts the momentum from k_x to $-k_x$, is associated with the intervalley transition from K to K' (or from K' to K). The transition between the two independent Dirac cones at K and K' causes mixing of two wave functions in the scattered wave. Accordingly, the wave function $\psi_B(\mathbf{R}_B)$ for a site on sublattice B is given by

$$\psi_B(\mathbf{R}_B) \propto (-\exp(-i\mathbf{K}\mathbf{R}_B) + \exp(i\mathbf{K}'\mathbf{R}_B)), \quad (6.6)$$

where \mathbf{R}_B is the translational vector of the site. Equation (6.6) describes the electron wave interference occurring in scattering at an armchair edge. This interference phenomenon was observed experimentally in the Raman spectra of graphene [23, 24, 26, 27, 104–107] and in the creation of an unconventional honeycomb superlattice pattern observed by STM [25].

The electron wave interference phenomenon in armchair edges can be understood also from chemistry aspect. In infinite-size graphene, three states represented by Clar's rule are degenerate as given in Figs. 6.41(a) and (b). In contrast, only one unique state is present in an armchair-edged molecule, as shown in Fig. 6.41(c). This is a consequence of electron wave interference at armchair edges. The interference gives a standing wave in an armchair-edged molecule, resulting in the presence of a unique Clar's representation. However, this is not the case for zigzag-edged molecules as shown in Fig. 6.41(d). There are many Clar's representations degenerate in a zigzag-edge molecule.

6.3.4.1 Raman spectra: G and D bands

The graphite E_{2g2} mode (G band) observed around 1600 cm^{-1} in the resonance Raman spectrum is an important signature indicating graphitic structure [23, 24, 26, 27, 38, 104–107]. The lattice vibration modulates the inter-atomic C–C distance, distorting the three-fold symmetric bond coordination surrounding the carbon atom. This breaks the symmetry between the A and B sublattices, similar to what happens in the creation of the edge state (see 6.3.1), generating the lattice-distortion-induced effective gauge field \mathbf{A}^q .

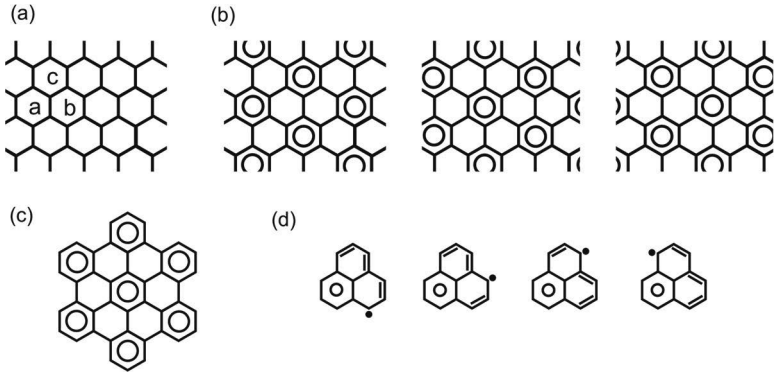


Figure 6.41 (a) Three independent equivalent hexagon rings (a,b,c) in infinite graphene. (b) Three degenerate states represented by Clar's rule in infinite graphene. (c) Unique state in an armchair-edged molecule. (d) Triangle phenalene represented as an example of zigzag edged molecule; there are 12 states, among which only four stases are shown. Note that three-fold symmetry of the molecule gives $4 \times 3 = 12$.

Eventually, the interaction of the incident laser beam with a graphene sheet subjected to lattice vibrations is given by the following equation by making the substitution $\mathbf{p} \rightarrow \mathbf{p} + \mathbf{A}^q - e\mathbf{A}$ in Eq. (6.2) [23, 24]

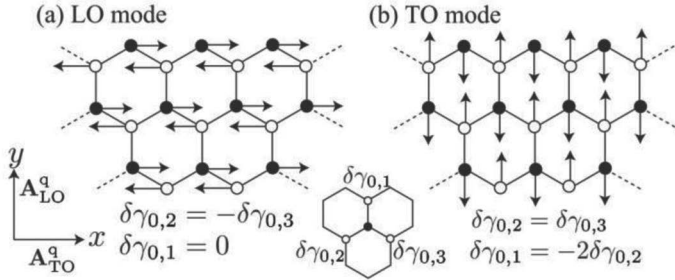
$$\hat{H} = v_F \sigma (\mathbf{p} + \mathbf{A}^q - e\mathbf{A}), \quad (6.7)$$

where \mathbf{A} is the electromagnetic gauge field of the incident laser beam. The electron-phonon interaction plays a key role in the Raman process. It is given by the deformation-induced gauge field $\mathbf{A}^q = (A_x^q, A_y^q)$, which can be expressed in terms of a change $\delta\gamma_0$ in the nearest-neighbor transfer integral from the average value γ_0 [24] as

$$v_F A_x^q = \delta\gamma_{0,1} - \frac{1}{2}(\delta\gamma_{0,2} + \delta\gamma_{0,3}), \quad v_F A_y^q = \frac{\sqrt{3}}{2}(\delta\gamma_{0,2} - \delta\gamma_{0,3}), \quad (6.8)$$

where $\delta\gamma_{0,1}$, $\delta\gamma_{0,2}$, and $\delta\gamma_{0,3}$ are the changes in the transfer integrals for the π bonds connected to three neighbors. The relationship between $\delta\gamma_{0,1}$, $\delta\gamma_{0,2}$, and $\delta\gamma_{0,3}$ and the displacement vectors are given in Fig. 6.42 for the longitudinal optical (LO) and transverse optical (TO) phonon modes in the zigzag and armchair regions. These two phonon modes, which are degenerate in bulk graphene,

zigzag edge



armchair edge

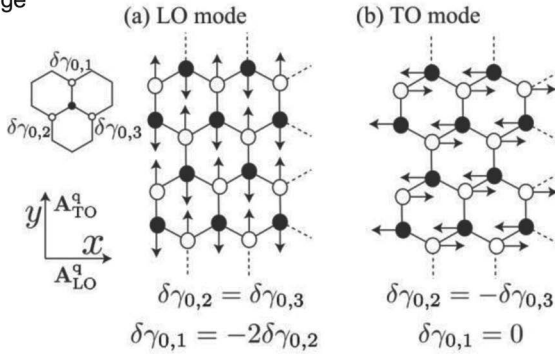


Figure 6.42 Displacement vectors for the (a) LO and (b) TO phonon modes for zigzag and armchair edges. Displacement vectors of the LO (TO) mode are parallel (perpendicular) to both the zigzag and armchair edges. The direction of the deformation-induced gauge field \mathbf{A}^q is perpendicular to the direction of atom displacement. After Ref. 24.

become nondegenerate in the edge regions owing to the lack of one bond. Near a zigzag edge subjected to the intravalley transition, $\mathbf{k} = (k_x, k_y) \rightarrow \mathbf{k}' = (k_x, -k_y)$, the wave functions in the conduction (c) and valence (v) bands are given by

$$\psi_{\mathbf{k}}^c(\mathbf{r}) = \frac{1}{\sqrt{2}} (\Phi_{\mathbf{k}}^c(\mathbf{r}) + \Phi_{\mathbf{k}'}^c(\mathbf{r})), \quad \psi_{\mathbf{k}}^v(\mathbf{r}) = \sigma_z \psi_{\mathbf{k}}^c(\mathbf{r}). \quad (6.9)$$

Thus, the intravalley transition allows only the TO phonon mode to be active, producing the polarization angle dependence of the G-band intensity, which is given as

$$M^{\text{opt}}(\mathbf{A}) = \langle \Psi_{\mathbf{k}}^c | -v_F e \sigma \mathbf{A} | \psi_{\mathbf{k}}^v \rangle, \quad |M^{\text{opt}}(\mathbf{A})|^2 \propto \sin^2 \Theta, \quad (6.10)$$

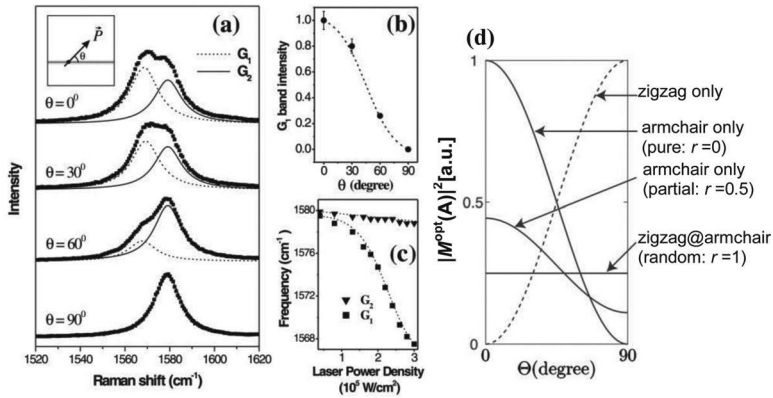


Figure 6.43 (a) Raman G-band spectra obtained for incident light having different polarization angles (θ). Inset shows a schematic of the graphene nanoribbon sample in Fig.6.8 (horizontal gray line) showing the angle θ between the ribbon's axis and the light polarization vector (\vec{P}). G_1 and G_2 are assigned to the G bands of the graphene nanoribbon and the HOPG substrate, respectively. (b) Intensity of the G_1 peak versus θ . Dotted line is a $\cos^2 \theta$ theoretical curve. (c) Raman frequencies of the G_1 (squares) and G_2 (triangles) peaks as a function of laser power density. Excitation laser energy is $E_{\text{laser}} = 2.41$ eV. After Ref. 26. (d) Theoretical polarization angle dependence of the G-band intensity for zigzag, armchair and zigzag/armchair mixed edges. After Ref. 24.

where Θ is the angle between the edge direction and the direction of \mathbf{A} . For armchair edges, in which the intervalley transition, $\mathbf{k} = (k_x, k_y) \rightarrow \mathbf{k}' = (-k_x, k_y)$, occurs, only the LO phonon mode can be active, so the G-band intensity is

$$\left| M^{\text{opt}}(\mathbf{A}) \right|^2 \propto \cos^2 \Theta. \quad (6.11)$$

The polarization angle dependence of the G-band intensity thus obtained is summarized in Fig. 6.43(d).

Let us investigate experimentally the laser beam polarization angle dependence of the G-band intensity for the graphene nanoribbon samples we discussed in Section 6.2.4 (see Fig. 6.8). Figures 6.43(a) and (b) present the G-band spectra of the graphene nanoribbons on the HOPG substrate with incident beams having various polarization angles. The peak intensity changes from 1 to 0 with a functional form of $\cos^2 \Theta$, which is the same as the

angular dependence theoretically predicted for the armchair-edged graphene nanoribbon (Fig. 6.43(d)).

Figure 6.43(c) shows the laser power density dependence of the G-band intensity. The dramatic softening of the G-band intensity with increasing laser power demonstrates easy heating of the graphene nanoribbons by laser beam irradiation owing to their small size. Eventually, the experiments demonstrated that the graphene nanoribbons prepared by heat-induced fractionalization are armchair-edged.

The Raman D band observed around 1300 cm^{-1} is another signature for discriminating between zigzag and armchair edges. It is related to the double resonance Raman process, which is caused by the $K \leftrightarrow K'$ intervalley transition [27, 104, 105]. Accordingly, electron wave interference at armchair edges, which is subjected to the intervalley transition, produces the D band, whereas the D band is absent for zigzag edges, which are governed by the intravalley transition. Raman observations of the edge dependence of the D band confirmed this trend, as illustrated in Fig. 6.44 [27].

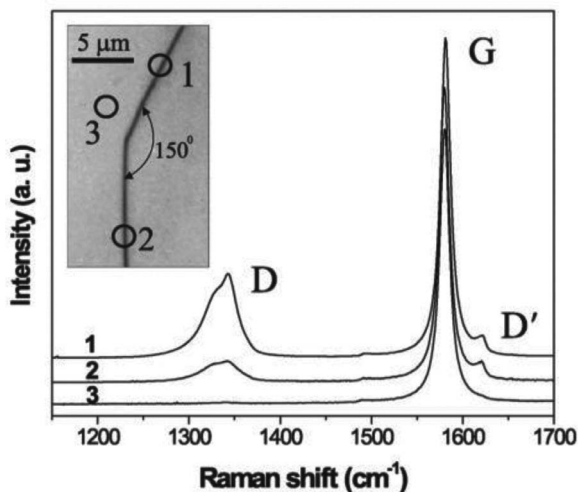


Figure 6.44 Raman spectra with D, G, and D' bands obtained in three different regions of the HOPG sample. Inset shows an optical image of the step and the regions where spectra are taken: 1, armchair edge; 2, zigzag edge; and 3, interior of the graphene sheet. After Ref. 27.

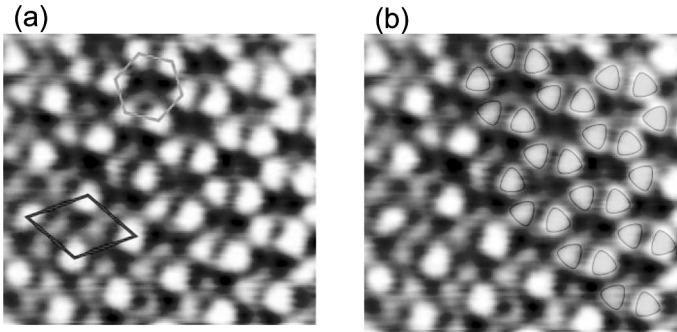


Figure 6.45 (a) Atomic-resolution STM lattice image ($1.4 \times 1.2 \text{ nm}^2$) taken near an armchair edge on the terrace near the step edge, which is approximately 1 nm away from the right end. Rhombus and hexagon indicate unit cells of the $\sqrt{3} \times \sqrt{3}R30^\circ$ and honeycomb superlattice patterns, respectively. (b) Same as (a) with an overlaid three-fold symmetry pattern. Sample bias voltage was 20 mV. After Ref. 25.

6.3.4.2 STM image of superlattice

A $\sqrt{3} \times \sqrt{3}$ superlattice has been observed in STM images of graphene sheets, as we discussed in Section 6.3.2.1. This is also the case for observations near a zigzag edge [25, 108, 109]. However, a honeycomb superlattice pattern has been observed near armchair edges [12, 25]. This difference is caused by scattering at the edges, similar to that observed in Raman spectra. Figure 6.45 shows the honeycomb superlattice pattern observed near an armchair edge. In addition to the $(\sqrt{3} \times \sqrt{3})R30^\circ$ superlattice, a honeycomb superlattice pattern appears. Importantly, individual sites on the honeycomb superlattice have three-fold symmetric fine structure, as exhibited in Fig. 6.45(b).

To understand the origin of the honeycomb pattern appearing at an armchair edge, we can recall the importance of electron wave interference in scattering events at the armchair edge in relation to intervalley transition ($K \leftrightarrow K'$). The wave function around the armchair edge is expressed by Eq. (6.6). Therefore, the spatial distribution of the LDOS, which corresponds to the STM superlattice pattern, is given by the 2D squared-amplitude mapping of the wave function. The result of this mapping using Eq. (6.6) is shown, with that for zigzag edges, in Figs. 6.46(b) and (c), which reproduce well

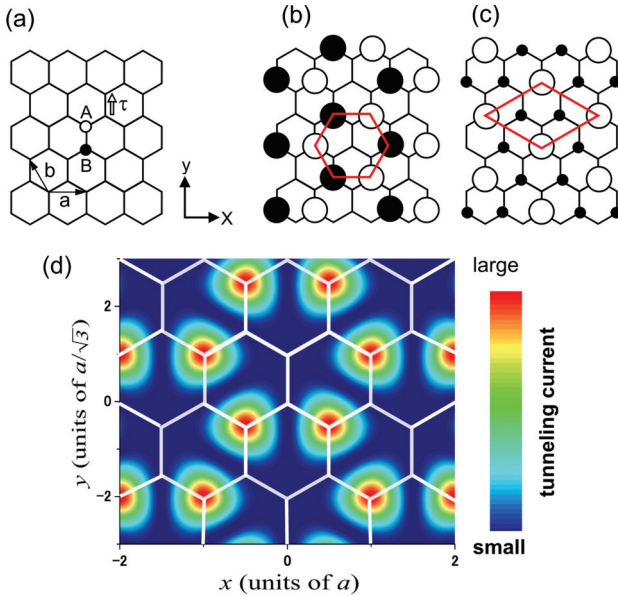


Figure 6.46 (a) Lattice structure of graphene. 2D squared-amplitude mappings of wave function near the (b) armchair edge and (c) zigzag edge. Hexagon and rhombus indicate the unit cells of the honeycomb and $\sqrt{3} \times \sqrt{3}R30^\circ$ superperiodic patterns, respectively. Open and filled circles correspond to + and - signs of the wave function phase, and their size corresponds to the amplitude of the wave function at each site. (d) 2D current mappings of honeycomb superlattice pattern. Variation from dark blue to red represents increasing tunneling current (in arbitrary units) (color). After Ref. 25.

the experimentally observed honeycomb superlattice and $(\sqrt{3} \times \sqrt{3})R30^\circ$ superlattice. Therefore, this confirms that intervalley scattering produces the honeycomb superlattice pattern at the armchair edge, whereas intravalley scattering causes the $(\sqrt{3} \times \sqrt{3})R30^\circ$ pattern at the zigzag edge. The wave function's phase is important here. In the honeycomb superlattice shown in Fig. 6.46(b), the signs of the wave functions at adjacent sites are opposite to each other, which suggests that they have an antiphase relationship.

To understand the three-fold symmetrical fine structure observed in the honeycomb superlattice, it is necessary to calculate the spatial distribution of the current between the graphene and

the STM tip [25, 110]. The calculated current distribution is shown in Fig. 6.46(d). The three-fold symmetrical fine structure observed in the STM atomic image is reproduced well in the calculated distribution. Taking into account the antiphase relationship between the wave functions at adjacent sites in the honeycomb superlattice, we conclude that the three-fold symmetry originates in antibonding coupling of the wave functions with a node in the middle between the two sites.

6.4 Magnetic Structures of Nanographene

Section 6.3 covers the role of edges in the electronic structure of graphene and nanographene. In particular, zigzag edges are important in terms of magnetism because the edge state appearing there is strongly spin polarized, producing localized spins, unlike diamagnetic graphene. Theoretical and experimental investigations have revealed unconventional magnetic features of the edge-state spins in nanographene [3, 8, 19, 31–35]. Indeed, strong ferromagnetic interaction between the edge-state spins in the zigzag edge, together with the inter-zigzag edge interaction mediated by conduction π electron carriers, causes a variety of carbon-based magnetism. In addition, chemical and structural modifications of the edges increase the amount of variation in the magnetism. Accordingly, edge-state spins are expected to be an important ingredient not only in building molecular magnets but also in developing carbon-based spintronics device applications. Here we discuss theoretical and experimental aspects of edge-state magnetism.

6.4.1 Theoretical Background

As early works pointed out [3], the edge-state spins are arranged in parallel along a zigzag edge with the aid of a strong ferromagnetic intra-zigzag exchange interaction having a strength of approximately several 10^3 K [111]. The inter-zigzag interaction has a strength of $10^{-1} - 10^{-2}$ times the intra-zigzag edge interaction and a sign of $+$ or $-$ (ferromagnetic or antiferromagnetic) depending on the mutual geometrical relationship between the relevant zigzag

edges in a nanographene sheet, whose periphery consists of a combination of zigzag and armchair edges. These interactions determine the magnetic structure of nanographene. We can see this in the zigzag-edged triangular and linear molecules discussed in Chapters 4 and 5 and Section 6.3.1, which have ferromagnetic [112, 113] and antiferromagnetic states [71, 114, 115], respectively. Many theoretical works have examined edge-state spin magnetism [71, 111–117]. Here, we discuss the magnetic structures of zigzag-edged triangular and hexagonal nanographene (see Fig. 6.47) because comparing the two is instructive regarding the way in which the geometry affects the magnetism [112].

The magnetism of the edge-state spins can be described in terms of the mean-field Hubbard Hamiltonian,

$$\hat{H} = \hat{H}_0 + U \sum_i (n_{i\uparrow} \langle n_{i\downarrow} \rangle + n_{i\downarrow} \langle n_{i\uparrow} \rangle),$$

$$\hat{H}_0 = -t \sum_{(i,j),\sigma} (c_{i\sigma}^\dagger c_{j\sigma} + H.C.), \quad (6.12)$$

\hat{H}_0 is the single-orbital Hamiltonian with a transfer integral t connecting neighboring sites i, j belonging to sublattices A and B, respectively, in the bipartite lattice. The second term is the on-site Coulomb interaction with U , where the summation is taken with i running over the number of sites $N_\eta, \eta = A, B$ (A, B sublattices). This term plays an essential role in creating magnetic moments. Figure 6.47 shows the energy spectra and the distribution of the local magnetic moments obtained by the Hubbard model and DFT calculations. A spin gap appears around the Fermi level, producing spin polarization in the edge-state spins, as shown in Fig. 6.47(b) for the triangular nanographene. Note that the results of the Hubbard model and DFT calculations have very similar structure in the vicinity of the Fermi level. The local magnetic moments, which are arranged in antiparallel between sublattices A and B, are well localized near the zigzag-shaped edges, and their strength decays sharply from the edge to the interior. In the three zigzag edges constituting the triangular nanographene, all the edge carbon atoms belong to sublattice A (B), and have up (down) spins arranged in parallel. Accordingly, triangular nanographene has a ferromagnetic structure with a spontaneous magnetization. The spin S of

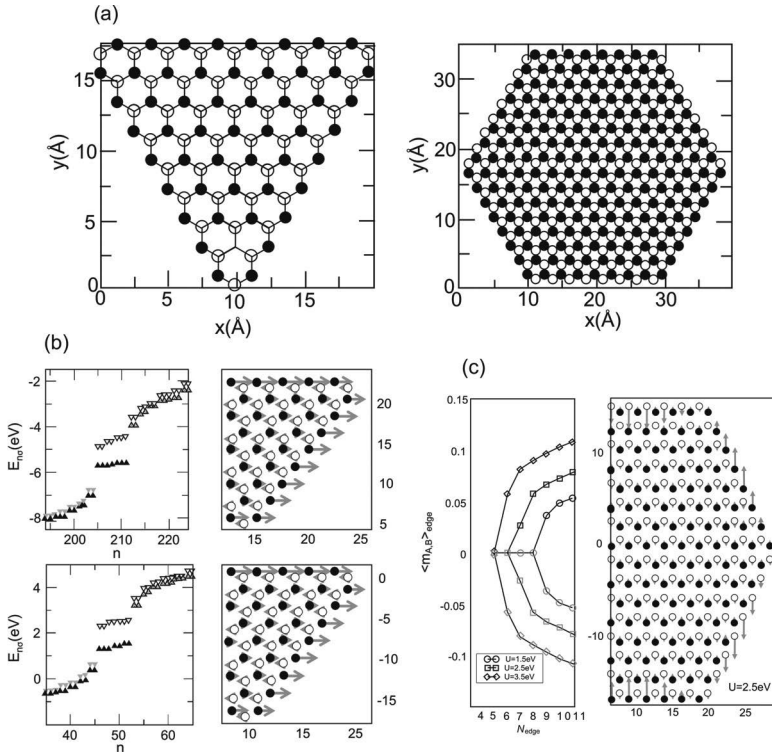


Figure 6.47 (a) (Left) Triangular and (right) hexagonal nanographene ($N_{\text{edge}} = 8$) with carbon atoms in A (filled circles) and B (open circles) sublattices. The size of a nanographene is given by the number N_{edge} of edge carbon atoms. (b) (Left) Energy spectra and (right) distributions of local magnetic moments for the triangular nanographene ($N_{\text{edge}} = 8$), calculated by a mean-field Hubbard model with $t = 2.5$ eV and $U = 3.85$ eV (lower row) and DFT calculation (upper row). Filled triangles (open triangles) in the energy spectra correspond to the full (empty) single particle state. Triangles (inverted triangles) represent up (down) spin states. Arrow represents the local moment whose strength is given by the length. (c) (Left) Sublattice-resolved average magnetic moment as a function of N_{edge} for hexagonal nanographene with $t = 2.5$ eV and $U = 1.5, 2.5$, and 3.5 eV calculated by a mean-field Hubbard model. (Right) Distributions of local magnetic moments for $N_{\text{edge}} = 8$ and $U = 2.5$ eV. After Ref. 112.

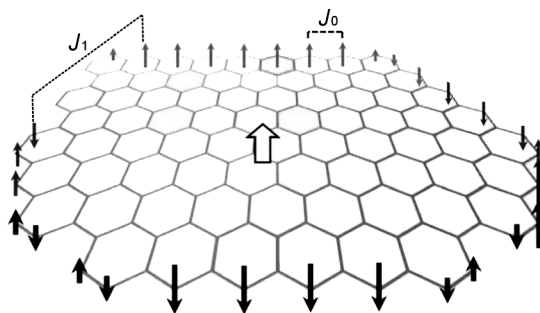


Figure 6.48 Schematic model of an arbitrarily shaped nanographene sheet and spatial distribution of edge-state spins (filled arrow). J_0 and J_1 are the intra- and inter-zigzag-edge interactions, respectively. Large open arrow is the net magnetic moment after compensation between ferromagnetic clusters in the zigzag edges.

the ground state in the Hubbard model in a bipartite lattice satisfies the relation $S = (1/2)|N_{\uparrow} - N_{\downarrow}| = (1/2)|N_A - N_B| = N_{\text{edge}} - 1$, where $N_{\uparrow(\downarrow)}$, $N_{A(B)}$ and N_{edge} are the number of sites having up (down) spins, that of the sites belonging to sublattice A (B), and that of edge carbon atoms in a zigzag edge, respectively. The spin state is simply related to the number of edge carbon atoms. This is consistent with Lieb's theorem (see Section 6.3.1). For hexagonal nanographene consisting of six zigzag edges, three edges belonging to sublattice A (B) have up (down) spins, whereas three edges belonging to sublattice B (A) have down (up) spins. Accordingly, compensation between up and down spins stabilizes an antiferromagnetic structure having no spontaneous magnetization.

An arbitrarily shaped nanographene sheet whose periphery is described by a combination of zigzag and armchair edges has a ferrimagnetic structure, as shown in Fig. 6.48 [35]. The localized edge-state spins are ferromagnetically arranged through a strong ferromagnetic intra-zigzag-edge exchange interaction ($J_0 \sim 10^3$ K) [111, 112, 116]. The ferromagnetically arranged edge-state spins in two zigzag edge regions separated by an armchair region interact with the aid of conduction- π -electron-mediated inter-zigzag-edge interaction J_1 , whose sign varies from positive (ferromagnetic) to negative (antiferromagnetic), depending on the mutual geometrical relationship between the relevant zigzag edges. J_1 has a moderate

strength ($J_1 \sim 10\text{--}100$ K). Consequently, depending on the shape of the nanographene sheet, the interplay between strong intra-zigzag-edge ferromagnetic interaction J_0 and moderate inter-zigzag-edge ferromagnetic/antiferromagnetic exchange interaction J_1 is expected to produce a ferrimagnetic structure with a non-zero net magnetic moment that remains after compensation between the antiferromagnetically coupled ferromagnetic spin clusters.

The creation of defects in the interior of a graphene sheet also creates a spin-polarized edge state. In this case, the magnetism has a geometrical dependence similar to that discussed above [117, 118]. In particular, when the presence of a defect makes sublattice A nonequivalent to sublattice B, a net magnetic moment is created, as we learned from Lieb's theorem. However, when defects possess unterminated carbon sites with σ -dangling bonds, nonbonding states of σ electron origin are also responsible for the magnetism. The edge-state spins of π electron origin are itinerant, with fractional magnetic moments, whereas the σ -dangling bond spins are localized, with a magnetic moment of $\sim 1\mu_B$ [86, 117].

Chemically modified zigzag-edged graphene nanoribbons exhibit interesting magnetism [119, 120]. In graphene nanoribbons having monohydrogenated zigzag edges on both sides, the compensation between up and down spins on opposite sides produces an antiferromagnetic structure with no spontaneous magnetization. However, when one side is dihydrogenated and the opposite side is monohydrogenated, uncompensation between the up and down spins yields a ferromagnetic structure in which even the carbon atoms in the interior are strongly spin polarized, as shown in Fig. 6.49(a). Dihydrogenation converts an ordinary zigzag edge to Klein edge, as shown in Fig. 6.26. The creation of ferromagnetic spontaneous magnetization is a consequence of the broken symmetry between the two sides. Here we recall the STM observations described in Section 6.3.2. The edge state near a Klein edge is less localized than an ordinary zigzag edge, so an appreciable population of edge-state spins appears in the interior of the graphene sheet, similar to the feature in Fig. 6.49(a) [13]. The fluorinated version of a graphene nanoribbon having the same structure is also in a ferromagnetic state, although the edge-state spins disappear on the difluorinated side, as illustrated in Fig. 6.49(b).

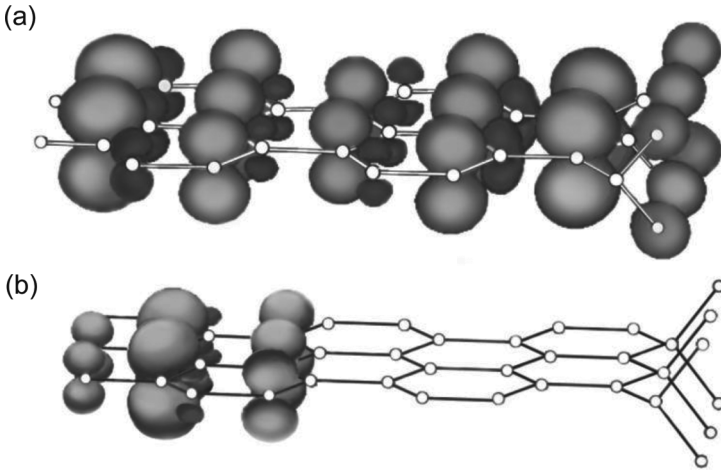


Figure 6.49 (a) Ferromagnetic structure of graphene nanoribbon having monohydrogenated zigzag edge on one side and dihydrogenated zigzag edge on the opposite side. Wave function represented by light (dark) color is polarized with up (down) spin. (b) Ferromagnetic structure of graphene nanoribbon having the same structure as (a) but with fluorine-terminated edges. After Ref. 120.

Let us discuss spin wave excitation and spin correlations in an edge-state spin system consisting of a 1D ferromagnet aligned along the zigzag direction. Owing to a small spin-orbit interaction of carbon atoms (5 cm^{-1}) [111,121], the edge-state spin is described in terms of a Heisenberg spin Hamiltonian with a small magnetic anisotropy,

$$\hat{H} = -2J m^2 \sum_i \mathbf{s}_i \mathbf{s}_{i+1} - 2\Delta J m^2 \sum_i s_i^z s_{i+1}^z - m\mathbf{H} \sum_i \mathbf{s}_i \quad (6.13)$$

where J , ΔJ , m , and \mathbf{H} are the isotropic ferromagnetic exchange interaction, the anisotropic exchange interaction along the z -axis ($\Delta J/J \sim 10^{-4}$), the strength of the magnetic moment in a unit cell, and the applied magnetic field, respectively. A DFT calculation [122] yields the estimated magnetic moments: $m = m_A + m_B \sim 0.3 \mu_B/\text{unit cell}$, with $m_A = 0.43 \mu_B$ for the moment at the edge carbon atom of sublattice A and $m_B = -0.13 \mu_B$ for that at the carbon atom of sublattice B next from the edge. The ferromagnetic exchange interaction is large; it is estimated as $J = 580 \text{ meV}$.

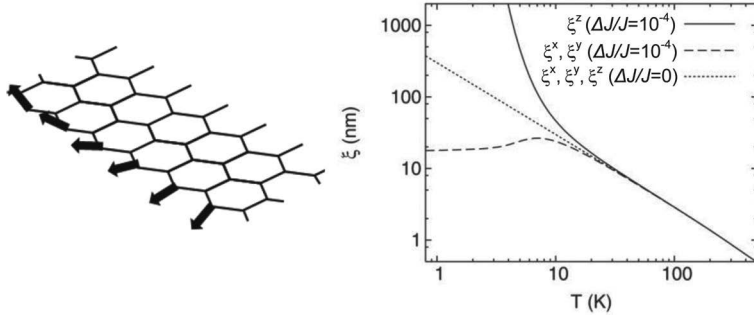


Figure 6.50 (Left) Spin wave excitation at a zigzag edge where the edge carbon atoms are assumed to belong to sublattice A. (Right) Temperature dependence of the correlation lengths ξ^x , ξ^y , ξ^z for $\Delta J/J = 10^{-4}$ and 0. After Ref. 122.

The corresponding ferromagnetic spin wave spectrum is $E(q) = \kappa q^2$, $\kappa = 320 \text{ meV}\text{\AA}^2$ ($\kappa = J m^2 a^2$ (a : lattice constant)). The spin correlation function with a correlation length of ξ^α ($\alpha = x, y, z$),

$$\langle s_i^\alpha s_{i+1}^\alpha \rangle \propto \langle s_i^\alpha s_i^\alpha \rangle \exp(-l/\xi^\alpha), \quad (6.14)$$

is shown as a function of temperature in Fig. 6.50. At high temperatures, the correlation lengths are isotropic and have a temperature dependence of $\xi^\alpha \approx 300/T$ (nm) for $\alpha = x, y, z$ as a consequence of the small anisotropy. The correlation length is about 1 nm (3.7 unit cells) at room temperature. The correlation length increases as the temperature decreases. Below ~ 10 K, it becomes anisotropic, and ξ^z increases nonlinearly,

$$\xi^z \propto \exp\left(\sqrt{8J \Delta J m^4 / k_B T}\right), \quad (6.15)$$

whereas ξ^x and ξ^y are less temperature dependent. The anisotropic Heisenberg feature of the edge-state spins is pronounced at low temperatures.

6.4.2 Experiments on Magnetic Properties of Edge-State Spins

6.4.2.1 Edge-state spins in defects

Defects created on graphene sheets by ion bombardment are an important system that can be used to experimentally investigate the

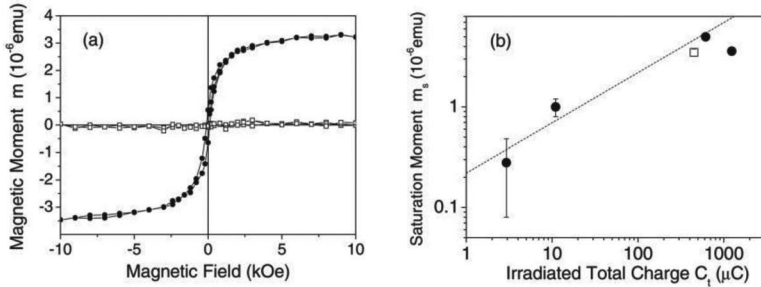


Figure 6.51 (a) Magnetization curve measured at 300 K for an HOPG sample before (open square) and after (filled circle) proton irradiation. Irradiation energy: 2.25 MeV, sample size: $570 \times 570 \mu\text{m}^2$, with 100×100 irradiated spots $2 \mu\text{m}^2$ in diameter, total charge: $8 \mu\text{C}$. Estimated saturation magnetic moment after proton irradiation is $m_s = 3.5 \times 10^{-6}$ emu. (b) Measured saturation magnetic moment m_s as a function of total irradiated charge C_t . Dashed line is the function $m_s = 0.22[10^{-6} \text{ emu}/\mu\text{C}^{0.5}]C_t^{0.5}$. After Ref. 32.

magnetism of edge-state spins [32, 33, 123–125]. Proton irradiation creates magnetic carbon sites on graphene and similar materials; carbon atoms in the defects are considered to be hydrogen-terminated. Figure 6.51 shows the magnetization curves of an HOPG sample at room temperature before and after proton irradiation, and the saturation magnetic moment as a function of total irradiated charge [32]. The proton-irradiated sample exhibited ferromagnetic magnetization curves with a small hysteresis having a remnant magnetization of $\sim 20\%$ and a coercive force of ~ 10 mT. The saturation magnetization is roughly proportional to the square root of the total irradiated charge of the proton irradiation. In addition, magnetic force microscopy observations at room temperature showed homogeneously distributed ferromagnetic domains in the irradiated areas. These experimental findings prove that ferromagnetic structure having a Curie temperature higher than room temperature is present at defects created by proton irradiation. Note that a strong ferromagnetic interaction plays an important role in the ferromagnetic structure.

This phenomenon raises a question about the origin of the spins in the ferromagnetic state. Soft x-ray dichroism provides an answer. Figure 6.52 presents the results of scanning transmission x-ray

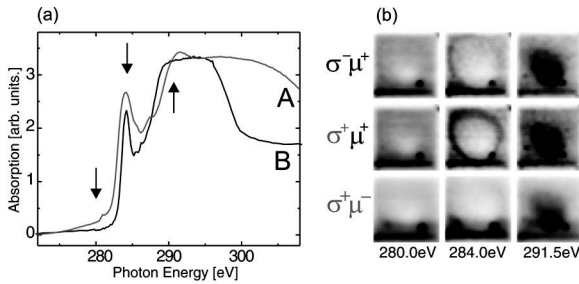


Figure 6.52 (a) Carbon K-edge absorption spectrum of carbon thin films prepared at room temperature (A) and 560°C (B). Arrows indicate photon energies at which the STXM images (b) in the corresponding columns were acquired for a spot proton-irradiated at 50 nC/μm² in film A. The circular polarization ($\sigma = \pm 1$) of the x-rays is reversed between the first and second rows of images. For the third row, the direction (μ) of the applied field ($H = \pm 600$ Oe) is reversed as well, so both the polarization and the applied field are opposite to those in the first row. Images acquired at the π^* resonance (284.0 eV) exhibit a clear x-ray magnetic circular dichroism signal. After Ref. 124.

microscopy (STXM) observations of carbon thin films prepared by pulsed laser deposition onto a Si₃N₄ window at room temperature and 560°C with different helicities of the x-ray and magnetic field directions, together with their carbon K-edge absorption spectrum. The x-ray absorption spectra exhibit a distinct π^* resonance around 284 eV, as we discussed in Section 6.3.2.3. In the thin film sample prepared at room temperature, the resonance is followed by a broad and mostly unstructured σ^* resonance feature around 290 eV, suggesting disordered graphitic structure. In contrast, the film prepared at 560°C shows a well-structured feature around 291.5 eV, indicating the development of graphitic structure. In the STXM images taken at 280.0 eV and 291.5 eV (σ^* resonance) for the disordered carbon thin film shown in Fig. 6.52, the changes in the polarization ($\sigma = \pm 1$) of the x-ray beam and the direction of the applied field ($H = \pm 600$ Oe [$\mu = \pm 1$]) produce no change in the images. This suggests that no magnetic ingredient is present. In contrast, the STXM images at the π^* resonance (284.0 eV), in which the magnetic edge-state is involved, depend on the polarization and the field direction. Indeed, observations with $\sigma^- \mu^+$ and its

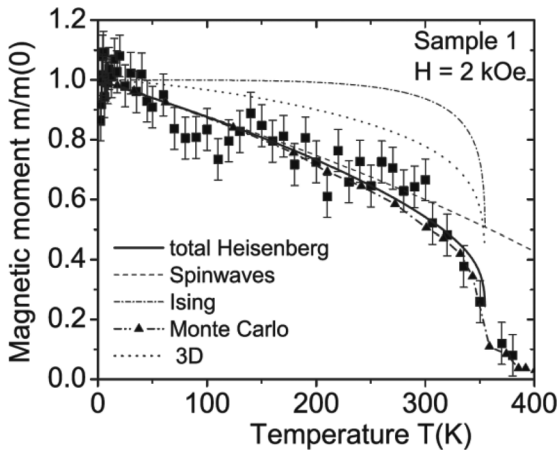


Figure 6.53 Temperature dependence of the normalized magnetic moment at 0.2 T for an HOPG sample after proton irradiation at 110 K. Irradiation energy was 2.25 eV. The fitting parameters of the theoretical curves are $T_c = 360$ K, $T_c^{sw} = 850$ K and $\Delta/J = 10^{-3}$. Solid line is obtained from Eq. (6.16) for the 2D Heisenberg model. Dotted line represents the 3D Bloch $T^{3/2}$ model with spin waves. Dash-dotted line with filled triangles shows the results of a Monte Carlo simulation with anisotropy. After Ref. 125.

geometric inverse $\sigma^+\mu^-$ show the same features, whereas the image with $\sigma^+\mu^+$ shows a dark ring assigned to magnetically ordered structure. This is an important demonstration of the magnetism's origin in the π electron state, which arises from the edge state. The image of the graphitic carbon thin film prepared at 560°C also shows this magnetic feature. A detailed analysis of the STXM image indicates that the spins are aligned in the graphitic plane.

The characteristics of the magnetic ordered state are observed in the temperature dependence of the magnetization, which is shown in Fig. 6.53. The behavior of the temperature-dependent magnetization can be explained well in terms of the 2D anisotropic Heisenberg ferromagnet model given by Eq. (6.13). Here the edge-state spins created by proton irradiation are considered to spread two-dimensionally. The magnetic moment in the Heisenberg system with the correction from the anisotropic exchange interaction is

effectively expressed by

$$M_z(T) \approx M_z^{\text{sw}}(T, J) M_z^1[T, \hat{J}(T)], \quad (6.16)$$

where the first factor on the right-hand side is the magnetization expected from spin waves in the isotropic Heisenberg spin, and the second comes from the anisotropy correction represented by the Ising system. $\hat{J}(T)$ is given by the Curie temperature predicted by spin wave theory T_c^{sw} and the anisotropy in the exchange interaction $\Delta J/J$,

$$\hat{J}(T) = J (1 - 2T/T_c^{\text{sw}}), \quad k_B T_c^{\text{sw}} = 2\pi J/K (1 - \Delta J/J), \quad (6.17)$$

where $K(x)$ is an elliptic function. The observed magnetization is reproduced well by the anisotropic Heisenberg model with an anisotropy of $\Delta J/J \sim 0.001$ and $T_c^{\text{sw}} = 850$ K, as shown in Fig. 6.53. Here the estimated Curie temperature is $T_c = 360$ K. This behavior is also confirmed by Monte Carlo simulation.

6.4.2.2 Edge-state spins in nanographene and nanographite

Here we employ a nanographene-based nanoporous carbon (activated carbon fiber (ACF)) as a model system in discussing the magnetism of edge-state spins. ACFs [35,126,127] consist of a 3D disordered network of nanographite domains, each of which is a stack of 3–4 nanographene sheets with a mean in-plane size of 2–3 nm, in which ~ 300 carbon atoms are involved, as illustrated in Fig. 6.54. The concentration of edge-state spins corresponds to several spins per nanographene sheet and has the magnitude predicted by Clar's aromatic sextet rule. The spins constituting an individual arbitrarily shaped nanographene sheet form a ferrimagnetic structure, as illustrated in Fig. 6.48. In the network of nanographite domains, a weak antiferromagnetic inter-nanographene-sheet interaction (J_2) appears ($J_0 > J_1 \gg J_2$). The magnetism of ACFs is ultimately a consequence of the cooperation of J_0 , J_1 , and J_2 .

Before discussing the magnetism, let us examine the electron transport properties of ACFs. Pristine ACFs exhibit insulating behavior (Anderson insulator [128]), as shown in Fig. 6.54(d) [126]. The conductivity obeys the formula of Coulomb-gap-type variable range hopping in an Anderson insulator,

$$\sigma(T) = \sigma_0 \exp[-(T_0/T)^{1/2}], \quad (6.18)$$

suggesting that the electron transport is governed by electron hopping between conductive nanographene sheets under the influence of a charging process in the disordered network of nanographene sheets [126, 127, 129]. The magnetism of ACFs reflects the electron transport features. Figures 6.54(a), (b), and (c) exhibit the temperature dependence of the electron spin resonance (ESR) intensity, ESR line width ΔH_{pp} , and static magnetic susceptibility χ of the edge-state spins in pristine ACFs [126]. The ESR intensity, which represents the dynamical magnetic susceptibility, obeys the Curie law down to 30 K, and suddenly drops by 50% below 20 K, unlike the static susceptibility, which obeys the Curie law in the entire temperature range. ΔH_{pp} follows a trend corresponding to the behavior of the intensity. It decreases linearly from 6.2 to 2.2 mT as the temperature decreases to 30 K and suddenly increases by 30% (0.6 mT) below 20 K. These experimental findings are therefore understood as representing a transition from the high-temperature homogeneous spin state to the low-temperature inhomogeneous state at ~ 20 K. This is clearly evident in a change in the ESR line profile that appears near the transition temperature ($T_c \sim 20$ K). The line shape deviates from a Lorentzian below 30 K. More importantly, the ESR signal at a strong microwave power of 16 mW shows a prominent hole-burning effect (irregular feature in the ESR signal) just below T_c , indicating a serious inhomogeneity in this temperature range. Above 25 K, the line shape becomes sharpened and purely Lorentzian, indicating exchange/motional narrowing.

The experimental findings presented above allow us to understand the magnetic structure and dynamics of the edge-state spin system. In electron hopping in the 3D random network of metallic nanographene sheets, π electron carriers interact strongly with the edge-state localized spins of a given sheet. At high temperatures, a rapid electron hopping process revealed by the high conductivity (Fig. 6.54(d)) subjects the edge-state spins to motional narrowing, yielding a homogeneous spin system in the entire network. Therefore, the spin system is modeled merely as a metallic system with interaction between localized edge-state spins and conduction π electron carriers. The strong carrier-localized spin interaction is demonstrated by the Korringa relation [130] in the linear temperature dependence of the line width (Fig. 6.54(b)).

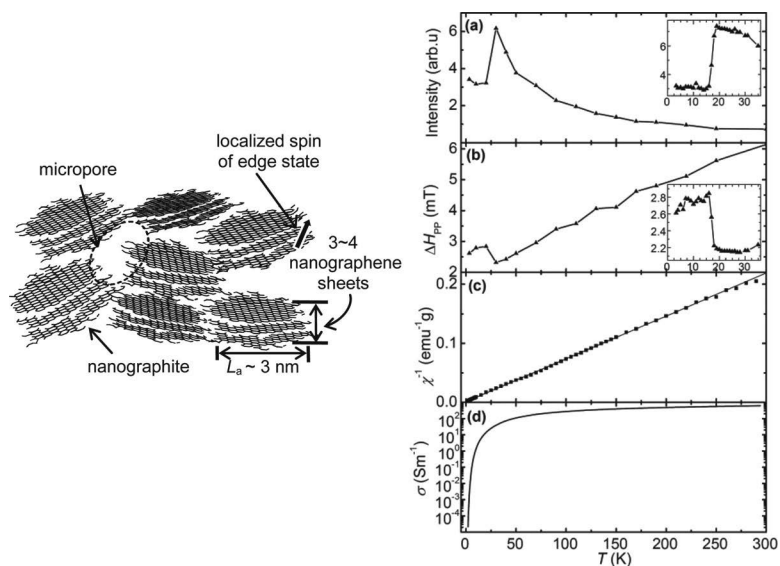


Figure 6.54 (Left) Structural model of activated carbon fiber (ACF) with localized edge-state spins at the zigzag edges. (Right) Temperature dependence of the (a) electronic spin resonance (ESR) intensity, (b) ESR line width (ΔH_{pp}), (c) reciprocal of the static susceptibility (χ), and (d) electrical conductivity (σ) of the pristine ACFs. ESR signals were observed with a microwave power of $1 \mu\text{W}$. Insets in (a) and (b) are close-ups in the low temperature range. After Ref. 126.

The situation becomes different in the low-temperature regime below T_c . The conductivity suggests strong electron localization due to Coulomb interaction at lower temperatures. The appearance of hole-burning near the transition temperature demonstrates the considerable effect of structural inhomogeneity on the edge-state spins. Indeed, an inhomogeneous distribution of on-resonance fields arises from the structural inhomogeneity originating in the hierarchical features of a 3D network with irregularly shaped nanographene sheets as the fundamental unit (Fig. 6.48). In the individual arbitrarily shaped nanographene sheets, a ferrimagnetic structure forms, having a net nonzero magnetic moment and its strength varies depending on its shape, causing an inhomogeneous static distribution of the ESR on-resonance fields. The inhomogeneous distribution of the on-resonance fields does not appear at high

temperatures owing to motional narrowing caused by rapid inter-nanographene-sheet electron hopping. However, as the temperature decreases, electron localization develops, and nanographene sheets become independent of each other because electron hopping becomes slower. Finally, the inhomogeneity survives at lower temperatures below T_c , below which the electron hopping frequency becomes small enough to reveal the inhomogeneous line width. This magnetic behavior unveils the ferrimagnetic structure of an arbitrarily shaped nanographene sheet.

Nanographene sheets in pristine ACFs have oxygen-containing functional groups bonded to their edge carbon atoms. Accordingly, these functional groups work as a barrier in the electron transport. Heat treatment at high temperatures can remove the functional groups bonded to the edge carbon atoms, which enhances the inter-nanographene-sheet interaction and creates coherent electron transfer paths between nanographene sheets in the disordered network of nanographene sheets. The development of coherent electron transfer paths enhances the conductivity, as indicated in Fig. 6.55(a), which shows the temperature dependence of the conductivity for ACF samples heat-treated at temperatures up to 2200°C [129, 131]. The extension of percolation path networks for coherent electron transport to the entire sample eventually causes metallic conductivity through an insulator-to-metal (I-M) transition around a heat-treatment temperature of 1200°C. The change in the conductivity is faithfully tracked by the susceptibility, as shown in Fig. 6.55(b). Namely, the Curie–Weiss behavior characteristic of localized edge-state spins in the Anderson insulator regime is converted to a less temperature dependent susceptibility of conduction electrons in the metallic regime. In the latter, the net negative susceptibility results from a combination of small positive Pauli paramagnetic and large negative orbital contributions. Note that an anomalous feature appears near the I–M transition: The susceptibility has a cusp at ~ 7 K with a negative Weiss temperature (antiferromagnetic) of -2 to -3 K. In addition, as shown in Fig. 6.55(c), the susceptibility of the sample near the I–M transition has a large field cooling effect, particularly around the temperature range in which the cusp emerges. The presence of a cusp and its large field cooling effect are important fingerprints of the development

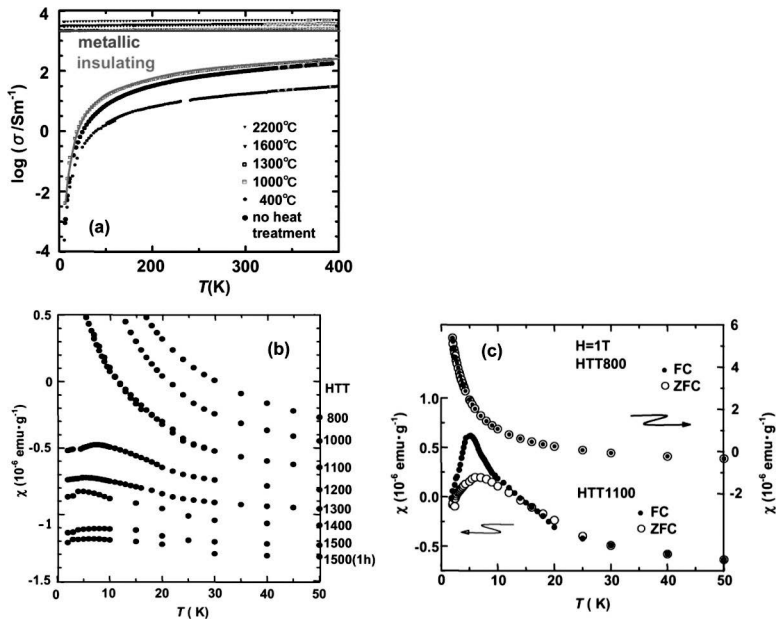


Figure 6.55 (a) Temperature dependence of the electrical conductivity (σ) of pristine ACFs and those heat-treated at temperatures up to 2200°C. After Ref. 129. (b) Temperature dependence of the magnetic susceptibility of ACF samples heat-treated at temperatures up to 1500°C for 15 min and at 1500°C for 1 h. (c) Effect of field cooling on the susceptibility vs. temperature plots for the samples heat-treated at 1100°C and 800°C, which are near and far from the I–M transition, respectively. Open and filled circles represent data from heating runs after zero field cooling and field cooling ($H = 1$ T), respectively. After Ref. 131.

of a spin glass state. Such a state generally develops when the strengths of exchange interactions J vary randomly in space. Here, the strengths of the net magnetic moments in the individual nanographene sheets, whose shapes and sizes vary randomly, are randomly distributed in space. In addition, the inter-nanographene-sheet interaction J_2 , which is enhanced by random strengthening of electron transfer paths through heat treatment, randomly couples the ferrimagnetic moments of nanographene sheets. This causes the anomalous spin glass state in the I–M transition region. Heat treatment well above the I–M transition converts electrons from

localized to itinerant as the localized spins of edge states diminish with the fusion of nanographene sheets upon the elevation of heat-treatment temperature in the metallic phase. However, a considerable number of edge-state spins still survive and form the unconventional magnetism near the I–M transition.

6.4.2.3 Interaction between edge-state spins and conduction π -electron carriers (Kondo effect)

As we discussed in Section 6.4.2.2, the line width of ESR spectra of nanographene, which obeys the Korringa relation [130], indicates that the π conduction carriers interact with the localized spins of the edge state. In addition, the electronic specific heat in disordered carbon that contains nanographene is greatly affected by the magnetic field [132]. This also suggests that electron transport is subject to the interaction between the π conduction carriers and the localized spins. Here we naturally recall the Kondo effect [133] appearing in electron transport in traditional s-d diluted alloys. In the Kondo effect, the s-electron conduction carriers interact with the localized spins of d-electrons, producing an anomalous $\ln T$ temperature dependence in the resistivity and forming a singlet ground state with the localized d-electron at low temperatures. Indeed, the Kondo effect in Dirac electrons was theoretically predicted in graphene having an edge state [134, 135], and it was observed in a graphene sheet with defects created by ion beam irradiation [136].

Field effect transistor (FET) devices (see Chapter 3) consisting of a graphene sheet with magnetic defects created by 500 eV He^+ irradiation at low temperature were used to investigate the Kondo effect as a function of the position of the Fermi level (ε_F). Figure 6.56(a) shows the temperature dependence of the resistivity ρ with variations in the gate voltage V_g that tunes ε_F from above the Dirac point to below it. At temperatures above 200 K, the increase in ρ with temperature is associated with phonon scattering. Between 100 K and 10 K, the resistivity exhibits a temperature dependence of $\ln T$ irrespective of the gate voltage. Below 10 K, ρ saturates. This temperature dependence is typical of the resistivity in a Kondo

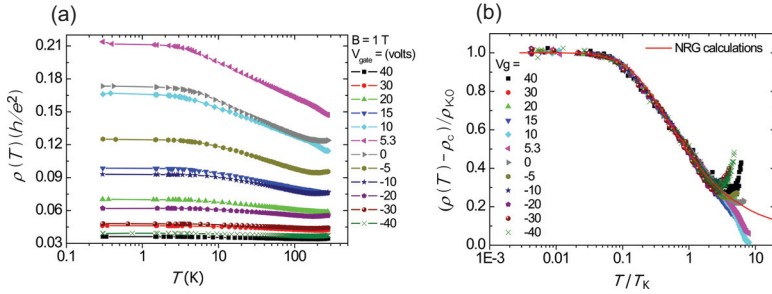


Figure 6.56 (a) Temperature dependence of the resistivity $\rho(T)$ of graphene having magnetic defects under a perpendicular magnetic field of 1 T at different gate voltages V_g between -40 and $+40$ V. (b) Normalized Kondo component of the resistivity $(\rho(T) - \rho_c)/\rho_{K,0}$ as a function of temperature, which is normalized with respect to the Kondo temperature T_K . ρ_c and $\rho_{K,0}$ represent the non-temperature-dependent part of the resistivity from nonmagnetic impurities and Kondo resistivity at $T = 0$ K, respectively. Solid line representing numerical renormalization group calculation is the expected universal Kondo behavior (see text). After Ref. 136.

system, which is expressed by

$$\rho(V_g, T) = \rho_c(V_g) + \frac{\rho_{K,0}(V_g)}{2} \left[1 - 0.470 \ln \left(\frac{1.2T}{T_K(V_g)} \right) \right] \quad (6.19)$$

and

$$\rho(V_g, T) = \rho_c(V_g) + \rho_{K,0}(V_g) \left[1 - \left(\frac{\pi}{2} \right)^4 \left(\frac{T}{T_K(V_g)} \right)^2 \right] \quad (6.20)$$

in the intermediate and lowest-temperature regimes, respectively. Here, $\rho_c(V_g)$, $\rho_{K,0}(V_g)$, and $T_K(V_g)$, which depend on the gate voltage V_g , are the non-temperature-dependent part of the resistivity due to nonmagnetic impurities, the Kondo resistivity at $T = 0$ K, and the Kondo temperature representing the strength of carrier-localized spin interactions, respectively. As shown in Fig. 6.56(b), the temperature dependence of the resistivity in the low-temperature regime $T < T_K$ collapses to a single functional form expressed by Eqs. (6.19) and (6.20) for all the experimental curves with different values of V_g . This is key evidence for Kondo behavior. The Kondo temperature is estimated as $T_K = 30\text{--}90$ K, with a specific

V_g (ε_F) dependence having a minimum at the Dirac point. In the conventional Kondo effect, T_K is given by

$$k_B T_K \approx W_b \exp(-1/J D(\varepsilon_F)) \quad (6.21)$$

where W_b , $D(\varepsilon_F)$, and J are the bandwidth, density of states at ε_F , and antiferromagnetic exchange interaction between the edge-state spin and conduction π -carriers, respectively. The density of states in graphene having zero-gap semiconductor structure is expressed as (see Chapter 2)

$$D(\varepsilon_F) = 8\pi |\varepsilon_F| / (h v_F)^2, \quad (6.22)$$

where v_F is the Fermi velocity. Therefore, Eq. (6.21) predicts that the Kondo temperature increases with increases in the absolute value of V_g ($\propto \varepsilon_F$) on both sides of electron and hole injection, and a minimum of $T_K = 0$ K occurs when ε_F is at the Dirac point. This is inconsistent with the observations, suggesting that the Dirac fermion in graphene does not follow the conventional Kondo effect behavior [134, 135]. The interaction of edge-state spins and conduction π carriers remains an important issue to be clarified in the future.

6.5 Chemical Activity of Nanographene and Graphene Edges

6.5.1 Stability and Chemical Activity of Graphene Edges

As we discussed in Chapter 4.5 and Section 6.3, zigzag edges having nonbonding edge states at the Fermi level are less stable than armchair edges. This is related to the question of the aromatic stability of graphene edges and can be understood in terms of Clar's aromatic sextet rule [16,21,22]. Zigzag and armchair edges can be modified in many ways by termination with various foreign species such as hydrogen and oxygen atoms or structural reconstruction. The stability varies with the type of modification. Figure 6.57 shows the electronic structures and formation energies of the five most stable hydrogen-terminated edges calculated by DFT [21]. The Clar representations and band structures in the figure show that a nanoribbon having edges reconstructed with a combination of five-

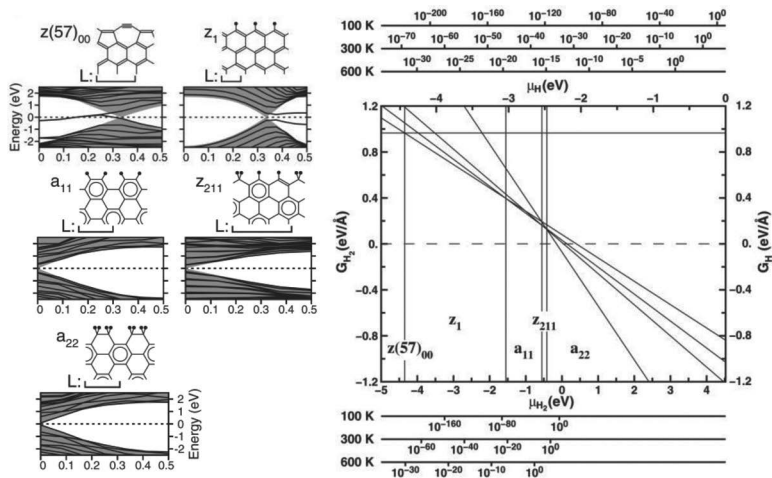


Figure 6.57 (Left) The five most stable hydrogen-terminated edges of graphene nanoribbons (Clar representations) and their band structures. Hydrogen atoms are small filled circles. The structures are periodic along the ribbon edge with periodicity L . Gray area corresponds to the electronic bands allowed in bulk graphene. Dashed line represents the Fermi level; z , a , and $z(57)$ represent a zigzag edge, an armchair edge, and an edge consisting of five and seven-membered rings, respectively. Subscripts 0, 1, and 2 represent edge carbon atoms with no hydrogen termination and mono-, and di-hydrogenated edge carbon atoms, respectively. (Right) Formation energies vs. chemical potential for the five most stable edges. Vertical lines distinguish the stability regions. Alternative bottom (top) axes show the pressure (bar) of molecular H_2 (atomic H) gas corresponding to the chemical potentials at $T = 100, 300,$ and 600 K. After Ref. 21.

and seven-membered rings with no hydrogen termination, $z(57)_{00}$, is nonmagnetic, metallic, and non-aromatic. Conventional zigzag edge z_1 is magnetic, metallic, and non-aromatic. Other edges are nonmagnetic, nonmetallic, and aromatic. Their stabilities vary depending on these electronic features, as indicated by the formation energies. The less aromatic and metallic $z(57)_{00}$ is the most unstable of these five types of edge, and z_1 having conventional edge states is the second most unstable. These two edge structures appear only at very low hydrogen pressures, as shown in Fig. 6.57. Depending on the aromaticity, the stability is in the order of $z(57)_{00} < z_1 < a_{11} < z_{211} < a_{22}$, and a_{22} appears at the highest hydrogen pressure.

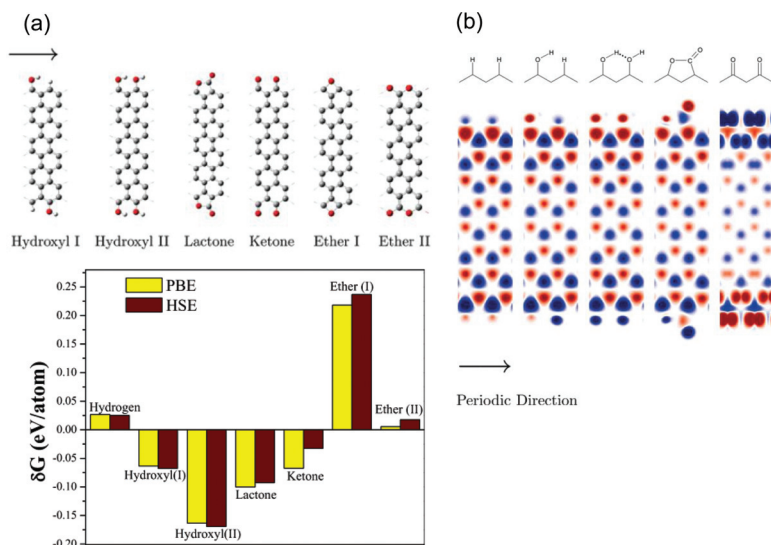


Figure 6.58 (a) Ground state relative stabilities of zigzag edges terminated by different oxygen-containing functional groups, calculated by the PBE and HSE methods. Dark circles and small circles at the edges are oxygen and hydrogen atoms, respectively. Negative values indicate stable structures with respect to the constituents. (b) Map of the ground state electron densities 0.16 Å above the surface of the ribbon for the five most stable zigzag edges. After Ref. 137.

In ambient atmosphere, graphene edges are terminated with oxygen-containing functional groups, since they are easily oxidized. Indeed, graphene edges prepared in ambient atmosphere at room temperature are terminated with functional groups containing more oxygen, such as carboxyl groups or lactone groups [91]. Annealing at high temperature converts the functional groups to those containing less oxygen, such as carbonyl and hydroxyl groups. Above $\sim 1000^\circ\text{C}$, most oxygen-containing groups are removed, and the edges are believed to be terminated mainly with hydrogen. Figure 6.58 shows the stabilities and electron density distributions of zigzag edges terminated with oxygen-containing functional groups and an ordinary monohydrogenated zigzag edge [137]. The edges terminated by hydroxyl, lactone, and ketone groups are stable, whereas those terminated with hydrogen and ether are rather

unstable. The distribution of electron populations around the edges varies considerably depending on how the edges are terminated.

The chemical activity is the inverse of the stability. Here again, nanographene differs from infinitely large graphene or bulk graphite because of the presence of edges and its finite size. In particular, the zigzag edge is active owing to the presence of a nonbonding edge state. An early work reported that the oxidation rate of edge carbon atoms is larger by 10–20% in zigzag edges than in armchair edges [138]. Thus, zigzag edges are more easily oxidized, which is consistent with their energetically unstable structure. In addition to the difference in the geometry of edge shapes, differences in edge carbon atom termination create a variety of chemical activity levels depending on the electronic features of the functional groups bonded to the edge carbon atoms. Therefore, edge-inherent chemical reactivity should be considered when discussing nanographene.

A theoretical approach indicated differences between zigzag and armchair regions of graphene nanoribbons in the dissociation reactions of several functional groups from carbon atoms [139]. The bond dissociation energy of a hydrogen atom from a dihydrogenated carbon site at a zigzag edge is 2.82–2.87 eV, whereas it is estimated to be 1.55 eV at an armchair edge. This suggests that the unstable structure of the zigzag edge is more strongly stabilized by dihydrogenation of the edge carbon atoms. The bond dissociation energy decreases with the ribbon width, suggesting that narrower

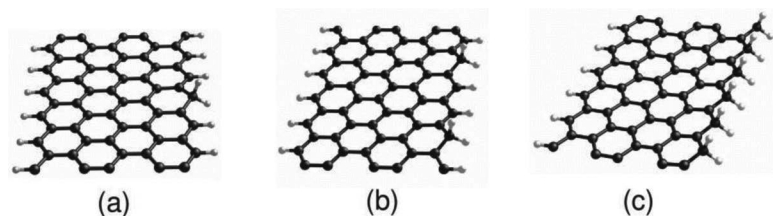


Figure 6.59 Chemical reaction of hydrogen atoms with graphene nanoribbons having a monohydrogenated zigzag edge at edge coverages of (a) 1/6, (b) 1/3, and (c) 1 for a 5 unit cell width. Small light circles at the edges denote hydrogen atom. Coverage is expressed as reacted hydrogen per edge carbon atom. After Ref. 139.

Table 6.2 Comparison of bond dissociation energy (BDE, in eV) of zigzag edge-X bonds with experimental BDE of C_2H_5-X . The coverage is at 1/6 X/edge C (see Fig. 6.59); zero-point-energy corrections not included. [Ref. 139]

Radical: X	H	OH	CH ₃	F	Cl	Br	I
BDE (edge X)	2.86	2.76	2.22	3.71	2.18	1.65	1.18
BDE (C_2H_5-X)	4.358	4.055	3.838	4.904	3.651	3.036	2.420

ribbons are more chemically active. The reactivity also depends on the coverage of the edges.

The dissociation energy decreases as the concentration of dihydrogenated sites increases. Thus, a zigzag edge structure with completely dihydrogenated edge carbon atoms is more stable than one with partially dihydrogenated carbon atoms. This is demonstrated in Fig. 6.59, in which the estimated dissociation energy is 2.86, 2.73, and 1.93 eV for coverages of 1/6, 1/3, and 1, respectively. Table 6.2 compares the bond dissociation energies of several functional groups with those of substituted ethane molecules. The smaller bond dissociation energy in zigzag edged nanoribbon than in C_2H_5-X proves partial radical nature of the edge state.

6.5.2 Interaction of Guest Molecules with Nanographene

Zero-gap semiconducting graphene and semimetallic graphite are amphoteric, both donating charge to guest molecules and accepting it from guest molecules [38]. In contrast, nanographene is semi-amphoteric owing to the presence of an energy gap and edge state, which depend on the edge geometry and chemical structure. The finite size and the presence of functional groups bonded to edge carbon atoms make charge transfer in nanographite (stacked nanographene sheets) different from that in bulk graphite, which forms graphite intercalation compounds (GICs) having a regular arrangement of guest molecules (intercalates) in the graphitic gallery [38]. Indeed, when the in-plane size is smaller than the coherence length of the density correlation function of intercalates in the intercalation process, an intercalation structure with a unique stage is not completed in nanographite owing to structural fluctua-

tions in the intercalate layers. In this case, the charge transfer rate deviates from that of bulk GICs. Actually, alkali-metal intercalation compounds of nanographite have a mixed stage structure consisting of stages 1 and 2 and non-reacted nanographene sheets [140, 141].

Here we discuss the charge transfer reaction with intercalates (or guest molecules) in nanographene. This is particularly important when discussing the electrochemical process. An important example is charge transfer with lithium, which is used in high-performance secondary batteries. The maximum guest/host composition ratio of conventional Li-GIC, $\text{Li}/\text{C} = 6$, is achieved for stage-1 GIC, in which Li atoms are intercalated in the close-packed manner in every graphitic gallery [38]. Interestingly, the ratio can reach $\text{Li}/\text{C} = 2$ for conventional reaction of lithium with nanographene or nanographite. This is considered to be associated with hydrogen-termination of the edge carbon atoms in a nanographene sheet [142–144]. The experimental findings suggest that nanographene can accept the amount of charges three times larger than that in bulk graphite. Therefore, nanographene has a strong advantage for achieving high performance in secondary batteries.

The charge transfer reaction of nanographene with Li proceeds differently from that in bulk graphite because of the presence of edges and its finite size [145–147]. Indeed, the charge transfer process and the arrangement of intercalates depend crucially on whether the edge carbon atoms are terminated with hydrogen atoms [142] or have σ -dangling bonds with no termination. When the edge carbon atoms are bare with dangling bonds, there is no stable site for guest Li atom in the interior of the nanographene sheet after the charge transfer reaction. Instead, a Li atom, which has a positive charge of +0.29, tends to form covalent bonds with edge carbon atoms that have σ -dangling bonds, as shown in Fig. 6.60(a). Interestingly, the charges transferred from the Li atom to the nanographene are distributed in the edge region. In contrast to the bare-edged nanographene sheet with σ -dangling bonds, Li guest atoms in a nanographene sheet in which all of the edge carbon atoms are completely hydrogen terminated are stabilized through charge transfer in the interior of the sheet. In this case, a $\sqrt{3} \times \sqrt{3}$ superlattice in-plane structure of Li atoms can form, similar to bulk stage-1 Li-GIC (LiC_6) [38]. However, the charges in

of partially hydrogenated nanographene lie between those of bare nanographene and completely hydrogenated nanographene sheets. The $\sqrt{3} \times \sqrt{3}$ superstructure is deformed by the finite size effect and the low degree of structural symmetry. What interests us here is the presence of dimerized (Li_2) or trimerized (Li_3) Li species created in partially hydrogenated nanographene sheets. The theoretical works on the electronic structures of Li-doped nanographene sheets cited above provide an important clue for explaining the electronic features of Li ion batteries.

The interactions of acceptors with nanographene also differ from those in bulk acceptor GICs. Iodine is a typical example. In bulk graphite, iodine molecules are not intercalated in the graphitic galleries [38]. In contrast, iodine molecules are intercalated in nanographite with a slight charge transfer ($f_c = 0.0027\text{--}0.0079$), where I_2 molecules and I_3^- ions coexist [129, 148]. Considering that polycyclic aromatic hydrocarbon molecules such as perylene and pyrene form charge transfer complexes with iodine [149], this suggests that nanographene has electronic features intermediate between those of small polycyclic aromatic hydrocarbon molecules and bulk graphite. Bromine, which is chemically more active, differs from iodine in its reaction with nanographene because of the presence of edges [150]. Bromine is bonded to the edge carbon atoms as covalent species in the substitution reaction, in addition to the formation of charge transfer species by bromine molecules. The charge transfer rate, which is estimated as $f_c \sim 0.0004$, is considerably smaller than that of bulk Br-GICs ($f_c \sim 0.002$) [150].

6.6 Summary

When a graphene sheet is cut into fragments, two types of edge are created: zigzag and armchair edges. The electronic structure of the nanographene or graphene edges thus created depends crucially on their geometrical shape. A nonbonding edge state originating in π electrons is created in zigzag edges, whereas electron wave interference occurs in armchair edges. This is a consequence of the singular physical behavior of a massless Dirac fermion in graphene edges. Chemists understand this in terms of the aromaticity in

polycyclic aromatic hydrocarbon molecules. The edge states, which are strongly spin polarized, have localized spins, which play an important role in the magnetism of nanographene, in contrast to diamagnetic infinite graphene sheets. Moreover, the edge states, which have a large LDOS in the edge region, make the edge carbon atoms chemically active. In addition, nanographene has an energy gap due to its finite size. In this chapter, we focused on graphene edges in our discussion of the fabrication of graphene nanostructures, their electronic and magnetic structure, and the chemical activity of nanographene and graphene edges in terms of experimental results.

Graphene nanostructures can be fabricated by several methods: CVD, graphene oxide, unzipping of carbon nanotubes, heat-induced structural changes, electron beam lithography, STM/AFM lithography, chemical reactions with crystallographic selectivity, and a bottom-up method from aromatic molecules.

Experimental investigations using STM/STS, ARPES, XAS, and TEM confirmed the presence of an edge state at zigzag edges at the Dirac point. Armchair edges were found to be energetically stable owing to aromatic stability, whereas the less-aromatic zigzag edges, which have edge states, are unstable, in good agreement with Clar's aromatic rule.

In contrast to the scattering at the zigzag edge, that at the armchair edge is accompanied by electron wave interference. The effect of the interference is observed in specific features in the Raman bands and in the superlattice pattern in STM lattice images near armchair edges.

The edge-state spins behave as Heisenberg spins with small magnetic anisotropy. The magnetic properties of the edge-state spins were discussed in terms of theory and experiments using magnetic defects created by ion irradiation and a 3D network of nanographene sheets. Depending on the edge structure and how the edge is terminated, a variety of magnetic structures is created: ferromagnetic, antiferromagnetic, ferrimagnetic, and spin glass structures.

Graphene edges, in which edge states exist, play an important role in chemical activity. The presence of an energy gap makes nanographene chemically different from graphene and graphite.

Nanographene and graphene edges are an important central issue in physics and chemistry. With the development of nanofabrication techniques, nanographene and graphene edges will be an important ingredient in promising future electronics and spintronics device applications.

References

1. Stein, S. E., and Brown, R. L. (1987). π -electron properties of large condensed polyaromatic hydrocarbons, *J. Am. Chem. Soc.*, **109**, pp. 3721–3729.
2. Tanaka, K., Yamashita, S., Yamabe, H., and Yamabe, T. (1987). Electronic properties of one-dimensional graphite family, *Synth Met.*, **17** (1–3), pp. 143–148.
3. Fujita, M., Wakabayashi, K., Nakada, K., and Kusakabe, K. (1996). Peculiar localized state at zigzag graphite edge, *J. Phys. Soc. Jpn.*, **65**, pp. 1920–1923.
4. Nakada, K., Fujita, M., Dresselhaus, G., and Dresselhaus, M. S. (1996). Edge state in graphene ribbons: nanometer size effect and edge shape dependence, *Phys. Rev. B*, **54**, pp. 17954–17961.
5. Wakabayashi, K., Fujita, M., Ajiki, H., and Sigrist, M. (1999). Electronic and magnetic properties of nanographite ribbons, *Phys. Rev. B*, **59**, pp. 8271–8282.
6. Okada, S., and Oshiyama, J. (2003). Nanometer-scale ferromagnet: carbon nanotubes with finite length, *J. Phys. Soc. Jpn.*, **72**, pp. 1510–1515.
7. Klusek, Z., Waqar, Z., Denisov, E. A., Kompaniets, T. N., Makarenko, I. V., Titkov, A. N., and Bhatti, A. S. (2000). Observations of local electron states on the edges of the circular pits on hydrogen-etched graphite surface by scanning tunneling spectroscopy, *Appl. Surf. Sci.*, **161**, pp. 508–514.
8. Andersson, O. E., Prasad, B. L. V., Sato, H., Enoki, T., Hishiyama, Y., Kaburagi, Y., Yoshikawa, M., and Bandow, S. (1998). Structure and electronic properties of graphite nanoparticles, *Phys. Rev. B*, **58**, pp. 16387–16395.
9. Kobayashi, Y., Fukui, K., Enoki, T., Kusakabe, K., and Kaburagi, Y. (2005). Observation of zigzag and armchair edges of graphite using scanning tunneling microscopy and spectroscopy, *Phys. Rev. B*, **71**, pp. 193406-1–4.

10. Niimi, Y., Matsui, T., Kambara, H., Tagami, K., Tsukada, M., and Fukuyama, H. (2005). Scanning tunneling microscopy and spectroscopy studies of graphite edges, *Appl. Surf. Sci.*, **241**, pp. 43–48.
11. Kobayashi, Y., Fukui, K., Enoki, T., and Kusakabe, K. (2006). Edge state on hydrogen-terminated graphite edges investigated by scanning tunneling microscopy, *Phys. Rev. B*, **73**, pp. 125415-1–8.
12. Niimi, Y., Matsui, T., Kambara, H., Tagami, K., Tsukada, M., and Fukuyama, H. (2006). Scanning tunneling microscopy and spectroscopy of the electronic local density of states of graphite surfaces near monoatomic step edges, *Phys. Rev. B*, **73**, pp. 085421-1–8.
13. Enoki, T., Kobayashi, Y., and Fukui, K. (2007). Electronic structures of graphene edges and nanographene, *Int. Rev. Phys. Chem.*, **26**, pp. 609–645.
14. Novoselov, K. S., Geim, A. K., Morozov, S. V., Jiang, D., Zhang, Y., Dubonos, S. V., Grigorieva, I. V., and Firsov, A. A. (2004). Electric field effect in atomically thin carbon films, *Science*, **306**, pp. 666–669.
15. Longuet-Higgins, H. C. (1950). Some studies in molecular orbital theory, I. resonance structures and molecular orbitals in unsaturated hydrocarbons, *J. Chem. Phys.*, **18**, pp. 265–274.
16. Clar, E. (1972). *The Aromatic Sextet* (Wiley, London).
17. Lieb, E. (1989). Two theorems on the Hubbard model, *Phys. Rev. Lett.*, **62**, pp. 1201–1204.
18. Nakasuji, K., and Kubo, T. (2004). Multi-stage amphoteric redox hydrocarbons based on a phenalenyl radical, *Bull. Chem. Soc. Jpn.*, **77**, pp. 1791–1801.
19. Radovic, L. R., and Bockrath, B. (2005). On the chemical nature of graphene edges: origin of stability and potential for magnetism in carbon materials, *J. Am. Chem. Soc.*, **127**, pp. 5917–5927.
20. Maksic, Z. B., Baric, D., and Muller, T. (2006). Clar's sextet rule is a consequence of the σ -electron framework, *J. Phys. Chem. A*, **110**, pp. 10135–10147.
21. Wassmann, T., Seitsonen, A. P., Saitta, A. M., Lazzeri, M., and Mauri, F. (2008). Structure, stability, edge states, and aromaticity of graphene ribbons, *Phys. Rev. Lett.*, **101**, pp. 096402-1–4.
22. Wassmann, T., Seitsonen, A. P., Marco Saitta, A., Lazzeri, M., and Mauri, F. (2010). Clar's theory, π -electron distribution, and geometry of graphene nanoribbons, *J. Am. Chem. Soc.*, **132**, pp. 3440–3451.
23. Sasaki, K., and Saito, R. (2008). Pseudospin and deformation-induced gauge field in graphene, *Prog. Theor. Phys. Suppl.*, **176**, pp. 253–278.

24. Sasaki, K., Saito, R., Wakabayashi, K., and Enoki, T. (2010). Identifying the orientation of edge of graphene using G band Raman spectra, *J. Phys. Soc. Jpn.*, **79**, pp. 044603-1-8.
25. Sakai, K., Takai, K., Fukui, K., Nakanishi, T., and Enoki, T. (2010). Honeycomb superperiodic pattern and its fine structure near the armchair edge of graphene observed by low-temperature scanning tunneling microscopy, *Phys. Rev. B*, **81**, pp. 235417-1-7.
26. Cançado, L. G., Pimenta, M. A., Neves, B. R. A., Medeiros-Ribeiro, G., Enoki, T., Kobayashi, Y., Takai, K., Fukui, K., Dresselhaus, M. S., Saito, R., and Jorio, A. (2004). Anisotropy of the Raman spectra of nanographite ribbons, *Phys. Rev. Lett.*, **93**, pp. 047403-1-4.
27. Cançado, L. G., Pimenta, M. A., Neves, B. R. A., Dantas, M. S. S., and Jorio, A. (2004). Influence of the atomic structure on the Raman spectra of graphite edges, *Phys. Rev. Lett.*, **93**, pp. 247401-1-4.
28. Yasuda, E., Inagaki, M., Kaneko, K., Endo, M., Oya, A., and Tanabe, Y. (2003). *Carbon Alloys, Novel Concepts to Develop Carbon Science and Technology* (Elsevier, UK).
29. Beguin, F., and Frackowiak, E. (2010). *Carbons for Electrochemical Energy Storage and Conversion Systems* (CRC Press, Taylor & Francis, USA).
30. Ingram, D. J. E., and Bennett, J. E. (1954). Paramagnetic resonance in activated carbon, *Phil. Mag.*, **45**, pp. 545-547.
31. Makarova, T. L., and Palacio, F., eds. (2006). *Carbon Based Magnetism: An Overview of the Magnetism of Metal Free Carbon-Based Compounds and Materials* (Elsevier, The Netherlands).
32. Esquinazi, P., Spemann, D., Höhne, R., Setzer, A., Han, K.-H., and Butz, T. (2003). Induced magnetic ordering by proton irradiation in graphite, *Phys. Rev. Lett.*, **91**, pp. 227201-1-4.
33. Esquinazi, P., Höhne, R., Han, K.-H., Spemann, D., Setzer, A., Diaconu, M., Schmidt, K., and Butz, T. (2006). Induced magnetic order by ion irradiation of carbon-based structures, in Makarova, T. L., and Palacio, F., eds., *Carbon Based Magnetism: An Overview of the Magnetism of Metal Free Carbon-based Compounds and Materials* (Elsevier, The Netherlands) chapter 19, pp. 437-462.
34. Enoki, T., and Takai, K. (2006). Unconventional magnetic properties of nanographite, in Makarova, T. L., and Palacio, F., eds., *Carbon Based Magnetism: An Overview of the Magnetism of Metal Free Carbon-based Compounds and Materials* (Elsevier, The Netherlands) chapter 17, pp. 397-416.

35. Enoki, T., and Takai, K. (2009). The edge state of nanographene and the magnetism of the edge-state spins, *Solid State Commun.*, **149**, pp. 1144–1150.
36. Biró, L. P., and Lambin, P. (2010). Nanopatterning of graphene with crystallographic orientation control, *Carbon*, **48**, pp. 2677–2689.
37. Jia, X., Campos-Delgado, J., Terrones, M., Meunier, V., and Dresselhaus, M. S. (2011). Graphene edges: a review of their fabrication and characterization, *Nanoscale*, **3**, pp. 86–95.
38. Enoki, T., Suzuki, M., and Endo, M. (2003). *Graphite Intercalation Compounds and Applications* (Oxford University Press, New York).
39. Li, X. S., Cai, W. W., An, J. H., Kim, S., Nah, J., Yang, D. X., Piner, R. D., Velamakanni, A., Jung, I., Tutuc, E., Banerjee, S. K., Colombo, L., and Ruoff, R. S. (2009). Large-area synthesis of high-quality and uniform graphene films on copper foils, *Science*, **324**, pp. 1312–1314.
40. Terai, M., Hasegawa, N., Okusawa, M., Otani, S., and Oshima, C. (1998). Electronic states of monolayer micrographite on TiC(111)-faceted and TiC(410) surfaces, *Appl. Surf. Sci.*, **130/132**, pp. 876–882.
41. Rümmele, M. H., Bachmatiuk, A., Scott, A., Börrnert, F., Warner, J. H., Hoffman, V., Lin, J.-H., Cuniberti, G., and Büchner, B. (2010). Direct low-temperature nanographene CVD synthesis over a dielectric insulator, *ACS Nano*, **4**, pp. 4206–4210.
42. Fujii, S., and Enoki, T. (2010). Cutting of oxidized graphene into nanosized pieces, *J. Am. Chem. Soc.*, **132**, pp. 10034–10041.
43. Li, J.-L., Kudin, K. N., McAllister, M. J., Prud'homme, R. K., Aksay, I. A., and Car, R. (2006). Oxygen-driven unzipping of graphitic materials, *Phys. Rev. Lett.*, **96**, pp. 176101-1–4.
44. Li, Z., Zhang, W., Luo, Y., Yang, J., and Hou, J. G. (2009). How graphene is cut upon oxidation, *J. Am. Chem. Soc.*, **131**, pp. 6320–6321.
45. Kosynkin, D. V., Higginbotham, A. L., Sinitskii, A., Lomeda, J. R., Dimiev, A., Price, B. K., and Tour, J. M. (2009). Longitudinal unzipping of carbon nanotubes to form graphene nanoribbons, *Nature*, **458**, pp. 872–876.
46. Jiao, L., Zhang, L., Wang, X., Diankov, G., and Dai, H. (2009). Narrow graphene nanoribbons from carbon nanotubes, *Nature*, **458**, pp. 877–880.
47. Terrones, M. (2009). Nanotubes unzipped, *Nature*, **458**, pp. 845–846.
48. Jiao, L., Zhang, L., Ding, L., Liu, J., and Dai, H. (2010). Aligned graphene nanoribbons and crossbars from unzipped carbon nanotubes, *Nano Res.*, **3**, pp. 387–394.

49. Affoune, A. M., Prasad, B. L. V., Sato, H., Enoki, T., Kaburagi, Y., and Hishiyama, Y. (2001). Experimental evidence of a single nanographene, *Chem. Phys. Lett.*, **348**, pp. 17–20.
50. Li, X., Wang, X., Zhang, L., Lee, S., and Dai, H. (2008). Chemically derived, ultrasmooth graphene nanoribbon semiconductors, *Science*, **319**, pp. 1229–1232.
51. Wang, X., Ouyang, Y., Li, X., Wang, H., Guo, J., and Dai, H. (2008). Room-temperature all-semiconducting sub-10-nm graphene nanoribbon field-effect transistors, *Phys. Rev. Lett.*, **100**, pp. 206803-1–4.
52. Berger, C., Song, Z., Li, T., Li, X., Ogbazghi, A. Y., Feng, R., Dai, Z., Marchenkov, A. N., Conrad, E. H., First, P. N., and de Heer, W. A. (2004). Ultrathin epitaxial graphite: 2D electron gas properties and a route toward graphene-based nanoelectronics, *J. Phys. Chem. B*, **108**, pp. 19912–19916.
53. Sprinkle, M., Ruan, M., Hu, Y., Hankinson, J., Rubio-Roy, M., Zhang, B., Wu, X., Berger, C., and de Heer, W. A. (2010). Scalable templated growth of graphene nanoribbons on SiC, *Nat. Nanotechnol.*, **5**, pp. 727–731.
54. Han, M. Y., Özyilmaz, B., Zhang, Y., and Kim, P. (2007). Energy band-gap engineering of graphene nanoribbons, *Phys. Rev. Lett.*, **98**, pp. 206805-1–4.
55. Chen, Z., Lin, Y.-M., Rooks, M. J., and Avouris, P. (2007). Graphene nanoribbon electronics, *Physica E*, **40**, pp. 228–232.
56. Xu, G., Bai, J., Torres, Jr., C. M., Song, E. B., Tang, J., Zhou, Y., Duan, X., Zhang, Y., and Wang, K. L. (2010). Low-noise submicron channel graphene nanoribbons, *Appl. Phys. Lett.*, **97**, pp. 073107-1–3.
57. Bischoff, D., Güttinger, J., Dröscher, S., Ihn, T., Ensslin, K., and Stampfer, C. (2011). Raman spectroscopy on etched graphene nanoribbons, *J. Appl. Phys.*, **109**, pp. 073710-1–4.
58. Tapasztó, L., Dobrik, G., Lambin, P., and Biró, L. P. (2008). Tailoring the atomic structure of graphene nanoribbons by scanning tunneling microscope lithography, *Nat. Nanotechnol.*, **3**, pp. 397–401.
59. Puddy, R. K., Scard, P. H., Tyndall, D., Connolly, M. R., Smith, C. G., Jones, G. A. C., Lombardo, A., Ferrari, A. C., and Buitelaar, M. R. (2011). Atomic force microscope nanolithography of graphene: cuts, pseudocuts, and tip current measurements, *Appl. Phys. Lett.*, **98**, pp. 133120-1–3.
60. Campos, L. G., Manfrinato, V. R., Sanchez-Yamagishi, J. D., Kong, J., and Jarillo-Herrero, P. (2009). Anisotropic etching and nanoribbon formation in single-layer graphene, *Nano Lett.*, **9**, pp. 2600–2604.

61. Datta, S. S., Strachan, D. R., Khamis, S. M., and Johnson, A. T. C. (2008). Crystallographic etching of few-layer graphene, *Nano Lett.*, **8**, pp. 1912–1915.
62. Schäffel, F., Warner, J. H., Bachmatiuk, A., Rellinghaus, B., Büchner, B., Schultz, L., and Rümeli, M. H. (2009). Shedding light on the crystallographic etching of multi-layer graphene at the atomic scale, *Nano Res.*, **2**, pp. 695–705.
63. Severin, N., Kirstein, S., Sokolov, I. M., and Rabe, J. P. (2009). Rapid trench channeling of graphenes with catalytic silver nanoparticles, *Nano Lett.*, **9**, pp. 457–461.
64. Müllen, K., and Rabe, J. P. (2008). Nanographenes as active components of single-molecule electronics and how a scanning tunneling microscope puts them to work, *Acc. Chem. Res.*, **41**, pp. 511–520.
65. Yang, X., Dou, X., Rouhanipour, A., Zhi, L., Räder, H. J., and Müllen, K. (2008). Two-dimensional graphene nanoribbons, *J. Am. Chem. Soc.*, **130**, pp. 4216–4217.
66. Cai, J., Ruffieux, P., Jaafar, R., Bieri, M., Braun, T., Blankenburg, S., Muoth, M., Seitsonen, A. P., Saleh, M., Feng, X., Müllen, K., and Fasel, R. (2010). Atomically precise bottom-up fabrication of graphene nanoribbons, *Nature*, **466**, pp. 470–473.
67. Hummers, W. S., and Offeman, R. E. (1958). Preparation of graphitic oxide, *J. Am. Chem. Soc.*, **80**, pp. 1339.
68. Affoune, A. M., Prasad, B. L. V., Sato, H., and Enoki, T. (2001). Electrophoretic deposition of nanosized diamond particles, *Langmuir*, **17**, pp. 547–551.
69. Nagayoshi, H. (1975). *Band Theory of Graphite; a New Method for Layer-Type Crystals*, PhD Thesis, University of Tokyo, Tokyo, Japan.
70. Kelly, B. T. (1981). *Physics of Graphite* (Applied Science Publishers, London).
71. Bendikov, M., Duong, H. M., Starkey, K., Houk, K. N., Carter, E. A., and Wudl, F. (2004). Oligoacenes: Theoretical prediction of open-shell singlet diradical ground states, *J. Am. Chem. Soc.*, **126**, pp. 7416–7417.
72. Ritter, K. A., and Lyding, J. W. (2009). The influence of edge structure on the electronic properties of graphene quantum dots and nanoribbons, *Nat. Mater.*, **8**, pp. 235–242.
73. Gass, M. H., Bangert, U., Bleloch, A. L., Wang, P., Nair, R. R., and Geim, A. K. (2008). Free-standing graphene at atomic resolution, *Nat. Nanotechnol.*, **3**, pp. 676–681.

74. Campos-Delgado, J., Rome-Herrera, J. M., Jia, X., Cullen, D. A., Muramatsu, H., Kim, Y. A., Hayashi, T., Ren, Z., Smith, D. J., Okuno, Y., Ohba, T., Kanoh, H., Kaneko, K., Endo, M., Terrones, H., Dresselhaus, M. S., and Terrones, M. (2008). Bulk production of a new form of sp^2 carbon: crystalline graphene nanoribbons, *Nano Lett.*, **8**, pp. 2773–2778.
75. Jia, X., Hofmann, M., Meunier, V., Sumpter, B. G., Campos-Delgado, J., Rome-Herrera, J. M., Son, H., Hsieh, Y.-P., Reina, A., Kong, J., Terrones, M., and Dresselhaus, M. S. (2009). Controlled formation of sharp zigzag and armchair edges in graphitic nanoribbons, *Science*, **323**, pp. 1701–1705.
76. Koskinen, P., Malola, S. and Häkkinen, H. (2009). Evidence for graphene edges beyond zigzag and armchair, *Phys. Rev. B*, **80**, pp. 073401-1–3.
77. Huang, J. Y., Ding, F., Yakobson, B. I., Lu, P., Qi, L., and Li, J. (2009). *In situ* observation of graphene sublimation and multi-layer edge reconstructions, *Proc. Nat. Acad. Sci.*, **106**, pp. 10103–10108.
78. Chuvilin, A., Meyer, J. C., Algara-Siller, G., and Kaiser, U. (2009). From graphene constrictions to single carbon chains, *New J. Phys.*, **11**, 083019-1–10.
79. Jin, C., Lan, H., Peng, L., Suenaga, K., and Iijima, S. (2009). Deriving carbon atomic chains from graphene, *Phys. Rev. Lett.*, **102**, pp. 205501-1–4.
80. Suenaga, K., and Koshino, M. (2010). Atom-by-atom spectroscopy at graphene edge, *Nature*, **468**, pp. 1088–1090.
81. Sugawara, K., Sato, T., Souma, S., Takahashi, T., and Suematsu, H. (2006). Fermi surface and edge-localized states in graphite studied by high-resolution angle-resolved photoemission spectroscopy, *Phys. Rev. B*, **73**, pp. 045124-1–4.
82. Sugawara, K., Sato, T., Souma, S., Takahashi, T., and Suematsu, H. (2006). Anomalous electronic states on graphite studied by angle-resolved photoemission spectroscopy, *Sci. Tech. Adv. Mater.*, **7**, pp. S94–S98.
83. Entani, S., Ikeda, S., Kiguchi, M., Saiki, K., Yoshikawa, G., Nakai, I., Kondoh, H., and Ohta, T. (2006). Growth of nanographite on Pt(111) and its edge state, *Appl. Phys. Lett.*, **88**, pp. 153126-1–3.
84. Pacilé, D., Papagno, M., Rodríguez, A. F., Grioni, M., Papagno, L., Girit, Ç. Ö., Meyer, J. C., Begtrup, G. E., and Zettl, A. (2008). Near-edge X-ray absorption fine-structure investigation of graphene, *Phys. Rev. Lett.*, **101**, pp. 066806-1–4.
85. Joly, V. L. J., Kiguchi, M., Hao, S.-J., Takai, K., Enoki, T., Sumii, R., Amemiya, K., Muramatsu, H., Hayashi, T., Kim, Y. A., Endo, M., Campos-Delgado,

- J., López-Urías, F., Botello-Méndez, A., Terrones, H., Terrones, M., and Dresselhaus, M. S. (2010). Observation of magnetic edge state in graphene nanoribbons, *Phys. Rev. B*, **81**, 245428-1-6.
86. Kiguchi, M., Takai, K., Joly, V. L. J., Enoki, T., Sumii, R., and Amemiya, K. (2011). Observation of magnetic edge state and dangling bond state on nanographene in activated carbon fibers, *Phys. Rev. B*, **84**, pp. 045421-1-6.
87. Hua, W., Gao, B., Li, S., Ågren, H., and Luo, Y. (2010). X-ray absorption spectra of graphene from first-principles simulations, *Phys. Rev. B*, **82**, pp. 155433-1-7.
88. Hou, Z., Wang, X., Ikeda, T., Huang, S.-F., Terakura, K., Boero, M., Oshima, M., Kakimoto, M., and Miyata, S. (2011). Effect of hydrogen termination on carbon K-edge X-ray absorption spectra of nanographene, *J. Phys. Chem. C*, **115**, 5392-5403.
89. Barone, V., Hod, O., and Scuseria, G. E. (2006). Electronic structure and stability of semiconducting graphene nanoribbons, *Nano Lett.*, **6**, pp. 2748-2754.
90. Kudin, K. N. (2008). Zigzag graphene nanoribbons with saturated edges, *ACS Nano*, **2**, pp. 516-522.
91. Sumanasekera, G. U., Chen, G., Takai, K., Joly, V. L. J., Kobayashi, N., Enoki, T., and Eklund, P. C. (2010). Charge transfer and weak chemisorption of oxygen molecules in nanoporous carbon consisting of a disordered network of nanographene sheets, *J. Phys. Condens. Matter*, **22**, pp. 334208-1-8.
92. Castro Neto, A. H., Guinea, F., Peres, N. M. R., Novoselov, K. S., and Geim, A. K. (2009). The electronic properties of graphene, *Rev. Mod. Phys.*, **81**, pp. 109-162.
93. Klein, D. J. (1994). Graphitic polymer strips with edge states, *Chem. Phys. Lett.*, **217**, pp. 261-265.
94. Klein, D. J., and Bytutas, L. (1999). Graphitic edges and unpaired π -electron spins, *J. Phys. Chem. A*, **103**, pp. 5196-5210.
95. Takahashi, T., Tokailin, H., and Sagawa, T. (1985). Angle-resolved ultra-violet photoelectron spectroscopy of the unoccupied band structure of graphite, *Phys. Rev. B*, **32**, pp. 8317-8324.
96. Sprinkle, M., Siegel, D., Hu, Y., Hicks, J., Tejada, A., Taleb-Ibrahimi, A., Le Fèvre, P., Bertran, F., Vizzini, S., Enriquez, H., Chiang, S., Soukiassain, P., Berger, C., de Heer, W. A., Lanzara, A., and Conrad, E. H. (2009). First direct observation of a nearly ideal graphene band structure, *Phys. Rev. Lett.*, **103**, pp. 226803-1-4.

97. Tatar, R. C., and Rabii, S. (1982). Electronic properties of graphite: A unified theoretical study, *Phys. Rev. B*, **25**, pp. 4126–4141.
98. McClure, J. W. (1957). Band structure of graphite and de Haas-van Alphen effect, *Phys. Rev.*, **108**, pp. 612–618.
99. Ezawa, M. (2006). Peculiar width dependence of the electronic properties of carbon nanoribbons, *Phys. Rev. B*, **73**, pp. 045432-1–8.
100. Son, Y.-W., Cohen, M. L., and Louie, S. G. (2006). Energy gaps in graphene nanoribbons, *Phys. Rev. Lett.*, **97**, pp. 216803-1–4.
101. Yang, L., Park, C.-H., Son, Y.-W., Cohen, M. L., and Louie, S. G. (2007). Quasiparticle energies and band gaps in graphene nanoribbons, *Phys. Rev. Lett.*, **99**, pp. 186801-1–4.
102. Berger, C., Song, Z., Li, X., Wu, X., Brown, N., Naud, C., Mayou, D., Li, T., Hass, J., Marchenkov, A. N., Conrad, E. H., First, P. N., and de Heer, W. A. (2006). Electronic confinement and coherence in patterned epitaxial graphene, *Science*, **312**, pp. 1191–1196.
103. Miao, F., Wijeratne, S., Zhang, Y., Coskun, U. C., Bao, W., and Lau, C. N. (2007). Phase-coherent transport in graphene quantum billiards, *Science*, **317**, pp. 1530–1533.
104. You, Y.-M., Ni, Z.-H., Yu, T. and Shen, Z.-X. (2008). Edge chirality determination of graphene by Raman spectroscopy, *Appl. Phys. Lett.*, **93**, pp. 163112-1–3.
105. Casiraghi, C., Hartschuh, A., Qian, H., Piscanec, S., Georgi, C., Fasoli, A., Novoselov, K. S., Basko, D. M., and Ferrari, A. C. (2009). Raman spectroscopy of graphene edges, *Nano Lett.*, **9**, pp. 1433–1441.
106. Krauss, B., Nemes-Incze, P., Skakalova, V., Biro, L.P., von Klitzing, K., and Smert, J. H. (2011). Raman scattering at pure graphene zigzag edges, *Nano Lett.*, **10**, pp. 4544–4548.
107. Sasaki, K., Yamamoto, M., Murakami, S., Saito, R., Dresselhaus, M. S., Takai, K., Mori, T., Enoki, T., and Wakabayashi, K. (2009). Kohn anomalies in graphene nanoribbons, *Phys. Rev. B*, **80**, pp. 155450-1–11.
108. Giunta, P. L., and Kelty, S. P. (2001). Direct observation of graphite layer edge states by scanning tunneling microscopy, *J. Chem. Phys.*, **114**, pp. 1807–1812.
109. Ruffieux, P., Melle-Franco, M., Gröning, O., Biemann, M., Zerbetto, F., and Gröning, P. (2005). Charge-density oscillation on graphite induced by the interference of electron waves, *Phys. Rev. B*, **71**, pp. 153403-1–4.
110. Nakanishi, T., and Ando, T. (2008). Conductance between two scanning-tunneling-microscopy probes in carbon nanotubes, *J. Phys. Soc. Jpn.*, **77**, pp. 024703-1–6.

111. Wakabayashi, K., Sigrist, M., and Fujita, M. (1998). Spin wave mode of edge-localized magnetic states in nanographite zigzag ribbons, *J. Phys. Soc. Jpn.*, **67**, pp. 2089–2093.
112. Fernández-Rossier, J., and Palacios, J. J. (2007). Magnetism in graphene nanoislands, *Phys. Rev. Lett.*, **99**, pp. 177204-1–4.
113. Wang, W. L., Meng, S., and Kaxiras, E. (2008). Graphene nanoflakes with large spin, *Nano Lett.*, **8**, pp. 241–245.
114. Jiang, D.-E., Sumpter, B. G., and Dai, S. (2007). First principle study of magnetism in nanographenes, *J. Chem. Phys.*, **127**, pp. 124703-1–5.
115. Jiang, D.-E., and Dai, S. (2008). Electronic ground state of higher acenes, *J. Phys. Chem. A*, **112**, pp. 332–335.
116. Hod, O., Barone, V., and Scuseria, G. E. (2008). Half-metallic graphene nanodots: A comprehensive first-principles theoretical study, *Phys. Rev. B*, **77**, pp. 035411-1–6.
117. Yazyev, O. V., and Helm, L. (2007). Defect-induced magnetism in graphene, *Phys. Rev. B*, **75**, pp. 125408-1–5.
118. Yazyev, O. V. (2008). Magnetism in disordered graphene and irradiated graphite, *Phys. Rev. Lett.*, **101**, 037203-1–4.
119. Kusakabe, K., and Maruyama, M. (2003). Magnetic nanographite, *Phys. Rev. B* **67**, pp. 092406-1–4.
120. Maruyama, M., and Kusakabe, K. (2004). Theoretical prediction of synthetic methods to create magnetic nanographite, *J. Phys. Soc. Jpn.*, **73**, pp. 656–663.
121. Matsubara, K., Tszukuku, T., and Sugihara, K. (1991). Electron spin resonance in graphite, *Phys. Rev. B*, **44**, pp. 11845–11851.
122. Yazyev, O. V., and Katsnelson, M. I. (2008). Magnetic correlations at graphene edges: basis for novel spintronics devices, *Phys. Rev. Lett.*, **100**, pp. 047209-1–4.
123. Lehtinen, P. O., Foster, A. S., Ma, Y., Krasheninnikov, A. V., and Nieminen, R. M. (2004). Irradiation-induced magnetism in graphite: a density functional study, *Phys. Rev. Lett.*, **93**, pp. 187202-1–4.
124. Ohldag, H., Tyliszczak, T., Höhne, R., Spemann, D., Esquinazi, P., Ungureanu, M., and Butz, T. (2007). π -electron ferromagnetism in metal-free carbon probed by soft-X-ray dichroism, *Phys. Rev. Lett.*, **98**, pp. 187204-1–4.
125. Barzola-Ququia, J., Esquinazi, P., Rothermel, M., Spemann, D., Butz, T., and García, N. (2007). Experimental evidence for two-dimensional magnetic order in proton bombarded graphite, *Phys. Rev. B*, **76**, pp. 161403-1–4.

126. Joly, V. L. J., Takahara, K., Takai, K., Sugihara, K., Enoki, T., Koshino, M., and Tanaka, H. (2010). Effect of electron localization on the edge-state spins in a disordered network of nanographene sheets, *Phys. Rev. B*, **81**, pp. 115408-1-6.
127. Fung, A. W. P., Wang, Z. H., Dresselhaus, M. S., Dresselhaus, G., Pekala, R. W., and Endo, M. (1994). Coulomb-gap magnetotransport in granular and porous carbon structures, *Phys. Rev. B*, **49**, pp. 17325–17335.
128. Shklovskii, B., and Efros, A. (1984). *Electronic Properties of Doped Semiconductors* (Springer-Verlag, Berlin).
129. Shibayama, Y., Sato, H., Enoki, T., Bi, X. X., Dresselhaus, M. S., and Endo, M. (2000). Novel electronic properties of a nano-graphite disordered network and their iodine doping effects, *J. Phys. Soc. Jpn.*, **69**, pp. 754–767.
130. Korringa, J. (1950). Nuclear magnetic relaxation and resonance line shift in metals, *Physica*, **16**, pp. 601–610.
131. Shibayama, Y., Sato, H., Enoki, T., and Endo, M. (2000). Disordered magnetism at the metal-insulator threshold in nano-graphite-based carbon materials, *Phys. Rev. Lett.*, **84**, pp. 1744–1747.
132. Mrozowski, S. (1979). Specific heat anomalies and spin-spin interactions in carbons: a review, *J. Low Temp. Phys.*, **35**, pp. 231–298.
133. Shiba, H., and Kuramoto, Y. (2005). Special Topics: Kondo effect – 40 years after the discovery of Kondo effect, *J. Phys. Soc. Jpn.*, **74**, pp. 1–238.
134. Sengupta, K., and Baskaran, G. (2008). Tuning Kondo physics in graphene with gate voltage, *Phys. Rev. B*, **77**, pp. 045417-1-5.
135. Vojta, M., Fritz, L., and Bulla, R. (2010). Gate-controlled Kondo screening in graphene: quantum criticality and electron-hole asymmetry, *Europhys. Lett.*, **90**, pp. 27006-1-6.
136. Chen, J.-H., Li, L., Cullen, W. G., Williams, E. D., and Fuher, M. S. (2011). Tunable Kondo effect in graphene with defects, *Nat. Phys.*, **7**, pp. 535–538.
137. Hod, O., Barone, V., Peralta, J. E., and Scuseria, G. E. (2007). Enhanced half-metallicity in edge-oxidized zigzag graphene nanoribbons, *Nano Lett.*, **7**, pp. 2295–2299.
138. Thomas, J. M. (1965). Microscopic studies of graphite oxidation, in Walker, P. L., ed., *Chemistry and Physics of Carbon, Vol. 1* (Marcel Dekker, New York) pp.122–204.
139. Jiang, D.-E., Sumpter, B. G., and Dai, S. (2007). Unique chemical reactivity of a graphene nanoribbon's zigzag edge, *J. Chem. Phys.*, **126**, pp. 134701-1-6.

140. Prasad, B. L. V., Sato, H., Enoki, T., Hishiyama, Y., Kaburagi, Y., Rao, A. M., Sumanasekera, G. U., and Eklund, P. C. (2001). Intercalated nanographite: structure and electronic properties, *Phys. Rev. B*, **64**, pp. 235407-1-10.
141. Takai, K., Eto, S., Inaguma, M., Enoki, T., Ogata, H., Tokita, M., and Watanabe, J. (2007). Magnetic potassium clusters in a nanographite host system, *Phys. Rev. Lett.*, **98**, pp. 017203-1-4.
142. Dahn, J. R., Zheng, T., Liu, Y., and Xue, J. S. (1995). Mechanisms for lithium insertion in carbonaceous materials, *Science*, **270**, pp. 590-593.
143. Sato, K., Noguchi, M., Demachi, A., Oki, N., and Endo, M. (1994). A mechanism of lithium storage in disordered carbons, *Science*, **264**, pp. 556-558.
144. Yata, S., Hato, Y., Kinoshita, H., Ando, N., Anekawa, A., Hashimoto, T., Yamaguchi, M., Tanaka, K., and Yamabe, T. (1995). Characteristics of deeply Li-doped polyacenic semiconductor material and fabrication of a Li secondary battery, *Synth. Met.*, **73**, pp. 273-277.
145. Zhou, P., Papanek, P., Bindra, C., Lee, R., and Fischer, J. E. (1997). High capacity carbon anode materials: structure, hydrogen effect, and stability, *J. Power Sources*, **68**, pp. 296-300.
146. Nakadaira, M., Saito, R., Kimura, T., Dresselhaus, G., and Dresselhaus, M. S. (1997). Excess Li ions in a small graphite cluster, *J. Mater. Res.*, **12**, pp. 1367-1375.
147. Yagi, M., Saito, R., Kimura, T., Dresselhaus, G., and Dresselhaus, M. S. (1999). Electronic states in heavily Li-doped graphite nanoclusters, *J. Mater. Res.*, **14**, pp. 3799-3804.
148. Shibayama, Y., Sato, H., Enoki, T., Seto, M., Kobayashi, Y., Maeda, Y., and Endo, M. (2000). ^{129}I Mössbauer effect of iodine adsorbed in activated carbon fibers, *Mol. Cryst. Liq. Cryst. Sci.* **340**, pp. 301-306.
149. Akamatsu, H., Inokuchi, H., and Matsunaga, Y. (1954). Electrical conductivity of the perylene-bromine complex, *Nature*, **173**, p.168-169.
150. Takai, K., Kumagai, H., Sato, H., and Enoki, T. (2006). Bromine-adsorption-induced change in the electronic and magnetic properties of nanographite network systems, *Phys. Rev. B*, **73**, pp. 035435-1-13.

This page intentionally left blank

“This book comprehensively covers graphene, addressing a broad range of physics- and chemistry-related aspects. This in itself is remarkable because so far books on graphene have been restricted to the physical aspects. The text plays a dual role: as a rich source of knowledge for graphene chemistry and as an introduction to graphene physics with an emphasis on reliable structure–property relations. Both the newcomer and the expert will find it extremely valuable.”

Dr. Klaus Müllen

Max Planck Institute for Polymer Research, Germany

Graphene has been attracting growing attention in physics, chemistry, and device applications after the discovery of micromechanically cleaved graphene sheet. The electronic structure of graphene, which is described in terms of massless Dirac fermion, brings about unconventional electronic properties, which are not only an important basic issue in condensed matter physics but also a promising target of cutting-edge electronics/spintronics device applications. Meanwhile, from the chemistry aspect, graphene is the extrapolated extreme of condensed polycyclic hydrocarbon molecules to infinite size. Here, the concept on aromaticity, which organic chemists utilize, is applicable. Interesting issues appearing between physics and chemistry are pronounced in nano-sized graphene (nanographene), as we recognize the importance of the shape of nanographene in understanding its electronic structure. This book comprehensively discusses the fundamental issues related to the electronic, magnetic, and chemical properties of condensed polycyclic hydrocarbon molecules, nanographene, and graphene.



Toshiaki Enoki graduated from Kyoto University in 1969 and received a Doctor of Science in 1975. Then, he became a research associate in the Institute for Molecular Science, Japan. He was appointed associate professor in the Tokyo Institute of Technology in 1987 and became a professor in 1991. He is currently a professor emeritus in the institute. Prof. Enoki's main research subject is the electronic and magnetic properties of π -electron systems, particularly nanocarbon materials.



Tsuneya Ando graduated in 1968 and received a Doctor of Science in 1973 from the University of Tokyo. Then, he became a research associate at the university. In 1979, he joined the University of Tsukuba, Japan, as an associate professor and later returned to the University of Tokyo and became a professor. In 2002, Prof. Ando moved to the Tokyo Institute of Technology, where, since his retirement in March 2011, he is institute professor. His main research subject is the theoretical study of electronic and transport properties of low-dimensional systems.